

IDO 11,104

MITNE - 21

# 6

THE IRRADIATION OF SANTOWAX OMP  
IN THE  
M.I.T. IN-PILE LOOP

Part I

Summary to October 5, 1961

Department of Nuclear Engineering  
Massachusetts Institute of Technology  
Cambridge 39, Massachusetts

IDO 11, 104  
MITNE - 21

THE IRRADIATION OF SANTOWAX OMP  
IN THE M. I. T. IN-PILE LOOP  
PART I. SUMMARY TO OCTOBER 5, 1961

by

D. T. MORGAN  
E. A. MASON

DEPARTMENT OF NUCLEAR ENGINEERING  
MASSACHUSETTS INSTITUTE OF TECHNOLOGY  
CAMBRIDGE, MASSACHUSETTS

M. I. T. DSR PROJECT NO. 8710

Work Performed under Contract No. AT(10-1)-1067  
with the  
Idaho Operations Office  
U. S. Atomic Energy Commission

Issued: May, 1962

## PREFACE

This report is divided into two parts, IDO-11, 104 which is the summary and IDO-11, 105 which presents the details of the equipment, procedures, and results (up to October 5, 1961) of the initial irradiation of Santowax OMP in the M. I. T. In-Pile Organic Loop. The complete results obtained in the initial irradiation of Santowax OMP, which is still under way in May, 1962, will be presented in subsequent IDO reports.

The work presented in this report is the cumulative effort of many people without which the program would have been impossible. Thanks are due to Dr. T. J. Thompson, E. J. Barnett, D. D. Lanning, and the entire reactor operation staff for their valuable assistance in incorporation of the loop into the reactor experimental programs.

To the loop operating staff, great credit is due for the diligent and careful work performed in obtaining the data presented in this report. Acknowledgment is made to W. N. Bley for supervision of the in-pile loop operation as well as aid in all phases of the program; to J. P. Casey who with the assistance of E. J. Fahimian and A. L. Seaver performed the physical and chemical measurements; to T. W. Carroll, G. L. Woodruff, and A. J. Pierni for their able assistance in operation of the loop; to A. Turricchia, P. Fischer, and E. Sefchovich as well as many others for the dosimetry and neutron flux measurements; and to T. J. Swierzawski, D. R. Edwards, and R. C. Sawyer for their aid in obtaining and correlating the heat transfer data.

## ABSTRACT

### THE IRRADIATION OF SANTOWAX OMP IN THE M. I. T. IN-PILE LOOP

An operational in-pile loop in the M. I. T. nuclear reactor is now available for testing organic materials suitable for use as moderator-coolants in nuclear reactors. A detailed description of the loop is presented. The first in-pile irradiation using Santowax OMP as the test material was started on August 9, 1961. The physical and chemical properties of the irradiated Santowax OMP are presented, covering the irradiation period up to October 5, 1961. During this period, the concentration of radiolytic degradation products in the coolant increased from ~0 to 39 wt %. Forced convection heat transfer measurements were made throughout the irradiation period and correlations of the data are presented. The use of Wilson's method for the study of fouling is also discussed and illustrated, using the heat transfer data.

Extensive calorimetric measurements of the dose rate in the position occupied by the in-pile section of the loop have been made, using a special adiabatic calorimeter developed for this purpose. Based on these results, the fast neutron and the gamma dose rates in any organic material of known composition can be estimated. Measurements of the thermal, epithermal, and fast neutron fluxes have also been made, both before and after installation of the in-pile section of the loop in the reactor, using neutron-absorbing foils.

Based on these dose rate measurements and the measured concentrations of each terphenyl isomer in the coolant (ortho-, meta-, and para-) in this experiment, the decomposition yields have been found to be:

$$G^* (-i) = \frac{G(-i)}{C} = 0.28 \pm 0.03 \frac{\text{molecules of component } i}{\text{wt fraction of component } i} \frac{\text{degraded/100 ev absorbed}}{\text{ev absorbed}}$$

for each of the terphenyl isomers.  $G^* (-i)$  is not significantly affected by the concentration of degradation products. This, as well as the other results of this investigation, to date, have generally been similar to those reported previously for Santowax R at the same temperature and thus generally support the reactor design studies that have been reported to date.

## TABLE OF CONTENTS

	<u>PAGE NO.</u>	
<u>CHAPTER I</u>		
<u>SUMMARY</u>		
THE IRRADIATION OF SANTOWAX OMP IN THE M.I.T. IN-PILE LOOP		
1.1	Introduction	1.1
1.1.1	Characteristics of Organic Cooled Nuclear Reactors	1.1
1.1.2	Behavior of Terphenyls When Irradiated	1.4
1.1.3	Characteristics of the M.I.T. In-Pile Loop Study	1.6
1.2	Description of the In-Pile Loop Facility at M.I.T.	1.7
1.2.1	Introduction	1.7
1.2.2	In-Pile Section	1.13
1.2.3	Out-of-Pile Section or Hydraulic Console	1.16
1.2.4	Instrumentation	1.16
1.2.5	Location of Equipment on Reactor	1.21
1.3	Measurement of Dose Rate in Organic Materials in Fuel Position No. 1 of the MITR	1.21
1.3.1	Introduction	1.21
1.3.2	Method of Calorimeter Measurements	1.26
1.3.3	Method of Estimating Fast Neutron and Gamma Dose Rate in Santowax OMP	1.31
1.3.4	Results of Calorimetric Dose Rate Measurements	1.38
1.3.5	Dose Rate in Santowax OMP in In-Pile Section	1.46
1.3.6	Thermal, Epithermal, and Fast Neutron Measurements	1.50

TABLE OF CONTENTS (CONTINUED)

	<u>PAGE NO.</u>
<u>CHAPTER I (CONTINUED)</u>	
1.4 Physical and Chemical Measurements on Irradiated Santomax OMP	1.63
1.4.1 Introduction	1.63
1.4.2 Coolant Composition and Decomposition Yield	1.66
1.4.2.1 Coolant Composition During Irradiation Period	1.66
1.4.2.2 Coolant Degradation Rate and Decomposition Yield	1.70
(A) Introduction	1.70
(B) Method of Calculating Degradation Rates and Decomposition Yields	1.70
(C) Calculated Decomposition Yields	1.71
1.4.2.3 Estimation of Relative Decomposition Yields of Fast Neutron Interactions and Gamma Interactions	1.78
1.4.2.4 Comparison With Previous Results	1.79
1.4.2.5 Coolant Cost for Hypothetical Reactor Based on Results Presented in this Report	1.80
1.4.3 Composition of Degradation Gases and Gas Evolution Rate	1.81
1.4.3.1 Introduction	1.81
1.4.3.2 Undissolved and Dissolved Gas Composition	1.84
1.4.3.3 Gas Evolution Rate	1.89
1.4.3.4 Comparison with Previous Results of In-Pile Irradiation of the Terphenyls	1.94
1.4.4 Density and Viscosity	1.95
1.4.4.1 Viscosity	1.95
1.4.4.2 Density	1.98

TABLE OF CONTENTS (CONTINUED)

	<u>PAGE</u> <u>NO.</u>
<u>CHAPTER I (CONTINUED)</u>	
1.4.5 Other Chemical and Physical Measurements	1.102
1.4.5.1 Carbon-Hydrogen Content	1.102
1.4.5.2 Average Molecular Weight	1.102
1.4.5.3 Melting Point	1.106
1.4.5.4 Inorganic Impurities in Coolant and Coolant Activation	1.106
1.4.5.5 Other Measurements	1.106
1.5 Heat Transfer Measurements	1.109
1.5.1 Introduction	1.109
1.5.2 Method of Determination of the Heat Transfer Coefficient	1.109
1.5.3 Use of Wilson's Method for Determination of Fouling and Check of Data	1.110
1.5.4 Correlation of Heat Transfer Data	1.114
1.6 Conclusions	1.116
Appendix 1.1 References for Chapter 1	A1.1
Appendix 1.2 Nomenclature for Chapter 1	A1.4

CHAPTER 2

INTRODUCTION

2.1 Characteristics of Organic Cooled Nuclear Reactors	2.1
2.2 Previous Work and Problem Areas in the Applica- tion of Organic Coolants	2.7
2.3 Characteristics of M.I.T. In-Pile Loop Study	2.13

TABLE OF CONTENTS (CONTINUED)

<u>CHAPTER 3</u>		PAGE NO.
DESCRIPTION OF THE ORGANIC MODERATOR-COOLANT IN-PILE LOOP		
3.1	General Characteristics of the M.I.T. Nuclear Reactor and the In-Pile Loop	3.1
3.2	Details of In-Pile Section	3.9
3.2.1	Introduction	3.9
3.2.2	Assembly of Thimble and Organic Holdup Capsule	3.10
3.2.3	Organic Holdup Capsule	3.10
3.2.4	Monitor Tube	3.14
3.2.5	Leak Detector	3.15
3.2.6	Reactivity of In-Pile Section	3.15
3.3	Details of Out-of-Pile Section or Hydraulic Console	3.16
3.3.1	Introduction	3.16
3.3.2	Surge Tank	3.16
3.3.3	Filters	3.18
3.3.4	Pumps	3.20
3.3.5	Flowmeters	3.20
3.3.6	Test Heaters	3.21
3.3.7	Main Loop Coolers	3.21
3.3.8	Samplers	3.25
3.3.9	Feed and Dump Tank	3.28
3.3.10	Safety Expansion Tank	3.28
3.3.11	Pressurizing System	3.30
3.3.12	Valves	3.32
3.3.13	Pressure Gages and Vapor Traps	3.32
3.3.14	Trace Heaters	3.34
3.3.15	Loop Layout	3.35
3.4	Instrumentation and Safety Controls and Signals	3.37
3.4.1	Introduction	3.37
3.4.2	Twelve Point Potentiometric Temperature Recorder	3.37
3.4.3	Temperature Indicators with Hi-Lo Limit Switches for Alarm Purposes	3.41
3.4.4	Temperature Indicator for Reactor Control Room	3.42



TABLE OF CONTENTS (CONTINUED)

PAGE  
NO.

CHAPTER 3 (CONTINUED)

3.4.5	Flowmeters	3.42
3.4.6	Precision Potentiometer	3.42
3.4.7	Power Measurement	3.43
3.4.8	Alarm System	3.43
3.4.9	Fire Control Systems	3.44
3.4.10	Safety Features of Wiring Layout	3.44
3.5	Volume of Loop	3.45
3.5.1	Introduction	3.45
3.5.2	Out-of-Pile Section	3.46
3.5.3	In-Pile Section	3.46
3.5.4	Total Loop Volume for One Flow Path	3.49

CHAPTER 4

DOSIMETRY METHODS AND RESULTS

4.1	Introduction	4.1
4.2	Technique of Dose Rate Estimation in Santowax OMP by Calorimetric Measurements	4.2
4.2.1	Introduction	4.2
4.2.2	General Description of Apparatus and Experimental Procedure	4.4
4.2.3	Details of Construction of Calorimeters	4.13
4.2.4	Method of Estimating Fast Neutron and Gamma Dose Rate in Santowax OMP	4.21
4.3	Technique of Thermal and Fast Neutron Flux Measurements	4.29
4.3.1	Introduction	4.29
4.3.2	Detectors Used for Flux Measurements	4.30
4.3.3	Thermal Flux	4.30
4.3.4	Epithermal Fast Flux (Above Thermal to ~ 1 Mev)	4.33

TABLE OF CONTENTS (CONTINUED)

	<u>PAGE</u> <u>NO.</u>
<u>CHAPTER 4 (CONTINUED)</u>	
4.3.5 Fast Neutron Flux (Above 1 Mev)	4.35
4.3.6 Calculation of Fast Neutron Dose Rate in Organic Material from Neutron Flux Spectrum	4.36
4.4 Experimental Results of Calorimeter and Thermal and Fast Neutron Flux Measurements	4.37
4.4.1 Introduction	4.37
4.4.2 Thermal and Fast Neutron Flux Measurements	4.39
4.4.2.1 Accuracy of Absolute Thermal and Fast Neutron Flux Measurements	4.40
4.4.2.2 Preliminary Measurements	4.42
4.4.2.3 Change of Thermal Flux and Epithermal Fast Flux when the Aluminum Thimble was Replaced by the Stainless Steel Thimble	4.46
4.4.2.4 Change of Thermal Flux, Epithermal Fast Flux, and Fast Flux when the Stainless Steel Thimble was Replaced by the In-Pile Section	4.48
4.4.2.5 Estimate of Fast Neutron Dose Rate in Santomax OMP and Values of $I_C/I_H$ and $I_{Al}/I_H$ from Neutron Flux Measurements.	4.61
4.4.3 Experimental Results of Calorimeter Measurements and Estimation of $R_{Al}^Y$ and $I_H$	4.66
4.4.3.1 Introduction	4.66
4.4.3.2 Accuracy of Calorimeter Measurement of Energy Generation Rate in Samples	4.67
(1) Errors in the Heat Capacity of the Samples	4.67

TABLE OF CONTENTS (CONTINUED)

	<u>PAGE</u> <u>NO</u>
<u>CHAPTER 4 (CONTINUED)</u>	
(2) Adiabatic Rate of Temperature Rise	4.69
(3) Net Loss of Energetic Compton Electrons from Samples	4.75
(4) Summary	4.76
4.4.3.3 Summary and Discussion of Results of Calorimetric Measurement of Energy Generation Rates	4.76
(1) Summary of Measurements Performed	4.76
(2) Results Obtained	4.79
(3) Discussion of Results	4.86
Reproducibility	4.86
Linearity of Measurements at Different Reactor Powers	4.89
Differences Among Results Obtained from Different Calorimeter Series	4.92
4.4.3.4 Values of $R_{Al}^Y$ and $I_H$ Calculated from the Calorimeter Data	4.94
(1) Method of Estimating Error in $R_{Al}^Y$ and $I_H$	4.95
(2) Calculated Values of $R_{Al}^Y$ and $I_H$ for Maximum Dose Rate	4.96
(3) Calculated Values of $R_{Al}^Y$ and $I_H$ Over Length of Core	4.106
4.5 Evaluation of Dose Rate in Circulating Santowax OMP in In-Pile Section	4.110

TABLE OF CONTENTS (CONTINUED)

PAGE  
NO.

CHAPTER 5

PHYSICAL AND CHEMICAL MEASUREMENTS ON IRRADIATED  
SANTOWAX OMP

5.1	Introduction	5.1
5.2	Coolant Composition and Decomposition Yield	5.5
5.2.1	Coolant Composition During Irradiation Period	5.5
5.2.2	Coolant Degradation Rate and Decomposition Yields	5.13
5.2.2.1	Introduction	5.13
5.2.2.2	Method of Calculation of Degradation Rate	5.16
5.2.2.3	Circulating Mass of Organic in Loop	5.21
5.2.2.4	Calculated Decomposition Yields and Comparison with Previous Work	5.24
	(A) Results and Discussion	5.24
	(B) Estimation of Relative Decomposition Yields of Fast Neutron Interactions and Gamma Interactions	5.33
	(C) Comparison with Previous Results of In-Pile Irradiation	5.37
5.2.2.5	Coolant Cost for Hypothetical Reactor Based on Results Presented in This Report	5.46
5.2.3	Future Plans for Coolant Composition Measurements on Irradiated Santowax OMP	5.47
5.3	Composition of Degradation Gases and Gas Evolution Rate	5.50
5.3.1	Introduction	5.50
5.3.2	Undissolved and Dissolved Gas Composition	5.51

TABLE OF CONTENTS (CONTINUED)

PAGE  
NO.

CHAPTER 5 (CONTINUED)

5.3.3	Gas Evolution Rate and Radiolytic Yield	5.57
5.3.3.1	Gas Balance on Loop	5.58
5.3.3.2	Gas Evolution Rate and Radiolytic Yield	5.61
5.3.3.3	Estimation of Relative Fast Neutron and Gamma Gas Yields	5.67
5.3.3.4	Comparison With Previous Results of In-Pile Irradiation of the Terphenyls	5.67
5.3.3.5	Preliminary Interpretation of Liquid Decomposition and Gas Evolution Yields	5.69
5.4	Density and Viscosity of Irradiated Santowax OMP	5.71
5.4.1	Viscosity Measurement	5.71
5.4.2	Density Measurement	5.78
5.5	Other Chemical and Physical Measurements	5.84
5.5.1	Carbon-Hydrogen Content	5.84
5.5.2	Average Molecular Weight	5.86
5.5.3	Melting Point	5.89
5.5.4	Inorganic Impurities in Coolant and Coolant Activation	5.89
5.5.5	Infrared and Ultraviolet Absorption Spectra	5.93
5.5.6	Thermal Conductivity and Heat Capacity	5.93

CHAPTER 6

HEAT TRANSFER MEASUREMENTS

6.1	Introduction	6.1
6.2	Method of Determination of the Heat Transfer Coefficient	6.2
6.2.1	Introduction	6.2

TABLE OF CONTENTS (CONTINUED)

	PAGE NO.
<u>CHAPTER 6 (CONTINUED)</u>	
6.2.2 Equipment and Apparatus	6.3
6.2.2.1 Text Heater	6.3
6.2.2.2 Bulk Organic Temperature Measurement	
6.2.2.3 Power Supply and Electrical Measurement Systems for Heat Transfer Measurements	6.4
6.2.2.4 Flowmeter and Calibration	6.6
6.2.3 Determination of Difference of Inside Wall ( $T_{wi}$ ) and Bulk Organic ( $T_{OR}$ ) Temperatures	6.8
6.2.3.1 Inside Temperature of Test Heater Wall, $T_{wi}$	6.8
6.2.3.2 Bulk Temperature and Evaluation of $T_{wi}-T_{OR}$	6.10
6.2.4 Determination of Heat Transfer Rate and Heat Balance	6.11
6.2.5 Estimated Accuracy of Each Individual Heat Transfer Coefficient	6.13
6.3 Use of Wilson's Method for Determination of Fouling and Check of Data	6.14
6.4 Correlation of Heat Transfer Data	6.21
6.4.1 Introduction	6.21
6.4.2 Summary of Correlation of Heat Transfer Data Up to November 10, 1961	6.23

TABLE OF CONTENTS (CONTINUED)

PAGE  
NO.

APPENDIX 3 FOR CHAPTER 3

DESCRIPTION OF THE ORGANIC MODERATOR-COOLANT  
IN-PILE LOOP

APPENDIX

3.1	Miscellaneous Components of the In-Pile Section and Components Necessary for Accommodation of the In-Pile Section in the MITR	A3.1
A3.1.1	Thimble for In-Pile Section	A3.1
A3.1.2	Organic Holdup Capsule Thermocouples, Trace Heaters, and Construction Photographs	A3.4
A3.1.3	Inlet-Outlet Lines for Flow of Organic To and From Holdup Capsule	A3.5
A3.1.4	Shielding	A3.8
A3.1.5	Lower Shield Plug and Upper and Lower Fuel Adapters	A3.8
A3.1.6	Upper Shield Plug	A3.15
A3.1.7	Replacement Shield Plug for In-Pile Section	A3.17
A3.1.8	Gas Supply Tube and Lead Tubes	A3.17
A3.1.9	Connections Between In-Pile Section and Hydraulic Console	A3.22
A3.1.10	Complete Assembly of In-Pile Section and Miscellaneous Parts	A3.22
3.2	Bases of Specifications for the Organic In-Pile Loop at M.I.T.	A3.22
3.3	Modifications to the Fuel Element and In-Pile Section Design to Permit a Larger In-Pile Organic Volume	A3.31
A3.3.1	Circular Plate Fuel Element	A3.31
A3.3.2	Modifications to Present Fuel Element Design	A3.33
3.4	Additional Details of Out-of-Pile Equipment	A3.36
A3.4.1	Surge Tank Liquid Level Gage	A3.36
A3.4.2	Operating History of the Chempumps	A3.36
A3.4.3	Pump Cooling System	A3.36
A3.4.4	Feed and Dump Tank Liquid Level Gage	A3.38
A3.4.5	Difficulties With Valves	A3.38
A3.4.6	Connections	A3.42

TABLE OF CONTENTS (CONTINUED)

	<u>PAGE</u> <u>NO.</u>
<u>APPENDIX 3 FOR CHAPTER 3</u> <u>(CONTINUED)</u>	
<u>APPENDIX</u>	
A3.4.7 Trace Heater Layout	A3.43
A3.4.8 Photographs of Hydraulic Console and Details of Piping Assembly	A3.43
A3.4.9 Hydraulic Console Cabinet	A3.43
A3.4.10 Pressure Drop and Velocities	A3.43
3.5 Miscellaneous Details of Instrumentation and Safety Systems	A3.53
A3.5.1 Thermocouple Schematic	A3.53
A3.5.2 Control Instrumentation for Trace Heat System for Weekend Operation	A3.54
A3.5.3 Organic Loop Alarms	A3.54
A3.5.4 Wiring Schematic and Valve Control System	A3.54
3.6 Measurement of the Total Volume in the Organic In-Pile Loop	A3.54
A3.6.1 Introduction	A3.54
A3.6.2 Out-of-Pile Volume Plus Volume of Lines Extending to Top of In-Pile Section	A3.59
(1) Method of Measurement	A3.59
(2) Results	A3.61
A3.6.3 Volume of In-Pile Section	A3.74
(1) Calculation of In-Pile Volume	A3.75
(2) Measurement of Total In-Pile Volume Including Header	A3.77

APPENDIX 4 FOR CHAPTER 4  
DOSIMETRY METHODS AND RESULTS

4.1 Energy Absorbed or Generated in the Organic Samples Because of Chemical Changes	A4.1
4.2 Sources of Fast Neutron and Gamma Radiation and Their Time Variation After Startup of a Nuclear Reactor	A4.2



TABLE OF CONTENTS (CONTINUED)

PAGE  
NO.

APPENDIX 4 FOR CHAPTER 4  
(CONTINUED)

APPENDIX

4.3	Estimation of Beta and Gamma Energy Absorbed in the Calorimeter Samples Due to Thermal Neutron Reactions	A4.6
	A4.3.1 Aluminum	A4.6
	A4.3.2 Plastic and Beryllium Absorbers	A4.14
4.4	Assumption of Only Compton Scattering of Gamma Radiation in Calorimeter Experiment	A4.14
4.5	Total Grams of Uranium in Central Fuel Element	A4.25
4.6	Method of Calculating Thermal Flux Differences for Aluminum and Stainless Steel Thimble	A4.29
4.7	Calculation of Fast Neutron Dose Rate, $I_C/I_H$ , and $I_{Al}/I_H$ from Fast Neutron Flux Measurements	A4.35
4.8	Equilibrium Temperature Difference between Thermocouple Bead and Calorimeter Samples	A4.39
4.9	Temperature-Time History of Center and Surface of Calorimeter Sample for Hypothetical Run	A4.42
4.10	Contribution to Energy Absorption from the Gamma and Beta Radiation emitted by the Aluminum Capsule	A4.46
	A4.10.1 Based on Turricchia's Calculations	A4.47
	A4.10.2 Based on Anderson and Waite's Calculations	A4.51
	A4.10.3 Discussion	A4.52
4.11	Net Absorbed Energy Loss from Samples Due to Escape of Compton Electrons from Samples and Capture of Compton Electrons Emanating from Aluminum Capsule.	A4.53

TABLE OF CONTENTS (CONTINUED)

PAGE  
NO

APPENDIX 4 FOR CHAPTER 4  
(CONTINUED)

APPENDIX

4.12	Sample Calculation of $R_{Al}^Y$ and $I_H$	A4.56
4.13	Estimation of Gamma and Fast Neutron Dose Rate Contribution from Central Fuel Element Relative to that from Surrounding Fuel Elements	A4.59
	A4.13.1 Gamma Dose Rate	A4.59
	A4.13.2 Fast Neutron Dose Rate	A4.67
4.14	Contribution of Gamma Radiation from the Stainless Steel and Aluminum Thimbles and from the In-Pile Section to the Dose Rate	A4.79
	A4.14.1 Stainless Steel Thimble	A4.81
	A4.14.2 Aluminum Thimble	A4.84
	A4.14.3 In-Pile Section	A4.86
4.15	Calculation of Average Energy Absorption Rate for Each Day of Irradiation of Santomax OMP	A4.87
4.16	Recommendations for Improving Accuracy of Dose Rate Determination	A4.90
	A4.16.1 Improvements in Accuracy of Calorimeter Measurements	A4.90
	A4.16.2 Measurement of Time Dependence of Dose Rate Over Long Period of Time	A4.93
	A4.16.3 Increase of Accuracy of Extrapolation of Calorimeter Measurements to Full Reactor Power	A4.94

APPENDIX 5 FOR CHAPTER 5

PHYSICAL AND CHEMICAL MEASUREMENTS ON IRRADIATED SANTOWAX OMP

5.1	Method of Gas Chromatography Analysis at M.I.T.	A5.1
5.2	Chemical Analyses of Liquid Samples	A5.4
	(1) Rejection of Extraneous Values	A5.4
	(2) Estimation of Average Concentration for Each Sample and of 70 Per cent Confidence Limit	A5.8

TABLE OF CONTENTS (CONTINUED)

APPENDIX 5 FOR CHAPTER 5  
(CONTINUED)

	<u>PAGE</u> <u>NO.</u>
<u>APPENDIX</u>	
5.3 Calculation of MWHR of Reactor Operation	A5.10
5.4 Least Squares Fit of Concentration vs. MWHR Data	A5.12
A5.4.1 Introduction	A5.12
A5.4.2 Method of Calculation	A5.12
A5.4.3 Sample Calculation	A5.14
5.5 Estimation of Thermal Decomposition Rate	A5.19
5.6 Mass of Circulating Organic in Loop	A5.20
A5.6.1 Summary of Loop Volumes and Temperatures Used in Estimating Circulating Mass in Loop	A5.20
A5.6.2 Circulating Mass of Organic In Loop Just Before Removal of Sample 62A, Based on Loop Volume and Organic Density	A5.20
A5.6.3 Circulating Mass in Organic Loop as Function of MWHR Exposure	A5.33
A5.6.4 Calculation of Expected Concentration Change on Dilution on 10-5-61, Just after Sample 62A Was Taken	A5.37
5.7 Sample Calculation of Total Terphenyl Degradation Rates by Methods I and II and Decomposition Yields from Degradation Rates	A5.41
A5.7.1 Method I for Calculation of Degradation Rates	A5.41
A5.7.2 Method II for Calculation of Degradation Rate and Decomposition Yield	A5.45
5.8 Method of Determining Gas Solubility	A5.45
5.9 Gas Balance on Loop	A5.48
A5.9.1 Gas Removed by Gas Sampling	A5.48
A5.9.2 Gas Removed by Liquid Sampling	A5.52

TABLE OF CONTENTS (CONTINUED)

APPENDIX 5 FOR CHAPTER 5  
(CONTINUED)

<u>APPENDIX</u>	<u>PAGE</u> <u>NO.</u>
A5.9.3 Volume of Undissolved Gas	A5.52
A5.9.4 Volume of Dissolved Gas Circulating in Loop	A5.53
A5.9.5 Total Gas in Loop Plus Gas Removed by Sampling	A5.53
5.10 Estimation of Gas Solubility	A5.53
5.11 Calculation of Radiolytic Gas Yields	A5.59
5.12 Measurement Technique for the Viscosity and Density of Santowax OMP up to 800°F.	A5.61
A5.12.1 Measurement of Viscosity	A5.61
A5.12.1A Introduction	A5.61
A5.12.1B Basic Equations and Errors of Viscosity Measurements	A5.61
A5.12.1C Viscometer Coefficient for Viscosity Measurement of Santowax OMP at Temperatures from 400-800°F.	A5.67
A5.12.1D Equipment and Experimental Procedures	A5.70
A5.12.1E Sample Experimental Results	A5.76
A5.12.2 Measurement of Density of Santowax OMP up to 800°F.	A5.83
A5.12.2A Method of Measurement	A5.83
A5.12.2B Calibration of Pycnometers	A5.84
A5.12.2C Density Measurement	A5.86

APPENDIX 6 FOR CHAPTER 6

HEAT TRANSFER MEASUREMENT

6.1 Dimensions of Test Heater TH-5	A6.1
6.2 Procedure and Sample Results for Calibration of Test Heater Thermocouples and Determina- tion of Heat Losses	A6.2

TABLE OF CONTENTS (CONTINUED)

APPENDIX 6 FOR CHAPTER 6  
(CONTINUED)

<u>APPENDIX</u>		<u>PAGE</u> <u>NO.</u>
6.3	Estimation of Temperature Difference Between Inside and Outside of Test Heater Wall	A6.4
6.4	Electrical Resistance of Test Heater TH-5	A6.10
6.5	Additional Results Obtained in Correlation of Heat Transfer Data	A6.10

APPENDIX 7

REFERENCES, CHAPTERS 2 THROUGH 6

7.1	Chapter 2	A7.1
7.2	Chapter 4	A7.3
7.3	Chapter 5	A7.5
7.4	Chapter 6	A7.8

APPENDIX 8

REFERENCES, APPENDICES FOR CHAPTERS 3 THROUGH 6

8.1	Chapter 3	A8.1
8.2	Chapter 4	A8.1
8.3	Chapter 5	A8.3

APPENDIX 9

<u>NOMENCLATURE</u>	A9.1
---------------------	------

## LIST OF TABLES

### PAGE NO.

#### CHAPTER 1

1.1	MIT Organic In-Pile Loop Design and Operating Characteristics	1.11
1.2	Tabulation of Out-of-Pile Components of Loop Comprising Hydraulic Console	1.17
1.3	Tabulation of Instrumentation Provided for Operation of Loop	1.22
1.4	Comparison of Z/A Ratios for Various Materials With the Corresponding Calculated Ratios of the Gamma Dose Rate in a Nuclear Reactor Core	1.35
1.5	Chronological Listing of Calorimeter Measurements Performed	1.38
1.6	Comparison of Dose Rates Obtained from Calorimeter Series III-2 at 50, 100, and 200 kw	1.42
1.7	Detectors Used for Thermal and Fast Neutron Measurements	1.51
1.8	Physical and Chemical Measurements Made on Santowax OMP During the Irradiation Period Covered by this Report	1.65
1.9	Terphenyl Irradiation Decomposition Yields	1.73
1.10	Composition of Dissolved Gases in Loop, Sample L-52E, 1170 MWHR	1.88
1.11	Semi-Quantitative Ash Analyses by Emission Spectroscopy	1.108

#### CHAPTER 2

2.1	Comparison of Nuclear Power Economics for Seven Reactor Types Based on AEC Evaluation in 1959	2.8
2.2	Chemical Composition of Polyphenyl Materials of Interest in the Study of Organic Coolants	2.9

LIST OF TABLES (CONTINUED)

PAGE NO.

CHAPTER 3

3.1	MIT Organic In-Pile Loop Design and Operating Characteristics	3.9
3.2	Volume of Different Sections of the Out-of-Pile Section of the Loop	3.47

CHAPTER 4

4.1	Materials Used for Calorimetric Measurements	4.3
4.2	Comparison of Z/A Ratios for Various Materials With the Corresponding Calculated Ratios of the Gamma Dose Rate in a Nuclear Reactor Core	4.25
4.3	Neutron Energy Transfer Integral Ratios for Various Elements	4.27
4.4	Detectors Used for Thermal and Fast Neutron Measurements	4.31
4.5	Chronological Survey of Calorimeter and Flux Measurements Made in Fuel Position No. 1	4.38
4.6	Estimated Errors in Absolute Neutron Fluxes	4.40
4.7	Calculated Values of $R_{SW}^n$ , $\frac{I_C}{I_H}$ , and $\frac{I_{Al}}{I_H}$	4.62
4.8	Calculated Fast Neutron Dose Rate in Santowax OMP at the MITR Core Center for Different Energy Intervals	4.65
4.9	Thermal Conductivity of Absorbers	4.70
4.10	Summary of Estimated Absolute Uncertainties in the Energy Generation Rate for Calorimeter Samples	4.77
4.11	Summary of Number of Runs, Purposes, and Difficulties for Each Calorimeter Series, Fuel Positions 1 and 6	4.78
4.12	Maximum Dose Rate for Each Calorimeter Series Normalized to 1.00 MW	4.87
4.13	Ratio of Measurements at Different Reactor Power Levels After Normalization to 1.00 MW	4.91

LIST OF TABLES (CONTINUED)

CHAPTER 4 (CONTINUED)

		<u>PAGE NO.</u>
4.14	Variation of Ratio of Dose Rate for Each Sample and Each Calorimeter Series to that for Calorimeter Series III-2	4.93
4.15	Calculated Dose Rate in Samples Based on Data of Table 4.12 and Comparison with Measured Dose Rates	4.97
4.16	Ratio of the Hydrogen Energy Transfer Integrals and Gamma Dose Rates Obtained from Measurements Made at Different Reactor Power Levels	4.99
4.17	Variation of the Hydrogen Energy Transfer Integral and the Gamma Dose Rate Through the Different Series of Calorimetric Experiments	4.100
4.18	Differences Between Calorimeter Measurements in Calorimeter Series III-2 and III-3	4.101
4.19	Calculation of Fraction of Gamma Dose Due to Stainless Steel Thimble for Various Conditions	4.105
4.20	Calculated Values of $I_H$ and $R_{Al}$ from Calorimeter Data	4.107
4.21	Vertical Distribution of Dose Rate in Santowax OMP	4.111
4.22	Dose Rate in Santowax OMP in In-Pile Section of Loop Based on Calorimeter Series III-3 in the Stainless Steel Thimble	4.114

CHAPTER 5

5.1	Physical and Chemical Measurements Made On Santowax OMP During the Irradiation Period Covered by This Report	5.4
5.2	Summary of Average Concentration of Samples Removed from Organic Loop-Based on MIT Analyses	5.7
5.3	Summary of Average Concentration of Samples Removed from Organic Loop-Based on Monsanto Analyses	5.8
5.4	Comparison of Degradation Rates Calculated by Methods I and II	5.25
5.5	Terphenyl Irradiation Decomposition Yields	5.27
5.6	Decomposition Yield of Terphenyls for Van de Graaff Irradiation Based on Data by Bates, <u>et al.</u> (5.7)	5.35



LIST OF TABLES (CONTINUED)  
CHAPTER 5 (CONTINUED)

	<u>PAGE NO.</u>	
5.7	Summary of Decomposition Yields Reported by Bley for the MTR In-Pile Loop (5.10)	5.38
5.8	Decomposition Yields for Santowax OMP Reported by Berg, et al. (5.6) for In-Pile Irradiation	5.41
5.9	Estimation of Decomposition Yields $G^*(-omp\phi_z)$ and $G^*(-p\phi_z)$ Based on "Smoothed Data" of Burns, et al. (5.5)	5.45
5.10	Composition of Dissolved and Undissolved Gases in Loop	5.53
5.11	Results of Gas Balance on Loop	5.59
5.12	Gas Evolution Yields	5.65
5.13	Viscosity of Irradiated Santowax OMP	5.73
5.14	Values of $\mu_o$ and $\beta$ obtained From Viscosity Measurements	5.76
5.15	Density of Irradiated Santowax OMP	5.79
5.16	Average Molecular Weight, Carbon-Hydrogen Content, and Melting Point of Irradiated Santowax OMP	5.85
5.17	Semi-Quantitative Ash Analysis by Emission Spectroscopy	5.92

CHAPTER 6

6.1	Summary of Uncertainties in Heat Transfer Coefficient Determination	6.14
-----	---	------

LIST OF  
TABLES FOR APPENDIX

PAGE NO.

CHAPTER 3

A3.1	MITR Fuel Element Modifications and Estimated In-Pile Volume	A3.35
A3.2	Frictional Pressure Drops and Organic Velocities in Different Loop Sections	A3.51
A3.3	Organic Loop Alarms	A3.56
A3.4	Volume Calibration of Surge Tank and Feed and Dump Tank	A3.62
A3.5	Volume Designations for Volume Measurements	A3.65
A3.6	Tabulation of Data and Results of Volume Measurements of Hydraulic Console	A3.66-67
A3.7	Summary of Results of Volume Calibration of Hydraulic Console	A3.73
A3.8	Total In-Pile Volume	A3.78

CHAPTER 4

A4.1	Calculation of Fraction of Gamma Energy Liberated by Thermal Neutron Capture Which is absorbed by the Aluminum Sample	A4.9
A4.2	Energy Absorption from Beta and Gamma Radiation in Aluminum Sample from Thermal Neutron Capture	A4.13
A4.3	The Energies, $E_{1/2}$ at Which the Photoelectric ( $\tau$ ) and Pair Production ( $\kappa$ ) Linear Attenuation Coefficients Are Equal to the Compton Coefficient ( $\sigma$ )	A4.15
A4.4	Calculations Made for Graphical Integration to Determine Relative Photoelectric, Compton, and Pair Production Absorption Rates in Aluminum, Attenuation by Aluminum Thimble (0.035 inch wall) and Capsule (0.10 inch wall)	A4.18

LIST OF  
TABLES FOR APPENDIX (CONTINUED)  
CHAPTER 4 (CONTINUED)

		<u>PAGE NO.</u>
A4.5	Calculations Made for Graphical Integration to Determine Relative Photoelectric, Compton, and Pair Production Absorption Rates in Aluminum, Attenuation by Stainless Steel Thimble (0.049 inch wall) and Aluminum Capsule (0.10 inch wall)	A4.19
A4.6	Calculated Energy Absorption Rates in Aluminum Due to Photoelectric, Compton, and Pair Production Interactions	A4.20
A4.7	Calculated Contributions of Photoelectric, Compton, and Pair Production Interactions to the Gamma Dose Rate for Different Materials	A4.21
A4.8	Comparison of Fluxes at Axial Center Position With Those Used for Curve V	A4.38
A4.9	Temperature Variation of Inside and Outside of Polystyrene Absorber	A4.46
A4.10	Energy Absorbed by Various Materials from Gamma and Beta Radiation Originating in the Aluminum Capsule	A4.50
A4.11	Loss of Absorbed Energy Due to Compton Gamma Interactions by Escape of Compton Electrons from Absorber	A4.55
A4.12	Comparison of Measured and Calculated Total Dose Rates	A4.57
A4.13	Calculations for Determination of Source Strength as Function of Neutron Lethargy	A4.69
A4.14	Information for Graphical Integration of Equation A4.75	A4.70
A4.15	Results of Calculation of Fast Neutron Dose Rate From Center Fuel Element Relative to that from Ring of Six Elements	A4.78
A4.16	Corrected Results of Calculation of Fast Neutron Dose Rate from Central Fuel Element Relative to that From Ring of Six Elements	A4.80
A4.17	Calculations Leading to Estimation of Dose Rate from Stainless Steel Thimble	A4.83
A4.18	Calculations Leading to Estimation of Dose Rate from Aluminum Thimble	A4.85
A4.19	Sample Calculations of $R_{SW}^{TI}$ for Individual Days of Loop Operation	A4.89

LIST OF  
TABLES FOR APPENDIX (CONTINUED)

<u>CHAPTER 5</u>		<u>PAGE NO</u>
A5.1	Operating Conditions for Burrell K-7 Gas Chromatograph at M.I.T.	A5.2
A5.2	Chemical Analyses of Irradiated Santowax OMP - MIT and Monsanto Data	A5.5
A5.3	Sample Calculation of MWHR's of Reactor Operation	A5.11
A5.4	Equations Used for Least Squares Calculation	A5.15
A5.5	Calculation Sheet for Least Squares Calculation for Total Terphenyl Concentration Based on M.I.T. Data	A5.16
A5.6	Summary of Volumes and Temperatures for Different Loop Sections Used in Estimating Effective Circulating Mass of Organic	A5.21
A5.7	Organic Mass on 10-5-61 in Sections with Positive Circulation of Organic and Known Temperature	A5.23
A5.8	Organic Mass on 10-5-61 in Chempump	A5.30
A5.9	Organic Mass on 10-5-61 in Coolers	A5.32
A5.10	Circulating Organic Mass in Loop as Function of MWHR Exposure	A5.34
A5.11	Three Occasions When Anomalous Drops Occurred in Surge Tank Level	A5.37
A5.12	Calculation Sheet for Total Degradation Rate of Ortho-, Meta-, and Para-Terpheyls	A5.42
A5.13	Comparison of $dH(Z)/dZ$ Calculated Using Samples 35E through 62A, 27G through 62A, and 16 through 62A	A5.44
A5.14	Equations Used and Sample Calculations for Degradation Rate and Decomposition Yields Using Method II	A5.46
A5.15	Gas Balance on Loop	A5.54
A5.16	Measured Values of Gas Solubility in Organic Coolant	A5.55
A5.17	Sample Calibration Runs for Viscometer A140	A5.77
A5.18	Sample Results of Viscosity Measurement on Santomax OMP	A5.80
A5.19	Calibration of Large Capillary Pycnometer for Density Determinations Reported in Section A5.12.2C	A5.87
A5.20	Density Measurement of Santowax OMP, Large Capillary Pycnometer	A5.89

## LIST OF FIGURES

PAGE NO.

### CHAPTER 1

1.1	Chemical Structure of Terphenyls and Biphenyl	1.2
1.2	Cross Sectional View of Reactor Illustrating Reactor Construction	1.8
1.3	Drawing of Cross Section of Reactor Core Showing Fuel and Control Rod Positions	1.9
1.4	Drawing of Fuel Element Cross Section With Position of In-Pile Section Shown	1.10
1.5	Flow Diagram	1.12
1.6	Assembly of Thimble and Organic Holdup Capsule	1.14
1.7	Photograph of Fuel Element Assembly	1.15
1.8	Front and Left Side of Hydraulic Console	1.19
1.9	Primary Instrument and Control Panel	1.20
1.10	Schematic Showing Location of Loop in M.I.T. Nuclear Reactor	1.24
1.11	Hydraulic Console and Instrument Panel in Position on Reactor Room	1.25
1.12	Assembly Drawing of Calorimeter II	1.28
1.13	Photograph of Calorimeter II	1.29
1.14	Schematic of Calorimeter Equipment Layout	1.30
1.15	Typical Example of the Time Variation of the Temperature of a Sample and of the Wall of the Calorimeter in the Center of the Core.	1.32
1.16	Sketch Illustrating Method of Determining $I_H$	1.37
1.17	Vertical Distribution of Dose Rate in Aluminum Sample	1.39
1.18	Vertical Distribution of Dose Rate in Polyethylene Sample	1.40
1.19	Vertical Distribution of Dose Rate in Polystyrene Sample	1.41
1.20	Vertical Distribution of the Gamma Dose Rate $R_{Al}^Y$ in Fuel Position No. 1	1.44
1.21	Vertical Distribution of the Energy Transfer Integral for Hydrogen, $I_H$ , in Fuel Position No. 1	1.45

LIST OF FIGURES (CONTINUED)  
CHAPTER 1 (CONTINUED)

		<u>PAGE NO.</u>
1.22	Vertical Distribution of Fast Neutron, Gamma, and Total Dose Rate in Santowax OMP	1.47
1.23	Variation With Time of Dose Rate, $R_{SW}^{TI}$ , in Santowax OMP in In-Pile Section	1.49
1.24	Thermal Neutron Flux (2200 meter/sec) at Different Reactor Powers after Extrapolation of All Results to 1.00 MW Reactor Power	1.53
1.25	Thermal Neutron Flux (2200 meter/sec) at 1.0 MW on Different Days During Normal Operating Week	1.54
1.26	Comparison of Thermal Flux Measurements (2200 meter/sec) in the Stainless Steel Thimble and in the In-Pile Section at 1.0 MW	1.55
1.27	Epithermal Neutron Flux as Measured With Copper (Resonance = 570 ev) and Cobalt (Resonance = 120 ev)	1.57
1.28	Integrated Fast Neutron Flux ( $\int_{2.9}^{\infty} \phi(E)dE$ ) From Sulfur Measurements	1.58
1.29	Integrated Fast Neutron Flux ( $\int_{5.0}^{\infty} \phi(E)dE$ ) From Nickel Measurements	1.59
1.30	Integrated Fast Neutron Flux ( $\int_{6.3}^{\infty} \phi(E)dE$ ) From Magnesium Measurements	1.60
1.31	Integrated Fast Neutron Flux ( $\int_{8.6}^{\infty} \phi(E)dE$ ) From Aluminum Measurements	1.61
1.32	Comparison of Fission Spectrum With Experimental Data For Fast Neutron Threshold Detectors With In-Pile Section in Place	1.62
1.33	Organic Concentrations During Initial Irradiation of Santowax OMP-MIT Data	1.67
1.34	Organic Concentrations During Initial Irradiation of Santowax OMP-MIT Data	1.68
1.35	Grams of Organic Circulating in Loop	1.72
1.36	Decomposition Yield, $G(-i)$ , for Ortho-, Meta-, and Para-Terphenyls	1.74
1.37	Decomposition Yield, $G^*(-i)$ , for Ortho-, Meta-, and Para-Terphenyls	1.76
1.38	Cost of Organic Makeup Based on 50% of Fast Neutron Energy Absorbed in Organic Coolant	1.82

LIST OF FIGURES (CONTINUED)  
CHAPTER 1 (CONTINUED)

	<u>PAGE NO.</u>	
1.39	Cost of Organic Makeup Based on 75% of Fast Neutron Energy Absorbed in Organic Coolant	1.83
1.40	Hydrogen Content of Undissolved Gases in Loop	1.85
1.41	Saturated Gas Content of Undissolved Gases in Loop	1.86
1.42	Unsaturated Gas Content of Undissolved Gases in Loop	1.87
1.43	Gas Present in Loop Plus Cumulative Removed as Function of MWHR'S of Reactor Operation and Gas Solubility	1.90
1.44	Comparison of Gas Evolution Calculations Based on Two Values of Gas Solubility	1.92
1.45	The Total Radiolytic Gas Yield for the Irradiation of Santowax OMP	1.93
1.46	Viscosity of Irradiated Santowax OMP	1.96
1.47	Variation of $\mu_0$ and $\beta$ with % DP	1.97
1.48	Viscosity of Irradiated Santowax OMP and Santowax R at Various Temperatures As Function of Concentration of Degradation Products or High Boilers	1.99
1.49	Density of Irradiated Santowax OMP	1.100
1.50	Variation of C in Correlating Density with % DP	1.101
1.51	Density of Irradiated Santowax OMP and Santowax R at Various Temperatures as Function of Degradation Products or High Boilers	1.103
1.52	Variation of Number-Average Molecular Weight of Irradiated Santowax OMP with % DP	1.105
1.53	Variation of Melting Point of Irradiated Santowax OMP With % DP	1.107
1.54	Typical Temperature Profile of the Test Heater	1.111
1.55	Wilson Plot for Heat Transfer Data on Unirradiated Santowax OMP	1.113
1.56	Wilson Plot for Heat Transfer Data on Irradiated Santowax OMP	1.115
1.57	Least Squares Correlation of Heat Transfer Data to Dittus-Boelter Type of Equation - Nominal $q/A \cong 200,000$ Btu/hr ft <sup>2</sup>	1.117

LIST OF FIGURES (CONTINUED)  
CHAPTER 1 (CONTINUED)

	<u>PAGE NO.</u>
1.58 Least Squares Correlation of Heat Transfer Data to Dittus-Boelter Type of Equation Nominal $q/A \approx 100,000$ Btu/hr-ft <sup>2</sup> .	1.118

CHAPTER 2

2.1 Chemical Structure of Terphenyls and Biphenyl	2.3
2.2 Comparative Energy Costs for Various Moderators in Organic Cooled Nuclear Reactors	2.6

CHAPTER 3

3.1 Cross Sectional View of Reactor Illustrating Reactor Construction	3.2
3.2 Drawing of Cross Section of Reactor Core Showing Fuel and Control Rod Positions	3.3
3.3 Drawing of Fuel Element Cross Section With Position of In-Pile Section Shown	3.4
3.4 Flow Diagram	3.6
3.5 Schematic Showing Position of Loop in MIT Nuclear Reactor	3.7
3.6 Hydraulic Console and Instrument Panel in Position on Platform in Reactor Room	3.8
3.7 Assembly of Thimble and Organic Holdup Capsule	3.11
3.8 Assembly of Irradiation Capsule	3.12
3.9 Details of Irradiation Capsule	3.13
3.10 Details of Surge Tank	3.17
3.11 Details of Filter	3.19
3.12 Test Heater	3.22
3.13 Photograph of Test Heater	3.23
3.14 Details of Main Loop Coolers	3.24
3.15 Photograph of Liquid and Gas Samplers	3.26
3.16 Details of Feed and Dump Tank	3.29
3.17 Details of Safety Expansion Tank	3.31
3.18 Details of Vapor Traps	3.33
3.19 Front and Left Side of Hydraulic Console	3.36



LIST OF FIGURES (CONTINUED)  
CHAPTER 3 (CONTINUED)

	<u>PAGE NO.</u>	
3.20	Primary Instrument and Control Panel	3.38
3.21	Auxiliary Instrument Panel in Reactor Control Room	3.39
3.22	Auxiliary Instrument Panel on Loop Platform	3.40
3.23	Capsule Volume per Unit Length at Different Axial Positions	3.48

CHAPTER 4

4.1	Assembly Drawing of Calorimeter II	4.5
4.2	Photograph of Calorimeter II	4.6
4.3	Schematic of Calorimeter Equipment Layout	4.8
4.4	T-Connection With Thermocouple Seal	4.9
4.5	Photograph of Equipment on Top of Reactor	4.10
4.6	Typical Example of the Time Variation of the Temperature of a Sample and of the Wall of the Calorimeter in the Center of the Core	4.12
4.7	Assembly Drawing of Calorimeter I	4.14
4.8	Santowax OMP Sample	4.16
4.9	Photograph of Calorimeter III	4.19
4.10	Construction Details of Calorimeter III	4.20
4.11	Sketch Illustrating Method of Determining $I_H$	4.28
4.12	Thermal Neutron Flux (2200 meter/sec) at Different Reactor Powers After Extrapolation of All Results to 1.00 MW Reactor Power	4.43
4.13	Thermal Neutron Flux (2200 meter/sec) at 1.0 MW on Different Days During Normal Operating Week	4.45
4.14	Calculated Relative Thermal Fluxes for Unit Cell With Various Geometries	4.47
4.15	Cadmium Ratios Measured with Co-Al Wire	4.49
4.16	Effect of Stainless Steel Thimble on Thermal Neutron Flux (2200 meter/sec) after Extrapolation of all Results to 1.0 MW, Tuesday Irradiation	4.50

LIST OF FIGURES (CONTINUED)  
CHAPTER 4 (CONTINUED)

PAGE NO.

4.17	Comparison of Thermal Flux Measurements (2200 meter/sec) in the Stainless Steel Thimble and in the In-Pile Section at 1.0 MW	4.52
4.18	Cadmium Ratios Measured With Copper Detectors	4.53
4.19	Epithermal Neutron Flux as Measured with Copper (Resonance = 560 ev) and Cobalt (Resonance = 120 ev)	4.55
4.20	Integrated Fast Flux ( $\int_{\infty}^{2.9} \phi(E) dE$ ) From Sulfur Measurements	4.56
4.21	Integrated Fast Flux ( $\int_{\infty}^{5.0} \phi(E) dE$ ) From Nickel Measurements	4.57
4.22	Integrated Fast Flux ( $\int_{\infty}^{6.3} \phi(E) dE$ ) From Magnesium Measurements	4.58
4.23	Integrated Fast Flux ( $\int_{\infty}^{8.6} \phi(E) dE$ ) From Aluminum Measurements	4.59
4.24	Comparison of Fission Spectrum with Experimental Data for Fast Neutron Threshold Detectors With In-Pile Section in Place	4.60
4.25	Fast Neutron Flux Spectra Used in Estimating $I_C/I_H$ , and Fast Neutron Dose Rate in Santowax OMP	4.63
4.26	Centerline and Surface Temperature for Polystyrene for Hypothetical Calorimeter Run	4.74
4.27	Vertical Distribution of Dose Rate in Aluminum Sample	4.80
4.28	Vertical Distribution of Dose Rate in Polyethylene Sample	4.81
4.29	Vertical Distribution of Dose Rate in Polystyrene Sample	4.82
4.30	Vertical Distribution of Dose Rate in Beryllium Sample	4.83
4.31	Vertical Distribution of Dose Rate in Santowax OMP Sample	4.84
4.32	Variation of the Total Dose Rate With Time After Startup, in Aluminum	4.88
4.33	Sketch Showing Method Used in Obtaining Errors for $R_{Al}$ and $I_H$	4.95
4.34	Vertical Distribution of the Energy Transfer Integral for Hydrogen, $I_H$ , in Fuel Position No. 1	4.108
4.35	Vertical Distribution of the Gamma Dose Rate, $R_{Al}$ , in Fuel Position No. 1	4.109
4.36	Vertical Distribution of Fast Neutron Gamma, and Total Dose Rate in Santowax OMP	4.112
4.37	Variation With Time of Dose Rate, $R_{SW}$ , in Santowax OMP in In-Pile Section	4.116

LIST OF FIGURES (CONTINUED)

PAGE NO.

CHAPTER 5

5.1	Organic Concentrations During Initial Irradiation of Santowax OMP-MIT Data	5.10
5.2	Organic Concentrations During Initial Irradiation of Santowax OMP-MIT Data	5.11
5.3	Organic Concentrations During Initial Irradiation of Santowax OMP-Monsanto Data	5.14
5.4	Plot of $M(Z) C_i(Z) + \sum_j S_{j,i}$ vs. Z for the Total Terphenyls - Based on MIT Data	5.18
5.5	Sketch of Actual and Assumed Variation of Mass in Organic Loop	5.20
5.6	Grams of Organic Circulating in Loop	5.23
5.7	Decomposition Yield, $G(-i)$ , for Ortho-, Meta-, and Para-Terphenyls	5.28
5.8	Decomposition Yield, $G^*(-i)$ for Ortho-, Meta-, and Para Terphenyls	5.30
5.9	Plot of Data Presented by Berg, <i>et al.</i> , (5.6) for the Irradiation of Santowax OMP	5.42
5.10	Cost of Organic Makeup Based on 50% of Fast Neutron Energy Absorbed in Organic Coolant	5.48
5.11	Cost of Organic Makeup Based on 75% of Fast Neutron Energy Absorbed in Organic Coolant	5.49
5.12	Hydrogen Content of Undissolved Gases in Loop	5.54
5.13	Saturated Gas Content of Undissolved Gases in Loop	5.55
5.14	Unsaturated Gas Content of Undissolved Gases in Loop	5.56
5.15	Gas Present in Loop Plus Cumulative Removed as Function of MWHRS of Reactor Operation and Gas Solubility	5.60
5.16	Comparison of Gas Evolution Calculations Based on Two Values of Gas Solubility	5.63
5.17	The Total Radiolytic Gas Yield for the Irradiation of Santowax OMP	5.66
5.18	Viscosity of Irradiated Santowax OMP	5.74
5.19	Variation of $\mu_o$ and $\beta$ with % DP	5.75
5.20	Viscosity of Irradiated Santowax OMP and Santowax R at Various Temperatures As Function of Concentration of Degradation Products or High Boilers	5.77

LIST OF FIGURES (CONTINUED)  
CHAPTER 5 (CONTINUED)

		<u>PAGE NO.</u>
5.21	Density of Irradiated Santowax OMP	5.80
5.22	Variation of C In Correlating Density With % DP	5.82
5.23	Density of Irradiated Santowax OMP and Santowax R at Various Temperatures As Function of Degradation Products or High Boilers	5.83
5.24	Variation of Number Average Molecular Weight of Irradiated Santowax OMP With % DP	5.88
5.25	Variation of Melting Point of Irradiated Santowax OMP With % DP	5.90

CHAPTER 6

6.1	Schematic of Power Supply for Test Heaters Showing Instruments Used for Power Input Measurements	6.5
6.2	Typical Temperature Profile of the Test Heater	6.9
6.3	Wilson Plot for Heat Transfer Data on Unirradiated Santowax OMP	6.19
6.4	Plot for Determination of Exponent on Velocity for Wilson Plot	6.19
6.5	Wilson Plot for Heat Transfer Data on Irradiated Santowax OMP	6.20
6.6	Least Squares Correlation of Heat Transfer Data to Dittus-Boelter Type of Equation Nominal $q/A \cong 200,000 \text{ Btu/hr-ft}^2$	6.25
6.7	Least Squares Correlation of Heat Transfer Data to Dittus-Boelter Type of Equation Nominal $q/A \cong 100,000 \text{ Btu/hr-ft}^2$	6.26

LIST OF  
FIGURES FOR APPENDIX

PAGE NO.

CHAPTER 3

A3.1	Details of In-Pile Section Thimble	A3.2
A3.2	Photographs of In-Pile Section Thimble	A3.3
A3.3	Photographs of the Organic Holdup Capsule Before Installation of Trace Heaters and Thermocouples	A3.6
A3.4	Photographs of the Organic Holdup Capsule after Installation of Trace Heaters and Thermocouples	A3.7
A3.5	Assembly of Lower Fuel Adapter and Thimble Guide	A3.10
A3.6	Lower Fuel Adapter (Photograph)	A3.11
A3.7	Detail of Lower Shield Plug	A3.12
A3.8	Details of Upper Fuel Adapter	A3.13
A3.9	Assembly of Lower Shield Plug and Upper Fuel Adapter	A3.14
A3.10	Photograph of Fuel Element Assembly	A3.16
A3.11	Assembly of Upper Shield Plug and Insert	A3.18
A3.12	Details of Upper Shield Plug	A3.19
A3.13	Replacement Shield Plug for In-Pile Section	A3.20
A3.14	Schematic of Thimble Pressurizing and Leak Detector System	A3.21
A3.15	Elbow Assembly	A3.23
A3.16	Details of Elbow	A3.24
A3.17	Conduit Tubes	A3.25
A3.18	Assembly of Conduit Tubes, Junction Box, and Lower Shield Plug Holddown	A3.26
A3.19	Photographs of Top of Lower Reactor Shield Showing Installation of Loop Lines and Sleeves	A3.27
A3.20	General Assembly of In-Pile Section	A3.28
A3.21	Miscellaneous Details	A3.29
A3.22	Design of Proposed Circular Fuel Element Capsule and Thimble Assembly of Proposed	A3.32
A3.23	In-Pile Section and Circular Fuel Element	A3.34
A3.24	Details of Surge Tank Liquid Level Gage	A3.37

LIST OF  
FIGURES FOR APPENDIX (CONTINUED)  
CHAPTER 3 (CONTINUED)

	<u>PAGE NO.</u>	
A3.25	Flow Diagram of Pump Cooling System	A3.39
A3.26	Pump Cooling System Heat Exchanger	A3.40
A3.27	Details of Feed and Dump Tank Liquid Level Gage	A3.41
A3.28	Schematic of Trace Heater System	A3.44
A3.29	Left Side of Hydraulic Console	A3.45
A3.30	Rear of Hydraulic Console	A3.46
A3.31	Right Side of Hydraulic Console	A3.47
A3.32	Piping Assembly of Hydraulic Console	A3.48
A3.33	Auxiliary Piping Assembly of Hydraulic Console	A3.49
A3.34	Details of Hydraulic Console Cabinet	A3.50
A3.35	Thermocouple Schematic	A3.52
A3.36	Schematic of Control Instrumentation for Trace Heating System Weekend Operation	A3.55
A3.37	Wiring Schematic for In-Pile Loop	A3.57
A3.38	Valve Control System	A3.58
A3.39	Surge Tank Volume to Valve 18	A3.63
A3.40	Feed and Dump Tank Volume to Valves 19 and 20	A3.64
A3.41	Volume Measurement, Run No. 3	A3.68
A3.42	Volume Measurement, Run No. 4	A3.69
A3.43	Volume Measurement, Run No. 4	A3.70
A3.44	Volume Measurement, Run No. 4 Based on $1/(\pi-p_a)$ rather than $1/\pi$	A3.71
A3.45	Volume Measurements, Run No. 5 and 6, plus Feed and Dump Tank Calibration	A3.72

CHAPTER 4

A4.1	Percentage of Equilibrium Gamma Dose Rate As a Function of Time After Reactor Startup	A4.4
A4.2	Differential Relative Energy Absorption Rate Due to Gamma Interactions 0.00-0.10 Mev	A4.22
A4.3	Differential Relative Energy Absorption Rate Due to Gamma Interactions 0.10-1.00 Mev	A4.23
A4.4	Differential Relative Energy Absorption Rate Due to Gamma Interactions, 1.00-7.00 Mev	A4.24
A4.5	Variation of the Total Grams of Uranium in Central Fuel Element (Fuel Position No. 1 with Date	A4.27

LIST OF  
FIGURES FOR APPENDIX (CONTINUED)  
CHAPTER 4 (CONTINUED)

	<u>PAGE NO.</u>
A4.6 Cross Section of the In-Pile Section in the Core of the Reactor and Equivalent Cylindrical Unit Cell	A4.30
A4.7 Cross Section of the Calorimeter in the Core of the Reactor and Equivalent Unit Cell	A4.31
A4.8 Neutron Flux Spectrum at Axial Center of Core Used for Calculation of Fast Neutron Dose Rate in Santowax OMP and $I_C/I_H$ and $I_{A\ell}/I_H$	A4.36
A4.9 Plot of $R_{A\ell}^Y$ vs $I_H$ , Used in Determining Best Value of $R_{A\ell}^Y$ and of $I_H$	A4.58
A4.10 Curves for Determination of Source Strength As Function of Neutron Lethargy	A4.71
A4.11 Plot for Graphical Integration to Determine Relative Contribution of Central Fuel Element to Fast Neutron Dose Rate	A4.72
A4.12 Plot for Graphical Integration to Determine Relative Contribution of Ring of Six Fuel Elements to Fast Neutron Dose Rate	A4.73
A4.13 Temperature of Santowax OMP in In-Pile Section, 8/15/61-8/20/61	A4.88
A4.14 Sketch of Dose Rate Variation With Weight Fraction of Carbon in Plastic for Proposed Calorimeter	A4.92

CHAPTER 5

A5.1 Gas Chromatogram for Sample Containing 1.50% Biphenyl, 9.47% O-Terphenyl, 22.96% Triphenylmethane, 39.68% M-Terphenyl, 24.89% P-Terphenyl, and 1.50% Triphenylene	A5.3
A5.2 Schematic of Apparatus for Gas Solubility Determination	A5.47
A5.3 Temperature of Gas Sample Capsule After Connection to Sampling Position	A5.49
A5.4 Photograph of Viscometer and Pycnometer	A5.72
A5.5 Schematic of Salt Bath	A5.73
A5.6 Photograph of Salt Bath	A5.74
A5.7 Schematic of Pressure and Evacuating System for Density and Viscosity Measurement	A5.75
A5.8 Variation of Viscometer Constant With Volume of Liquid in Viscometer	A5.78
A5.9 Variation of Viscosity with $l/T$ on Semi Log Plot	A5.81

LIST OF  
FIGURES FOR APPENDIX (CONTINUED)

CHAPTER 5 (CONTINUED)

		<u>PAGE NO.</u>
A5.10	Variation of $\mu v^{1/3}$ with $1/vT$ on Semi-Log Plot	A5.82
A5.11	Calibration for Pycnometers for Density Measurement	A5.88
A5.12	Density of Unirradiated Santowax OMP	A5.90

CHAPTER 6

A6.1	Sample of Method Used to Determine Thermocouple Calibration	A6.5
A6.2	Sample of Thermocouple Calibration	A6.6
A6.3	Total Heat Losses from Both Heater Sections vs. Outside Wall Temperature	A6.7
A6.4	Least Squares Correlation of Heat Transfer Data with Seider Tate Type of Equation - Nominal $q/A \cong 200,000$ and $100,000 \text{ Btu/hr-ft}^2$	A6.12
A6.5	Least Squares Correlation of Heat Transfer Data to Dittus-Boelter type of Equation - Nominal $q/A \cong 200,000 \text{ Btu/hr-ft}^2$ - All three constants Determined	A6.14
A6.6	Least Squares Correlation of Heat Transfer Data to Dittus-Boelter Type of Equation- Nominal $q/A \cong 100,000 \text{ Btu/hr-ft}^2$ - All Three Constants Determined.	A6.15



## CHAPTER 1

## SUMMARY

THE IRRADIATION OF SANTOWAX OMP  
IN THE M. I. T. IN-PILE LOOP

## 1. 1 INTRODUCTION

Previous work has indicated that organic cooled nuclear reactors have an excellent potential for the economic production of electrical power (1. 1, 1. 2). As a result of this potential, a study sponsored by the U. S. Atomic Energy Commission was started in October, 1958, at the Massachusetts Institute of Technology, on the effects of in-pile irradiation on organic liquids suitable for use as coolants and moderators in nuclear reactors. To date, the principal activities at M. I. T. have been the design, construction, and initial operation of an in-pile loop; Santowax OMP is the first material being tested. The primary purposes of the program at M. I. T. are the study of (1) the nature and rate of irradiation degradation of various organic materials having physical and chemical properties satisfactory for use as primary coolants in nuclear reactors and (2) the effect of the irradiation degradation products on the heat transfer rate and other characteristics pertinent to use of the materials in organic cooled nuclear reactors.

## 1. 1. 1 Characteristics of Organic Cooled Nuclear Reactors

Organic cooled nuclear reactors now being designed or constructed are generally based on the use of mixtures of ortho-, meta-, and para-terphenyls. Previous work has indicated that these materials have desirable nuclear, chemical, and physical properties for use as organic coolants in nuclear power reactors (1. 3, 1. 4, 1. 5, 1. 6, 1. 7). The chemical structure of the terphenyls as well as biphenyl is shown in Figure 1. 1. Most current reactor designs are based on the use of

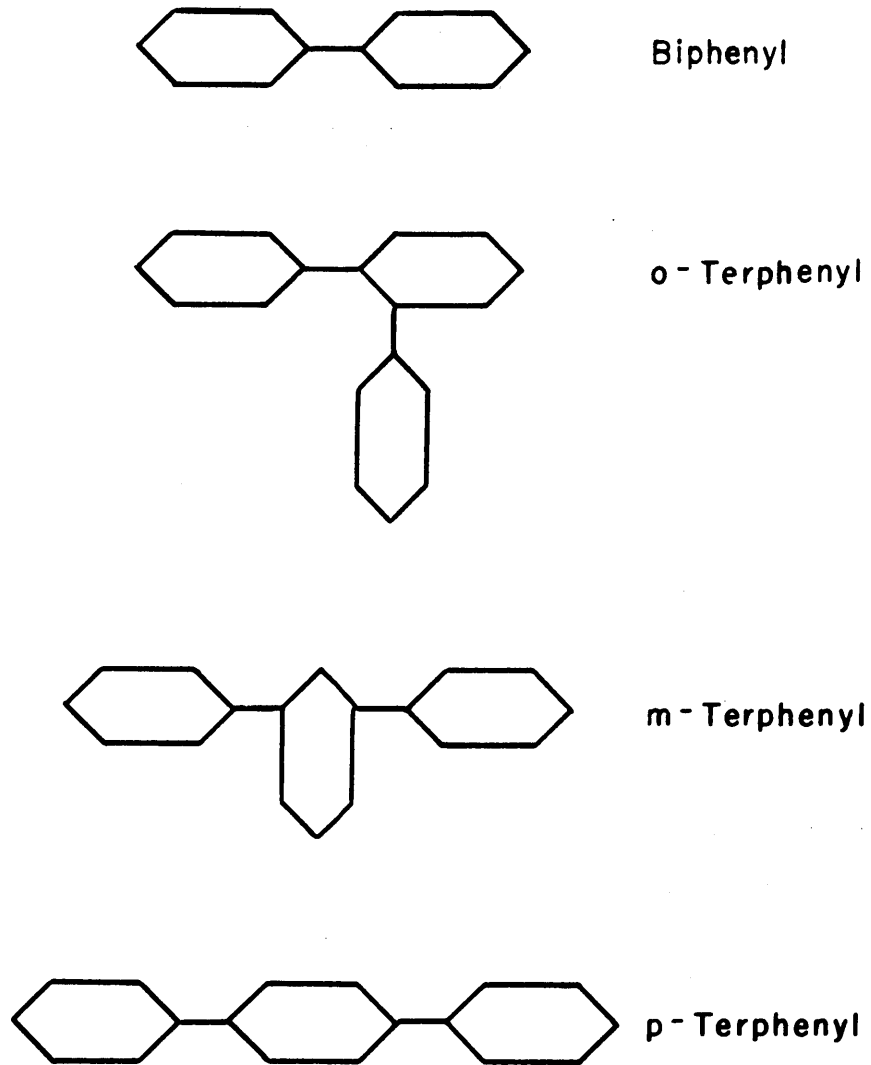


FIG. 1.1 CHEMICAL STRUCTURE OF TERPHENYLS AND BIPHENYL

Santowax OMP (1.1) which is an isomeric mixture of ortho-, meta-, and para-terphenyls having the following nominal composition:

Less than 2% biphenyl plus degradation products  
~12-1/2% o-terphenyl  
~62-1/2% m-terphenyl  
~25% p-terphenyl

Nuclear reactors cooled by this or similar organic liquids have the following desirable characteristics:

- (1) Low operating pressure at high coolant temperatures. Due to the low vapor pressure of the organics, organic-cooled reactors are generally designed for operating pressures of about 100 psig at organic temperatures of about 600-700°F.
- (2) Negligible corrosion of conventional structural materials such as carbon steel.
- (3) Low induced activity in the coolant significantly reducing shielding requirements for the primary coolant loop as well as permitting ease of maintenance.
- (4) Feasibility of use of the organic coolant as moderator because of its hydrogen content permitting compact and simple core designs.

There are, however, some undesirable characteristics in the use of organic moderated and cooled nuclear reactors, the most important of which are summarized below:

- (1) Irreversible radiolytic and thermal degradation of the organic coolant. At concentrations greater than 30-40 wt %, the degradation products seriously affect the coolant heat transfer performance. Consequently, the degradation products must be continually removed during operation of the reactor and fresh organic makeup added. Makeup costs of 0.75-0.90 mills/kwhr(e) have been reported (1.8) for organic moderated and cooled power reactors.

(2) Poor heat transfer performance due to the low thermal conductivity of the organic coolant. The coolants also have a tendency to foul heat transfer surfaces if excessive temperatures and/or large concentrations of particulate material are allowed during operation of an organic cooled reactor (1. 9).

The desirable characteristics of organic cooled and moderated nuclear reactors result in a significant reduction in the capital costs for a nuclear power plant, compared to other reactor types. In 1959, the U. S. Atomic Energy Commission reported on an extensive economic evaluation of seven different reactor concepts as well as organic cooled reactors with various moderators. These studies indicated that organic moderated and cooled nuclear power reactors have the lowest projected energy costs of any of the systems studied (1. 1, 1. 2).

#### 1. 1. 2 Behavior of Terphenyls When Irradiated

Organic materials, when irradiated in nuclear reactor cores, are radiolytically decomposed, due to energy released in the material by fast neutron moderation (by the hydrogen and carbon atoms) and by gamma radiation (primarily Compton interactions). Screening tests have indicated that the aromatics (materials containing the resonance-stabilized benzene ring) are the organic materials most resistant to irradiation and high temperature. As previously mentioned, it has been found that the terphenyls in particular have desirable nuclear, chemical, and physical properties for use as the primary coolant in nuclear power reactors. In previous work at several different laboratories, electron, gamma, and in-pile irradiation of these materials have been carried out to determine the processes occurring on irradiation (1. 8, 1. 10). Based on these studies, the chemical changes occurring on irradiation of the coolant are very complex and a diverse mixture of degradation products are produced. It is difficult, if not impossible, to completely characterize the chemical structure of all of these degradation products. They can, however, be divided into the following four groups based on volatility, each of which consists of a complex mixture of materials (1. 11, 1. 12):

(1) High Boiling Material consisting of components having a lower volatility than para-terphenyl. The formation of these materials, which have molecular weights ranging from around 230 (that of the terphenyls) up to about 3000 with a number average of about 460-500, is the predominant and most important process occurring on irradiation of the polyphenyl materials. These "high boilers" have a pronounced effect on the physical properties of the coolant, particularly the viscosity. This change in physical properties results in a significant decrease in the heat transfer performance of the coolant at concentrations of 30-40 wt % and above.

(2) Intermediate Boilers consisting of components other than the three terphenyl isomers, having a volatility lower than ortho-terphenyl but greater than para-terphenyl and

(3) Low Boilers consisting of compounds having a volatility greater than ortho-terphenyl. The molecular weight of the intermediate boilers is generally of the same order as that of the terphenyls (230), and that of the low boilers is generally less than that of the terphenyls. These two groups are believed to compose about 5 to 10 per cent of the degradation products and probably have no serious effect on the performance of the coolant.

(4) Non-Condensable Gases consisting of components such as hydrogen, methane, ethane, ethylene, etc., which are non-condensable at the temperatures and pressures of interest in organic cooled nuclear reactors. These gases do, however, dissolve in the organic coolant to an appreciable extent. While hydrogen gas appears to be the primary component, a large variety of saturated and unsaturated hydrocarbon gases are also produced. It should be mentioned that the line of distinction between "non-condensable" gases and "low boilers" cannot always be clearly established.

As a result of comparison of electron and gamma irradiations with in-pile irradiations, it has been established that fast neutron irradiation is significantly more effective in causing chemical

degradation of the terphenyls than is gamma irradiation (1.8, 1.13). This fact is of particular importance in estimating the organic degradation rate in an organic cooled and moderated nuclear reactor. Not only must the total energy absorption rate in the coolant due to fast neutron and gamma interactions be known, but also the fraction of the total dose rate due to each source.

### 1.1.3 Characteristics of the M. I. T. In-Pile Loop Study

The M. I. T. in-pile loop and accompanying experimental program have been designed to give quantitative information on the physical and chemical changes which occur in the irradiated organic material, as well as the effect of the degradation products on the heat transfer characteristics of the material. A large variety of organic materials can be tested at temperatures up to 800°F and pressures up to 600 psig. Dosimetry measurements have been carried out calorimetrically from which the fast neutron dose rate and the gamma dose rate in any organic material can be estimated. Extensive measurements of the thermal and fast neutron fluxes have also been made. The dose rate information is used in conjunction with chemical analyses of the coolant and measurement of the volume of gases evolved to estimate the radiolytic decomposition yield and the total gas evolution yield of the terphenyl isomers. The importance of the method used in the determination of these yields from the experimental data is stressed. Heat transfer rates at coolant velocities up to 20 ft/sec and fouling of the heat transfer surface are studied.

The loop began in-pile operation August 9, 1961. The first irradiation experiment at M. I. T. is a study of the behavior of Santowax OMP on irradiation. The loop was operated on the original batch of terphenyls without additional feed of unirradiated Santowax OMP until the concentration of degradation products in the coolant had increased from approximately 0% to 39%. At that time (October 5, 1961), unirradiated Santowax OMP was added to the loop to replace material removed by liquid sampling. The remainder of this chapter summarizes the results obtained up to this

first dilution with fresh Santowax OMP as well as the dosimetry measurements performed.

Results obtained during the irradiation which followed this date will be presented in subsequent reports issued by the M. I. T. project.

## 1.2 DESCRIPTION OF THE IN-PILE LOOP FACILITY AT M. I. T.

### 1.2.1 Introduction

The in-pile loop at M. I. T. has been designed and constructed for use in the M. I. T. Nuclear Reactor, which is a heavy water moderated and cooled research reactor presently operating at a power level of 1.8 MW. Measurements indicate that, at a power level of 1.8 MW and at the center of the core, the 2200 meter/sec thermal neutron flux and dose rate in Santowax OMP are  $2.5 \times 10^{13}$  n/cm<sup>2</sup>-sec and 0.63 watts/gm, respectively. The reactor construction is illustrated in Figure 1.2 which is a cross sectional drawing of the reactor and Figure 1.3 which is a cross section of the reactor core showing the location of the fuel elements and control rods. The in-pile volume for irradiation of the organic material is situated along the axis of the central fuel element (fuel position No. 1). The fuel element used has the eight central fuel plates of the normal 16 fuel plates removed as illustrated in Figure 1.4, which shows a cross section of the fuel element with the in-pile thimble and capsule in place. This construction leaves four fuel plates on each side of the gap into which the in-pile section fits, providing a relatively high fast neutron dose rate.

The design and operating characteristics of the loop are tabulated in Table 1.1. An additional factor which has been considered is reliability, since it was desired to perform long-term tests of the organic coolants. In Figure 1.5, the hydraulic flow diagram of the loop is given. For purposes of discussion, the loop equipment is considered to consist of three principal parts:

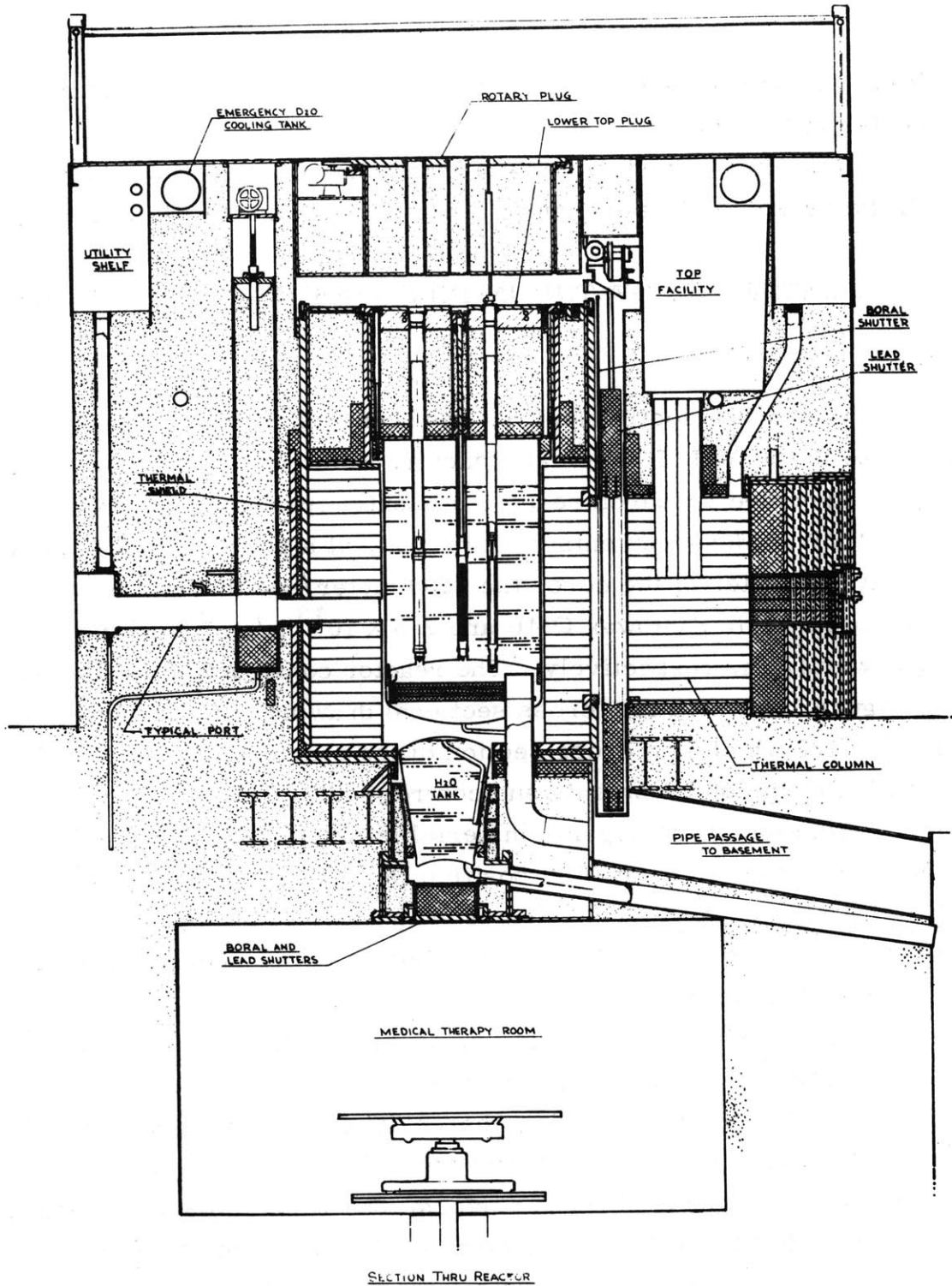


FIG. 1.2 CROSS SECTIONAL VIEW OF REACTOR ILLUSTRATING REACTOR CONSTRUCTION



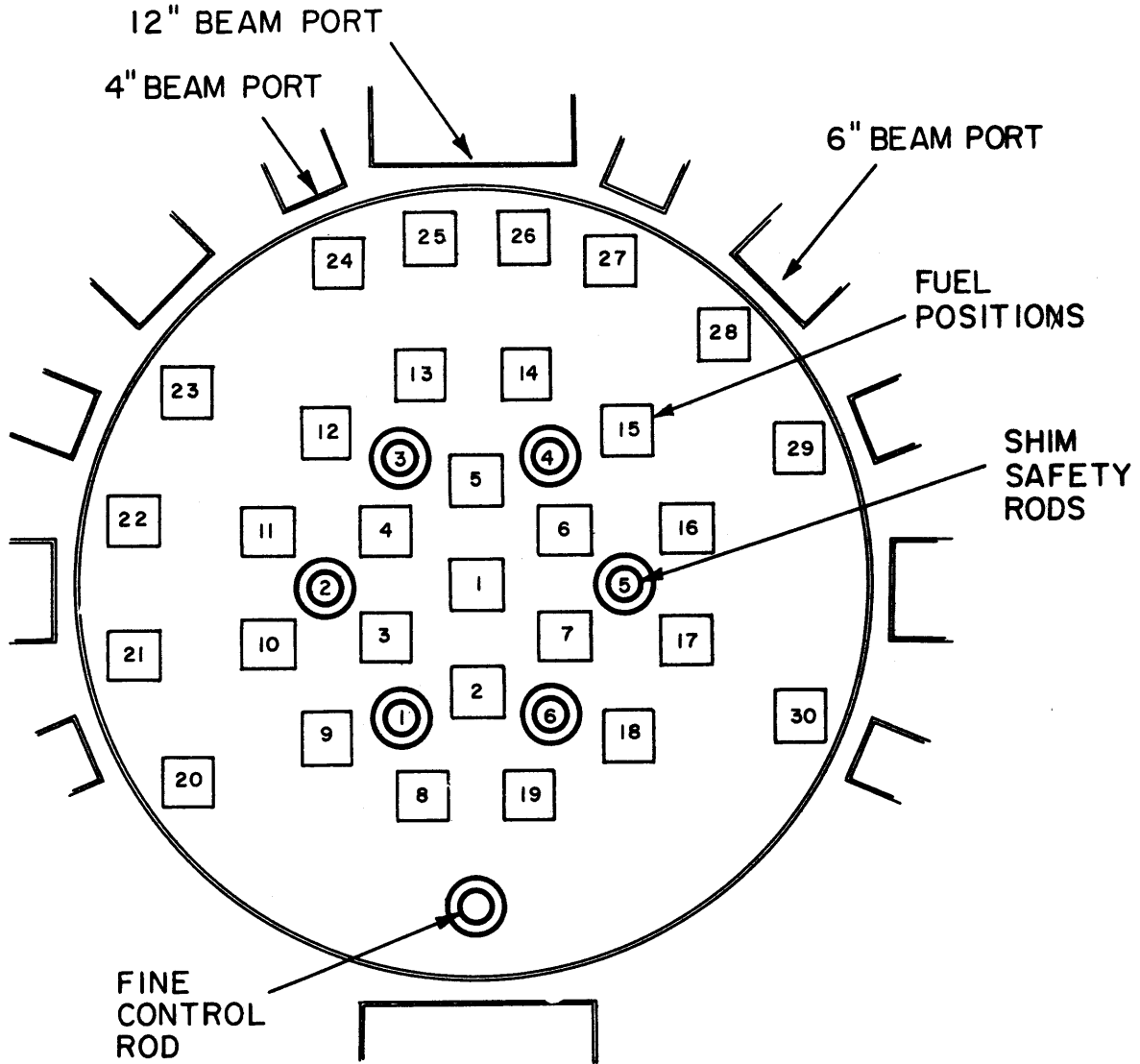


FIG. 1.3 DRAWING OF CROSS SECTION OF REACTOR CORE SHOWING POSITION OF FUEL AND CONTROL ROD POSITIONS

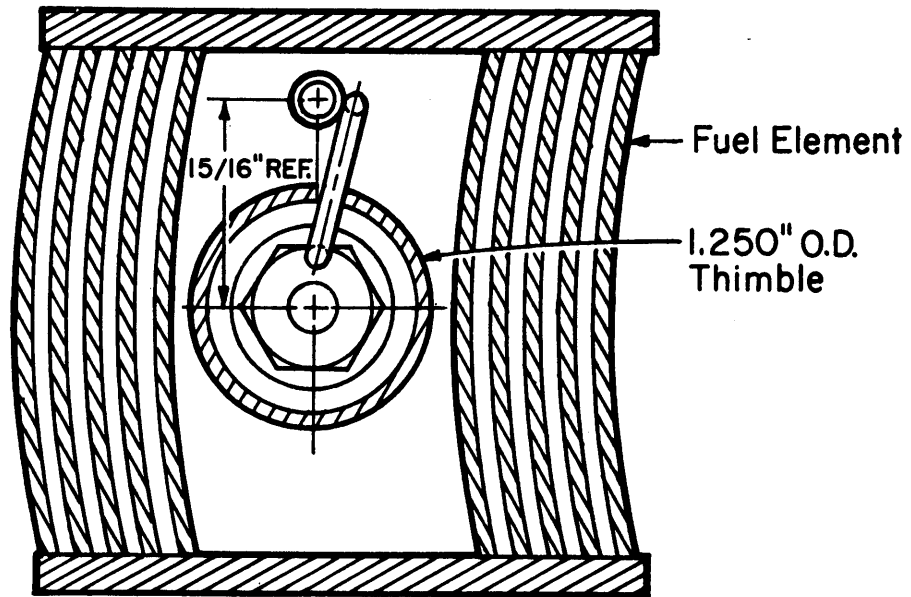


FIGURE I.4 DRAWING OF FUEL ELEMENT CROSS SECTION WITH POSITION OF IN-PILE SECTION SHOWN

Table 1. 1. M. I. T. Organic In-Pile Loop Design and Operating Characteristics.

Bulk temperature	to 800°F
Loop Pressure	to 600 psig
Materials of construction	Type 304 and 316 stainless steel
In-pile capsule volume	205 cm <sup>3</sup>
Circulating volume of one flowpath with surge tank level of 19.5 inches	5680 cm <sup>3</sup>
Maximum heat flux of test heaters	400,000 Btu/hr-ft <sup>2</sup>
Test heater wall temperature	to 1000°F
Velocity in test heater	to 20 ft/sec
Organic melting temperature	to 350°F

LEGEND

- |                            |                       |
|----------------------------|-----------------------|
| ⊗ NEEDLE VALVE (HAND)      | Ⓟ PRESSURE GAGE       |
| ⊗ DIAPHRAGM OPERATED VALVE | GG GAGE GLASS         |
| Ⓡ RUPTURE DISK             | PR PRESSURE REGULATOR |

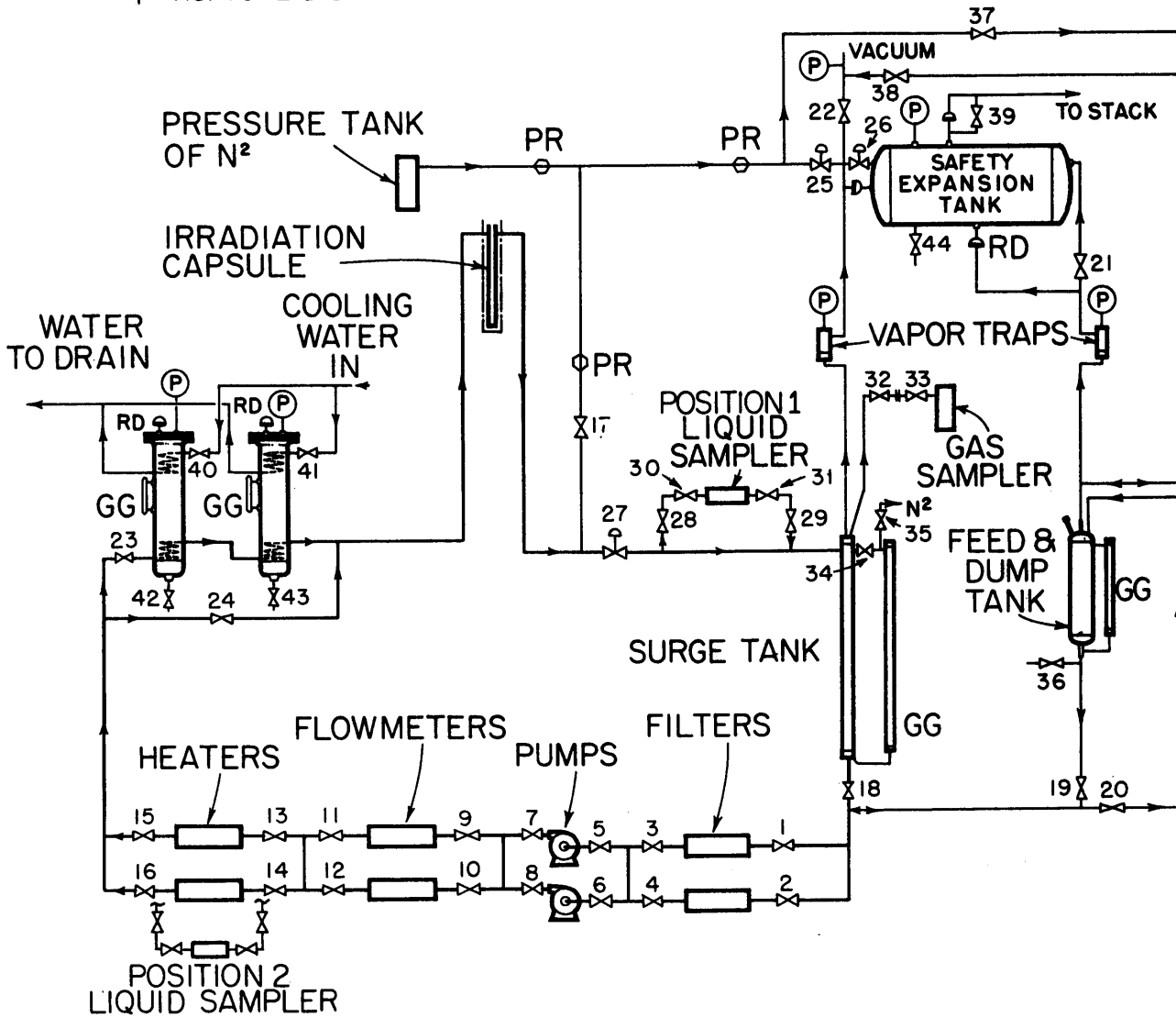


FIGURE I.5 FLOW DIAGRAM

- (1) In-Pile Section consisting of an aluminum thimble containing a stainless steel capsule to provide volumetric holdup in the reactor core.
- (2) Out-of-Pile Section consisting of pumps, flowmeters, valves, and other equipment necessary for operation of the loop. Provision is included for heat transfer measurements and liquid and gas sampling.
- (3) Instrumentation for monitoring and control of the loop operation.

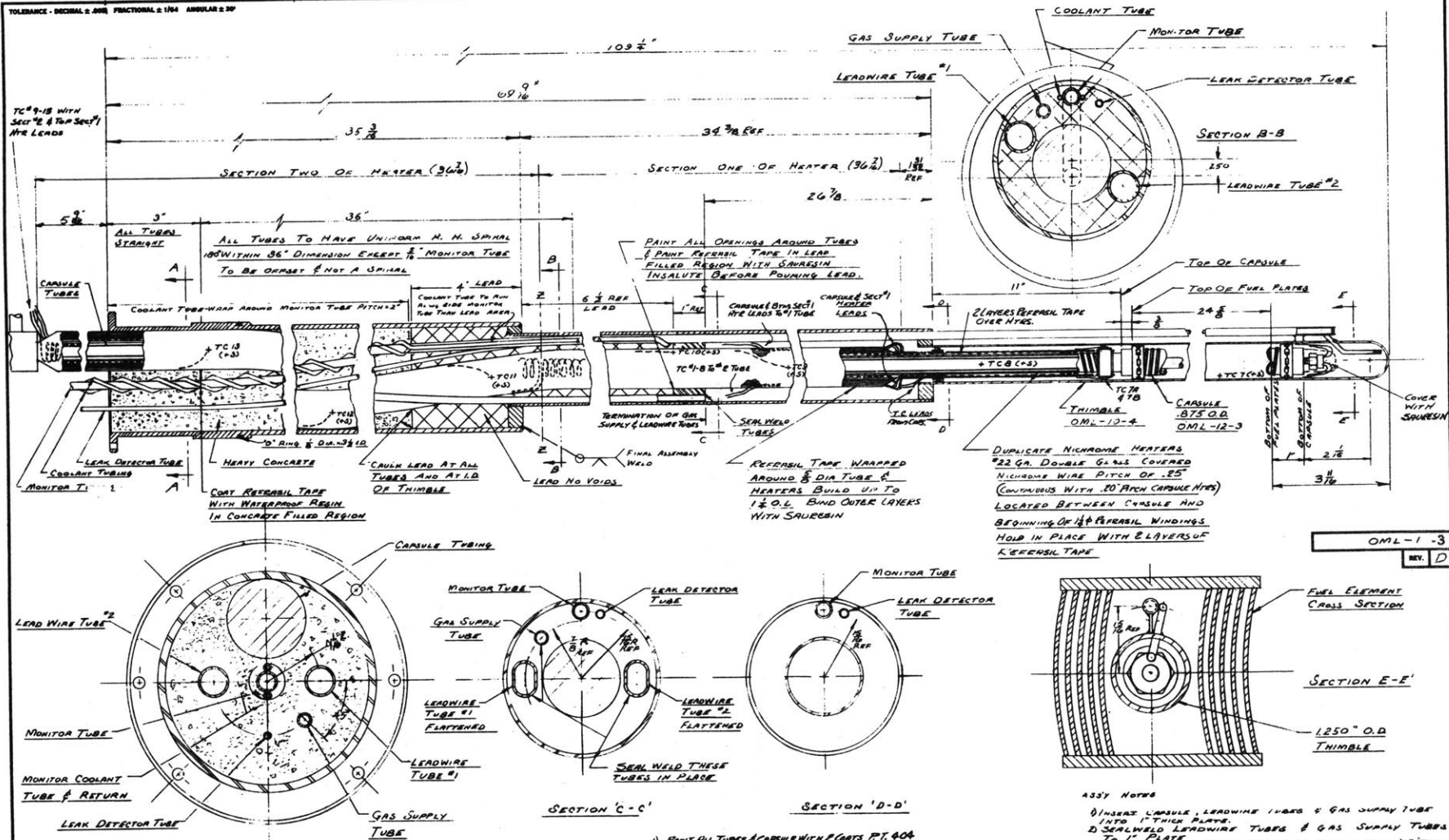
A brief description of these different parts is presented in the following sections.

### 1. 2. 2 In-Pile Section

As mentioned previously, the in-pile section is designed to fit down the axis of the central fuel element from which eight of the normal 16 fuel plates have been removed. This provides space in the fuel element sufficient for a 1-1/4 inch maximum diameter thimble with four fuel plates on each side to provide a large fast neutron dose rate. The in-pile section used in the present case consists of a 1-1/4 inch OD  $\times$  0.035 inch wall aluminum thimble containing a stainless steel capsule (7/8 inch OD  $\times$  0.035 inch wall) which provides 205 cm<sup>3</sup> of organic holdup in the reactor core. The aluminum thimble is used to separate the D<sub>2</sub>O of the reactor from the hot organic holdup capsule.

In Figure 1.6, the assembly of the thimble, irradiation capsule, and inlet-outlet lines for flow of organic to and from the capsule is illustrated. This entire in-pile section is constructed as a single unit and is inserted inside a specially constructed lower shield plug and upper fuel element adapter (see Chapter 3 for details). The lower part of the assembly which extends into the fuel element is centered in the fuel element by the upper and lower fuel adapters. The cross sectional position of the thimble in the fuel element may be seen by reference to section E-E of Figure 1.6. The fuel element assembly is illustrated in Figure 1.7, along with the in-pile section which fits

TOLERANCE - DECIMAL 2.000 FRACTIONAL 2.100 ANGULAR 2.000



NOTE!  
HEAVY CONCRETE TO HAVE A DENSITY GRADE TO 200 PPM THICK 1/4 IN. MAGNETITE SAND - 2000 1000 POUNDS - 4160 PORTLAND CEMENT - 775

- SECTION 'A-A'
- (1) MONITOR TUBE 1/2 O.D. x .035 WALL 3052-0 AL
  - (2) MONITOR COOLANT TUBE 3/8 O.D. x .015 WALL 3052-0 AL
  - (3) LEAK DETECTOR TUBE 1/2 O.D. x .030 WALL 3052-0 AL
  - (4) GAS SUPPLY TUBE 1/2 O.D. x .030 WALL 3052-0 AL
  - (5) LEADWIRE TUBE 1/2 O.D. x .030 WALL 3052-0 AL

- 1) PAINT ALL TUBES & CAPSULE WITH 2 COATS P.T. 404
- 2) BEFORE & AFTER ASSY ALL HEATER & THERMOCOUPLE CIRCUITS MUST BE CHECKED FOR CONTINUITY & LACK OF SHORTS
- 3) DIVIDE HEATER COIL INTO TWO PARTS. SECTION ONE FROM BOTTOM TO LINE Z-Z, LENGTH APPROX (36 3/4) SECTION TWO FROM LINE Z-Z TO LENGTH APPROX (36 3/4) EACH HEATER 22 GA DOUBLE GLASS COVERED NICHROME WIRE, 55" NICHROME WIRE PER HEATER, WINDING PITCH OF APPROX 0.11" HTS TO BE COVERED WITH PERID PREHEAT SLEEVING & PROVIDED IN DUPLICATE - LOOP ENDS 3" & SOLDER UNDER TO DOUBLE GLASS INSULATED NICKEL PLATED COPPER WIRE (HOT LEADS). SEE DETAIL ON DWG OML-12-B
- 4) HEATER LEADS TO BE GROUNDED IN #1 LEADWIRE TUBE & THERMOCOUPLE LEADS #1 THRU #2 LEADWIRE TUBE & LEAD WIRE TUBE #2 THRU #3 LEADWIRE TUBE UNDER OUTER LAYER OF TUBES
- 5) SEE CAPSULE DWG FOR ADDITIONAL DATA ON THERMOCOUPLES & HEATERS

- ASSY NOTES
- 1) INSERT CAPSULE, LEADWIRE LEADS & GAS SUPPLY TUBE INTO 1" THIMBLE
  - 2) SEALWELD LEADWIRE TUBES & GAS SUPPLY TUBES TO 1" PLATE
  - 3) POSITION CAPSULE & PULL ALL LEADS THRU 1/2" TUBES
  - 4) PASS MONITOR TUBE & LEAK DETECTOR TUBE THRU HOLES IN 1" PLATE & SLIDE ASSEMBLY INTO LOWER HALF OF THIMBLE
  - 5) PAINT SPIRALS & OXIDIZERS IN TUBES
  - 6) POSITION COILING COIL ON MONITOR TUBE
  - 7) PAINT WITH SAUREGIN
  - 8) POUR LEAD
  - 9) COAT REFRASIL TAPE WITH WATERPROOF RESIN
  - 10) MAKE FINAL ASSEMBLY WELD
  - 11) POOR CONCRETE

REV.	DESCRIPTION	BY	DATE
D	Re BUINY	OL	4/6/53
C	MONITOR TUBE MTS - 100 MTS	WAL	3/24/53
B	REVISION: THIMBLE & LEAD WIRE TUBE	WAL	10/15/52
A	ORIGINAL DRAWING	WAL	1/1/53

MATERIAL	QUANTITY
3-2-50	P.C.
DATE	DRAWN BY

MASSACHUSETTS INSTITUTE OF TECHNOLOGY REACTOR  
FIG. I.6 ASSEMBLY OF THIMBLE AND ORGANIC HOLDUP CAPSULE

OML-1-3  
REV. D

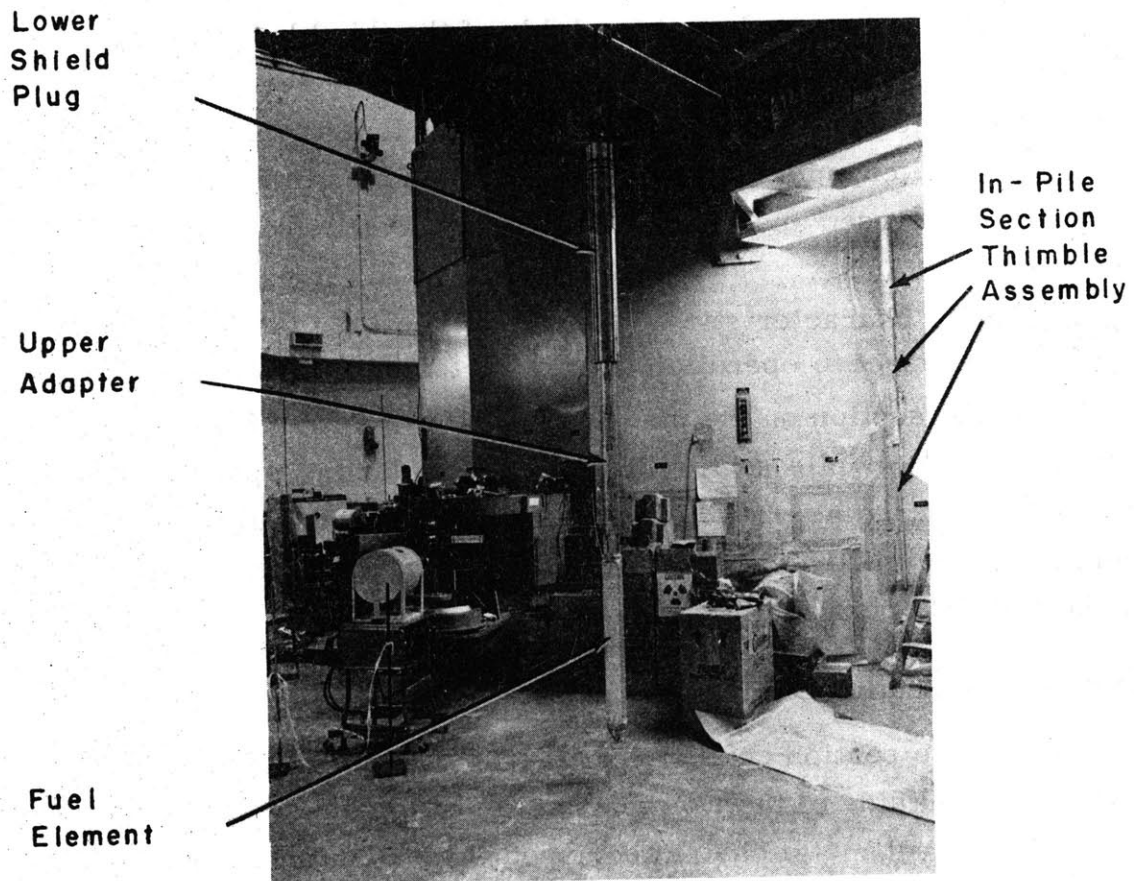


FIG. I.7 FUEL ELEMENT ASSEMBLY AND IN-PILE SECTION THIMBLE ASSEMBLY

down the inside of the fuel element assembly.

To monitor the fast and thermal neutron fluxes in the reactor core while the reactor and loop are operating, a 5/16 inch OD X 0.035 inch wall aluminum tube is provided on the outside of the thimble beside the holdup capsule, as illustrated in Figure 1.6. At any reactor power, various types of detectors may be shoved down this tube from the reactor top until opposite the capsule and removed after completion of the irradiation. The detectors used and measurements performed are described in section 1.3.

One important characteristic of the in-pile section is the reactivity effect, both with respect to operation of the reactor and to estimation of the effect of the in-pile section on the measured dose rates (which were measured without the in-pile section in place due to lack of space). The reactivity was measured as  $-940 \pm 25$  milli-beta without organic which is well under the  $\pm 1330$  milli-beta limit permitted per experiment in the MITR by the USAEC operating license.

### 1. 2. 3 Out-of-Pile Section or Hydraulic Console

The out-of-pile section consists of all loop components containing organic which are outside of the reactor shield. All of these components are enclosed in a sheet metal cabinet equipped with an automatic fire extinguisher because of the flammable nature of the organics to be tested. The equipment contained in this cabinet is tabulated in Table 1.2 (see also the flow sheet, Figure 1.5). For additional detail, reference is made to Chapter 3. In Figure 1.8, a photograph of the front of the hydraulic console is given before installation of the thermal insulation.

### 1. 2. 4 Instrumentation

One primary instrument panel illustrated in Figure 1.9 and two auxiliary panels are used in operation of the loop. The primary panel is located on the loop platform and contains instruments for measuring and monitoring loop temperatures, flow rate, and electrical power input to the test heater, as well as controls for all electrical equipment. One



Table 1.2. Tabulation of Out-of-Pile Components of Loop  
Comprising Hydraulic Console.

Component	Purpose	Description
Surge tank	Provide holdup of excess organic for sampling and for temperature expansion. Also has gas space in which gases evolved collect.	Tank with total volume of 1450 cm <sup>3</sup> and having volume per unit inch of length of 61.1 cm <sup>3</sup> /inch.
Filters	Remove particulates from coolant.	One filter has sintered stainless steel element with 98% removal rating of 55 microns. Other has element with 98% removal rating of 2 microns.
Pumps	Circulate organic at rates up to 2 GPM equivalent to velocity of 20 ft/sec through test heater.	Chempump Model CFHT-3-3/4S canned rotor stainless steel pumps
Flowmeters	Measure volumetric rate of organic flow.	3/8 inch Potter turbine-type volumetric flowmeter.
Test heaters	Measure heat transfer coefficients.	1/4 inch OD X 0.020 inch wall stainless steel tube heated by passage of up to 450 amps through two sections, each 12 inches in length. Thermocouples are welded to test heater wall for temperature measurements.
Main loop coolers	Remove excess energy introduced during heat transfer measurements.	Reflux condenser type using Dowtherm A as cooling medium with water-cooled coil as condenser.
Sampling stations	To take liquid and gas samples.	Gas sample--taken in stainless steel capsule from surge tank. Liquid sample--taken in stainless steel capsule substituted for test heater and through which organic flows before sample is collected.

Table 1. 2 (continued)

Component	Purpose	Description
Feed and dump tank	To melt organic prior to charging to loop and to collect organic discharged from loop.	Tank with total volume of 5200 cm <sup>3</sup> and volume per unit length of 223 cm <sup>3</sup> /inch.
Safety expansion tank	Rapid depressurization of loop in case of emergency involving danger to reactor or personnel.	Tank volume $\cong$ 7 ft <sup>3</sup> .
Pressurizing system	To provide high pressure nitrogen gas for pressurizing loop.	Purified nitrogen gas cylinder plus regulators and valves for control.
Valves	Control of organic flow.	Bellows-sealed stainless steel valves.
Pressure gages	Measure pressure in surge tank and feed and dump tank.	Diaphragm type pressure probes connected to gage by capillary tube.
Trace heaters	Melt Santowax OMP for operation of loop (M. P. = 314°F).	Double glass insulated heating tapes.

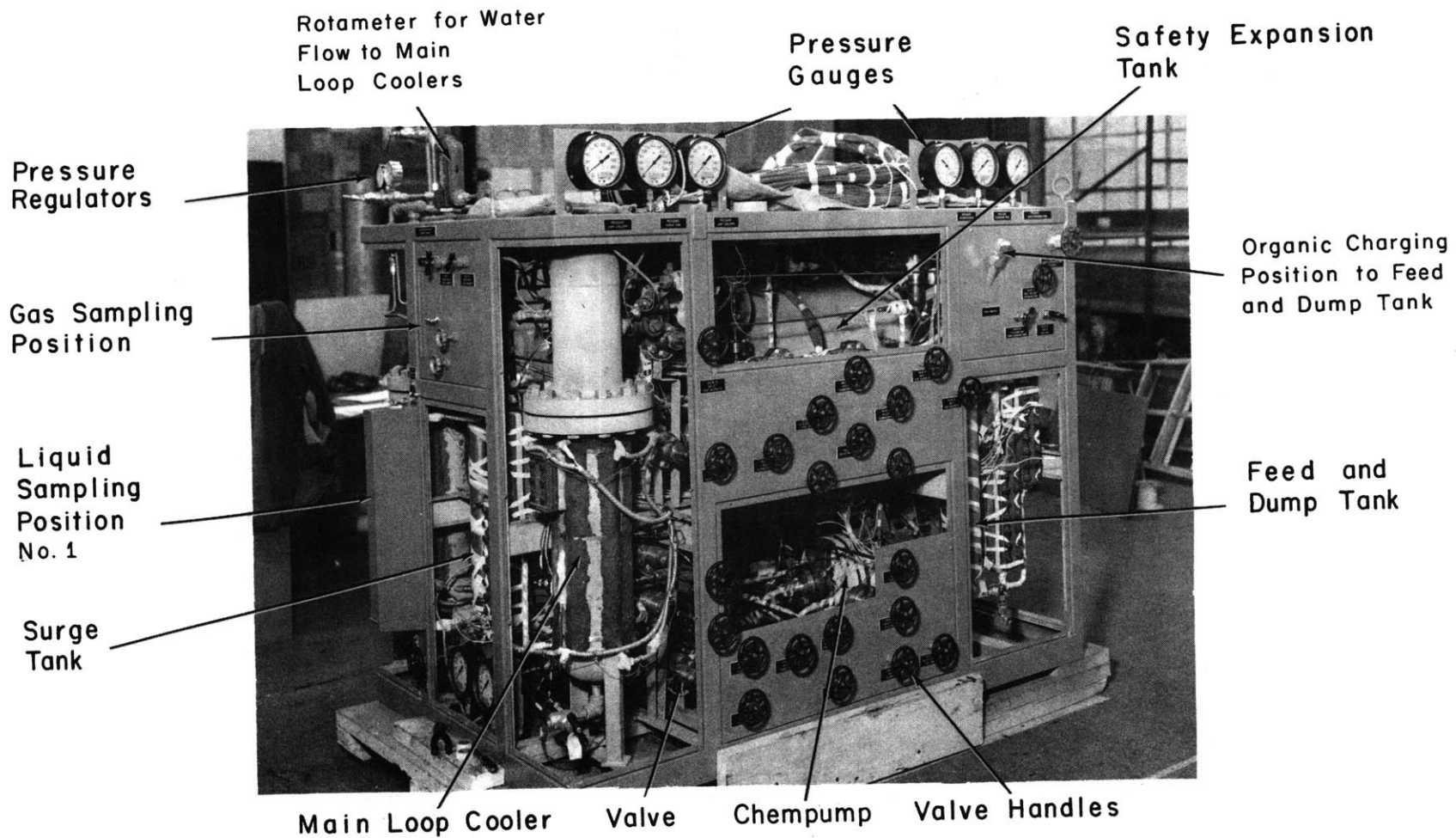


FIG. 1.8 FRONT AND LEFT SIDE OF HYDRAULIC CONSOLE - BEFORE INSTALLATION OF THERMAL INSULATION, PANELS REMOVED

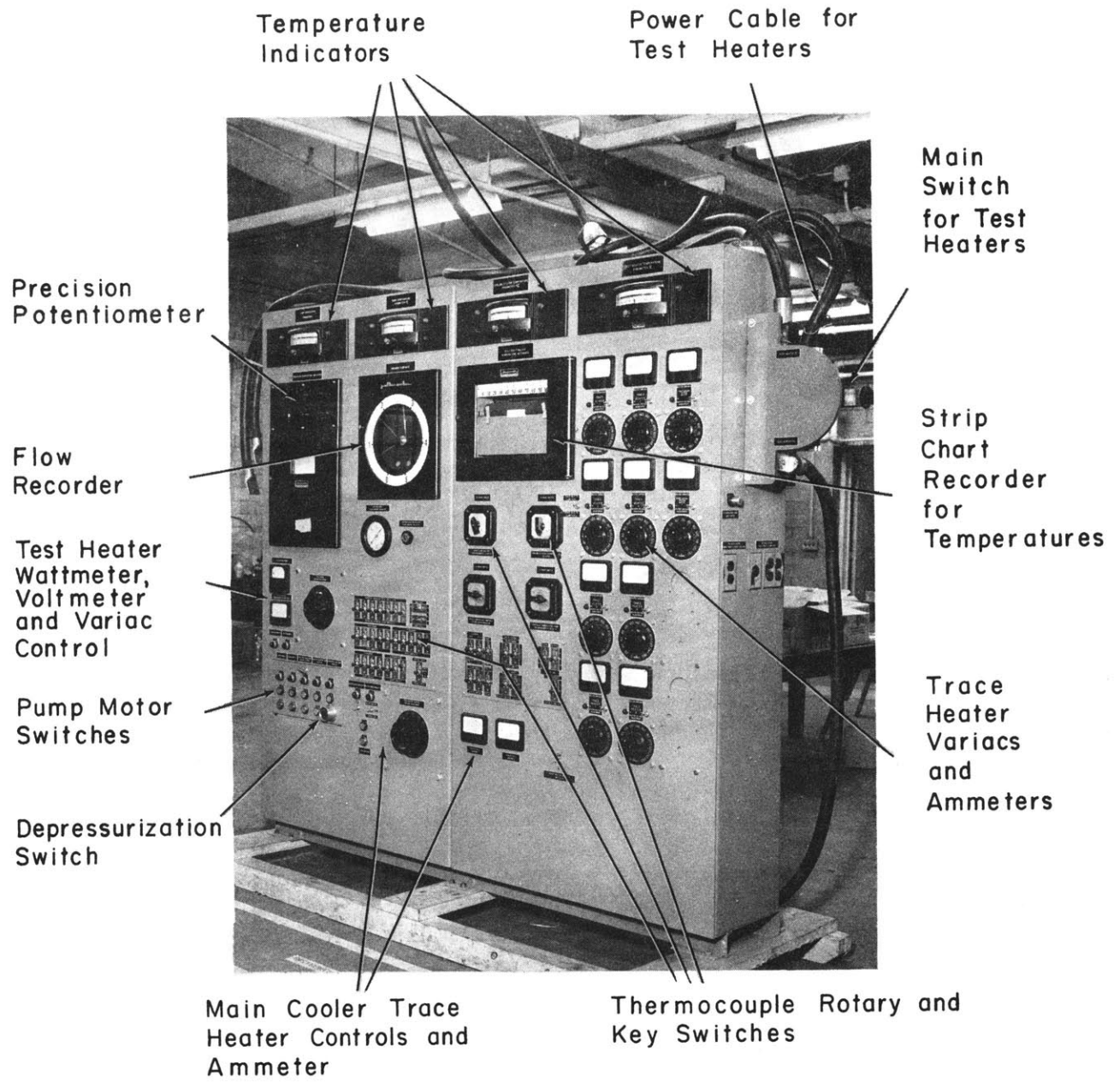


FIG. I.9 PRIMARY INSTRUMENT AND CONTROL PANEL

of the auxiliary panels is located in the reactor control room to provide information to the reactor operators on the operating behavior of the loop. The other supplements the primary instrument panel. The principal functions of the instruments and circuits provided are given in Table 1. 3.

#### 1. 2. 5 Location of Equipment on Reactor

In Figure 1. 10, a schematic is presented showing the location of the in-pile and out-of-pile equipment on the M. I. T. nuclear reactor. The primary instrument panel, one auxiliary panel, and the hydraulic console are supported on a special platform, 10-1/2 feet above the reactor floor. In Figure 1. 11, a photograph is given, illustrating the primary instrument panel and hydraulic console in position on this platform.

### 1. 3 MEASUREMENT OF DOSE RATE IN ORGANIC MATERIALS IN FUEL POSITION NO. 1 OF THE MITR

#### 1. 3. 1 Introduction

As previously mentioned, when organic materials are placed in the radiation field of a nuclear reactor, energy is absorbed in the material due to fast neutron moderation by the hydrogen and carbon atoms of the organic and to gamma interactions in the material. The energy absorbed in the organic by these processes leads to chemical changes in the coolant. One important phase of this study is the relation of the chemical changes produced in the irradiated organic coolant to the absorbed energy due to fast neutron and gamma interactions in the coolant. In addition, since previous work (1. 8, 1. 13) has indicated that fast neutron radiation is considerably more effective in causing chemical changes in the polyphenyls than gamma radiation, it is necessary to know not only the total radiation energy absorbed in the coolant, but also the fraction of this energy caused by fast neutron interactions and the fraction caused by gamma interactions.

Table 1. 3. Tabulation of Instrumentation Provided for Operation of Loop

Instrument	Purpose
Twelve-point strip chart potentiometric recorder.	Measure and record the organic bulk temperature at several positions around the loop and the test wall temperature. It is equipped with Hi-Lo limit switches which are used for alarm purposes and to cut off the test heater if an excessive temperature is reached. This instrument is also used for control of the trace heaters during the weekend when there are no reactor or loop personnel present to monitor loop operation.
Millivoltmeter-type temperature indicators.	<p>Pyrometer I - Used with 24-point thermocouple switches to monitor various temperatures throughout the loop. Hi-Lo alarms provided.</p> <p>Pyrometer II - Monitor pump motor temperature to prevent shutdown of the pump due to excessive temperatures. Hi-Lo alarms provided.</p> <p>Pyrometer III - Used with 6-point thermocouple switch to monitor operation of the two main loop coolers and the pump-cooling systems.</p> <p>Pyrometer IV - Monitor test heater temperature. Hi-Lo alarms and an automatic cutoff for the test heater power, if excessive temperatures are encountered, are provided.</p> <p>Pyrometer V - Provided on auxiliary panel in reactor control room with 8-point switch for reading various temperatures around loop.</p>
Flowrate indicator	The turbine-type flowmeters are used with a circular chart recorder to monitor the organic flowrate. Hi-Lo alarms are provided.
Precision potentiometer	An automatically balanced precision potentiometer (accuracy = $\pm 2$ microvolts) is used for measuring the heater wall and bulk organic temperatures for heat transfer measurements.

Table 1. 3 (continued)

Instrument	Purpose
Precision indicating wattmeter (range 0-15 kw).	Used for measuring power input to test heater circuits during heat transfer measurements.
Precision voltmeter (range 0-7.5 and 0-15 volts A. C.).	Used to measure voltage at various points throughout test heater circuits for estimating power input into test heater during heat transfer measurements.
Alarm system.	Used in conjunction with Hi-Lo limit switches on instruments to provide visual and audio indication of abnormal operation of loop.
Variacs and ammeters.	To control and indicate power input to all trace heater circuits, the heaters on the main loop coolers, and the heaters on the pump cooling system.

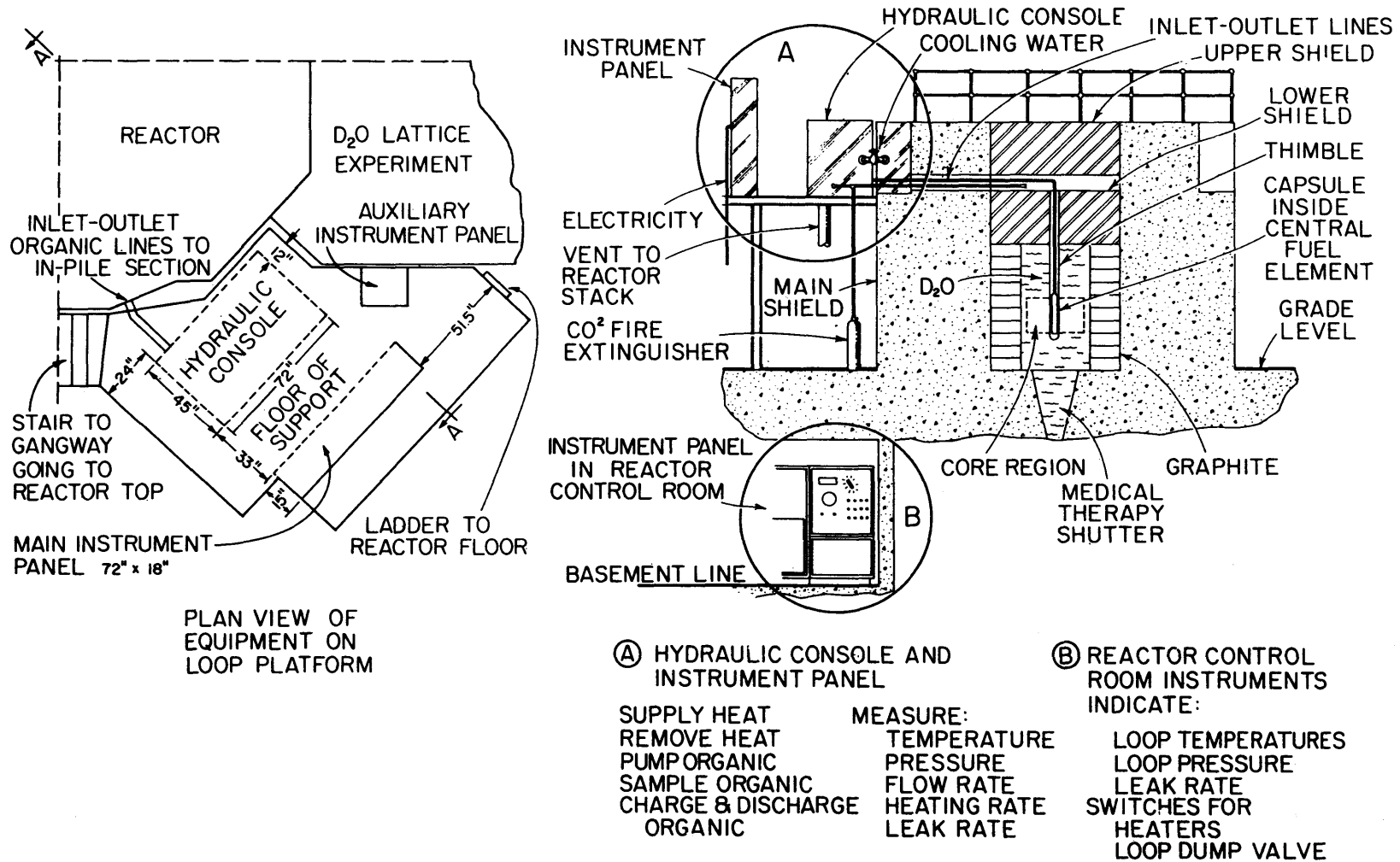


FIGURE I.10 SCHEMATIC SHOWING LOCATION OF LOOP IN THE M.I.T. NUCLEAR REACTOR



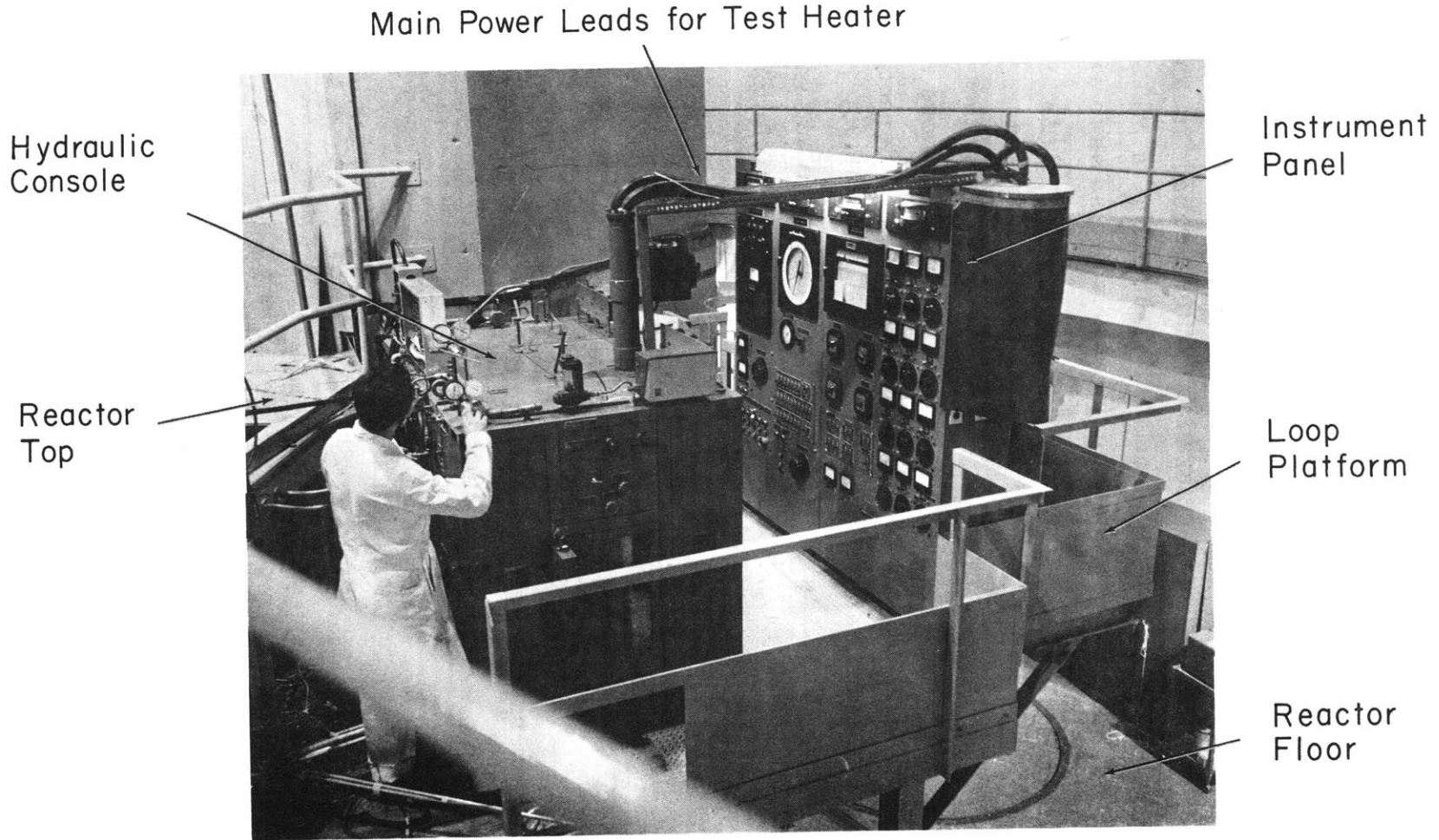


FIG. I.II HYDRAULIC CONSOLE AND INSTRUMENT PANEL IN POSITION ON PLATFORM IN REACTOR ROOM

With these objectives in mind, calorimetric measurements of the dose rate in aluminum, polyethylene, polystyrene, beryllium, and Santowax OMP have been made along the axis of the central fuel element (fuel position No. 1) of the MITR. The measurements were not made with the in-pile section in place due to the limited space available but were made inside aluminum and stainless steel thimbles inserted in place of the in-pile section. The dimensions of the stainless steel thimble were selected so as to approximate the reactivity and flux depression of the in-pile section, and the estimated dose rates in Santowax OMP in the in-pile section are based on the measurements in this thimble. From the measured dose rates in the different materials, it is possible to estimate the fraction of the dose rate due to fast neutron interactions and the fraction due to gamma interactions.

In addition to the calorimeter measurements, measurements of the thermal, epithermal, and fast neutron fluxes have been made, using various wire flux monitors. These measurements have aided the interpretation of the calorimeter results.

### 1. 3. 2 Method of Calorimeter Measurements

The method of calorimetry used was the measurement of the adiabatic rate of temperature rise in the materials for which the dose rate was desired. From this rate of temperature rise, the dose rate was calculated by:

$$R^T = C \left( \frac{dT(t)}{dt} \right)_{q=0} \frac{\text{watts}}{\text{gm}} \quad (1. 1)$$

where

$R^T$  = total dose rate in material, watts/gm.

$C$  = heat capacity of material, watt-sec/gm-°C.

$T(t)$  = temperature, °C, as a function of time,  $t$ .

$\left( \frac{dT(t)}{dt} \right)_{q=0}$  = adiabatic rate of temperature rise, °C/sec.

The method of measuring the adiabatic rate of temperature rise used in these experiments is unique in that it permits simultaneous measurements on several different materials to be made and does not require maintenance

of a zero  $\Delta T$  between the capsule wall (surrounding the sample) and the sample. In perfecting the technique, three different adiabatic calorimeters have been used, all of which were based on the same principle but each of which was constructed in a slightly different manner. In each of these calorimeters, the different samples were suspended inside an aluminum capsule as shown in Figures 1. 12 and 1. 13, which illustrate calorimeter II. Two thermocouples were placed on the centerline of each absorber and three thermocouples were placed on the aluminum capsule, one at the center and one at each end. The samples were thermally insulated by evacuating the capsule to reduce conduction losses and by vacuum coating the samples with a thin layer of aluminum to reduce thermal radiation losses. The samples were suspended in the capsule by means of 1/16-inch polystyrene pins and polystyrene discs. A polyethylene tube was connected to the calorimeter and extended to the outside of the reactor. This tube permitted evacuation of the calorimeter and was used to move the calorimeter to various positions in the reactor core. The thermocouple leads also passed up this tube.

To perform a dose rate measurement, the calorimeter was suspended inside a thimble inserted along the axis of the central fuel element in the reactor core as previously described. The equipment layout is illustrated schematically in Figure 1. 14. Between calorimeter measurements, the calorimeter was pulled into a recess in the lower shield out of the main radiation field for cooling the sample in preparation for the next measurement. When the capsule and absorber temperatures had cooled to about the shield temperature, which was approximately  $5^{\circ}\text{C}$  lower than the  $\text{D}_2\text{O}$  reactor coolant, the calorimeter was evacuated and rapidly lowered by means of the polyethylene tube to the desired axial position in the fuel element. The capsule wall and sample temperatures were then read and recorded once per minute. Due to rapid heat transfer between the walls of the calorimeter capsule and the thimble, as well as energy generated in the capsule by radiation absorption, the capsule wall temperature initially rose rapidly until it exceeded the  $\text{D}_2\text{O}$  temperature and

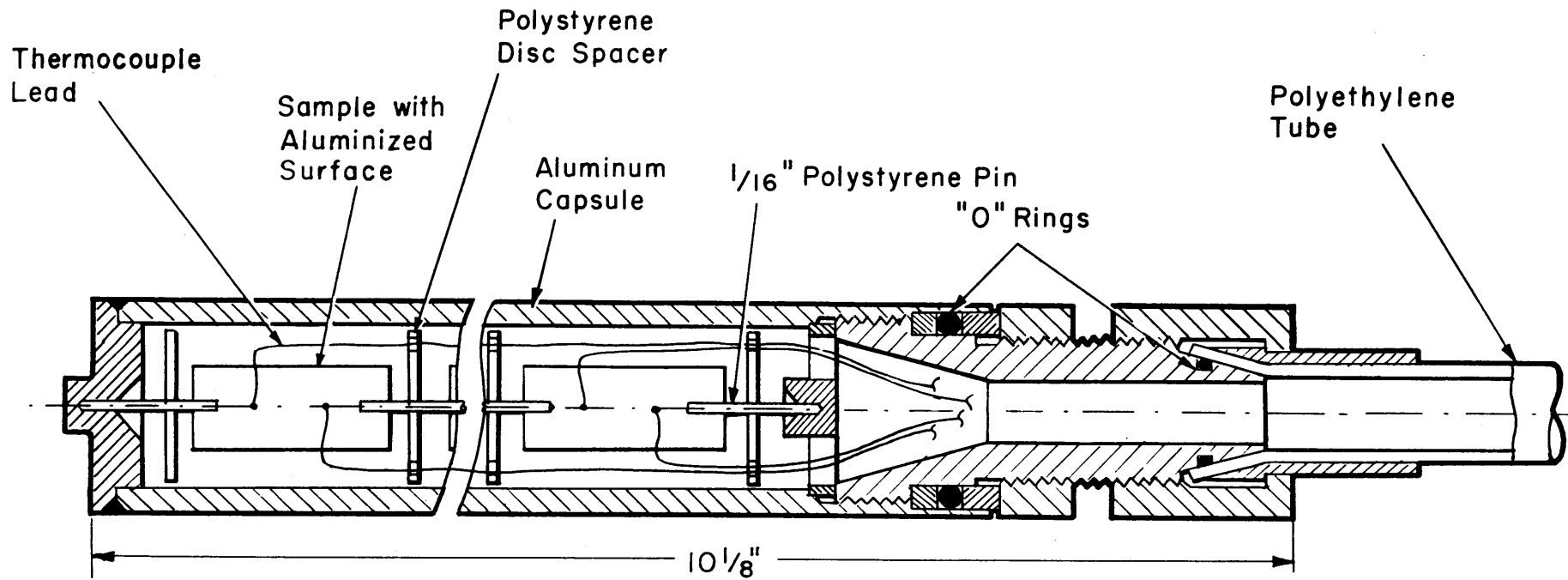


FIG. I.12 ASSEMBLY DRAWING OF CALORIMETER II

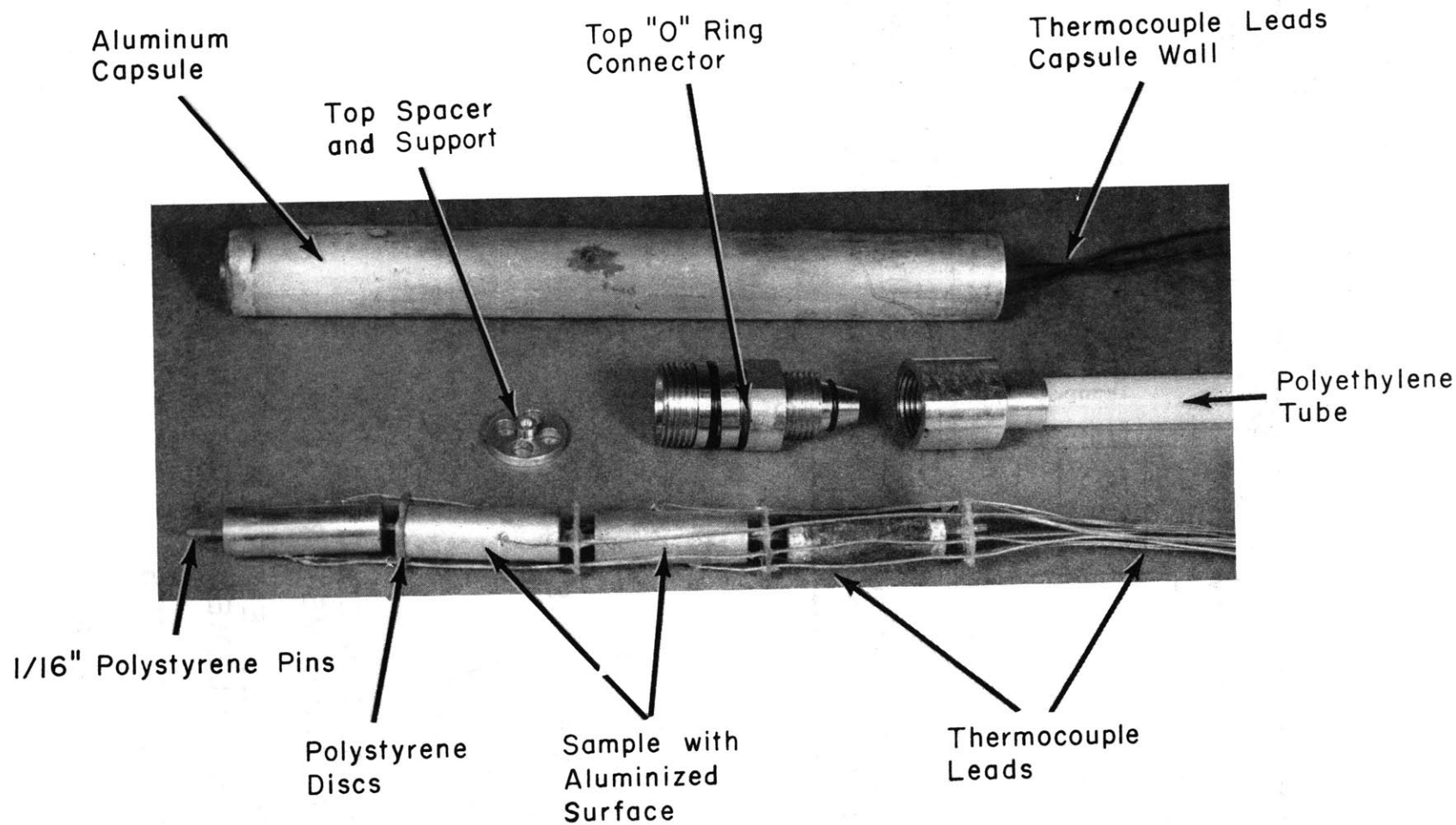


FIG. I.13 PHOTOGRAPH OF CALORIMETER II

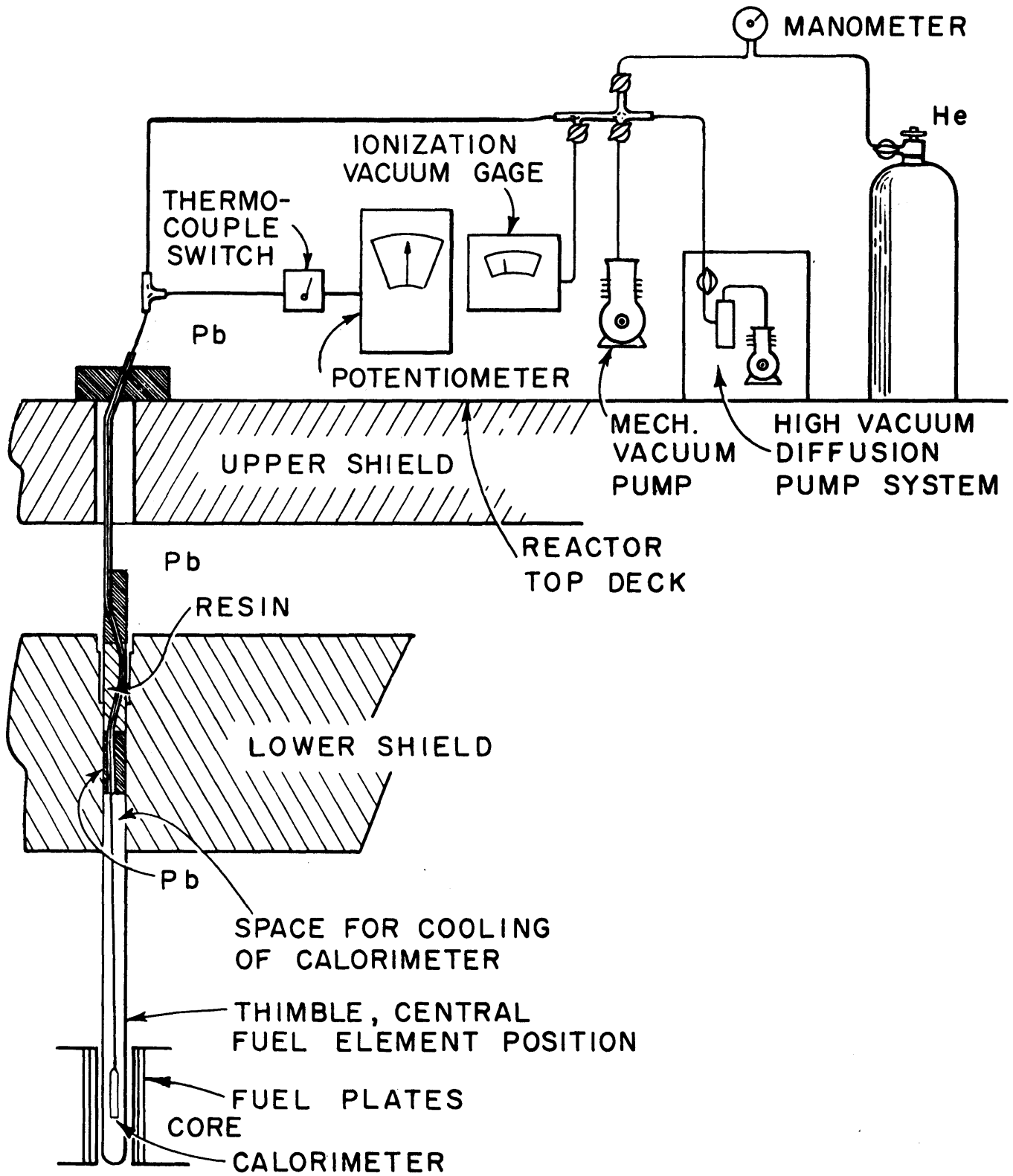


FIG. I.14 SCHEMATIC OF CALORIMETER EQUIPMENT LAYOUT

then slowly approached an asymptotic value at which the energy generated in the capsule wall by radiation absorption was equalized by heat losses to the thimble. The sample temperature, on the other hand, initially rose more slowly than the capsule temperature, but eventually equaled and then exceeded the capsule wall temperature. At the position where the sample and capsule wall temperatures were equal, no heat was transferred to or from the absorber and the slope of the sample temperature vs. time curve at this point is the adiabatic rate of temperature increase. A typical temperature vs. time curve is given in Figure 1.15. Most of the calorimeter measurements were made at reactor power levels of 50 and 100 kw, with a few measurements at 200 and 500 kw. With the present instrumentation which required manual reading of the thermocouples, measurements could only be made at these low powers, since the rate of temperature rise of the absorbers would be too fast to measure conveniently at high reactor powers.

To minimize the gamma background from fission product decay from previous full power reactor operation, the calorimetric dose rate measurements were made Monday mornings after the regular weekend shutdown of approximately 2-1/4 days. The gamma background present at this time (approximately 5 to 10 per cent of the total dose rate at 100 kw) was subtracted from the measurements so that extrapolation of the results to different reactor power levels could be made. The gamma background was measured before each series of calorimeter measurements was started. In addition, in the first series of measurements made, the fission product decay was measured over the entire weekend to get a decay curve which could be extrapolated over the time required for each series of measurements.

### 1. 3. 3 Method of Estimating Fast Neutron and Gamma Dose Rate in Santowax OMP

The dose rate in Santowax OMP can be expressed by the following relation:

$$R_{SW}^T = R_{SW}^\gamma + N_H^{SW} I_H + N_C^{SW} I_C \quad (1. 2)$$

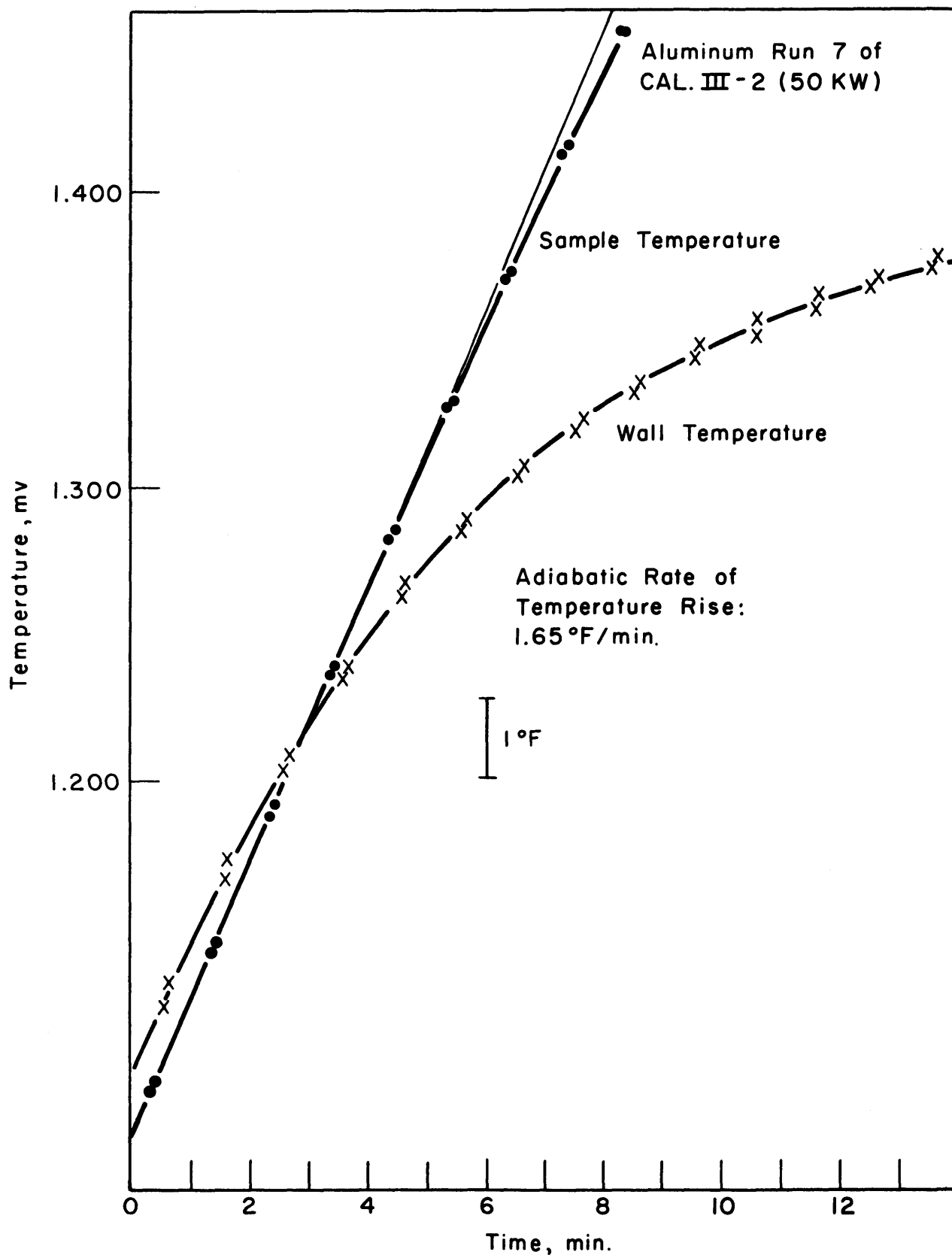


FIG. 1.15 TYPICAL EXAMPLE OF THE TIME VARIATION OF THE TEMPERATURE OF A SAMPLE AND OF THE WALL OF THE CALORIMETER IN THE CENTER OF THE CORE



where

$$I_j = g_j F \int_0^{\infty} \sigma_s^j(E) \phi(E) E dE \frac{\text{watts}}{\text{atom}} = \text{energy transfer integral}$$

where j refers to either hydrogen or carbon.

$$R_{SW}^T = \text{total fast neutron and gamma dose rate in Santowax OMP, watts/gm.}$$

$$R_{SW}^\gamma = \text{gamma dose rate in Santowax OMP, watts/gm.}$$

$$F = \text{conversion factor, ev/sec-gm to watts/gm.}$$

$$g_H, g_C = \frac{2A_H}{(A_H+1)^2}, \frac{2A_C}{(A_C+1)^2} = \text{average fraction of the neutron energy lost on collision with a hydrogen or carbon atom, respectively.}$$

$$A_H, A_C = \text{atomic weights of hydrogen and carbon, respectively.}$$

$$N_H^{SW}, N_C^{SW} = \text{atoms/gm of hydrogen and carbon, respectively, in Santowax OMP.}$$

$$\sigma_s^H(E), \sigma_s^C(E) = \text{scattering cross section of hydrogen and carbon, respectively, as a function of neutron energy, cm}^2.$$

$$\phi(E) = \text{neutron flux per unit energy, n/cm}^2\text{-sec-ev.}$$

$$E = \text{neutron energy, ev.}$$

Values of  $R_{SW}^\gamma$ ,  $I_H$ , and  $I_C$  are the quantities to be determined from the calorimeter measurements.

In order to determine  $R_{SW}^\gamma$ ,  $I_H$ , and  $I_C$ , calorimetric measurements of the dose rate in aluminum, polyethylene, and polystyrene were used. (Measurements in beryllium and Santowax OMP were also made, but uncertainty in the heat capacity values for these materials limited the reliability of these results and they were not used in determining  $R_{SW}^\gamma$ ,  $I_H$ , and  $I_C$ .) Following the same procedure for these materials as for Santowax OMP, the following generalized relation for the dose rate can be written:

$$R_i^T - R_i^{th} = R_i^\gamma + \sum_j N_j^i I_j \quad (1. 3)$$

where  $R_i^{th}$  = dose rate in material due to thermal neutron interactions, watts/gm. Some refinements can be made to this equation, based on consideration of the nuclear processes occurring. For the gamma interactions, since only low  $Z$  materials ( $Z \leq 13$ ) have been used, Compton collisions are the predominant and controlling mode over a wide range of gamma energies. Hence, it would be expected that the assumption that all gamma interactions are Compton collisions is reasonable. With this assumption, the relative gamma dose rate in the different materials can be shown to be:

$$\frac{R_1^\gamma}{R_2^\gamma} = \frac{(Z_{avg}/A)_1}{(Z_{avg}/A)_2} \quad (1. 4)$$

where

$Z_{avg}$  = average atomic number for materials 1 and 2, respectively, electrons/molecule or atom.

$A$  = atomic or molecular weight of material, grams/gram molecule, for materials 1 and 2.

This assumption has been checked by calculating the relative gamma dose rates in the materials of interest due to photoelectric, Compton, and pair production reactions. These calculations are described in Chapter 4 and Appendix 4.4 and are based on use of a gamma spectrum from the fission process as reported by Goldstein (1.14). Attenuation of the gamma spectrum by the stainless steel thimble and aluminum calorimeter capsule was used in these calculations in approximation of the actual geometry of the calorimeter measurements; this procedure provides an effective cutoff on the low energy end of the spectrum of approximately 0.05 Mev. The results obtained by this calculation are summarized in Table 1.4 where it can be seen that the ratios of  $R_H^\gamma/R_{A1}^\gamma$  and  $R_C^\gamma/R_{A1}^\gamma$  agree with the corresponding  $Z/A$  ratios within about 3 per cent. The ratio of  $R_C^\gamma/R_H^\gamma$  is seen to agree exactly with the corresponding  $Z/A$  ratio. The assumption of Compton interactions only

Table 1.4. Comparison of Z/A Ratios for Various Materials with the Corresponding Calculated Ratios of the Gamma Dose Rate in a Nuclear Reactor Core (see Appendix 4.4) -- Based on Attenuation of Gamma Spectrum by Stainless Steel Thimble and Aluminum Calorimeter Capsule.

Material i	$\frac{(Z/A)_i}{(Z/A)_{Al}}$	$\frac{R_i^\gamma}{R_{Al}^\gamma}$	$\frac{(Z/A)_i}{(Z/A)_H}$	$\frac{R_i^\gamma}{R_H^\gamma}$
Hydrogen	2.06	2.01	1.00	1.00
Carbon	1.034	1.010	0.503	0.503
Aluminum	1.00	1.00	0.486	0.497
Polyethylene	1.184	1.152	0.574	0.574

is therefore practically exact for hydrogen and carbon and good within about 3 per cent for aluminum. The gamma dose rate in each material can thus be written in terms of the gamma dose rate in aluminum with good accuracy so that Equation (1.3) can be written as:

$$R_i^T - R_i^{th} = R_{Al}^\gamma \frac{(Z/A)_i}{(Z/A)_{Al}} + \sum_j N_j^i I_j \quad (1.5)$$

Application of this equation to aluminum, polyethylene, and polystyrene results in three equations and five unknowns,  $R_{Al}^{th}$ ,  $R_{Al}^\gamma$ ,  $I_H$ ,  $I_C$ , and  $I_{Al}$ .  $R_{Al}^{th}$  was calculated from the measured thermal neutron flux in the central fuel element (see Appendix 4.3). Since  $R_{Al}^{th}$  is only about 8 per cent of the total dose rate,  $R_{Al}^T$ , even a relatively large error in this calculation introduces only a small error in  $R_{Al}^T - R_{Al}^{th}$ . To further reduce the variables, ratios of  $I_C/I_H$  and  $I_{Al}/I_H$  have been calculated, using the measured fast neutron spectra in the central fuel element. While the absolute values of  $I_H$ ,  $I_C$ , and  $I_{Al}$  are difficult to accurately calculate, the ratios can be calculated with good accuracy. Calculations with different spectra have indicated that the calculated ratios are quite insensitive to the flux spectrum used in the calculation. In addition, neutron moderation by carbon and aluminum atoms contribute only a

small percentage to the total dose rates, so that a relatively large error in the calculated ratios would have only a small effect on the final results. Using these calculated ratios,  $(I_j/I_H) I_H$  can be substituted for  $I_j$  and Equation (1.5) can be written as:

$$R_i^T - R_i^{th} = R_{Al}^\gamma \frac{(Z/A)_i}{(Z/A)_{Al}} + I_H \sum_j N_j^i \left( \frac{I_i}{I_H} \right) \quad (1.6)$$

The unknowns are thus reduced to two,  $R_{Al}^\gamma$  and  $I_H$ . With  $\frac{(Z/A)_{PE}}{(Z/A)_{Al}} = 1.184$ ,  $\frac{(Z/A)_{PS}}{(Z/A)_{Al}} = 1.119$ ,  $\frac{(Z/A)_{SW}}{(Z/A)_{Al}} = 1.100$ ,  $I_C/I_H = 0.164$ , and  $I_{Al}/I_H = 0.0993$ , and substitution of the atoms of each element per gram of each material, the final equations for the materials of interest become:

$$R_{Al}^T - R_{Al}^{th} = R_{Al}^\gamma + 0.221 \times 10^{22} I_H \quad (1.7)$$

$$R_{PE}^T = 1.184 R_{Al}^\gamma + 9.32 \times 10^{22} I_H \quad (1.8)$$

$$R_{PS}^T = 1.119 R_{Al}^\gamma + 5.39 \times 10^{22} I_H \quad (1.9)$$

$$R_{SW}^T = 1.100 R_{Al}^\gamma + 4.43 \times 10^{22} I_H \quad (1.10)$$

A graphical procedure was used to determine  $R_{Al}^\gamma$  and  $I_H$  from the first three of these equations and the calorimeter data for aluminum, polyethylene, and polystyrene. Values of  $R_{Al}^\gamma$  corresponding to several values of  $I_H$  were calculated and plotted vs.  $I_H$  for each material as indicated in Figure 1.16. Since  $R_{Al}^\gamma$ , based on the aluminum data, is believed to represent the best estimate of this quantity for the three samples, a value of  $R_{Al}^\gamma$  and a value of  $I_H$  were selected from this plot so that  $R_{Al}^\gamma$  determined from the aluminum measurement is the average of that calculated from the two plastic samples. Once  $R_{Al}^\gamma$  and  $I_H$  have been determined, the dose rate in Santowax OMP may be calculated, using Equation (1.10).

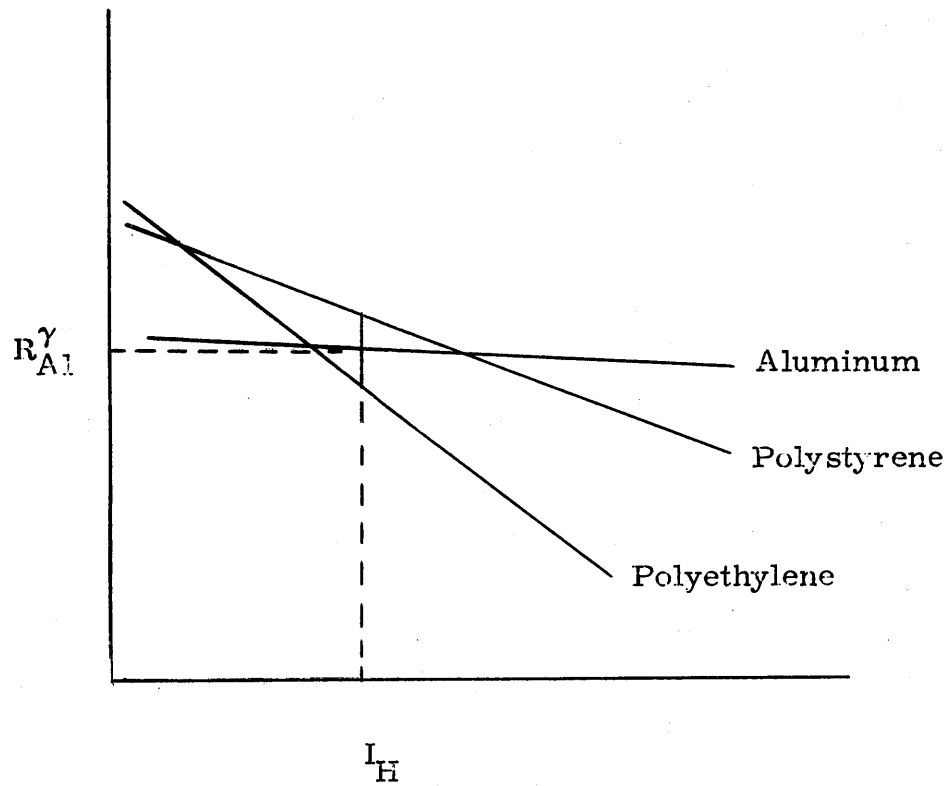


Figure 1. 16. Sketch Illustrating Method of Determining  $I_H$ .

### 1. 3. 4 Results of Calorimetric Dose Rate Measurements

Calorimeter dose rate measurements have been performed on six occasions over a period of about one year, as indicated in Table 1. 5.

Table 1. 5. Chronological Listing of Calorimeter Measurements Performed

Date	Calorimeter Series	Thimble	Fuel Element
3/28/60	I	Aluminum	2MR-12
7/18/60	II	Aluminum	2MR-12
9/6/60	III-1	Aluminum	2MR-12
12/19/60	III-2	Aluminum	2MR-12
3/20/61	III-3	Stainless steel	2MR-11
3/27/61	III-4	Stainless steel	2MR-11

All measurements were performed in thimbles positioned along the axis of the central fuel element in the core (see Figures 1. 3 and 1. 4) which is the position used for the in-pile irradiation. On the first four of these occasions (calorimeter series I, II, III-1, and III-2), the measurements were made in an aluminum thimble and fuel element 2MR-12. On the last two occasions (calorimeter series III-3 and III-4), the measurements were performed in a stainless steel thimble and in fuel element 2MR-11 which is the fuel element actually used for the irradiation of Santowax OMP in this experiment. The dimensions of the stainless steel thimble were selected to give a close approximation to the flux behavior and dose rate with the in-pile section in place. The measured reactivity effect of the stainless steel thimble was  $-735 \text{ m}\beta$ , compared to  $-940 \text{ m}\beta$  for the in-pile section. The estimated dose rate in Santowax OMP in the in-pile section is based on measurements in this stainless steel thimble and, in particular, on the measurements made in calorimeter series III-3.

In Figures 1. 17, 1. 18, and 1. 19, a graphical summary of the measured dose rates in aluminum, polyethylene, and polystyrene are presented. The

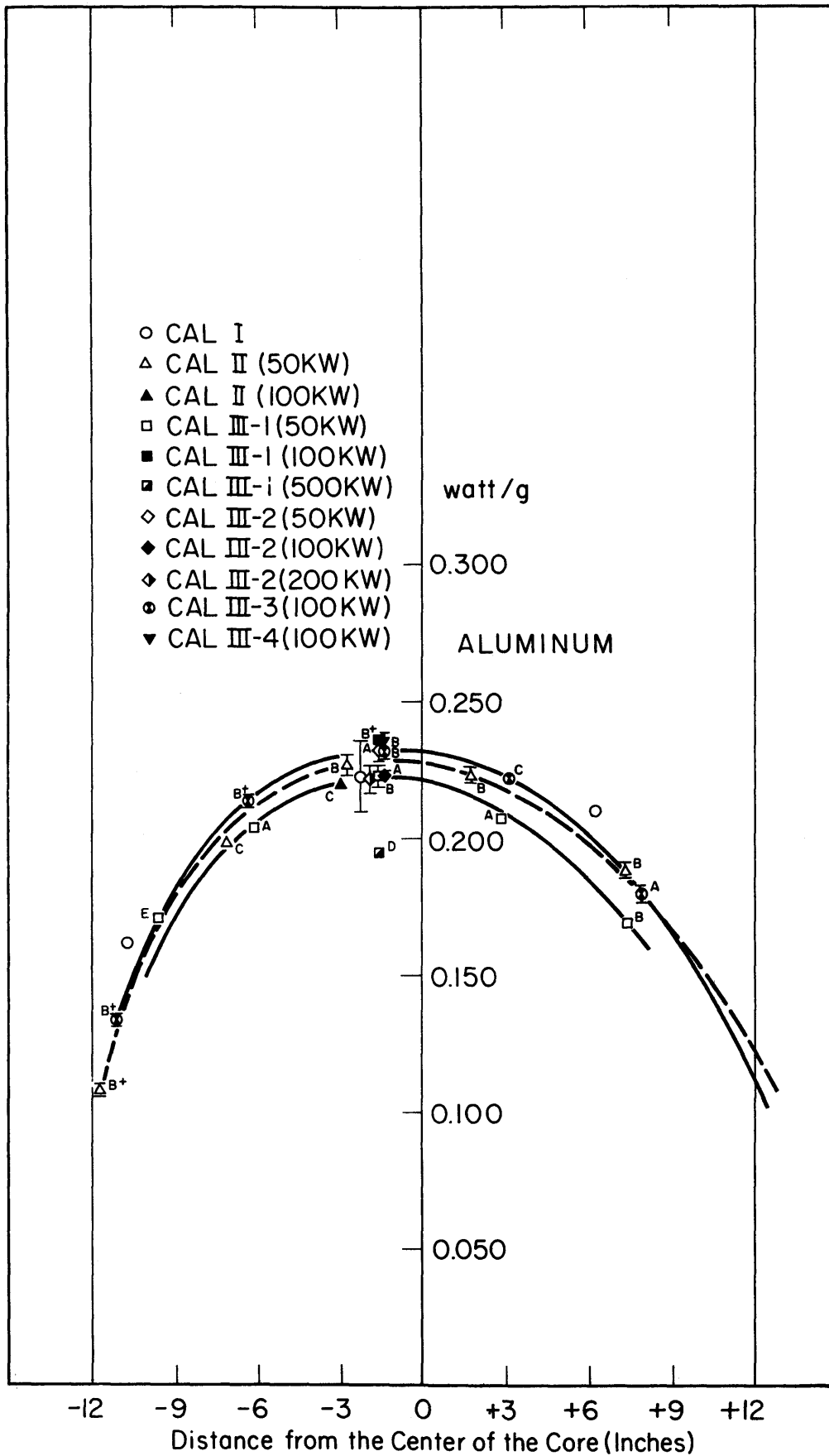


FIG. 1.17 VERTICAL DISTRIBUTION OF DOSE RATE IN ALUMINUM SAMPLE

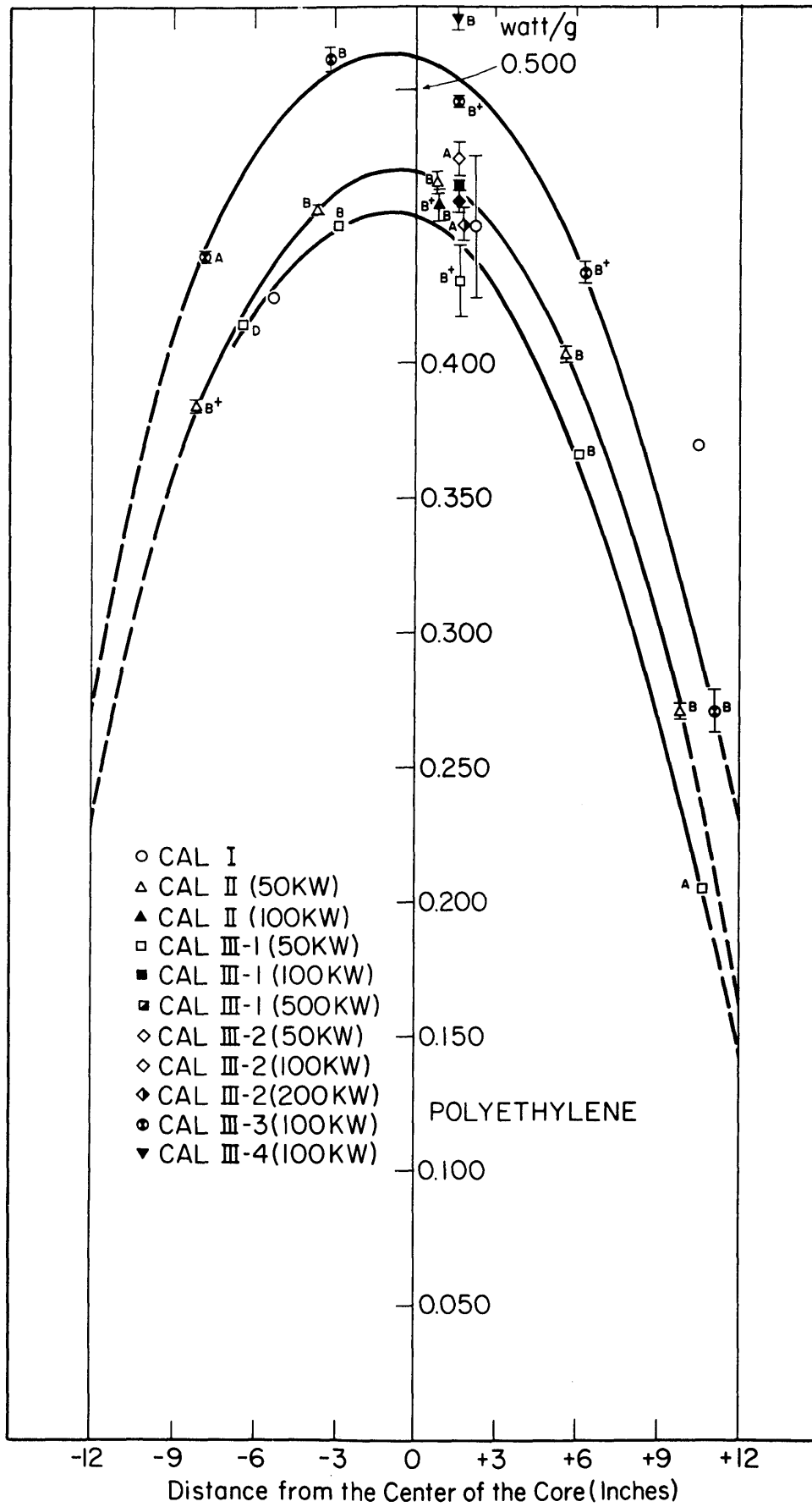


FIG. I.18 VERTICAL DISTRIBUTION OF DOSE RATE IN POLYETHYLENE SAMPLE



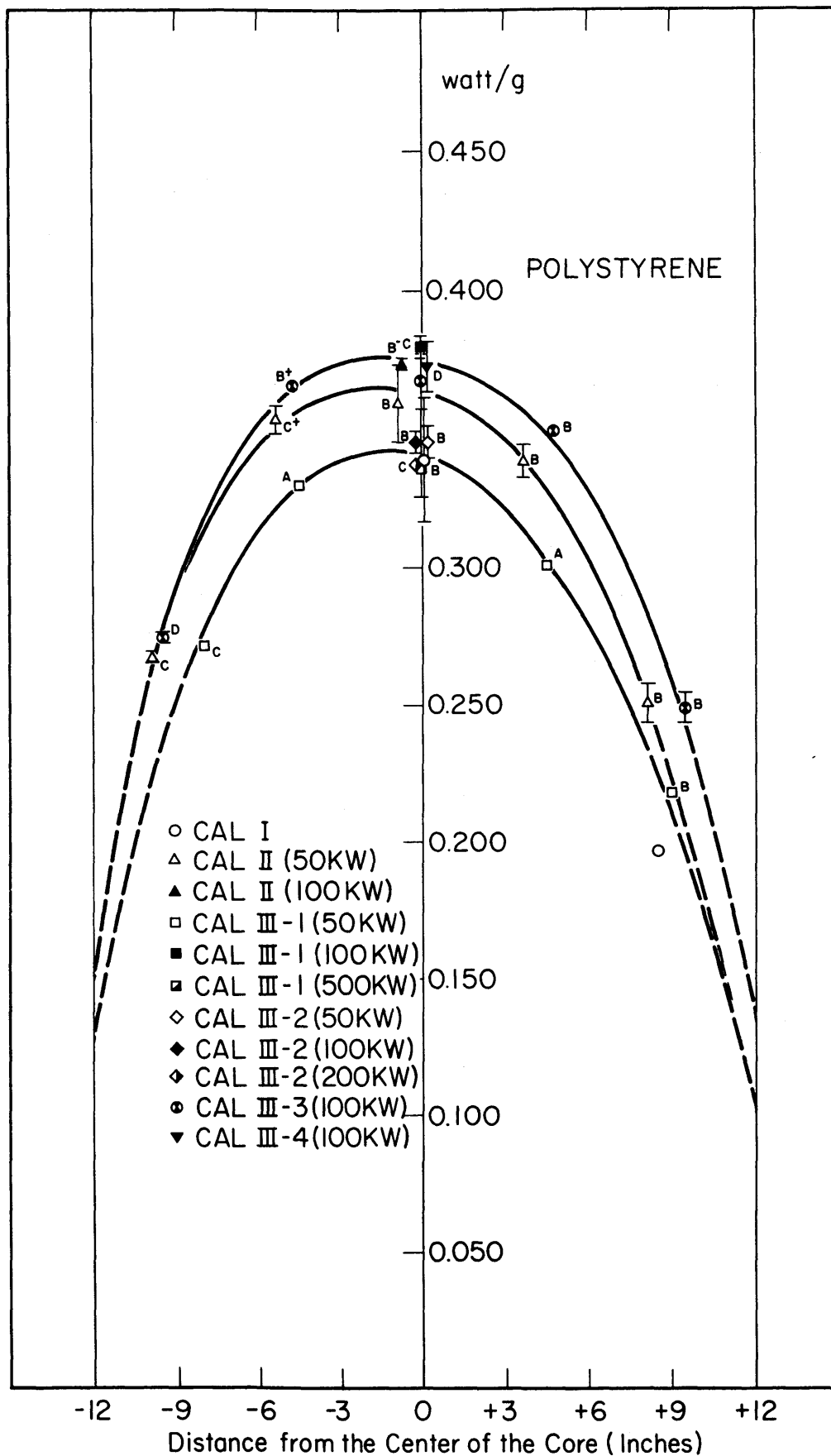


FIG. I.19 VERTICAL DISTRIBUTION OF DOSE RATE IN POLYSTYRENE SAMPLE

results in these figures have been normalized to a reactor power level of 1.00 MW based on the assumption of linearity between the reactor power indicated by the reactor instrumentation and the dose rate. The curves drawn in these figures are based on the measurements for calorimeter series II (50 kw), III-1 (50 kw), and III-3 (100 kw). The measurements were all performed at nominal reactor powers of 50 kw, 100 kw, and 200 kw, with a few (and, in general, unreliable) measurements at 500 kw. The measurements were made at these different reactor power levels to check the reliability of extrapolating the calorimeter measurements up to 1800 kw which was the nominal reactor power at which the irradiation of Santowax OMP was carried out. The ratios of measurements at different reactor power levels at the center of the core are presented in Table 1.6, for calorimeter series III-2 (after normalization of all measurements to 1.0 MW). It is seen that the deviation from the expected ratio of one ranges from 0 to 5 per cent.

Table 1.6. Comparison of Dose Rates Obtained from Calorimeter Series III-2 at 50, 100, and 200 kw. (Data Normalized to 1.0 MW).

Ratio*	Material		
	Al	PE	PS
$\frac{R_{100}}{R_{50}}$	0.963	0.967	1.000
$\frac{R_{200}}{R_{50}}$	0.955	0.950	0.975
$\frac{R_{200}}{R_{100}}$	0.900	0.983	0.975
* The values, 50, 100, and 200, on the dose rate, R, indicate the nominal reactor power level at which the dose rates were measured.			

Following the procedure outlined in section 1.3.3, values of the dose rate in aluminum, polyethylene, and polystyrene have been used to estimate  $I_H$  and  $R_{Al}^\gamma$ . The results based on the curves for calorimeter series II

(50 kw), III-1 (50 kw), and III-3 (100 kw) are presented as a function of axial position in the reactor core in Figures 1. 20 for  $R_{A1}^{\gamma}$  and 1. 21 for  $I_H$ . It is seen from these figures that the gamma dose rate,  $R_{A1}^{\gamma}$ , is practically the same for all three series of calorimeter measurements. In contrast, it will be noted that the fast neutron dose rate is not the same for the three calorimeter series but shows a slight decrease on going from calorimeter series II to calorimeter series III-1, and a relatively large increase on going to calorimeter series III-3.

As discussed in more detail in Chapter 4, this behavior is believed to be primarily the result of changes in the fuel loading in the central fuel element for the different calorimeter series. Calculations presented in Appendix 4. 13 indicate that approximately 30 per cent of the gamma dose rate and greater than 90 per cent of the fast neutron dose rate at the center of the central fuel position is due to the central fuel element; the remainder of these dose rates are due to the 18 fuel elements surrounding the central fuel position (see Figure 1. 3). It is thus seen that a change in the fission rate in the central fuel element should have a relatively large effect on the fast neutron dose rate and only a minor effect on the gamma dose rate. Between calorimeter series III-2 and III-3, the fuel element in the central fuel position was changed from 2MR-12 to 2MR-11, resulting in an 18 per cent increase in the grams of uranium in this fuel position. It is therefore believed that the relatively large increase in the fast neutron dose rate, compared to the gamma dose rate noted in Figures 1. 20 and 1. 21, is the result of the following factors:

- (a) The fission rate in the central fuel element increases by 10 to 18 per cent on insertion of the new fuel element (2MR-11) and the stainless steel thimble. This increase occurs due to the increase in fuel loading with this element and results in:
  - (1) A 10 to 18 per cent increase in the fast neutron dose rate.
  - (2) A reduction in the total fission rate in the outer fuel elements by  $\sim 3$  per cent to maintain a constant reactor power level.

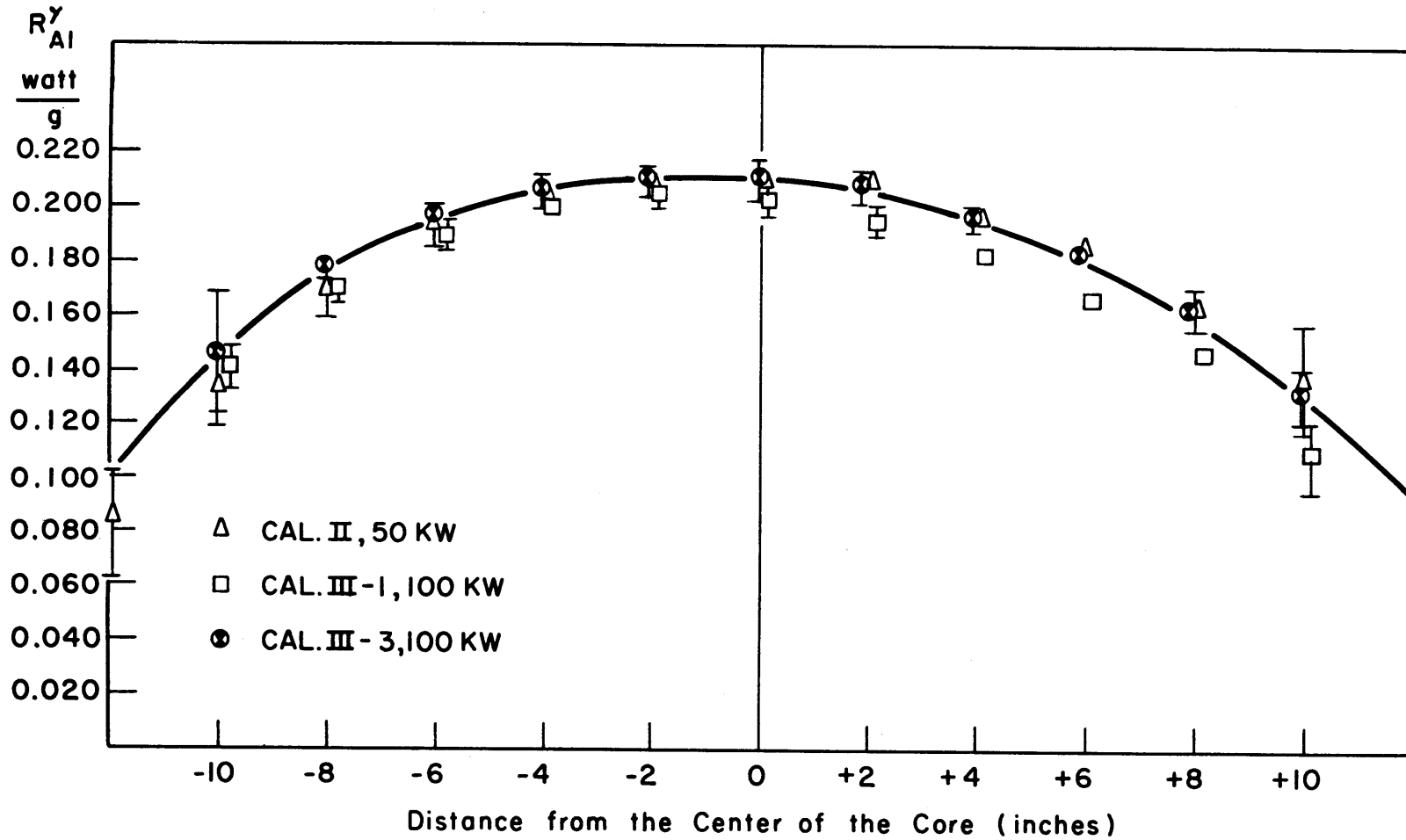


FIG. 1.20 VERTICAL DISTRIBUTION OF THE GAMMA DOSE RATE,  $R_{Al}^{\gamma}$ , IN FUEL POSITION NO. 1. (DATA NORMALIZED TO 1.0 MW)

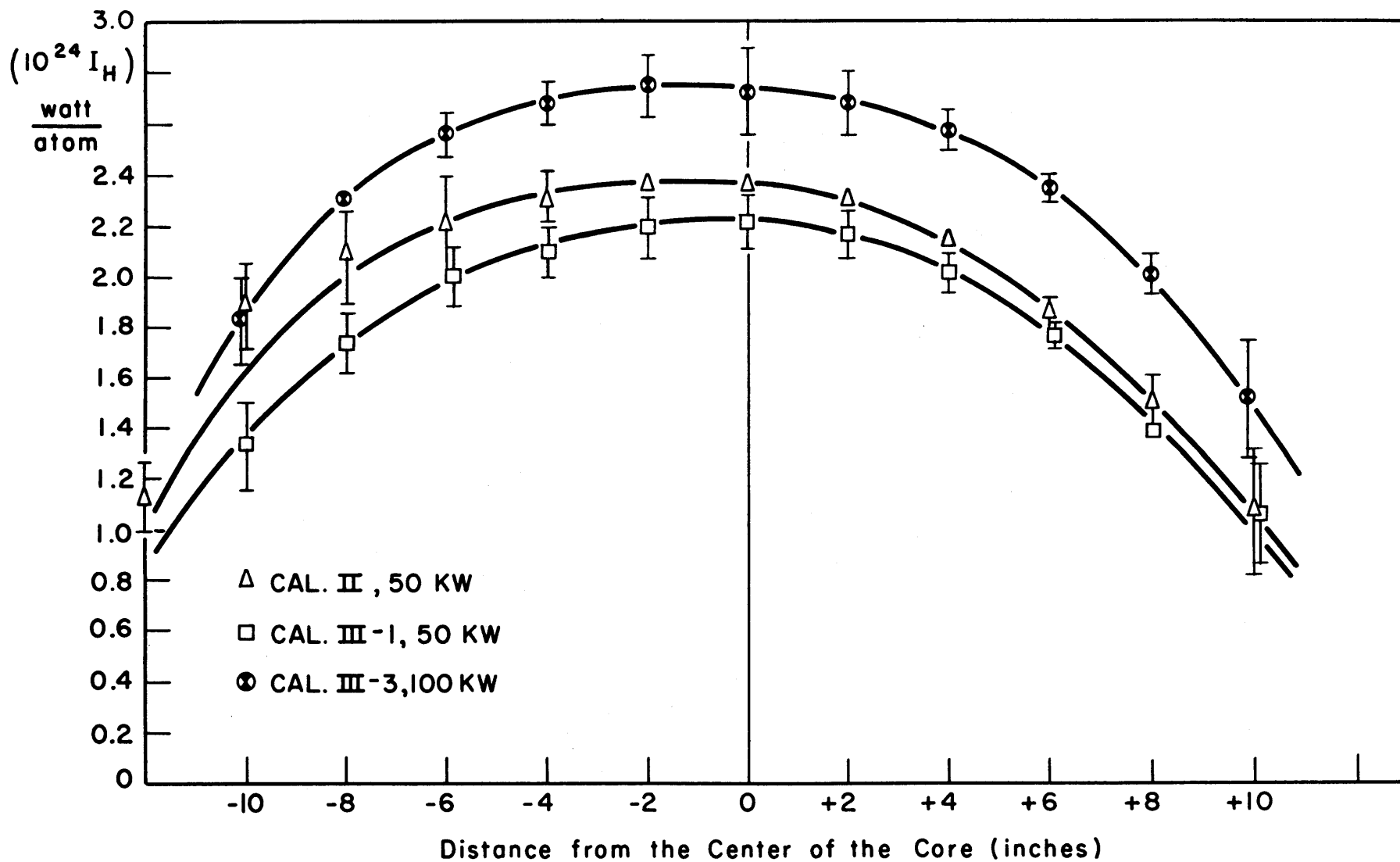


FIG. 1.21 VERTICAL DISTRIBUTION OF THE ENERGY TRANSFER INTEGRAL FOR HYDROGEN,  $I_H$ , IN FUEL POSITION NO. 1. (DATA NORMALIZED TO 1.0 MW)

(b) The gamma dose rate increases by a small percentage (5% or less) due to a combination of two factors:

- (1) The addition of the stainless steel thimble introduces an added source of gamma radiation ( $\sim 4$  per cent) because of thermal neutron interactions in the thimble.
- (2) The contribution of the central fuel element increases because of the increased fission rate in this element, whereas the contribution of the outer fuel elements decreases because of their decrease in fission rate required to maintain a constant reactor power.

### 1. 3. 5 Dose Rate in Santowax OMP in In-Pile Section

The fast neutron and gamma dose rates in Santowax OMP have been calculated at various axial positions in the reactor core, using Equation (1. 10) and the values of  $I_H$  and  $R_{A1}^\gamma$  presented in Figures 1. 20 and 1. 21. The calculated values are presented in Figure 1. 22 as a function of position in the reactor core. As previously discussed, the measurements with calorimeter series III-3 were made under conditions approximating those with the in-pile section in the reactor and hence provide the best estimate of the dose rate in Santowax OMP in the in-pile section. The values above and below 10 inches from the center of the core (where calorimeter measurements were not made due to the low dose rate) were obtained by extrapolation of  $I_H$ , using the fast flux measurements, and of  $R_{A1}^\gamma$ , using ionization chamber measurements.

In correlating the amount of Santowax OMP degraded during operation of the loop with the total amount of radiation energy absorbed, an integration of the dose rate (as given in Figure 1. 22) over the length of the core is required. Assuming the dose rate to be constant with time, the average absorbed dose rate in the organic material over a period of one day can be written as:

$$\left(R_{SW}^{TI}\right)_{avg} = \rho_{avg} \left\{ \int_{-l_l}^{+l_u} \frac{R_{SW}^T}{P_o} x_1 dl + \int_{+l_u}^{\infty} \frac{R_{SW}^T}{P_o} x_2 dl \right\} \frac{\text{watt hr.}}{\text{MWHR}} \quad (1. 11)$$

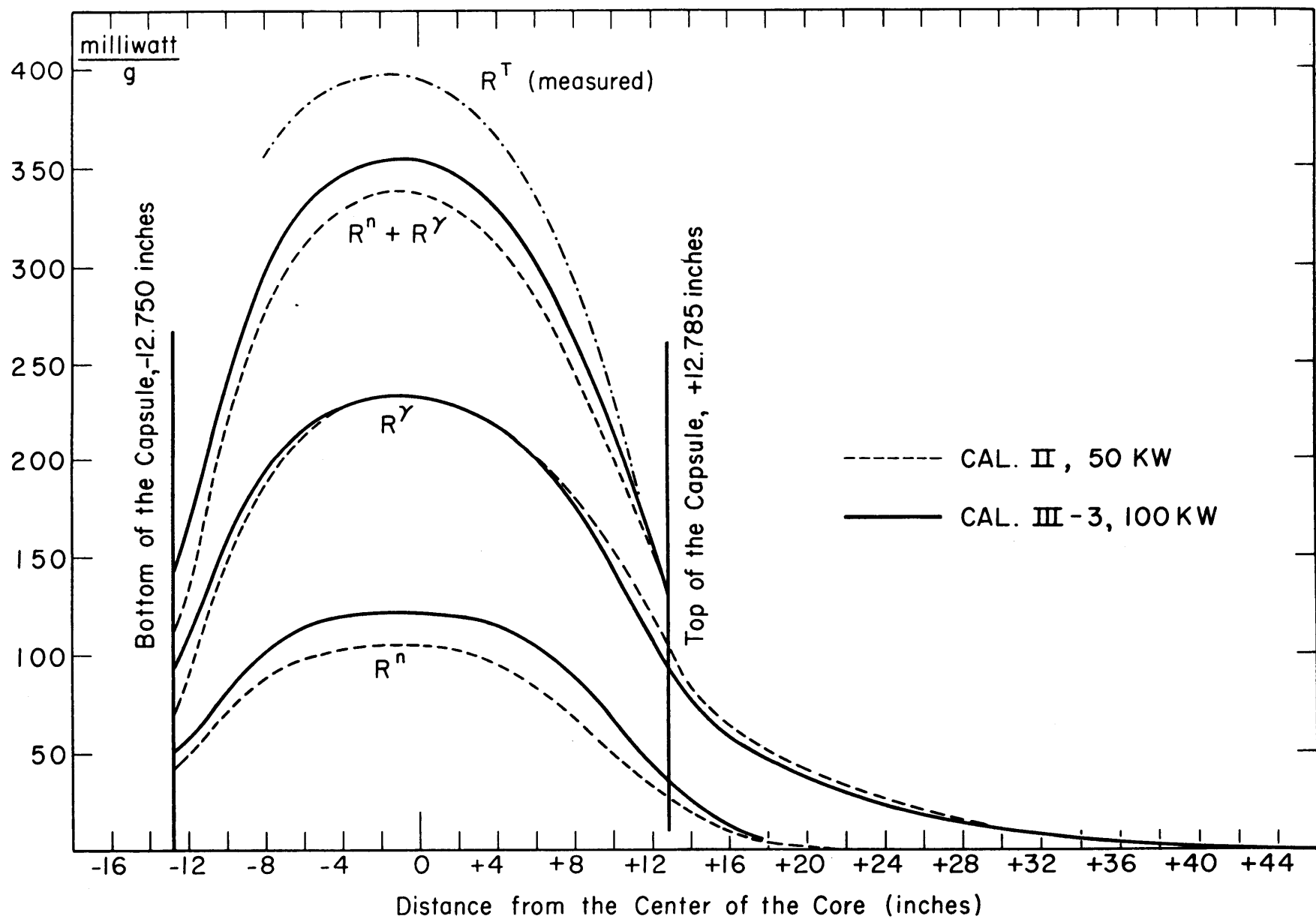


FIG. 1.22 VERTICAL DISTRIBUTION OF FAST NEUTRON, GAMMA AND TOTAL DOSE RATE IN SANTOWAX OMP. (Fuel Element Position No. 1) (Data Normalized to 1.0 MW)

where

$(R_{SW}^{TI})_{avg}$  = average (over one day) total energy absorption rate in the organic coolant, watt-hr/MWHR.

$\rho_{avg}$  = time averaged density of the organic in the radiation field, gms/cm<sup>3</sup>, for a period of one day.

$+l_u$  = distance in inches of the top of the holdup capsule from the reactor core center.

$-l_l$  = distance in inches of the bottom of the capsule from the reactor core center, inches.

$R_{SW}^T/P_o$  = total dose rate in organic material as a function of position in the core (Figure 1.22) normalized to a reactor power of 1.0 MW, watts/gm-MW.

$l$  = axial position in the reactor core, inches.

$x_1, x_2$  = organic volume per unit length of the capsule and tubing above the capsule, respectively, cm<sup>3</sup>/in.

For the present case,  $x_1 = 8.02$  cm<sup>3</sup>/inch,  $x_2 = 3.21$  cm<sup>3</sup>/inch,  $-l_l = -12.75$  inches, and  $+l_u = +12.875$  inches. Substitution of these quantities into Equation (1.11) and graphical integration using Figure 1.22 (for calorimeter series III-3) gives:

$$R_{SW}^{TI} = (61.3 \pm 2.9) \rho_{avg} \frac{\text{watt-hr}}{\text{MWHR}} \quad (1.12)$$

Separate calculations for the fast neutron and gamma dose rates indicate that 67 per cent of the total dose rate is due to gamma interactions and 33 per cent to fast neutron interactions.

The average density for each day of the irradiation has been calculated from Equation (1.33) (which expresses the density as a function of %DP and temperature) and the time-averaged organic temperature in the in-pile section for that day. The calculated energy absorption rates are plotted in Figure 1.23 as a function of MWHR of reactor operation since the start of the in-pile irradiation.



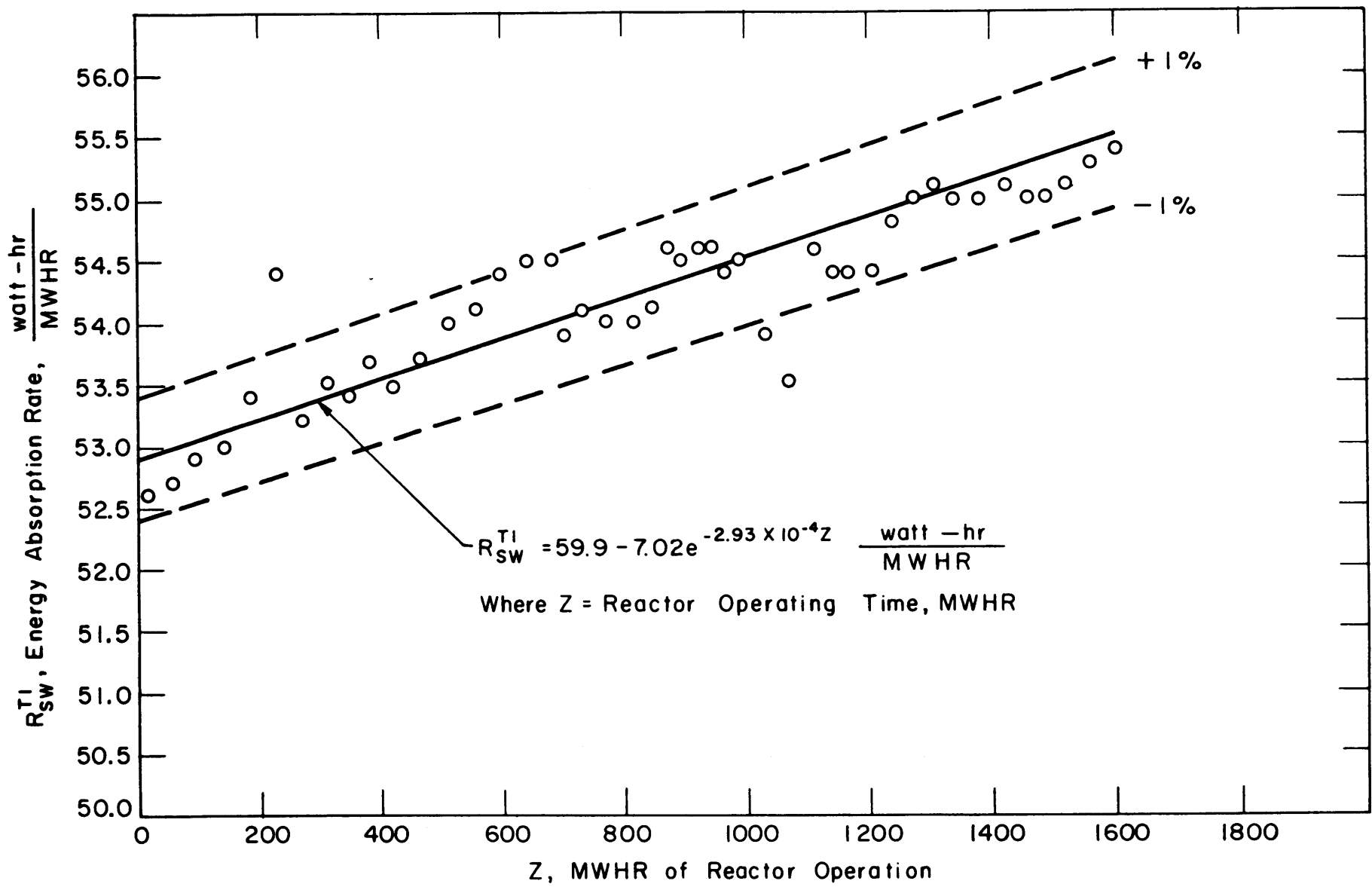


FIGURE 1.23 VARIATION WITH TIME OF DOSE RATE,  $R_{SW}^{TI}$  IN SANTOWAX OMP IN IN-PILE SECTION

For ease in calculation, an equation has been derived which is plotted in Figure 1. 23 and is seen to fit the data very well. This equation is based on an average organic temperature of 601°F for the irradiation period covered in this report. Using this average temperature, Equation (1.15) for the %DP vs. MWHR, and Equation (1. 33) for the coolant density, the following equation is obtained.

$$R_{SW}^{TI} = [ 59. 9 - 7. 02 e^{-2. 93 \times 10^{-4} Z} ] \pm 5\% \frac{\text{watt hr}}{\text{MWHR}} \quad (1. 13)$$

This equation has been used in estimating the total dose rate in the irradiated Santowax OMP throughout the irradiation period covered in this report.

### 1. 3. 6 Thermal, Epithermal, and Fast Neutron Measurements

Thermal, epithermal, and fast neutron flux measurements have been performed both before and after the in-pile section was inserted in the loop. These measurements were made for the following purposes:

(1) To establish the magnitude and energy distribution of the neutron flux to which the organic coolant being tested is exposed.

(2) To determine any changes in the dose rate throughout an experiment on a coolant due to changes in the neutron flux in the reactor.

(3) To compare the neutron fluxes in the stainless steel thimble where the last two calorimeter experiments were performed with those in the in-pile section.

(4) To determine the fast neutron spectrum for use in calculating  $I_C/I_H$  and  $I_{Al}/I_H$  as well as for a calculation of the fast neutron dose rate in Santowax OMP for comparison with that from the calorimeter measurements. The detectors used and their pertinent properties are listed in Table 1. 7. For details of the methods of measurement, reference is made to Chapter 4. Some of the results obtained will be presented in the remainder of this section.

To investigate the linearity of the neutron flux with the reactor power obtained from the reactor instrumentation and the variation of the neutron

TABLE 1.7

## Detectors Used for Thermal and Fast Neutron Measurements

Reaction	$E_{\text{eff.}}$ (Mev)	Resonance Energy ev	$\bar{\sigma}_{\text{eff.}}$ barns	Neutron Energy Region	$t_{1/2}$	Radiation Emitted on Decay of Product Isotope
$S^{32}(n,p)P^{32}$	2.9	---	0.300	Fast	14.3d	$\beta^{-}$ (1.70Mev)
$Ni^{58}(n,p)Co^{58}$	5.0	---	1.23	Fast	72d	19% $\beta^{+}$ (0.65Mev) 42%EC 39% $\beta^{-}$ (0.57Mev) -0.5% $\gamma$ (1.34Mev)
$Mg^{24}(n,p)Na^{24}$	6.3	---	0.048	Fast	15.0h	$\beta^{-}$ (1.39Mev) $\gamma_1$ (1.38Mev) $\gamma_2$ (2.76Mev)
$Al^{27}(n,\alpha)Na^{24}$	8.6	---	0.110	Fast	15.0h	$\beta^{-}$ (1.39Mev) $\gamma_1$ (1.38Mev) $\gamma_2$ (2.76Mev)
$Co^{59}(n,\gamma)Co^{60}$ Bare and Cadmium Covered	---	120	---	Resonance and Thermal	5.3y	$\beta^{-}$ (0.31Mev) $\gamma_1$ (1.17Mev) $\gamma_2$ (1.33Mev)
$Cu^{63}(n,\gamma)Cu^{64}$ Cadmium Covered	---	570	---	Resonance	12.8h	$\beta^{-}$ (0.57Mev) $\beta^{+}$ (0.65Mev) $\gamma$ (1.34Mev)

flux on different days of the week, measurements of the thermal neutron flux were made in the aluminum thimble and fuel element 2MR-12, using pure cobalt wire and 0.595 per cent cobalt-aluminum wire. In Figure 1. 24, the thermal fluxes measured at different reactor powers (as given by the reactor instrumentation) are compared after linear extrapolation to a reactor power of 1.00 MW. It is seen that the same flux is obtained within  $\pm 3$  per cent, indicating that extrapolation of flux or dose rate measurements at low reactor powers to higher reactor powers can be done with good accuracy, using the reactor control room indication of reactor power.

In Figure 1. 25, the thermal neutron fluxes measured on different days of a normal operating week are presented. It is seen that small differences of the order of 10 per cent are observed throughout the week. These changes are believed to be due to the movement of the control rods in the MITR throughout the week due to Xenon buildup. On Monday morning at reactor startup, the bottom of the control rods is normally at a level of approximately 8 inches above the core center. By Thursday and Friday, the control rods have generally been moved out approximately 4 inches to a level even with the top of the core (fuel extends  $\pm 12$  inches from midplane of the core).

Thermal and fast flux measurements have been performed in both the stainless steel thimble and the monitor tube of the in-pile section, and these results will be presented in the remainder of this section. It should be remembered, however, in comparing these measurements, that those made in the in-pile section were made in the monitor tube which is located on the outside of the thimble and immersed in the  $D_2O$  coolant, whereas those made in the stainless steel thimble were made inside the thimble. It would be expected that the fluxes as measured in the monitor tube would be at least slightly different from those measured in the stainless steel thimble because of the difference in position and the fact that  $D_2O$  surrounds the monitor tube for the in-pile section.

In Figure 1. 26, the thermal flux measurements made in the stainless steel thimble and in the monitor tube of the in-pile section are compared. It is seen that in contrast to the expected depression of the thermal flux

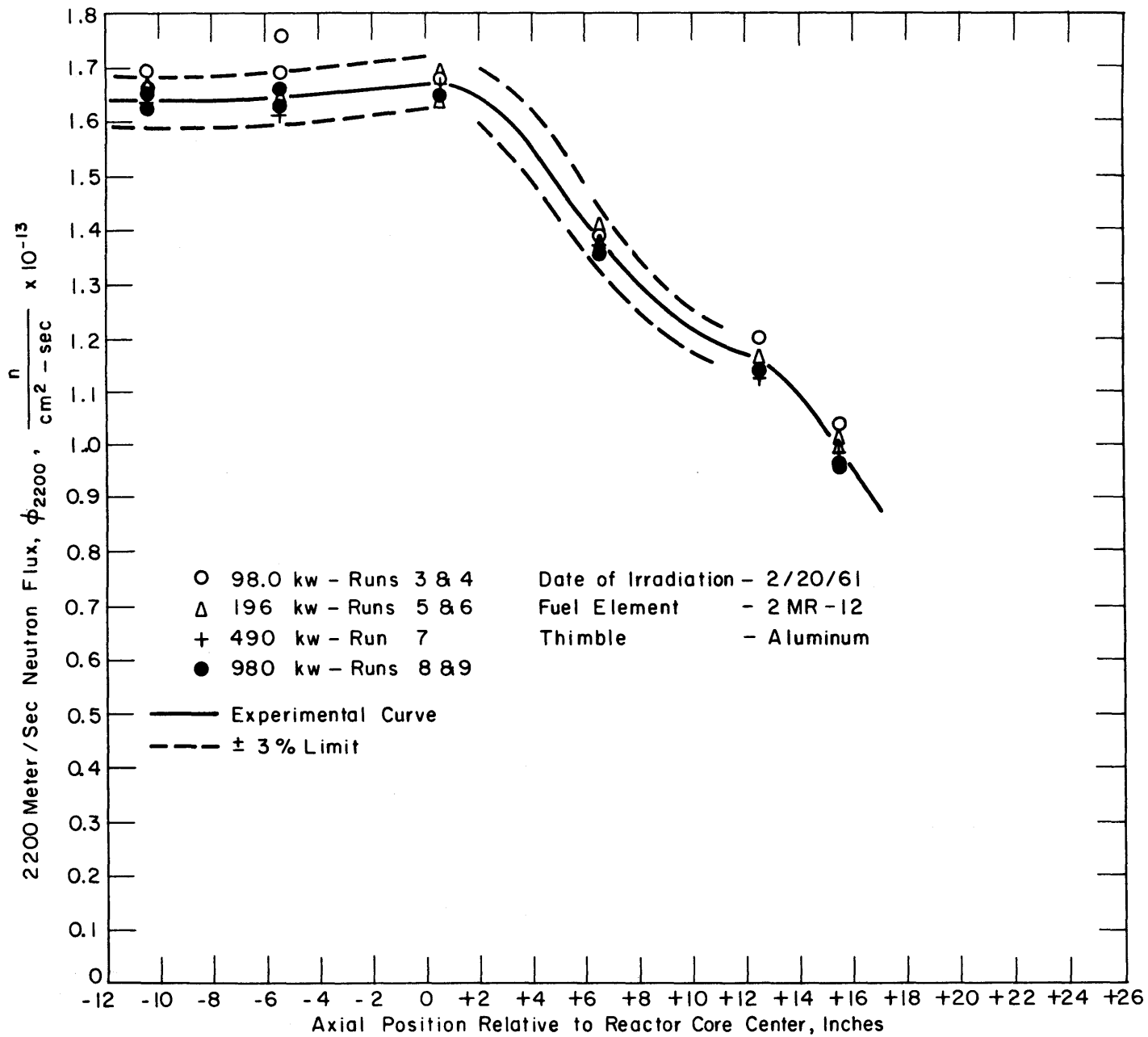


FIGURE 1.24 THERMAL NEUTRON FLUX (2200 METER/SEC) AT DIFFERENT REACTOR POWERS AFTER EXTRAPOLATION OF ALL RESULTS TO 100 MW REACTOR POWER

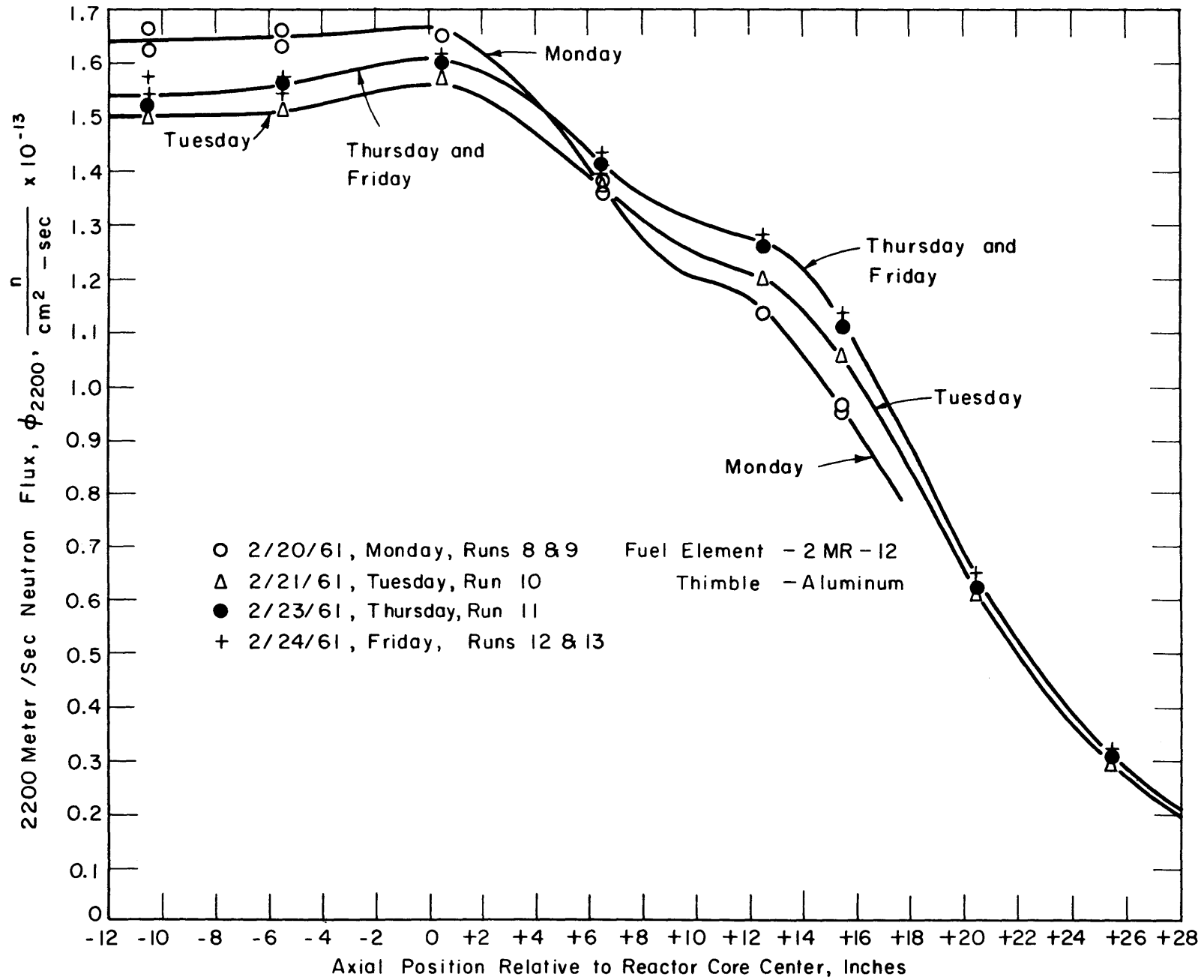


FIGURE 1.25 THERMAL NEUTRON FLUX (2200 METER/SEC) AT 1.0 MW ON DIFFERENT DAYS DURING NORMAL OPERATING WEEK

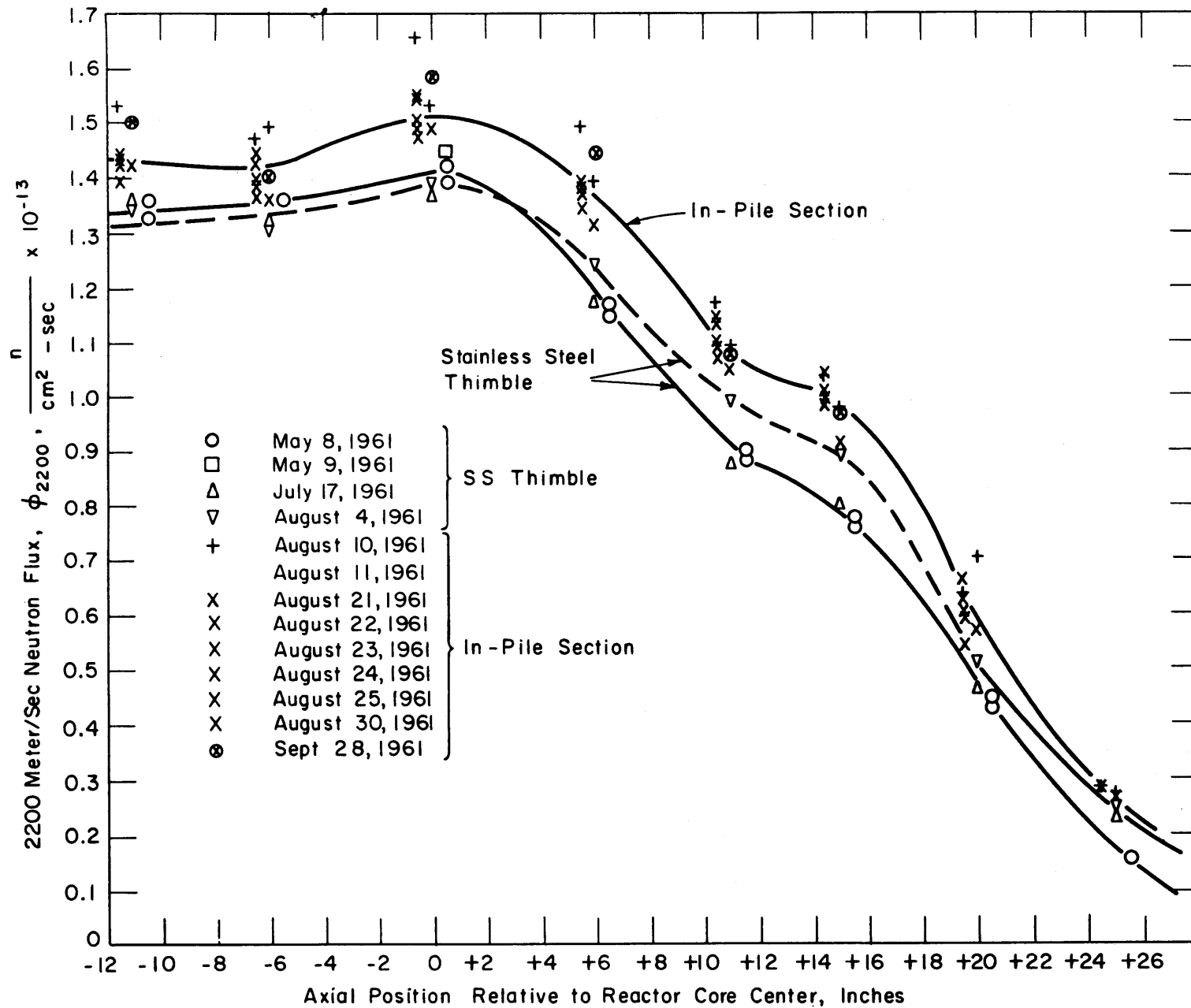


FIGURE I.26 COMPARISON OF THERMAL FLUX MEASUREMENTS (2200 METER/SEC) IN THE STAINLESS STEEL THIMBLE AND IN THE IN-PILE SECTION AT 1.0 MW

with the in-pile section in place, because of its greater reactivity (-940 mβ compared to -735 mβ for the stainless steel thimble), the measurements indicate an 8 per cent higher thermal flux with the in-pile section in place. It is believed that this increase is due to the difference of location of the measurements rather than an actual increase in the thermal flux. It is also evident from this figure that no significant changes in the thermal neutron flux have occurred throughout the irradiation period.

In Figure 1. 27, measurements of the epithermal flux constant,  $\phi_0 = \int \phi(E) E$ , using cobalt and copper irradiations are presented. Based on the cobalt measurements, the epithermal flux in the monitor tube is slightly higher than that in the stainless steel thimble. It is also seen that a large difference exists between the  $\phi_0$  measured with cobalt and that measured with copper; the cobalt measurements are believed to be the more reliable measurements and have been used in all calculations involving the neutron flux.

Measurements of the integrated fast neutron fluxes  $\left( \int_{E_{\text{eff}}}^{\infty} \phi(E) dE \right)$  above effective neutron energy thresholds of 2.9 Mev [ $S^{32}(n, p) P^{32}$ ], 5.0 MEV [ $Ni(n, p) Co^{58}$ ], 6.3 Mev [ $Mg^{24}(n, p) Na^{24}$ ], and 8.6 Mev [ $Al^{27}(n, \alpha) Na^{24}$ ], are presented in Figures 1. 28-1. 31, inclusive; measurements using Ni were made only in the in-pile section monitor tube. In all cases (with the exception of the Ni measurements), it is seen that the fluxes in the stainless steel thimble are higher than those in the monitor tube, in contrast to the inverse behavior of the thermal flux. Again, it is believed most of this difference is due to the different position of the measurements rather than due to a large change in the fast flux.

In Figure 1. 32, the data for each neutron detector obtained in the monitor tube are plotted as a function of neutron energy and are compared with the Watt fission spectrum. The data are reasonably consistent, although the nickel results appear to be somewhat higher than the curve indicated by the other three threshold detectors. The decrease in the magnitude of the flux with energy appears to be slightly less than that of the Watt fission spectrum. There appears to be no difference between the shape of the flux spectrum at 0 inches, -8 inches, and +8 inches.



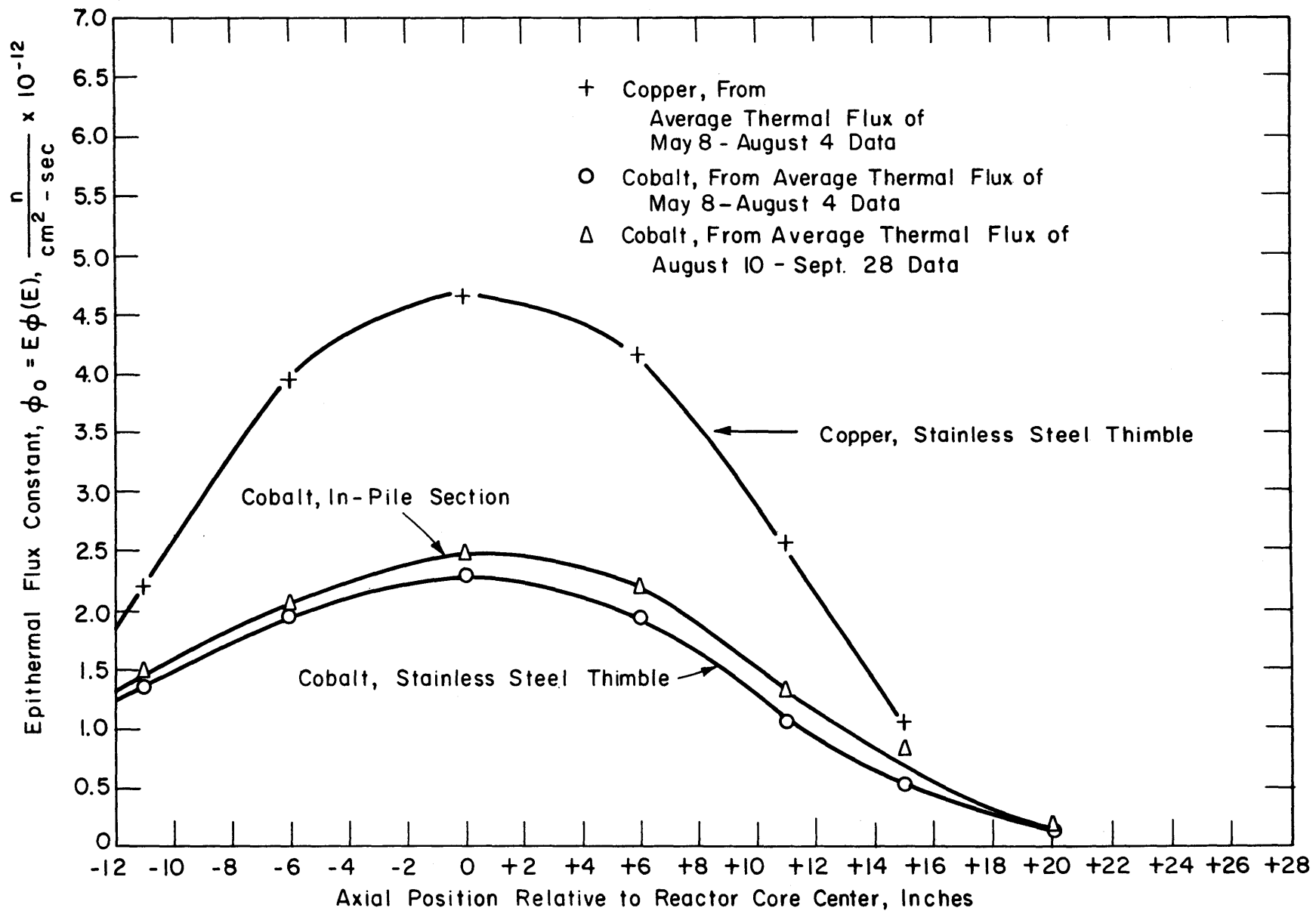


FIGURE 1.27 EPITHERMAL NEUTRON FLUX AS MEASURED WITH COPPER (RESONANCE = 560ev) AND COBALT (RESONANCE = 120ev)

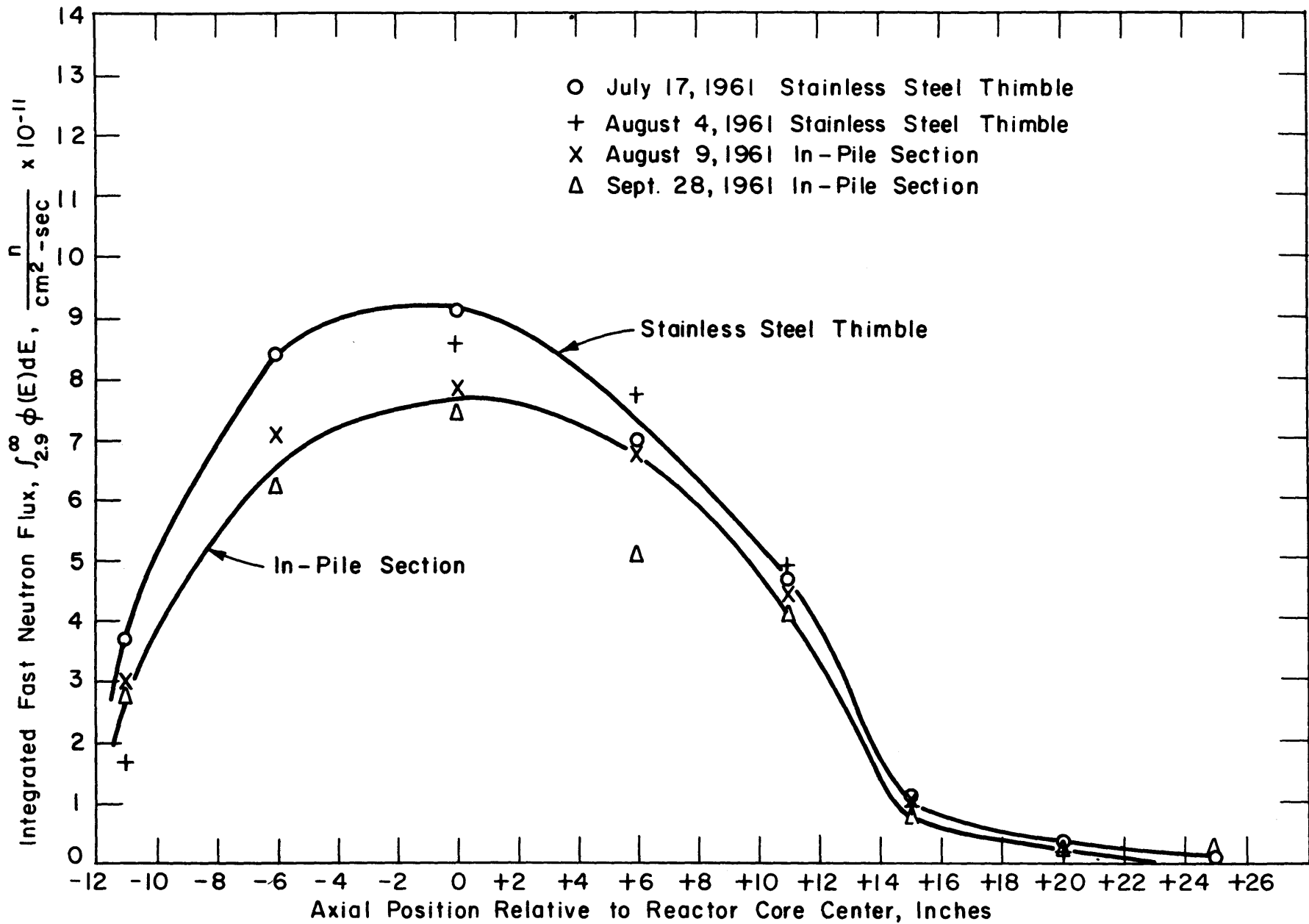


FIGURE 1.28 INTEGRATED FAST NEUTRON FLUX ( $\int_{2.9}^{\infty} \phi(E) dE$ ) FROM SULFUR MEASUREMENTS  
 EFFECTIVE THRESHOLD = 2.9 MEV, REACTOR POWER = 1.0 MW

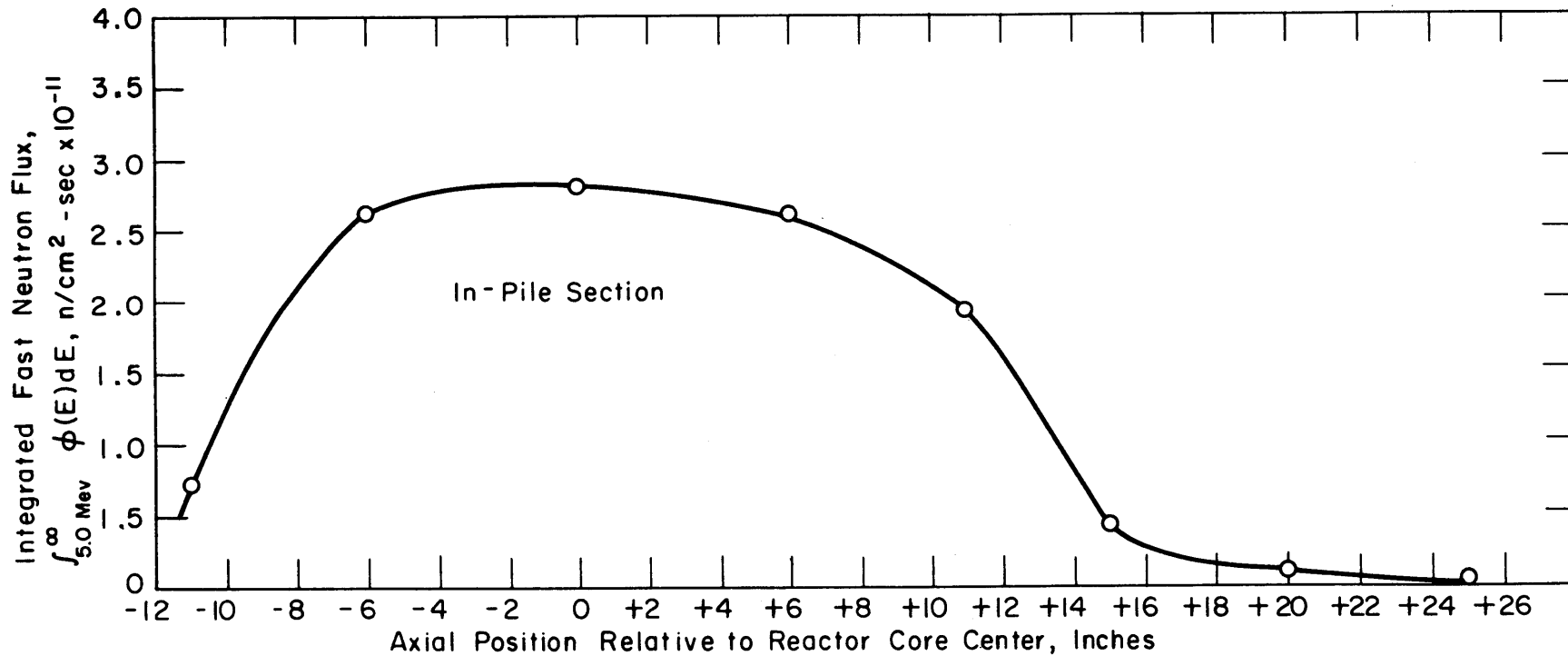


FIGURE 1.29 INTEGRATED FAST FLUX ( $\int_{5.0}^{\infty} \phi(E)dE$ ) FROM NICKEL MEASUREMENTS, EFFECTIVE THRESHOLD = 5.0 MEV, REACTOR POWER = 1.0 MW. DATE OF IRRADIATION = OCTOBER 20, 1961

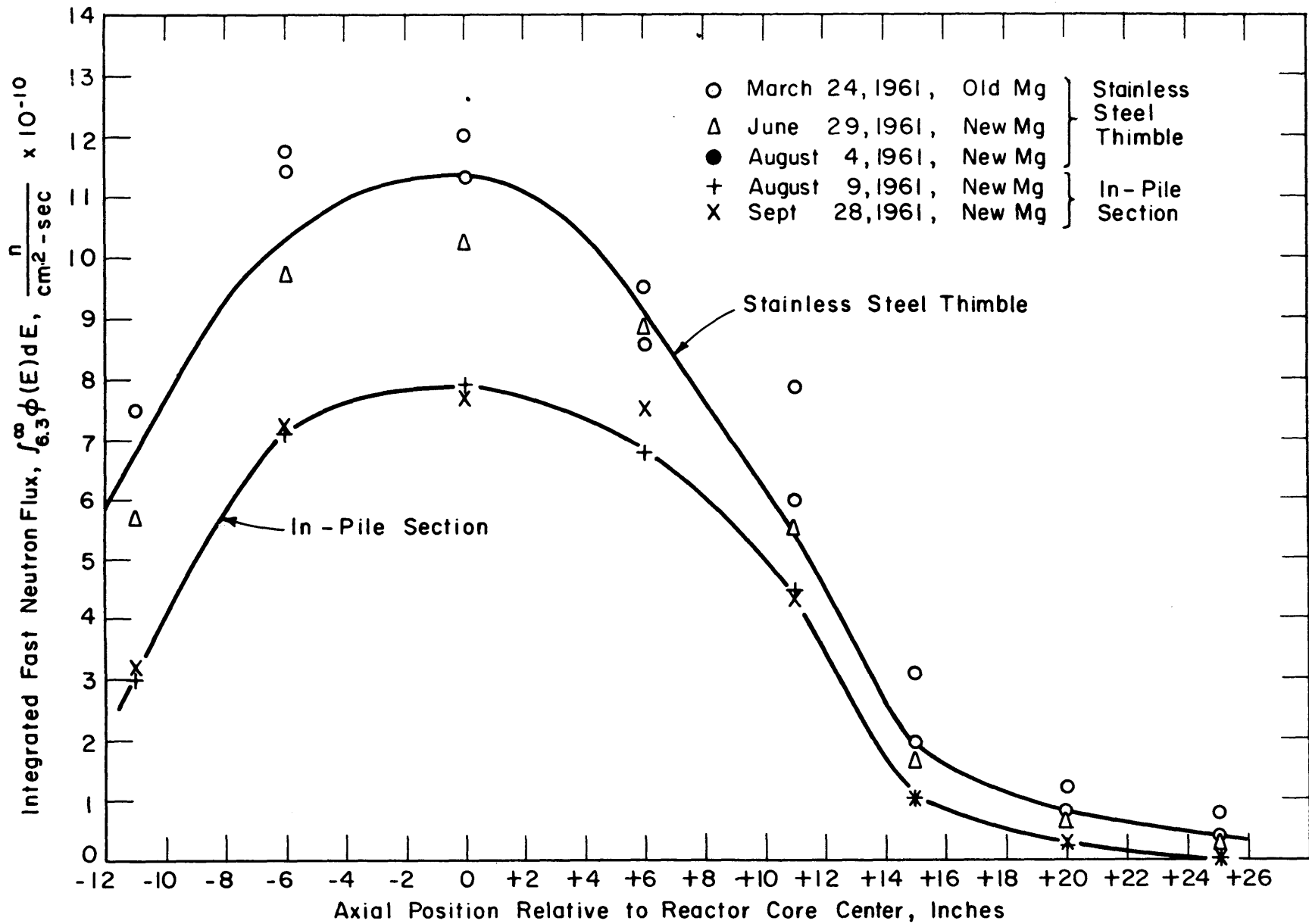


FIGURE 1.30 INTEGRATED FAST FLUX ( $\int_{6.3}^{\infty} \phi(E)dE$ ) FROM MAGNESIUM MEASUREMENTS  
EFFECTIVE THRESHOLD = 6.3 MEV, REACTOR POWER = 1.0 MW

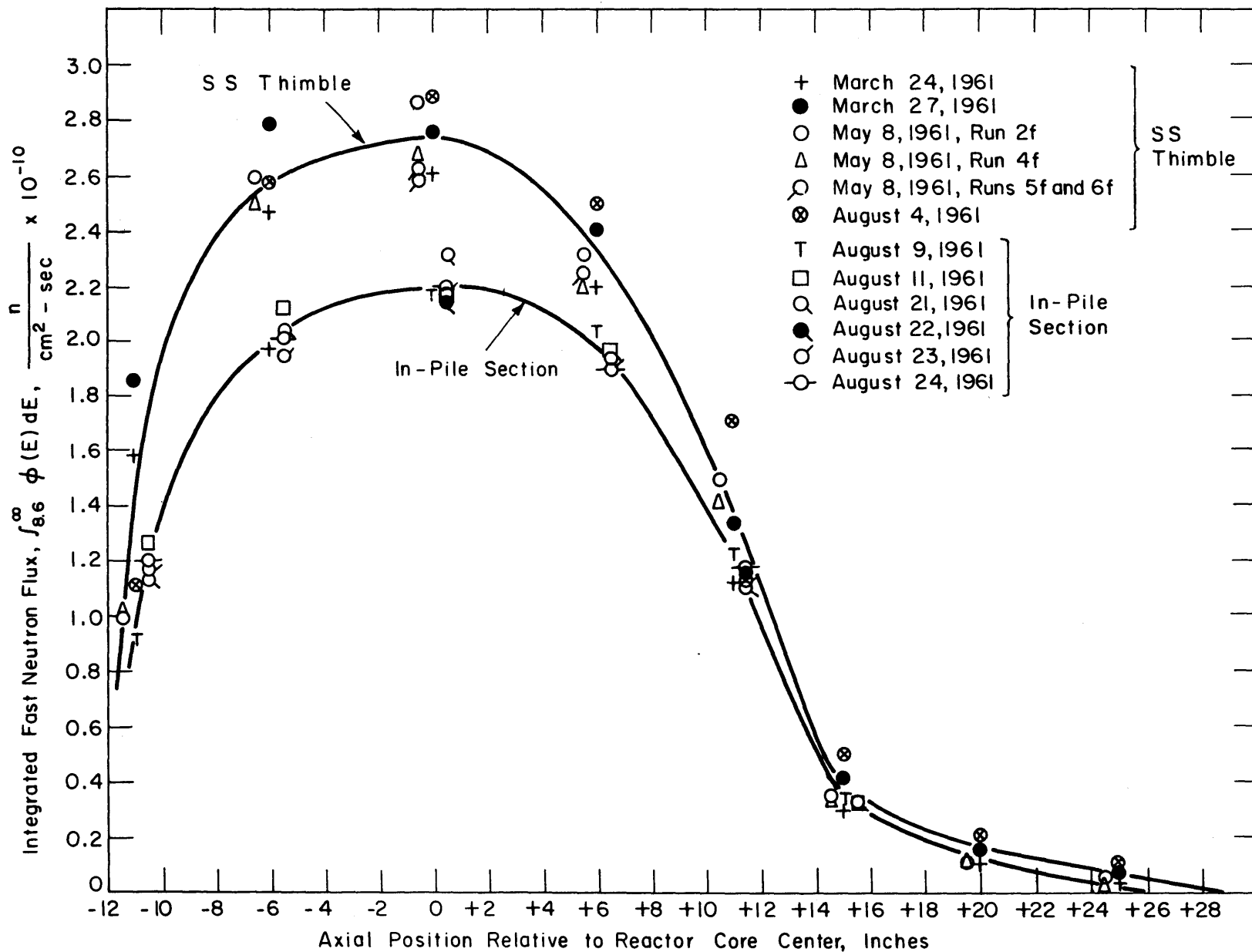


FIGURE 1.31 INTEGRATED FAST FLUX ( $\int_{8.6}^{\infty} \phi(E) dE$ ) FROM ALUMINUM MEASUREMENTS  
EFFECTIVE THRESHOLD = 8.6 MEV, REACTOR POWER = 1.0 MW

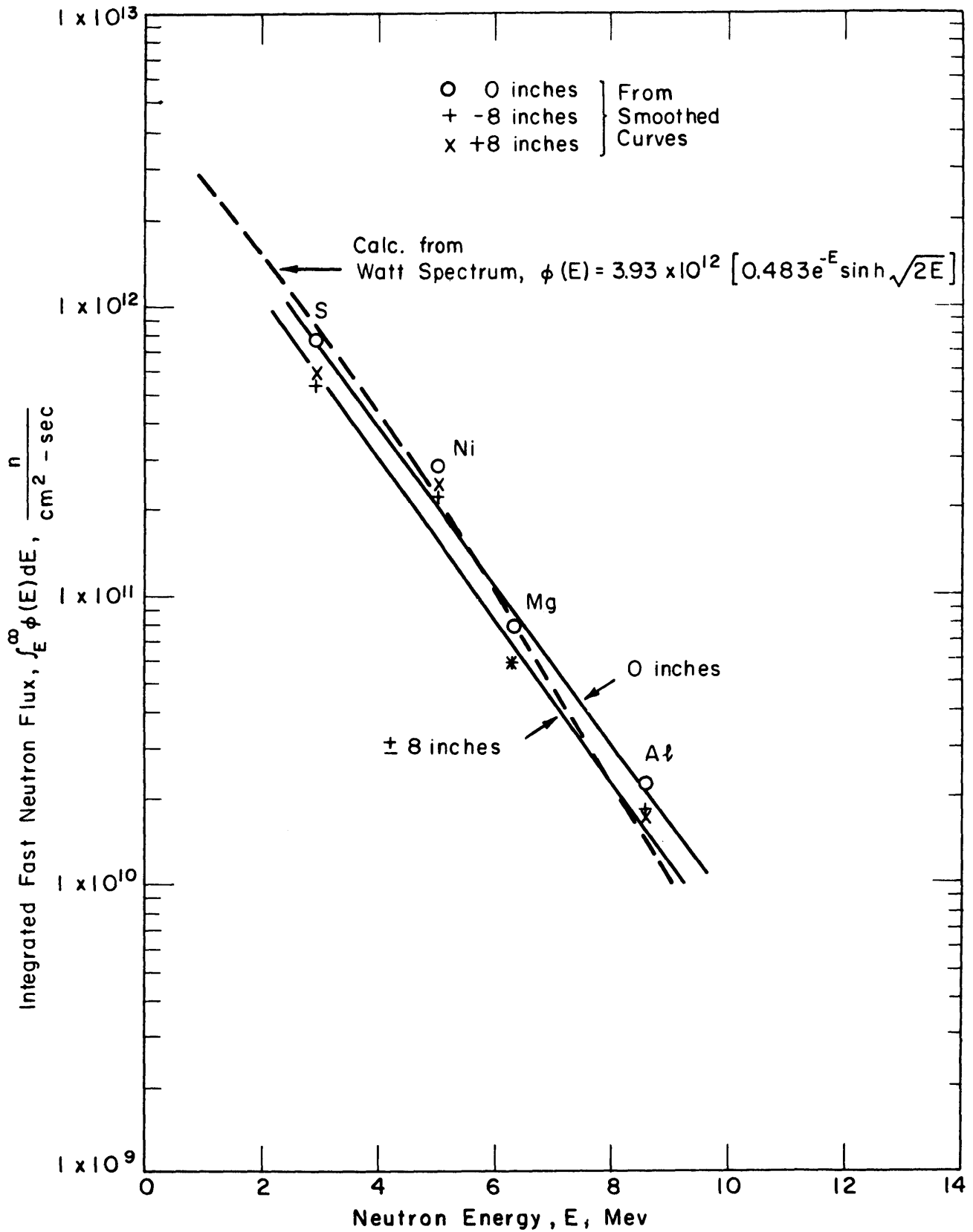


FIGURE I.32 COMPARISON OF FISSION SPECTRUM WITH EXPERIMENTAL DATA FOR FAST NEUTRON THRESHOLD DETECTORS WITH IN-PILE SECTION, REACTOR POWER = 1.00 MW

The fast and epithermal neutron flux measurements have been used to derive neutron flux spectra above thermal energies in the stainless steel thimble and in the monitor tube. Using these spectra, the fast neutron dose rate,  $R_{SW}^n$ , as well as values of  $I_C/I_H$  and  $I_{Al}/I_H$  have been calculated. Since no flux measurements have been made between neutron energies of 570 eV and 2.9 MeV, the flux spectrum in this energy range is somewhat uncertain and the calculations have been made for several different assumed spectra in this energy range. It has been found that the ratios of  $I_C/I_H$  and  $I_{Al}/I_H$  are insensitive to the spectra used in the calculation (see Chapter 4 for details). Also, the calculations based on the measurements in the stainless steel thimble, assuming a  $1/E$  thermal neutron spectrum up to about 1 MeV, give a value (at 1.0 MW) of  $R_{SW}^n$  of 0.128 watts/gram (at the core center), which is in excellent agreement with the measured value of 0.124 watts/gram using the calorimeter. The calculations have also indicated that 53.1 per cent of the total fast neutron dose rate results from interactions with neutrons having energies above 1.0 MeV.

## 1.4 PHYSICAL AND CHEMICAL MEASUREMENTS ON IRRADIATED SANTOWAX OMP

### 1.4.1 Introduction

When ortho-, meta-, and para-terphenyls are irradiated, a very complex mixture of degradation products are produced. The process of most importance with respect to use of organics as moderator-coolants in nuclear reactors is the formation of high molecular weight materials which have a lower volatility than para-terphenyl. These high boiling products have a significant effect on the physical properties of the coolant, particularly viscosity, and at concentrations of the order of 30 to 40 wt %, result in a significant decrease in the heat transfer performance of the coolant. In addition to this process, low and intermediate molecular weight materials (relative to that of the terphenyls, 230) as well as hydrogen and saturated and unsaturated hydrocarbon

gases are produced but in significantly lower quantities on a mass basis.

The basic objectives of this program are to determine the effect of these degradation products on the engineering performance of the organic coolant as the concentration of degradation products increase and, if possible, to determine or predict the mechanisms responsible for the chemical changes observed. With these objectives in mind, the first in-pile irradiation using the M. I. T. in-pile loop was started on August 9, 1961; the behavior of Santowax OMP under nuclear radiation at 600°F and 100 psig was studied. Irradiation was continued until October 5, 1961, without addition of new material to the loop. At this time, it was necessary to add organic makeup to replace material removed by liquid sampling during this first irradiation period. This section describes the physical and chemical characteristics of the irradiated Santowax OMP up to this first addition of organic makeup. At the time of removal of liquid sample 62A, just prior to addition of the organic makeup, 1616 MWHR of reactor operation had been logged, which is equivalent to a total energy absorption in the coolant of approximately 19 watt-hours per gram of organic circulating in the loop. The %DP, defined as 100 minus the total weight per cent of ortho-, meta-, and para-terphenyl (as determined by gas chromatography), increased from ~ 0 per cent to 39.1 per cent during this period.

In order to characterize the type and rate of changes occurring in irradiated Santowax OMP, the physical and chemical measurements summarized in Table 1.8 have been made. Since this report covers the initial commissioning run of the loop, the methods of measurement were not fully developed in all cases and the status of the various measurements are also described in this table. The available data have been correlated, however, with the chemical composition of the coolant, and the liquid decomposition yields of the individual terphenyl isomers have been determined.



Table 1.8. Physical and Chemical Measurements Made on Santowax OMP During the Irradiation Period Covered by this Report.

Measurement	Status of Measurement
Coolant composition and decomposition yield	The ortho-, meta-, and para-terphenyl content of the coolant have been measured throughout the period of irradiation using gas chromatography and the liquid decomposition yield determined by difference. Plans are under way for distillation measurements of the %HB and analysis of the high boiling material using gas chromatography and mass spectrophotographic techniques.
Gas evolution rate and composition of degradation gases	The composition of the undissolved degradation gases has been measured throughout the period of irradiation. Only a limited number of measurements of the dissolved degradation gas composition and of the gas solubility are available. As a result, it has been possible to determine only the total gas evolution rate and not that of the gaseous components individually.
Density and viscosity	Density and viscosity measurements have been made at temperatures of 400°F to 750°F throughout the period of irradiation.
Carbon-hydrogen content	The carbon-hydrogen content of the coolant has been measured throughout the period of irradiation. However, the uncertainty of the measurement is considerably larger than the changes which have occurred in the period covered by this report.
Ash content and coolant activation	Satisfactory ash content measurements and coolant activation measurements have not yet been developed and are currently being developed. The data available are presented, however.
Average molecular weight	The average molecular weight of the coolant has been measured. However, because of the diluent effect of the undegraded coolant coupled with the relatively large uncertainty of the measurement, it has been difficult to follow changes of the molecular weight of the degradation products. Measurements on only the high boiling materials after the distillation method has been developed will greatly increase the usefulness of this measurement.

Table 1. 8 (continued)

Measurement	Status of Measurement
Infrared and ultra-violet absorption spectra	These measurements have been made throughout the irradiation period. The usefulness of the results is still to be demonstrated, however, because of the large number of different compounds in the coolant.
Melting point	Measurements have been made throughout the irradiation period.
Thermal conductivity and heat capacity	Measurements are not yet available. Samples of material have been submitted to Monsanto Research Corporation for measurement.

#### 1. 4. 2 Coolant Composition and Decomposition Yield

##### 1. 4. 2. 1 Coolant Composition During Irradiation Period

To determine the decomposition yield of Santowax OMP on irradiation as well as to provide a basis for correlating physical property changes, quantitative analyses of the biphenyl, ortho-terphenyl, meta-terphenyl, and para-terphenyl concentrations have been determined at different times during the irradiation period covered in this report. The analyses have been performed using high-temperature gas chromatography. The concentrations are plotted vs. the MWHR's of reactor operation in Figure 1. 33 on a semi-log plot, and in Figure 1. 34 on a rectangular plot. It is seen from Figure 1. 33 that the data can be represented up to the time the loop was recharged by a straight line on a semi-log plot. Hence, the concentration as a function of the MWHR's of reactor operation can be expressed by an equation of the following type:

$$C_i = B_i e^{-b_i Z} \quad (1. 14)$$

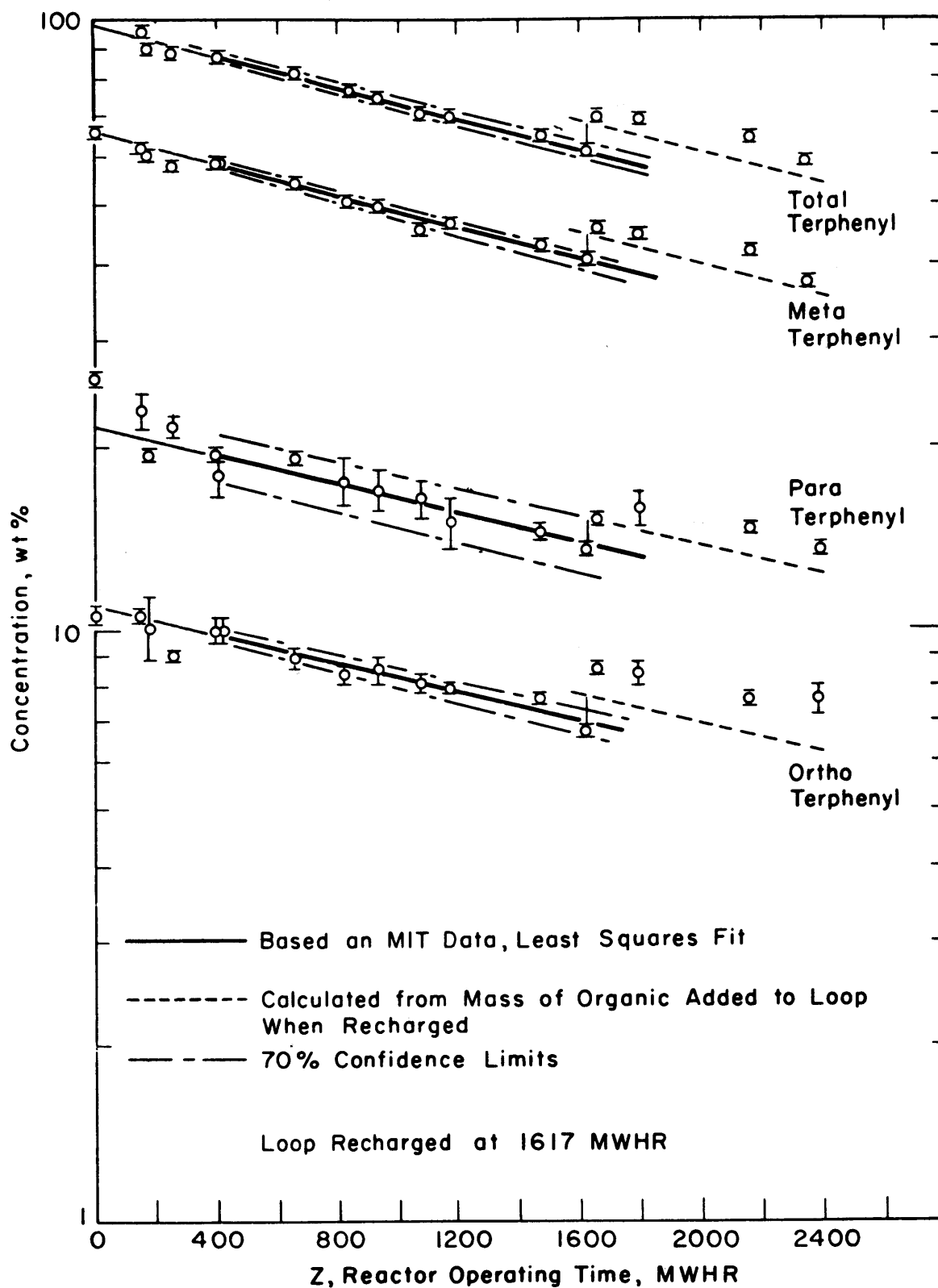


FIG. I.33 ORGANIC CONCENTRATIONS DURING INITIAL IRRADIATION OF SANTOWAX OMP - MIT Data

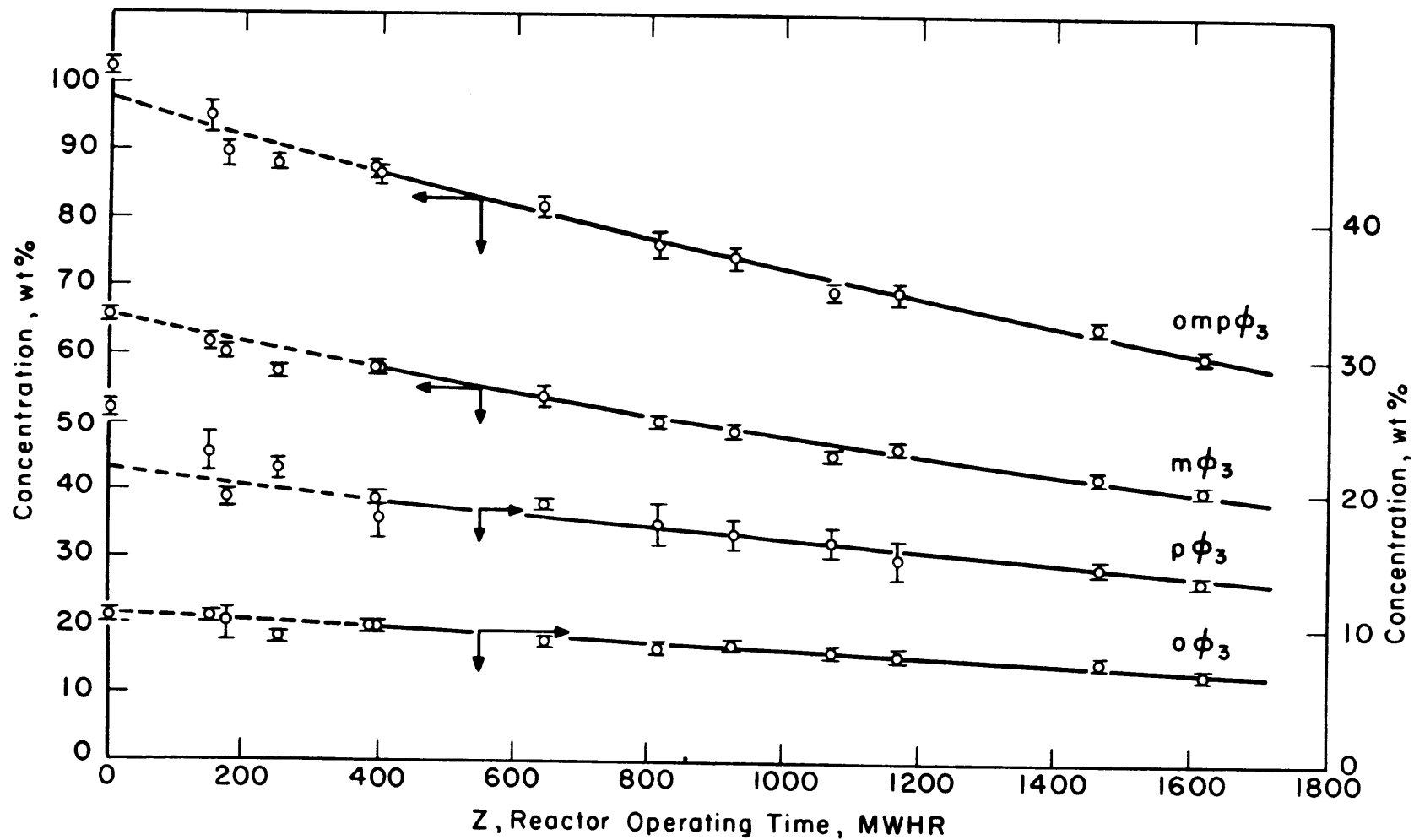


FIG. I.34 ORGANIC CONCENTRATIONS DURING INITIAL IRRADIATION OF SANTOWAX OMP - MIT DATA - THE CURVES DRAWN REPRESENT A LEAST SQUARES FIT TO MIT'S DATA

where

$B_i$  and  $b_i$  = constants to be determined from the data for the material,  $i$ .

$Z$  = MWHR of reactor operation.

$C_i$  = concentration of the material,  $i$ , wt %.

This equation has been fitted to the data using a least squares calculation in which equal weight has been given to each sample except the first four at 0 MWHR, 150 MWHR, 175 MWHR, and 250 MWHR; these four samples were not used in the least squares calculations because of difficulties encountered in obtaining representative liquid samples in this initial period of loop operation. The equations obtained for each terphenyl isomer, as well as the total terphenyl isomer concentration, are summarized below and are also plotted in Figures 1.33 and 1.34; the uncertainties quoted represent the 70 per cent confidence limits.

Total terphenyl

$$C_{\text{omp}\phi_3} = (97.7 \pm 1.6) e^{-(2.93 \pm 0.18) \times 10^{-4} Z} \quad (1.15)$$

Meta-terphenyl

$$C_{\text{m}\phi_3} = (65.4 \pm 0.9) e^{-(3.02 \pm 0.19) \times 10^{-4} Z} \quad (1.16)$$

Para-terphenyl

$$C_{\text{p}\phi_3} = (21.5 \pm 1.8) e^{-(2.71 \pm 0.41) \times 10^{-4} Z} \quad (1.17)$$

Ortho-terphenyl

$$C_{\text{o}\phi_3} = (10.9 \pm 0.3) e^{-(2.80 \pm 0.27) \times 10^{-4} Z} \quad (1.18)$$

The biphenyl concentration has remained constant at 0.2 to 0.4 per cent throughout the irradiation period.

#### 1. 4. 2. 2 Coolant Degradation Rate and Decomposition Yield

##### (A) Introduction

In most previous work on the determination of the radiolytic decomposition yields of the polyphenyls, the final results only have been given, without any indication of the method used in calculating the decomposition yields from the data and without any reliable estimate of the experimental uncertainty given. As a result, it is impossible to evaluate the reliability of the measurements performed. This factor is of particular importance since the decomposition yields reported by different laboratories have often been considerably different and it is difficult to obtain definitive reasons for the differences. It should be noted also that the method used in analyzing the data obtained can have a strong influence on the calculated decomposition yields; this is particularly true where only limited data are available (as has generally been the case in in-pile irradiations) and graphical techniques are used in determining the decomposition yield.

In the present experiment, techniques have been developed for the accurate and reproducible calculation of decomposition yields from the data which provides a statistical estimate of the uncertainty in the calculated values. The method involves fitting an applicable equation to the data by the method of least squares. It has been found that the data can be represented remarkably well as a function of the MWHR's of reactor operation by simple equations. The derivatives of these equations then give directly the degradation rates and, most importantly, a statistical estimate of the reliability.

##### (B) Method of Calculating Degradation Rates and Decomposition Yields

The primary method used in calculating the degradation rates has been to use Equations (1. 15) through (1. 18) giving the concentration of the terphenyl components as a function of the MWHR's of reactor operation. As indicated in Chapter 5, the degradation rate can be written as:

$$\frac{dH_i(Z)}{dZ} = -M(Z) \frac{dC_i(Z)}{dZ} \frac{\text{grams}}{\text{MWHR}} \quad (1. 19)$$

where

$M(Z)$  = mass of organic in loop as a function of  $Z$ , the MWHR's of reactor operation.

$\frac{dC_i(Z)}{dZ}$  = derivatives of Equations (1. 15) through (1. 18) for each terphenyl isomer,  $i$  (after division by 100 to give concentration as weight fraction rather than wt %).

$\frac{dH_i(Z)}{dZ}$  = degradation rate for material,  $i$ , grams/MWHR of reactor operation.

A similar calculation in which  $\frac{dH_i(Z)}{dZ}$  was calculated from a mass balance on the loop gave good agreement with the above method for the total terphenyl concentration.

Once  $\frac{dH_i(Z)}{dZ}$  has been determined, the decomposition yield can be calculated, using Equation (1. 13) for the total dose rate in the organic coolant,  $R_{SW}^{TI}$  watt hr/MWHR, as follows:

$$G_m(-i) = \frac{dH_i(Z)/dZ}{R_{SW}^{TI}} \frac{\text{grams}}{\text{watt-hr}} \quad (1. 20)$$

$$G(-i) = 11.65 G_m(-i) \frac{\text{molecules}}{100 \text{ ev}} \quad (1. 21)$$

### (C) Calculated Decomposition Yields

Following the procedures outlined above, the degradation rates and decomposition yields have been calculated for ortho-terphenyl, meta-terphenyl, para-terphenyl, and the total terphenyls. The circulating mass in the loop used in these calculations is indicated in Figure 1. 35. In Table 1. 9 and Figure 1. 36, the calculated decomposition yields,  $G(-i)$ , are presented as a function of %DP for each of the terphenyl isomers as well as the total terphenyls. The uncertainties quoted

FIG. 1.35 GRAMS OF ORGANIC CIRCULATING IN LOOP - THE POSITIONS OF SAMPLE REMOVAL ARE SHOWN

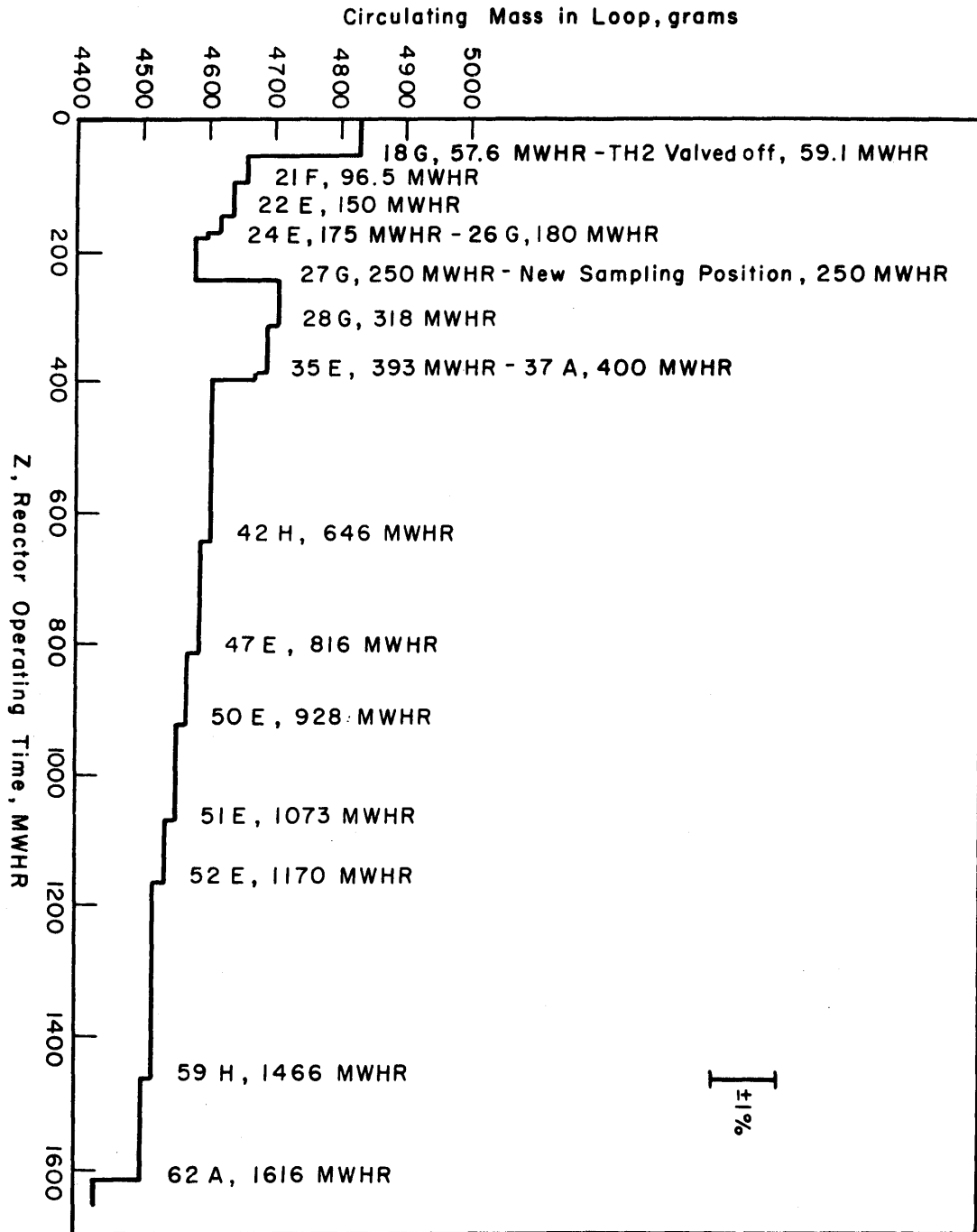




TABLE 1.9

TERPHENYL IRRADIATION DECOMPOSITION YIELDS

Z	%DP	ORTHO TERPHENYL			META TERPHENYL			PARA TERPHENYL			TOTAL TERPHENYL			
		$G_m(-o\phi_3)$ grams watt-hr	$G(-o\phi_3)$ molecules 100 ev	$G^*(-o\phi_3)$ molecules 100 ev	$G_m(-m\phi_3)$ grams watt-hr	$G(-m\phi_3)$ molecules 100 ev	$G^*(-m\phi_3)$ molecules 100 ev	$G_m(-p\phi_3)$ grams watt-hr	$G(-p\phi_3)$ molecules 100 ev	$G^*(-p\phi_3)$ molecules 100 ev	$G_m(-omp\phi_3)$ grams watt-hr	$G(-omp\phi_3)$ , $\frac{\text{molecules}}{100 \text{ ev}}$		$G^*(-omp\phi_3)$ molecules 100 ev
												$G(-o\phi_3)+G(-m\phi_3)+G(-p\phi_3)$	From Least Squares Calc.	
400	12.2	0.00235 ±0.00023	0.0274 ±0.0027	0.281 ±0.029	0.0150 ±0.0013	0.174 ±0.015	0.301 ±0.027	0.00449 ±0.00077	0.0522 ±0.0090	0.272 ±0.052	0.0218 ±0.0019	0.253	0.254 ±0.022	0.289 ±0.027
600	18.1	0.00221 ±0.00022	0.0258 ±0.0024	0.280 ±0.028	0.0140 ±0.0012	0.164 ±0.014	0.300 ±0.026	0.00424 ±0.00070	0.0493 ±0.0081	0.271 ±0.051	0.0204 ±0.0018	0.239	0.238 ±0.024	0.291 ±0.026
800	22.7	0.00207 ±0.00019	0.0241 ±0.0022	0.276 ±0.026	0.0131 ±0.0011	0.152 ±0.013	0.296 ±0.025	0.00395 ±0.00063	0.0460 ±0.0073	0.267 ±0.048	0.0192 ±0.0016	0.222	0.224 ±0.019	0.290 ±0.025
1000	27.1	0.00194 ±0.00017	0.0226 ±0.0019	0.274 ±0.026	0.0122 ±0.0010	0.142 ±0.012	0.293 ±0.025	0.00370 ±0.00057	0.0431 ±0.0066	0.264 ±0.047	0.0178 ±0.0015	0.208	0.207 ±0.017	0.284 ±0.024
1200	31.3	0.00180 ±0.00015	0.0210 ±0.0017	0.269 ±0.025	0.0113 ±0.0009	0.132 ±0.010	0.290 ±0.024	0.00346 ±0.00051	0.0402 ±0.0059	0.260 ±0.046	0.0166 ±0.0013	0.193	0.193 ±0.015	0.281 ±0.024
1400	36.2	0.00169 ±0.00013	0.0197 ±0.0015	0.267 ±0.024	0.0106 ±0.0008	0.123 ±0.009	0.287 ±0.024	0.00325 ±0.00046	0.0378 ±0.0054	0.258 ±0.045	0.0155 ±0.0012	0.181	0.181 ±0.014	0.279 ±0.023
1600	38.9	0.00158 ±0.00012	0.0184 ±0.0013	0.264 ±0.023	0.00983 ±0.00074	0.115 ±0.009	0.284 ±0.233	0.00304 ±0.00042	0.0354 ±0.0049	0.255 ±0.044	0.0145 ±0.0011	0.168	0.169 ±0.013	0.277 ±0.023

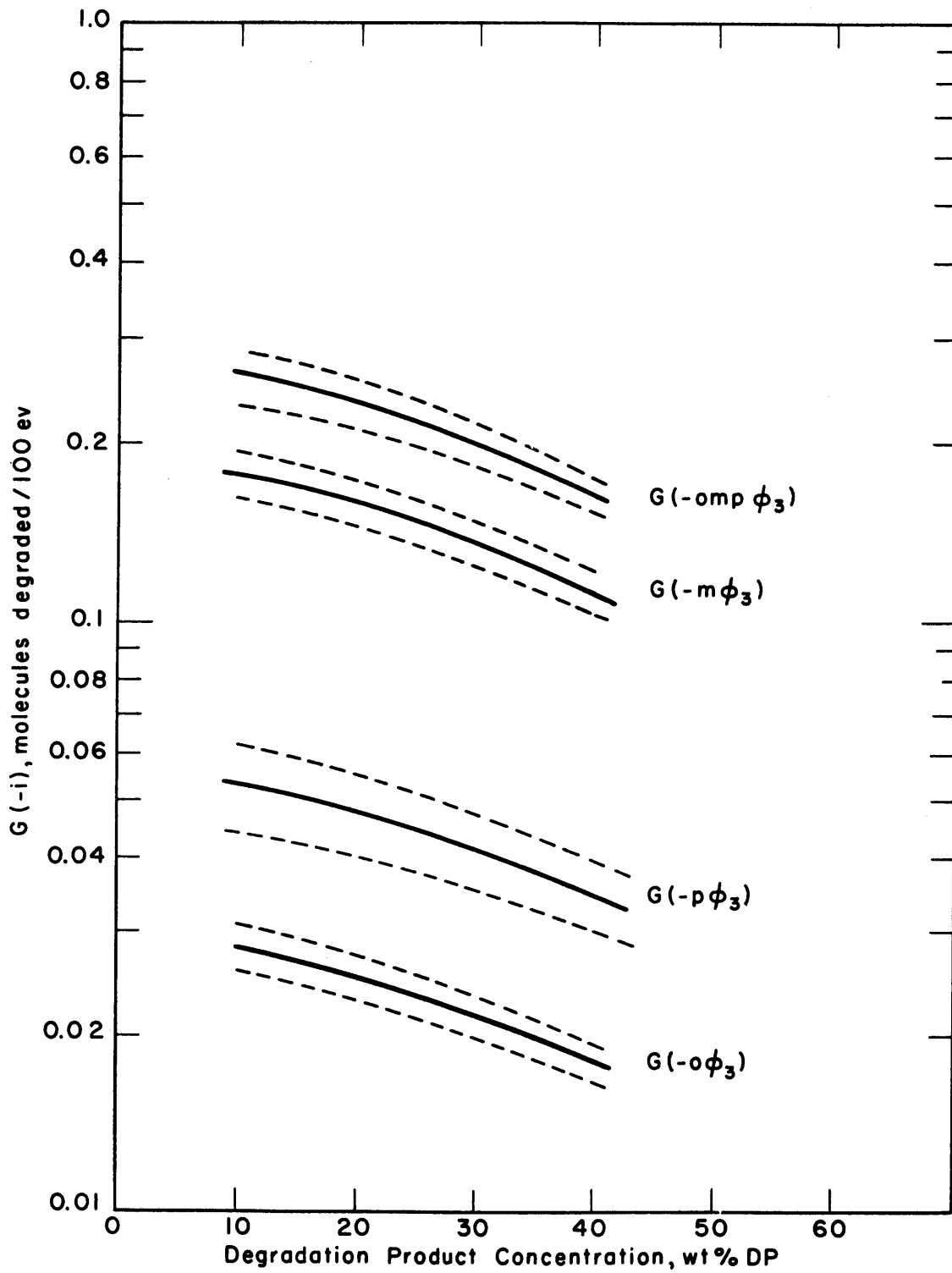


FIG. I.36 DECOMPOSITION YIELD,  $G(-i)$  FOR ORTHO-, META-, AND PARA-TERPHENYLS, 70% CONFIDENCE LIMITS SHOWN

correspond to 70 per cent confidence limits (approximately one standard deviation).

From Figure 1. 36, it will be noted that the decomposition yields expressed in this manner decrease with increasing %DP (and decreasing concentration of the species themselves). Also, there is a large difference in the apparent decomposition yields of the different terphenyl isomers with the order of decreasing decomposition yield corresponding in all cases to the order of decreasing concentration. Both of these observations are not surprising, however, since it is to be expected that components present in the greatest amount will absorb the greatest amount of radiation and hence would be apt to show the greatest amount of degradation per unit of energy absorbed by the entire mixture. For instance, as the concentration of any material tends to zero, its decomposition yield, when defined on the basis of the total energy absorption in the coolant, will tend to zero.

Based on the above considerations, it is desirable to eliminate this concentration dependence of the decomposition yields so that a more meaningful evaluation and comparison of the relative radiation stability of the terphenyl isomers can be made. Accordingly, the decomposition yields given in Figure 1. 36 (and Table 1. 9) have been divided by the concentration of the terphenyl material to which the decomposition yield applies. That is,

$$G^* (-i) = \frac{G(-i)}{C_i(Z)} \frac{\text{molecules}}{100 \text{ ev}} \quad (1. 22)$$

where  $C_i(Z)$  is expressed as the weight fraction. Values of  $G^* (-i)$  are given in Table 1. 9 and Figure 1. 37. From this figure, it will be noted that the decomposition yields expressed in this manner are almost identical for each of the three terphenyl isomers. Furthermore, there is only a slight and statistically insignificant decrease in the decomposition yield with increasing %DP (in Chapter 5, it is shown that this result comes directly from the form of equation found applicable to the data). Hence, the variation of  $G(-i)$  with %DP and the large differences

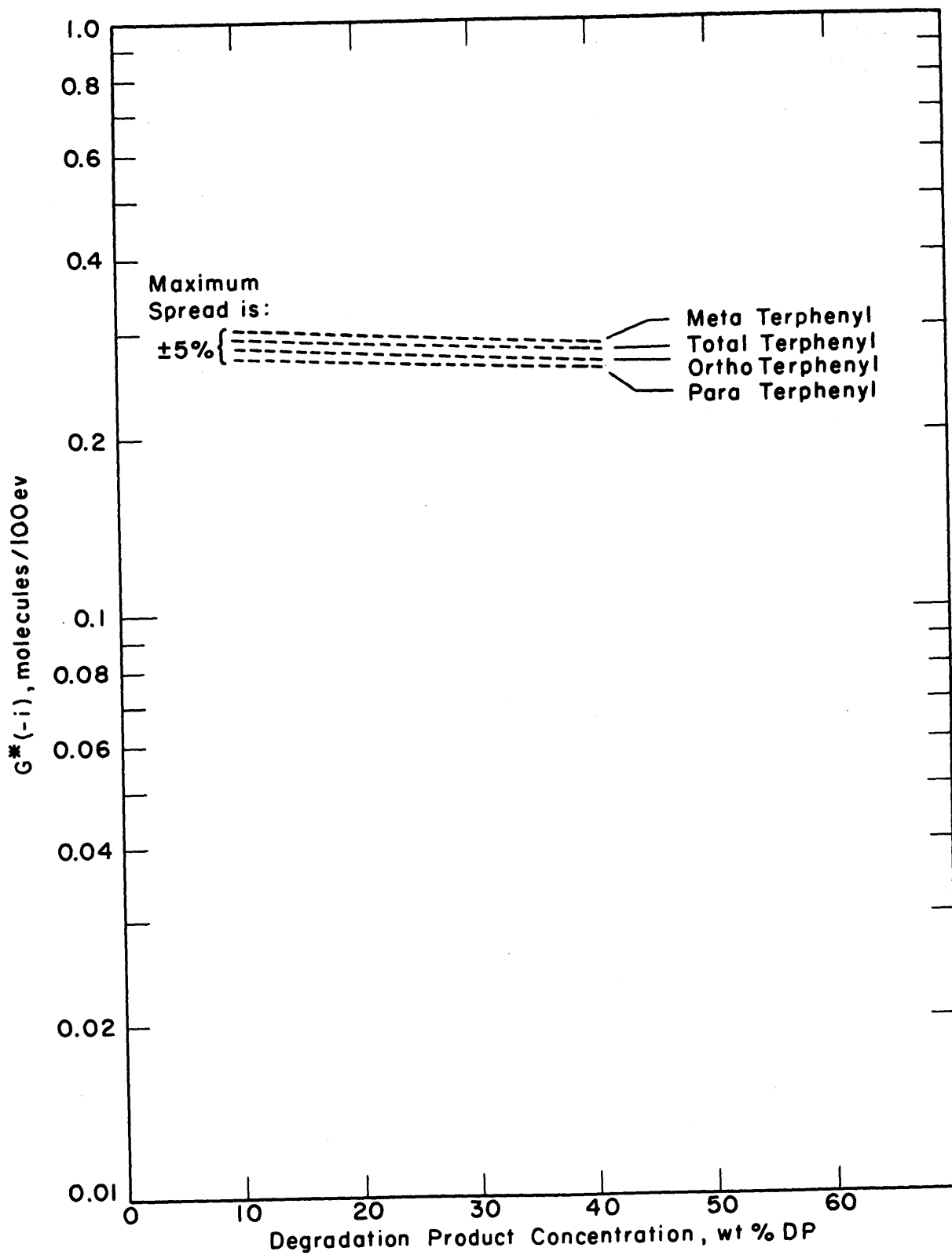


FIG. I. 37 DECOMPOSITION YIELD,  $G^*(-i)$  FOR ORTHO-, META-, AND PARA- TERPHENYLS

noted between the different terphenyl isomers in Figure 1.36 can be interpreted as due almost completely to variations in the concentration of the individual components. Within the limits of the experimental error, the following value of  $G^*(-i)$  can be used independent of the % DP and the particular terphenyl isomer:

$$G^*(-i) = 0.28 \pm 0.03 \frac{\text{molecules}}{100 \text{ ev}}$$

Two interesting interpretations of  $G^*(-i)$  can be made. First, since the carbon-hydrogen ratio of the coolant has been affected only very slightly by the buildup of degradation products in the period covered by this report,

$$\begin{aligned} G^*(-i) &= \frac{\text{molecules isomer degraded}}{100 \text{ ev absorbed in coolant}} \times \frac{1}{\text{wt. fraction isomer in coolant}} \\ &\cong \frac{\text{molecules isomer degraded}}{100 \text{ ev absorbed in coolant}} \times \frac{\text{ev absorbed in coolant}}{\text{ev absorbed in isomer}} \\ &\cong \frac{\text{molecules isomer degraded}}{100 \text{ ev absorbed in isomer}} \end{aligned} \quad (1.23)$$

Hence, the values of  $G^*(-i)$  are seen to represent the decomposition yield expressed as molecules of  $i$  degraded per 100 ev of radiation energy absorbed due only to radiation absorbed by material  $i$ . The results presented in Figure 1.37, therefore, indicate that the relative stabilities of the three terphenyl isomers to ionizing radiation are equal and constant within the uncertainty of the experimentally determined values.

Secondly, defining  $\tau_m$  as the specific absorbed dose, watt-hr of radiation energy absorbed per gram of total coolant, the following relation is obtained:

$$-\frac{dC_i(Z)}{d\tau_m} = G_m^*(-i) C_i(Z) \quad (1.24)$$

Hence,  $G_m^*(-i)$  or  $G^*(-i)$  can be considered as rate constants for the first-order degradation of component  $i$  and the degradation processes occurring in the terphenyls under the conditions of this experiment are shown to be compatible with the assumption of first-order reaction kinetics.

#### 1. 4. 2. 3 Estimation of Relative Decomposition Yields of Fast Neutron Interactions and Gamma Interactions

The  $G^*(-i)$  decomposition yields presented in the preceding section are based on the total energy absorbed in the various terphenyls due to both fast neutron and gamma interactions. In the present case, 33 per cent of the energy absorbed is due to fast neutron and 67 per cent due to gamma interactions. Since previous work (1.8, 1.13) has indicated that combined fast neutron and gamma irradiation is more effective (per unit of energy absorbed in the material) in causing chemical degradation in terphenyls than is gamma irradiation alone, the decomposition yields are dependent on the relative fraction of the energy absorbed due to fast neutron interactions. Assuming that the effects of fast neutron and gamma irradiation are independent of each other, the following relation can be written:

$$G^*(-i) = xG^{*\gamma}(-i) + (1-x) G^{*n}(-i) \quad (1. 25)$$

where  $x$  is the fraction of the total dose due to gamma interactions. Previous work by other investigators (1.10) indicates that  $G^{*\gamma}(-i) \cong 0.12 \pm 0.03$  molecules/100 ev. With  $x = 0.67 \pm 0.03$  and  $G^*(-i) = 0.28 \pm 0.03$  molecules/100 ev for the present experiment,

$$G^{*n}(-i) = 0.61 \pm 0.12 \text{ molecules/100 ev}$$

$$\frac{G^{*n}(-i)}{G^{*\gamma}(-i)} = 5.1 \pm 1.6$$

It is therefore seen that the results of this experiment indicate that fast neutron irradiation is about five times as effective per unit of energy absorbed in causing chemical degradation as gamma radiation.

#### 1. 4. 2. 4 Comparison with Previous Results

In comparing the present results with previous results, it should be remembered that the previous data have, in general, been correlated vs. wt % HB (High Boiler), whereas the present results are correlated vs. %DP (Degradation Products). Also, no reliable estimates of the uncertainty have been reported for the earlier work and, in some cases, only the initial decomposition yields at 0%HB have been presented.

Bley (1. 15) operated on an in-pile loop in the MITR in which Santowax R, a mixture of the three terphenyl isomers quite similar to Santowax OMP, and Santowax O-Santowax M, a mixture of ortho- and meta-terphenyls, were tested. The material was analyzed for % HB by distillation. Eighteen per cent of the energy absorbed in the coolant was estimated by Bley to come from fast neutron interactions and 82 per cent from gamma interactions. Based on Bley's results,  $G^*(-i) = 0.25 \pm 0.06$  molecules/100 ev. The present results, assuming additivity of the fast neutron and gamma effects (Equation (1. 25)), and using the value of  $G^{*\gamma}(-i)$  and  $G^{*n}(-i)$  given in section 1.4. 2. 3, give 0.21 molecules/100 e for the conditions of Bley's experiment; the values thus agree within the experimental uncertainty.

Berg, et al., (1. 8) performed irradiations of Santowax OMP in the Curtiss-Wright Research Reactor with a primary objective of studying the fast neutron effect in the irradiation of the terphenyls. The ortho-, meta-, and para-terphenyl concentrations were determined by gas chromatography. The method of equation fitting for calculating the decomposition yields was used in a manner similar to that described in this report, but with a different type of equation; the equation used by Berg, et al., in fitting their data was of the form corresponding to second-order kinetics. However, as indicated in Chapter 5, the data are equally as well represented by an equation of the type used in this experiment (Equation (1. 14)) as by an equation corresponding to second-order kinetics. Application of the methods used in analyzing the data for the present experiment to Berg's data gives  $G^*(-i) \cong 0.41$  molecules/100 ev. This value compares favorably with the value of  $G^*(-i) = 0.44$  molecules /100 ev obtained from the results of the present

experiment using Equation (1. 25) and Berg's estimate of 65 per cent as the fraction of the absorbed dose due to fast neutron interactions in the Curtiss-Wright Reactor.

Burns, Burns, et al, and Bates, et al, (1. 16, 1. 13, 1. 17) at Harwell have presented the results of electron and in-pile irradiation of the terphenyls. In these experiments, a sublimation method was used for the analysis of % HB and 54. 4 per cent of the dose rate was estimated to come from fast neutron radiation. Using Equation (1. 25) and the results of the present experiment for  $G^{*\gamma}(-i)$  and  $G^{*n}(-i)$ , a  $G^*(-i)$  value of 0. 38 molecules/100 ev would have been expected for the Harwell experiments. A rough estimation of  $G^*(-i)$  values from "smoothed" data presented by Burns, et al, (1. 13) has been made which indicates that  $G^*(-i)$  is constant at  $\sim 0. 6$  molecules/100 ev, up to about 18% HB where it rapidly drops with increasing % HB to a value significantly less than that obtained using the results of the present experiment. This discrepancy is believed to be due to the limited amount of data obtained in the Harwell experiments which makes the determination of accurate decomposition yields difficult.

#### 1. 4. 2. 5 Coolant Cost for Hypothetical Reactor Based on Results Presented in This Report

Assuming the additivity of fast neutron and gamma radiation as implied in Equation (1. 25), the cost of organic makeup for a nuclear power reactor has been estimated as a function of the fractions of the fast neutron energy and gamma energy produced on fission which are absorbed in the organic coolant. The calculation is based on the following conditions:

- (a) All of the terphenyl isomers have the same decomposition yield.
- (b)  $G^*(-omp\phi_3)$  is independent of %DP.

$$G^{*n}(-omp\phi_3) = 0. 61 \pm 0. 10 \text{ molecules/100 ev.}$$

$$G^{*\gamma}(-omp\phi_3) = 0. 12 \pm 0. 03 \text{ molecules/100 ev.}$$

- (c) Thermal efficiency of nuclear power plant = 30%.



- (d) Fraction of reactor thermal energy due to fast neutrons emitted on fission  $\cong 2.51\%$ .
- (e) Fraction of reactor thermal energy due to gamma radiation emitted on fission and by  $(n, \gamma)$  reactions  $\cong 9.55\%$ .
- (f) Cost of organic makeup = \$0.17 per pound.

With these conditions, the organic makeup cost can be written as follows:

$$\text{Organic Makeup Cost} = C[1.6X + 1.2Y][1 \pm 0.3] \frac{\text{mills}}{\text{kwhr (e)}} \quad (1.26)$$

where

C = weight fraction of terphenyls in the coolant.

X = fraction of the fission neutron energy absorbed in the coolant.

Y = fraction of the fission gamma energy absorbed in the coolant.

The results obtained from this equation are presented in Figures 1.38 and 1.39, respectively, for 50 per cent and 75 per cent absorption of the fission neutron energy in the coolant. In each figure, curves are given for 25 per cent, 50 per cent and 75 per cent absorption of the fission gamma energy in the organic. It is seen that at 30% DP, the cost varies from 0.8 to 1.5 mills/kwhr(e), depending on the fraction of the fast neutron and gamma energy absorbed directly in the coolant.

### 1.4.3 Composition of Degradation Gases and Gas Evolution Rate

#### 1.4.3.1 Introduction

Part of the decomposition products produced on irradiation of Santowax OMP are gases consisting of hydrogen and various saturated and unsaturated gases. The rate of evolution and the composition of these gases are important, both with respect to understanding the irradiation degradation mechanism and in designing gas removal and handling systems for organic cooled nuclear reactors.

For these reasons, features permitting the measurement of the

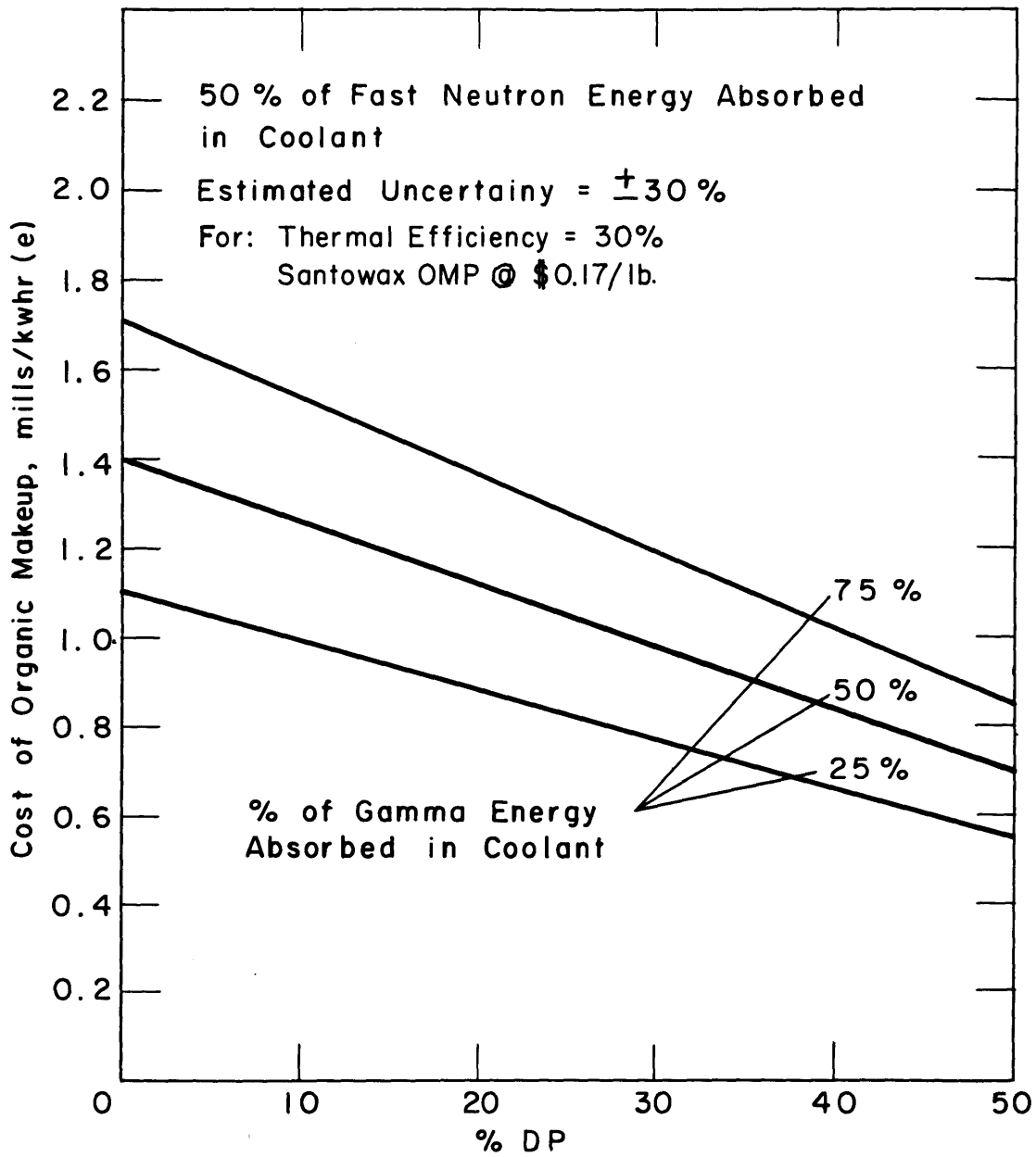


FIG. 1.38 COST OF ORGANIC MAKEUP BASED ON 50% OF FAST NEUTRON ENERGY ABSORBED IN COOLANT

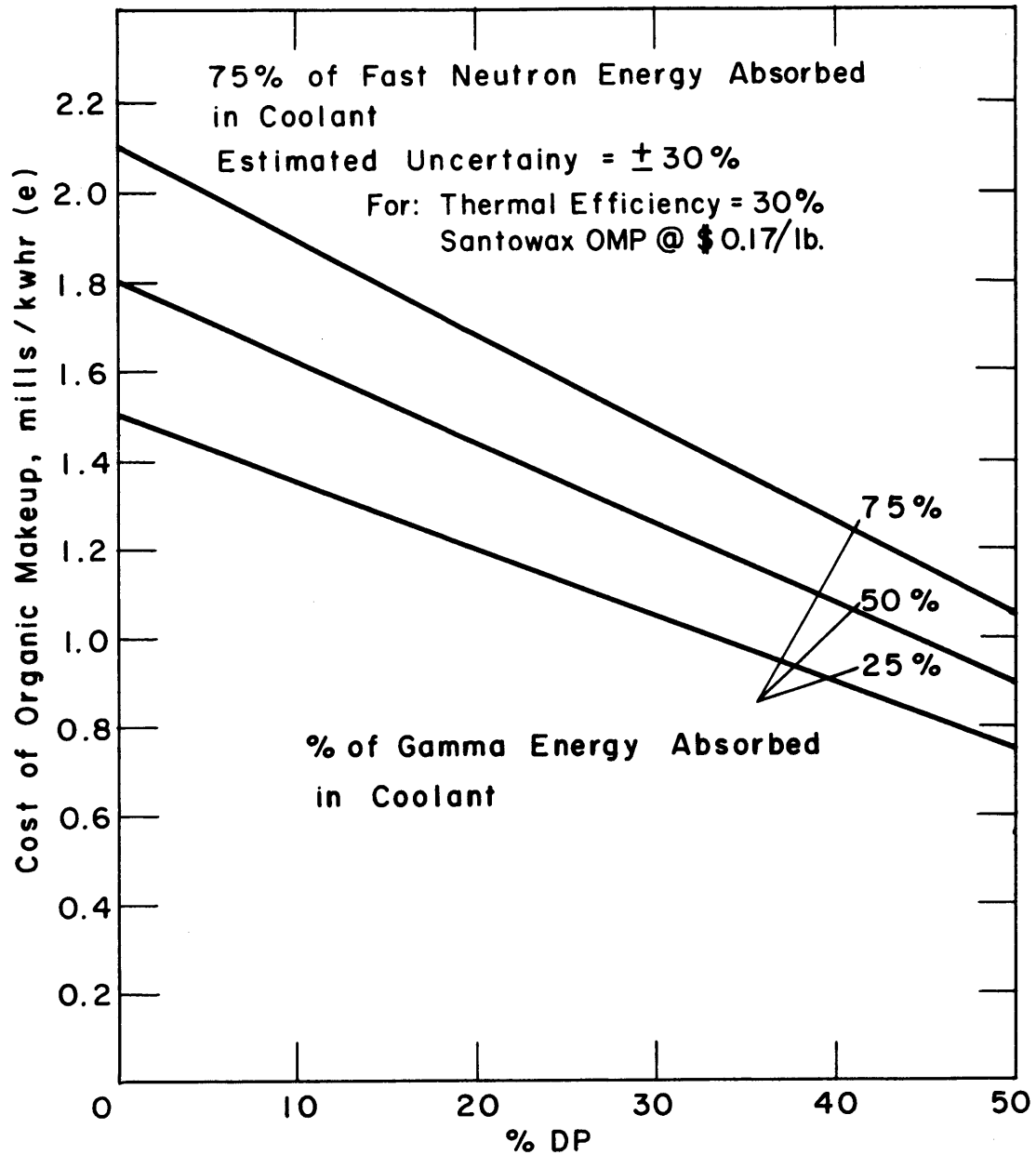


FIG. 1.39 COST OF ORGANIC MAKEUP BASED ON 75% OF FAST NEUTRON ENERGY ABSORBED IN ORGANIC COOLANT

gas composition and evolution rate were included in the design of the loop. The gases in the loop consist of undissolved gases in the gas space in the surge tank and dissolved gases in the circulating organic coolant. Provision has been included in the loop for taking gas samples from the surge tank and liquid samples from the loop. By measuring the volume and composition of the gas removed in the gas samples, as well as the solubility and composition of the gases in the liquid, a gas balance can be performed on the loop and the gas evolution rate determined. Since only limited data on the solubility and composition of the dissolved gas in this first irradiation were available, it has been possible to determine only the total gas evolution rate and not that of each gaseous component produced on irradiation of Santowax OMP.

#### 1. 4. 3. 2 Undissolved and Dissolved Gas Composition

The compositions of the undissolved and dissolved gases in the organic loop have been measured, using mass spectroscopy. The results for the undissolved gas composition are presented in Figures 1. 40, 1. 41, and 1. 42 in which the hydrogen, saturated hydrocarbon, and unsaturated hydrocarbon gas contents are given, respectively. These plots are based on an  $N_2$ ,  $CO$ ,  $CO_2$ , and  $O_2$  free basis (nitrogen was the pressurizing gas and  $CO_2$ ,  $CO$ , and  $O_2$  are believed to be due to leakage of air into the samples before the mass spectrometer analyses were made). It is seen from Figure 1. 40 that hydrogen is the largest component of the undissolved gases. At short exposure times, it appears that between 90 per cent and 100 per cent of the undissolved decomposition gas is hydrogen. With continued operation of the loop, the concentration of hydrogen in the undissolved decomposition gas decreased to 50 per cent at about 1500 MWHR's of reactor operation, with the remainder of the gas being saturated and unsaturated hydrocarbons.

The composition of the saturated hydrocarbon gases in the undissolved gases increase linearly with the MWRH's of reactor operation (see Figure 1. 41). Furthermore, extrapolation of the straight lines to 0 MWHR's indicates that the concentration of these gases in the undissolved radiolytic gas was zero at the beginning of the irradiation. The two largest components of

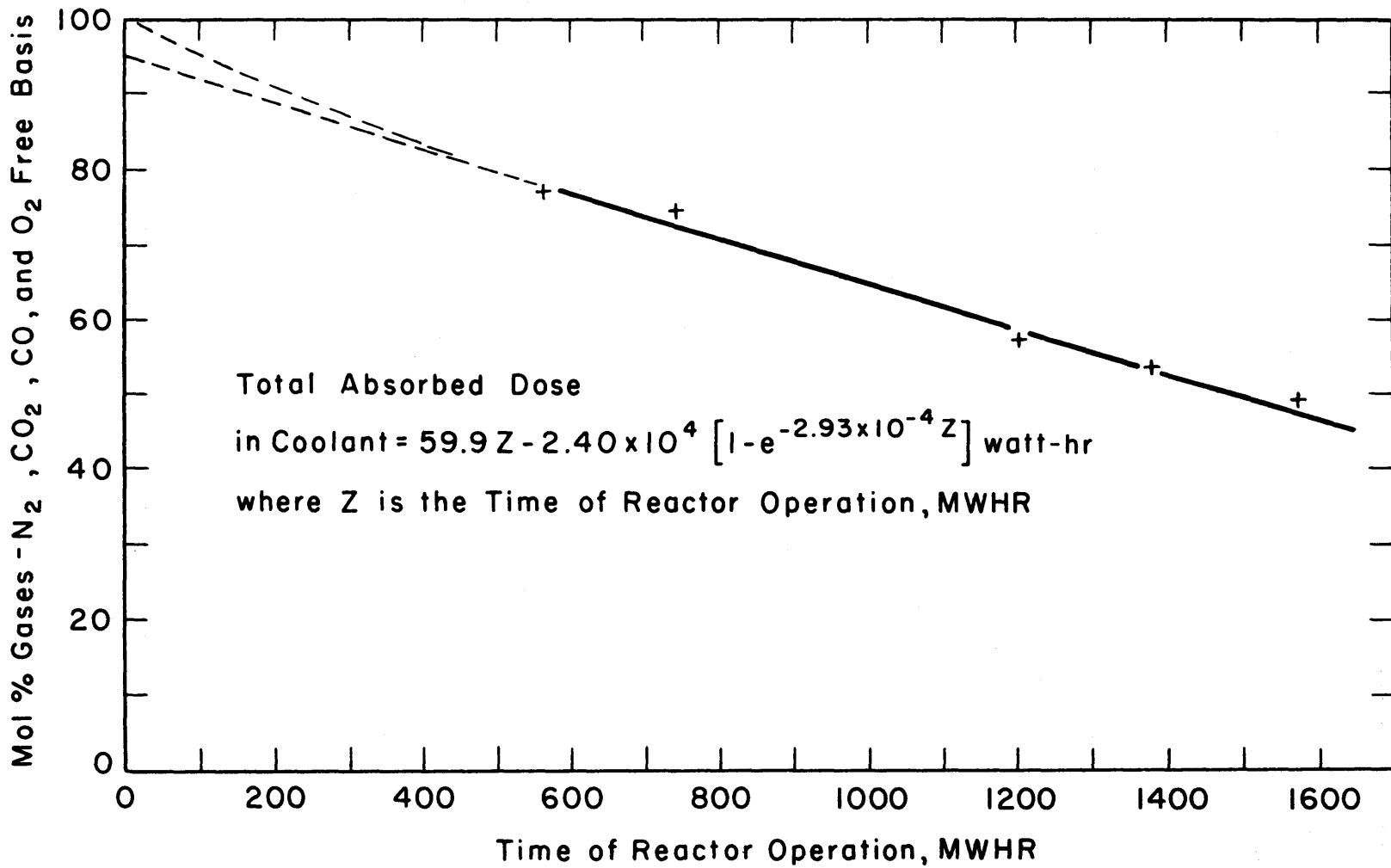


FIG. I.40 HYDROGEN CONTENT OF UNDISSOLVED GASES IN LOOP

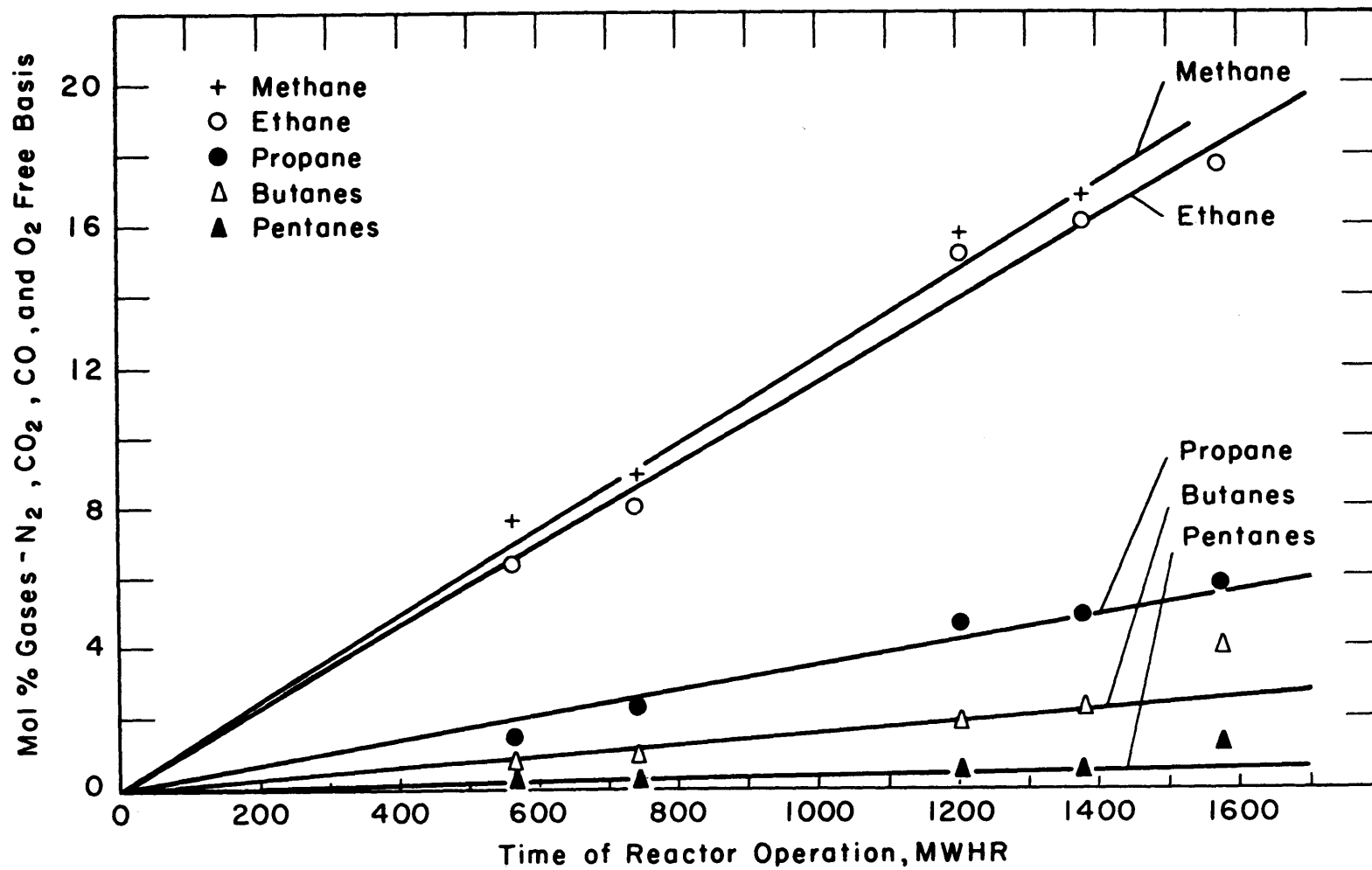


FIG. 1.41 SATURATED GAS CONTENT OF UNDISSOLVED GASES IN LOOP

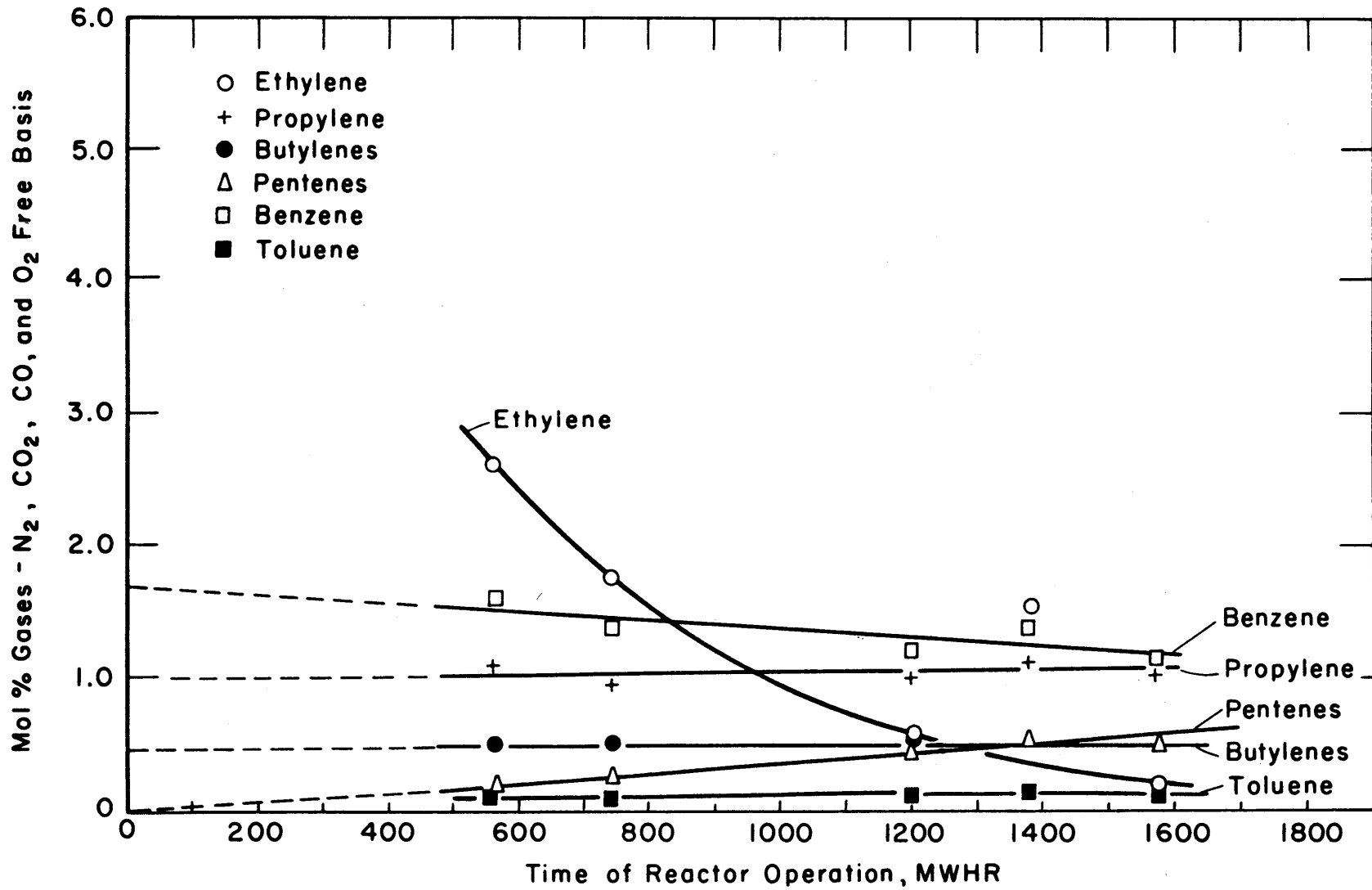


FIG. 1.42 UNSATURATED GAS CONTENT OF UNDISSOLVED GASES IN LOOP

these gases are methane and ethane which compose 18 per cent and 17 per cent of the undissolved degradation gases at 1500 MWHR's of reactor operation.

In contrast to the saturated hydrocarbons, it can be seen from Figure 1. 42 that the unsaturated hydrocarbon gases do not extrapolate to zero concentration at zero MWHR's of reactor operation. This may indicate that the undissolved radiolytic gases produced during the initial period of irradiation consist of hydrogen and a small amount (< 10 per cent) of unsaturated hydrocarbons.

Table 1. 10 presents the one analysis available (during the period covered in this report) on the composition of the dissolved gas. As can be seen from this table, no hydrogen gas was reported. Whether this is actually the case or not must await future measurements. Considering the large hydrogen content of undissolved gases, it is believed the results presented in Table 1. 10 may be in error with respect to the hydrogen content.

Table 1. 10. Composition of Dissolved Gases in Loop, Sample L-52E, 1170 MWHR.

Surge Tank Temperature = 603°F  
Loop Pressure = 115 psig

<u>Component</u>	<u>mol %</u>
Hydrogen	-
Carbon monoxide	1. 76
Oxygen	3. 45
Carbon dioxide	1. 56
Nitrogen	17. 17
Methane	8. 92
Ethane	26. 14
Ethylene	0. 28
Propane	12. 23
Propylene	5. 80
Butanes	10. 76
Butylenes	2. 55
Pentanes	2. 63
Pentenenes	2. 50
Hexanes	0. 51
Benzene	3. 63
Toluene	0. 10
Xylene	0. 01



### 1. 4. 3. 3 Gas Evolution Rate

By performing a gas balance on the loop at various times, the total gas evolution rate has been determined. Due to lack of data on the composition of the dissolved gases throughout this irradiation period, it has not been possible to derive the evolution rate for each component of the evolved gases but only for the total gases evolved on irradiation.

A gas balance on the loop at Z MWHR's can be written in terms of the following gas volumes at standard temperature and pressure (32°F, 14. 7 psia):

$$\begin{aligned}
 V &= [ \text{Gas evolved + undissolved gas in loop at } Z = 0 \\
 &\quad + \text{dissolved gas in loop at } Z = 0 ] \\
 &= [ \text{Undissolved gas in loop + dissolved gas in loop} \\
 &\quad + \text{cumulative total of gas removed by gas sampling} \\
 &\quad + \text{cumulative total of gas removed by liquid sampling} ] \\
 &\hspace{15em} (1. 27)
 \end{aligned}$$

The derivative of this equation gives the gas evolution rate,  $\text{cm}^3 \text{ (STP)/MWHR}$

In performing a gas balance, the solubility of the gases in the coolant must be known so the total gas dissolved in the coolant, as well as the gas removed in the liquid samples, can be determined. Two different values for the gas solubility have been determined in the present case. The first,  $7. 1 \times 10^{-3} \text{ cm}^3 \text{ (STP)/psia}$ , is based on measurements performed on liquid samples removed from the loop in which the dissolved gases were determined when the sample was boiled under a vacuum. These measurements indicated that the gas solubility could be assumed constant and independent of the gas and coolant compositions. The second,  $2. 6 \times 10^{-2} \text{ cm}^3 \text{ (STP)/psia}$ , is based on changes in the loop pressure when six consecutive gas samples were removed from the loop. The value of  $7. 1 \times 10^{-3} \text{ cm}^3 \text{ (STP)/psia}$  is believed to be the more reliable value. Additional measurements will be made in the future, to provide a better estimate of the dissolved gas content of the irradiated coolant.

In Figure 1. 43, the results of the gas balance are presented for both values of the gas solubility which have been assumed to be constant

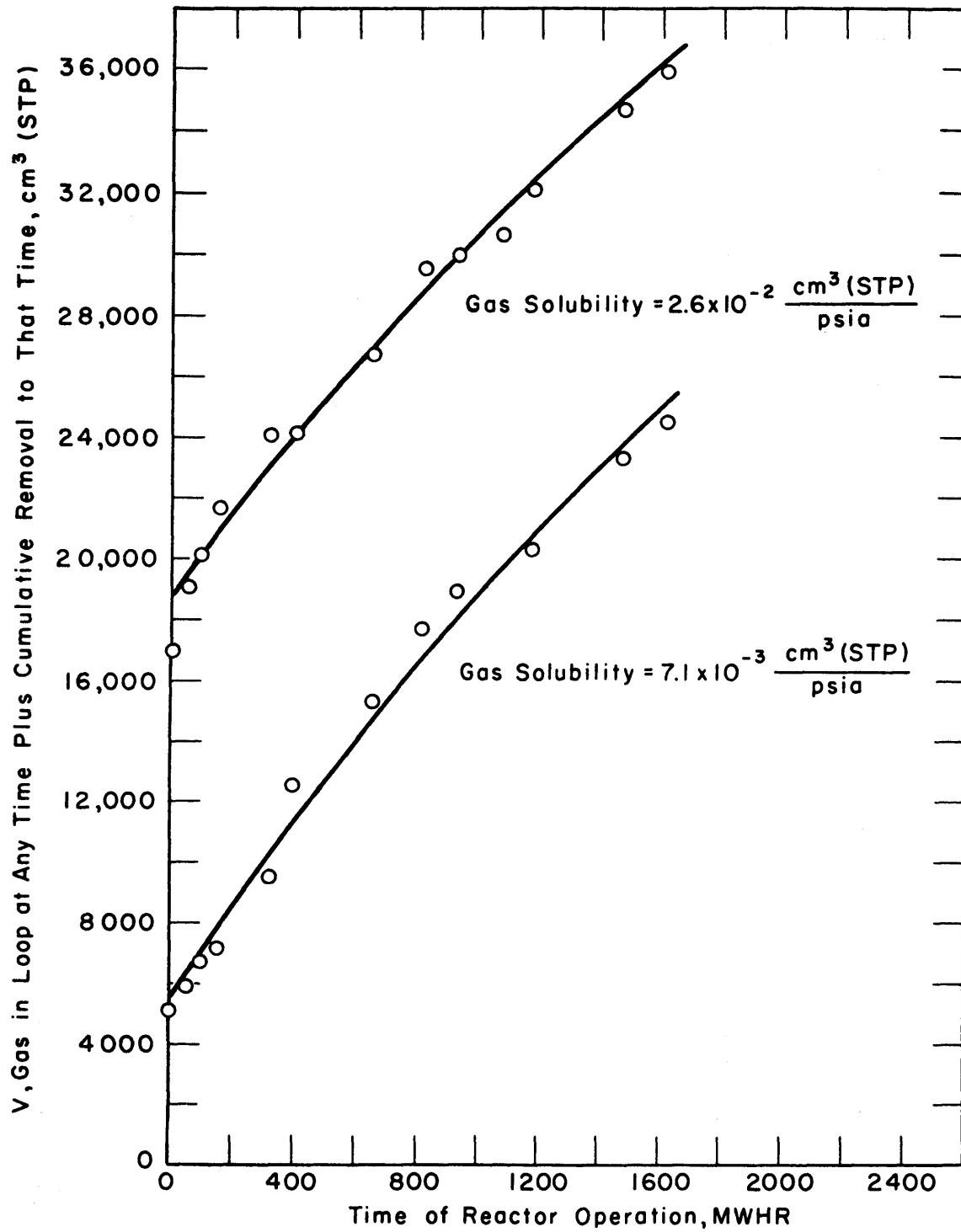


FIG. 1.43 GAS PRESENT IN LOOP PLUS CUMULATIVE REMOVED AS FUNCTION OF MWHR'S OF REACTOR OPERATION AND GAS SOLUBILITY

throughout the irradiation period. It will be noticed from this figure that the curves based on both gas solubilities are almost parallel, indicating that the effect of the gas solubility on the calculated evolution rate is quite small. This would be expected, since the circulating organic mass, as well as the loop pressure, have remained approximately constant throughout the irradiation period, so that with the assumption of constant gas solubility, the amount of dissolved gas is almost constant.

The procedure followed in estimating the gas evolution rate and radiolytic yield from this data is similar to that used in determining the liquid decomposition yield. In Figure 1. 44, the data are plotted vs.

$(1 - e^{-2.93 \times 10^{-4} Z})$ , where it is seen that the data can be represented by a straight line on this plot. The constant,  $2.93 \times 10^{-4}$ , comes from Equation (1. 15) for the total terphenyl concentration in the coolant.

Hence, the data can be represented by an equation of the following type:

$$V = V_1 + P(1 - e^{-(2.93 \pm 0.18) \times 10^{-4} Z}) \quad (1. 28)$$

A least squares calculation using the data based on a gas solubility of  $7.1 \times 10^{-3} \text{ cm}^3 \text{ (STP)/psia}$  gives (with 70 per cent confidence limits):

$$V = (5560 \pm 920) + (5.21 \pm 0.51) \times 10^4 (1 - e^{-(2.93 \pm 0.18) \times 10^{-4} Z}) \quad (1. 29)$$

With conversion of units, the derivative of this equation divided by the dose rate,  $R_{SW}^{TI}$ , gives the radiolytic gas yield,  $G(\text{gas})$  molecules/100 ev. Analogous to the liquid composition yield,  $G^*(\text{gas})$  is defined as  $G(\text{gas})/C$  where  $C$  is the weight fraction of terphenyls in the coolant.

The results obtained are presented for both  $G(\text{gas})$  and  $G^*(\text{gas})$  in Figure 1. 45, where the limits represent the 70 per cent confidence limits. It will be noted from Figure 1. 45 that  $G(\text{gas})$  decreases with increasing % DP. However, as in the case of the liquid decomposition yield, the form of equation selected to represent the data results in almost constant values for  $G^*(\text{gas})$ . Within the experimental error,  $G^*(\text{gas})$  can be assumed independent of % DP and the following value is recommended:

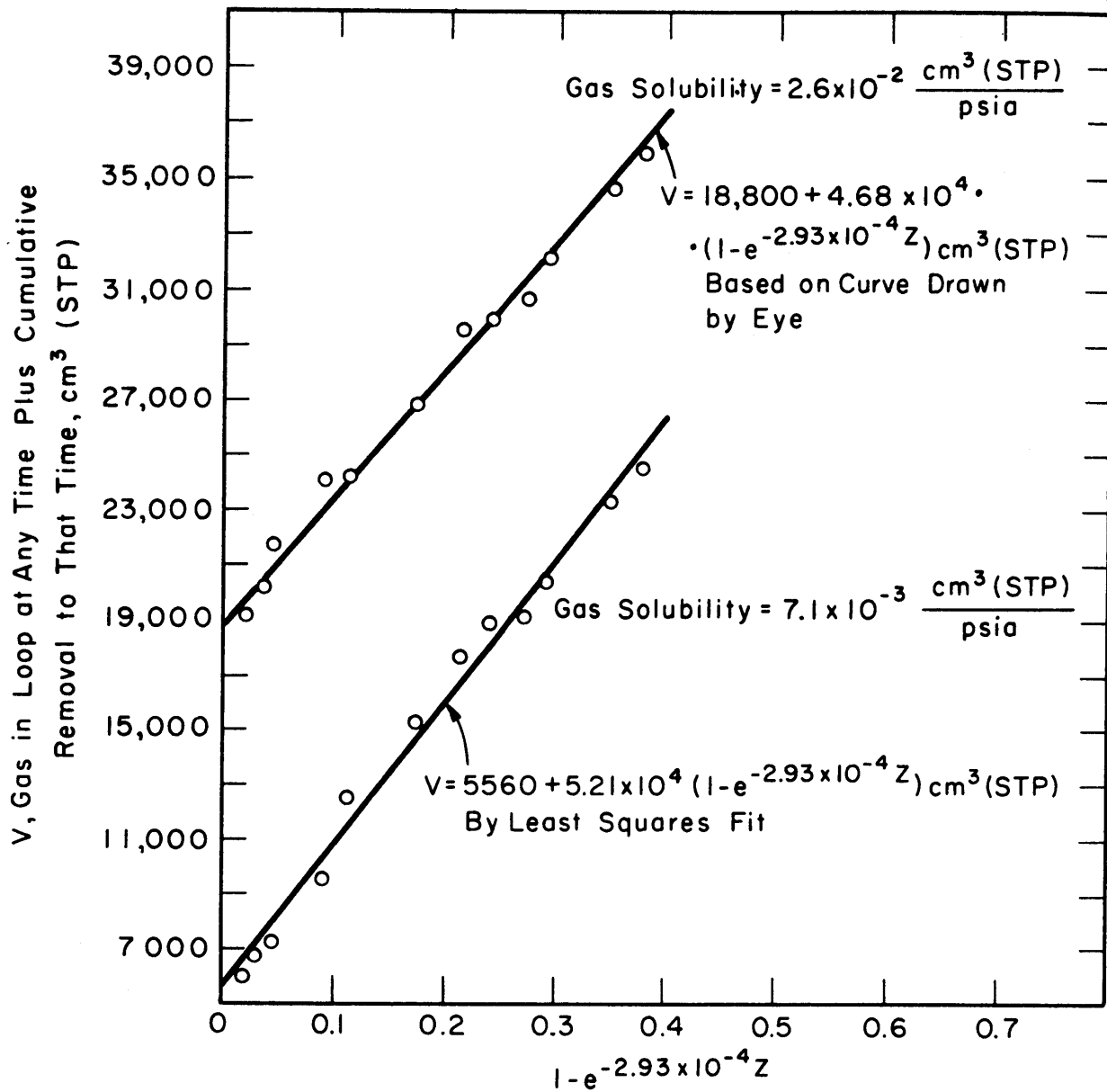


FIG. I.44 COMPARISON OF GAS EVOLUTION CALCULATIONS BASED ON TWO VALUES OF GAS SOLUBILITY

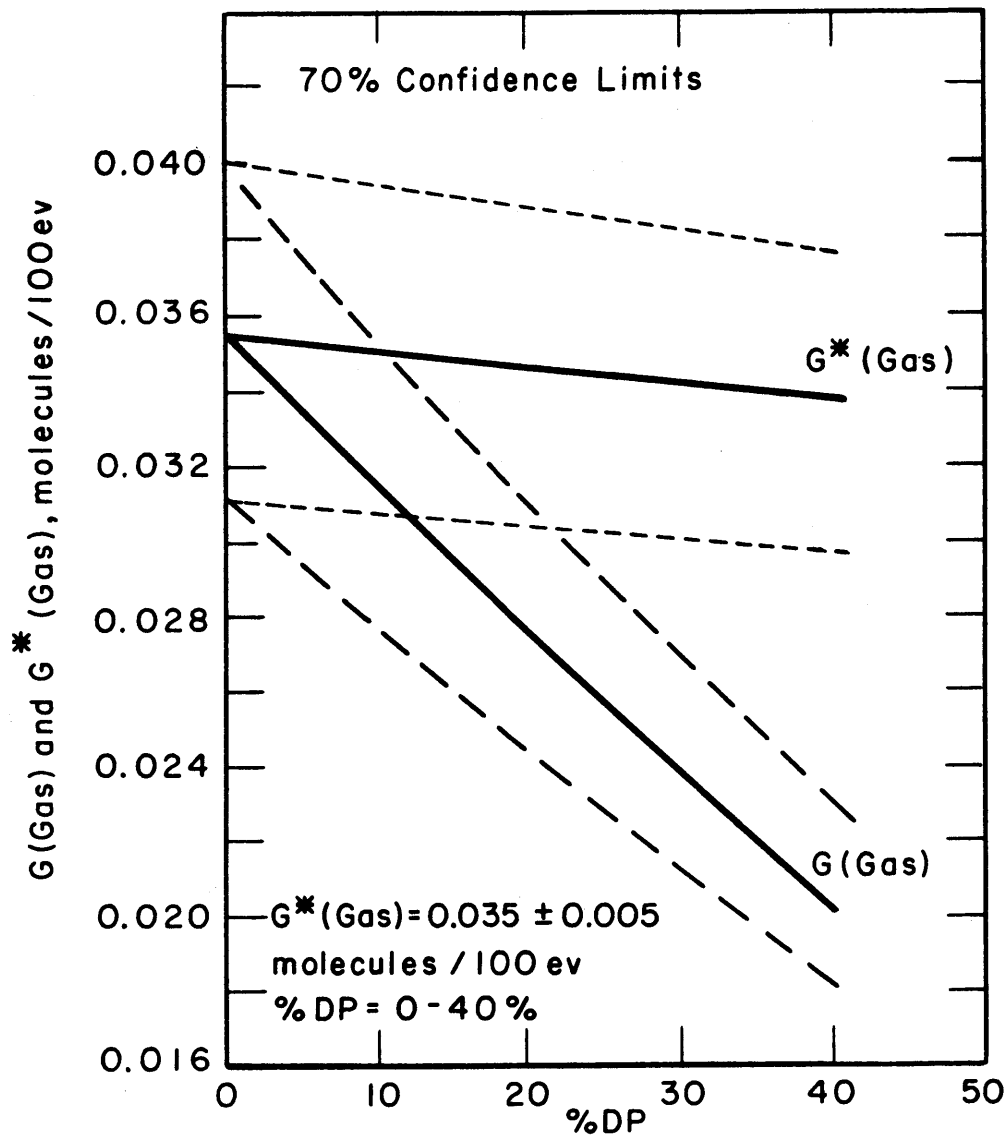


FIG. I.45 THE TOTAL RADIOLYTIC GAS YIELD FOR THE IRRADIATION OF SANTOWAX OMP

$$G^*(\text{gas}) = 0.035 \pm 0.005 \text{ molecules/100 ev}$$

The value obtained using a gas solubility of  $2.6 \times 10^{-2} \text{ cm}^3 \text{ (STP)/psia}$  is 0.031 molecules/100 ev, a difference of about 11 per cent.

As for the liquid decomposition yield and subject to the same assumptions, fast neutron and gamma gas yields can be determined. Following Equation (1.25), this can be expressed as:

$$G^*(\text{gas}) = xG^{*\gamma}(\text{gas}) + (1-x)G^{*n}(\text{gas}) \quad (1.30)$$

Based on the results of Bates, et al., (1.17),  $G^{*\gamma}(\text{gas}) \cong 0.013 \pm 0.002$  molecules/100 ev. Substitution of this quantity into Equation (1.30), along with the results of the present experiment, gives:

$$G^{*n}(\text{gas}) = 0.080 \pm 0.017 \text{ molecules/100 ev}$$

$$\frac{G^{*n}(\text{gas})}{G^{*\gamma}(\text{gas})} = 6.1 \pm 1.6$$

Hence, based on the results of the present experiment, the effect of fast neutrons in producing gases on irradiation of Santowax OMP is definitely greater than the effect of gamma radiation.

#### 1.4.3.4 Comparison with Previous Results of In-Pile Irradiation of the Terphenyls

Berg, et al., (1.8) have reported gas yields for the irradiations of Santowax OMP in the Curtiss-Wright Research Reactor described in section 1.4.2.4. Based on these results, an average value of 0.054 molecules/100 ev was obtained. Using Equation (1.30) and the results of the present experiment for  $G^{*\gamma}(\text{gas})$  and  $G^{*n}(\text{gas})$ , a value of  $G^*(\text{gas}) = 0.057$  molecules/100 ev would be expected for the conditions of Berg's experiments (65 per cent of total dose rate due to fast neutron interactions). The agreement is excellent, considering the approximations involved in the comparison.

Burns, Burns, et al., and Bates, et al., (1.16, 1.13, 1.17) have reported the initial gas evolution yields at 0% DP; these values can be taken as approximately equal to  $G^*(\text{gas})$ . In these experiments,

54.4 per cent of the total dose rate was due to fast neutron interactions. Hence, based on the present results, a gas yield of  $G^*$  (gas) = 0.049 molecules/100 ev would have been expected. At an irradiation temperature of 300°C, values of 0.062 and 0.064 molecules/100 ev are reported for para-terphenyl and Santowax R. The reason for the discrepancy of ~28 per cent is unknown but could be due to any one or a combination of several indeterminate factors.

#### 1.4.4 Density and Viscosity

The density and viscosity of irradiated Santowax OMP, up to a degradation product concentration of 39.1 per cent, have been measured over the temperature range of 400 to 800°F. All measurements have been performed in a molten nitrate salt constant temperature bath with a maximum temperature variation of 1 to 2°F.

##### 1.4.4.1 Viscosity

The kinematic viscosity of the irradiated Santowax OMP was determined by measuring the efflux time in a semi-micro capillary viscometer of the Ostwald type. The viscometer calibration constant was determined as a function of liquid volume in the viscometer, using water at 25°C. Calculations indicated that the temperature correction for the viscometer constant could be neglected. The estimated accuracy is ±1% at 400°F and ±4% at 800°F.

The viscosity results are presented in Figure 1.46 where the dynamic viscosity,  $\mu$ , is plotted vs.  $1/T$ , °R<sup>-1</sup>. It is seen that the data form a straight line and can therefore be represented as a function of temperature by an equation of the following type:

$$\mu = \mu_0 e^{\beta/T} \quad (1.31)$$

This equation has been fitted to the data and the calculated values of  $\mu_0$  and  $\beta$  are given in Figure 1.47 as a function of %DP. It is seen that both  $\mu_0$  and  $\beta$  increase as the concentration of degradation products in the coolant increases.

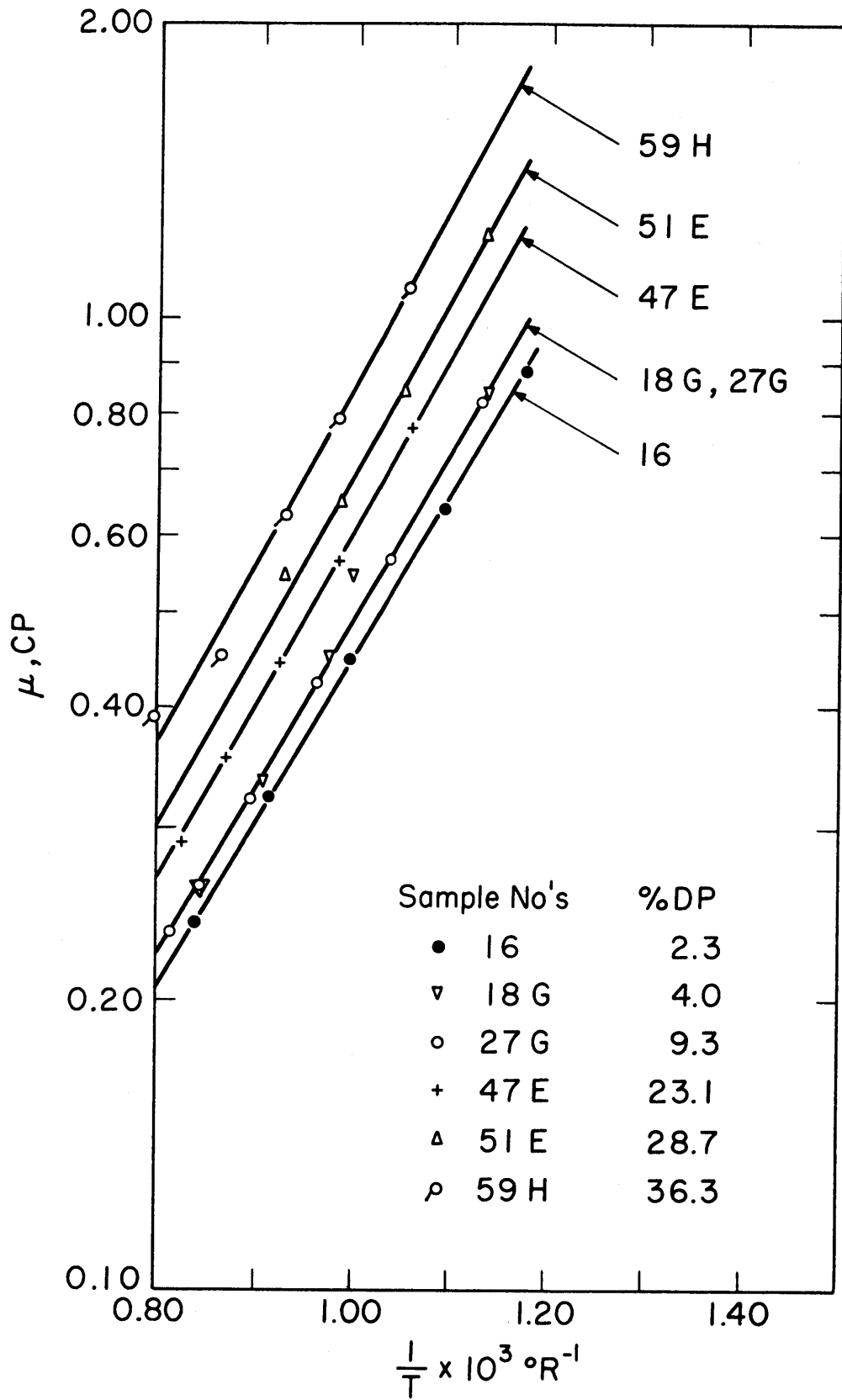
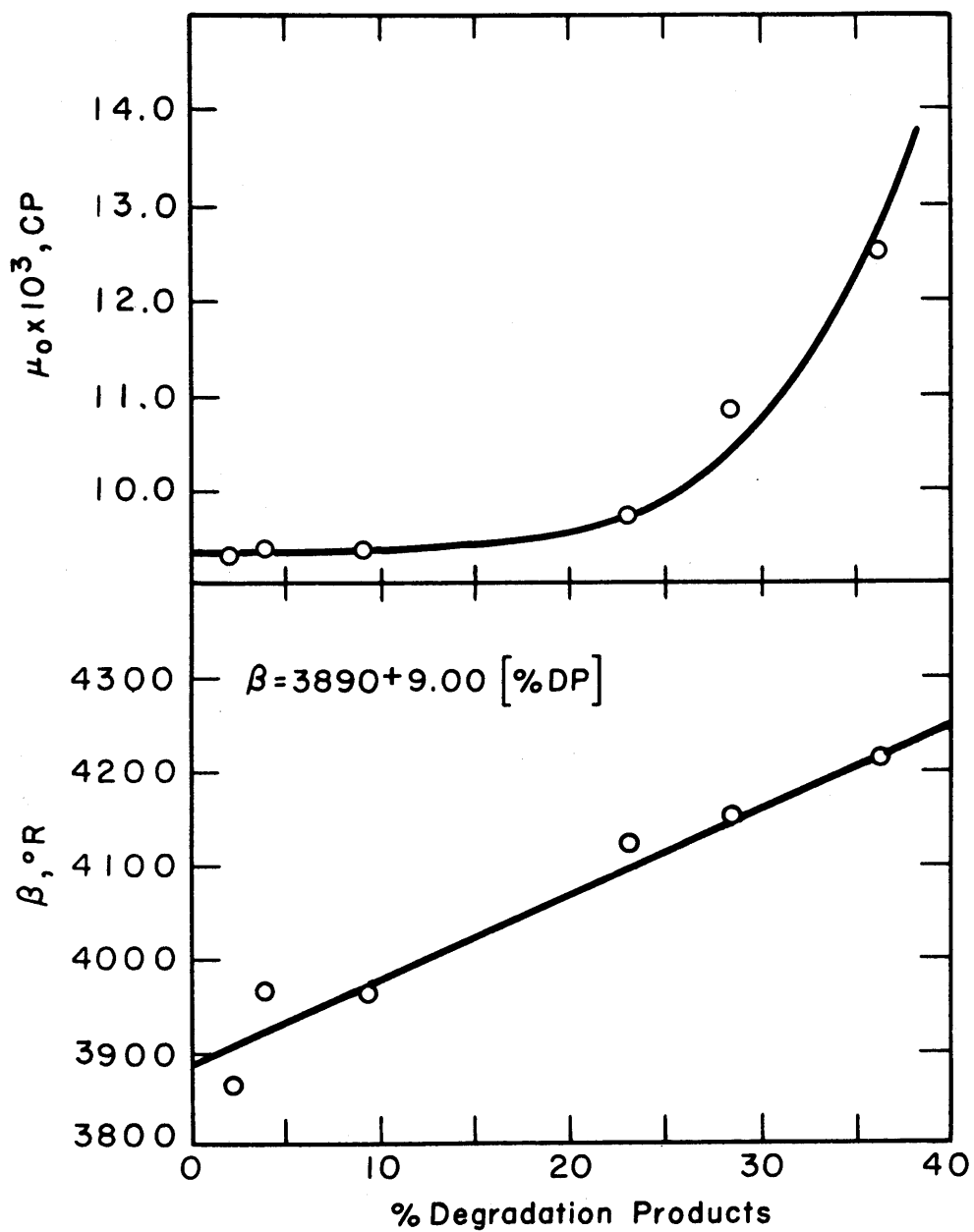


FIG. I.46 VISCOSITY OF IRRADIATED SANTOWAX OMP



FIG. 1.47 VARIATION OF  $\mu_0$  AND  $\beta$  WITH % DP

In Figure 1.48, the viscosity at various temperatures measured for the Santowax OMP irradiated in this experiment is presented as a function of %DP. The results are compared in this figure with the viscosity of irradiated Santowax R measured at Atomics International (1.18) and at Harwell (1.19), which are presented as a function of % HB.

#### 1.4.4.2 Density

The density of the irradiated Santowax OMP was determined by use of a pycnometer in which the volume of a known mass of organic was determined by measuring the liquid height in two capillary tubes connected to a small reservoir of fluid. The volume of the pycnometer at different capillary heights was determined by measuring the height in the capillaries when the pycnometer contained a known volume of mercury at 25°C. Calculations indicate that the volume change of the pycnometer with temperature due to thermal expansion of the glass can be neglected.

The results are presented in Figure 1.49 as a function of temperature for the various samples. It is seen that a linear plot of density vs. temperature is obtained at all concentrations, so that the data can be represented by an equation of the type:

$$\rho = C + aT \quad (1.32)$$

where

$$\rho = \text{density, gms/cm}^3.$$

$$T = \text{temperature, } ^\circ\text{F}.$$

C and a are constants independent of temperature.

Values of C and a have been determined from the data. The quantity, a, has been found to be approximately constant and independent of % DP, so that an average value of  $-4.37 \times 10^{-4} \text{ gm}/(\text{cm}^3\text{-}^\circ\text{F})$  can be used for all degradation product concentrations. C, on the other hand, is linearly dependent on the % DP as indicated in Figure 1.50; C can therefore be expressed as  $1.122 + 1.18 \times 10^{-3}[\%DP]$ , so that the density is given as a function of % DP and temperature by the following equation:

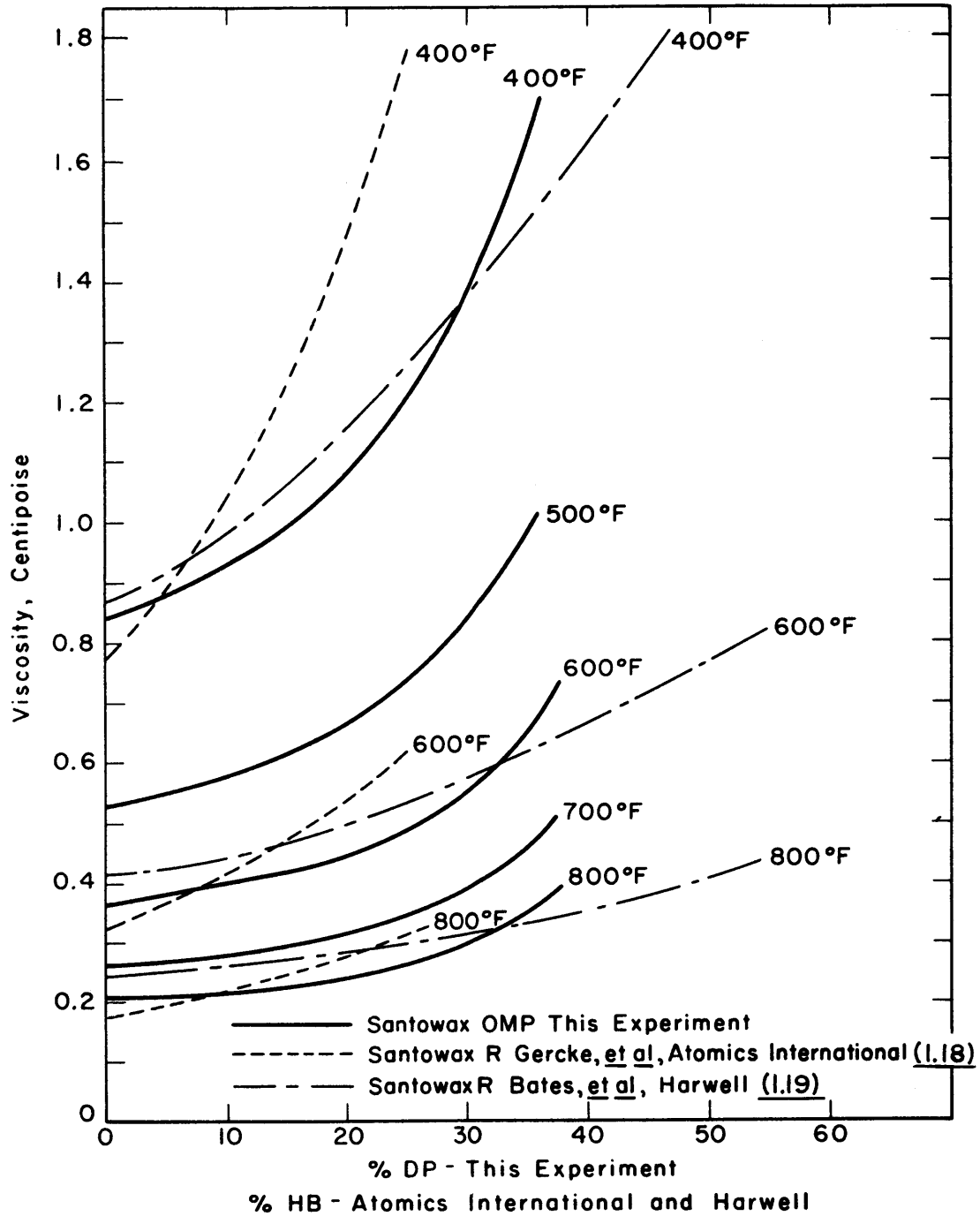


FIG. 1.48 VISCOSITY OF IRRADIATED SANTOWAX OMP AND SANTOWAX R AT VARIOUS TEMPERATURES AS FUNCTION OF CONCENTRATION OF DEGRADATION PRODUCTS OR HIGH BOILERS

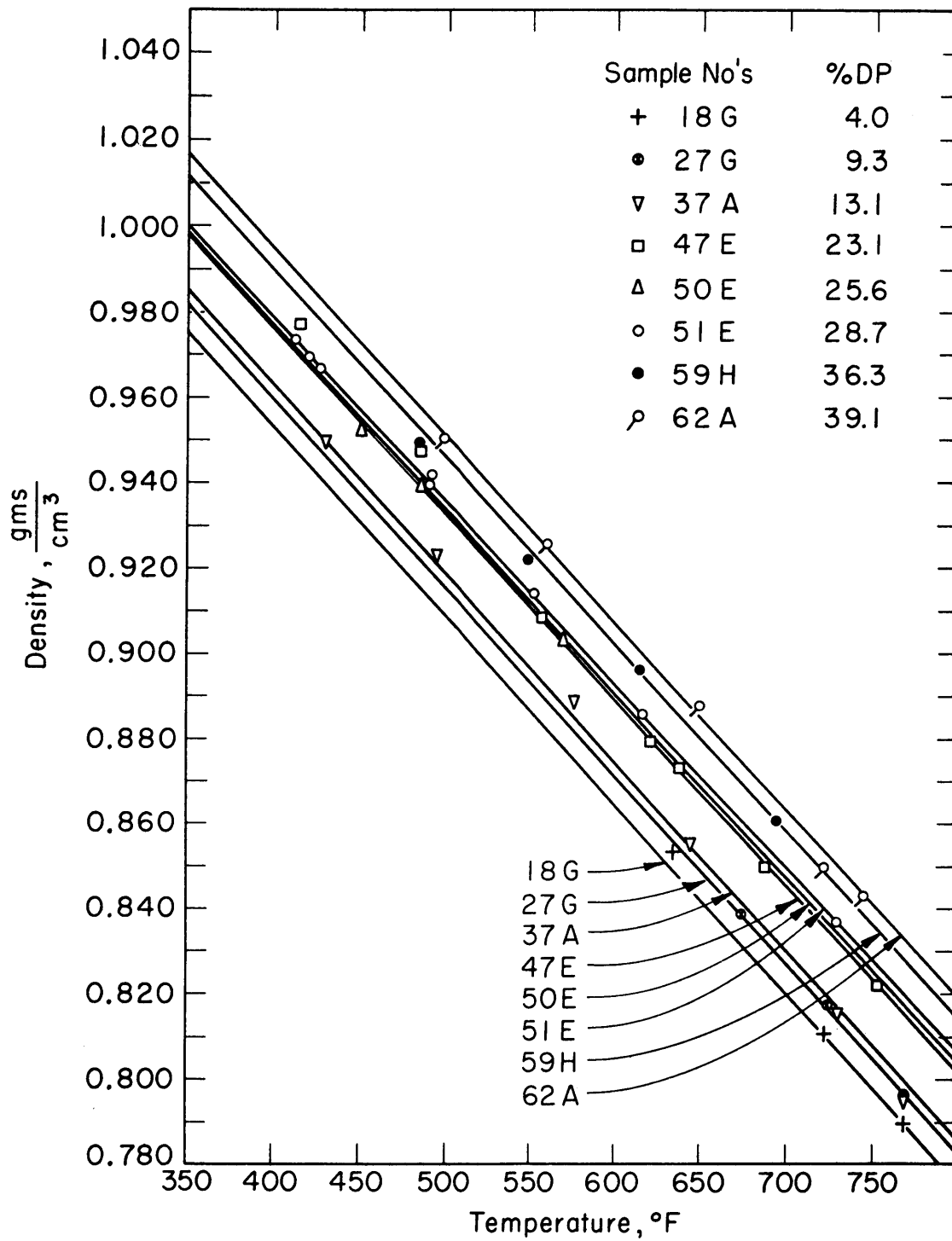


FIG. I.49 DENSITY OF IRRADIATED SANTOWAX OMP

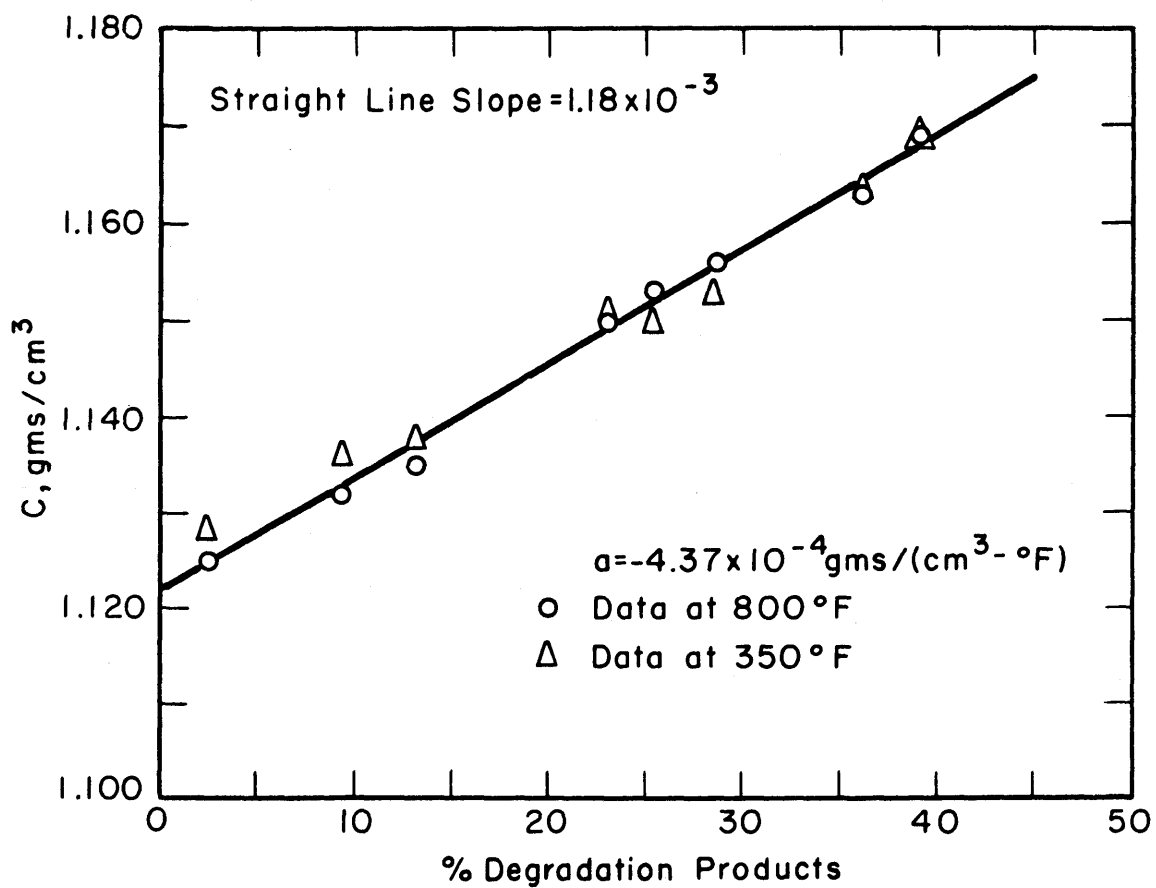


FIG. 1.50 VARIATION OF  $C$  IN CORRELATING DENSITY WITH % DP

$$\rho = 1.122 + 1.18 \times 10^{-3} \%DP - 4.37 \times 10^{-4}T \quad (1.33)$$

It should be noted, however, that recent results at M. I. T. indicate that the density of irradiated Santowax OMP is a function not only of the % DP but also of the irradiation history of the degradation products. This factor will be discussed in future reports.

In Figure 1.51, the density at various temperatures measured for the Santowax OMP irradiated in this experiment is presented as a function of % DP. The results are also compared in this figure with the density of irradiated Santowax R measured at Atomics International (1.18) and at Harwell (1.19), which are presented as a function of % HB.

#### 1.4.5 Other Chemical and Physical Measurements

To further characterize the irradiated Santowax OMP, various other chemical and physical measurements have been performed. Most of these measurements have not yet been fully developed, however, since the primary emphasis for this first irradiation has been in development of methods of measuring the liquid and gas composition and the density and viscosity of the coolant. The available results are presented, however.

##### 1.4.5.1 Carbon-Hydrogen Content

The carbon-hydrogen content of the coolant has been measured throughout the irradiation period using combustion techniques. The estimated precision of the determination is  $\pm 0.5$  per cent. However, based on the radiolytic gas evolved from the coolant, the maximum change in the hydrogen content is only about 0.5 per cent so that the precision of the measurement is not capable of detecting the small change which has occurred. The measured values have fluctuated around the value for pure Santowax OMP of 93.88 wt % carbon and 6.12 wt % hydrogen.

##### 1.4.5.2 Average Molecular Weight

The average molecular weight of the irradiated Santowax OMP has been measured throughout the irradiation period by a cryoscopic method using diphenyl ether as a solvent. This method of measurement for a

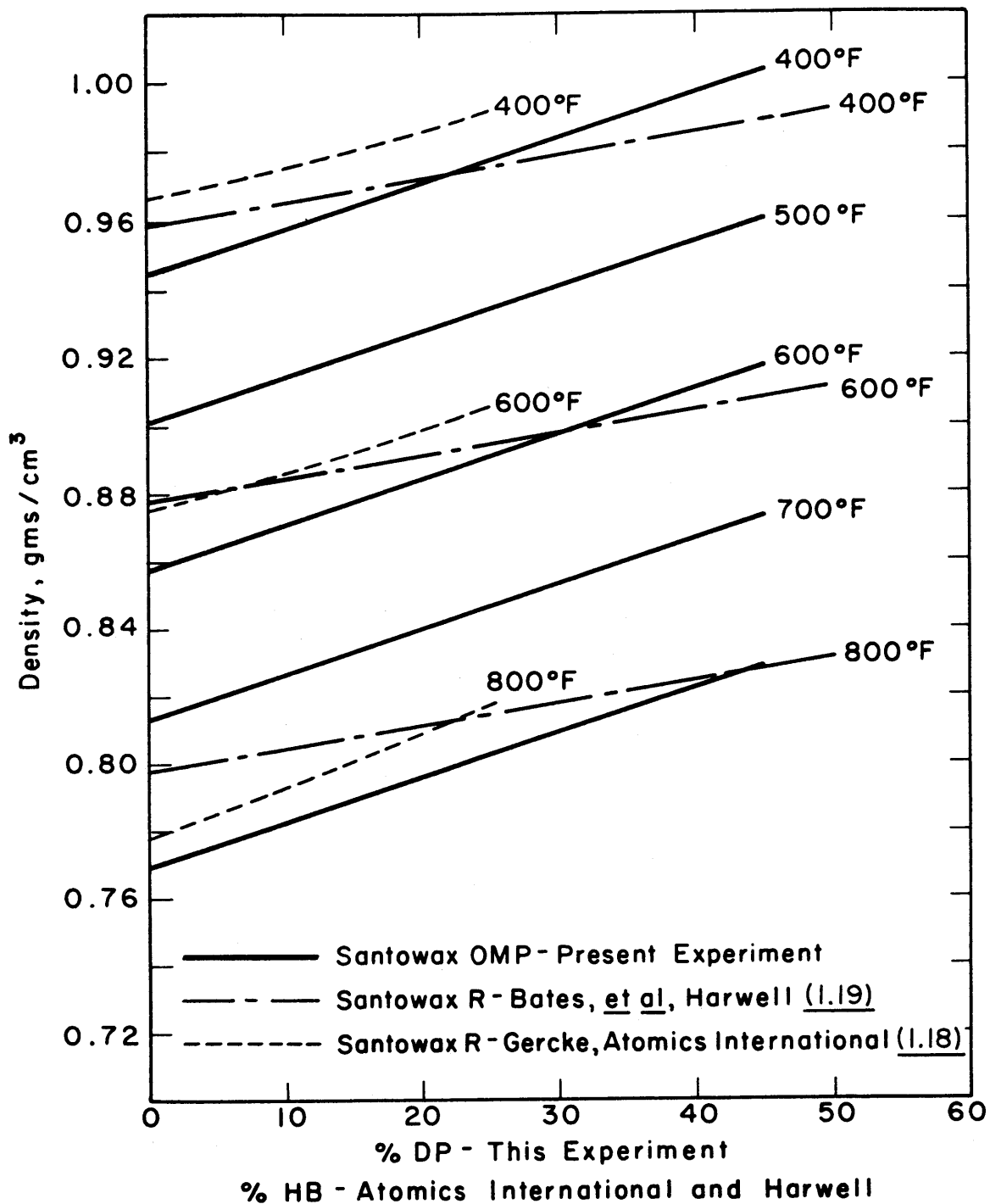


FIG. 1.51 DENSITY OF IRRADIATED SANTOWAX OMP AND SANTOWAX R AT VARIOUS TEMPERATURES AS FUNCTION OF DEGRADATION PRODUCTS OR HIGH BOILERS

mixture as in the present case, provides a number average molecular weight defined as:

$$M_N = \frac{\sum C_i}{\sum C_i / M_i} \quad (1. 34)$$

where

$C_i$  is the wt % of component,  $i$ .

$M_i$  is the molecular weight of component,  $i$ , grams/gram mole.

$M_N$  is the number average molecular weight, grams/gram mole.

For a mixture containing a wide molecular weight range, the number averaging process gives emphasis to low values and is consequently insensitive to high molecular weight materials.

The results obtained in the present case are given in Figure 1. 52 for the organic coolant consisting of the undegraded terphenyls plus all degradation products. Since the molecular weight of the high boiling materials are of primary interest, the usefulness of a number average molecular weight determination of the complete coolant is somewhat limited due to the influence of the undegraded terphenyls as well as low molecular weight degradation products. From the present data, it is impossible to evaluate accurately the average molecular weight of the high boiler material. In Figure 1. 52, the measured average molecular weight of the coolant at various MWHR exposures is compared with two curves calculated (using Equation (1. 34)) for coolant having high boiler with an average molecular weight of 460 (twice that of terphenyl) and 540 (arbitrary), respectively. It is seen that the data have a large scatter. However, as would be expected, an upward trend of the molecular weight of the coolant is apparent with increasing % DP; it also is apparent that the average molecular weight of the high boiler is of the order of 500 but the data are not precise enough to provide a reliable estimate.



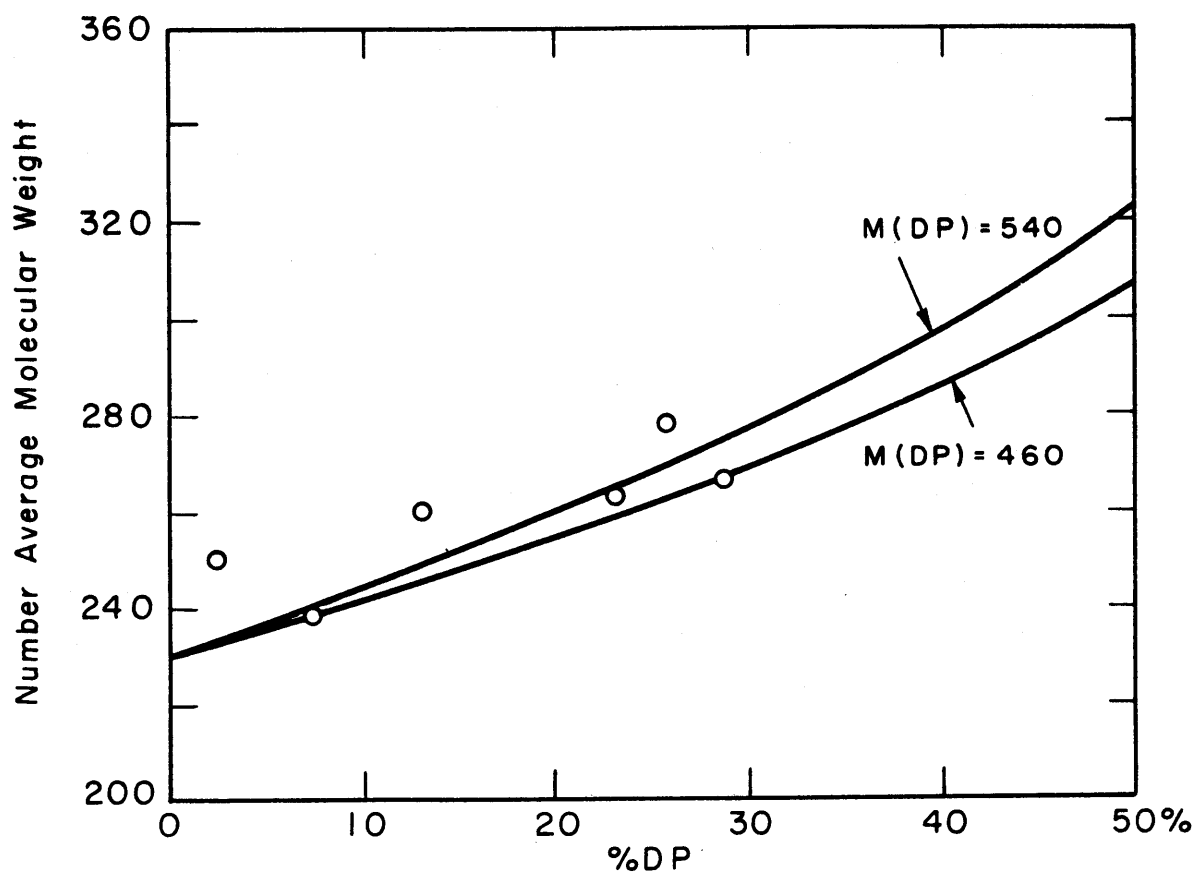


FIG. I.52 VARIATION OF NUMBER AVERAGE MOLECULAR WEIGHT OF IRRADIATED SANTOWAX OMP WITH % DP

#### 1. 4. 5. 3 Melting Point

In Figure 1. 53, the initial liquidus point defined as the temperature at which the liquid phase first appears, and the final liquidus point defined as the temperature at which the final crystal disappears, are presented as a function of % DP. It will be noted that, in agreement with previously reported results (1. 15), the melting point decreases with increasing degradation product concentrations.

#### 1. 4. 5. 4 Inorganic Impurities in Coolant and Coolant Activation

In Table 1. 11, the inorganic concentrations in the coolant, as determined by emission spectroscopy, are presented. It is seen that in all cases, the detectable elements have a maximum concentration of the order of 20 ppm or less. However, there do not appear to be any consistent trends in the data indicating a large uncertainty in the measured quantities and the values quoted can be considered only as an indication that the inorganic content of the coolant is low.

The low inorganic content of the coolant is supported by the low activity induced on irradiation. The dose rate measured approximately 6 inches from the surge tank containing approximately 750 grams of coolant has been of the order of 2 to 4 mr/hr. The dose rate at the surge tank is the largest on the outside of the hydraulic console cabinet. Attempts have been made to count liquid samples removed from the loop, using a scintillation counter, but the activity of the coolant has been too low to give reliable counting rates up to the present time.

#### 1. 4. 5. 5 Other Measurements

The infrared and ultraviolet absorption spectra of the irradiated Santowax OMP have been measured. It is questionable, however, if any significant results can be obtained from this data due to the complex nature of the irradiated Santowax OMP.

Arrangements have been made for the measurements of the thermal conductivity and heat capacity of the coolant and samples 37A (16. 6% DP) and 62A (39. 1% DP), as well as a sample of the unirradiated material have been submitted for these measurements. The results are not yet available, but will be reported in future reports.

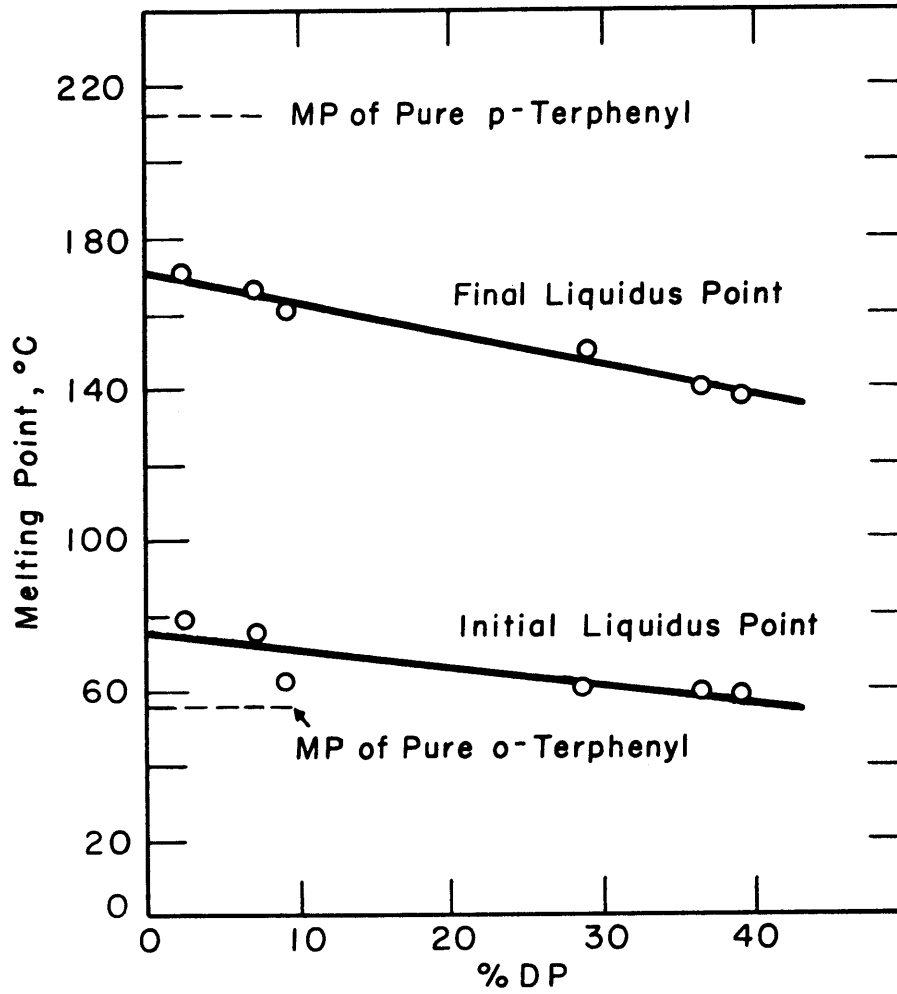


FIG. I.53 VARIATION OF MELTING POINT OF IRRADIATED SANTOWAX OMP WITH % DP

Table 1.11  
SEMI-QUANTITATIVE ASH ANALYSES BY EMISSION SPECTROSCOPY  
CONCENTRATION OF ELEMENTS DETECTED\* -ppm  
OF COOLANT

Sample No.	Ag	Al	Cr	Cu	Fe	Mg	Mn	Mo	Na	Ni	Pb	Si
18G	10-31	<4	6-19	< 2	13-38	2-6	< 2	8-25	1-4	4-13	4	2-6
24E	3-8	<6	<6	-	3-8	< 3	< 1	6-17	-	< 3	6	2-7
27G	-	<4	-	< 4	< 4	< 4	-	-	2-7	-	-	12-35
35E	-	<2	-	-	-	2	-	-	1-3	-	-	3-9
47E	-	3-8	-	<1.3	1-2	4-12	-	< 1	13-39	<2.6	-	15-15 <sup>4</sup>
50E	-	1-4	1-4	< 2	2-7	7-21	< 1	-	6-17	< 5	-	28-57
51E	-	< 2	< 2	< 2	2-6	< 2	-	-	< 4	-	-	3-10
59HL	-	1-3	-	< 1	1-3	< 1	Trace	< 1	-	-	-	2-5

\* From the ash resulting after ignition at temperature of 750°C to 1000°C

Higher ignition temperatures are required at lower % coolant and some oxides may be lost.

## 1. 5 HEAT TRANSFER MEASUREMENTS

### 1. 5. 1 Introduction

One of the more important considerations in the design of an organic-cooled nuclear reactor is estimation of the heat transfer performance of the organic coolant. Provision was therefore incorporated in the M. I. T. loop for the out-of-pile measurement of the heat transfer coefficients of the irradiated organic. Throughout the period covered in this report, measurements of the forced convection heat transfer coefficient have been performed at intervals of approximately every 5 per cent increase in the degradation product concentration. The measurements have been performed at nominal heat fluxes of 100,000 Btu/hr-ft<sup>2</sup> and 200,000 Btu/hr-ft<sup>2</sup> and a bulk organic temperature entering the test heater of 600°F; for each series of heat transfer measurements at a given heat flux, and % DP, the measurement has been made at approximately five different velocities between 10 and 20 ft/sec.

In analyzing the data, consideration has been given to (1) determining the effect of the degradation products on the heat transfer coefficient and providing a correlation for the heat transfer data and (2) determining the out-of-pile fouling characteristics of the organic material. The use of a Wilson plot has been found useful in checking the consistency of the data and in providing a measure of the fouling characteristics of the organic coolant.

### 1. 5. 2 Method of Determination of the Heat Transfer Coefficient

The heat transfer measurements have been made, using a stainless steel tube, nominally 1/4 inch OD by 0.020 inch wall with two heater sections, each 12 inches long. An unheated inlet calming section with L/D = 40.5 was provided. The tube is resistance heated by the passage of large A. C. currents (up to 450 amps) along the test heater wall. The heat transfer coefficients were determined from the measured energy input rate and the difference between the

test heater wall and bulk organic temperatures (all temperature measurements have been made using chromel-alumel thermocouples). The heat transfer coefficient,  $U$ , is thus given by:

$$U = \frac{q}{A_i(T_{wi} - T_{OR})} \quad (1.35)$$

where

$q$  is the heat transfer rate, Btu/hr, for a given test heater section.

$A_i$  is the inside surface area of the test heater wall,  $\text{ft}^2$ , for a given heater section.

$T_{wi} - T_{OR}$  is the (constant) temperature difference between the inside wall and organic temperature along the test heater section.

In performing the measurements,  $q$  was determined from the voltage drop across the test heater section and the measured resistance of the test heater; the measured heat losses were subtracted from the heat input to give the heat transfer rate into the coolant. In Figure 1.54, a typical temperature plot is given, illustrating the procedure used in evaluating  $T_{wi} - T_{OR}$ ; a correction for the temperature drop across the wall thickness was applied to the measured outside wall temperature to give the inside wall temperature,  $T_{wi}$ . For additional details on the procedure, reference is made to Chapter 6. The absolute uncertainty of each individual heat transfer coefficient is estimated to be  $\pm 10$  per cent.

### 1.5.3 Use of Wilson's Method for Determination of Fouling and Check of Data

Wilson's method (1.20) has been used throughout this first experiment to provide current information on fouling, as well as to aid in interpretation of the data. The heat transfer experiments have been designed and performed for the optimum use of this method. Assuming any scale thickness is small relative to the radius of the tube, the measured heat transfer coefficient can be considered to consist of two resistances, one due to coolant convective heat transfer layer and the

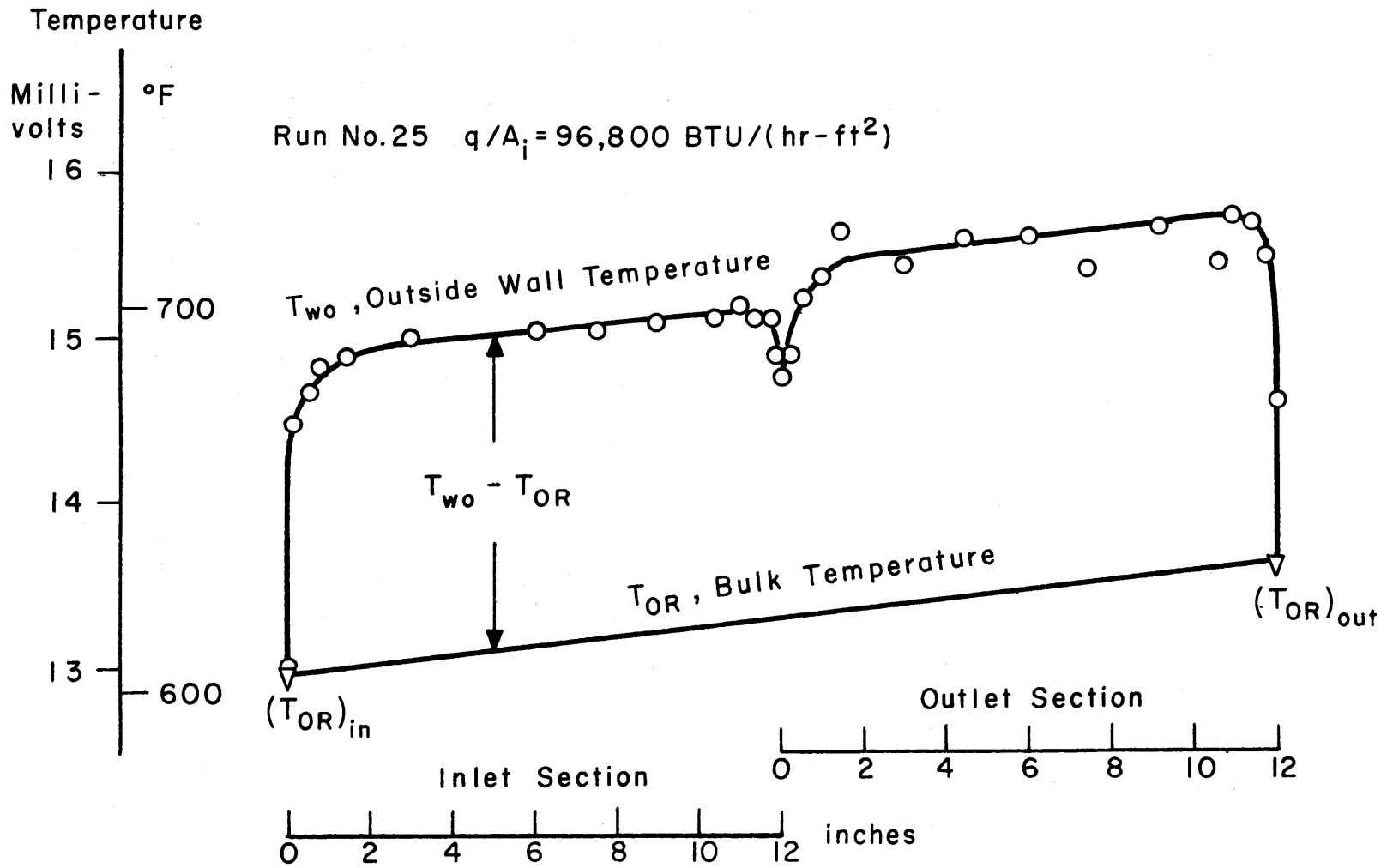


FIG. I.54 TYPICAL TEMPERATURE PROFILE OF THE TEST HEATER

other due to the scale resistance:

$$\frac{1}{U} = \left[ \frac{1}{h} + \frac{1}{k_s/d} \right] = R_f + R_s \quad (1. 36)$$

where

$h$  = the fluid convective heat transfer coefficient, Btu/hr-ft<sup>2</sup>-°F.

$k_s$  = the thermal conductivity of the scale, Btu/hr-ft-°F.

$d$  = the scale thickness, ft.

Now, since the bulk coolant properties at any given time are constant,  $h$  is a function of velocity only, and, according to the standard heat transfer correlations, can be written as  $h = CV^a$ , where both  $C$  and  $a$  are constants. Substitution of this relation into Equation (1. 36) gives:

$$\frac{1}{U} = \frac{1}{CV^a} + R_s \quad (1. 37)$$

Hence, a plot of  $1/U$  vs.  $1/V^a$  should give a straight line when plotted on rectangular coordinates. Furthermore, the intercept at  $1/V^a = 0$  should be the fouling or scale resistance,  $R_s = 1/(k_s/d)$ . For turbulent flow,  $a$  is generally taken as 0. 8 (1. 20, 1. 21).

In Figure 1. 55, a Wilson plot of the data for unirradiated Santowax OMP, using both test heater TH-5 and TH-6, is given. From the data plotted with an exponent,  $a$ , of 0. 8, it is seen that Runs 1-6 and 12-16 fall, respectively, above and below the line based on Runs 9-11, 17-21, and 22-26. The data from these last three series of runs fall closely on the same line and are believed to represent the best data for the unirradiated Santowax OMP. It is also seen that with an exponent,  $a$ , of 0. 8, the data extrapolate to a value of  $1/U$  less than zero, a physical impossibility if the Wilson method is strictly applicable and the data are accurate. It is seen, however, that a plot of Runs 9-11, 17-21, and 22-26, using  $a = 0. 967$ , extrapolates to  $1/U = 0$  at  $1/V^{0. 967} = 0$ , with a straight line again being obtained; this value of  $a$  is appreciably larger than the value of 0. 8 normally specified for the Reynolds number dependence in the heat transfer correlations.



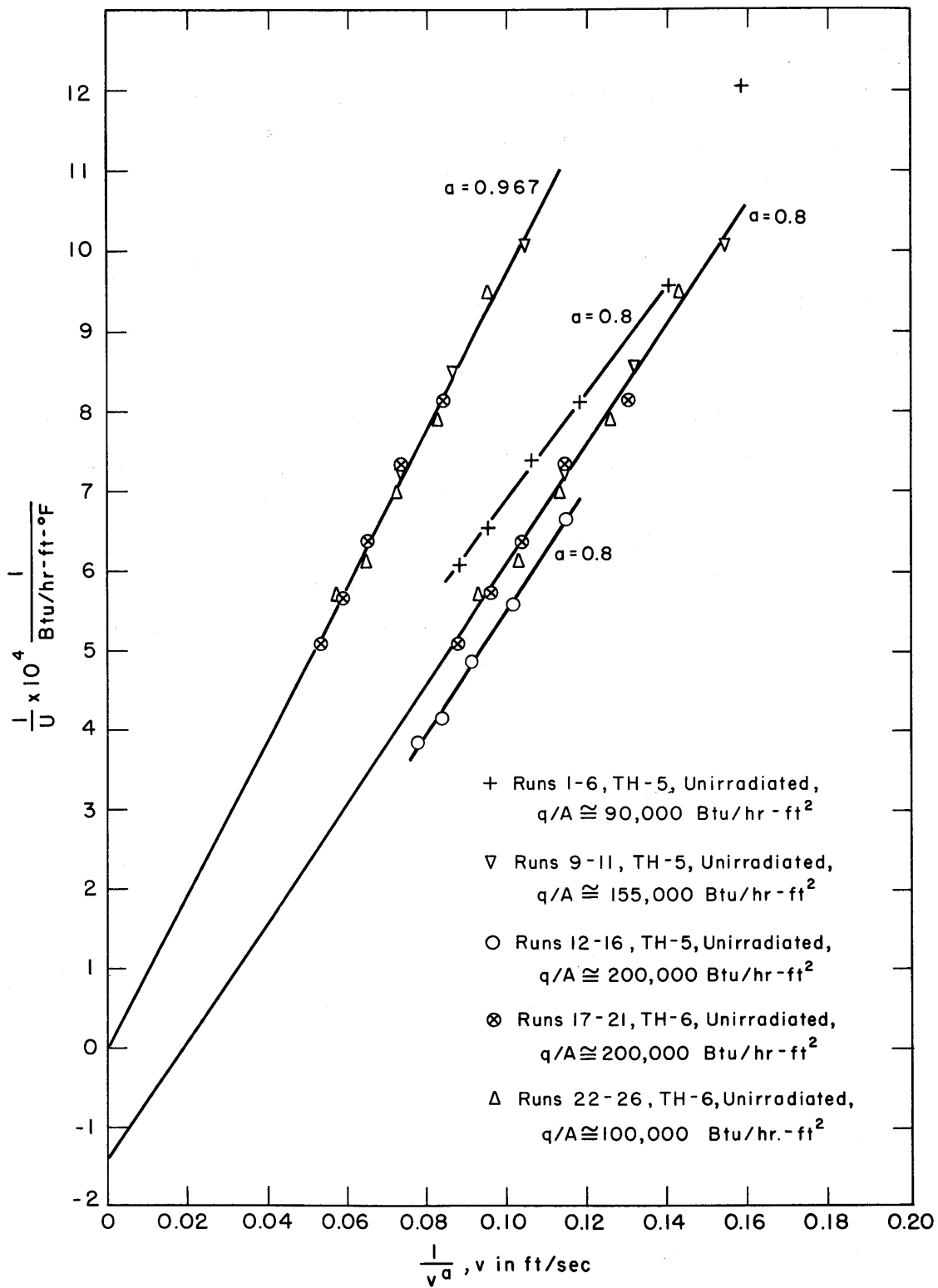


FIG. I.55 WILSON PLOT FOR HEAT TRANSFER DATA ON UNIRRADIATED SANTOWAX OMP

In Figure 1. 56, a comparison of heat transfer data for irradiated Santowax OMP is made with that for unirradiated Santowax OMP, using  $a = 0.8$ . It will be noted that while the slope of the straight lines obtained increase with increasing %DP because of the change in physical properties, the lines all extrapolate to about the same point as the unirradiated material; this indicates that little or no fouling of the heat transfer surface has occurred during the irradiation period covered in this report. Test heater TH-5 has operated continuously throughout this period.

The reason for the possible discrepancy in the exponent and extrapolation to a  $1/U$  of less than zero on the Wilson plot is under investigation at the present time. In view of the large amount of previously reported information indicating a 0.8 power dependence of heat transfer coefficients with velocity and the fact that the Wilson method lines for unirradiated and irradiated coolant all converge to approximately the same point, the discrepancy is probably due to some small systematic error in the heat transfer measurements rather than to the suggested 0.97 power dependence on velocity.

#### 1. 5. 4 Correlation of Heat Transfer Data

A least squares fit of correlation of the heat transfer data has been made using the conventional relationship:

$$(\text{Nu})_b = A(\text{Re})_b^{0.8} (\text{Pr})_b^{0.4} \quad (1. 38)$$

where

$$\text{Nu} = \text{Nusselt number} = \frac{hD}{k}$$

$$\text{Re} = \text{Reynolds number} = \frac{DV\rho}{\mu}$$

$$\text{Pr} = \text{Prandtl number} = \frac{C_p \mu}{k}$$

A = constant to be determined by least squares calculation.

b = subscript corresponding to evaluation of coolant properties at the bulk temperature of the coolant.

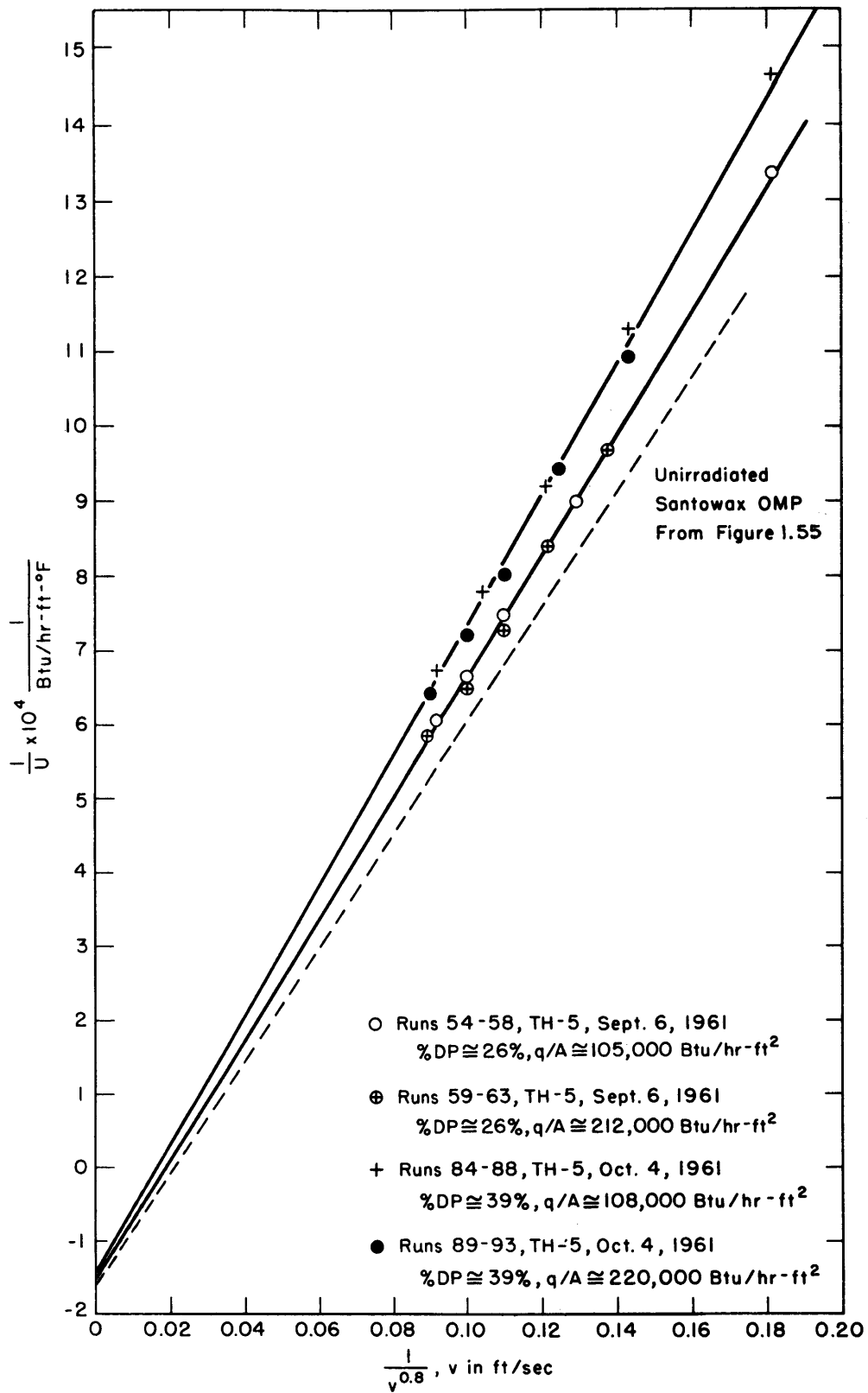


FIG. I.56 WILSON PLOT FOR HEAT TRANSFER DATA ON IRRADIATED SANTOWAX OMP

A least squares evaluation of A gave the following results (1.22):

$$q/A \cong 200,000 \text{ Btu/hr-ft}^2 \text{ data}$$

$$(\text{Nu})_b = 0.0259 (\text{Re})_b^{0.8} (\text{Pr})_b^{0.4}$$

$$\text{RMS deviation} = \pm 9.6\%$$

$$q/A \cong 100,000 \text{ Btu/hr-ft}^2 \text{ data}$$

$$(\text{Nu})_b = 0.0246 (\text{Re})_b^{0.8} (\text{Pr})_b^{0.4}$$

$$\text{RMS deviation} = \pm 9.7\%$$

It is seen that practically the same relation is obtained in both cases; furthermore, the relations are in good agreement with previously reported correlations of the type of Equation (1.38) in which the coefficient, A, has varied from 0.023 to 0.027 (1.20).

The relations obtained in the present case are compared in Figures 1.57 and 1.58 with the experimental data. It is seen that while the data suggest a slightly higher Reynolds number dependence than 0.8, the data all lie within  $\pm 10$  per cent of the line based on the correlation.

## 1.6 CONCLUSIONS

Based on the results from the loop operating period from August 9, 1961, to October 5, 1961, during which the % DP in the irradiated Santowax OMP increased from  $\sim 0\%$  to 39.1%, the following conclusions can be drawn:

- (1)  $G^*(-i) = \frac{G(-i)}{C_i} = 0.28 \pm 0.03 \frac{\text{molecules of } i \text{ degraded/100 ev absorbed in coolant}}{\text{wt. fraction of } i \text{ in coolant}}$   
 for each of the three terphenyl isomers.  $G^*(-i)$  is not significantly affected by the concentration of degradation products.
- (2)  $G^*(\text{gas}) = \frac{G(\text{gas})}{C_{\text{omp}\phi_3}} = 0.035 \pm 0.005 \frac{\text{molecules gas produced/100 ev absorbed in coolant}}{\text{wt. fraction of o-, m-, and p-terphenyl in coolant}}$   
 for the irradiation of the terphenyls.  $G^*(\text{gas})$  is not significantly affected by the concentration of degradation products.

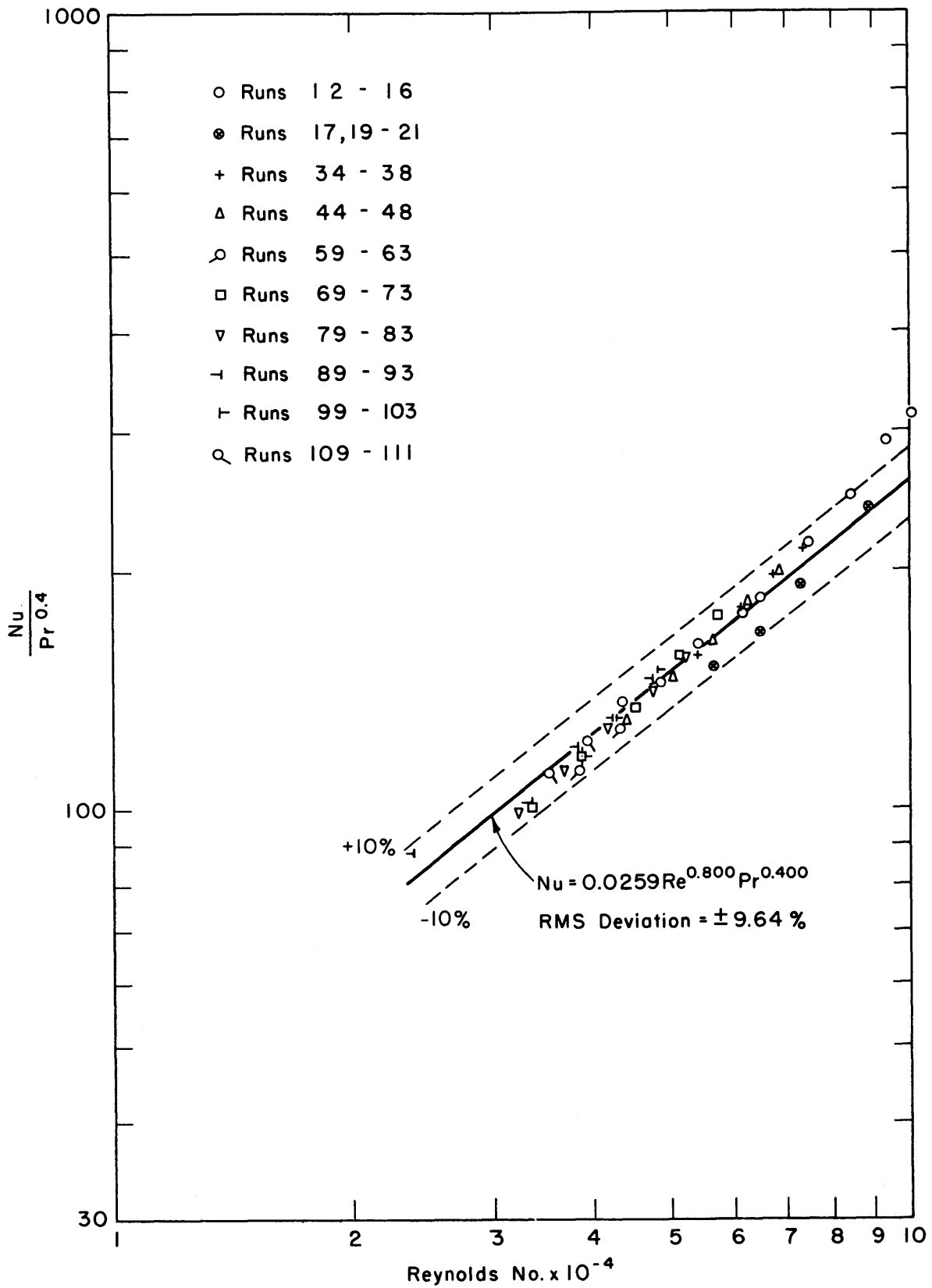


FIG. 1.57 LEAST SQUARES CORRELATION OF HEAT TRANSFER DATA TO DITTUS - BOLTER TYPE OF EQUATION - NOMINAL  $q/A \cong 200,000 \text{ Btu/hr-ft}^2$  (1.22)

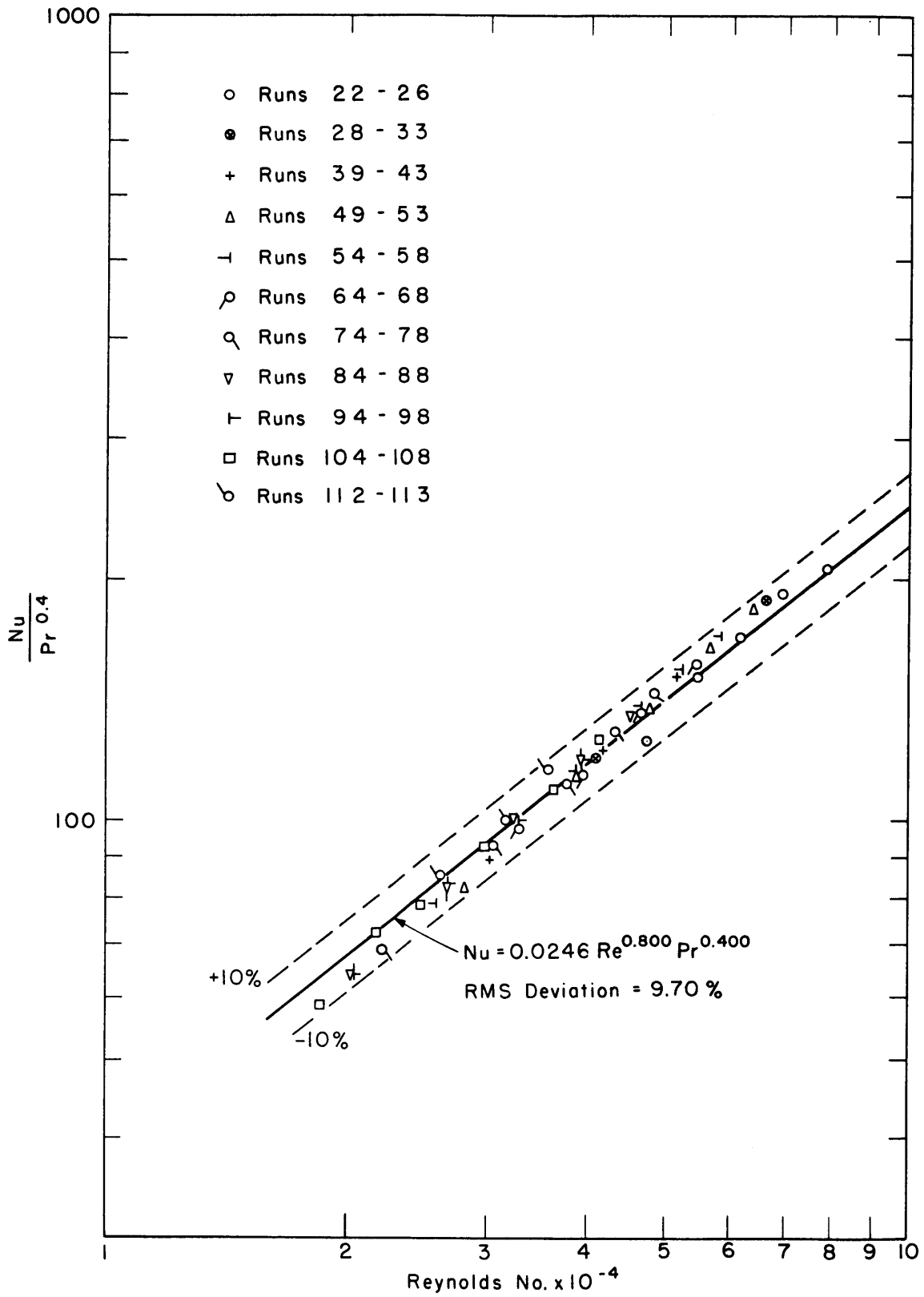


FIG. 1.58 LEAST SQUARES CORRELATION OF HEAT TRANSFER DATA TO DITTUS-BOELTER TYPE OF EQUATION NOMINAL  $q/A \cong 100,000$  Btu/hr-ft<sup>2</sup> (1.22)

- (3) The data on the amount of terphenyls degraded or of gas produced on irradiation can be fitted by a number of different mathematical relations, each of which results in somewhat different values of the decomposition and gas evolution yields, as well as a somewhat different dependence of the yields on concentration of the degradation products.
- (4) The decomposition yields,  $G^*(-i) = G(-i)/C$ , are first-order rate constants for the disappearance of the terphenyls and also can be considered to represent the inherent decomposition yields for each isomer, i. e., molecules of the  $i^{\text{th}}$  species degraded per 100 ev of energy absorbed in the  $i^{\text{th}}$  species alone.
- (5) The relative degradation effects of fast neutron and gamma radiation are estimated to be  $G^{*n}(-i)/G^{*\gamma}(-i) = 5.1 \pm 1.6$  for the terphenyl degradation and  $G^{*n}(\text{gas})/G^{*\gamma}(\text{gas}) = 6.1 \pm 1.6$  for the total gas production.
- (6) No fouling of heat transfer surfaces has been noted during the period covered in this report.
- (7) The coefficients of heat transfer for forced convection are correlated within about  $\pm 10\%$  by the conventional relationships.
- (8) The density and viscosities of irradiated Santowax OMP increase with increasing concentration of degradation products and decreasing temperature and provide information of use in organic reactor design.
- (9) The methods of application and calculation for dosimetry by adiabatic calorimetry developed in this study is convenient and accurate and should be generally useful for in-pile irradiation studies.

- (10) The results of this investigation, to date, have been generally similar to those reported previously for Santowax R at the same temperature and thus generally support the reactor design studies that have been reported to date.
- (11) Further in-pile studies of Santowax OMP are required at higher temperatures and over extended periods of irradiation during which decomposition products are continually removed from the system.
- (12) Operation of the loop equipment has shown that it provides a convenient, safe, and versatile facility for studying the effects of radiation on organic fluids under conditions of elevated temperatures and pressures.



APPENDIX 1.1 REFERENCESCHAPTER I

- (1.1) "Organic Cooled Reactor Study, Summary of Study", TID 8501 (Pt. 1), Bechtel Corporation and Atomics International, June, 1959.
- (1.2) "AEC Puts Together a Long Range Power Reactor Program - Nucleonics Digests it For You", Nucleonics, 18, No. 4, pp. 71-82, April, 1960.
- (1.3) Bolt, R.O., and J. G. Carroll, "Organic Reactor Moderator - Coolants, Some Aspects of Their Thermal and Radiation Stability", Proc. Int. Conf. on the Peaceful Uses of Atomic Energy, 2, p. 547, 1956.
- (1.4) Colichman, E. L., and R. H. J. Gercke, "Radiation Stability of Polyphenyls", Nucleonics, 14, pp. 50-54, 1956.
- (1.5) Colichman, E. L., and R. F. Fish, "Resistance of Terphenyls to Heat and Radiation", Nucleonics, 15, pp. 72-74, 1957.
- (1.6) Smith, H. P., "Compilation of Organic Moderator and Coolant Technology", TID-7007 (Parts I and II), Office of Technical Services, Washington, D. C., 1957.
- (1.7) Civilian Power Reactor Program Part III, "Status Report on Organic-Cooled Power Reactors as of 1959", TID - 8518 (7), U. S. Atomic Energy Commission, 1960.
- (1.8) Berg, S., N. W. Ewbank, R. J. Mack, J. Scarborough, and J. F. Zack, Jr., "Irradiations of Santowax OMP at the Curtiss-Wright Research Reactor", NAA-SR-5892, Atomics International, Canoga Park, Calif., January 3, 1961.

APPENDIX 1.1 REFERENCES (CONT.)CHAPTER I (CONT.)

- (1.9) "Evaluation of the Organic Fouling Problem in the OMRE", TID-6882, Office of Technical Information, U.S. Atomic Energy Commission, June 3, 1960.
- (1.10) Gercke, R.H.J., and C.A. Trilling, "A Survey of the Decomposition Rates of Organic Reactor Coolants", NAA-SR-3835, Atomics International, Canoga Park, Calif., June 10, 1959.
- (1.11) Annual Technical Progress Report, AEC Unclassified Programs, Fiscal Year, 1959, NAA-SR-3850, Atomics International, Canoga Park, Calif., August 1, 1959.
- (1.12) Annual Technical Progress Report, AEC Unclassified Programs, Fiscal Year, 1961, NAA-SR-6370, Atomics International, Canoga Park, Calif., August 15, 1961.
- (1.13) Burns, W.G., W. Wild, and T.F. Williams, "The Effect of Fast Electrons and Fast Neutrons on Polyphenyls at High Temperatures", 2nd United Nations International Conference on the Peaceful Uses of Atomic Energy, Paper A/Conf. 15/P/51, May 26, 1958.
- (1.14) Goldstein, H., Fundamental Aspects of Reactor Shielding, Addison-Wesley Publishing Co., Inc., Reading, Mass., 1959.
- (1.15) Bley, W.N., "An In-Pile Loop Study of the Performance of Polyphenyl Reactor Coolants", NAA-SR-2470, Atomics International, Canoga Park, Calif., September 15, 1958.
- (1.16) Burns, W.G., "The Irradiation of Polyphenyls With Different Types of Radiation", Estratto Dagli Atti Ufficial: Del Congresso Scientifico, Sezione Nucleare, Roma 16-20 Giugno, 1959.
- (1.17) Bates, T.H., W.G. Burns, B. Morris, R.W. Wilkinson, and T.F. Williams, "The Radiation and Thermal Stability of Some Potential Organic Moderator-Coolants, Part II, Pile Irradiation of Para Terphenyl and Santowax R.", AERE C/R 2185, Harwell, July, 1959.

APPENDIX 1.1 REFERENCES (CONT.)CHAPTER I (CONT.)

- (1.18) Gercke, R.H.J., and Asanovick, G., "Thermo-Physical Properties of Irradiated Polyphenyl Coolants, Part I, Density and Viscosity," NAA-SR-4484, Atomics International, Canoga Park, Calif., December 1, 1960.
- (1.19) Bates, T. H., W. G. Burns, B. Morris, R. W. Wilkinson, and T. F. Williams, "The Radiation and Thermal Stability of Some Potential Organic Moderator-Coolants, Part I, Electron Irradiation of Para-Terphenyl and Santowax R," AERE C/R 2121, Harwell, England, 1957.
- (1.20) McAdams, W. H., Heat Transmission, McGraw-Hill Book Company, Inc., New York, 1954.
- (1.21) Eckert, E.R.G., and Drake, R.M. Jr., Heat and Mass Transfer, McGraw-Hill Book Company, Inc., New York, 1959.
- (1.22) Sawyer, C., Personal Communication, MIT Department of Nuclear Engineering, Cambridge 39, Mass., May, 1962.

## APPENDIX 1. 2

## NOMENCLATURE FOR CHAPTER 1

$A$  = constant.

$A_i$  = atomic or molecular weight of material  $i$  where  $i$  refers to aluminum (Al), polyethylene (PE), and polystyrene (PS), grams/gram mole or atom.

$a$  = constant.

$B_i$  = constant.

$b$  = subscript corresponding to evaluation of coolant properties at the bulk temperature of the coolant.

$b_i$  = constant.

$C, C_p$  = heat capacity of material, watt-sec/gm-°C.

$C$  = weight fraction of terphenyls in the coolant.

$C_i$  = concentration of component,  $i$ , in coolant, wt % or wt fraction, where  $i$  refers to meta-terphenyl ( $m\phi_3$ ), para-terphenyl ( $p\phi_3$ ), ortho-terphenyl ( $o\phi_3$ ), and the total terphenyls ( $omp\phi_3$ ).

$D$  = diameter, ft.

$d$  = the scale thickness, ft.

$E$  = neutron energy, ev.

$E_{\text{eff}}$  = effective threshold energy, Mev, for fast neutron threshold detectors.

$F$  = conversion factor,  $\frac{\text{ev}}{\text{atom-sec}}$  to watts/atom.

$G(\text{gas})$  = molecules of total gas evolved per 100 ev absorbed in the coolant.

$$G^*(\text{gas}) = \frac{G(\text{gas})}{C} \frac{\text{molecules}}{100 \text{ ev}}$$

$G^{*n}(\text{gas}), G^{*\gamma}(\text{gas})$  = gas evolution yield for fast neutrons and gamma radiation, respectively, for the coolant.

$G_m(-i), G(-i)$  = radiolytic decomposition yield of component  $i$  in the coolant expressed in units of grams/watt-hr and molecules/100 ev, respectively, where  $i$  refers to meta-terphenyl ( $m\phi_3$ ), para-terphenyl ( $p\phi_3$ ), ortho-terphenyl ( $o\phi_3$ ), and the total terphenyls ( $omp\phi_3$ ).

$$G^*(-i) = \frac{G(-i)}{C_i(Z)} \text{ molecules/100 ev.}$$

$G^{*n}(-i), G^{*\gamma}(-i)$  = decomposition yield for fast neutron and gamma radiation, respectively, for material  $i$ .

$g_j$  = average fraction of the neutron energy lost on collision with an atom of element  $j$  where  $j$  refers to aluminum (Al), hydrogen (H), and carbon (C).

$H_i(Z)$  = grams of component  $i$  degraded at  $Z$  MWHR's, where  $i$  refers to meta-terphenyl ( $m\phi_3$ ), para-terphenyl ( $p\phi_3$ ), ortho-terphenyl ( $o\phi_3$ ) and the total terphenyls ( $omp\phi_3$ ).

$h$  = the fluid convective heat transfer coefficient, Btu/hr-ft<sup>2</sup> °F.

$I_j$  = energy transfer integral for element,  $j$ , watts/atom, where  $j$  refers to aluminum (Al), hydrogen (H), and carbon (C).

$k$  = thermal conductivity, Btu/hr-ft-°F.

$k_s$  = the thermal conductivity of the scale, Btu/hr-ft-°F.

$L$  = length, ft.

$l$  = axial position in the reactor core, inches.

$+l_u$  = distance in inches of the top of the holdup capsule from the reactor core center.

$-l_l$  = distance in inches of the bottom of the capsule from the reactor core center, inches.

A 1. 6

$M_i$  = molecular weight of component, i, of the coolant, grams/gram mole.

$M_N$  = number average molecular weight, grams/gram mole.

$M(DP)$  = molecular weight of degradation products.

$M(Z)$  = mass of organic in loop as a function of Z, the MWHR's of reactor operation.

$N_j^i$  = atoms of element j per gram of material i where j refers to hydrogen (H), carbon (C), and aluminum (Al) and i refers to aluminum (Al), polyethylene (PE), and polystyrene (PS).

$Nu$  = Nusselt number =  $\frac{hD}{k}$ .

P = constant.

Pr = Prandtl number,  $\frac{C_p \mu}{k}$ .

q = heat transfer rate, Btu/hr.

Re = Reynolds number,  $\frac{DV\rho}{\mu}$ .

$R_f = \frac{1}{h}$  = coolant boundary layer resistance to heat flow.

$R_s$  = fouling or scale resistance to heat flow.

$R_i^n$  = fast neutron dose rate in material, i, watts/gm, where i refers to aluminum (Al), polyethylene (PE), and polystyrene (PS).

$R^T, R_i^T$  = total dose rate in material i, watts/gm, where i refers to aluminum (Al), polyethylene (PE), and polystyrene (PS).

$R_{SW}^T/P_o$  = total dose rate in organic material as a function of position in the core normalized to a reactor power of 1.0 MW, watts/gm-MW.

$R_i^{th}$  = dose rate due to thermal neutron activation in material i, watts/gm, where i refers to aluminum (Al).

$\left( R_{SW}^{TI} \right)_{avg}$  = average (over one day) total energy absorption rate in the organic coolant, watt-hr/MWHR.

$R_i^\gamma$  = gamma dose rate in material i, watts/gram where i refers to aluminum (Al), polyethylene (PE), and polystyrene (PS).

T = absolute temperature, °R, or temperature, °F.

T(t) = temperature, °C, as a function of time, t.

$T_{OR}$  = bulk organic temperature along the test heater, °F.

$T_{wi}$  = inside wall temperature of test heater, °F.

t = time.

U = heat transfer coefficient, Btu/hr-ft<sup>2</sup>-°F, from inside of test heater wall to flowing organic.

V = velocity, ft/sec.

V = undissolved and dissolved gas in loop plus cumulative removal by liquid and gas sampling, cm<sup>3</sup> (STP).

$V_1$  = value of V, cm<sup>3</sup> (STP), at Z = 0 MWHR's.

X = fraction of the fission neutron energy absorbed in the coolant.

x = fraction of total dose rate due to fast neutron interactions.

$x_1, x_2$  = organic volume per unit length of the capsule and tubing above the capsule, respectively, cm<sup>3</sup>/in.

Y = fraction of the fission gamma energy absorbed in the coolant.

Z = MWHR's of reactor operation.

$Z_i$  = average atomic number of material i where i refers to aluminum (Al), polyethylene (PE), and polystyrene (PS).

$\beta$  = constant, °R<sup>-1</sup>.

$\mu$  = viscosity, cp.

$\mu_o$  = constant, cp.

$\rho$  = density, gms/cm<sup>3</sup>.

A 1. 8

$\rho_{\text{avg}}$  = time averaged density of the organic in the radiation field, gms/cm<sup>3</sup>,  
for a period of one day.

$\Sigma$  = summation sign.

$\sigma_s^j(E)$  = scattering cross section of element j, cm<sup>2</sup>, where j refers to  
hydrogen (H) and carbon (C).

$\tau_m$  = specific absorbed dose, watt-hr of radiation energy absorbed per  
gram of total coolant.

$\phi_{2200}$  = 2200 meter/sec neutron flux, n/cm<sup>2</sup>-sec.

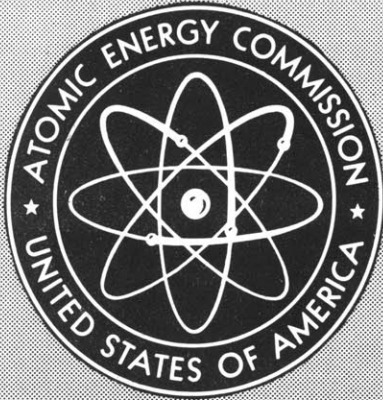
$\phi_0$  = epithermal flux constant, n/cm<sup>2</sup>-sec =  $\phi(E) E$ .

$\phi(E)$  = neutron flux per unit energy, n/cm<sup>2</sup>-sec-ev.

% DP = per cent of degradation products in the coolant.

$\infty$  = infinity.





MITNE-22(Bk. II)

THE IRRADIATION OF SANTOWAX OMP IN THE  
M.I.T. IN-PILE LOOP

Part II. Equipment Design, Procedures and Results of  
Irradiation to October 5, 1961

By  
D. T. Morgan  
E. A. Mason

May 1962

Department of Nuclear Engineering  
Massachusetts Institute of Technology  
Cambridge, Massachusetts

## CHAPTER 6

### HEAT TRANSFER MEASUREMENTS

#### 6. 1 INTRODUCTION

One of the more important considerations in the design of an organic cooled nuclear reactor is estimation of the heat transfer performance of the organic coolant. Provision was therefore incorporated in the M. I. T. loop for the out-of-pile measurement of the heat transfer coefficients of the irradiated organic. Throughout the period covered in this report, measurements of the heat transfer coefficient of forced convection have been performed at intervals of approximately every 5 per cent increase in the degradation product concentration. The measurements have been performed at nominal heat fluxes of 100,000 Btu/hr-ft<sup>2</sup> and 200,000 Btu/hr-ft<sup>2</sup> and a bulk organic temperature entering the test heater of 600°F; for each series of heat transfer measurements at a given heat flux and % DP, the measurement has been made at approximately five different velocities between 10 and 20 ft/sec.

A detailed description of the method of measurement is given in section 6. 2. Briefly, the measurements have been made using a stainless steel tube nominally 1/4 inch OD by 0. 020 inch thick wall. The tube is resistance heated by the passage of large A. C. currents (up to 450 amps) along the test heater wall. The heat transfer coefficient is determined from the measured energy input rate and the difference between the test heater wall temperature and bulk temperature of the organic material. All temperature measurements have been made using chromel-alumel thermocouples.

In analyzing the data, consideration has been given to (1) determining the effect of the degradation products on the heat transfer coefficient and providing a correlation for the heat transfer data, and (2) determining the out-of-pile fouling characteristics of the organic material. The use of a "Wilson" plot has been found

useful in checking the consistency of the data, and, more importantly, in providing a measure of the fouling characteristics of the organic coolant. The preliminary results and analysis are given in section 6.3 which considers use of "Wilson's" plot and fouling, and in section 6.4 which considers correlation of the heat transfer data. A more detailed evaluation of the results will be given in a subsequent report which will cover the entire period of irradiation of Santowax OMP.

## 6. 2 METHOD OF DETERMINATION OF THE HEAT TRANSFER COEFFICIENT

### 6. 2. 1 Introduction

The measured quantity in each heat transfer measurement is,  $U$ , the local heat transfer coefficient from the inside test heater wall to the organic coolant; this coefficient may be defined as:

$$U = \frac{dq}{dA_i(T_{wi} - T_{OR})} \quad (6. 1)$$

where

$dq$  is the heat transfer rate, Btu/hr, for a differential length of test heater.

$dA_i$  is the inside surface area of the test heater wall,  $ft^2$ , for a differential length of test heater.

$T_{wi}$  is the temperature of the inside surface of the test heater wall, °F, at the differential element.

$T_{OR}$  is the average bulk temperature of the organic, °F, at the differential element.

In the present case,  $T_{wi} - T_{OR}$  has been found to be constant (except near the electrodes) along the test heater length within the experimental error of the measurement;  $dq$  and  $dA_i$  can also be considered as constant along the test heater length. With these conditions, the average heat transfer coefficient over each section of the test heater is equivalent

to the local heat transfer coefficient and Equation (6. 1) can be integrated to give:

$$U = \frac{q}{A_i(T_{wi} - T_{OR})} \quad (6. 2)$$

The heat transfer area,  $A_i$ , is determined from the heater dimensions given in Appendix 6. 1 as  $0.0541 \text{ ft}^2$  for each of the two sections of the test heater. The heat transfer rate,  $q$ , and the temperature difference,  $T_{wi} - T_{OR}$ , must therefore be measured for the determination of  $U$ . The equipment and procedures used in the determination of these quantities will be discussed in the following sections.

## 6. 2. 2 Equipment and Apparatus

### 6. 2. 2. 1 Test Heater

The test heater used for heat transfer measurements has been previously described in section 3. 3. 6 and Figures 3. 12 and 3. 13. The inside diameter and wall thickness of the test heater (TH-5) used for the measurements presented in this report are given in Appendix 6. 1. As indicated in Figure 3. 12, three chrome-plated copper electrodes are provided for connection to bus bars supplying the large alternating currents necessary. These electrodes are spaced 12 inches apart and essentially divide the heated portion of the test heater into two separate sections. The two outer electrodes are maintained at ground potential and a variable voltage from 0 to 12 volts is applied to the central electrode.

Each 12-inch section of the test heater is provided with fifteen 28-gage chromel-alumel thermocouples for measuring the temperature profile on the outside of the heater wall down the length of the test heater section. From these temperature measurements and the energy input to the heater section, the inside wall temperature can be calculated. The thermocouples are spot-welded to the outside of the tube. As indicated in Figure 3. 13, the thermocouple leads are passed along the surface of the test heater to the central

electrode and covered with a high temperature cement to reduce the temperature gradient in the leads and to provide protection to the thermocouple junctions. The test heater has also been thermally insulated with approximately 2 inches of glass wool to reduce heat losses.

On the inlet end of the test heater, an unheated calming section, 8-1/2 inches in length, is provided. With an ID of 0.210 inches, the L/D ratio for this section is 40.5 which should be sufficient for removal of upstream disturbances and attainment of fully developed turbulent flow at the entrance to the heated section of the test heater (6.1).

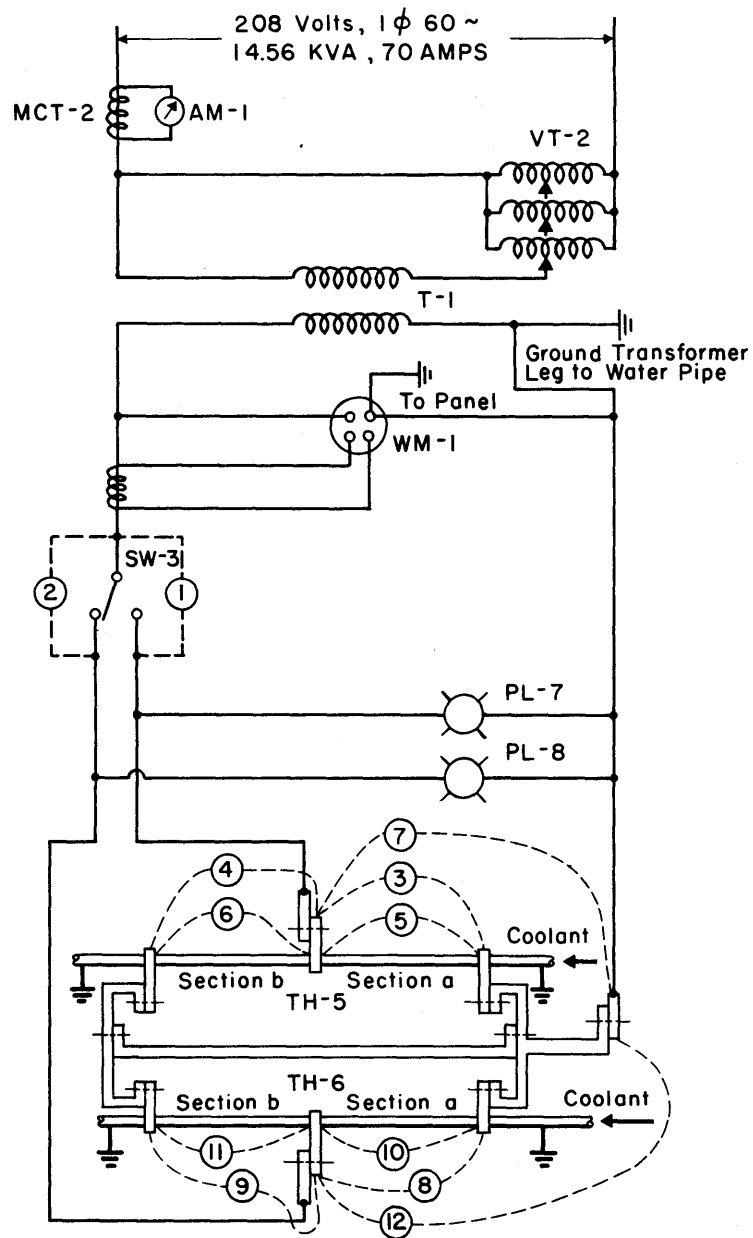
#### 6.2.2.2 Bulk Organic Temperature Measurement

The bulk organic temperature entering and leaving the test heater is measured, using chromel-alumel thermocouples. On each end of the test heater, a mixing chamber has been provided for this measurement to insure accurate measurement of the average bulk temperature of the coolant. Each chamber is provided with two stainless-steel clad thermocouple probes for the temperature measurements. These probes are 1/8 inch diameter and are immersed in the organic for a depth of about one inch; the thermocouple junctions are welded directly to the stainless-steel clad to provide accurate temperature measurements.

#### 6.2.2.3 Power Supply and Electrical Measurement Systems for Heat Transfer Measurements

In Figure 6.1, a schematic of the electrical system is illustrated, showing the instruments provided for measuring the power input into each section of test heater TH-5 which was used for the measurements given in this report. The provisions for TH-6 in the other test heater position are also shown. This test heater position is normally used for measurements only at the beginning and end of the irradiation of a coolant to aid in detection of fouling of the heat transfer surface (see section 6.3).

From Figure 6.1, the following features may be noted. A wattmeter (see section 3.4.7) is provided for a direct measurement of the power input into the test heater circuit. However, because of possible contact



ITEM	DESCRIPTION
AM-1 With MCT-2	Ammeter and Current Transformer, 4 1/2" GE # 549x57, 0-100 AMP Scale, 208 Volt
WM-1 With MCT-1	Wattmeter and Current Transformer, 15 kw Scale @ 15 Volt, Weston # 610 With # 604 CT, Current Transformer Ratio 1000:5
VT-2	Variac, General Radio # W50H G3, 75 AMP @ 230 Volt, 3 Gang
T-1	Transformer, 60 ~, 208 Volt / 15 Volt, 900 AMP, Isolated Secondary, Mystic Transformer Co. # A540-01
PL-7 and PL-8	Pilot Lights
Portable Voltmeter	General Electric Model BAP97-Y261, Type AP-9, Dual Range 0-7.5 and 0-15.0 Volts AC
<p>FIG. 6.1 SCHEMATIC OF POWER SUPPLY FOR TEST HEATERS SHOWING INSTRUMENTS USED FOR POWER INPUT MEASUREMENTS - CIRCLED NUMBERS REFER TO POSITION ACROSS WHICH VOLTAGE IS MEASURED USING 12 POINT SWITCH</p>	

resistances in the electrode connections, voltage measurements were also made at various positions throughout the electrical system; the circled numbers of Figure 6. 1 refer to positions on a multipoint switch which are connected to a precision voltmeter (see section 3. 4. 7). These voltage measurements were used with the measured electrical resistance of the test heater (known as a function of temperature) to determine the power input into each section of the test heater. The variable power input to the test heater circuit was provided by a constant voltage-ratio stepdown transformer with isolated secondary. The input to this transformer was controlled by a variac as indicated in Figure 6. 1.

In Figure A3. 35 of Appendix 3. 5, the thermocouple schematic is given which illustrates the circuitry used for measuring the test heater wall and bulk organic temperatures. A precision potentiometer, accurate to  $\pm 2$  microvolts (see section 3. 4. 6), was used for all temperature measurements; an ice-water cold bath was used as the reference temperature for these measurements. Thermocouple switches are provided so all test heater wall thermocouples as well as the bulk organic thermocouples can be read on the strip chart recorder. Furthermore, these switches make it possible to always keep a test heater temperature on pyrometer IV for safety cutoff of the power to the test heater if an excessive temperature is encountered. Generally, the strip chart recorder was used to monitor the test heater temperatures, to insure existence of steady state before a set of temperature measurements was started. The thermocouples were then read by means of the precision potentiometer. A complete set of readings of 32 thermocouples can be made in about 5 minutes and duplicate readings are generally taken.

#### 6. 2. 2. 4 Flowmeter and Calibration

For determining the velocity or equivalently the volumetric rate of organic flow through the test heater, a Potter turbine flowmeter (see section 3. 3. 5) is used. As mentioned in section 3. 3. 5, this instrument measures the volumetric flowrate and is insensitive to changes in the density and viscosity of the flowing fluid. While the instruments are

supplied with a calibration chart determined with water, the calibration of each meter has been checked, using tap water, before installation in the loop. In all cases, the calibration has agreed closely with that supplied by the manufacturer.

In addition to these checks on operation of the meter, the variation of the calibration with density and viscosity was measured with two meters. Measurements with water at various temperatures provided an indication of the effect of viscosity only on the flowmeter response since the density remained essentially constant with temperature. Measurements with methanol, when compared with the water measurements, provided an indication of the effect of density changes. In both cases, the change of flowmeter response with density and viscosity was less than one per cent for the range of density and viscosity of interest in these experiments.

Because of thermal expansion of the meter, a slight change in the calibration factor occurs when measurements are performed at higher temperatures than that used in the calibration. Based on information supplied by the manufacturer, the temperature correction is estimated to be  $[1 + 1.9 \times 10^{-5}(T-60)]$  where T is the temperature of the fluid passing through the flowmeter in °F. Since the organic temperature is about 600°F in the present case, the correction is about 1.1 per cent.

Based on the above considerations, it is seen that the effect of density, viscosity, and temperature changes from the conditions used in calibration of the meter amount to approximately one per cent. Considering that the instrument used to indicate the flowrate can be read with an accuracy of only one to two per cent, depending on the flowrate, no correction has been applied to the flowmeter calibration for variations in the density, viscosity or temperature. The estimated maximum uncertainty in the flowrate measurements is  $\pm 3$  per cent at flow rates corresponding to 10 ft/sec and  $\pm 2$  per cent at flow rates corresponding to 20 ft/sec in the test heater.



### 6. 2. 3 Determination of Difference of Inside Wall ( $T_{wi}$ ) and Bulk Organic ( $T_{OR}$ ) Temperatures

As indicated in Equation (6. 2), the difference of inside wall temperature ( $T_{wi}$ ) and bulk organic temperature ( $T_{OR}$ ) is required for calculation of the heat transfer coefficient; this section describes the procedure used in evaluating this quantity. Corrections to the thermocouple readings are first applied to give the correct temperatures; the calibration procedure used in determining these correction factors is discussed in Appendix 6. 2.

#### 6. 2. 3. 1 Inside Temperature of Test Heater Wall, $T_{wi}$

As previously discussed, the outside wall temperature of the test heater is measured in performing heat transfer measurements. In Figure 6. 2, the outside temperature profile down the test heater for a typical test heater run is given, illustrating the sharp drop-off in temperature near the copper electrodes which act as a heat sink. A correction must be applied to these measurements to obtain the inside wall temperature. Assuming that the heat is uniformly generated in the tube wall by the electric current, the temperature drop across the tube wall can be expressed as (see Appendix 6. 3):

$$T_{wi} = T_{wo} + \frac{Qr_o^2}{4k} \left[ 1 + 2 \ln \frac{r_i}{r_o} - \frac{r_i^2}{r_o^2} \right] + \frac{H_{loss}/L}{2\pi k} \left[ \ln \frac{r_o}{r_i} \right] \quad (6. 3)$$

where

$T_{wi}$ ,  $T_{wo}$  = inside and outside wall temperatures of test heater, respectively, °F.

$Q$  = volumetric energy generation rate in tube wall, Btu/hr-ft<sup>3</sup>.

$r_i$ ,  $r_o$  = inside and outside radius of tube, ft.

$k$  = thermal conductivity of stainless steel, Btu/hr-ft-°F.

$\frac{H_{loss}}{L}$  = heat loss rate from test heater, Btu/hr-ft.

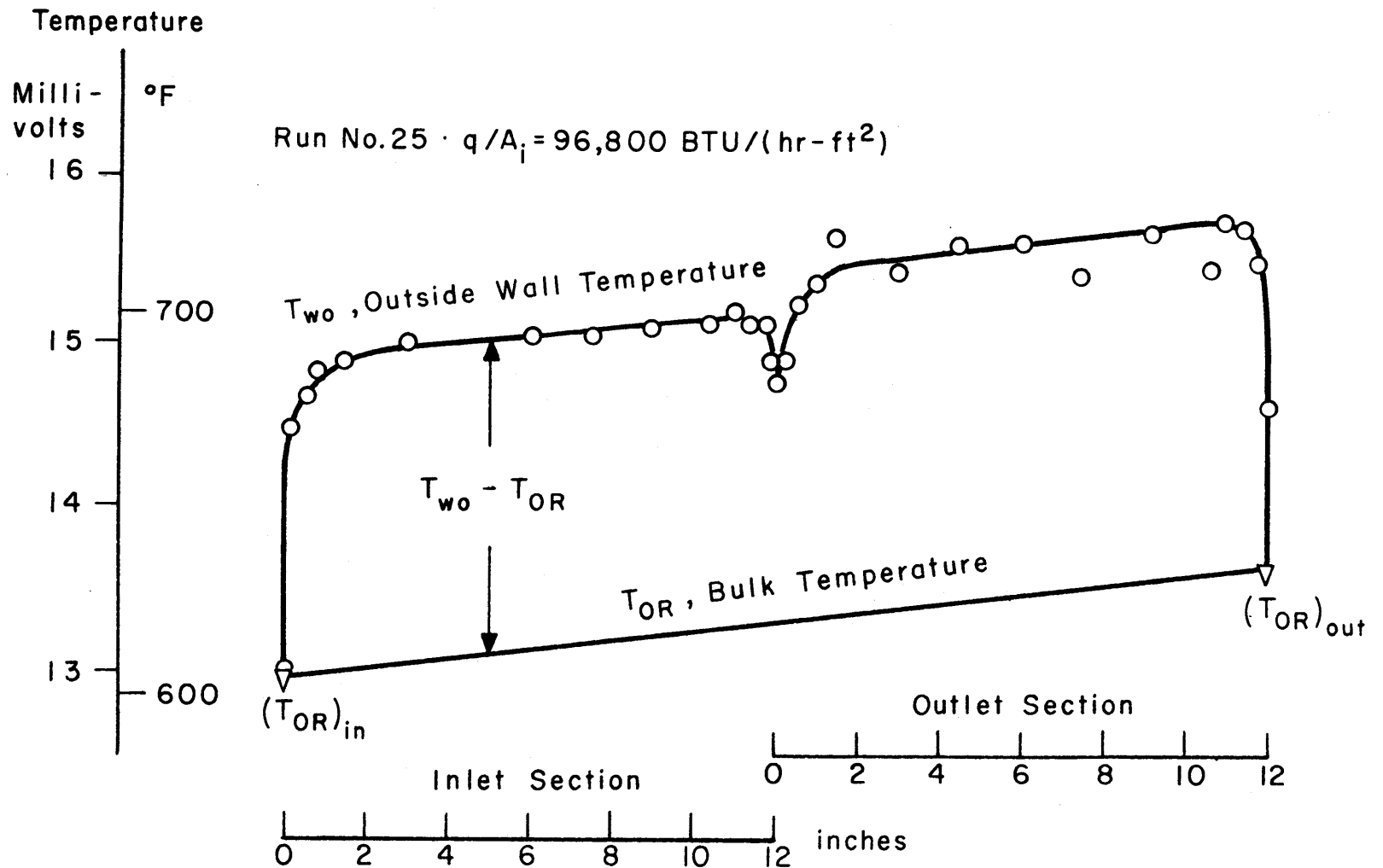


FIG. 6.2 TYPICAL TEMPERATURE PROFILE OF THE TEST HEATER

Substitution of dimensions and thermal conductivity gives:<sup>(1)</sup>

$$T_{wo} - T_{wi} = 4.20 \times 10^{-3} \frac{q}{L} - 8.09 \times 10^{-3} \left( \frac{H_{loss}}{L} \right) \quad (6.4)$$

For one heater section,  $H_{loss}/L \cong 150$  watts/ft including losses to the electrode;  $q/L$  is approximately 1800 watts/ft for a heat flux of 100,000 Btu/hr-ft<sup>2</sup>. Substitution of these typical properties give  $T_{wo} - T_{wi} = 7.6 - 1.2 = 6.4^\circ\text{F}$ . In performing the heat transfer calculations, the effect of heat losses on the temperature correction ( $1.2^\circ\text{F}$ ), as given in the second term on the right of Equation (6.4), has generally been neglected, since the correction is small relative to  $T_{wi} - T_{OR}$  ( $50-130^\circ\text{F}$  at  $q/A = 100,000$  Btu/hr-ft<sup>2</sup>) and since the heat loss per unit length away from the electrodes is considerably smaller than that used in the above calculations which include heat losses through the electrodes.

#### 6. 2. 3. 2 Bulk Temperature and Evaluation of $T_{wi} - T_{OR}$

Assuming no change in heat capacity and heat transfer rate down the length of the test heater, the bulk organic temperature can be assumed to vary linearly with distance from the beginning of the heated section of the test heater. While there have been variations on the order of 10 per cent in the heat input to each section of the test heater (see section 6. 2. 4), the assumption of a linear variation from the inlet to the outlet bulk temperatures is well within the experimental uncertainty and has been used in the present case. The variation of the bulk organic temperature is indicated in Figure 6. 2. From plots such as that of Figure 6. 2 and using the temperature drop across the test heater wall from Equation (6. 4), the values of  $T_{wi} - T_{OR}$  used in evaluating the heat transfer coefficients for all runs have been obtained as follows:

$$T_{wi} - T_{OR} = (T_{wo} - T_{OR}) - (T_{wo} - T_{wi}) \quad (6.5)$$

The heat transfer coefficients have been based on the inlet section of the test heater in all cases since there was considerably less scatter of the thermocouple measurements in this section than in the exit section.

(1) The units of  $q/L$  and  $H_{loss}/L$  are watts/ft in Equation (6. 4).

#### 6. 2. 4 Determination of Heat Transfer Rate and Heat Balance

The electrical heat input into each section of the test heater has been determined from the measured voltage drop,  $E$ , across the test heater section and from the test heater wall resistance,  $R(T)$ :

$$q_{el} = \frac{E^2}{R(T)} \text{ watts} \quad (6.6)$$

where

$q_{el}$  = electrical input into test heater section, watts.

$E$  = potential drop across test heater section, volts.

$R(T)$  = electrical resistance of test heater section as function of temperature, ohms.

The electrical resistance of the test heater has been measured as a function of temperature as described in Appendix 6. 4. The sum of  $q_{el}$  from both heater sections has generally been of the order of 10 to 15 per cent less than the power input to the test heater circuits as measured with the wattmeter; the difference is interpreted as due to contact resistances at various bus-bar connections between the transformer and the test heater section. This effect is also believed to account for the 10 per cent difference in the heat inputs into the inlet and outlet sections of the test heater, respectively.

The total heat input into the test heater can be written as:

$$q_{el}^T = q_{el}^a + q_{el}^b \text{ watts} \quad (6.7)$$

where  $a$  and  $b$  refer to the two test heater sections, respectively. In order to obtain the total heat transferred into the coolant from both heater sections,  $(q_{el}^T)_{in}$ , it is necessary to subtract the heat losses from  $q_{el}^T$ :

$$(q_{el}^T)_{in} = q_{el}^T - H_{loss} \text{ watts} \quad (6.8)$$

The heat loss,  $H_{\text{loss}}$ , was determined at various test heater wall temperatures during calibration of the thermocouples (see Appendix 6. 2).

As previously mentioned, only the wall temperature data of the inlet section were used in evaluating  $T_{\text{wi}} - T_{\text{OR}}$  for calculation of the heat transfer coefficient. Hence, the value of  $q$  to be used in Equation (6. 2) for the inlet section (a) in evaluating  $U$  is:

$$q = \frac{q_{\text{el}}^{\text{a}}}{T} (q_{\text{el}}^{\text{T}})_{\text{in}} \quad \text{watts} \quad (6. 9)$$

Transformation of units and division by  $A_i = 0. 0541 \text{ ft}^2$  gives:

$$\frac{q}{A_i} = 63. 0 \frac{q_{\text{el}}^{\text{a}}}{T} (q_{\text{el}}^{\text{T}})_{\text{in}} \frac{\text{Btu}}{\text{hr-ft}^2} \quad (6. 10)$$

This relation along with  $T_{\text{wi}} - T_{\text{OR}}$  permits calculation of the heat transfer coefficient,  $U \text{ Btu/hr-ft-}^\circ\text{F}$ .

As a check on the reliability of the measurement, a heat balance has been performed on all heat transfer runs. The heat balance can be written as:

$$100 \frac{3. 413 (q_{\text{el}}^{\text{T}})_{\text{in}} - w C_p [(T_{\text{OR}})_o - (T_{\text{OR}})_i]}{3. 413 (q_{\text{el}}^{\text{T}})_{\text{in}}} \% \quad (6. 11)$$

where

$w$  = pounds/hr of organic flow.

$c_p$  = heat capacity of organic coolant,  $\text{Btu/lb-}^\circ\text{F}$ .

$(T_{\text{OR}})_o - (T_{\text{OR}})_i$  = temperature difference between outlet and inlet to test heater of bulk organic coolant,  $^\circ\text{F}$ .

If the heat balance as computed above is greater than  $\pm 5$  per cent, that heat transfer run has been discarded and not used in correlating the heat transfer data.

### 6. 2. 5 Estimated Accuracy of Each Individual Heat Transfer Coefficient

Each measured quantity on the right hand side of Equation (6. 2) contributes to an uncertainty in the calculated heat transfer coefficient. The absolute error in these quantities is difficult to determine. With respect to  $T_{wi} - T_{OR}$ , plots such as Figure 6. 2 used in determining  $T_{wi} - T_{OR}$  indicate that an uncertainty in  $T_{wi} - T_{OR}$  of about  $\pm 3^\circ\text{F}$  exists due to scatter of the temperature measurements down the length of the inlet test heater section. Assuming an additional uncertainty in the wall correction of 1 to  $2^\circ\text{F}$ , a total uncertainty in  $T_{wi} - T_{OR}$  of about  $\pm 4^\circ\text{F}$  is obtained. At a  $q/A_i \cong 100,000 \text{ Btu/hr-ft}^2$ ,  $T_{wi} - T_{OR}$  varies from about 50 to  $130^\circ\text{F}$ , depending on the fluid velocity. The uncertainty is thus equivalent to a  $\pm 8$  per cent to  $\pm 3$  per cent uncertainty in  $T_{wi} - T_{OR}$  at this heat flux. The per cent uncertainties at  $q/A_i \cong 200,000 \text{ Btu/hr-ft}^2$  are approximately half these values.

The uncertainty in  $q$  is very difficult to accurately evaluate. The uncertainty in  $q_{el}^a$  can be written as (from Equation (6.6)):

$$\delta^2(q_{el}^a) = (q_{el}^a)^2 \left[ 4 \left( \frac{\delta E}{E} \right)^2 + \left( \frac{\delta R}{R} \right)^2 \right] \quad (6.12)$$

Assuming a 2 per cent uncertainty in the voltage and 5 per cent uncertainty in  $R$ ,

$$\frac{\delta(q_{el}^a)}{q_{el}^a} \cong 6\%$$

At  $q/A_i \cong 100,000 \text{ Btu/hr-ft}^2$ ,  $q_{el}^a \cong 1800 \text{ watts}$ . This uncertainty is thus equal to 108 watts at this  $q/A_i$  and about 216 watts at  $q/A_i \cong 200,000 \text{ Btu/hr-ft}^2$ . The uncertainty in the heat loss will be assumed as about 50 watts ( $\sim \pm 30\%$ ) so that the RMS error becomes 119 watts ( $\sim \pm 6\text{-}1/2\%$ ) and 222 watts ( $\sim \pm 6\%$ ) for each  $q/A_i$ , respectively.

Assuming the uncertainties in the area,  $A_i$ , are negligible compared to the other uncertainties, the RMS summation of the uncertainties

Table 6. 1. Summary of Uncertainties in Heat Transfer Coefficient Determination.

$q/A_i$ , Btu/hr-ft <sup>2</sup>	Velocity, ft/sec	Estimated Uncertainty in U		
		$T_{wi} - T_{OR}$	$q_{el}^a$	RMS
100,000	10 ± 3%	± 3%	6-1/2%	~ 7%
	20 ± 2%	± 8%	6%	~ 10%
200,000	10 ± 3%	± 2%	6-1/2%	~ 7%
	20 ± 2%	± 4%	6%	~ 7%

are summarized in Table 6. 1. As discussed in section 6. 2. 2. 4, the estimated error in the coolant velocity is ± 2% at velocities of 20 ft/sec and ± 3% at velocities of 10 ft/sec. From Table 6. 1, it is seen that the final estimated RMS uncertainty is about 7 to 10% in all cases. Considering the difficulty in estimating the uncertainty as well as the neglect of such factors as the effect of the electrodes on reducing  $T_{wi} - T_{OR}$  near the electrodes (see Figure 6. 2), an estimated uncertainty of ± 10% for each heat transfer coefficient is believed to represent the best estimate presently available. It would, however, be expected that the data obtained at  $q/A_i \cong 200,000$  Btu/hr-ft<sup>2</sup> would be the more accurate, primarily because of increased per cent accuracy in  $T_{wi} - T_{OR}$ . The increase in accuracy over the data from the lower heat flux runs is not significantly apparent, however.

### 6. 3 USE OF WILSON'S METHOD FOR DETERMINATION OF FOULING AND CHECK OF DATA

One of the objectives of the heat transfer measurements of the loop is to provide information on the fouling of heat transfer surfaces. One method of achieving this goal is based on the incorporation of two identical test heaters in the loop. At the beginning of a run on a particular coolant, the heat transfer coefficient is measured using both test heaters. One of the

test heaters is then valved off or removed from the loop entirely and is not used again until the end of that irradiation. The other test heater, on the other hand, is used continuously throughout the run, both for heat transfer measurements and for providing heat to the loop. At this conclusion of the run, the heat transfer coefficient is again measured using both test heaters. Comparison of the data from both test heaters should indicate the degree of fouling which has occurred in the test heater heater used continuously. This procedure eliminates the effect of physical property changes of the organic on irradiation and provides a direct indication of any fouling.

The second method involves the use of Wilson's method (6. 1) of detecting fouling or scale deposits on heat transfer surfaces. This method has been used throughout this first experiment to provide current information on fouling as well as to aid in interpretation of the data. The heat transfer experiments have been designed and performed for the optimum use of this method. The Wilson method will now be described.

In the present experiment, the measured heat transfer coefficients have been based on the difference between the inside wall temperature and the bulk organic temperature. Hence, the coefficient includes not only the thermal resistance due to the coolant boundary layer, but also any resistances due to coating (or fouling) of the heat transfer surface by deposits. Assuming the scale thickness is small relative to the radius of the tube,

$$\frac{1}{U} = \left[ \frac{1}{h} + \frac{1}{k_s/d} \right] = R_f + R_s \quad (6. 13)$$

where

U = the over-all coefficient of heat transfer from inner tube wall to bulk of flowing coolant, Btu/hr-ft<sup>2</sup>°F.

h = the fluid convective heat transfer coefficient, Btu/hr-ft<sup>2</sup>°F.

k<sub>s</sub> = thermal conductivity of scale, Btu/hr-ft-°F.



$d$  = scale thickness, ft.

$R_f = \frac{1}{h}$  = thermal resistance of fluid film.

$R_s = \frac{1}{k_s/d}$  = thermal resistance of scale.

Now, at any given time the bulk coolant properties (thermal conductivity, heat capacity, density, and viscosity) are essentially constant, so that the heat transfer coefficient,  $h$ , is a function of velocity only and, according to the standard heat transfer correlations (see section 6.4), can be written as:

$$h = CV^a \quad (6.14)$$

where both  $C$  and  $a$  are constants. Substitution into Equation (6.13) thus gives:

$$\frac{1}{U} = \frac{1}{CV^a} + R_s \quad (6.15)$$

Hence, a plot of  $1/U$  vs.  $1/V^a$  should give a straight line when plotted on rectangular coordinates. Furthermore, the intercept at  $1/V^a = 0$  should be the fouling or scale resistance,  $R_s = 1/(k_s/d)$ . For turbulent flow,  $a$  is generally taken as 0.8 (6.1).

In this work, heat transfer measurements have almost always been taken in sets of approximately five runs. At a given  $q/A$ , the measurements have been made at about five different velocities ranging from 8 to 21 ft/sec for preparation of the Wilson plot. The inlet temperature to the test heater during these measurements has been maintained constant at  $600^\circ\text{F} \pm 5^\circ\text{F}$ . While the change in velocity results in a change in the outlet organic temperature, the temperature change is generally small enough so that the change in physical properties is negligible.

In Figure 6.3, a Wilson plot of the data for unirradiated Santowax OMP, using both test heaters TH-5 and TH-6, is given. From the data plotted with an exponent,  $a$ , of 0.8, it is seen that Runs 1-6 and 12-16, respectively, fall above and below the line based on Runs 9-11, 17-21, and 22-26. The data from these last three series of runs fall closely on

the same straight line and are believed to represent the best data for the unirradiated Santowax OMP. This plot illustrates the usefulness of the Wilson method in checking the consistency of the data. In all cases, it is seen that the data form a straight line on a Wilson plot.

From Figure 6. 3, it is also seen that the plot based on an exponent,  $a$ , of 0. 8 extrapolates to a value of  $1/U$  less than zero, a physical impossibility if the Wilson method is strictly applicable and the data are accurate. To find an exponent,  $a$ , which fits the unirradiated data, logarithms of Equation (6. 15) were taken, assuming  $R_s = 0$ :

$$\text{Log} \left( \frac{1}{U} \right) = \text{Log} \frac{1}{C} - a \text{Log} V \quad (6. 16)$$

Hence, a plot of  $\text{Log} (1/U)$  vs.  $\text{Log} V$  should be a straight line with slope of  $a$ . This plot is presented in Figure 6. 4 where it is noted that a straight line is obtained; the slope of the line drawn by eye is 0. 967, a value much higher than the value of 0. 8 normally specified for the Reynolds number dependence in the heat transfer correlations. The data for unirradiated Santowax OMP (Runs 9-11, 17-21, and 22-26) are also plotted in Figure 6. 3, using  $a = 0. 967$  where it is seen, as expected, that use of this exponent results in extrapolation through  $1/U = \text{zero}$ ; a straight line is again obtained.

In Figure 6. 5, a comparison of some heat transfer data for irradiated Santowax OMP is made with that for unirradiated Santowax OMP. It will be noted that while the slope of the straight lines obtained increase with increasing % DP because of the change in physical properties with increasing % DP, the lines all extrapolate to about the same point as the unirradiated material; this indicates that little or no fouling of the heat transfer surface has occurred during the irradiation period covered in this report. The test heater (TH-5) was operated continually throughout this period, even when heat transfer measurements were not in progress.

In view of the large amount of previously reported information indicating a 0. 8 power dependence of heat transfer coefficients on velocity and the fact that the Wilson method lines for unirradiated

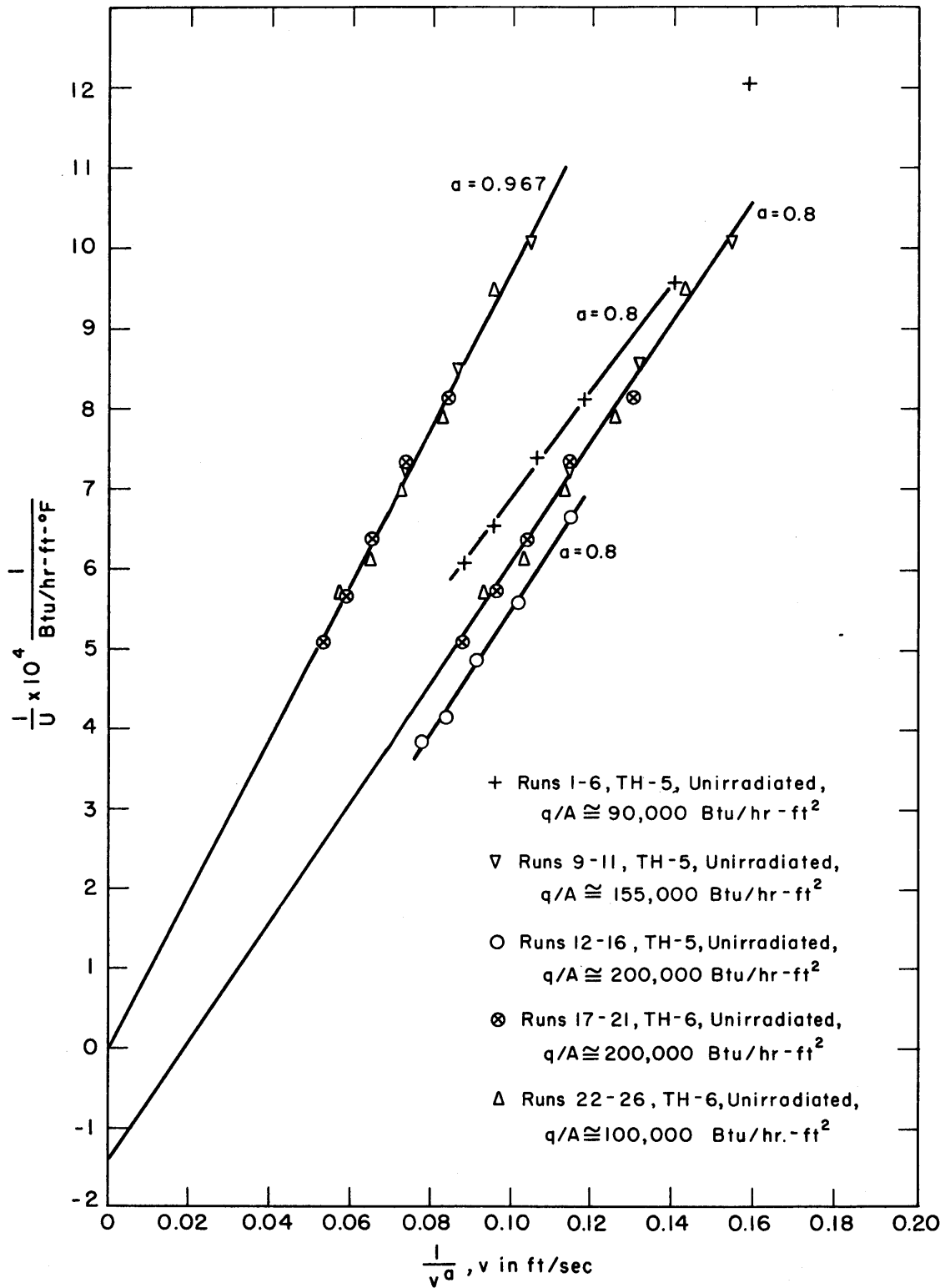


FIG. 6.3 WILSON PLOT FOR HEAT TRANSFER DATA ON UNIRRADIATED SANTOWAX OMP

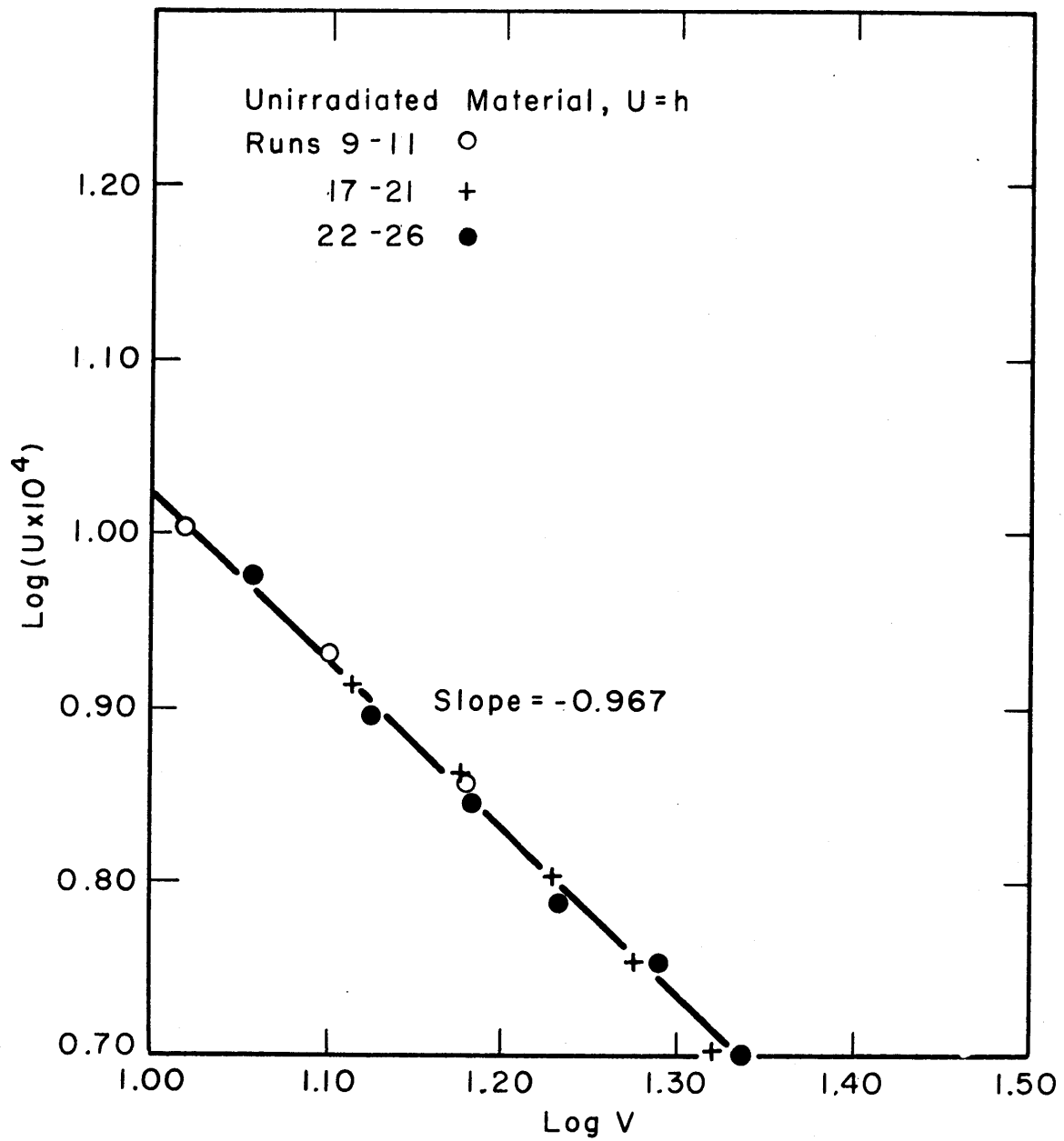


FIG. 6.4 PLOT FOR DETERMINATION OF EXPONENT VELOCITY FOR WILSON PLOT

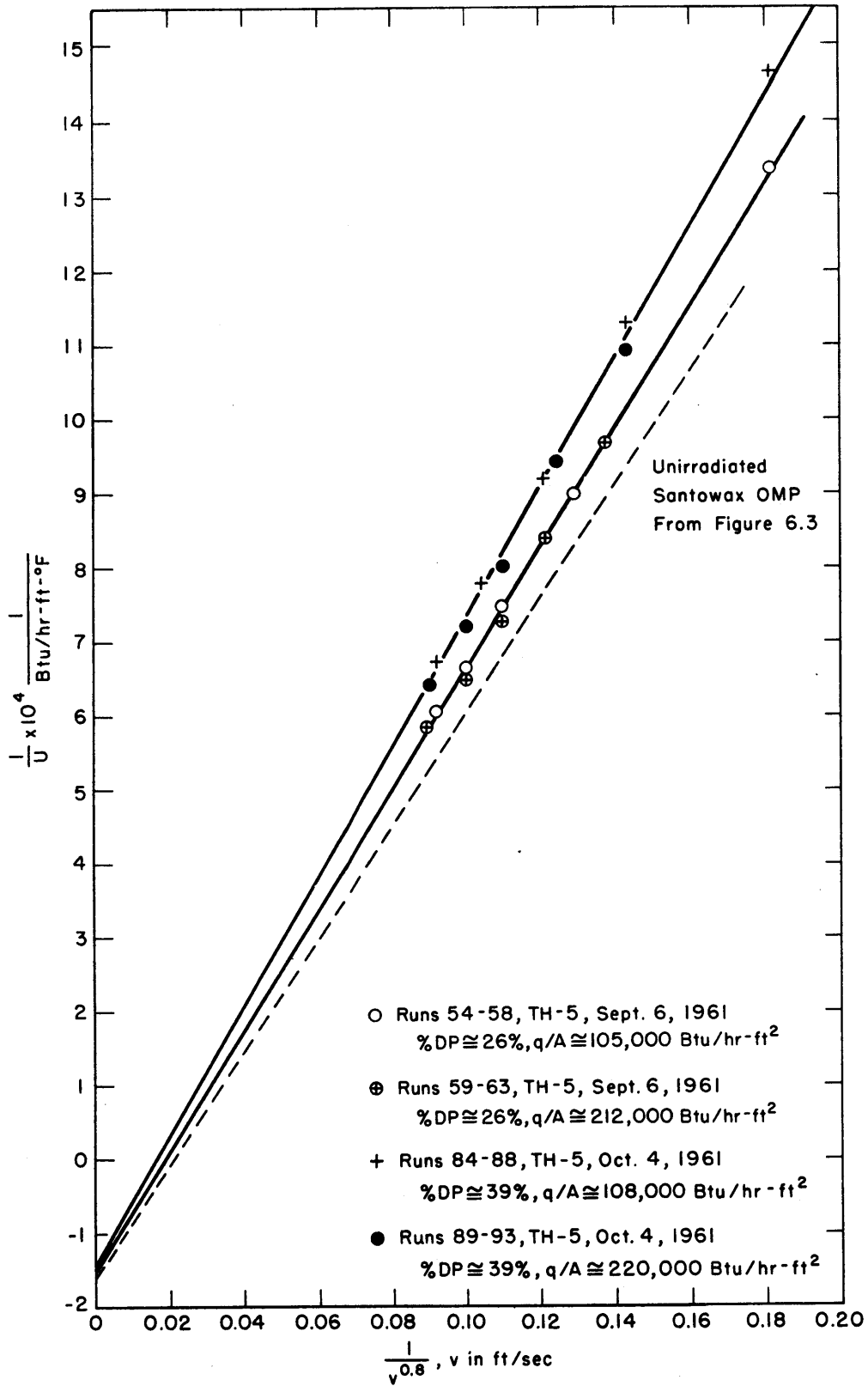


FIG. 6.5 WILSON PLOT FOR HEAT TRANSFER DATA ON IRRADIATED SANTOWAX OMP

and irradiated coolant all converge to approximately the same point (i. e., show the same velocity dependence), the discrepancy is probably due to some small systematic error in the heat transfer measurement rather than to a 0.97 power dependence on velocity. The discrepancy may be related to the slight, but unexpected, separation of the data in Figure 6.3 on the basis of heat flux level. This matter is receiving further consideration, and will be discussed in future reports as more information becomes available.

## 6.4 CORRELATION OF HEAT TRANSFER DATA

### 6.4.1 Introduction

In the extensive previous work reported in the literature (6.1, 6.2) for forced convection heat transfer, it has been found that remarkable correlation between the heat transfer rate and the physical properties of the coolant is provided by an equation of the following type:

$$(\text{Nu})_b = A(\text{Re})_b^B (\text{Pr})_b^C \quad (6.17)$$

where

$\text{Nu}$  = Nusselt number =  $hD/k$ .

$\text{Re}$  = Reynolds number =  $DV\rho/\mu$ .

$\text{Pr}$  = Prandtl number =  $C_p\mu/k$ .

$b$  = subscript indicating that all physical properties are evaluated at the bulk coolant temperature.

$A, B, C$  = constants.

For example, Dittus and Boelter obtained the following relation for heat flow from the wall to a liquid (6.2):

$$(\text{Nu})_b = 0.0243(\text{Re})_b^{0.8} (\text{Pr})_b^{0.4} \quad (6.18)$$

Various modifications have been incorporated into Equation (6.17) by various investigators in attempts to obtain better correlation; these

modifications generally involve estimation of some of the physical properties of the coolant at the average film temperature of the coolant to correct for variation of properties with temperature. The addition of another dimensionless term on the right of Equation (6. 17),

$\left(\frac{\mu_b}{\mu_w}\right)^D$ , to correct for variation of the viscosity with temperature across the film, has also been considered by Sieder and Tate (6. 1, 6. 2) where  $\mu_b$  and  $\mu_w$  are the viscosity of the coolant at the bulk and wall temperatures, respectively:

$$(\text{Nu})_b = A(\text{Re})_b^B (\text{Pr})_b^C \left(\frac{\mu_b}{\mu_w}\right)^D \quad (6. 19)$$

This relation would be expected to be especially applicable to fluids for which the variation of viscosity is a dominating one.

In the present case, a computer program has been written by Sawyer (6. 3) for the least squares fit of the heat transfer data, obtained in the present experiment by Swierzawski (6. 4), to Equations (6. 17) and (6. 19). While the work of correlating the results is still proceeding and will be given in detail in the final report covering the entire Santowax OMP irradiation, the preliminary results obtained using the heat transfer data obtained up to November 10, 1961, will be summarized in this section. In performing the correlations, values of density and viscosity measured in the present experiment have been used. Values of  $k$  and  $C_p$  have been assumed independent of % DP and have been taken from work by Ziebland and Burton (6. 5) and Bowring, *et al*, (6. 6), respectively:

$$k \times 10^4 = 3. 516 - 0. 00228T \quad (6. 20)$$

where  $k$  is the thermal conductivity, cal/cm-sec-°C.

$T$  is the temperature in °C.

$$C_p = 0. 382 + 5. 86 \times 10^{-4}T \text{ cal/gm-}^\circ\text{C.} \quad (6. 21)$$

where

$C_p$  is the heat capacity, cal/gm-°C.

$T$  is the temperature in °C.

#### 6. 4. 2 Summary of Correlation of Heat Transfer Data Obtained up to November 10, 1961

In correlating the data, the attempt was made to evaluate all constants (A, B, C, and D) in Equations (6. 17) and (6. 19). However, when this procedure has been followed, the constants have generally been significantly different from those usually reported (see discussion in Appendix 6. 5). It is believed that the discrepancies are probably due to the small variation of the various parameters employed in the present experiment which prohibits the accurate evaluation of the constants. The variations in the variables used in the correlation encountered in the present experiment are summarized below:

Re	$3 \times 10^4$ to $10 \times 10^4$
Pr	6. 5 to 16
q/A	100, 000 and 200, 000 Btu/hr-ft <sup>2</sup>
$\mu_b / \mu_w$	1. 2 to 1. 9

It is recommended that the range of these variables be extended to provide better correlation of the heat transfer data. One method of doing this would be to perform heat transfer measurements at different organic temperatures. An inlet temperature of 600°F has been used for all of the heat transfer experiments up to the present time.

As a result of these difficulties, the recommended correlation is based on the values of B = 0. 8 and C = 0. 4, which are the coefficients usually reported for the correlation of heat transfer data. With these assumed values, the least squares evaluation of A has been performed with the following results:

$$q/A \cong 200, 000 \text{ Btu/hr-ft}^2 \text{ data}$$

$$\text{Nu} = 0. 0259 \text{ Re}^{0. 8} \text{ Pr}^{0. 4} \quad (6. 20)$$

RMS deviation of Nusselt number =  $\pm 9. 6\%$

$$q/A \cong 100, 000 \text{ Btu/hr-ft}^2 \text{ data}$$

$$\text{Nu} = 0. 0246 \text{ Re}^{0. 8} \text{ Pr}^{0. 4} \quad (6. 21)$$

RMS deviation of Nusselt number =  $\pm 9. 7\%$



It is seen that practically the same relation is obtained in both cases, which is in good agreement with Equation (6.18). The root mean square errors of these correlations are only a few per cent greater than those obtained when the values of A, B, C, and D are determined by a computed least squares fit (see Appendix 6.5). These relations are compared with the experimental data in Figures 6.6 and 6.7, where the  $\pm 10$  per cent limits are also drawn. It is seen that while the data indicate a slightly higher Reynolds number dependence than 0.8, the data all lie within  $\pm 10$  per cent of the line based on the correlation. The equations given above thus represent the data obtained in this experiment very well, especially considering that the data spread around a correlation of this type is generally of the order of  $\pm 25$  to 40 per cent (6.1).

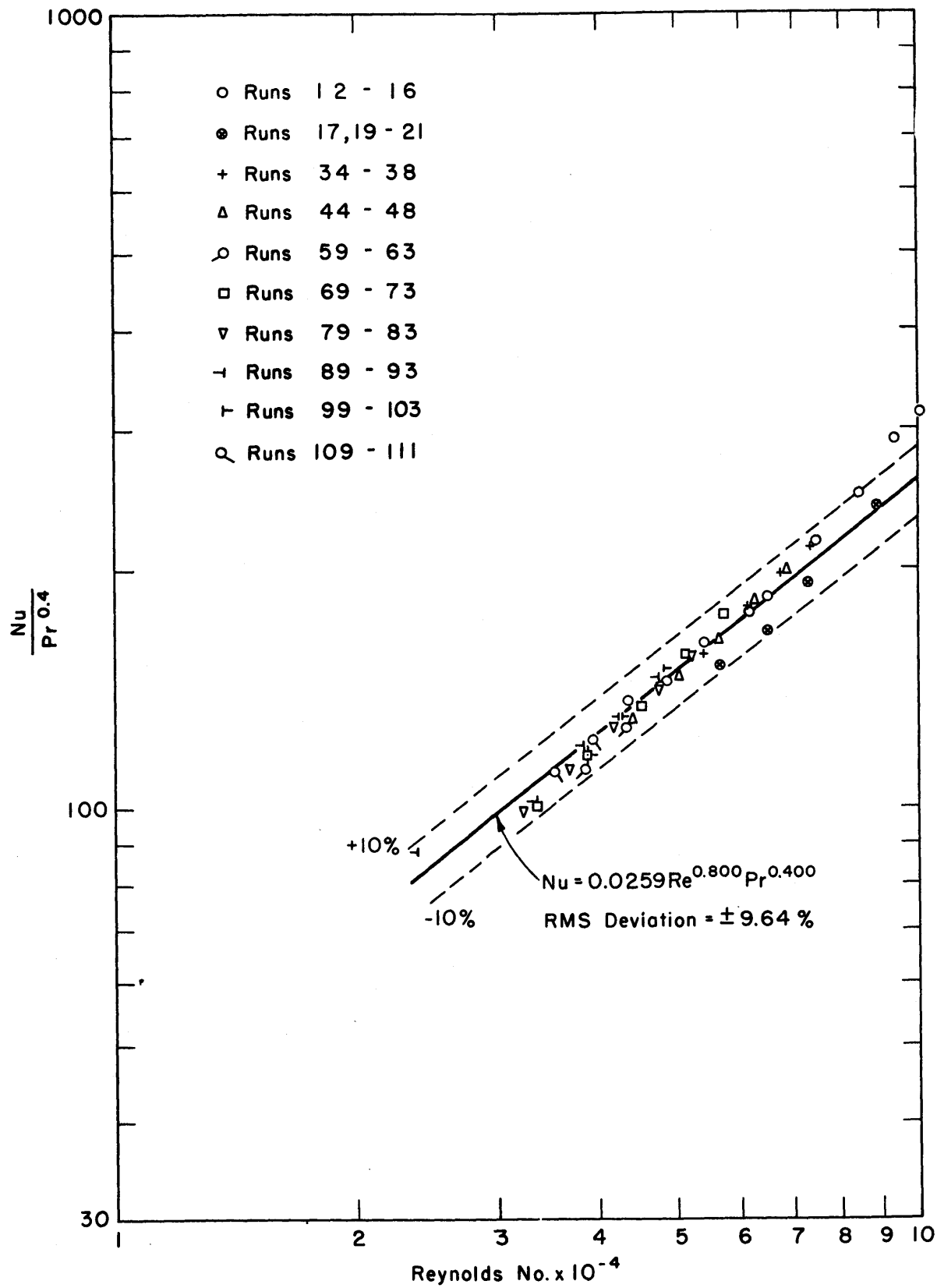


FIG. 6.6 LEAST SQUARES CORRELATION OF HEAT TRANSFER DATA TO DITTUS - BOLTER TYPE OF EQUATION - NOMINAL  $q/A \cong 200,000$  Btu/hr-ft<sup>2</sup> (6.3)

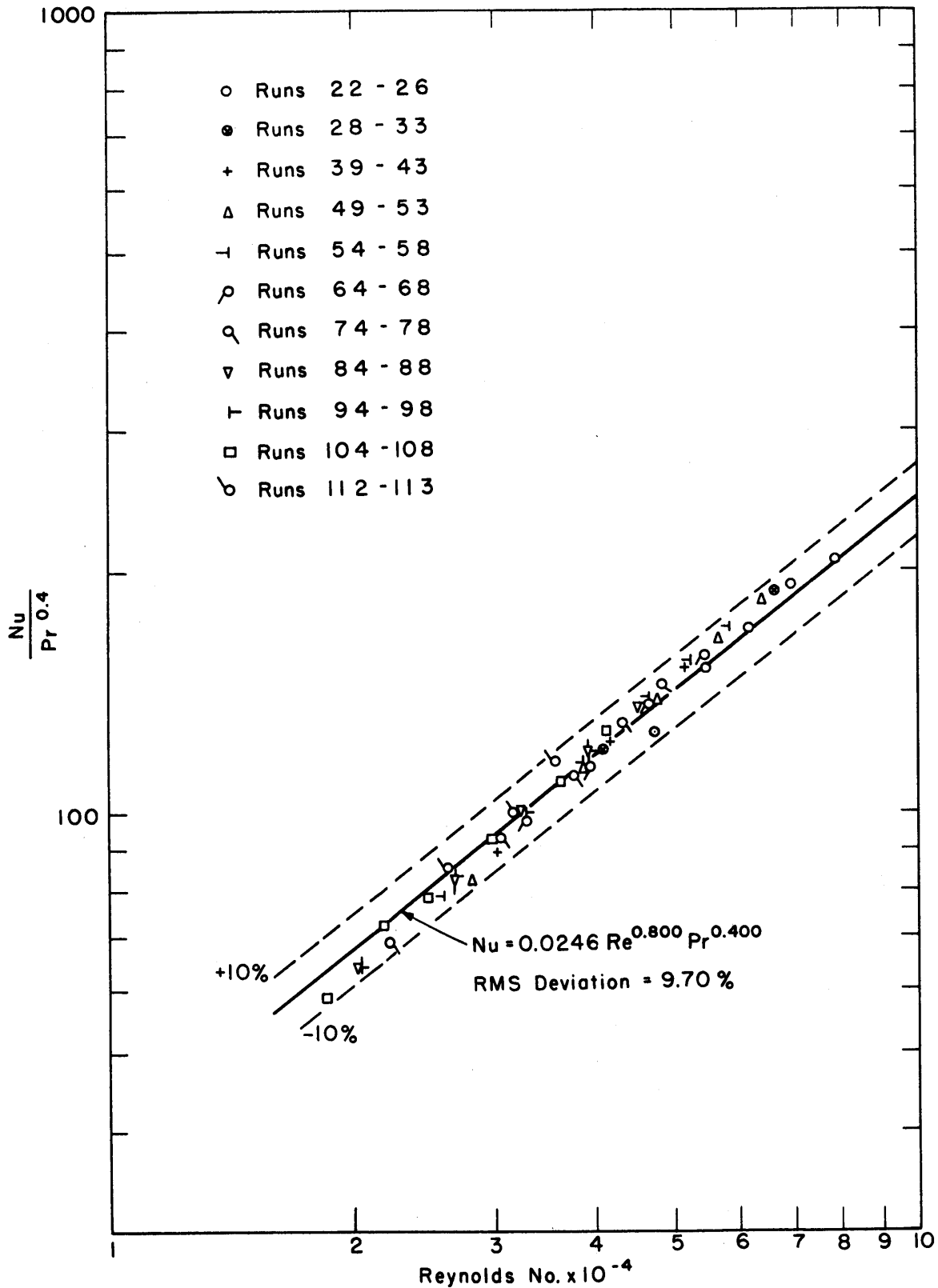


FIG. 6.7 LEAST SQUARES CORRELATION OF HEAT TRANSFER DATA TO DITTUS - BOELTER TYPE OF EQUATION NOMINAL  $q/A \cong 100,000$  Btu/hr-ft<sup>2</sup> (6.3)

## APPENDIX 3. 1

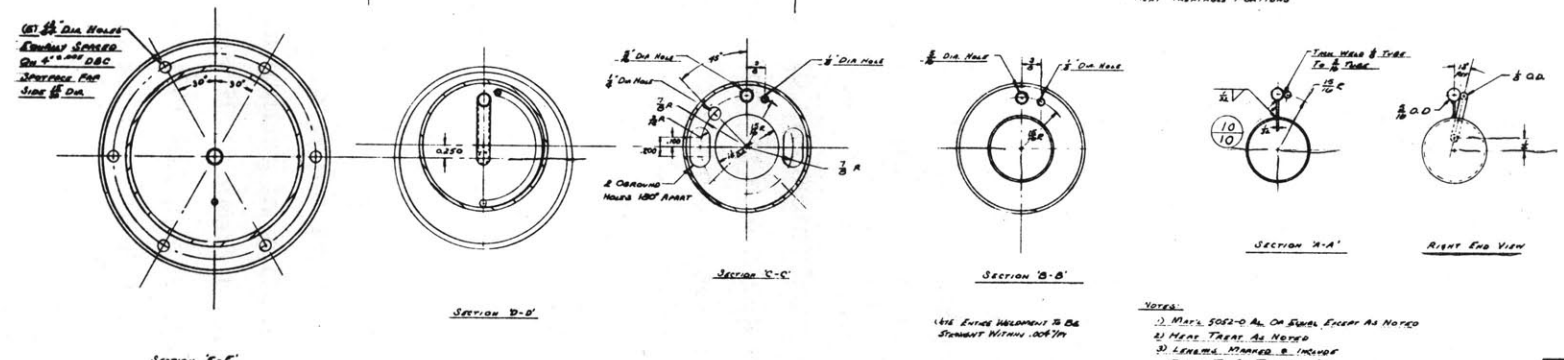
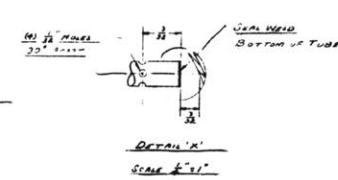
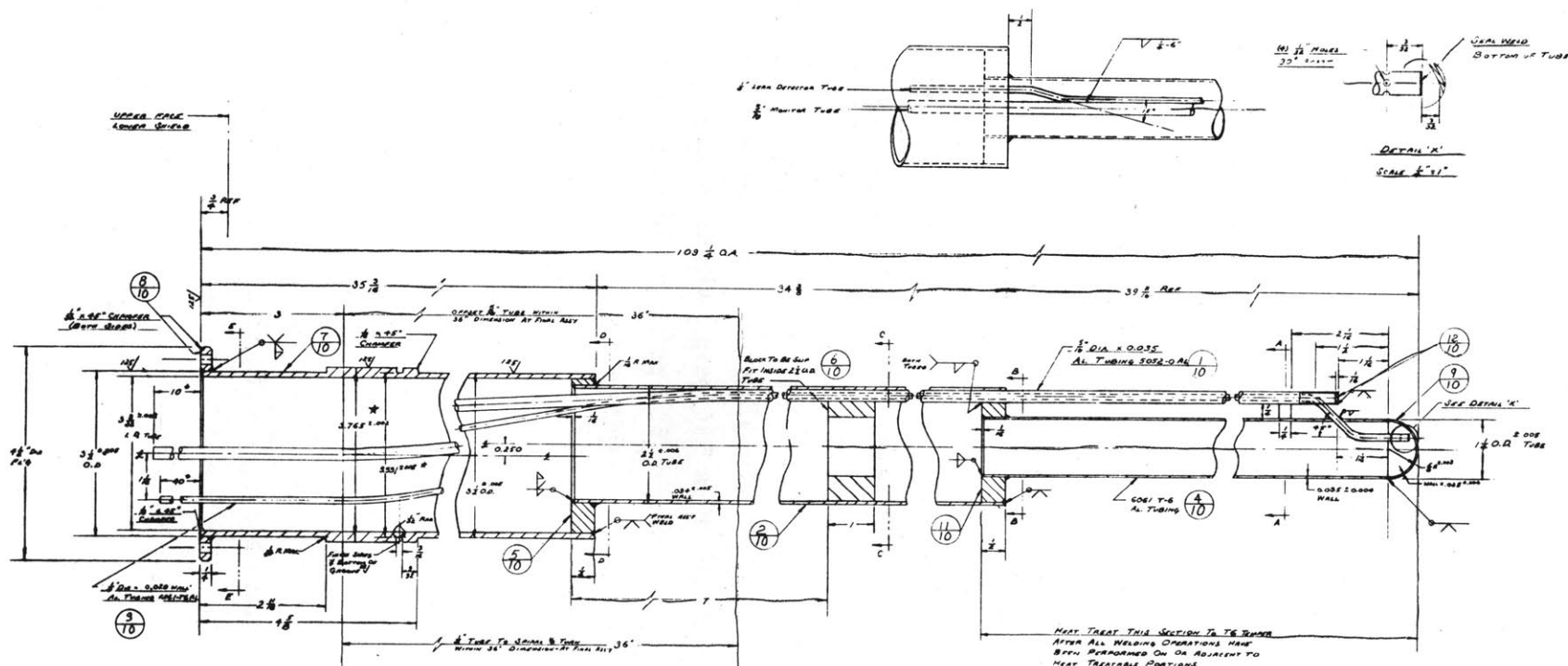
MISCELLANEOUS COMPONENTS OF THE IN-PILE SECTION  
AND COMPONENTS NECESSARY FOR ACCOMMODATION OF THE  
IN-PILE SECTION IN THE MITR

## A3. 1. 1 Thimble for In-Pile Section

The thimble which contains the in-pile holdup capsule and inlet-outlet organic lines is illustrated in Figures A3. 1 and A3. 2. Figure A3. 1 is the construction drawing and Figure A3. 2 is a presentation of photographs of (1) the thimble before the final assembly welding and (2) the thimble tip showing the monitor tube and leak detector tube.

The OD of the lower section of the thimble which extends into the center of the fuel element is limited to 1-1/4 inches by the opening available in the fuel element. This section of the thimble is constructed of 6061 aluminum alloy which was heat treated to the T6 specification after welding, to get the greatest possible tensile strength. With a wall thickness of 0.035 inches, the allowable working pressure of this section of the thimble at 250° F is 540 psig, which is only slightly less than the maximum pressure (600 psig) of the loop itself. The thimble is protected by means of a rupture disc rated for release at 100 psig on the thimble gas supply system, and leaks of gas through the thimble shielding normally prohibits any large pressure buildup in any case. The thimble is pressurized slightly above atmospheric with carbon dioxide gas during operation of the loop.

The two upper sections of the thimble are constructed of 5052-0 aluminum alloy (rolled into tubes and turned to the proper dimensions) because of its superior strength in the annealed state and the practical consideration of getting maximum strength without requiring heat treating of these sections. The middle and upper sections have allowable working pressures of 270 psig and 230 psig, respectively, at 400° F which is the maximum estimated temperature of these sections; space limitations prohibited use of thicker tubing. The thimble was not pressure-tested but was x-rayed for defects and helium leak-tested.



- Notes:
- 1) MAX. SO2-O AL ON SURF EXCEPT AS NOTED
  - 2) WELD TREAT AS NOTED
  - 3) WELDING MATERIALS TO BE INSURED TO BE TENSILE ST FINAL ASBY
  - 4) SPALLS & OFFSET OF 1/8 IN THREE TO BE DONE AT FINAL ASBY
  - 5) 1/2" THICK BLOK TO BE INSERTED AT FINAL ASBY
  - 6) OAL FINISH TO BE CONCERNING WITHIN 100 1/4

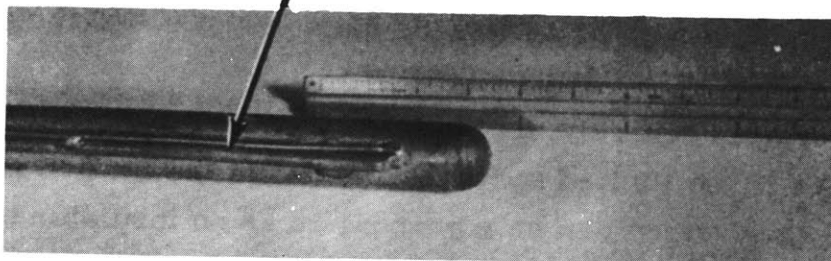
MASSACHUSETTS INSTITUTE OF TECHNOLOGY REACTOR

FIG. A3.1 DETAILS OF IN-PILE SECTION THIMBLE

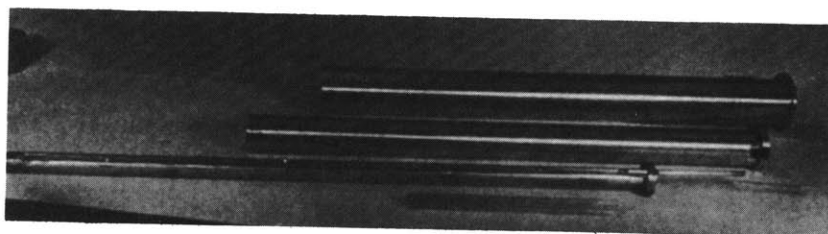
C	Aluminum	1/2"	100"
D	Aluminum	3/8"	100"
E	Aluminum	1/2"	100"
F	Aluminum	1/2"	100"
G	Aluminum	1/2"	100"

DATE	REV	BY	CHK
8/20/59	PC		

Monitor and Leak Detector Tubes



A. Bottom Tip of Thimble



B. All Components of Thimble Before Final Assembly Welding

FIG. A 3.2 - PHOTOGRAPHS OF IN-PILE SECTION THIMBLE

### A3. 1. 2 Organic Holdup Capsule Thermocouples, Trace Heaters, and Construction Photographs

For measuring temperatures around the organic holdup capsule, the use of the smallest thermocouple lead wires compatible with reliability is necessary because of space limitations imposed on the thimble and the desire for the largest possible in-pile organic holdup. Single conductor "Ceramo" stainless steel sheathed thermocouples (28 gage wires, Chromel-Alumel) with MgO insulation and an outside diameter of 0. 040 inches are used. <sup>(1)</sup>

The incorporation of a reliable trace heater for heating the capsule is difficult because of the limited space available and the limited amount of boron-silicate glass which can be incorporated as an insulator on the holdup capsule because of reactivity effects. It was originally planned to cover the capsule and heating wires with No. 27 "Scotch" glass tape, <sup>(2)</sup> but the reactivity limitation of one per cent  $\delta k/k$  per experiment in the MITR is exceeded with this design due to the boron in the glass tape. The procedure finally followed was to paint the capsule and those tubes which were to be trace heated with "PT-404," a ceramic insulating paint. <sup>(3)</sup> As additional protection, the 22-gauge nichrome heater wire used was purchased with double-glass insulation with an over-all OD of 0. 033 inches maximum and was further covered by hand with 1/32-inch "Refrasil" silica sleeving. <sup>(4)</sup> The length of nichrome heating wire required for each of the duplicate trace heaters on the capsule and the 13 inches of tubing above the capsule (to the "Refrasil" tape-insulated tubing -- see Figure 3. 7 of Chapter 3) is 40 feet based on conservatively calculated heating requirements of 600 watts for the capsule and 125 watts for the 13 inches of tubing. This heat load is obtained at approximately 175 volts and is equivalent to a heating density of 2. 9 watts/cm<sup>2</sup> of wire. Operation of the

---

(1) Thermo Electric Company, Inc., Saddle Brook, New Jersey

(2) Minnesota Mining and Mfg. Company, St. Paul, Minnesota

(3) Product Techniques, Inc., Los Angeles, California

(4) H. I. Thompson Fiber Glass Company, Los Angeles, California

in-pile section during the first run on Santowax OMP has indicated that the trace heater on the capsule operates satisfactorily, even after exposure to large radiation doses. On October 10, 1961, after 1690 MWHR of irradiation, circulation of the organic in the loop was interrupted by the failure of the electrical power to the loop, and the Santowax OMP froze in all sections of the loop. By use of the trace heaters, the organic was remelted and circulation restarted once power had been restored. The total radiation exposure of the trace heater at the axial center of the capsule at that time was  $1.4 \times 10^{11}$  rads or a thermal nvt of  $8.8 \times 10^{19}$  n/cm<sup>2</sup>.

Figures A3. 3 and A3. 4 are photographs of the organic holdup capsule before and after installation of the trace heaters and thermocouples.

### A3. 1. 3 Inlet-Outlet Lines for Flow of Organic to and from Holdup Capsule

As illustrated in Figures 3. 7 and 3. 8 of Chapter 3, two annular tubes are provided to transport the organic between the top of the lower reactor shield and the irradiation capsule. The organic flows down the inner tube (3/8 inch OD by 0. 020 inch wall Type 304 stainless steel) to the bottom of the irradiation capsule. The outflow is through the annulus between the inner tube and the outer tube (5/8 inch OD by 0. 049 inch wall Type 316 stainless steel). With this arrangement, any gases are removed from the capsule and emptying of the capsule by means of a gas purge is simplified. The 5/8 inch OD tube can be used up to pressures of 2800 psig at 800°F and the 3/8 inch OD tube up to 1100 psig at 800°F. In addition, the inner tube, which has the thinnest wall, is not likely ever to be subjected to a large differential pressure since it is always completely immersed in the organic liquid. The tubes were pressure tested to 1670 psig at 70°F.

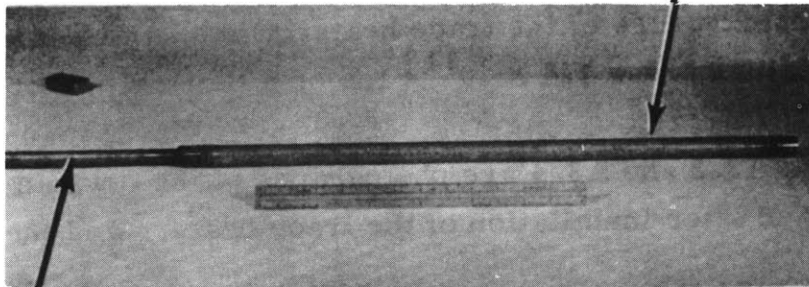
The lines are insulated by "Refrasil" tape wrapped to a minimum OD of 1-1/4 inches except over the lower 13 inches of tubing where the diameter of the thimble does not permit any such insulation. The outside of the insulation was painted with "Sauereisen" cement<sup>(1)</sup> to act as a

---

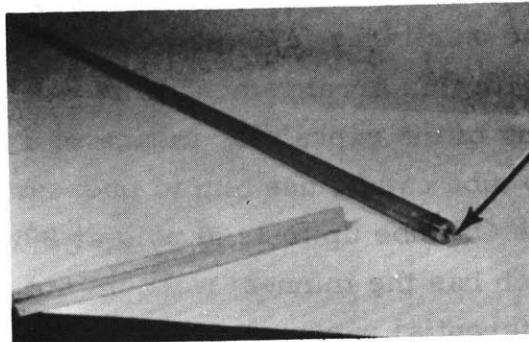
(1) Sauereisen Cement Company, Pittsburgh, Pennsylvania



Capsule 7/8" O.D. x  
0.035 inch Wall  
Type 316 SS



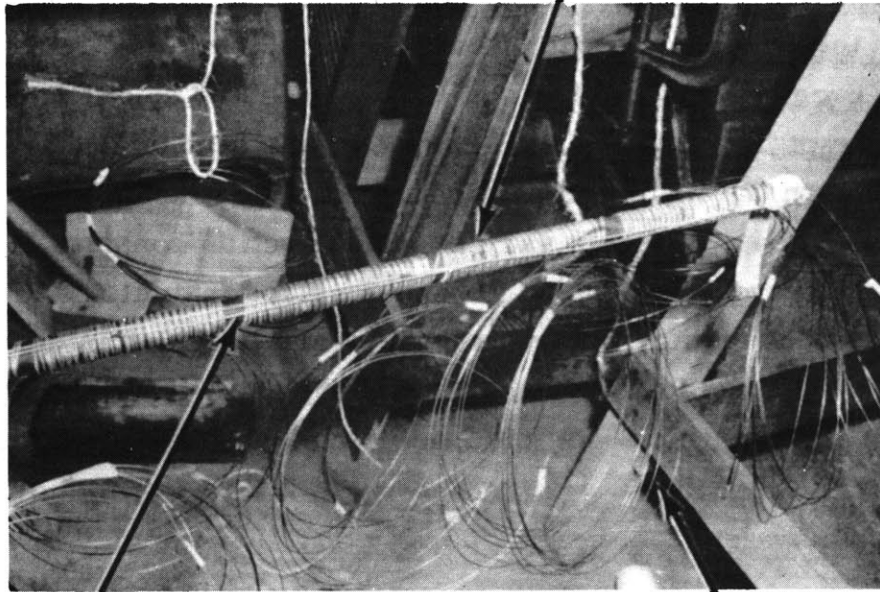
Outlet Tube 5/8" O.D. x 0.049 inch Wall  
Type 316 SS -  
Contains Inlet Tube 3/8" O.D. x 0.020 inch Wall  
Type 304 SS



Threaded Hole  
for Installation  
of Thermocouple  
Probe  
Seal-Welded After  
Installation of  
Probe

FIG A3.3 PHOTOGRAPHS OF THE ORGANIC  
HOLDUP CAPSULE BEFORE  
INSTALLATION OF TRACE HEATERS  
AND THERMOCOUPLES

Trace Heaters  
on Capsule



Trace Heater  
Leadwire

0.040 inch O.D. "Ceramo"  
Thermocouple Lead Wires  
Single Conductor

FIG. A3.4 PHOTOGRAPHS OF THE ORGANIC HOLDUP  
CAPSULE AFTER INSTALLATION OF TRACE  
HEATERS AND THERMOCOUPLES

binder for the tape and to prevent penetration of the "Refrasil" when the lead shielding was poured. In the region where concrete shielding was poured, a waterproof resin was used to coat the "Refrasil" and prevent water penetration and shorting of the trace heaters. Some difficulty was encountered with use of "Refrasil" due to its approximately 10 per cent water of crystallization which is driven out at around 300°F. Until all of this water was removed by baking at a temperature somewhat greater than 300°F, trouble was continually encountered with short circuiting of the trace heaters due to the water liberated on heating. After final removal of the water, operation has been satisfactory.

The trace heaters on the inlet-outlet lines are constructed similarly to those of the capsule in all respects (see section A3. 1. 2). The trace heaters on the insulated portion are divided into two sections, each controlled by a different variac. Each section consists of 55 feet of 22-gauge nichrome heating wire, double-glass insulated and covered with "Refrasil" sleeving; the trace heaters are provided in duplicate for reliability. The heat load was conservatively estimated at 770 watts for each heater section which, for the heater wire specified, requires 218 volts and is equivalent to a heating density of 2.3 watts/cm<sup>2</sup> of wire.

#### A3. 1. 4 Shielding

In the part of the thimble contained within the lower shield plug, lead and heavy concrete are provided for radiation shielding. All lines passing through this section are curved to prevent streaming of radiation (see Figure 3. 7 of Chapter 3).

#### A3. 1. 5 Lower Shield Plug and Upper and Lower Fuel Adapters

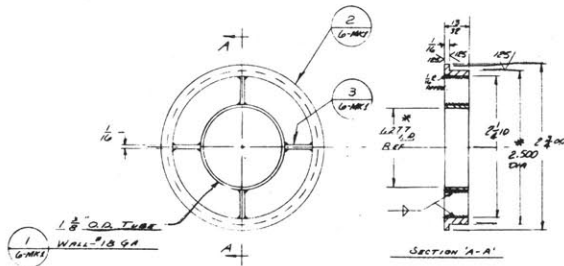
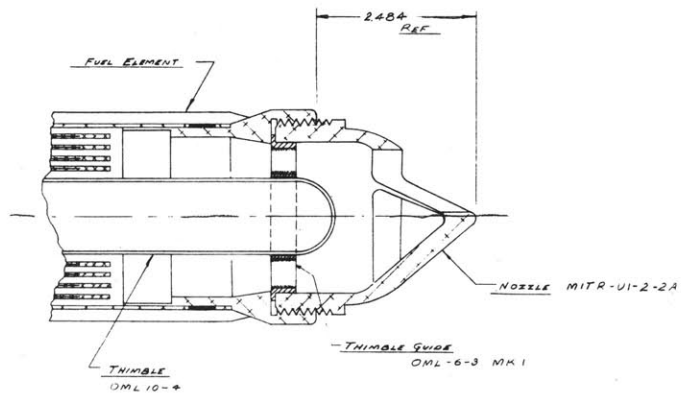
A special lower shield plug and upper and lower fuel adapters have been constructed for this study. The fuel element is connected to the upper shield plug by means of the upper fuel adapter; the lower fuel adapter on the lower end of the fuel element mates with a hole in the plenum plate and is used to position the lower end of the fuel element in the reactor as well as to divert D<sub>2</sub>O coolant flow through the fuel

element. The in-pile section (Figure 3. 7 of Chapter 3) fits inside this assembly.

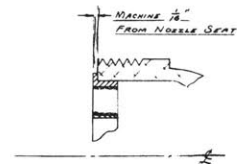
In the fuel element used in the first experiment, no thimble positioners or guides are built into the fuel element itself. The thimble guides usually constructed integral with the MITR removable plate fuel elements prohibit the use of the monitor and leak detection tubes on the outside of the thimble. In order to position the thimble at the bottom of the fuel element, the lower adapter used on the MITR fuel elements has been modified as shown in Figures A3. 5 and A3. 6 to include a thimble guide. The lower adapter is screwed into the fuel element in the usual fashion. The thimble used with this design is approximately 1-1/4 inches longer than the aluminum thimble normally used in the MITR for irradiation of samples in the center of the fuel element. However, the increase in length does not cause any significant change in the D<sub>2</sub>O coolant flow to the fuel element. The upper fuel adapter is used to position the thimble above the fuel element.

In Figures A3. 7 and A3. 8, the lower shield plug and upper fuel adapter are illustrated; the connection between the lower shield plug and upper fuel adapter is shown in Figure A3. 9. The contemplated change at a future date to a new fuel element having space for a larger in-pile section required the incorporation of some flexibility in the design of this lower shield plug and upper fuel adapter. For reasons of economy, it was desired to be able to: (1) use in some other experiment the reactivity left in the initial fuel element when the changeover to the new fuel element is made, and (2) to transfer the special shield plug to the new fuel element, which will probably require a larger OD upper fuel adapter than that presented in Figure A3. 8. Since no method is presently available for making a connection between a hot fuel element and an upper adapter, it is necessary to make the change at the connection between the adapter and the shield plug. Consequently, at changeover, when the special shield plug has been disconnected, a standard shield plug will be connected to the adapter of the initial fuel element so that it can be returned to other MITR use. The special shield plug will then be connected

TOLEANCE - DECIMAL ± .005 FRACTIONAL ± 1/64 ANGULAR ± 30'



MAT'L 6061-T6 ALUMINUM (MK 1)

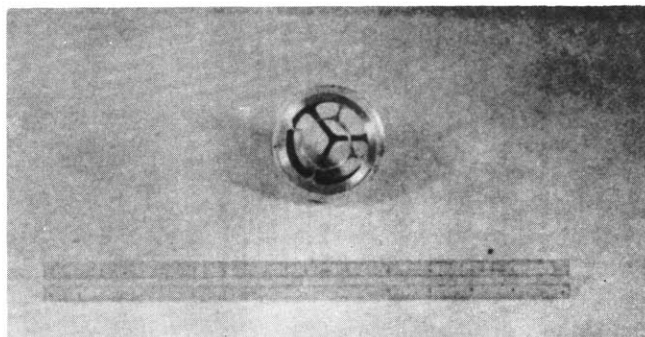


NOTES

- 1) NOZZLE SUPPLIED BY M.I.T.R.
- 2) THIMBLE GUIDE MUST BE LOOSE FIT ON THIMBLE (1.250 O.D.)
- 3) DIAS MARKED \* TO BE CONCENTRIC WITHIN .005 TIE

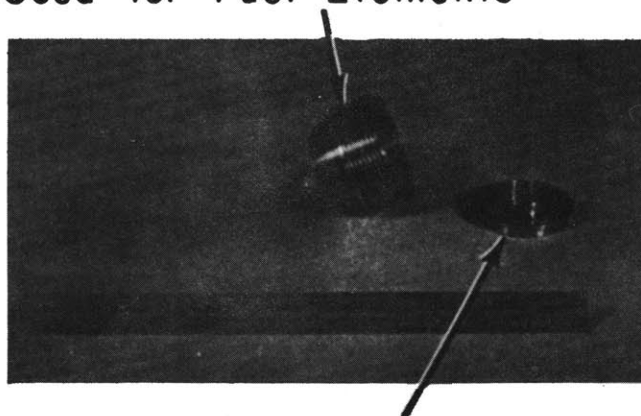
1	AS BUILT	PC #64
2	1.250 DIA X 1.250	WL 5000
3	GUIDE HAS HOLE TO MTR-UI-2-2A	#1 7/17/59
REV.	DESCRIPTION	BY DATE

FIG. A3.5 A	
DATE	APPROVED
8/2/59	PC



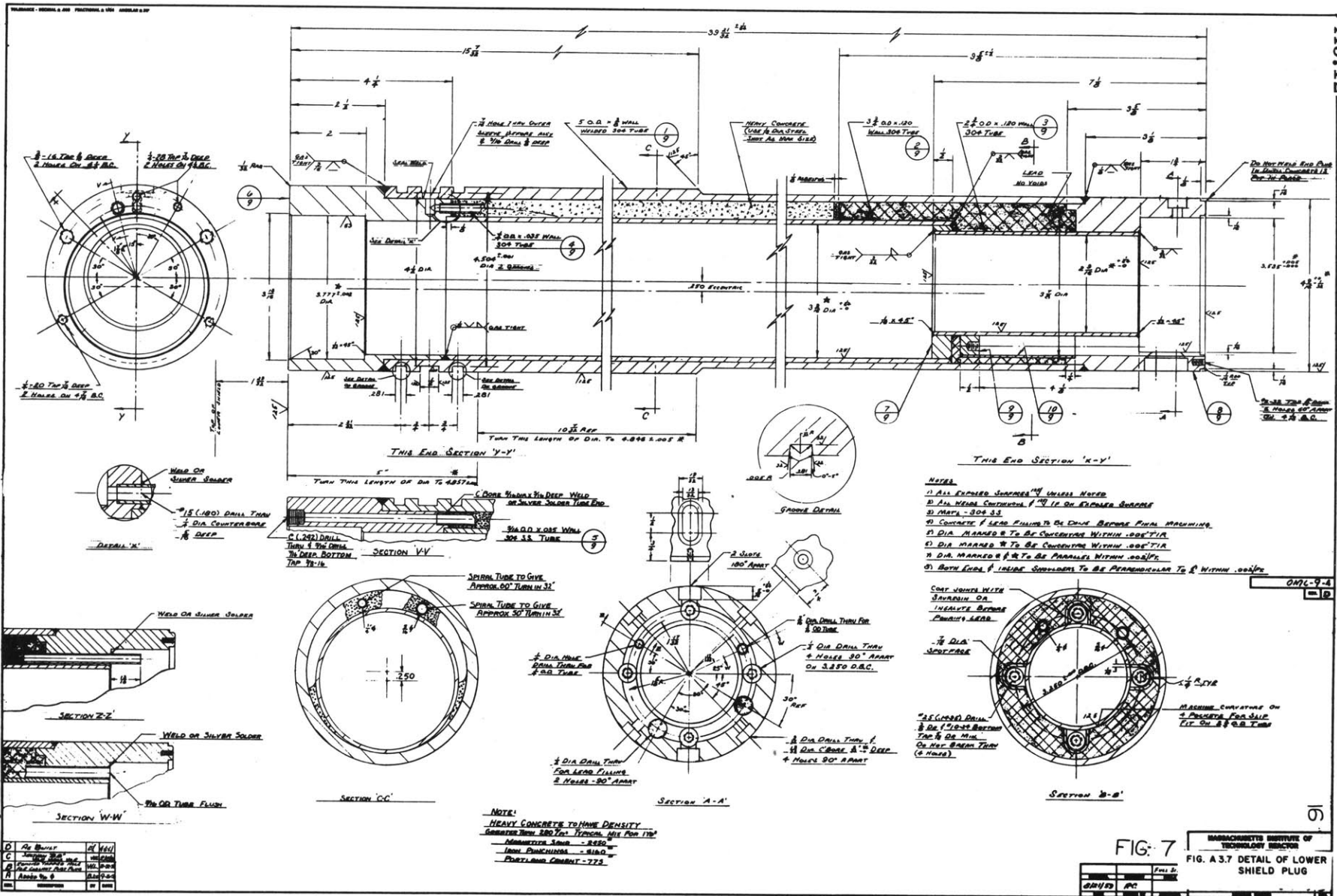
Top View of Assembled Lower Fuel Adapter

Lower Fuel Adapter Normally Used for Fuel Elements



Special Insert to Guide and Position Lower End of In-Pile Section Thimble

FIG. A 3.6 LOWER FUEL ADAPTER



- NOTES
- 1) ALL DIMENSIONS UNLESS NOTED
  - 2) ALL WELDS CONTINUOUS 1/4" IF ON FLANGES SHOULD BE WELD - 305 1/2"
  - 3) CONCRETE LEAD FINISH TO BE DONE BEFORE FINAL WELDING
  - 4) DIA MARKED \* TO BE CONCENTRIC WITHIN .002" TIR
  - 5) DIA MARKED # TO BE PARALLEL WITHIN .002" TIR
  - 6) BOTH ENDS OF INSIDE SHOULDERS TO BE PERPENDICULAR TO & WITHIN .002" TIR

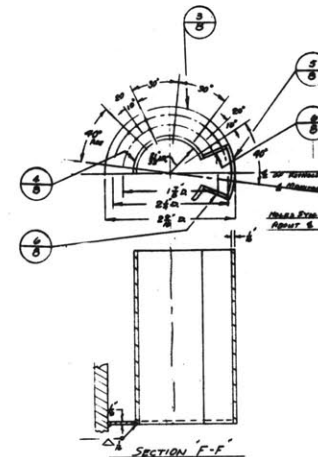
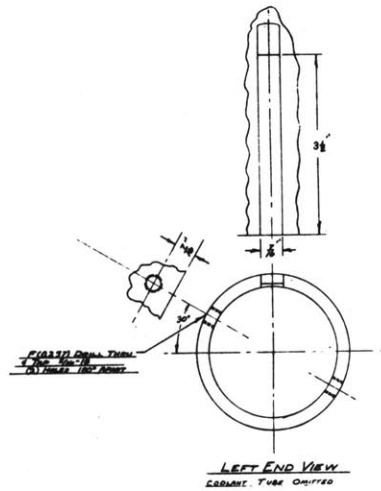
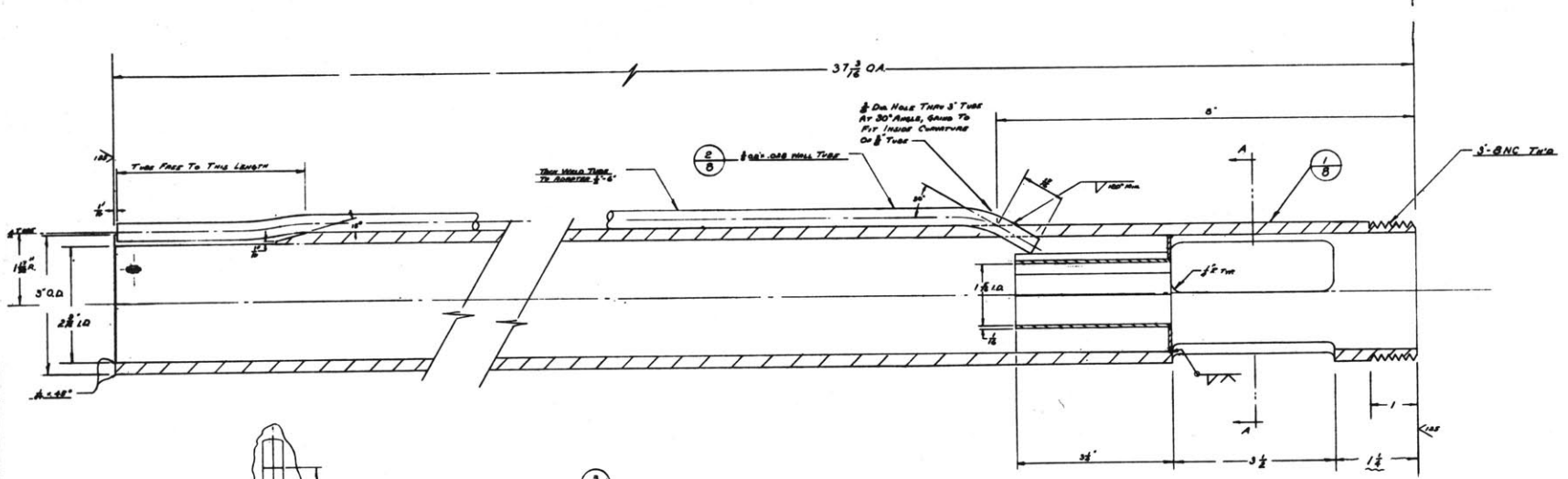
- CONCRETE JOINTS WITH SHROUDING OR INCOMPLETE BONDING FINISHES LEAD
- 3/8" DIA HOLES 30" APART
- 3/8" DIA DRILL THRU & HOLES 30" APART ON 3.350 O.D.C.
- 3/8" DIA DRILL THRU & HOLES 30" APART ON 3.350 O.D.C.
- 3/8" DIA DRILL THRU & HOLES 30" APART
- 3/8" DIA DRILL THRU & HOLES 30" APART
- 3/8" DIA DRILL THRU & HOLES 30" APART
- 3/8" DIA DRILL THRU & HOLES 30" APART
- 3/8" DIA DRILL THRU & HOLES 30" APART

NOTE:  
HEAVY CONCRETE TO HAVE DENSITY  
GREATER THAN 880 LBS PER CU FT  
MINIMUM STRENGTH - 8500  
TENSILE STRENGTH - 8500  
PORTLAND CEMENT - 775

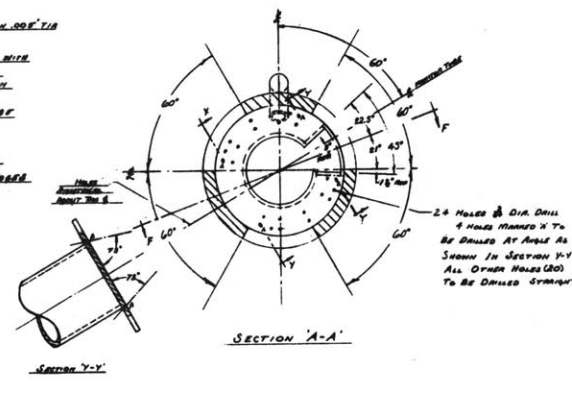
FIG. 7  
BARRACLETTE INSTITUTE OF TECHNOLOGY INDIAN  
FIG. A.3.7 DETAIL OF LOWER SHIELD PLUG

Q	Q	Q	Q
Q	Q	Q	Q
Q	Q	Q	Q
Q	Q	Q	Q
Q	Q	Q	Q

REVISIONS: 000001 & 0001 PARTIAL & 0002 COMPLETE 0017



- NOTES
- 1. I.D. & O.D. TO BE CONSIDERED WITHIN .002" TIA
  - 2. PARALLEL WITHIN .002"
  - 3. TUBES MUST BE ORIENTED WITH TUBE O.D. WITHIN .002" TIA - PARALLEL WITH TUBE AX. WITHIN .002" TIA
  - 4. FREE ENDS PERPENDICULAR TO TUBE AX. WITHIN .002" TIA
  - 5. HOLE TO BE DRILLED TO TUBE EDGE - D.O.
  - 6. REMOVE ALL BURRS & SHARP EDGES



0001-B-4

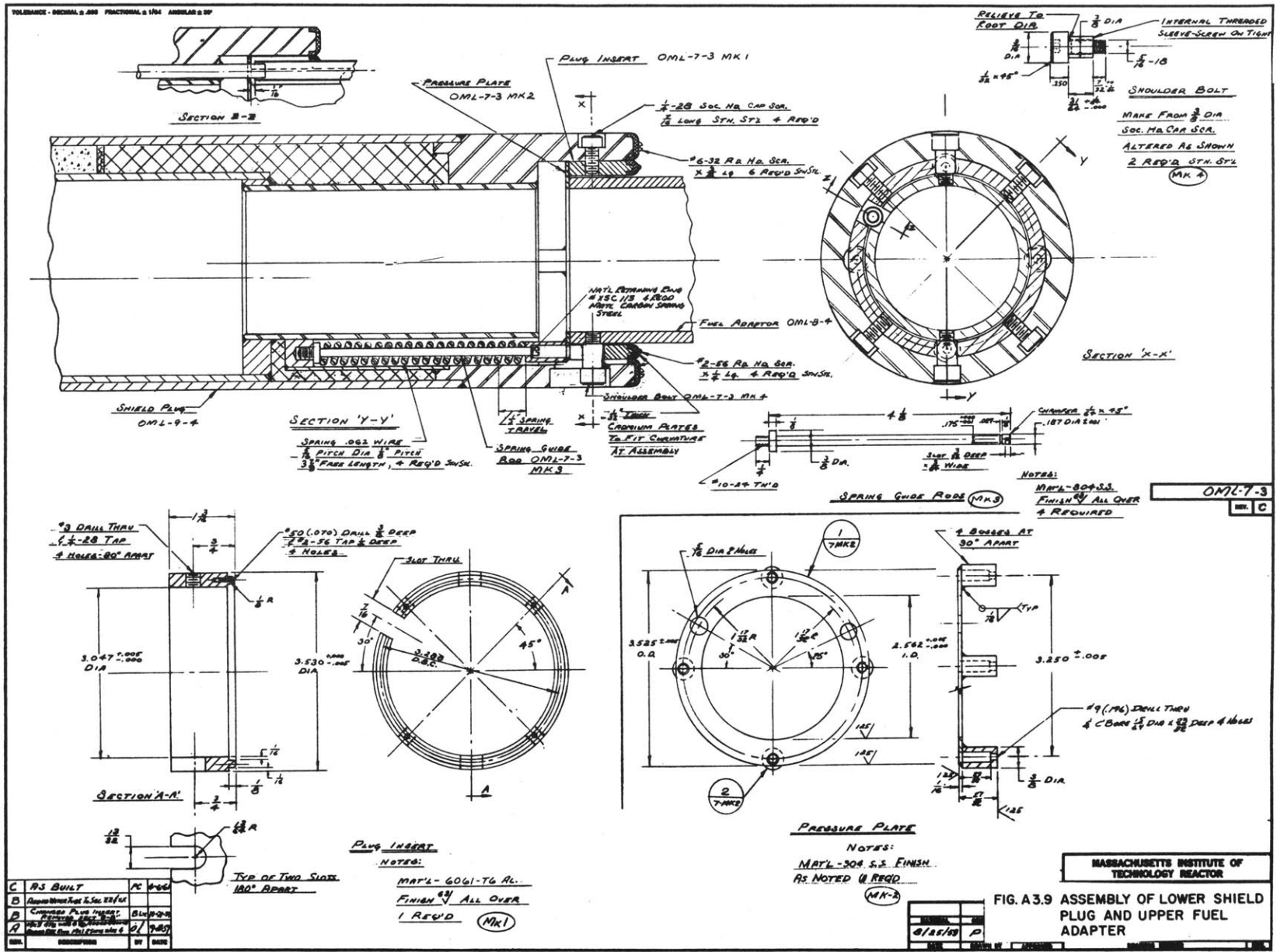
MASSACHUSETTS INSTITUTE OF TECHNOLOGY REACTOR

REV.	DATE	BY	CHKD.	APP'D.
1	3/1/59	J.P.C.		
2				
3				
4				

FIG. A3.8 DETAILS OF UPPER FUEL ADAPTER

BY	CHKD.	DATE
A.A.		





REV.	DESCRIPTION	DATE	BY	CHKD.
C	RS BUILT	PC	0-66	
B	Assembly Test 5 Sec 12/64			
A	Changes Plus Insert		8-11-64	
	REVISIONS			

REV.	DESCRIPTION	DATE	BY	CHKD.

to the new fuel element for the loop by means of the upper adapter constructed for that fuel element. This procedure required that (1) the upper adapter used with the initial fuel element have an inside diameter sufficient to take the thimble diameter shown in Figure 3. 7 of Chapter 3, (2) that this upper adapter fit into both the special and the standard MITR lower shield plugs, and (3) that the special shield plug also fit the upper adapter required for the new fuel element. The lower shield plug design and upper fuel adapter shown in Figures A3. 7 and A3. 8, respectively, incorporate this flexibility. This is accomplished by inserting a removable sleeve in the end of the special lower shield plug (which can be used with an upper adapter having an outside diameter up to 3-1/2 inches). With this sleeve, the inner diameter of the special lower shield plug is the same as that of the standard MITR lower shield plugs which are designed for use with a 3-inch OD upper adapter (see Figure A3. 9).

Emergency  $D_2O$  cooling for the fuel element has been incorporated in the design of the upper fuel element adapter; cooling would thus be provided if the  $D_2O$  level in the reactor tank dropped below the element. The hole size in the spray head used for this purpose has been selected to give roughly the same  $D_2O$  flow rate as in the standard MITR fuel element assembly; this flow is estimated to be 0. 3 gallons/min through 24 holes; flow tests have indicated satisfactory operation of the emergency cooling system.

A photograph of the assembled fuel element, upper adapter, and lower shield plug is presented in Figure A3. 10. The assembled in-pile section which fits into this assembly can be seen at the right hand side of this photograph.

#### A3. 1. 6 Upper Shield Plug

The monitor tube on the in-pile section extends to the space between the upper and lower shields of the MITR. A new upper shield plug with a removable insert has been constructed, so that detectors can be inserted in this tube from the top of the reactor with the reactor operating at full power. A tube (1/2-inch OD  $\times$  0. 035-inch wall) extends

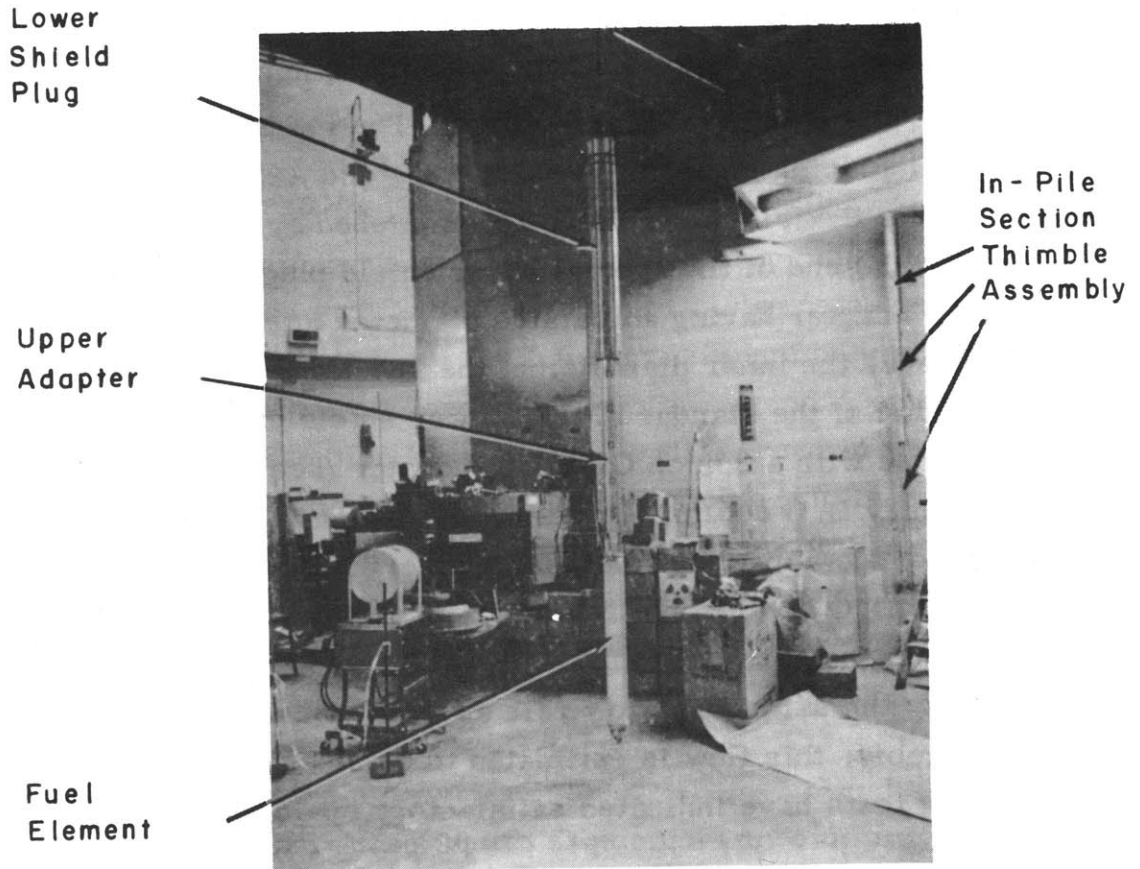


FIG. A3.10 FUEL ELEMENT ASSEMBLY AND IN-PILE SECTION THIMBLE ASSEMBLY

through this insert and mates with the monitor tube (which has a funnel-shaped guide on top) so that detectors may be inserted into the monitor tube from the top of the reactor. Figure A3. 11 illustrates construction of the upper shield plug and monitor tube extension. With the design shown, the entire upper rotary shield of the reactor can be removed or rotated without disturbing the monitor tube or in-pile section. Details of the upper shield plug and insert are given in Figure A3. 12.

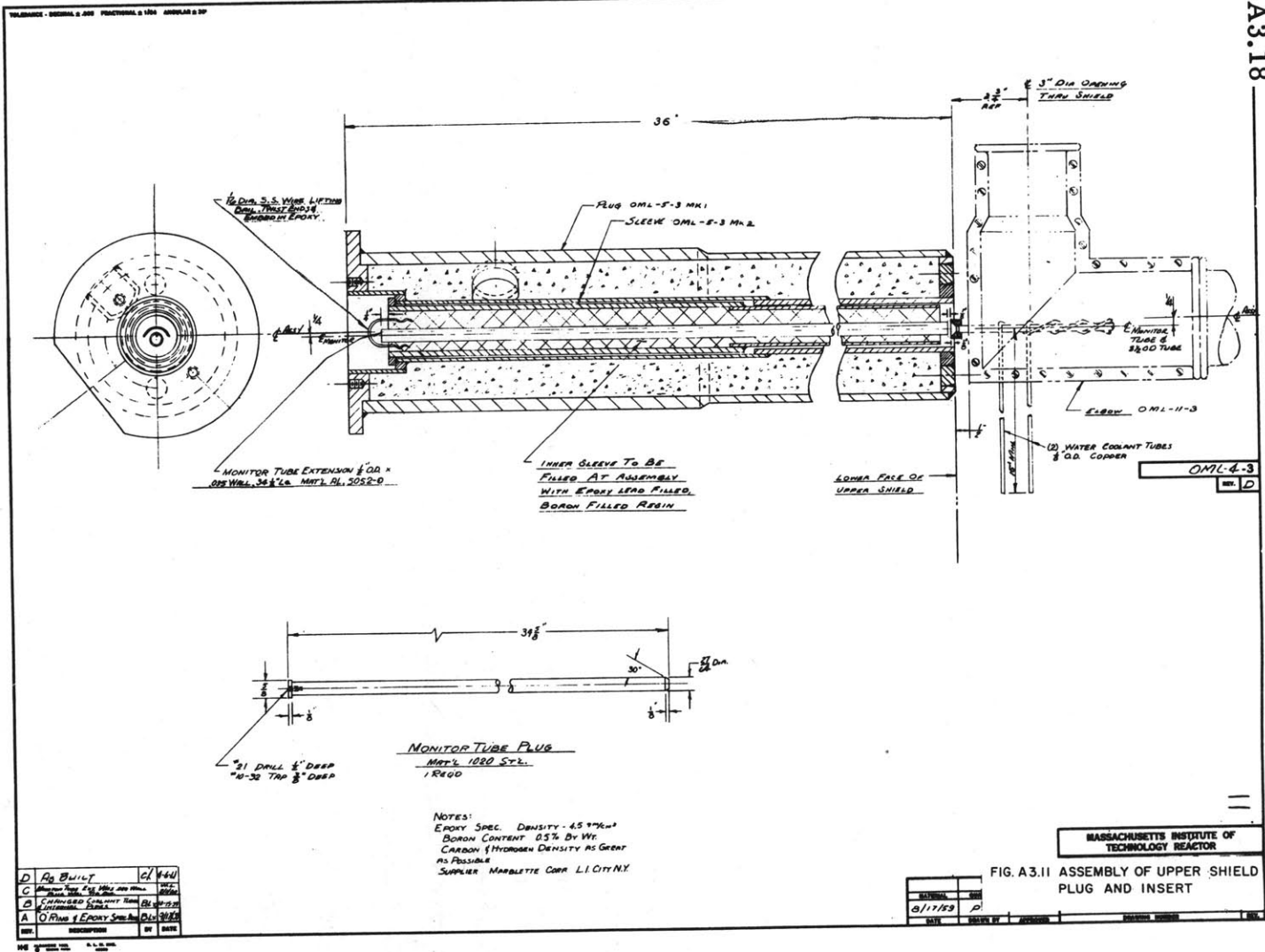
#### A3. 1. 7 Replacement Shield Plug for In-Pile Section

Whenever the in-pile section is not in the reactor, the opening left in the lower shield plug (Figure A3. 7) must be closed. Figure A3. 13 is a drawing of the shield plug constructed for this purpose. The outside dimensions of the plug are the same as those of the in-pile section thimble. The inside dimensions are the same as those of the standard MITR lower shield plugs. This arrangement permits a 1-1/4 inch OD thimble to be located in the center of the fuel element; the neutron flux and calorimetric dose rate measurements reported in Chapter 4 were thus made in the fuel element before the in-pile section was installed in the reactor.

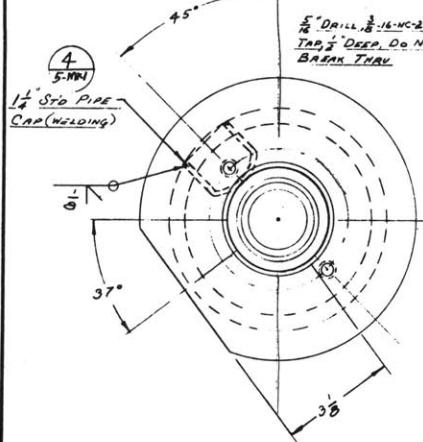
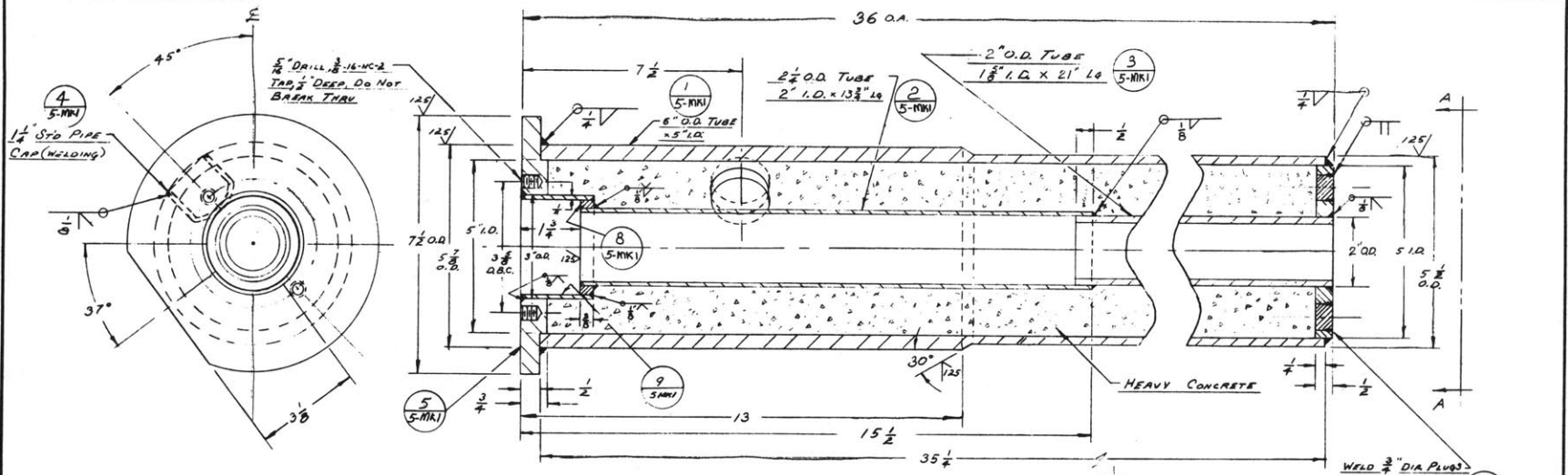
#### A3. 1. 8 Gas Supply Tube and Lead Tubes

An aluminum tube (1/4-inch OD  $\times$  0. 028-inch wall) supplies purified carbon dioxide gas to the bottom of the shielded section inside the thimble of the in-pile section. This gas is normally maintained at a slight positive pressure to force carbon dioxide through the leak detector tube and to prevent leakage of  $D_2O$  into the thimble in case the thimble develops a leak. A pressure relief system set at 100 psig, illustrated in Figure A3. 14 along with the leak detector system, is used to prevent the formation of excess pressure in the thimble.

Two aluminum tubes (1/2-inch OD  $\times$  0. 049-inch wall) which run from the bottom to the top of the shield inside the thimble, are provided for passage of the thermocouple and heater leads to the instrument panel outside of the reactor.

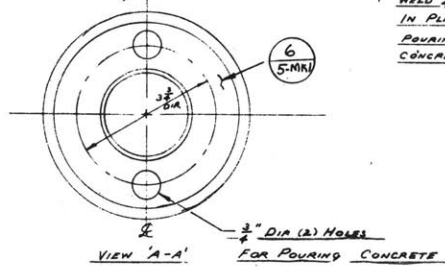


TOLERANCE - DECIMAL & .005 FRACTIONAL & 1/64 ANGULAR & 30'

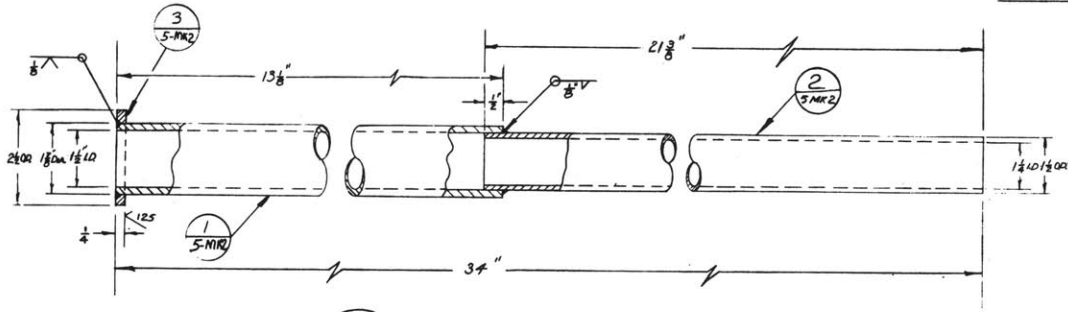


HEAVY CONCRETE TO HAVE A DENSITY GREATER THAN 230 PCF  
 TYPICAL MIX FOR 1 YD<sup>3</sup>  
 MAGNETITE SAND 285#  
 IRON FURNINGS 410#  
 PORTLAND CEMENT 775#

**PLUG MK 1**  
 MAT'L TUBING - COLD DRAWN ST'L MECHANICAL  
 P.L.T. FLANGES - H.R. MILD ST'L  
 INNER TUBES I.D. MUST BE STRAIGHT  
 PARALLEL & CONCENTRIC TO O.D. OF  
 OUTER TUBE WITHIN 0.002/FT.  
 FINISH MACHINING AFTER POURING CONCRETE  
 & WELDING PLUGS IN PLACE



OML-S-3  
 REV. C



**SLEEVE MK 2**  
 MAT'L  
 COLD DRAWN ST'L MECH TUBING  
 TUBE I.D. STRAIGHT & PARALLEL  
 WITHIN 0.002/FT.

MASSACHUSETTS INSTITUTE OF  
 TECHNOLOGY REACTOR

C	AS BUILT	AC	6-6-64
D	REMOVED TO PRIME & CORROSE AND TUBING	EL	11-17-59
N	REMOVED TO PRIME & CORROSE SHELL LEAKING ON MK 2	AL	7-7-58
REV.	DESCRIPTION	BY	DATE

MATERIAL	QUANTITY	SCALE	HALF
3/17/59	P.C.		
DATE	DRAWN BY	APPROVED	DRAWING NUMBER

FIG. A 3.12 DETAILS OF UPPER  
 SHIELD PLUG

A3.19

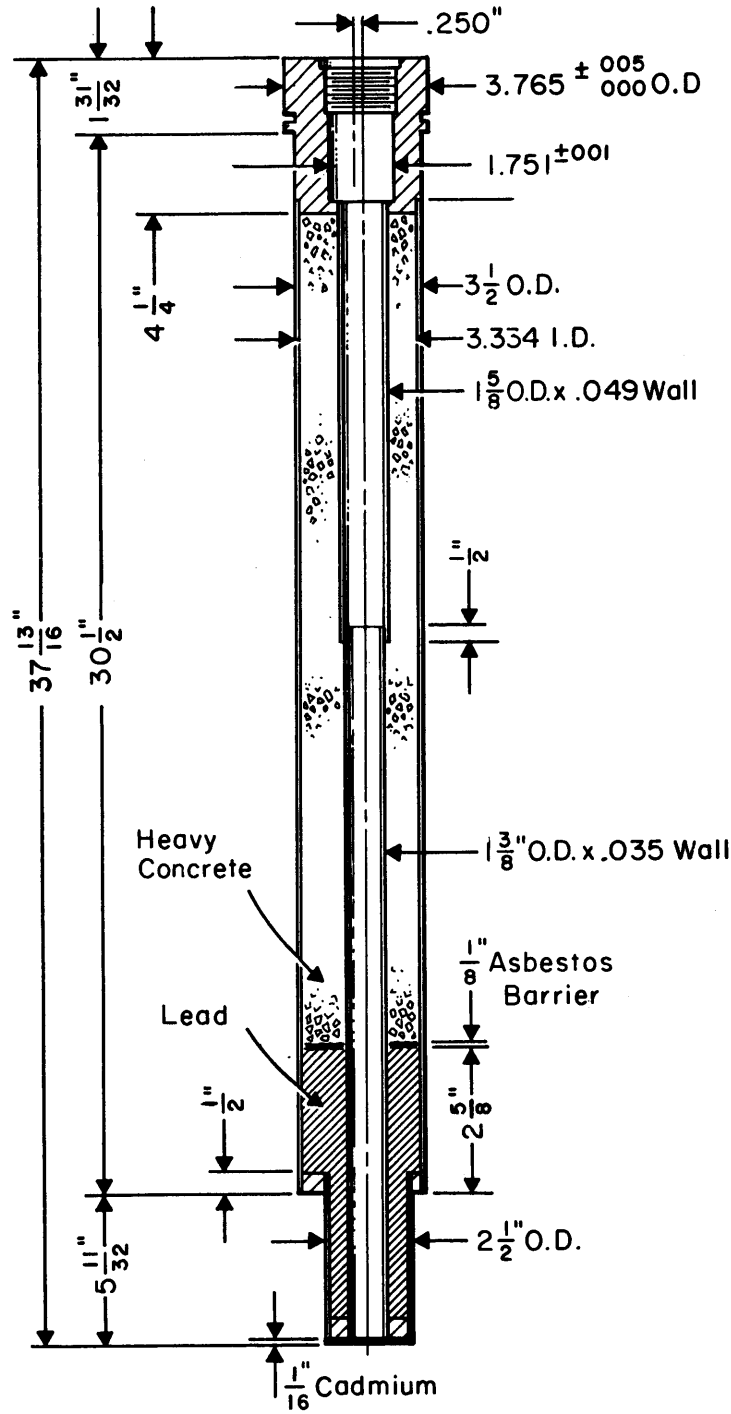


Fig. A3.13 Filler Plug for Lower Shield Plug

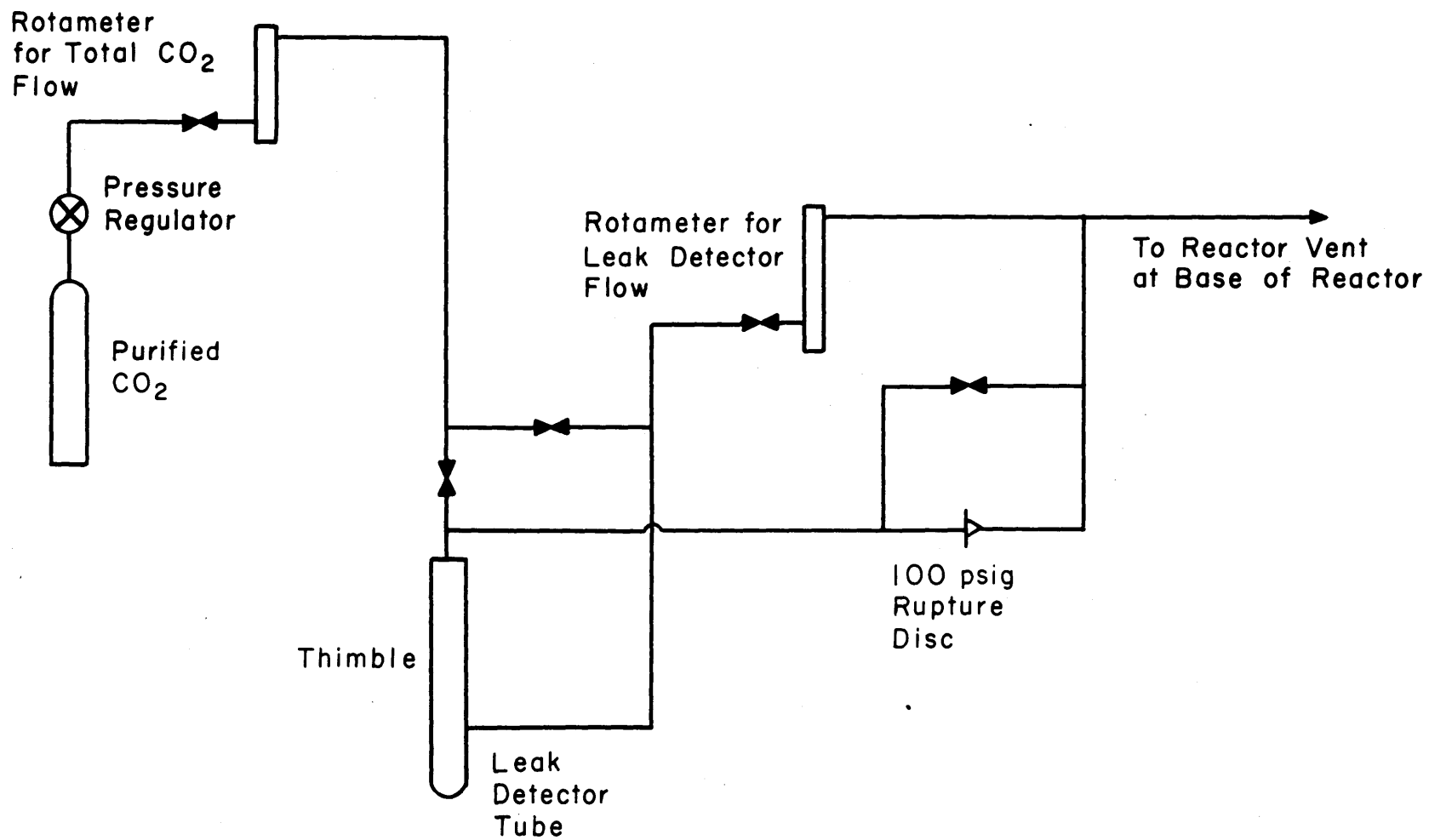


FIG. A 3.14 SCHEMATIC OF THIMBLE PRESSURIZING AND LEAK DETECTOR SYSTEM



### A3.1.9 Connections Between In-Pile Section and Hydraulic Console

In addition to the items described above, it is necessary to have lines carrying the organic material, thermocouple leads, and electrical leads through the main biological shield. A 3-inch ID sleeve passing horizontally through the reactor shield at a position between the upper and lower shields is used for this purpose. In all cases, the loop lines are completely enclosed by an aluminum elbow and aluminum conduit tubes to prevent contamination of the reactor by the organic in case leaks develop in these sections (see Figures A3. 15-A3. 19). The junction box used to provide a connecting point for electrical and thermocouple leads at the hydraulic console is also illustrated in Figure 3. 18.

It should be noted that the union design illustrated in Figure A3. 15 prevents any large pressure differences between the inside and outside of the relatively thin-walled 3/8-inch OD tube carrying the organic down to the irradiation capsule. Also, the method of positively holding the thimble and shield plug in the reactor are shown in Figures A3. 15 and A3. 18, respectively. Figure A3. 19 is a photograph of the top of the reactor showing installation of these sleeves. A detailed drawing of the elbow at the top of the thimble is given in Figure A3. 16.

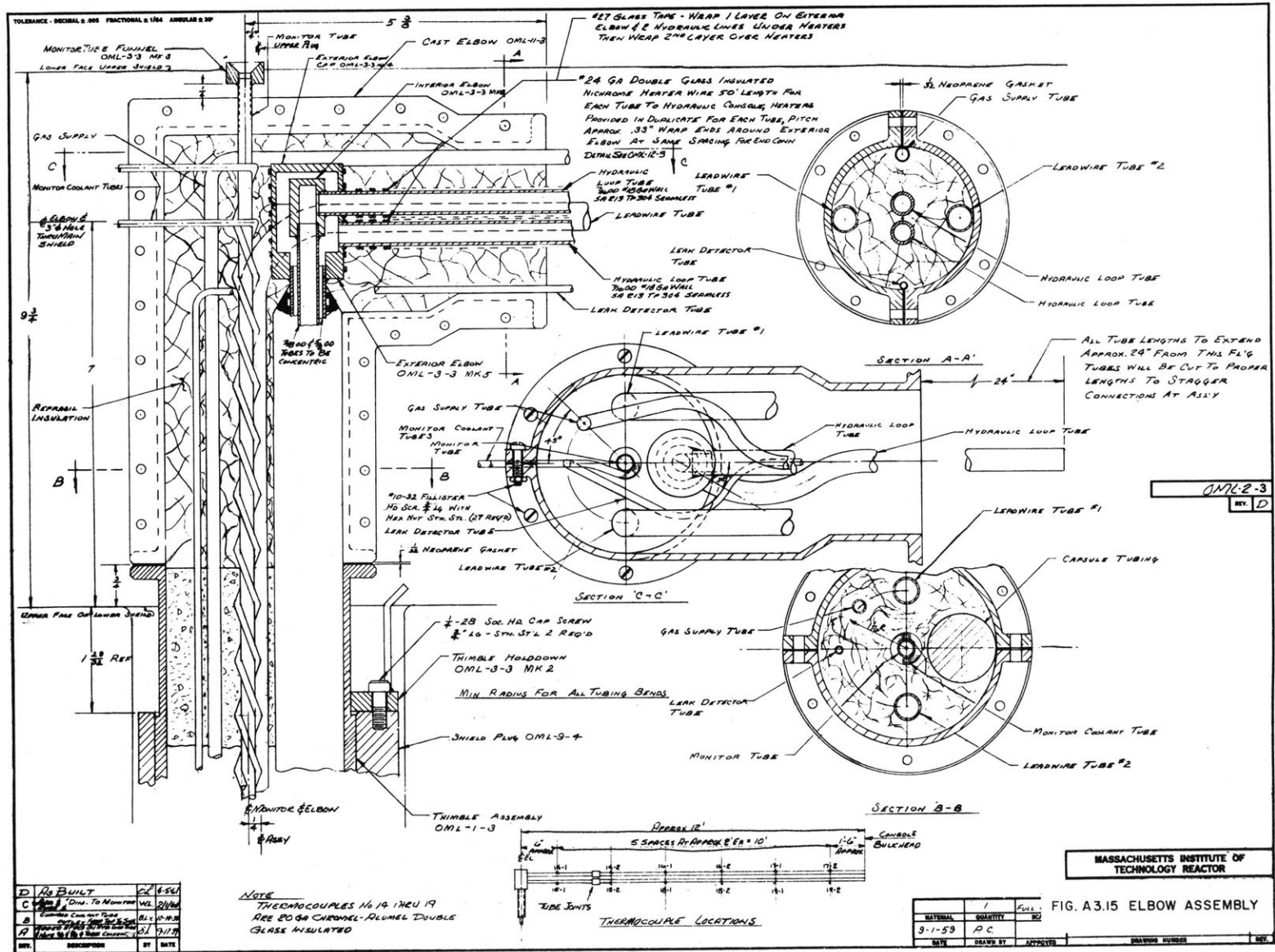
### A3.1.10 Complete Assembly of In-Pile Section and Miscellaneous Parts

A complete assembly drawing of the in-pile section, including all shield plugs and a detailed drawing of some miscellaneous parts are given in Figures A3. 20 and A3. 21.

## APPENDIX 3. 2

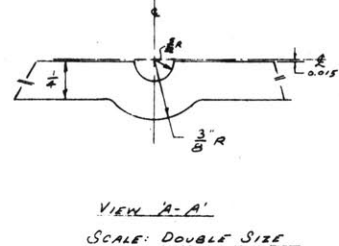
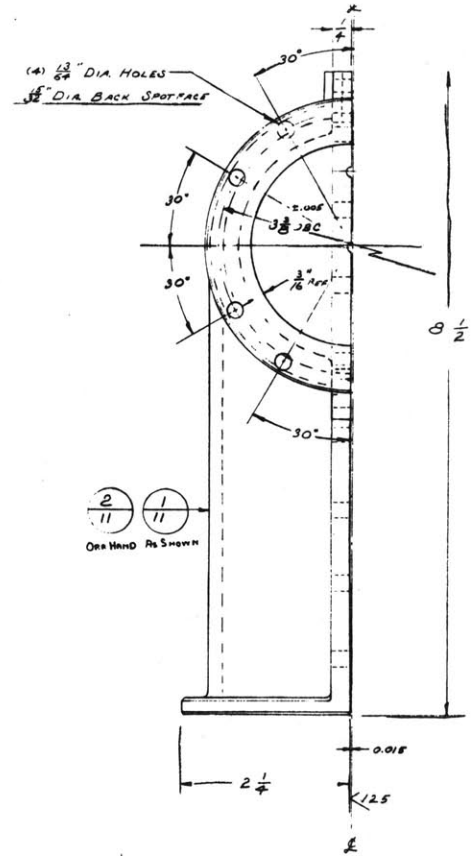
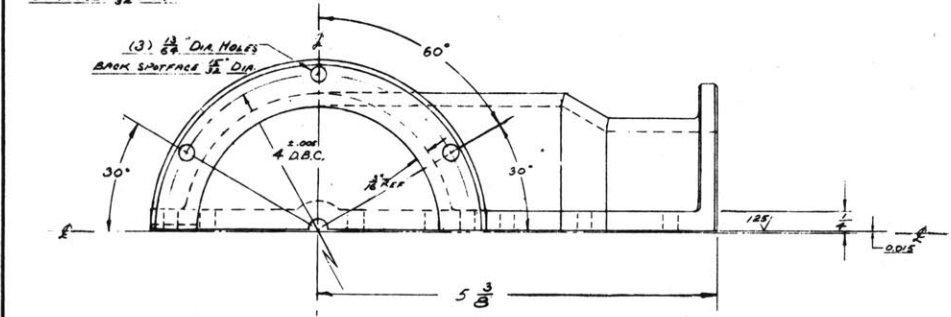
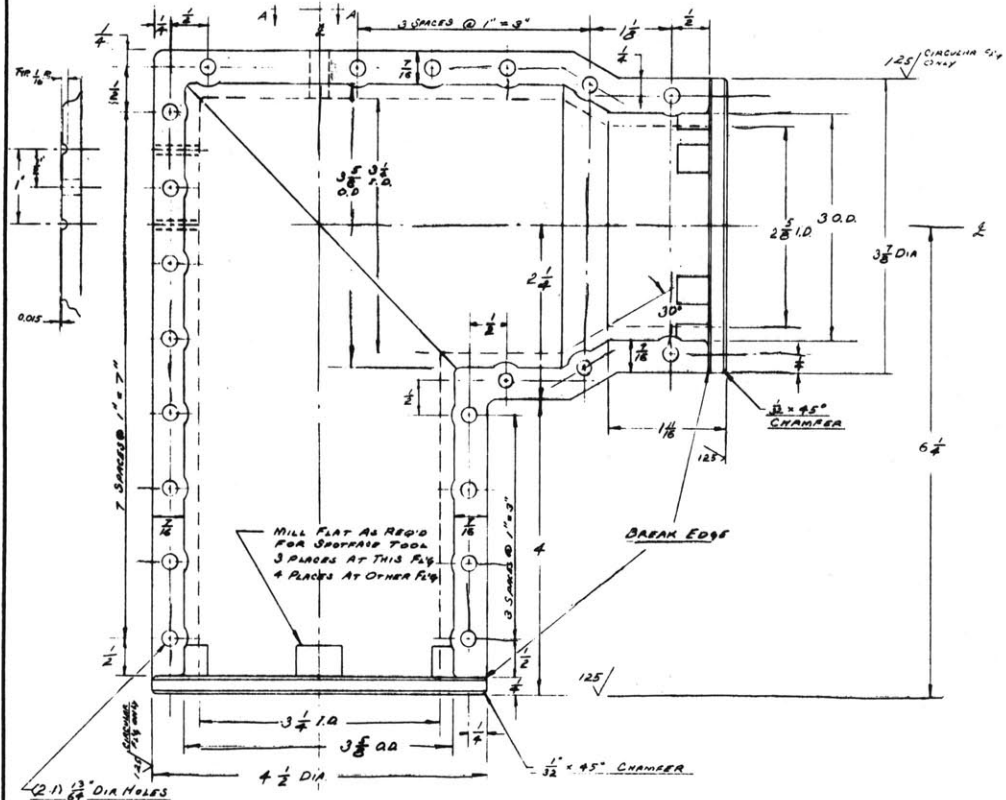
### BASES OF SPECIFICATIONS FOR THE ORGANIC IN-PILE LOOP AT M. I. T.

In deciding on specifications as a guide in designing the organic in-pile loop, consideration was given to the requirements imposed by the organic materials which might be tested for use in organic cooled nuclear reactors and the type of information desired from operation of the loop. The bases



A3.23

TOLERANCE - DECIMAL & .005 FRACTIONAL & 1/64 ANGULAR & 30°



NOTES:  
 MAT'L: CAST ALUM.  
 ALLOY 356 OR 195  
 MACHINE FINISHES AS NOTED  
 2 REQUIRED: 1 AS SHOWN  
 1 ORA HAND  
 LOCATE 3/8 DIA HOLES WITHIN .005 OF TRUE LOCATION

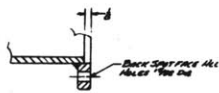
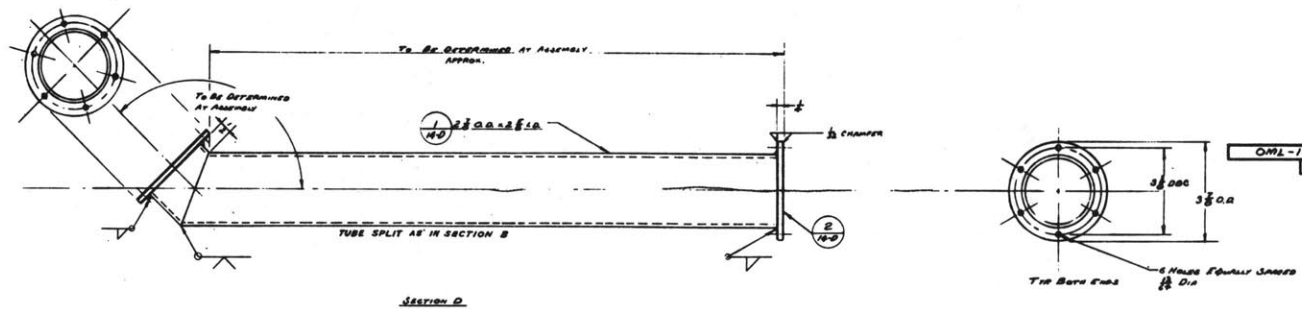
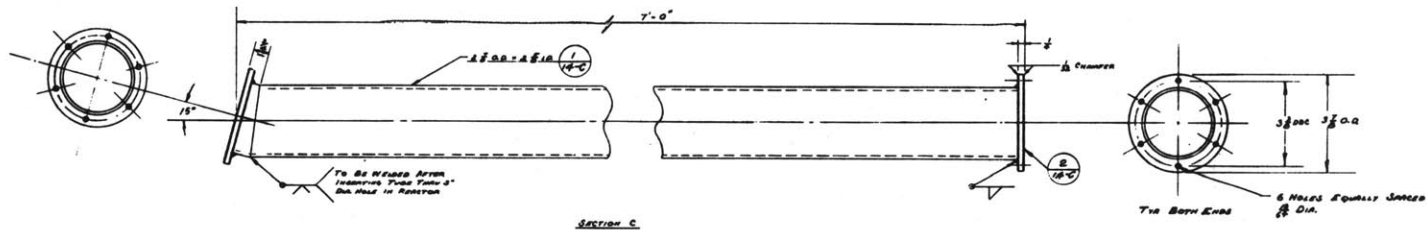
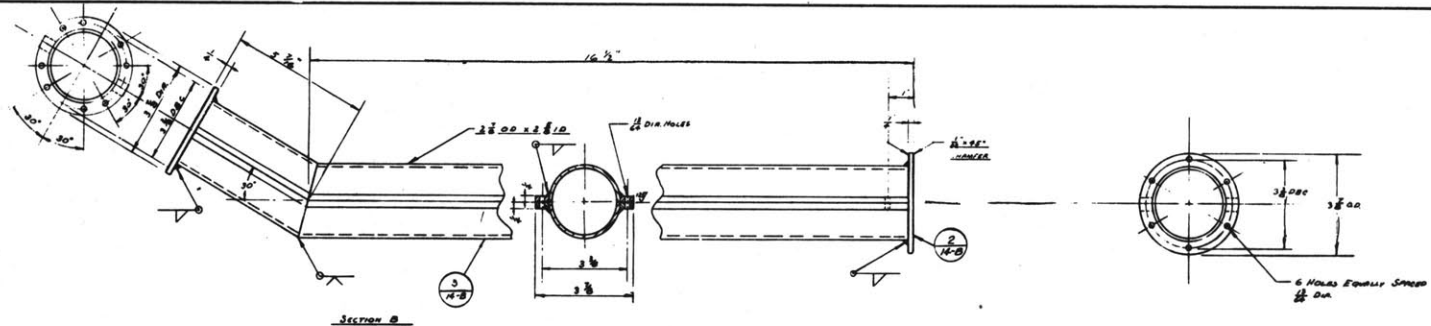
ORNL-11-3  
 REV. C

MASSACHUSETTS INSTITUTE OF TECHNOLOGY REACTOR

FIG. A3.16 DETAILS OF ELBOW

C	AS BUILT	PC	666
B	1/8" DIA HOLES	WC	824
A	CHAMFERED CORNER	AL	824
REV.	DESCRIPTION	BY	DATE

MATERIAL	QUANTITY	FILE #
8/13/59	P.C.	SEA
DATE	DRAWN BY	APPROVED
		DRAWING NUMBER
		REV.



TYPICAL FLANGE CONSTRUCTION

MATL: ALUM.  
5052-O

NOTE ALL HOLES ON FLANGES  
TO BE LOCATED WITHIN ±.005"  
OF TRUE LOCATION

NO BUILT	PC 5-30
DATE	BY

5-11-63	PC
---------	----

MASSACHUSETTS INSTITUTE OF  
TECHNOLOGY REACTOR

FIG. A3.17 CONDUIT TUBES

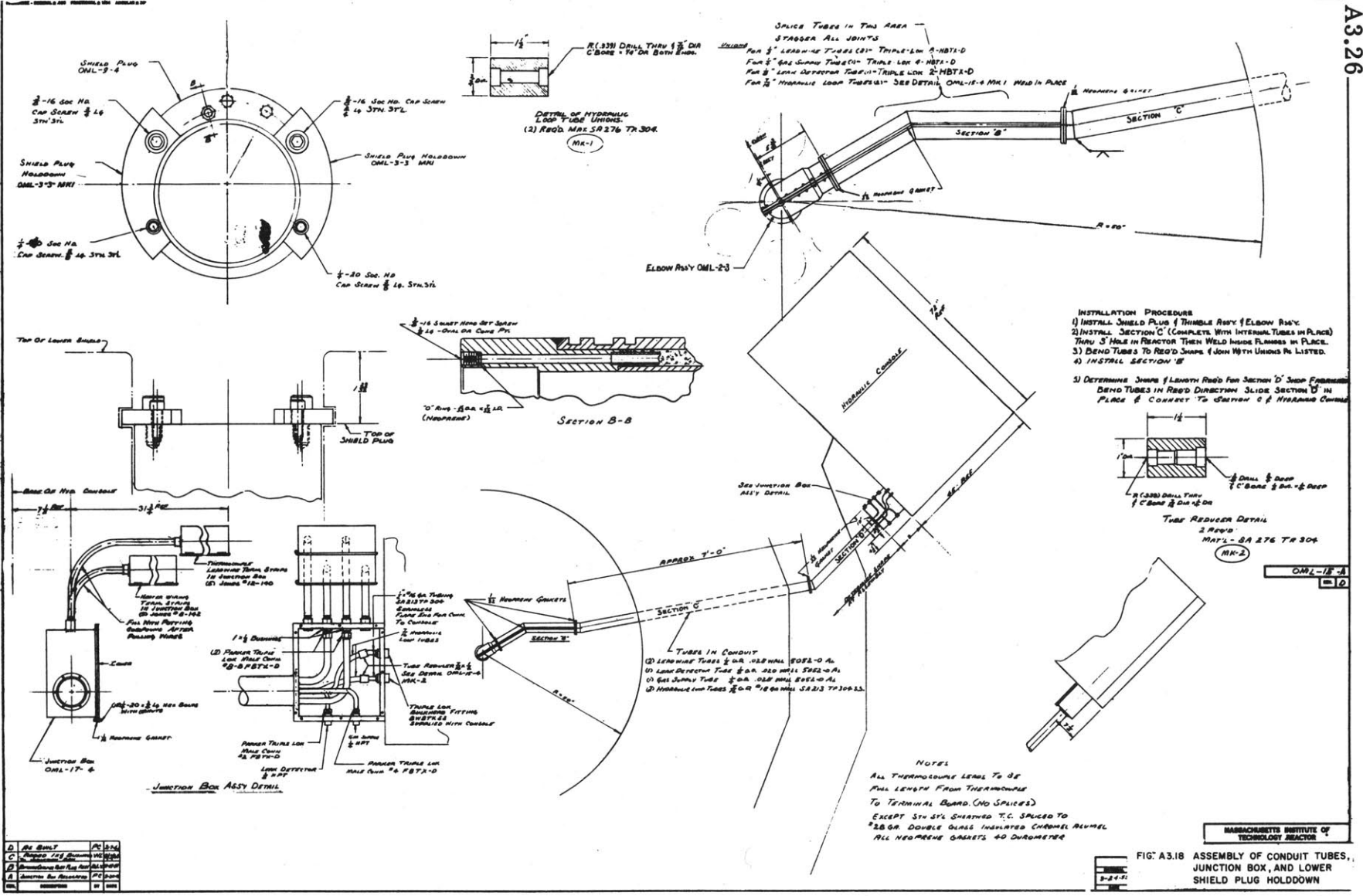
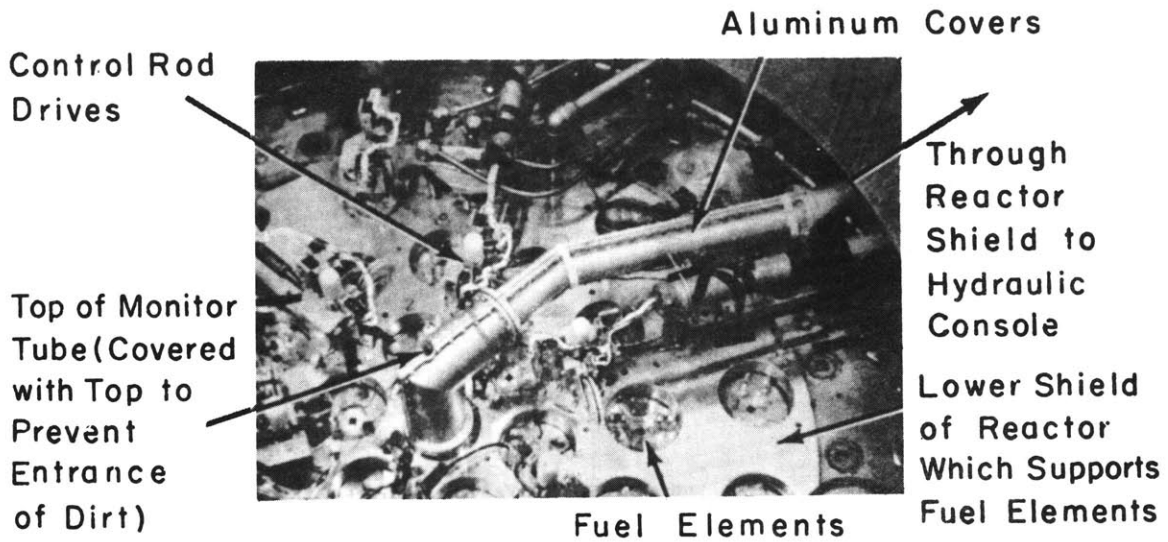
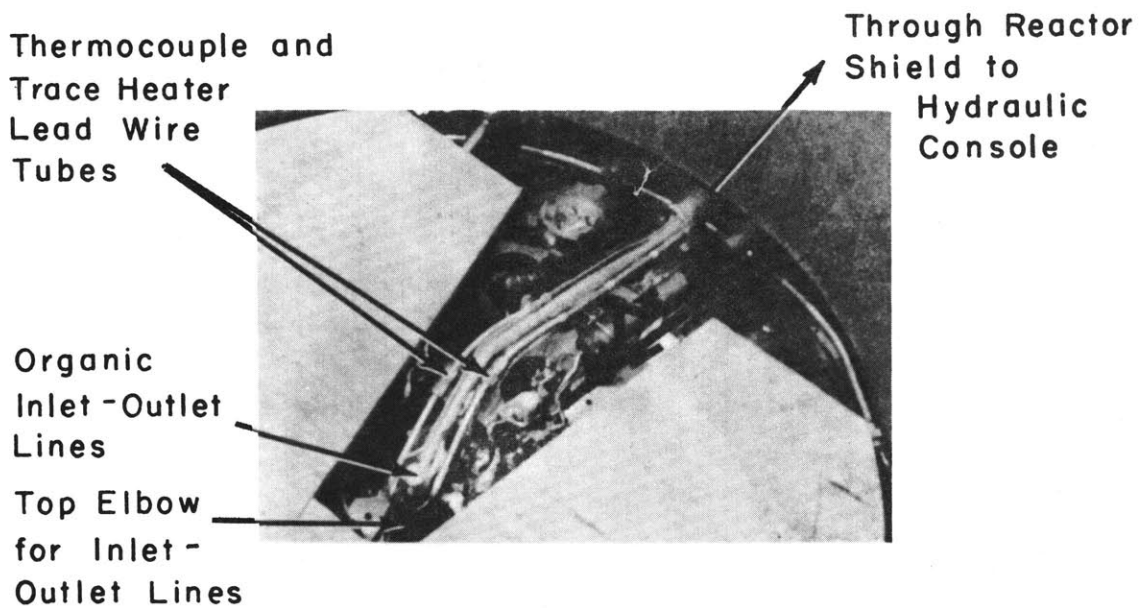


FIG. A3.18 ASSEMBLY OF CONDUIT TUBES, JUNCTION BOX, AND LOWER SHIELD PLUG HOLD-DOWN

NO.	REV.	DATE	BY	CHKD.
1	A	11/18/64	[Signature]	[Signature]
2	B	12/15/64	[Signature]	[Signature]
3	C	1/21/65	[Signature]	[Signature]
4	D	2/11/65	[Signature]	[Signature]
5	E	3/11/65	[Signature]	[Signature]
6	F	4/11/65	[Signature]	[Signature]
7	G	5/11/65	[Signature]	[Signature]
8	H	6/11/65	[Signature]	[Signature]
9	I	7/11/65	[Signature]	[Signature]
10	J	8/11/65	[Signature]	[Signature]

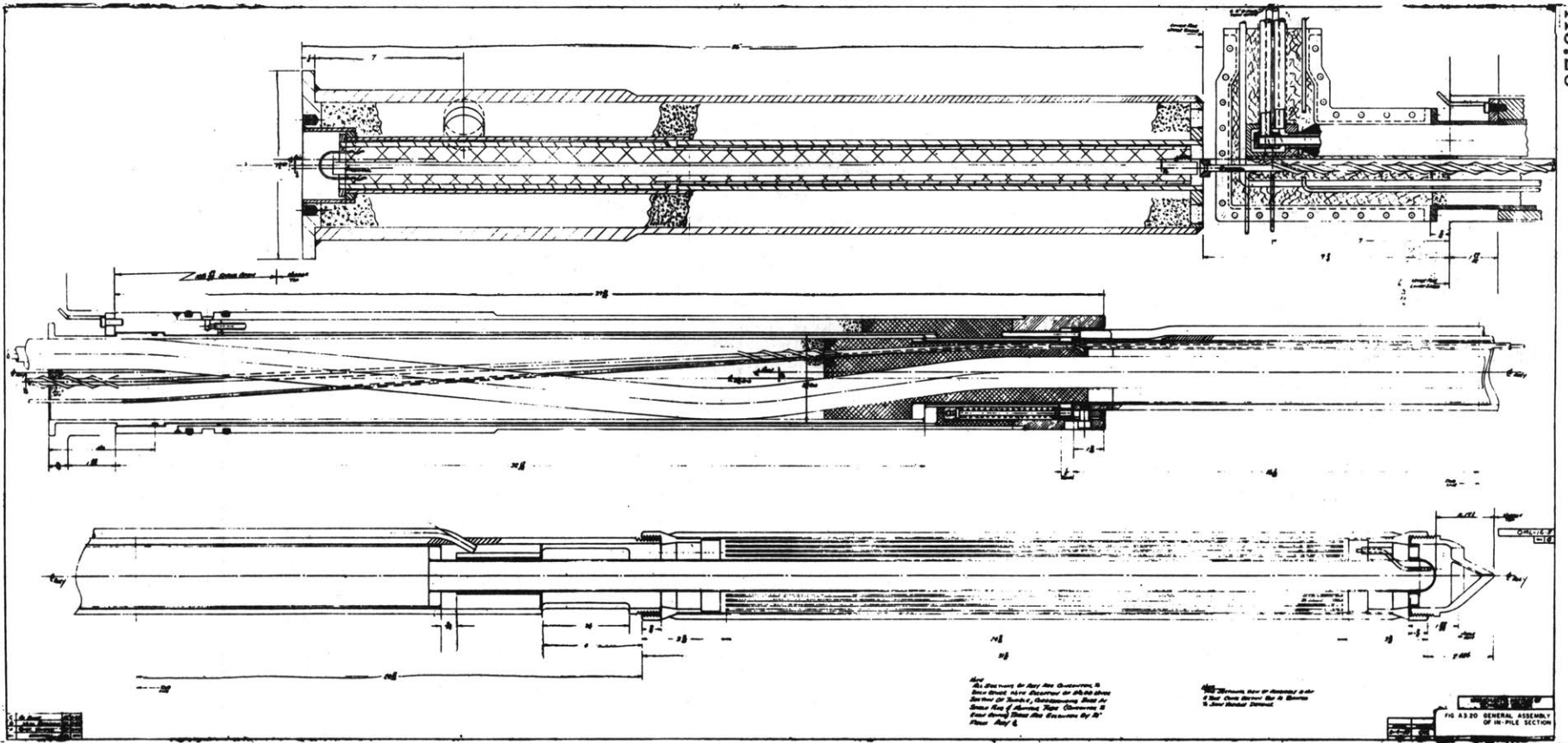


(A) With Thermal Insulation and Outer Aluminum Covers

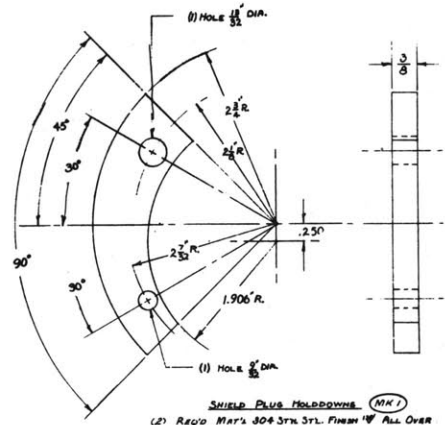


(B) Before Installation of Thermal Insulation and Outer Aluminum Covers

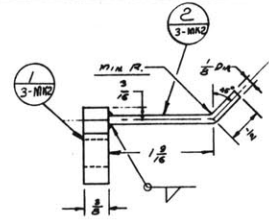
FIG. A 3.19 PHOTOGRAPHS OF TOP OF LOWER REACTOR SHIELD SHOWING INSTALLATION OF LOOP LINES AND SLEEVES



TOLEANCE - DECIMAL ± .005 FRACTIONAL ± 1/64 ANGULAR ± 30'

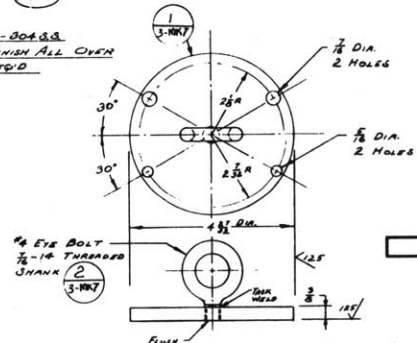
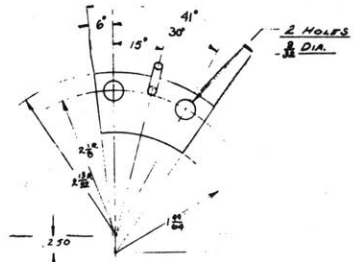


**SHIELD PLUS HOLDDOWNS (MK1)**  
 (2) REQ'D MAT'L 304 STN. STL. FINISH  $\nabla$  ALL OVER



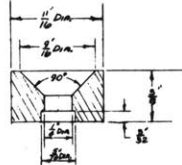
**THIMBLE HOLDDOWN (MK2)**

NOTES  
 MAT'L 304 S.S.  
 $\nabla$  FINISH ALL OVER  
 1 REQ'D

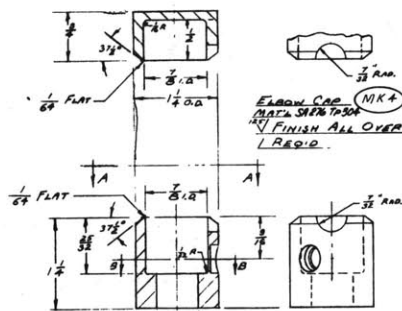


**INTERIOR ELBOW (MK6)**

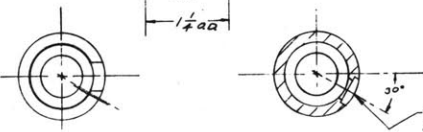
NOTES  
 MAT'L 302 1/2 TP304  
 FINISH  $\nabla$  ALL OVER  
 1 REQ'D



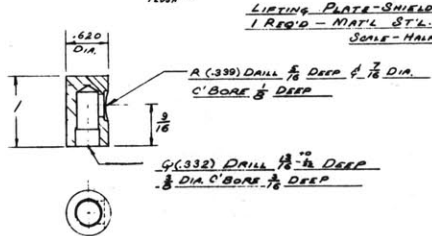
**MONITOR TUBE FUNNEL (MK3)**  
 MAT'L AL 5052-O SCALE 2\"/>



**ELBOW CAP (MK4)**  
 MAT'L 302 1/2 TP304  
 $\nabla$  FINISH ALL OVER  
 1 REQ'D



**EXTERIOR ELBOW (MK5)**  
 MAT'L 302 1/2 TP304 FINISH  $\nabla$  ALL OVER 1 REQ'D



**LIFTING PLATE - SHIELD PLUG (MK7)**  
 1 REQ'D - MAT'L ST.L.  
 SCALE - HALF SIZE

OML-9-3  
 MK 2

REV.	DESCRIPTION	BY	DATE
D	As BUILT	CT	4-24
C	Change Monitor Tube Funnel	MS	4-16
B	Port Plus Illuminated Observation Tube Elbow	SL	3-18
A	Thimble Hold Down Revised	CK	3-20
P	Rev. Spec. Rev. To An 4.6.6	CP	3-25

MATERIAL	QUANTITY
8-31-59	P.C.
DATE	DRAWN BY
	APPROVED
	DRAWING NUMBER
	REV.

FIG. A.3.21 MISCELLANEOUS DETAILS

MASSACHUSETTS INSTITUTE OF TECHNOLOGY REACTOR



of the specifications are summarized below:

(1) In order to decrease the radiation time per experiment, the ratio of in-pile to out-of-pile column was made as large as possible within the limitations imposed by the in-pile space available and the experimental information required.

(2) Since organic materials having a high vapor pressure would, in general, not be of interest in organic cooled nuclear reactors, and since thermal degradation limits the maximum organic temperature which can be used, it was estimated that the maximum pressure and bulk temperature at which the loop would ever be operated was 600 psig and 800°F, respectively.

(3) Heat transfer measurement capability up to heat fluxes of 400,000 Btu/hr-ft<sup>2</sup> and wall temperatures of 1000°F were selected as the maximum requirements which might be needed; a desired velocity of 20 ft/sec through the test heater was used in determining the pump capacity and head as well as the loop tubing sizes (see Appendix A3.4.10 for pressure drop calculations). Study of heat transfer surface fouling was also desirable.

(4) Provision for representative liquid and gas sampling for the determination of chemical and physical changes in the organic material was an obvious provision.

(5) All components of the loop which might come in contact with the organic material being tested were selected to be either of Type 304 or Type 316 stainless steel to prevent or reduce the addition of inorganic impurities to the coolant by corrosion.

(6) Since some of the organics which show promise for use as organic moderator-coolants have melting points up to approximately 315°F, electric trace heating of all lines was employed.

(7) In order to insure long-term operation of the loop in an experiment in which the concentration of degradation products is maintained

constant over a long period of time by periodic removal of degraded organic and feed of fresh organic, it was decided to provide in duplicate those components such as pumps, flowmeters, essential thermocouples, and trace heaters which were deemed most likely to fail during an experiment.

(8) Finally, considering that the organic materials presently proposed for use in nuclear reactors are flammable at the temperatures in question and the in-pile section of the experiment extends directly into the center of a fuel element, it was necessary to take precautions to reduce the hazard to the reactor and to personnel.

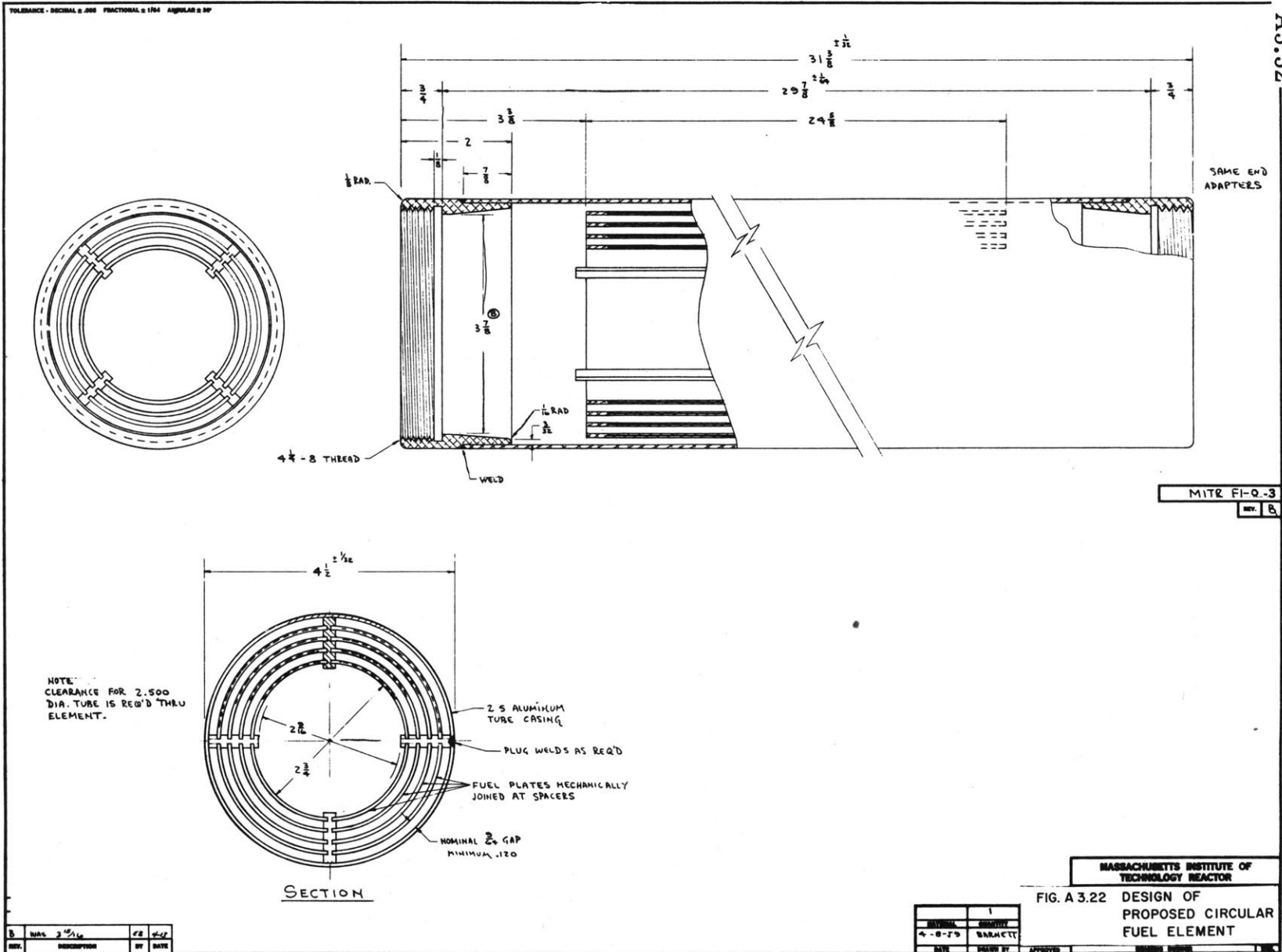
### APPENDIX 3. 3

#### MODIFICATIONS TO THE FUEL ELEMENT AND IN-PILE SECTION DESIGN TO PERMIT A LARGER IN-PILE ORGANIC VOLUME

During the first experiment on Santowax OMP, 1616 MWHR were required to increase the degradation product concentration from 0 per cent to 39.1 per cent. This irradiation time is equivalent to almost 8 weeks of irradiation in the MITR, based on operation at 2.0 MW for 4-1/4 days/week. While not prohibitively long, it would be desirable to increase the in-pile organic column to reduce the time required for each experiment on an organic material. This increase in in-pile volume is particularly desirable for the long-term runs at a constant concentration of degradation products. This appendix presents various schemes which have been suggested for increasing this volume.

##### A3. 3. 1 Circular Plate Fuel Element

The method which would result in a maximum in-pile volume as well as maximum dose rate is use of a new circular plate fuel element illustrated in Figure A3. 22. This fuel element would not only have an irradiation space of 2-9/16 inch diameter but would completely surround the irradiation capsule with fuel, probably resulting in an increased fast



neutron and gamma dose rate. The fuel element would contain approximately 160 gms of  $U^{235}$  vs. the 80 grams in the present fuel element and thimble assembly.

An in-pile section design, illustrated in the drawing of Figure A3. 23, has been completed by Morgan (A3.1) for the circular plate fuel element. In his design, the in-pile organic volume would be approximately  $640 \text{ cm}^3$ . Though the design of both the fuel element and in-pile capsule and thimble are complete, approval for their insertion in the MITR must be secured from the AEC. The estimated reactivity of the in-pile section for this fuel element is  $1.1\% \delta k/k$ , which exceeds the one per cent allowed per experiment by the AEC operating license for the MITR.

### A3. 3. 2 Modifications to Present Fuel Element

Modifications to the present fuel element assembly are presented here which would result in an increased in-pile volume. The simplest modification is simply removal of ten fuel plates (of sixteen) instead of the present eight, although the increased organic in-pile volume will be counterbalanced to some extent by a probable decrease in the dose rate due to removal of fuel surrounding the capsule. Additional modifications involve using an element in which the bow of the fuel plates on opposite sides of the irradiation volume is opposed and either eight or ten fuel plates are again removed. Fuel elements of this type have been ordered for the MITR. Preliminary estimates of the thimble and capsule dimensions and the in-pile volume for the different modifications are presented in Table A3. 1. An additional factor to be considered in selection of one of these modifications is the reactivity which should be less than one per cent.

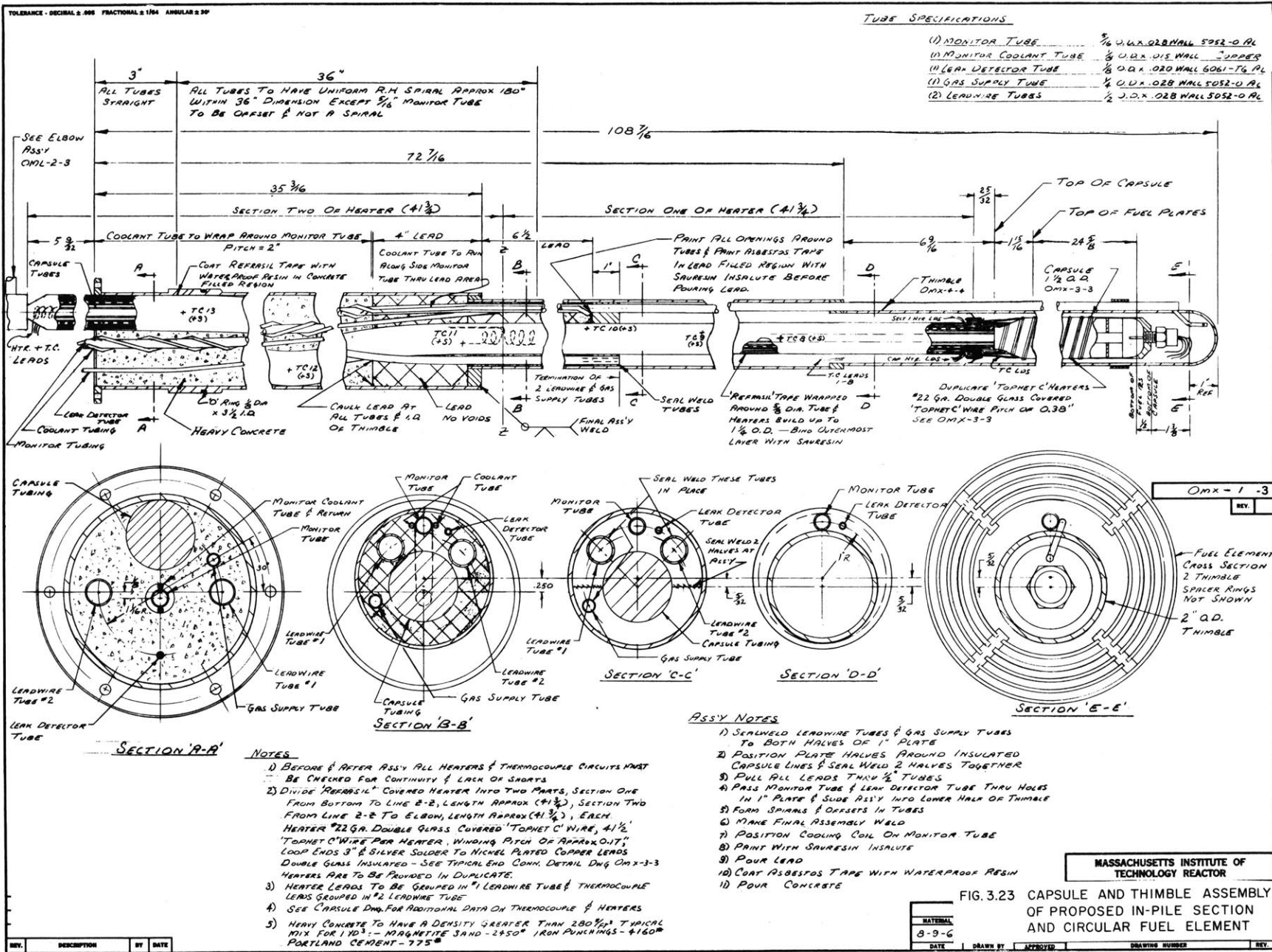
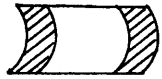
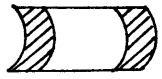
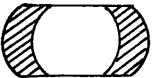
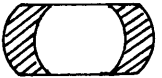
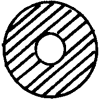


TABLE A3.1

MITR FUEL ELEMENT MODIFICATIONS AND ESTIMATED  
ORGANIC IN-PILE VOLUME

CONFIGURATION AND PLATES IN FUEL ELEMENT	THIMBLE INCHES		CAPSULE		
	O.D.	WALL	O.D.	WALL	VOL. cm <sup>3</sup>
PRESENT DESIGN  8	1 1/4"	0.035"	7/8"	0.035	205
 6	1 5/8"	0.065"	1.120"	0.035	350
 8	1 9/16	0.065	1 1/16"	0.035	310
 6	2.00	0.083	1 1/2	0.035	640
	2.00	0.083	1 1/2"	0.035	640

## APPENDIX 3.4

## ADDITIONAL DETAILS OF OUT-OF-PILE EQUIPMENT

## A3.4.1 Surge Tank Liquid Level Gage

The surge tank liquid level gage is illustrated in Figure A3.24; for details of the surge tank, reference is made to Figure 3.10 of Chapter 3.

## A3.4.2 Operating History of the Chempumps

Because of difficulties encountered with both of the Chempumps during out-of-pile testing, it has been necessary to return the pumps to the manufacturer three separate times, each of which resulted in a one to three-month delay in the project. The first trouble encountered was rapid erosion of the thrust bearings due to a hydraulic imbalance on the impeller at the low flow rates used for the loop. Both pumps were rebuilt as a result to include a thrust equalizer which automatically maintains the impeller in hydraulic balance and prevents thrust on the thrust bearings. Operation of this feature has been satisfactory. In addition to this trouble, both pumps have developed shorts in the stator on two separate occasions, requiring rewinding of the stators on each occasion. This trouble is believed to be due to immersion of the stator in silicone oil (for heat removal purposes) which attacked the electrical insulation. A dry N<sub>2</sub> atmosphere is now used to prevent reoccurrence of this trouble and reliable operation has been obtained from the pump used in the first experiment; as of November 1, 1961, this pump had operated continuously for approximately 2200 hours without trouble.

## A3.4.3 Pump Cooling System

Because of the high temperature of the circulating organic (up to 800°F) and the fact that the motor section of the pump cannot exceed 450°F, a heat exchanger for cooling the motor section is constructed integral with the pump. Since the melting point of some of the organics

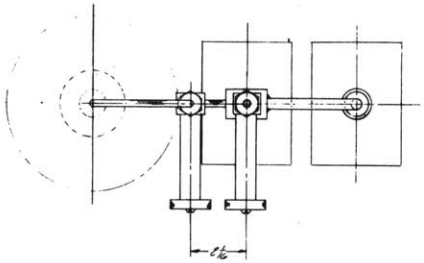
1-66511 ON D.M.G.

NO. 00. #106. TUBING SA 213 TO SOE SENSORS

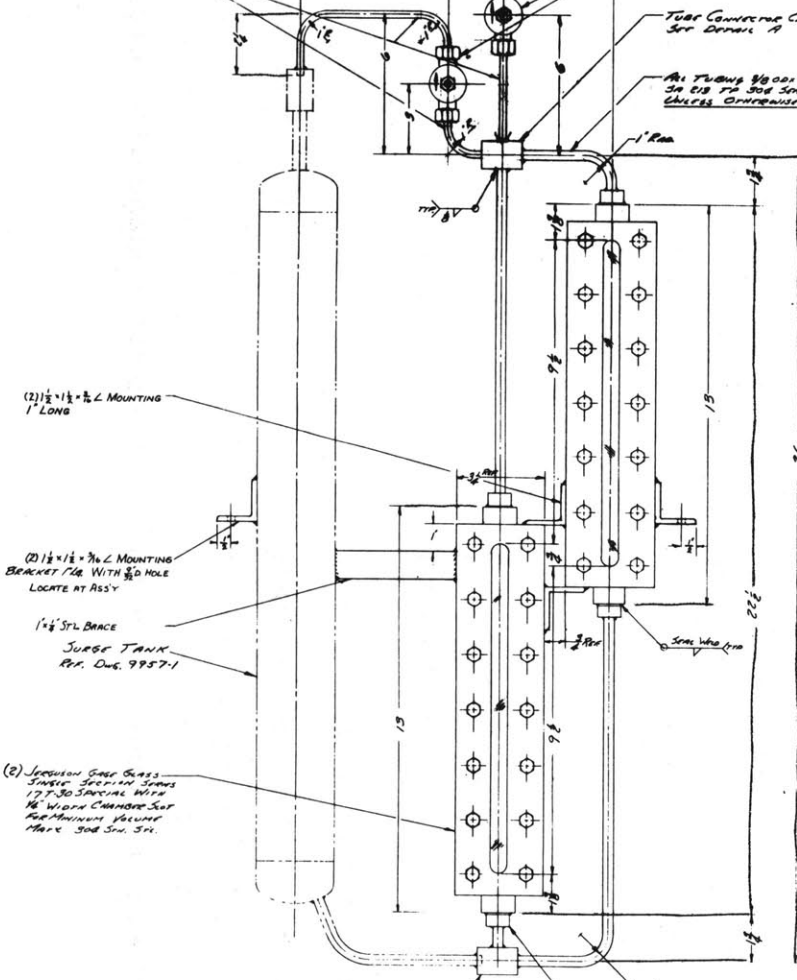
Hand Valve #20 Series 1/2" 30 S.S. #1197 2 PROD.

TUBE CONNECTOR CROSS SEE DETAIL A

All Tubing #300. #600. SA 213 TO SOE SENSORS CHECK OTHERWISE MARKED



PLAN VIEW



(2) 1 1/2 x 1/2 x 3/8 L MOUNTING 1" LONG

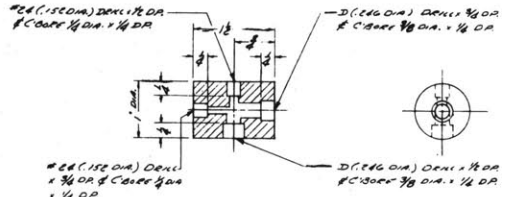
(2) 1 1/2 x 1/2 x 3/8 L MOUNTING BRACKET 1/2" WITH 3/8" HOLE LOCATE AT ASSY

1/2" STL BRACE SURGE TANK Ref. Dwg. 9957-1

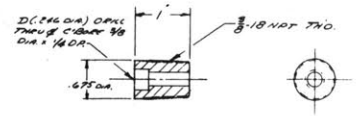
(2) JOHNSON SAE BRASS SENSITIVE SECTION SERIES 177-30 SENSITIVE WITH 1/2" WIDE CHANNEL SUR FOR MOUNTING BELOW MARK SOE S.S. STL.

TUBE CONNECTOR TIT See Detail A Comp. 11617-1

ADAPTER See Detail B



DETAIL A  
TUBE CONNECTOR CROSS  
MAX. SA 213 TO SOE  
Cue Prod.



DETAIL B  
ADAPTER  
3/8" DIA - 3/8" DIA  
MAX. SA 213 TO SOE  
# Prod. FOR SURGE TANK

REV	REVISION	BY	DATE
IV	ADDED ADAPTER BRACKET	BLJ	9-3-59
III	ADDED VALVE DESCRIPTION	AD	6-1-59
II	REVISED	AD	6-2-59
I	ISSUED	AD	5-29-59

ARTISAN METAL PRODUCTS, INC.  
POND STREET, WALTHAM,  
BOSTON 54, MASS.

FIG. A3.24 DETAILS OF SURGE TANK  
LIQUID LEVEL GAGE

FIG. NO.	DATE		LIMITS ON DIMENSIONS UNLESS OTHERWISE SPECIFIED	FRAC. S DEC. 2 ANG. 2
	REV.	DATE		
2147	NOV. 1959	11/27-59	IV	DWG. NO. 11593-1



to be tested is about 315°F, it was necessary that the coolant used be capable of operating at least as high as this temperature. To eliminate the high pressures that would be present with a water cooled system, Dowtherm A was used as the cooling medium.

In Figure A3. 25, the flow sheet of the pump cooling system is presented. The Dowtherm A is circulated from a heat exchanger to either or both Chempumps by an Eastern stainless steel centrifugal pump<sup>(1)</sup> (Model No. DH-11-100RST) rated for use with Dowtherm A at 350°F; as of November 1, 1961, this pump had operated continuously for approximately 2200 hours without trouble. The heat exchanger is illustrated in Figure A3. 26 and contains two cooling coils through which water flows and two Chromalox immersion heaters<sup>(2)</sup> rated at 1000 watts each (Model No. MTO-110); a temperature controller (Chromalox thermostat AR5534) is provided to control one of the immersion heaters and hence maintain the Dowtherm A at a constant temperature. The cooling system is normally operated at 250-260°F which maintains the pump motor temperature at 300-325°F, depending on the circulating organic temperature. Operation of the pump cooling system has been satisfactory in all respects.

#### A3. 4. 4 Feed and Dump Tank Liquid Level Gage

The liquid level gage for the feed and dump tank is illustrated in Figure A3. 27; for details of the feed and dump tank, reference is made to Figure 3. 16 of Chapter 3.

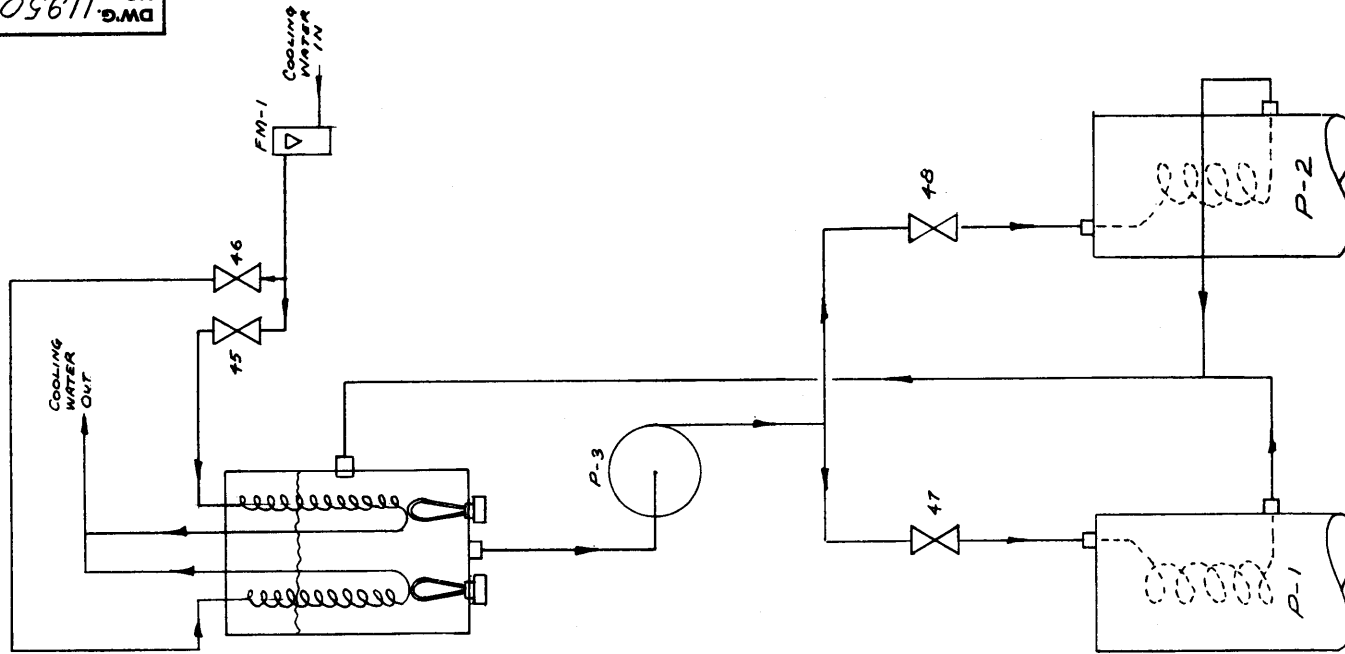
#### A3. 4. 5 Difficulties with Valves

Considerable difficulty has been encountered with the "Aveco" valves after the valve has been used several times, due to leakage through the valve seats. Several of the valves have been disassembled and resealed or new plugs installed, but some leakage still occurs after the valve is used several times. Such leakage is particularly important as it would

(1) Eastern Industries, Hamden, Connecticut

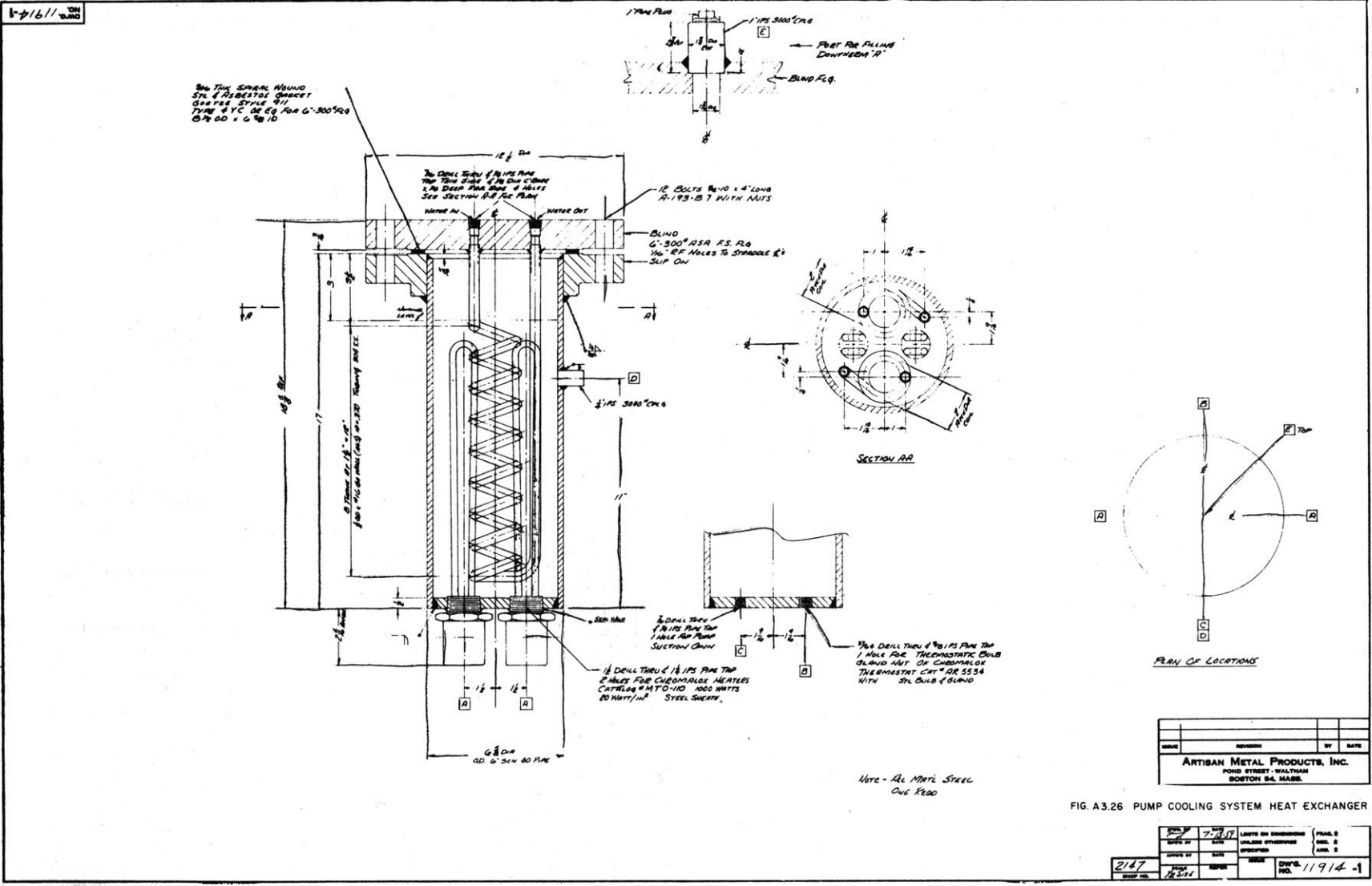
(2) Edwin L. Wiegand Company, Pittsburgh, Pennsylvania

DWG. 11950-3 ON NO.

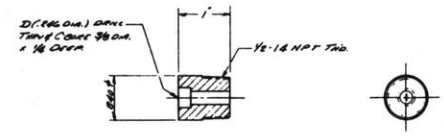
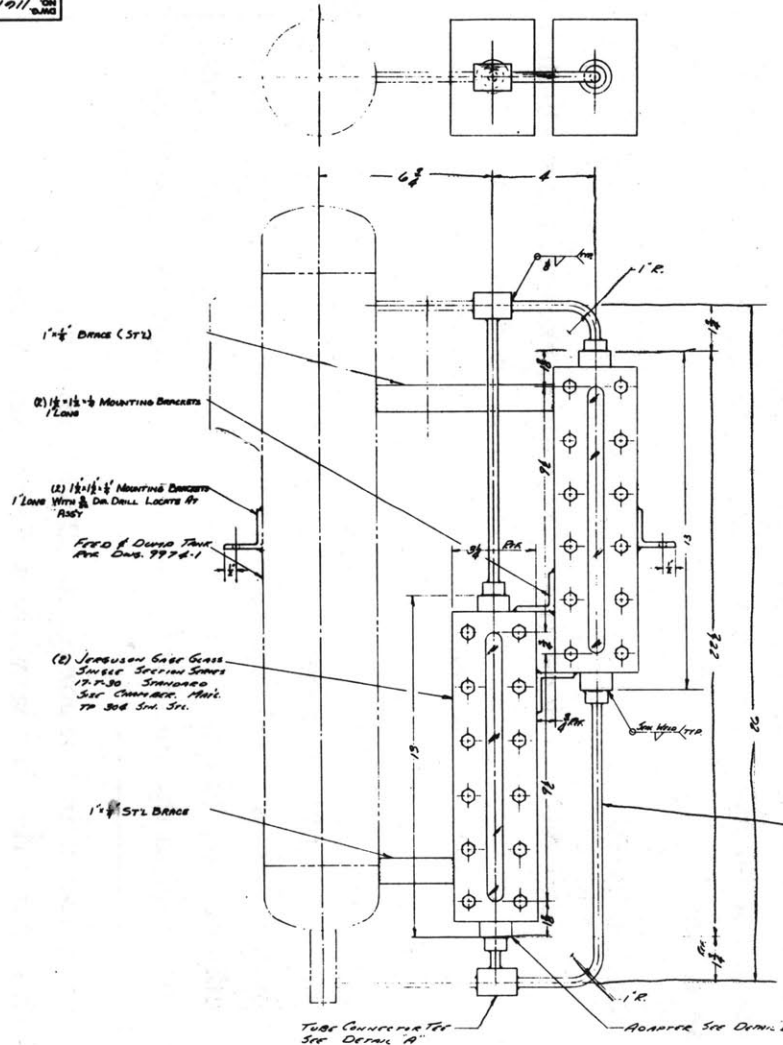


ISSUE	REVISION	BY	DATE
<b>ARTISAN METAL PRODUCTS, INC.</b> POND STREET - WALTHAM BOSTON 54, MASS.			
<b>FIG. A3.25 FLOW DIAGRAM OF PUMP COOLING SYSTEM</b>			
DRAWN BY <i>PA</i>	DATE 9-29-59	LIMITS ON DIMENSIONS UNLESS OTHERWISE SPECIFIED	
CHECK'D BY	DATE		
APPRO'D BY	DATE	ISSUE	
SCALE	REFER		
2147 SHOP NO.		DWG. NO. 11950	

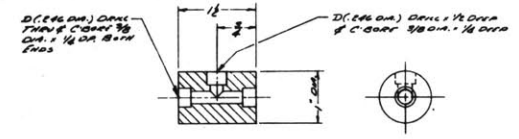
A3.39



1-61911



ADAPTER - 1/2" NPT 1/2" DIA.  
 MATERIAL - SA 304 TP 304  
 USE FOR FEED & DUMP TANK  
 DETAIL B



TUBE CONNECTOR TEE  
 MATERIAL - SA 304 TP 304  
 USE FOR FEED & DUMP TANK  
 AND FEED FOR FEED & DUMP TANK  
 DETAIL A

ALL TUBING 3040  
 1/2" DIA. SA 304  
 TP 304 SCHLIES

1	BRACKET & BENCH HOODS	REV	9/3/57
ISSUE	REVISION	BY	DATE
ARTISAN METAL PRODUCTS, INC. FOND STREET - WALTHAM BOSTON 54, MASS.			

FIG. A3.27 DETAILS OF FEED AND DUMP TANK LIQUID LEVEL GAGE

APP'D BY	DATE	SCALE	1/4" = 1"	NO. OF SHEETS	1	SHEET NO.	1
5/27	1957	NONE					
DWG. NO.	11619-1						

A3.41

affect the measurement of the gas evolution rate. As discussed in section 3. 3. 11 of Chapter 3, a nitrogen balance can be kept on the system so that the leakage rate and hence the amount of radiolytic gases lost by leakage can be determined; this procedure has not been necessary during the Santowax OMP irradiation since the gas leakage rate in this experiment is negligible.

Flow control valve V-27, which could be operated remotely, is no longer used; rupture of the actuating diaphragm occurred during out-of-pile testing of the loop. Since the loop can be operated satisfactorily without the diaphragm, a decision against replacement was made and the valve is now blocked open. Valve 27 was included in the initial design when it appeared that the instrument panel would have to be located some distance from the hydraulic console; in such a case, remote control of the flow rate from the instrument and control panel would be desirable. The failure of the diaphragm is believed to be due to weakness resulting from the high temperature (approximately 200°F) inside the hydraulic console cabinet. As a result, water-cooled copper coils have been placed on the valve operators of V-25 and V-26 to prevent rupture of the diaphragms for these valves.

#### A3. 4. 6 Connections

All pipe and tubing connections are welded except those which may need to be broken during operation of the loop, such as the gas and liquid samplers, test heaters, pumps, and filters. "Triple-Lok"<sup>(1)</sup> flared tube fittings are used for connecting the samplers and heaters to the loop. Ring-joint flanges are used for connecting the pumps and filter housings to the loop. Excellent leak-tightness has been obtained with both the "Triple-Lok" and ring-joint flanges. As originally constructed, the loop had some screwed connections (using "Plastiseal-F"<sup>(2)</sup> as a sealer) in the main organic lines and in the main loop coolers. Satisfactory operation was

---

(1) Parker-Hannifin Corporation, Cleveland, Ohio

(2) Johns-Manville Company, New York, New York

never attained with these connections and seal welding of all of them was necessary to prevent leakage.

#### A3. 4. 7 Trace Heater Layout

The layout of the trace heaters for all parts of the out-of-pile section of the loop is given in Figure A3. 28.

#### A3. 4. 8 Photographs of Hydraulic Console and Details of the Piping Assembly

In Figures A3. 29-A3. 31, photographs of the left, rear, and right sides of the hydraulic console are illustrated; the front side is illustrated in Figure 3. 19 of Chapter 3.

In Figures A3. 32 and A3. 33, drawings of the piping assembly of the hydraulic console are presented. As can be seen from Details "X" and "Y" of Figure A3. 32, the attempt has been made to eliminate stagnant areas which could lead to poor mixing of the organic material. Sections of 1/16-inch OD  $\times$  0. 010-inch wall tubing have been placed inside two sections of the loop tubing which are normally valved off at one end; this small tubing should provide a small purge flow of the circulating organic into these dead end sections.

#### A3. 4. 9 Hydraulic Console Cabinet

In Figure A3. 34, a detailed drawing of the hydraulic console cabinet is presented.

#### A3. 4. 10 Pressure Drop and Velocities

The pressure drop calculations considered in selecting the pumps and tubing sizes are presented in this section. The values are based on a desired maximum velocity of 20 ft/sec in the test heaters. Values of  $\mu = 0. 9$  cp and  $\rho = 1. 00$  gms/cm<sup>3</sup> were used in estimating the frictional pressure drops. The calculated results are summarized in Table A3. 2. Contraction and expansion losses were calculated from Equation (A3. 1) where the subscripts are explained by the sketch.



FIG. A3.28 SCHEMATIC OF TRACE HEATER SYSTEM

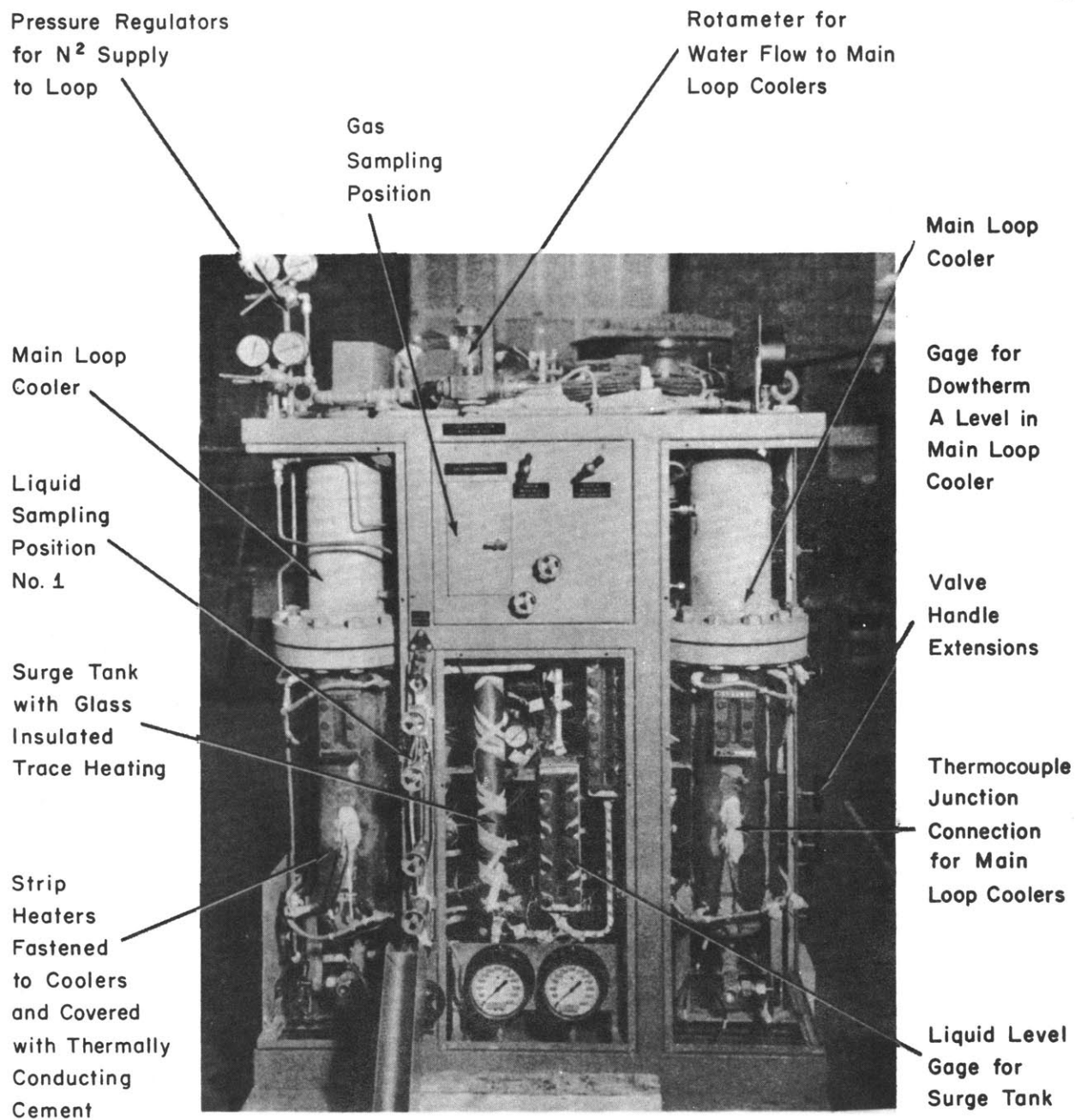


FIG. A3.29 LEFT SIDE OF HYDRAULIC CONSOLE—BEFORE INSTALLATION OF THERMAL INSULATION, PANELS REMOVED



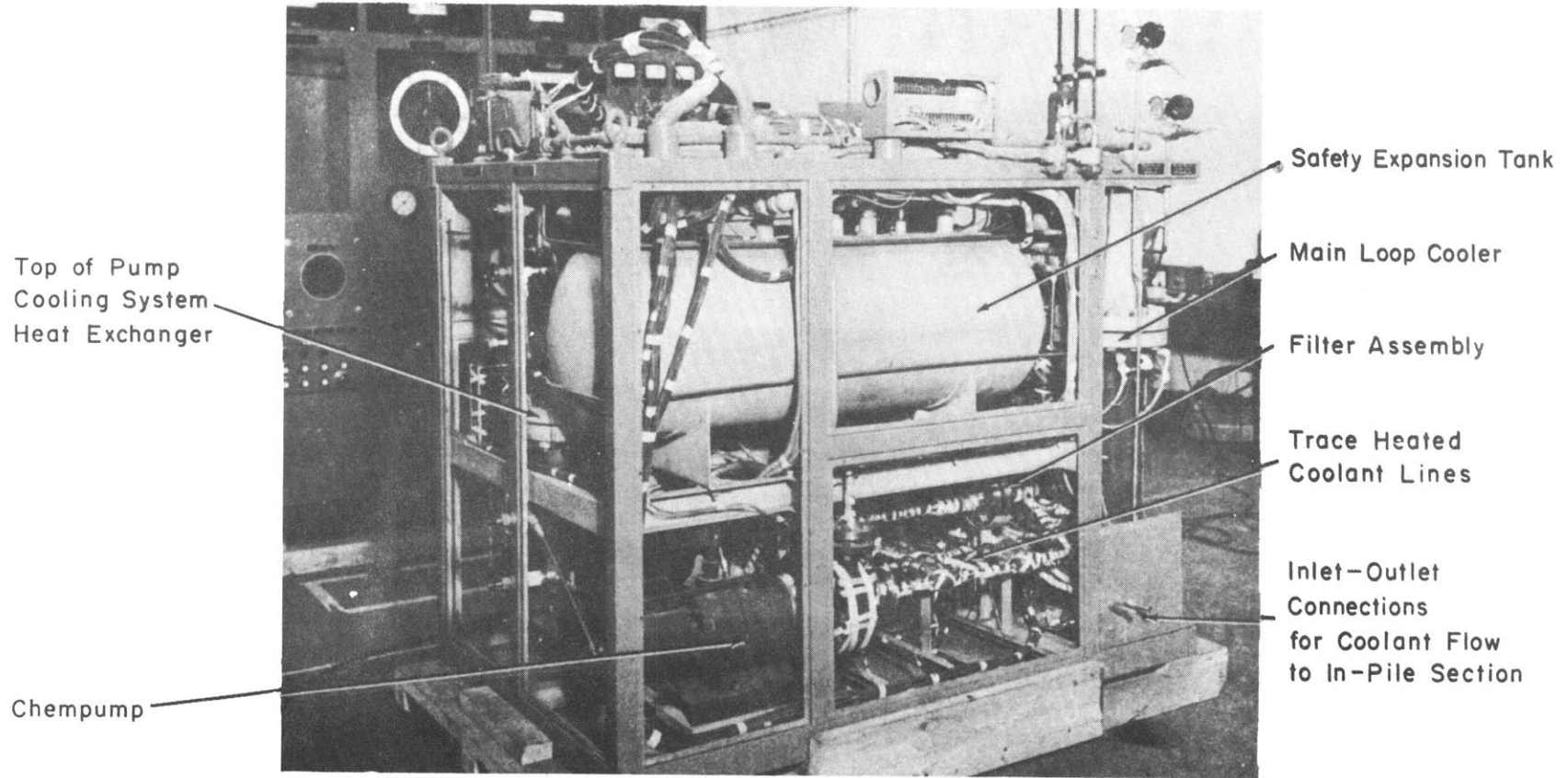


FIG. A3.30 REAR OF HYDRAULIC CONSOLE-BEFORE  
INSTALLATION OF THERMAL INSULATION,  
PANELS REMOVED

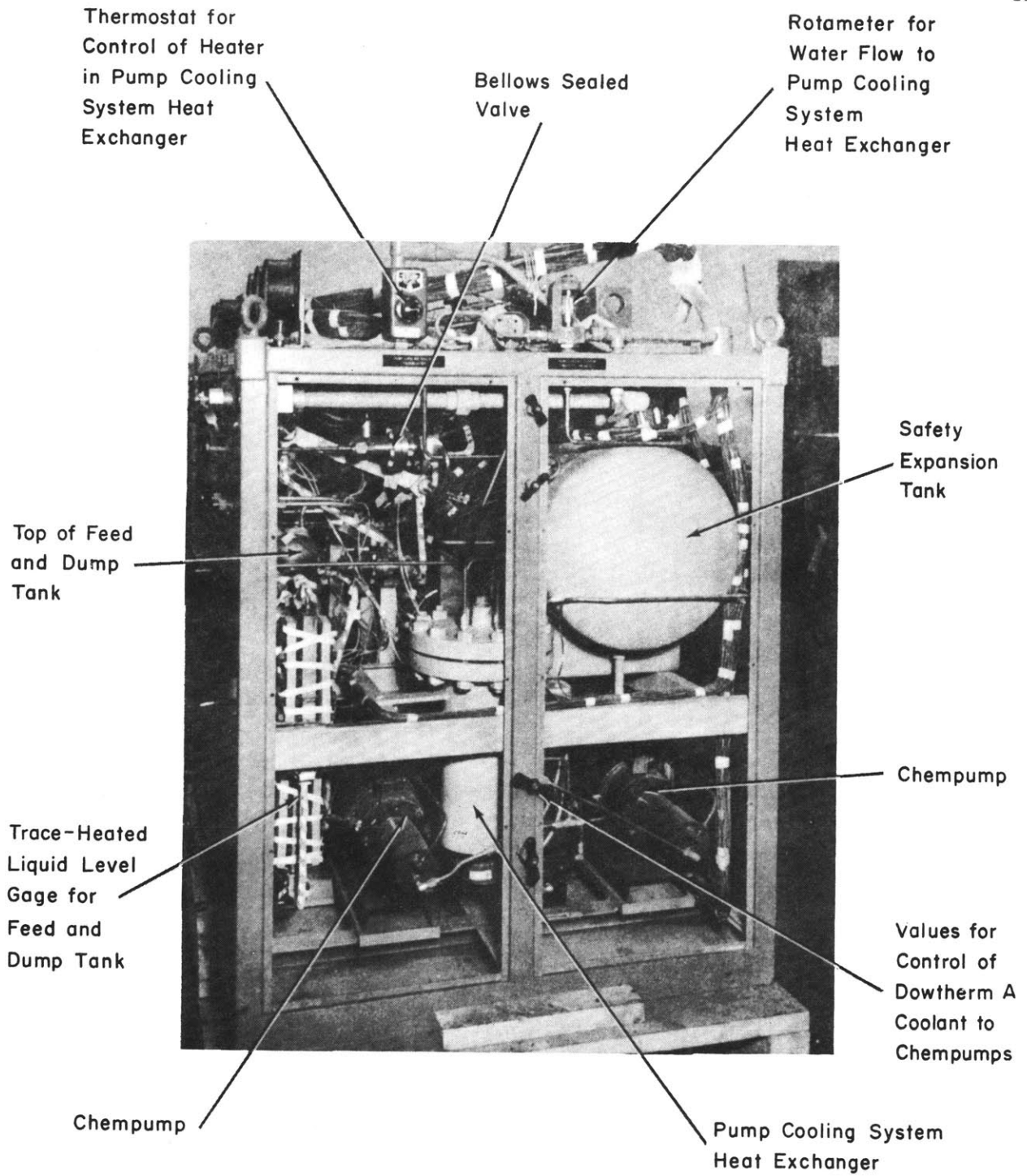
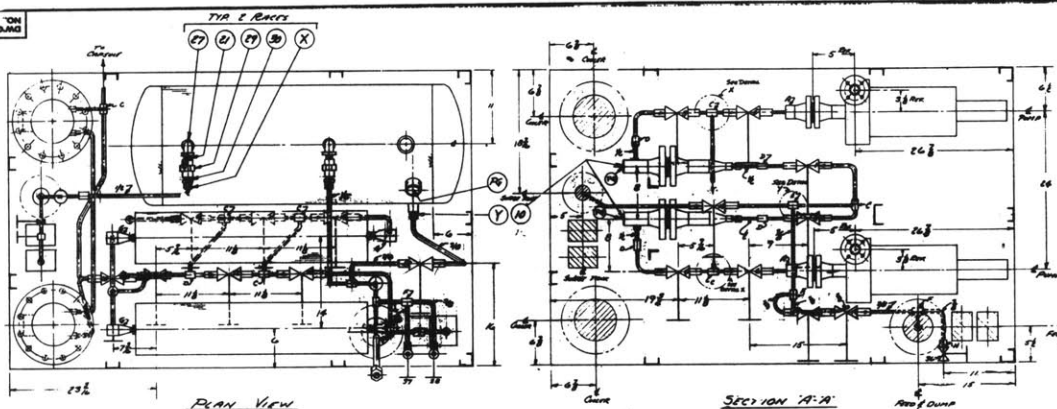


FIG. A3.31 RIGHT SIDE OF HYDRAULIC CONSOLE - BEFORE INSTALLATION OF THERMAL INSULATION, PANELS REMOVED

1-92111 ON DANG

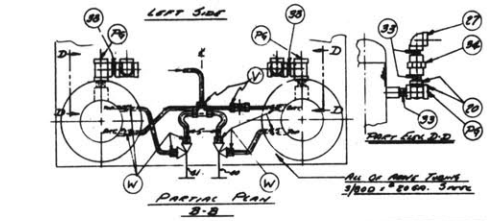
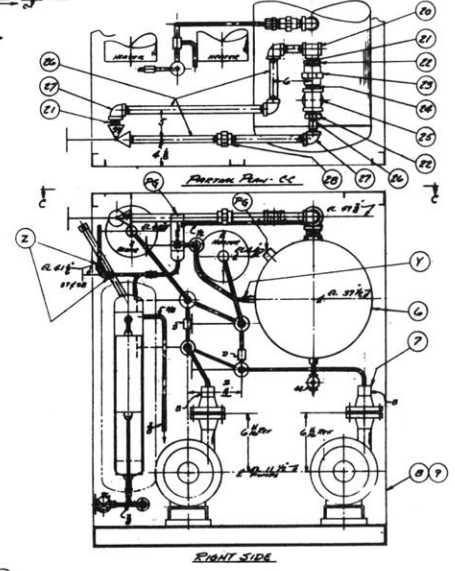
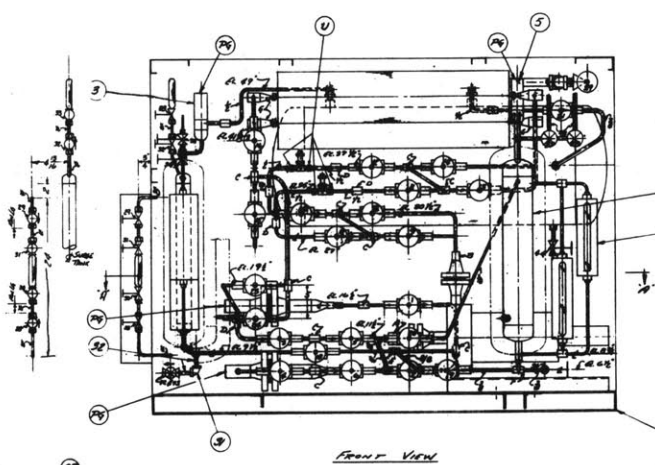
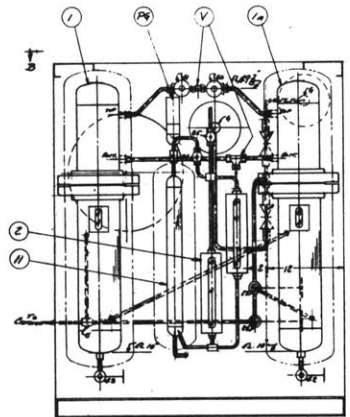
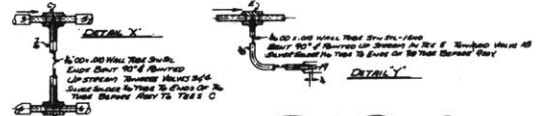


**PIPING TABLE OF FITTINGS**

Pr.	Description	Qty.	Pr.	Description	Qty.
R	1/2" S.W.P. 1/2"	1	U	1/2" S.W.P. 1/2" x 1/2" x 1/2" Tee	1
Y	1/2" S.W.P. 1/2"	1			
X	1/2" S.W.P. 1/2"	1			
W	1/2" S.W.P. 1/2"	1			
V	1/2" S.W.P. 1/2"	1			
U	1/2" S.W.P. 1/2" x 1/2" x 1/2" Tee	1			

**EQUIPMENT Dwg.**

Pr.	Description	Dwg. No.
1	COIL (2)	9767-1
2	COIL (2)	1167-1
3	VALVE (2)	1167-1
4	VALVE (2)	1167-1
5	VALVE (2)	1167-1
6	VALVE (2)	1167-1
7	VALVE (2)	1167-1
8	VALVE (2)	1167-1
9	VALVE (2)	1167-1
10	VALVE (2)	1167-1
11	VALVE (2)	1167-1
12	VALVE (2)	1167-1



- Notes:**
1. See Section Fittings See Memo
  2. 1/2" S.W.P. Tee to be kept in line with pressure when closed in the Tee Run
  3. Bends & Coils to be allowed to keep the Tee Run to the center position
  4. All tubing to be 1/2" S.W.P. or better
  5. Elbow 1/2" S.W.P. or better
  6. Valves 17, 22, 23, 24, 25 to be closed when
  7. 1/2" S.W.P. or better
  8. 1/2" S.W.P. or better
  9. 1/2" S.W.P. or better
  10. 1/2" S.W.P. or better
  11. 1/2" S.W.P. or better
  12. 1/2" S.W.P. or better
  13. 1/2" S.W.P. or better
  14. 1/2" S.W.P. or better
  15. 1/2" S.W.P. or better
  16. 1/2" S.W.P. or better
  17. 1/2" S.W.P. or better
  18. 1/2" S.W.P. or better
  19. 1/2" S.W.P. or better
  20. 1/2" S.W.P. or better
  21. 1/2" S.W.P. or better
  22. 1/2" S.W.P. or better
  23. 1/2" S.W.P. or better
  24. 1/2" S.W.P. or better
  25. 1/2" S.W.P. or better
  26. 1/2" S.W.P. or better
  27. 1/2" S.W.P. or better
  28. 1/2" S.W.P. or better
  29. 1/2" S.W.P. or better
  30. 1/2" S.W.P. or better
  31. 1/2" S.W.P. or better
  32. 1/2" S.W.P. or better

**PIPING FITTINGS**

Pr.	Description	Qty.	Pr.	Description	Qty.
33	1/2" S.W.P. Tee	1	34	1/2" S.W.P. Tee	1
35	1/2" S.W.P. Tee	1	36	1/2" S.W.P. Tee	1
37	1/2" S.W.P. Tee	1	38	1/2" S.W.P. Tee	1
39	1/2" S.W.P. Tee	1	40	1/2" S.W.P. Tee	1
41	1/2" S.W.P. Tee	1	42	1/2" S.W.P. Tee	1
43	1/2" S.W.P. Tee	1	44	1/2" S.W.P. Tee	1
45	1/2" S.W.P. Tee	1	46	1/2" S.W.P. Tee	1
47	1/2" S.W.P. Tee	1	48	1/2" S.W.P. Tee	1
49	1/2" S.W.P. Tee	1	50	1/2" S.W.P. Tee	1
51	1/2" S.W.P. Tee	1	52	1/2" S.W.P. Tee	1
53	1/2" S.W.P. Tee	1	54	1/2" S.W.P. Tee	1
55	1/2" S.W.P. Tee	1	56	1/2" S.W.P. Tee	1
57	1/2" S.W.P. Tee	1	58	1/2" S.W.P. Tee	1
59	1/2" S.W.P. Tee	1	60	1/2" S.W.P. Tee	1
61	1/2" S.W.P. Tee	1	62	1/2" S.W.P. Tee	1
63	1/2" S.W.P. Tee	1	64	1/2" S.W.P. Tee	1
65	1/2" S.W.P. Tee	1	66	1/2" S.W.P. Tee	1
67	1/2" S.W.P. Tee	1	68	1/2" S.W.P. Tee	1
69	1/2" S.W.P. Tee	1	70	1/2" S.W.P. Tee	1
71	1/2" S.W.P. Tee	1	72	1/2" S.W.P. Tee	1
73	1/2" S.W.P. Tee	1	74	1/2" S.W.P. Tee	1
75	1/2" S.W.P. Tee	1	76	1/2" S.W.P. Tee	1
77	1/2" S.W.P. Tee	1	78	1/2" S.W.P. Tee	1
79	1/2" S.W.P. Tee	1	80	1/2" S.W.P. Tee	1
81	1/2" S.W.P. Tee	1	82	1/2" S.W.P. Tee	1
83	1/2" S.W.P. Tee	1	84	1/2" S.W.P. Tee	1
85	1/2" S.W.P. Tee	1	86	1/2" S.W.P. Tee	1
87	1/2" S.W.P. Tee	1	88	1/2" S.W.P. Tee	1
89	1/2" S.W.P. Tee	1	90	1/2" S.W.P. Tee	1
91	1/2" S.W.P. Tee	1	92	1/2" S.W.P. Tee	1
93	1/2" S.W.P. Tee	1	94	1/2" S.W.P. Tee	1
95	1/2" S.W.P. Tee	1	96	1/2" S.W.P. Tee	1
97	1/2" S.W.P. Tee	1	98	1/2" S.W.P. Tee	1
99	1/2" S.W.P. Tee	1	100	1/2" S.W.P. Tee	1

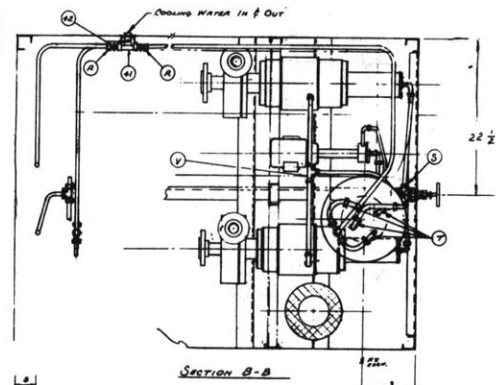
**ARTIBAN METAL PRODUCTS, INC.**  
 1000 STREET, WALTHAM  
 BOSTON 24, MASS.

**FIG. A3.32 PIPING ASSEMBLY OF HYDRAULIC CONSOLE**

DATE: 1-17-53  
 DRAWN BY: J. J. ...  
 CHECKED BY: ...  
 APPROVED BY: ...

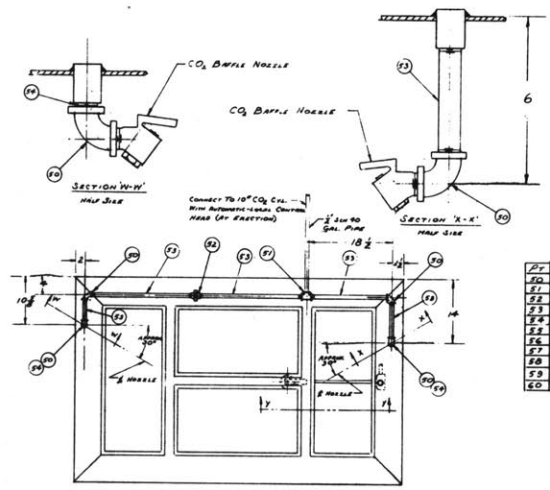
2167  
 1-17-53

1-94611 DWG

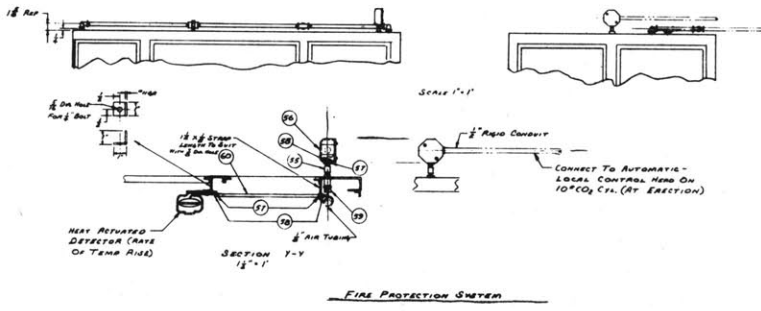
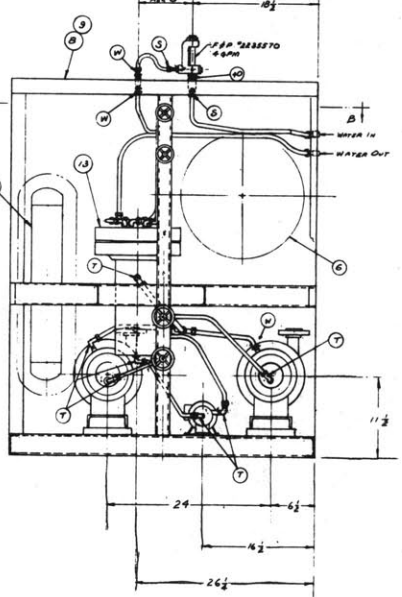
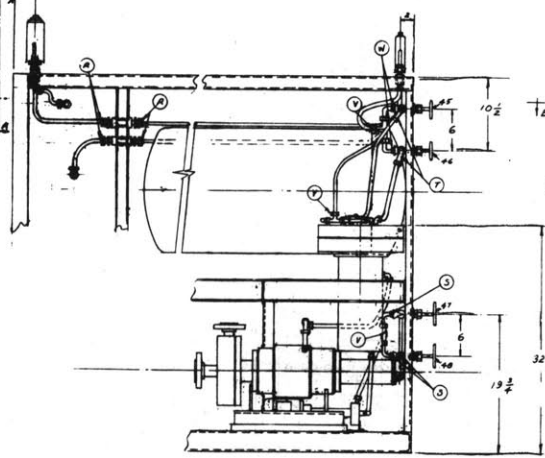


PARTS TRIM-LON FITTINGS		
PT	DESCRIPTION	REQD
R	6-6-FBTK-S	4
S	6-8-FBTK-S	8
T	6-CBTK-S	14
V	6-VBTK-S	4
W	6-FBTK-S	6

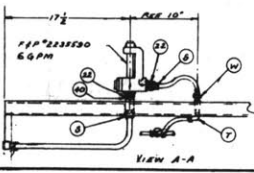
EQUIPMENT OWNER		
PT	DESCRIPTION	DWG. NO.
A	SACRETT EXHAUSTION TANK	3960-1
B	HYDRAULIC LINE CABINET	11712-1
C	PUMP FOR LOGS CRANE	11716-1
D	FRESH AIR PUMP TANK	3978-1
E	HEAT EXCHANGER	11710-1



PT	DESCRIPTION	REQD
60	1/2" IPS 90° SWEEPED ELBOW 1/2" x 1/2" x 1/2"	4
61	1/2" IPS STRAIGHT PIPE 1/2" x 1/2" x 1/2"	1
62	1/2" IPS PIPE UNION 1/2" x 1/2" x 1/2"	1
63	1/2" IPS 90° ELBOW 1/2" x 1/2" x 1/2"	1
64	1/2" IPS 90° ELBOW 1/2" x 1/2" x 1/2"	3
65	1/2" IPS 90° ELBOW 1/2" x 1/2" x 1/2"	1
66	1/2" IPS 90° ELBOW 1/2" x 1/2" x 1/2"	1
67	1/2" IPS 90° ELBOW 1/2" x 1/2" x 1/2"	3
68	1/2" IPS 90° ELBOW 1/2" x 1/2" x 1/2"	3
69	1/2" IPS 90° ELBOW 1/2" x 1/2" x 1/2"	1
70	1/2" IPS 90° ELBOW 1/2" x 1/2" x 1/2"	1



SCALE 1 1/2" = 1'



PUMP COOLING SYSTEM		
PT	DESCRIPTION	REQD
22	1 1/2" IPS BUSHING 8"x4"	2
20	1/2" IPS 90° CLOSE NIPPLE 3"x4"	2
41	1/2" IPS 90° CLOSE NIPPLE 1/2"x1/2"	2
42	1/2" IPS 90° CLOSE NIPPLE 1/2"x1/2"	2

NOTE: ALL TUBING 3/8" O.D. x 20 GA WALL STEEL

REFER TO DWG NO. 11724-1 FOR HYDRAULIC PIPING

REVISION	BY	DATE
ARTISAN METAL PRODUCTS, INC. 1000 STREET WALTHAM BOSTON 54, MASS.		

FIG. A3.33 AUXILIARY PIPING ASSEMBLY OF HYDRAULIC CONSOLE

DWG. NO.	DATE	LIMITS OR DIMENSIONS	PAGE	
			NO.	TOTAL
2147	10-23	UNLESS OTHERWISE SPECIFIED	2	2
2147	10-23	UNLESS OTHERWISE SPECIFIED	2	2
DWG. NO. 11348-1				

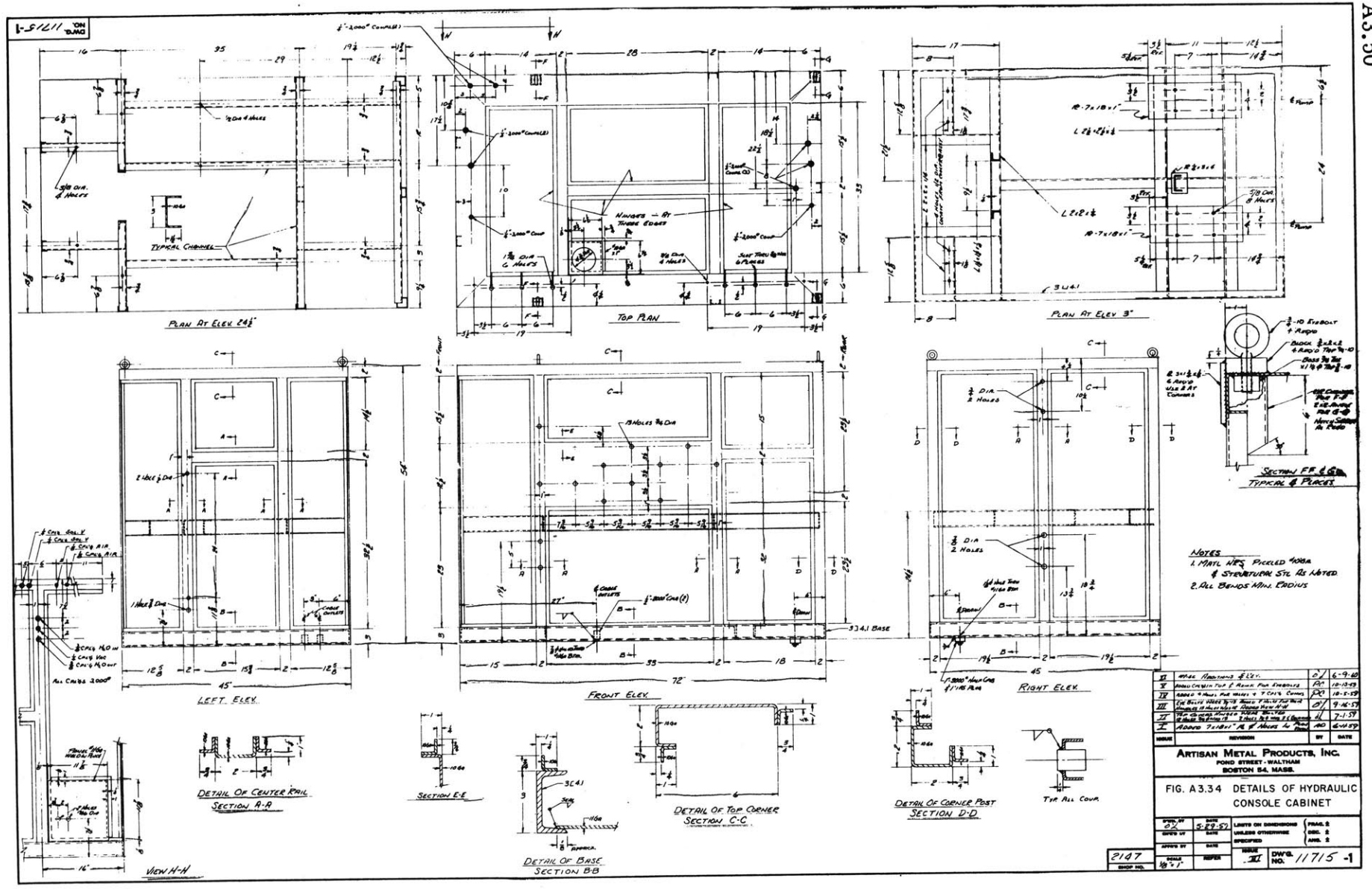


TABLE A3.2

## FRICTIONAL PRESSURE DROPS AND ORGANIC VELOCITIES IN DIFFERENT LOOP SECTIONS

## A. Tubing

LOOP SECTION	VELOCITIES FT./SEC.	REYNOLDS No., Re	FRICTION FACTOR, f	LENGTH FT.	PRESSURE DROP PER	TOTAL PRESSURE DROP $\Delta P$ , psi
					FT. $\frac{\Delta P}{\Delta L}$ $\frac{\text{psi}}{\text{ft}}$	
Test Heater 1/4" O.D. x 0.020" Wall	20	$3.61 \times 10^4$	0.0058	3	3.57	10.7
7/16" Tubing x 0.049" Wall	7.66	$2.23 \times 10^4$	0.0066	~60	0.370	22.2
3/8" Tubing x 0.020" Wall	7.86	$2.26 \times 10^4$	0.0066	$9 \frac{1}{4}$	0.394	3.6
Annular Space 5/8" O.D. x 0.049" Wall Containing 3/8" O.D. Tube	6.43	$8.43 \times 10^3$ <sup>(a)</sup>	0.0080	$7 \frac{1}{4}$	0.702	5.1
Capsule 0.875" O.D. x 0.035" Wall Containing 3/8" O.D. Tube	1.73	-	-	-	-	Negligible
Fittings <sup>(b)</sup>	-	-	-	-	-	6.7
TOTAL						48.3 psi

(a) Based on Equivalent Diameter.

(b) Based on an equivalent length of 32D for elbows and an approximate number of 20 elbows as a conservative estimate.

## B. Components and Contraction-Expansion Losses

Component	$\Delta P$ , psi
Flowmeter	1.6
Filter (165 micron element)	Negligible
Valves (based on 11 valves in one flow loop with a 0.5 psi drop per valve)	5.5
Contraction - Expansion Losses	
(i) Capsule	0.5
(ii) Test Heater (mixing chamber at each end)	3.1
(iii) Pump inlet and outlet	0.5
TOTAL	11.2 psi

## C. Cumulative Total = 59.5 psi

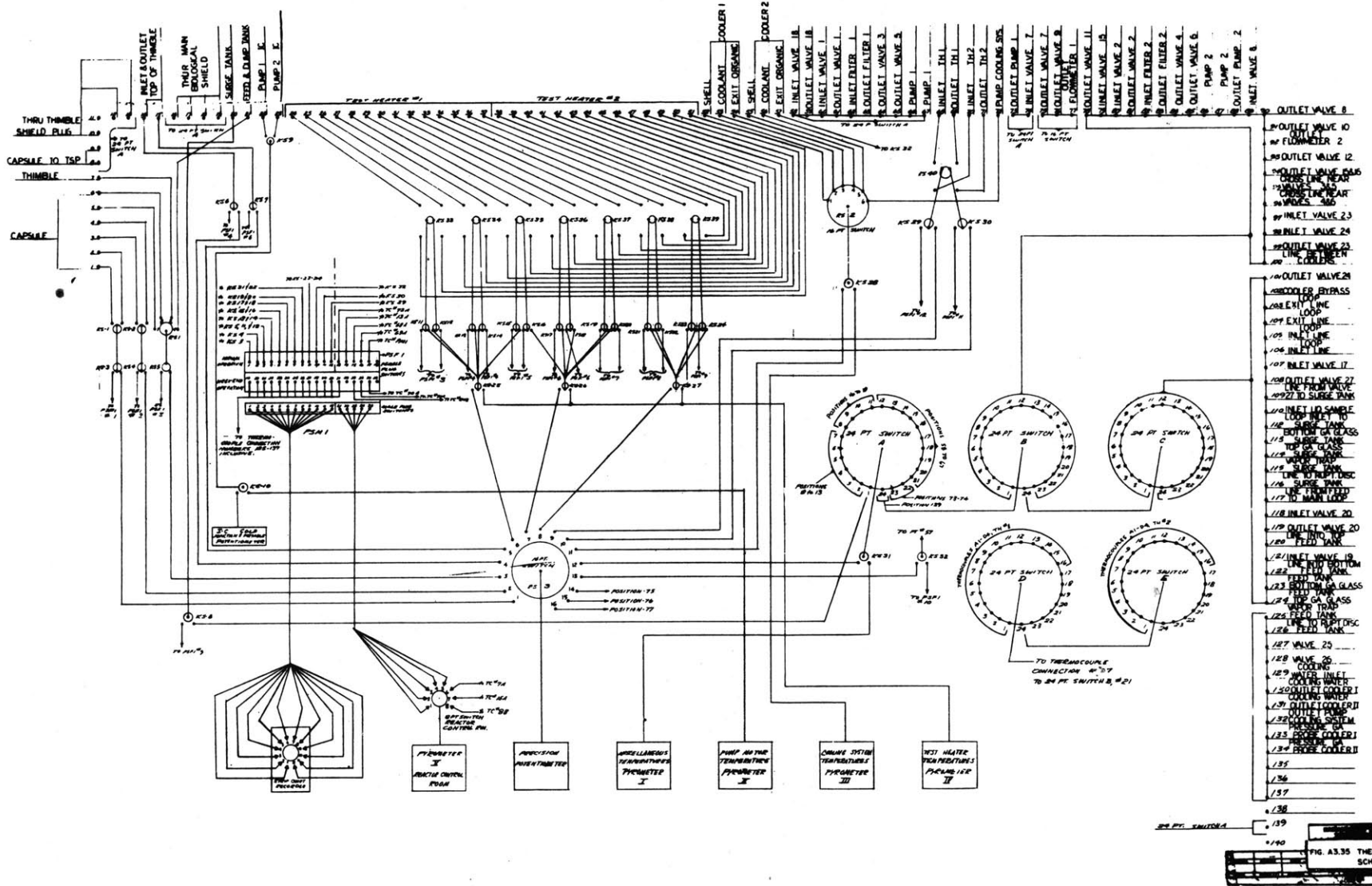
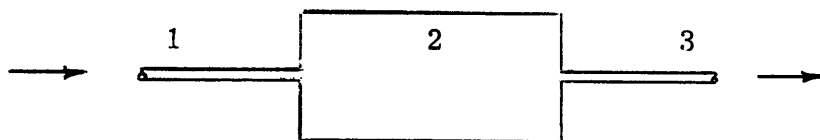


FIG. A3.35 THERMOCOUPLE SCHEMATIC

$$\begin{aligned} \frac{1}{\rho} [P_1 - P_3] &= \frac{V_2^2 - V_1^2}{2g_c} + \frac{(V_1 - V_2)^2}{2g_c} + \frac{V_3^2 - V_2^2}{2g_c} + K_c \frac{V_3^2}{2g_c} \\ &= \frac{(V_1 - V_2)^2}{2g_c} + K_c \frac{V_1^2}{2g_c} \quad \text{where } V_1 = V_3 \end{aligned} \quad (\text{A3. 1})$$



P = pressure

V = velocity

$K_c$  = contraction coefficient

$g_c$  = gravitational constant

While it has not been possible to check any of these pressure drops during loop operation, it has been possible to get velocities in the test heater of slightly greater than 20 ft/sec, using both monoisopropyl biphenyl and Santowax OMP, indicating that the design calculations are reasonably accurate. With a density of 1.0 gm/cm<sup>3</sup>, the pump should deliver a  $\Delta P$  of 77.1 psi, whereas the estimated pressure drop through the loop was 60 psi.

## APPENDIX 3.5

### MISCELLANEOUS DETAILS OF INSTRUMENTATION AND SAFETY SYSTEMS

In this appendix, miscellaneous details of instrumentation and safety systems are presented.

#### A3.5.1 Thermocouple Schematic

Figure A3.35 is the thermocouple schematic showing the switching arrangements possible for each thermocouple.



### A3. 5. 2 Control Instrumentation for Trace Heat System for Weekend Operation

Figure A3. 36 is the schematic of the circuit used for control of the trace heating system during weekend operation. This circuit is controlled by the strip chart recorder and reduces the possibility of any hot spots on the loop tubing during weekend operation when the loop is left unattended. Operation of the circuit is explained in section 3. 4. 2 of Chapter 3.

### A3. 5. 3 Organic Loop Alarms

The alarms provided to indicate abnormal operation of the organic loop are given in Table A3. 3.

### A3. 5. 4 Wiring Schematic and Valve Control System

In Figures A3. 37 and A3. 38, the complete electrical wiring schematic (with the exception of the weekend control circuit for operation of the trace heaters) is given. In Figure A3. 38, the pneumatic system for control of valves V-25 and V-26 is illustrated. Valve V-27 is no longer used in loop operation.

## APPENDIX 3. 6

### MEASUREMENT OF THE TOTAL VOLUME IN THE ORGANIC IN-PILE LOOP

#### A3. 6. 1 Introduction

This section describes the measurement of the volume of the in-pile and out-of-pile volumes of the loop; the methods used and the results obtained are described in detail. A summary of the results is presented in section 3. 5 of the main report.

In discussing the measurements, it is convenient to divide the loop volume into two sections, one the volume of the in-pile section up to the right angle bend at the center of the reactor and the other the out-of-pile volume consisting of all components and lines contained in the hydraulic

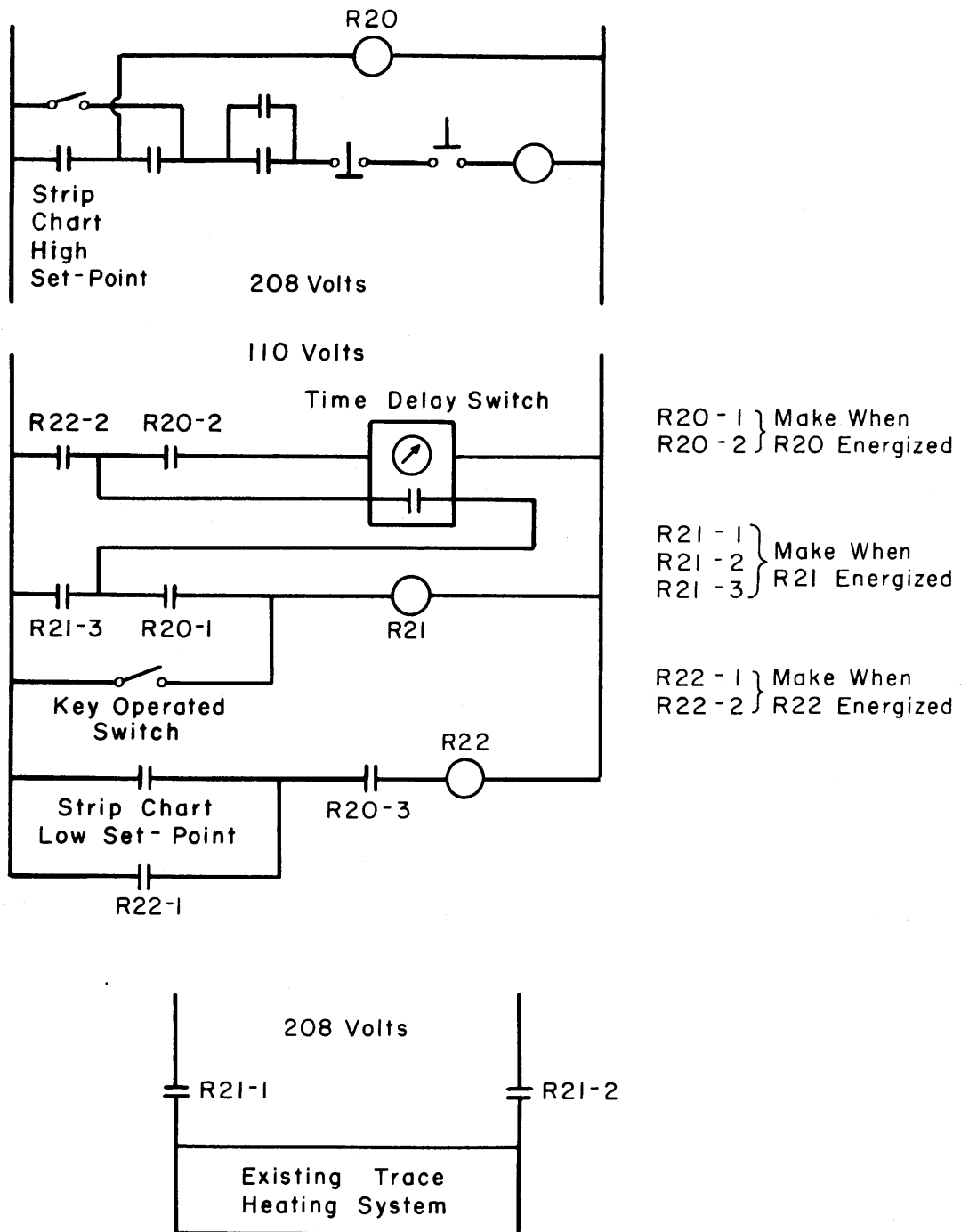


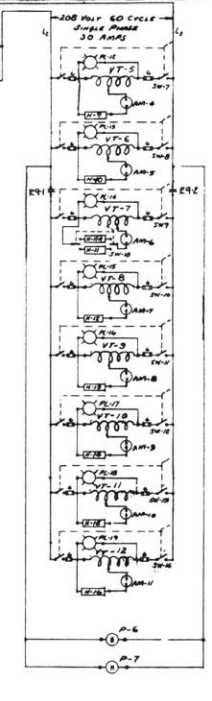
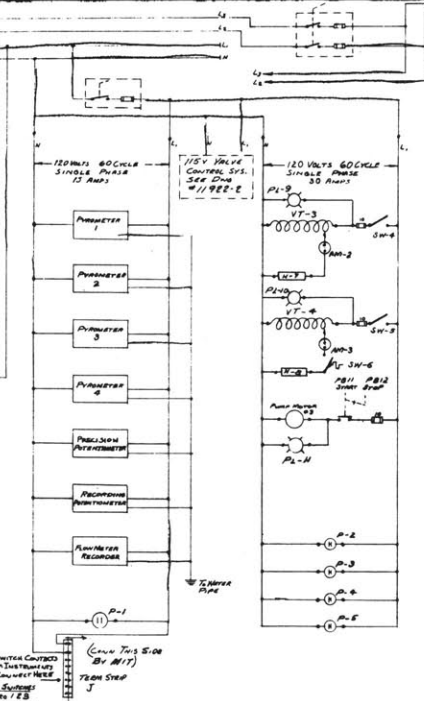
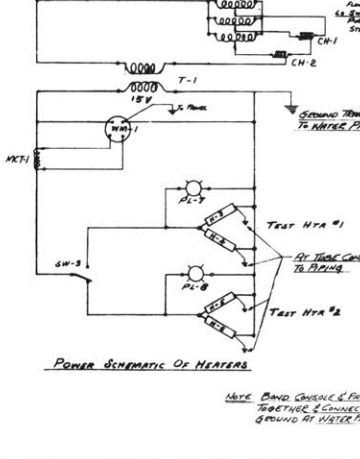
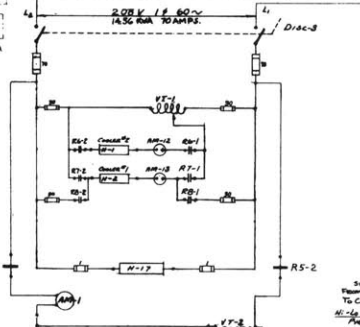
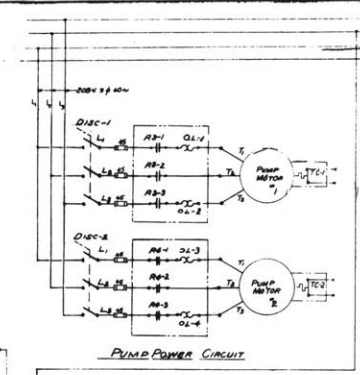
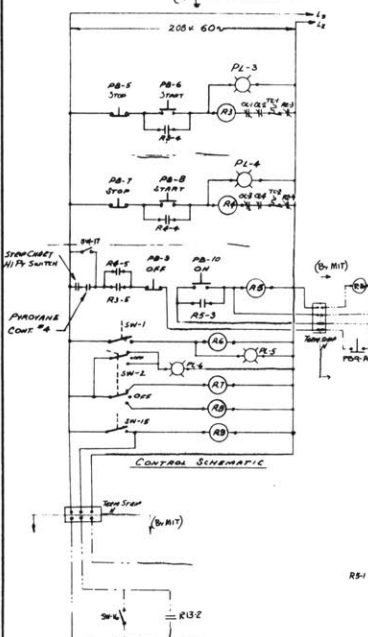
FIG. A3.36 SCHEMATIC OF CONTROL INSTRUMENTATION FOR TRACE HEATING SYSTEM WEEKEND OPERATION

TABLE A3.3  
ORGANIC LOOP ALARMS

LOOP VARIABLE	DETECTING INSTRUMENT	CONTROL CONTACTS		MEANING
		UPPER OR LOWER	SET NORMAL POINT	
Temperature	Strip Chart Recorder	Upper	925°F	Temperature of one or more of 12 thermocouples has exceeded 925°F and test heater is cut-off.
	Pyrometer IV	Upper	925°F	Temperature of test heater has exceeded 925°F and test heater is cut-off.
	Strip Chart Recorder	Lower	850°F	Temperature of one or more of 12 thermocouples has exceeded 850°F.
	Pyrometer I	Upper	800°F	Temperature of thermocouple switched into pyrometer I has exceeded 800°F.
	Pyrometer III	Lower	600°F	Test heater wall temperature has decreased below 600°F
	Pyrometer I	Lower	400°F	Loop organic temperature has decreased below 400°F and close to freezing point of Santowax OMP
	Pyrometer II	Upper	375°F	Pump motor temperature has exceeded 375°F and is rising toward thermal cut-off temperature of 425°F.
	Pyrometer II	Lower	330°F	Pump motor temperature has decreased below 330°F and is approaching freezing point of Santowax OMP.
Organic Flow Rate	Circular Chart Recorder	Upper	1.8 GPM	Organic flow rate has dropped below 1.8 GPM
	Circular Chart Recorder	Lower	0.5 GPM	Organic flow rate has dropped below 0.5 GPM
Pressure	Surge Tank Pressure Gauge	Upper	300 psig	Loop pressure has exceeded 300 psig
	Surge Tank Pressure Gauge	Lower	75 psig	Loop pressure has decreased below 75 psig
	Thimble Pressure Gauge	Upper	25 psig	Thimble pressure has exceeded 25 psig
	Thimble Pressure Gauge	Lower	0 psig	Thimble pressure has decreased to 0 psig
Flow Rate From Leak Detector	Rotameter with Thermocap Relay	One Contact	One-half Normal Flow	Gas flow rate from leak detector has dropped below one-half of normal flow and there is a possibility of an organic leak in the in-pile section.

1-22611 ON BOARD

200V 60W  
200V 60W  
200V 60W  
200V 60W



37	AM-12, 13	AMMETER 4 1/2" GE #549 X 54 0-30 AMP SCALE 200P
38	A-8	AC CONTACTOR GE CR18E1103 SIZE 2 NEMA 1 ENCL 208 V CUL 2 NO MAIN CONTACTS
37	CH-1	CHOKE-GENERAL RADIO TYPE 50 P1
38	CH-2	CHOKE-GENERAL RADIO TYPE 50 P2
39	SW-17	CHURCHILL SELECTOR SWITCH GE TYPE 12731-3
40	SW-18	TABLE SWITCH MICROSWITCH #12731-3
41	SW-14	TONGUE SWITCH MICROSWITCH #12731-2

ITEM NO.	QUANTITY	DESCRIPTION	USE MATL LISTED OR EQUAL
1	3	AB-5, 6, 7, 8, 9, 10	PUSH BUTTON GE CO CR2940 UN202C WITH RED PUSH BUTTON 2 1/4" DIA 2 1/4" NAME PLATE STOP 1" NAME PLATE OFF
2	3	AB-4, 10	PUSH BUTTON GE CO CR2940 UN202B WITH BLACK PUSH BUTTON 2 1/4" DIA 2 1/4" NAME PLATE - START 1" NAME PLATE ON
3	1	AB-11, 12	MAINTAINED CONTACT PUSH BUTTON GE CO #CR2940 UM 202A NAME PLATE START-STOP
4	4	AB-3, 4, 5, 6, 7, 8, 9, 10	230V INDICATOR LIGHT GE CO CR2940-10012 B3 WITH 2" NAME PLATES ON 2" NAME PLATES "RUN"
5	2	PL-3, 8	18 V INDICATOR LIGHT UNITS GE #CR2940-UC12 A11 WITH RED COLORED GLASS GE #CR2940 UC100 2 NAME PLATES "ON"
6	2	PL-9, 10	INDICATOR LIGHT DIALS #51308-991 WITH NE-11 LAMP FOR 180V
7	1	PL-11	120 V INDICATOR LIGHT GE #CR2940 UC12 B NAME PLATE "RUN"
8	8	PL-12-19	INDICATOR LIGHT DIALS #51308-991 WITH NE-11 LAMP FOR 180V
9	2	SW-14, 15	TONGUE SWITCH MICROSWITCH #12731-2 SPST
10	1	SW-2	TONGUE SWITCH MICROSWITCH #12731-2 SPST
11	1	SW-3	TONGUE SWITCH MICROSWITCH #12731-2 SPST
12	2	SW-15	TONGUE SWITCH MICROSWITCH #12731-2 SPST
13	1	SW-6	COMMON TRANSDUCER CH #12731-2 SPST
14	1	VT-1	VARIABLE GEN RADIO #12731-2 SPST
15	1	VT-2	VARIABLE GEN RADIO #12731-2 SPST
16	2	VT-3, 4	VARIABLE GEN RADIO #12731-2 SPST
17	2	VT-5, 6	VARIABLE GEN RADIO #12731-2 SPST
18	1	VT-7	VARIABLE GEN RADIO #12731-2 SPST
19	1	AM-1	AMMETER 4 1/2" GE #549 X 54 0-30 AMP SCALE 200P
20	2	AM-2, 3	AMMETER 4 1/2" GE #549 X 54 0-30 AMP SCALE 200P
21	8	AM-4-11	AMMETER 4 1/2" GE #549 X 54 0-10 AMP SCALE 200P
22	2	A-8, 9	AC CONTACTOR GE CR18E1103 SIZE 2 NEMA 1 ENCL 208 V CUL
23	2	R-6, 7, 8	AC CONTACTOR GE CR18E1103 ADA SIZE 1 NEMA 1 ENCL 208 V CUL 1 NO MAIN CONTACT
24	3	R-6, 7, 8	AC CONTACTOR GE CR18E1103 ADA SIZE 1 NEMA 1 ENCL 208 V CUL 1 NO MAIN CONTACT
25	1	T-1	TRANSFORMER 60W 200V 120V 3000 AMP
26	2	H-1, 2	HEATER 150W 200V 120V 3000 AMP
27	1	H-3	HEATER 150W 200V 120V 3000 AMP
28	2	H-4, 5	HEATER 150W 200V 120V 3000 AMP
29	1	H-6	HEATER 150W 200V 120V 3000 AMP
30	1	H-7	HEATER 150W 200V 120V 3000 AMP
31	1	H-8	HEATER 150W 200V 120V 3000 AMP
32	1	H-9	HEATER 150W 200V 120V 3000 AMP
33	1	H-10	HEATER 150W 200V 120V 3000 AMP
34	1	H-11	HEATER 150W 200V 120V 3000 AMP
35	1	H-12	HEATER 150W 200V 120V 3000 AMP
36	1	H-13	HEATER 150W 200V 120V 3000 AMP
37	1	H-14	HEATER 150W 200V 120V 3000 AMP
38	1	H-15	HEATER 150W 200V 120V 3000 AMP
39	1	H-16	HEATER 150W 200V 120V 3000 AMP
40	1	H-17	HEATER 150W 200V 120V 3000 AMP
41	1	P-1	PUMP MOTOR 1/2 HP 200V 120V 3000 AMP
42	1	P-2	PUMP MOTOR 1/2 HP 200V 120V 3000 AMP
43	1	P-3	PUMP MOTOR 1/2 HP 200V 120V 3000 AMP
44	1	P-4	PUMP MOTOR 1/2 HP 200V 120V 3000 AMP
45	1	P-5	PUMP MOTOR 1/2 HP 200V 120V 3000 AMP
46	1	P-6	PUMP MOTOR 1/2 HP 200V 120V 3000 AMP
47	1	P-7	PUMP MOTOR 1/2 HP 200V 120V 3000 AMP
48	1	P-8	PUMP MOTOR 1/2 HP 200V 120V 3000 AMP
49	1	P-9	PUMP MOTOR 1/2 HP 200V 120V 3000 AMP
50	1	P-10	PUMP MOTOR 1/2 HP 200V 120V 3000 AMP
51	1	P-11	PUMP MOTOR 1/2 HP 200V 120V 3000 AMP
52	1	P-12	PUMP MOTOR 1/2 HP 200V 120V 3000 AMP
53	1	P-13	PUMP MOTOR 1/2 HP 200V 120V 3000 AMP
54	1	P-14	PUMP MOTOR 1/2 HP 200V 120V 3000 AMP
55	1	P-15	PUMP MOTOR 1/2 HP 200V 120V 3000 AMP
56	1	P-16	PUMP MOTOR 1/2 HP 200V 120V 3000 AMP
57	1	P-17	PUMP MOTOR 1/2 HP 200V 120V 3000 AMP
58	1	P-18	PUMP MOTOR 1/2 HP 200V 120V 3000 AMP
59	1	P-19	PUMP MOTOR 1/2 HP 200V 120V 3000 AMP
60	1	P-20	PUMP MOTOR 1/2 HP 200V 120V 3000 AMP
61	1	P-21	PUMP MOTOR 1/2 HP 200V 120V 3000 AMP
62	1	P-22	PUMP MOTOR 1/2 HP 200V 120V 3000 AMP
63	1	P-23	PUMP MOTOR 1/2 HP 200V 120V 3000 AMP
64	1	P-24	PUMP MOTOR 1/2 HP 200V 120V 3000 AMP
65	1	P-25	PUMP MOTOR 1/2 HP 200V 120V 3000 AMP
66	1	P-26	PUMP MOTOR 1/2 HP 200V 120V 3000 AMP
67	1	P-27	PUMP MOTOR 1/2 HP 200V 120V 3000 AMP
68	1	P-28	PUMP MOTOR 1/2 HP 200V 120V 3000 AMP
69	1	P-29	PUMP MOTOR 1/2 HP 200V 120V 3000 AMP
70	1	P-30	PUMP MOTOR 1/2 HP 200V 120V 3000 AMP

LEGEND

- PL-1 - PUMP LIGHT
- PL-2 - PUMP LIGHT
- PL-3 - PUMP LIGHT
- PL-4 - PUMP LIGHT
- PL-5 - PUMP LIGHT
- PL-6 - PUMP LIGHT
- PL-7 - PUMP LIGHT
- PL-8 - PUMP LIGHT
- PL-9 - PUMP LIGHT
- PL-10 - PUMP LIGHT
- PL-11 - PUMP LIGHT
- PL-12 - PUMP LIGHT
- PL-13 - PUMP LIGHT
- PL-14 - PUMP LIGHT
- PL-15 - PUMP LIGHT
- PL-16 - PUMP LIGHT
- PL-17 - PUMP LIGHT
- PL-18 - PUMP LIGHT
- PL-19 - PUMP LIGHT
- PL-20 - PUMP LIGHT
- PL-21 - PUMP LIGHT
- PL-22 - PUMP LIGHT
- PL-23 - PUMP LIGHT
- PL-24 - PUMP LIGHT
- PL-25 - PUMP LIGHT
- PL-26 - PUMP LIGHT
- PL-27 - PUMP LIGHT
- PL-28 - PUMP LIGHT
- PL-29 - PUMP LIGHT
- PL-30 - PUMP LIGHT
- PL-31 - PUMP LIGHT
- PL-32 - PUMP LIGHT
- PL-33 - PUMP LIGHT
- PL-34 - PUMP LIGHT
- PL-35 - PUMP LIGHT
- PL-36 - PUMP LIGHT
- PL-37 - PUMP LIGHT
- PL-38 - PUMP LIGHT
- PL-39 - PUMP LIGHT
- PL-40 - PUMP LIGHT
- PL-41 - PUMP LIGHT
- PL-42 - PUMP LIGHT
- PL-43 - PUMP LIGHT
- PL-44 - PUMP LIGHT
- PL-45 - PUMP LIGHT
- PL-46 - PUMP LIGHT
- PL-47 - PUMP LIGHT
- PL-48 - PUMP LIGHT
- PL-49 - PUMP LIGHT
- PL-50 - PUMP LIGHT
- PL-51 - PUMP LIGHT
- PL-52 - PUMP LIGHT
- PL-53 - PUMP LIGHT
- PL-54 - PUMP LIGHT
- PL-55 - PUMP LIGHT
- PL-56 - PUMP LIGHT
- PL-57 - PUMP LIGHT
- PL-58 - PUMP LIGHT
- PL-59 - PUMP LIGHT
- PL-60 - PUMP LIGHT
- PL-61 - PUMP LIGHT
- PL-62 - PUMP LIGHT
- PL-63 - PUMP LIGHT
- PL-64 - PUMP LIGHT
- PL-65 - PUMP LIGHT
- PL-66 - PUMP LIGHT
- PL-67 - PUMP LIGHT
- PL-68 - PUMP LIGHT
- PL-69 - PUMP LIGHT
- PL-70 - PUMP LIGHT
- PL-71 - PUMP LIGHT
- PL-72 - PUMP LIGHT
- PL-73 - PUMP LIGHT
- PL-74 - PUMP LIGHT
- PL-75 - PUMP LIGHT
- PL-76 - PUMP LIGHT
- PL-77 - PUMP LIGHT
- PL-78 - PUMP LIGHT
- PL-79 - PUMP LIGHT
- PL-80 - PUMP LIGHT

ARTISAN METAL PRODUCTS, INC.  
1000 BOSTON STREET, WALTHAM, MASS.

FIG. A3.37 WIRING SCHEMATIC FOR IN-PILE LOOP

REVISED BY DATE

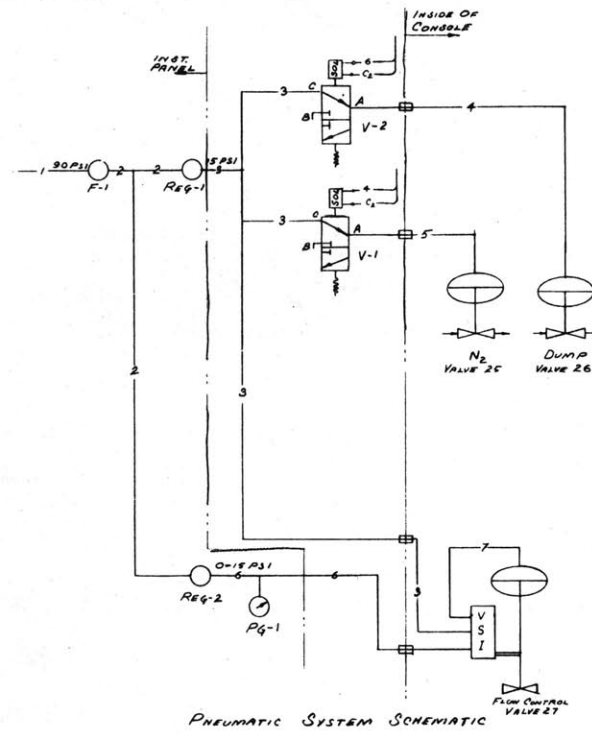
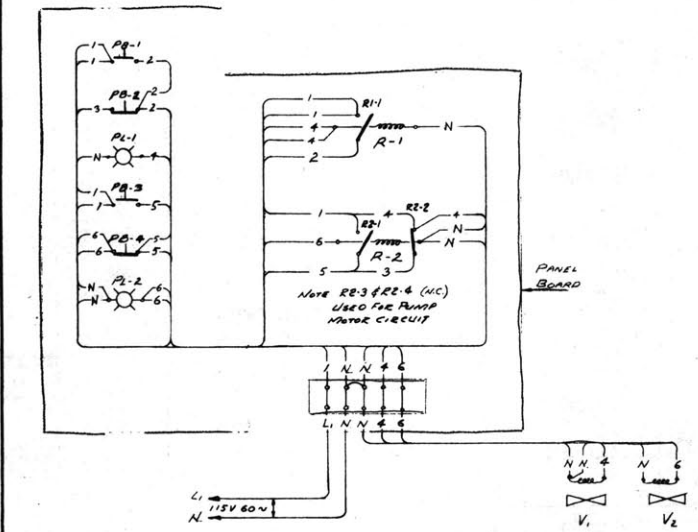
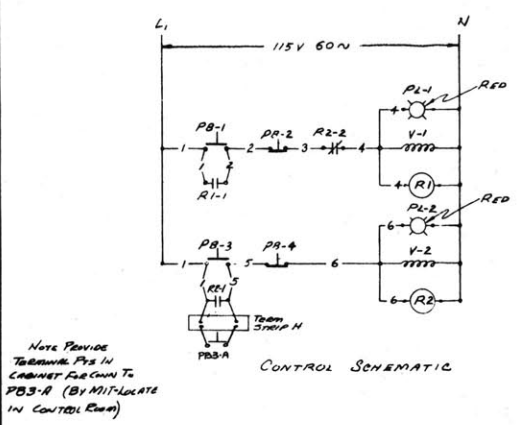
APPROVED BY DATE

DWG. NO. 11977-1

A3.57

2-22611 ON  
D.M.C.

A3.58



LIST OF MATERIALS

QUANTITY REQ'D - ONE OF EACH

- 1) PB-1 PUSH BUTTON GE CO. CR2940UA202C WITH RED PUSH BUTTON & RING NAME PLATE MARKED 'OPEN'
- 2) PB-2 PUSH BUTTON GE CO. CR2940UA202B WITH BLACK PUSH BUTTON & RING NAME PLATE MARKED 'CLOSE'
- 3) PB-3 PUSH BUTTON GE CO. CR2940UA202C WITH RED MUSHROOM BUTTON & RING, NAME PLATE MARKED 'OPEN'
- 4) PB-4 PUSH BUTTON GE CO. CR2940UA202B WITH BLACK PUSH BUTTON & RING NAME PLATE MARKED 'CLOSE'
- 5) PL-1 PILOT LIGHT GE CO. CR2940UC212B NAME PLATE MARKED 'OPEN' 115V/60CY
- 6) PL-2 PILOT LIGHT GE CO. CR2940UC212B NAME PLATE MARKED 'OPEN' 115V/60CY
- 7) R-1 RELAY ASCO CAT. NO. 5401 1PNO 115V/60CY COIL
- 8) R-2 RELAY GE #CE105 B10E SIZE 0 NEMA 1 ENCL 115V COIL 3 N.E. DRAW CONT. NO. 2 NO. 2 AUX CONT.
- 9) V-1 SOLENOID VALVE ASCO 1/4 IPS CAT. NO. B31454 115V/60CY
- 10) V-2 SOLENOID VALVE ASCO 1/4 IPS CAT. NO. B31454 115V/60CY
- 11) REG-1 PRESSURE REGULATOR ARROW CAT. NO. 1483-1 3/8 IPS 0-50PSI SECONDARY
- 12) REG-2 PRESSURE REGULATOR GOVERNOR CAT. NO. 1032 1/2-30PSI RANGE 1/2 NPT
- 13) F-1 FILTER ARROW CAT. NO. 3103 3/8 SIZE
- 14) PG-1 PRESSURE GA. ASHCROFT #4 1/2-10TTA GRADUATIONS 0-30 PSI

III	MISC REV.	DA	5/12/60
II	ADD PB3-A	BT	1/25/60
I	REV WMS #501 IPAD 1PVC	BT	11-18-59
ISSUE	REVISION	BY	DATE

ARTISAN METAL PRODUCTS, INC.  
POND STREET · WALTHAM  
BOSTON 54, MASS.

FIG. A3.38 VALVE CONTROL SYSTEM

DESIGN BY	DATE	LIMITS ON DIMENSIONS (UNLESS OTHERWISE SPECIFIED)	FRAC. 2 DEC. 2 ANG. 2
APPROV BY	DATE		
SCALE	REFER	ISSUE III	DWG. NO. 11922-2
2147 SHOP NO.			

console plus the lines carrying organic from the top of the in-pile section at the radial center of the reactor to the hydraulic console. In addition, in those parts of the in-pile section exposed to the radiation field, the volume distribution as a function of position must be known so that the integrated average dose rate in the organic material can be determined.

#### A3.6.2 Out-of-Pile Volume Plus Volume of Lines Extending to Top of In-Pile Section

The method of determining the out-of-pile volume will be presented along with all experimental results.

##### (1) Method of Measurement

Referring to the loop flowsheet in Figure 3.4 of Chapter 3, a short bypass was connected between the inlet-outlet lines of the hydraulic console leading to the in-pile section. The volume in different sections of the hydraulic console was then determined by evacuating the loop and adding acetone section by section, starting from either the pressurized feed and dump tank or the surge tank; the volume in both of these tanks had been calibrated by adding measured quantities of acetone from a graduated cylinder and measuring the incremental heights in the gage glass of each tank. Acetone was used as it is impossible to completely drain the loop or to force the remaining liquid out using gas pressure, and acetone with its high vapor pressure could easily be removed between runs by connecting a vacuum pump to the loop outlet and evacuating the loop.

During the initial attempts at measuring the volume, it was noticed that increasing the gas pressure exerted on the calibrated surge tank or feed and dump tank when a section had apparently been filled, resulted in further addition of acetone (i. e., drop in level in the gage glass). This was taken to indicate that some gas was present in the section of the loop whose volume was being measured. This effect was due to the impossibility of obtaining a high vacuum in the loop and the compression of the remaining gas in the loop into a smaller and smaller volume as the loop was filled section by section. The effect

was particularly significant for the last sections measured where the gas in the entire loop had been compressed into a small volume. In order to eliminate this error, the following procedure was used:

Let:  $V_A$  = volume of acetone added to section at any pressure,  $\pi$ ,  $\text{cm}^3$ .

$V_S$  = actual volume of section on which measurement is being performed.

$V_T$  = total volume filled by acetone vapor plus gas after filling the section with acetone,  $\text{cm}^3$ .

$p_a$  = partial pressure of acetone in the volume,  $V_T$ , psia.

$p_g$  = partial pressure of gas in the volume,  $V_T$ , psia.

$\pi = p_a + p_g$  = total pressure exerted on system, psia.

$n_g$  = moles of gas in  $V_T$ .

$T$  = temperature of measurement, °F.

Assuming the ideal gas law, the partial pressure of gas in the volume  $V_T$  can be written as:

$$p_g = n_g \frac{RT}{V_T} \quad (\text{A3. 2})$$

Then

$$V_T = V_S - V_A = n_g \frac{RT}{p_g} = n_g \frac{RT}{\pi - p_a} \quad (\text{A3. 3})$$

or

$$V_S = V_A + n_g \frac{RT}{\pi - p_a} \quad (\text{A3. 4})$$

Now,  $n_g RT$  is taken as constant and independent of the total pressure  $\pi$  so that

$$V_S = V_A + \frac{C}{\pi - p_a} \quad (\text{A3. 5})$$

If now, the volume,  $V_A$ , of acetone is determined at different pressures and plotted vs.  $1/(\pi - p_a)$ , a straight line should be obtained which, on extrapolation of  $V_A$  to a  $1/(\pi - p_a)$  of zero, should give  $V_S$  or the volume of the section without

any gas space. Actually, it was found in analyzing the data that a plot of  $V_A$  vs.  $1/\pi$  was generally more linear than the plot of  $V_A$  vs.  $1/(\pi-p_a)$  where  $p_a$  was taken as the vapor pressure of acetone at 75°F (210 mm Hg) or 4.1 psia). The reason for this behavior is not known but could be due to one or an accumulation of effects such as inaccuracies in the pressure gage and solubility of the pressurizing gas in the acetone. However, since only a very small extrapolation is required from the measurement at the highest pressure (214.7 psia) to a  $1/\pi$  or  $1/(\pi-p_a)$  of zero, essentially the same extrapolated volume is obtained from either plot. The plots used for analysis of the data have been based on use of the total pressure,  $\pi$ , because of the better linearity.

## (2) Results

As the surge tank and feed and dump tank were used as calibrated reservoirs, these were calibrated by adding acetone by means of a graduated cylinder and measuring the liquid level by means of the gage glass on each tank. The results are presented in Table A3.4 and Figures A3.39 and A3.40. The volume per unit length is 61.1 cm<sup>3</sup>/inch for the surge tank and 223 cm<sup>3</sup>/inch for the feed and dump tank. The total volume for each tank to the top of the gage glass is 1305 cm<sup>3</sup> and 4500 cm<sup>3</sup>, respectively; the surge tank and the feed and dump tank have an additional volume at levels above the gage glass top of approximately 200 cm<sup>3</sup> and 700 cm<sup>3</sup>, respectively.

In reporting the results for the different loop sections, the designations for each section given in Table A3.5 were used; the valve positions can be seen from the flow sheet given in Figure 3.4. Results for four different calibration runs are given in Table A3.6 and Figures A3.41 through A3.45; a final summary of the recommended volumes is given in Table A3.7. For comparison, a plot for some volumes measured on calibration run No. 4 are given, based on  $1/(\pi-p_a)$  rather than  $1/\pi$ . Comparing Figures A3.43 and A3.45, it is seen that the same result is obtained from both plots and that the plot vs.  $1/\pi$  results in better linearity. The volumes,  $Q$ , of the tubing from the hydraulic



TABLE A3.4  
VOLUME CALIBRATION OF SURGE TANK AND FEED AND DUMP TANK

TANK	LEVEL, INCHES <sup>(1)</sup>	VOL. ACETONE ADDED, cm <sup>3</sup> (3)	EFFECT OF INCREASING PRESSURE			SLOPE cm <sup>3</sup> /inch
			P psia	$\frac{P}{\text{atm}}$ <sup>-1</sup>	Level <sup>(2)</sup> inches	
Surge	1 3/8	200	Negligible			61.1
	3.0	300				
	4 5/8	400				
	6 5/16	500				
	8.0	600				
	9 9/16	700				
	11 3/16	800				
	12 13/16	900				
	14 1/2	1000				
	16 1/8	1100				
Feed and Dump	1	500				223
	3 5/16	1000				
	5 1/2	1500	14.7	1.0	19.0	
	7 3/4	2000	56.7	0.259	18 7/8	
	10.0	2500	214.7	0.0684	18 13/16	
	12 1/4	3000	$\infty$	0	18 13/16	
	14 7/16	3500				
	16 11/16	4000				
	19.0	4500				

(1) Accuracy of Reading  $\cong \pm \frac{1}{16}$

(2) See Fig. A3.45

(3) For the Surge Tank, a 100 cm<sup>3</sup> graduated cylinder was used.  
For the Feed and Dump Tank, a 500 cm<sup>3</sup> graduated cylinder was used.

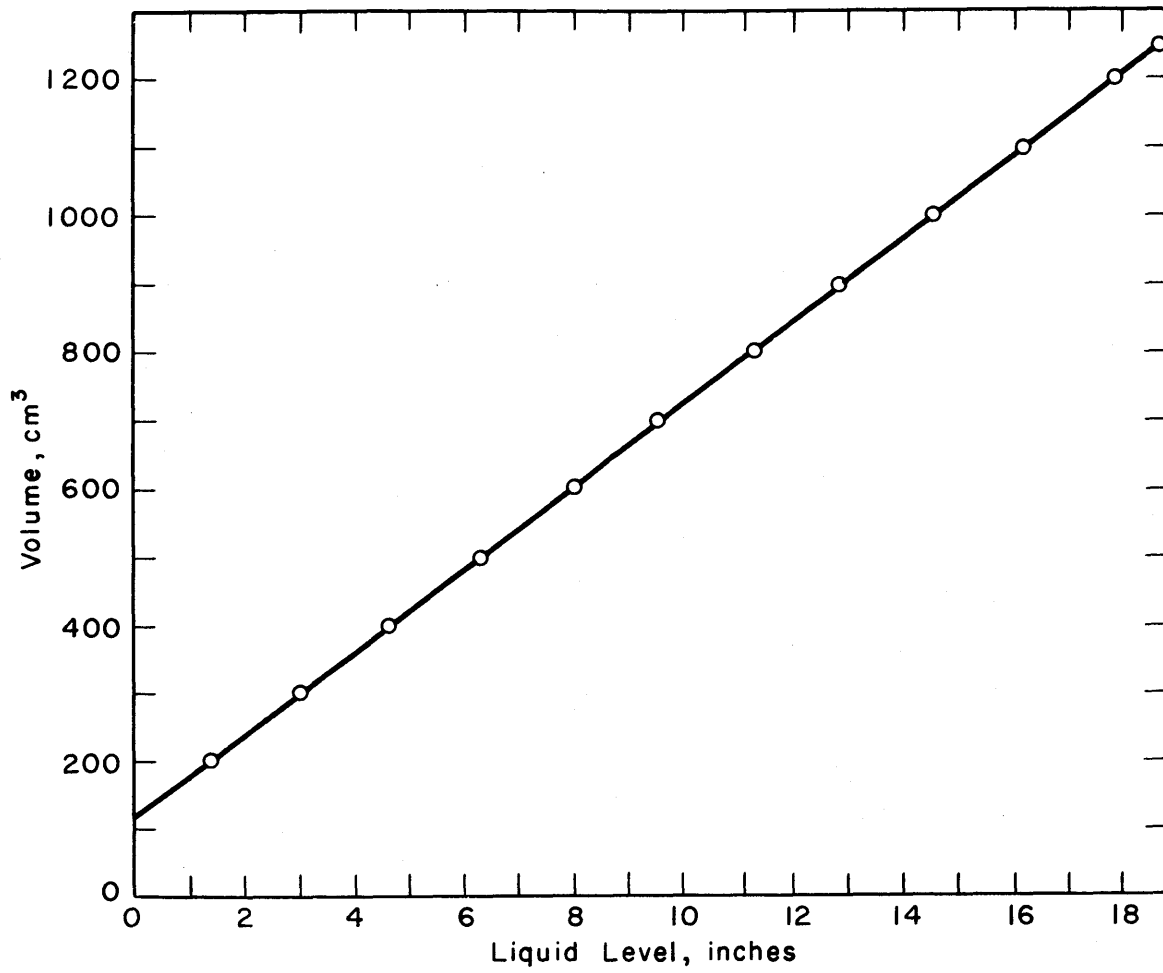


FIG. A 3.39 SURGE TANK VOLUME TO VALVE 18

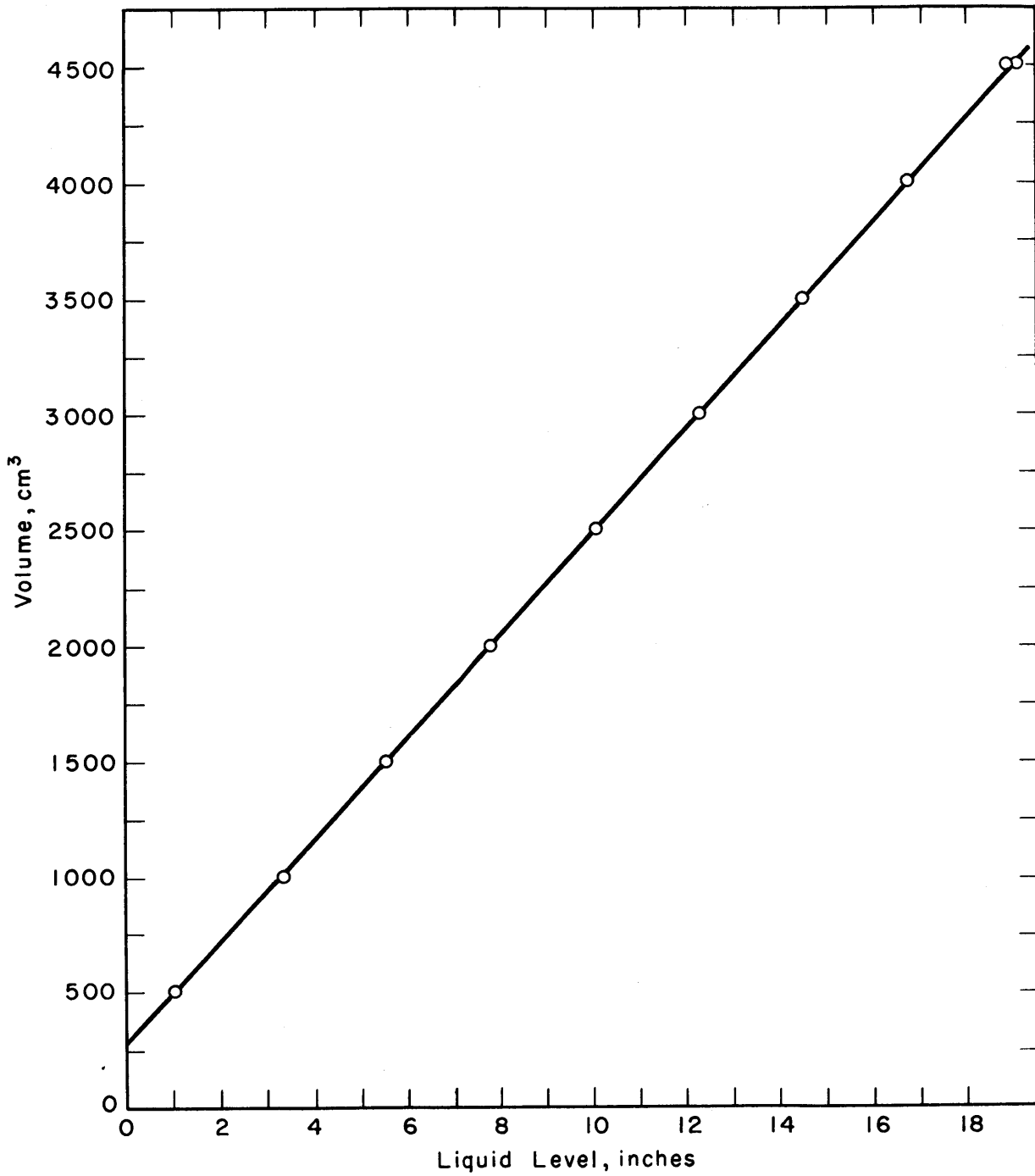


FIG. A3.40 FEED AND DUMP TANK VOLUME TO VALVES 19 AND 20

Table 3. 5. Volume Designations for Volume Measurements.

Volume Designation	Volume Location between Valves
A	18, 19, 20, 1, 2
B	1, 3 [ Filter #1 without element]
C	2, 4 [ Filter #2 with element]
D	3, 5, 4, 6
E	5, 7 [ Pump #1]
F	6, 8 [ Pump #2]
G	7, 9, 8, 10
H	9, 11 [ Flowmeter #1]
I	10, 12 [ Flowmeter #2]
J	11, 13, 12, 14
K	13, 15 [ Test Heater #1]
L	14, 16 [ Test Heater #2]
M	15, 16, 23, 24
N	23, 24, 27 Including bypass
O	Bypass
P	27 to Surge tank
Q	Inlet-outlet to reactor center

TABLE A3.6

TABULATION OF DATA AND RESULTS OF VOLUME MEASUREMENT OF HYDRAULIC CONSOLE

A3.66

CALIBRATION RUN NO.	VOLUME DESIGNATION	SURGE TANK LEVEL, INCHES		FEED AND DUMP TANK LEVEL, INCHES		PRESSURE psia	$\frac{1}{\pi}$ atm <sup>-1</sup>	VOLUME OF SECTION, cm <sup>3</sup>
		L <sub>1</sub>	L <sub>f</sub>	L <sub>1</sub>	L <sub>f</sub>			
3	A	17 3/4	14.0	-	-	14.7	1.0	(17 5/8 - 13 1/2) (61.1) = 252
		17 3/4	13 3/4	-	-	34.7	0.424	
		17 3/4	-	-	-	74.7	0.197	
		17 5/8	13 1/2	-	-	214.7	0.0684	
		17 5/8	13 1/2	-	-	∞	0.000	
	C	-	7 7/8	-	-	14.7	1.0	(13 1/2 - 6 5/8) (61.1) = 420
		-	7 1/4	-	-	34.7	0.424	
		13 1/2	6 3/4	-	-	214.7	0.0684	
	B	-	6 5/8	-	-	∞	0.000	(16 7/8 - 8 1/2) (61.1) = 512
		18 1/8	10 7/8	-	-	14.7	1.0	
		17 5/8	9 1/2	-	-	34.7	0.424	
		17.0	8 11/16	-	-	214.7	0.0684	
	D	-	8 1/2	-	-	∞	0.000	(8 1/2 - 5 1/4) (61.1) = 199
		-	7 7/8	-	-	14.7	1.0	
		-	6 3/8	-	-	34.7	0.424	
		-	5 7/16	-	-	214.7	0.0684	
4	A	8 1/2	5 1/4	-	-	∞	0.000	(17 1/2 - 13 3/16) (61.1) = 264
		-	7 7/8	-	-	14.7	1.0	
		-	6 3/8	-	-	34.7	0.424	
		-	5 7/16	-	-	214.7	0.0684	
		-	5 1/4	-	-	14.7	1.0	
		17 1/2	13 3/16	-	-	∞	0.000	
	B	-	6 3/4	-	-	14.7	1.0	(13 3/16 - 4 15/16) (61.1) = 506
		-	6 1/8	-	-	20.7	0.710	
		-	5 5/8	-	-	34.7	0.424	
		-	5.0	-	-	214.7	0.0684	
		13 3/16	4 15/16	-	-	14.7	1.0	
	C	-	4 15/16	-	-	∞	0.000	(16 15/16 - 10.0) (61.1) = 425
		18 1/2	12 3/8	-	-	14.7	1.0	
		18.0	11 1/2	-	-	20.7	0.710	
		17 1/2	10 7/8	-	-	34.7	0.424	
	D	-	10 1/8	-	-	214.7	0.0684	(10.0 - 6 3/4) (61.1) = 199
		16 15/16	10.0	-	-	∞	0.000	
		-	8 15/16	-	-	14.7	1.0	
		-	8 5/16	-	-	20.7	0.710	
	E	-	7 5/8	-	-	34.7	0.424	1000+(16 1/4-11 9/16) (61.1) = 1286
		-	6 7/8	-	-	214.7	0.0684	
		10.0	6 3/4	-	-	∞	0.000	
		18 1/8	15 3/4	-	-	14.7	1.0	
		17 9/16	14 3/16	-	-	20.7	0.710	
17 1/8		13 1/16	-	-	34.7	0.424		
F	16 9/16	11 13/16	-	-	214.7	0.0684	1000+(11 9/16-6 7/8) (61.1) = 1286	
	18 1/16	-	-	-	14.7	1.0		
	16 3/8	-	-	-	214.7	0.0684		
	16 1/4	11 9/16	-	-	∞	0.000		
	-	13 1/2	-	-	14.7	1.0		
1000 cc Acetone Added to Surge Tank	-	11 1/4	-	-	20.7	0.710	-	
	-	9 3/8	-	-	34.7	0.424		
	-	7 5/16	-	-	214.7	0.0684		
	11 9/16	6 7/8	-	-	∞	0.000		
	-	6 7/8	-	-	14.7	1.0		

TABLE A3.6 (Continued)

TABULATION OF DATA AND RESULTS OF VOLUME MEASUREMENT OF HYDRAULIC CONSOLE

CALIBRATION RUN NO.	VOLUME DESIGNATION	SURGE TANK LEVEL, INCHES		FEED AND DUMP TANK LEVEL, INCHES		PRESSURE psia	$\frac{1}{w}$ atm <sup>-1</sup>	VOLUME OF SECTION, cm <sup>3</sup>
		L <sub>i</sub>	L <sub>f</sub>	L <sub>i</sub>	L <sub>f</sub>			
	G	-	10 1/16	-	-	14.7	1.0	(6 7/8 - 4 1/16) (61.1) = 172
	-	-	7 7/8	-	-	22.7	0.648	
	-	-	6 3/8	-	-	34.7	0.424	
	-	6 7/8	4 1/16	-	-	214.7	0.0684	
	-	-	-	-	-	∞	0.000	
	H	-	15 15/16	-	-	14.7	1.0	500-(10 1/4-4 1/16) (61.1) = 122
	500 cc Acetone	-	13 15/16	-	-	21.7	0.678	
Added to	-	12 7/16	-	-	34.7	0.424		
Surge Tank	4 1/16	10 5/8	-	-	214.7	0.0684		
-	-	10 1/4	-	-	∞	0.000		
I	-	13 1/2	-	-	14.7	1.0	(10 1/4 - 8 5/16) (61.1) = 118	
-	-	11 15/16	-	-	20.7	0.710		
-	-	10 3/8	-	-	35.7	0.412		
-	10 1/4	8 5/8	-	-	214.7	0.0684		
-	-	8 5/16	-	-	∞	0.000		
J	-	10 1/2	-	-	14.7	1.00	(8 5/16 - 5 5/8) (61.1) = 164	
-	-	8 15/16	-	-	20.7	0.710		
-	-	7 1/2	-	-	34.7	0.424		
-	8 5/16	5 7/8	-	-	214.7	0.0684		
-	-	5 5/8	-	-	∞	0.000		
K	-	7 1/4	-	-	14.7	1.00	(5 5/8 - 2 1/2) (61.1) = 191	
-	-	5 13/16	-	-	20.7	0.710		
-	-	4 7/16	-	-	34.7	0.424		
-	5 5/8	2 13/16	-	-	214.7	0.0684		
-	-	2 1/2	-	-	∞	0.000		
L	-	15 5/8	-	-	14.7	1.00	700-(11.0- 2 1/2) (61.1) =181	
700 cc Acetone	-	14 1/8	-	-	20.7	0.710		
Added to	-	12 7/8	-	-	34.7	0.424		
Surge Tank	2 1/2	11 1/4	-	-	214.7	0.0684		
-	-	11.0	-	-	∞	0.000		
M	-	12 7/16	-	-	14.7	1.00	(11.0- 7 7/8) (61.1) =191	
-	-	11.0	-	-	20.7	0.710		
-	-	9 3/4	-	-	34.7	0.424		
-	11.0	8 1/8	-	-	214.7	0.0684		
-	-	7 7/8	-	-	∞	0.000		
5	A through M	-	-	-	10 15/16	14.7	1.0	2500+(18 13/16-7 5/8)(223) =5020
2500 cc Acetone	-	-	-	-	8 11/16	56.7	0.259	
Added	-	-	-	18 13/16	7 7/8	214.7	0.0684	
-	-	-	-	-	7 5/8	∞	0.000	
-	-	-	-	-	10 1/2	14.7	1.00	
	N	-	-	-	7 5/8	14.7	1.0	(7 5/8 - 4 3/4) (223) =641
-	-	-	-	-	5 3/4	56.7	0.259	
-	-	-	-	7 5/8	5.0	214.7	0.0684	
-	-	-	-	4 3/4	∞	0.000		
6	A through F	-	-	-	3 9/16	14.7	1.0	(18 7/8 - 1 3/8) (223) =3900
-	-	-	-	-	2 5/16	28.2	0.572	
-	-	-	-	-	2 1/16	35.2	0.414	
-	-	-	18 7/8	-	1 1/2	214.7	0.0684	
-	-	-	-	-	1 3/8	∞	0.000	
	G through M	-	-	17 9/16	12 3/4	14.7	1.0	(15 3/4 - 11 1/6) (223) =1050
-	-	-	-	16 1/2	11 3/4	24.6	0.596	
-	-	-	-	16 3/8	-	34.6	0.425	
-	-	-	-	15 13/16	11 1/8	214.7	0.0684	
-	-	-	-	15 3/4	11 1/16	∞	0.000	
-	-	-	-	17 3/8	12 1/2	14.7	1.0	
-	-	-	-	-	11 9/16	35.6	0.412	

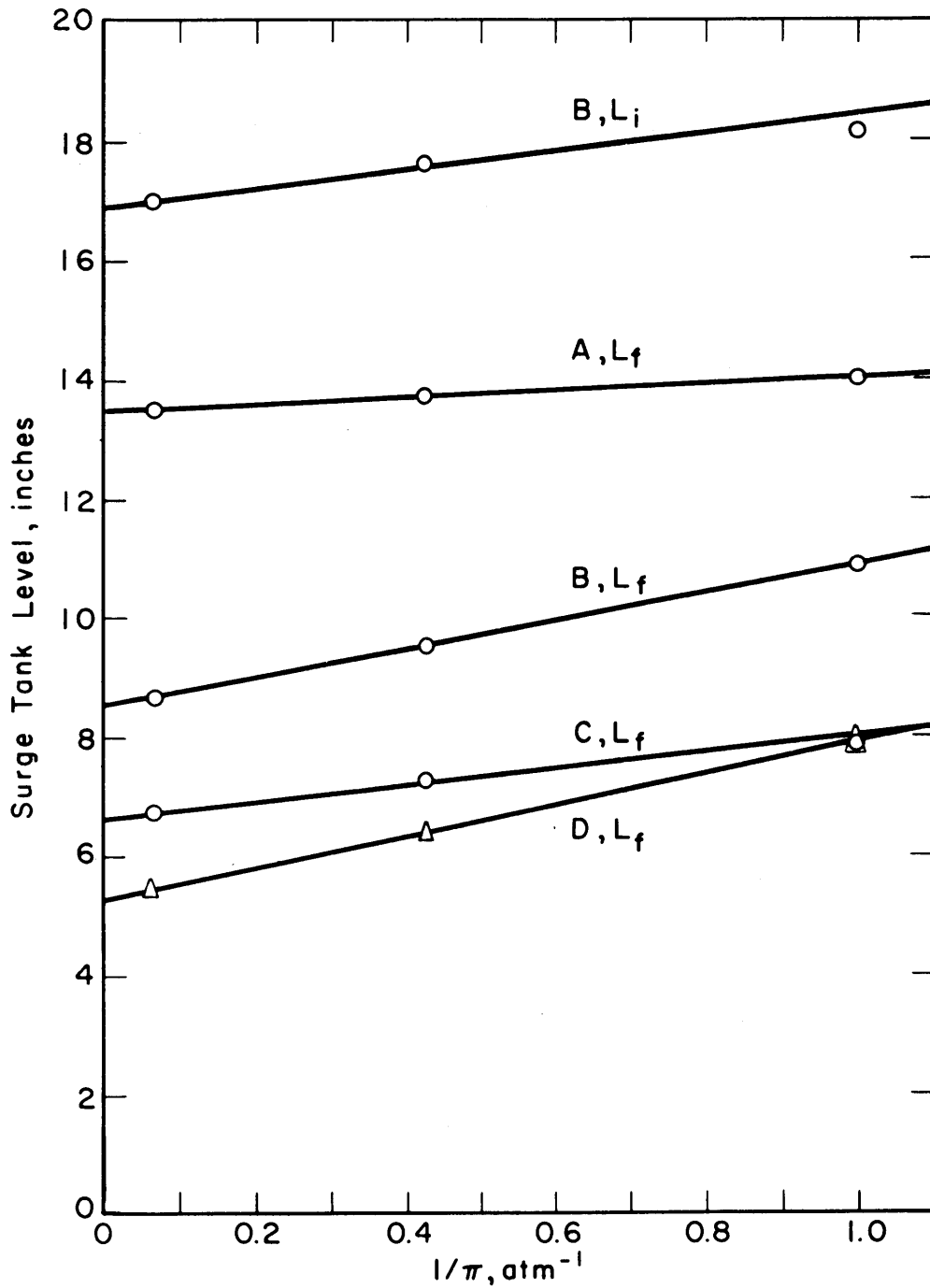


FIG. A3.41 VOLUME MEASUREMENT, RUN No. 3  
 L<sub>i</sub> = INITIAL LIQUID LEVEL  
 L<sub>f</sub> = FINAL LIQUID LEVEL  
 SEE TABLE A.3.5 FOR VOLUMES  
 CORRESPONDING TO LETTERS

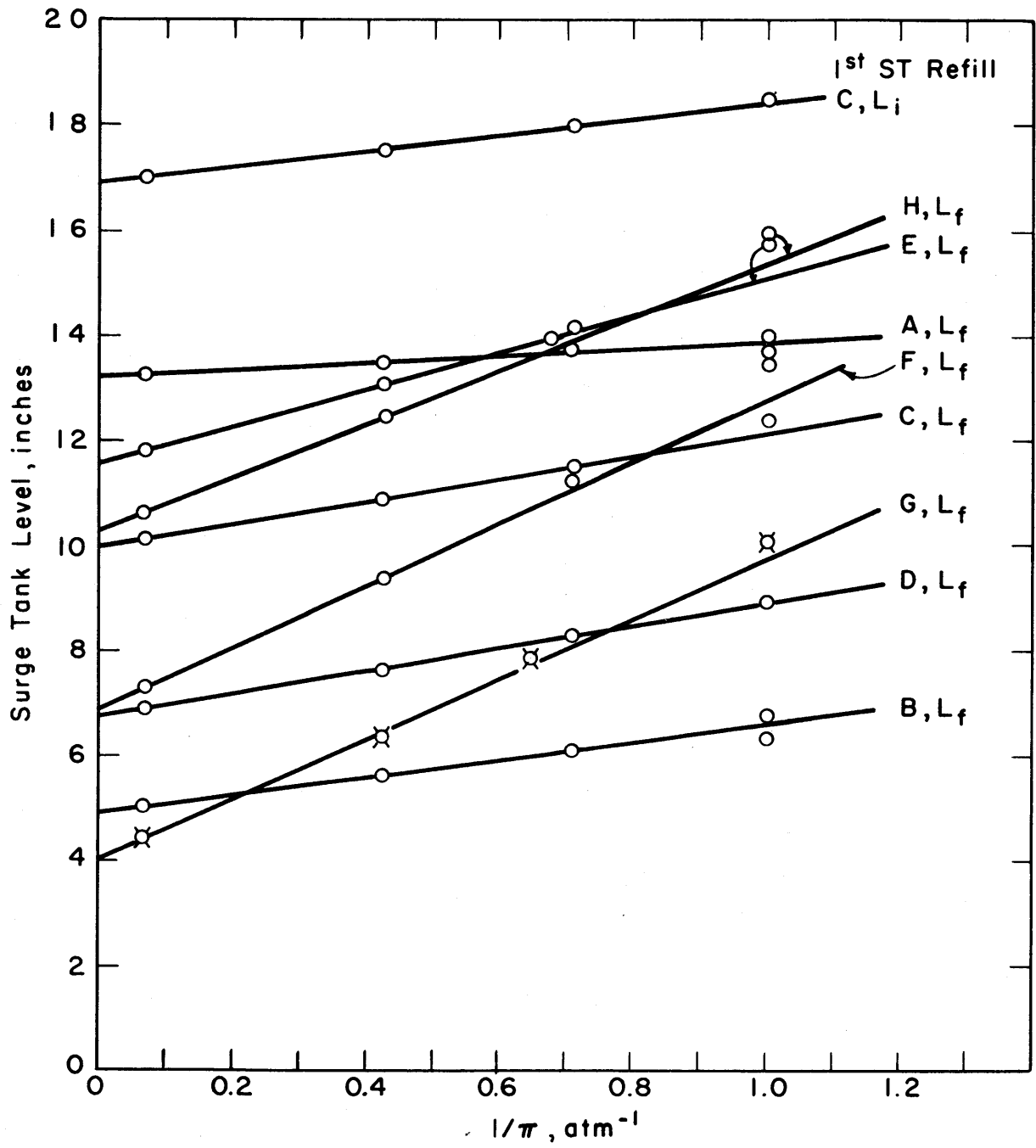


FIG. A3.42 VOLUME MEASUREMENT, RUN No.4 L<sub>i</sub>= INITIAL LIQUID LEVEL, L<sub>f</sub>=FINAL LIQUID LEVEL, SEE TABLE A3.5 FOR VOLUMES CORRESPONDING TO LETTERS



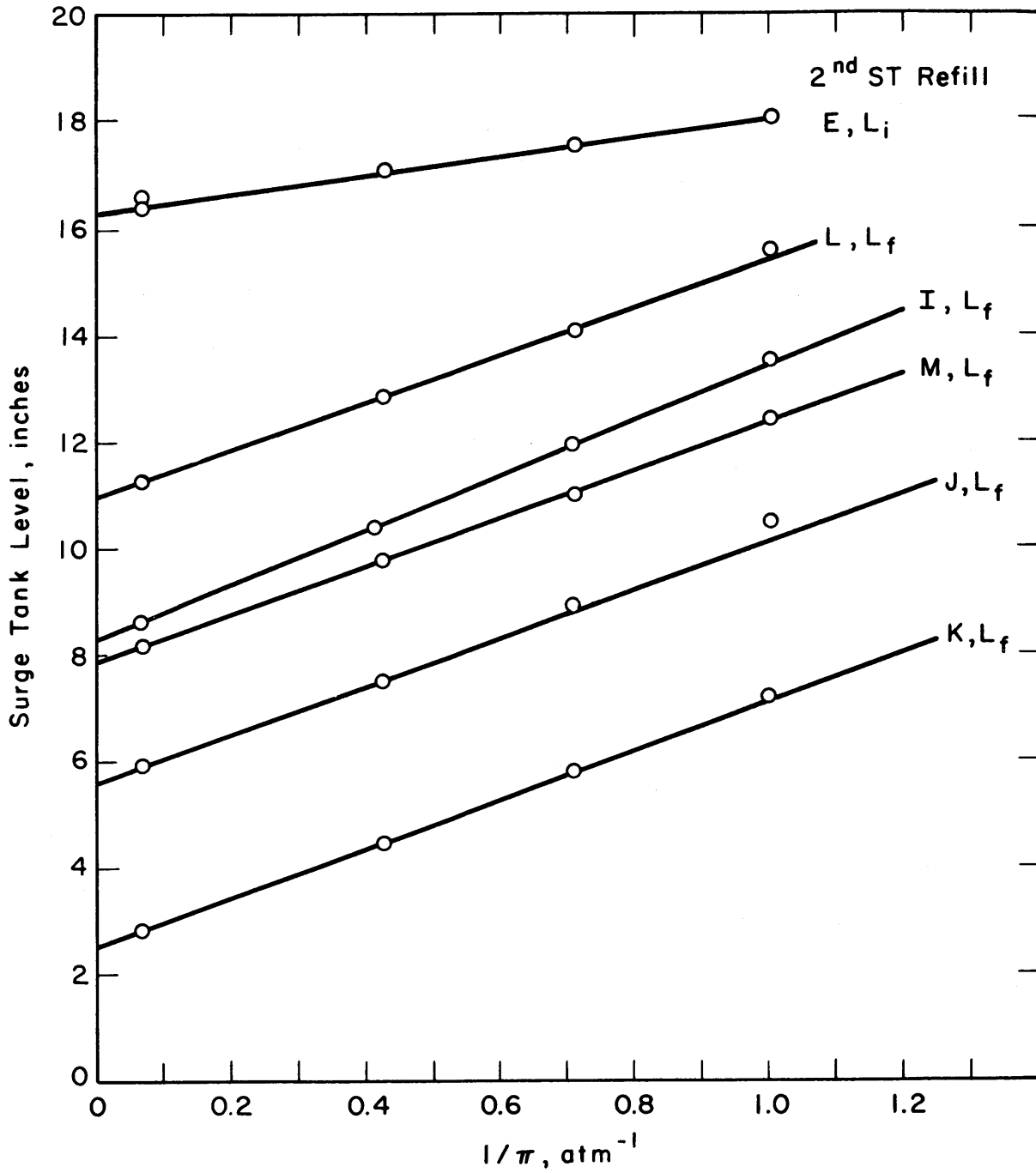


FIG. A3.43 VOLUME MEASUREMENT, RUN No. 4, L<sub>i</sub>= INITIAL VOLUME, L<sub>f</sub>=FINAL VOLUME, SEE TABLE A 3.5 FOR VOLUMES CORRESPONDING TO LETTERS

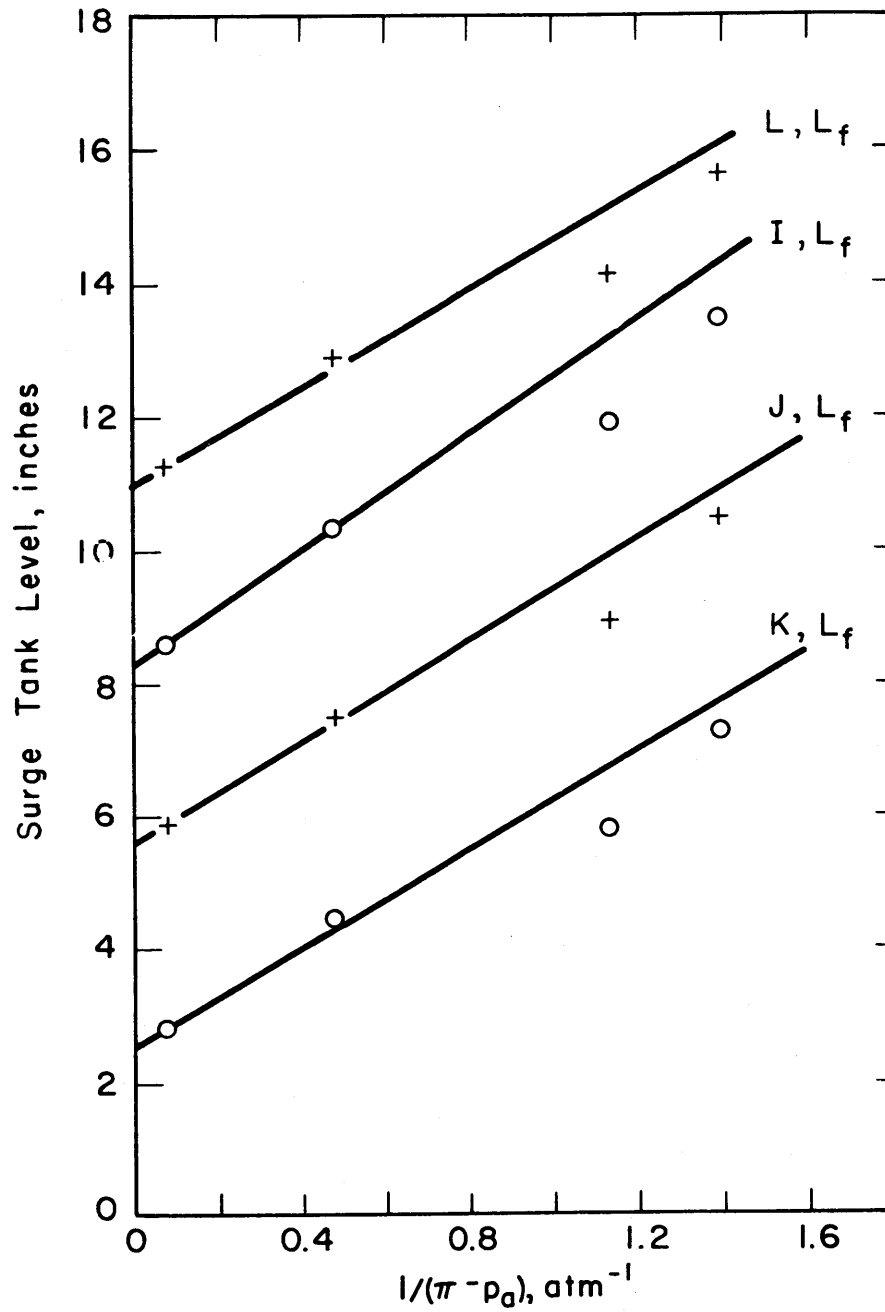


FIG. A3.44 VOLUME MEASUREMENT RUN No. 4,  
 BASED ON  $1/(\pi - \rho_0)$  RATHER THAN  $1/\pi$   
 $L_i$  = INITIAL LIQUID LEVEL  
 $L_f$  = FINAL LIQUID LEVEL  
 SEE TABLE A3.5 FOR VOLUMES  
 CORRESPONDING TO LETTERS

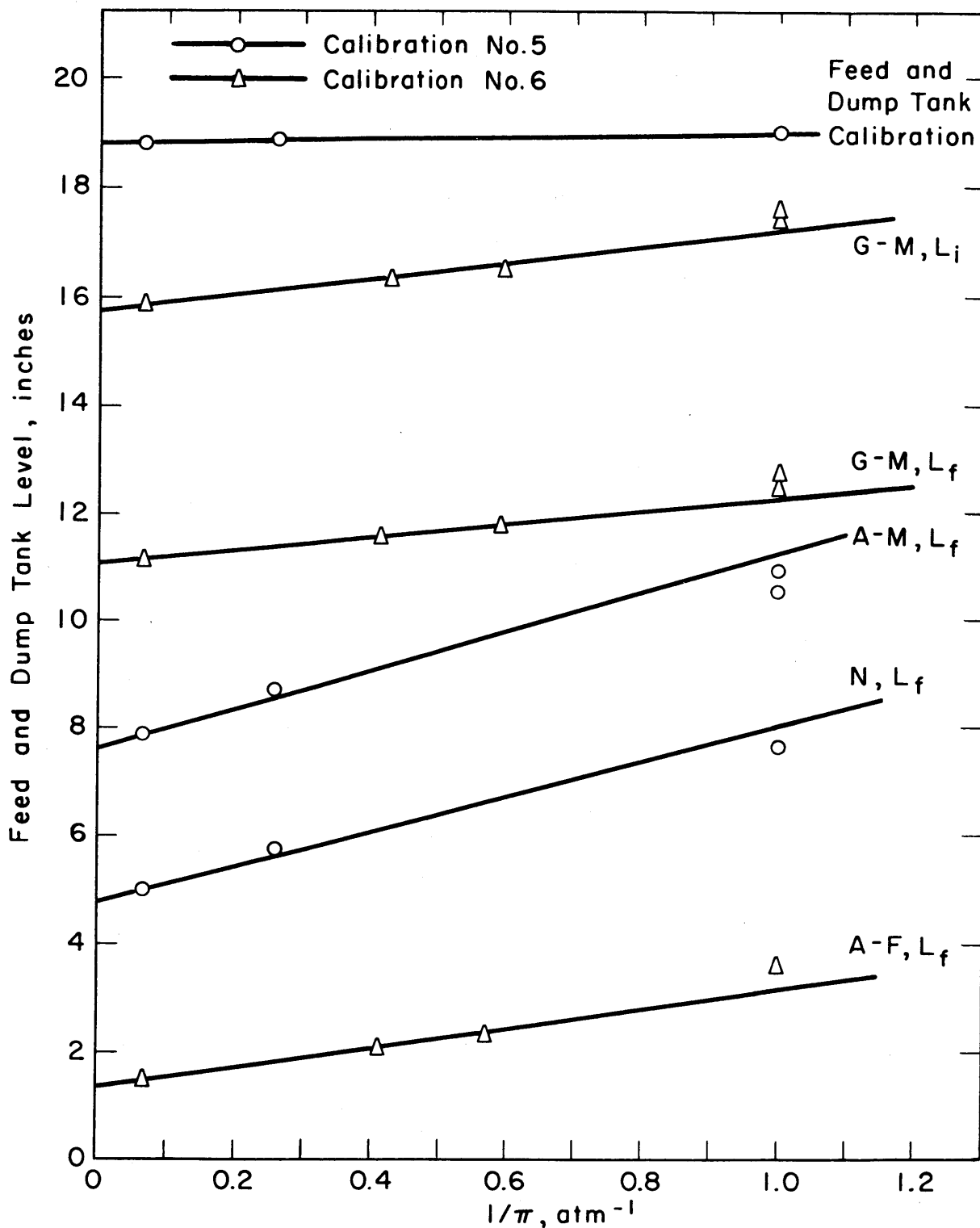


FIG. A3.45 VOLUME MEASUREMENT, RUNS No. 5 and 6, PLUS FEED AND DUMP TANK CALIBRATION  
 $L_i$  = INITIAL LIQUID LEVEL,  $L_f$  = FINAL LIQUID LEVEL, SEE TABLE A3.5 FOR VOLUMES  
 CORRESPONDING TO LETTERS

TABLE A3.7  
SUMMARY OF RESULTS OF VOLUME CALIBRATION  
OF HYDRAULIC CONSOLE

(A) Vol. A through M

CALIBRATION RUN NO.	VOL. DESIGNATION	VOLUME cm <sup>3</sup>	TOTALS
3 and 4	A	258	A through F
	B	509	3960
	C	422	G through M
	D	199	1139
	E	1286	A through M
	F	1286	5099
	G	172	
	H	122	
	I	118	
	J	164	
	K	191	
	L	181	
	M	191	
5	A through M	5020	A through M 5020
6	A through F G through M	3900 1050	A through M 4950

Avg = 5020 ml

(B) Vol. N, O, P, QCalibration 5 gave: N = 641 cm<sup>3</sup>Calculated Vol. of Bypass O = 33 cm<sup>3</sup>N-O = 608 cm<sup>3</sup>Calculations gave: P = 106  
Q = 465(C) Best Estimate of Volumes

The volumes for equivalent sections of flow path 1 and flow path 2 are assumed equal as the difference is generally within the experimental error.

VOLUME DESIGNATION	VOLUME cm <sup>3</sup>
A	256
B or C - Filter With Element	420
Filter Without Element	506
D	198
E or F - Pump	1260
G	169
H or I - Flowmeter	118
J	161
K or L - Test Heater	183
M	188
N-O	608
P	106
Q	465

Total vol. = 4132 ml  
for one flow path  
only not including  
surge tank

console inlet-outlet to the in-pile section header at the vertical center of the reactor, P, from value 27 to the surge tank and O, the bypass, were not measured but were calculated from the total length of tubing and tube size as indicated below:

## (i) Volume Q

$$\text{Tube OD} = 7/16 \text{ inch}$$

$$\text{Tube wall} = 0.049 \text{ inch}$$

$$\text{Tube ID} = 0.3395 \text{ inch}$$

$$\text{Volume/length} = 1.48 \text{ cm}^3/\text{inch}$$

$$\text{Length} = 2(157) = 314 \text{ inches}$$

$$\text{Tube volume, Q} = (1.48)(314) = 465 \text{ cm}^3$$

## (ii) Volume P

$$\text{Tube OD} = 7/16 \text{ inch}$$

$$\text{Tube wall} = 0.049 \text{ inch}$$

$$\text{Tube ID} = 0.3395 \text{ inch}$$

$$\text{Volume/length} = 1.48 \text{ cm}^3/\text{inch}$$

$$\text{Length} = 41 \text{ inches}$$

$$\text{Volume} = 61 \text{ cm}^3$$

$$1 \text{ Downstream}^{(1)} \text{ side of value} = 45 \text{ cm}^3.$$

$$\text{Volume, P} = 106 \text{ cm}^3$$

## (iii) Bypass

$$\text{Tube OD} = 0.500 \text{ inch}$$

$$\text{Tube wall} = 0.049 \text{ inch}$$

$$\text{Tube ID} = 0.402 \text{ inch}$$

$$\text{Volume/length} = 2.08 \text{ cm}^3/\text{inch}$$

$$\text{Length} = 16 \text{ inches}$$

$$\text{Volume, O} = 33 \text{ cm}^3$$

## A3. 6. 3 Volume of In-Pile Section

The in-pile volume was determined by calculation from the tube sizes

---

(1) See Appendix A5.7

used in the in-pile section and was checked by measuring the total volume with acetone.

(1) Calculation of In-Pile Volume

The volume of the in-pile section of the loop was calculated, starting from the inside bottom of the irradiation capsule; reference is made to Figure 3. 8 of Chapter 3 for a drawing of the in-pile section.

- (a) Volume, bottom of capsule to tip of T-C well (1/2 inch from inside bottom)

$$\text{Capsule OD} = 0.875 \text{ inch}$$

$$\text{Wall} = 0.035 \text{ inch}$$

$$\text{ID} = 0.805 \text{ inch}$$

$$\text{Volume of capsule/inch} = (\pi/4)(0.805)^2(1)(16.4) = 8.35 \text{ cm}^3/\text{inch}$$

$$\text{T-C well OD} = 0.125 \text{ inch}$$

$$\text{Length} = 1/2 \text{ inch}$$

$$\text{Volume/inch} = (\pi/4)(0.125)^2(1)(16.4) = 0.20 \text{ cm}^3/\text{inch}$$

$$\text{Net volume/inch} = 8.35 - 0.20 = 8.15 \text{ cm}^3/\text{inch}$$

$$\frac{\text{Volume}}{-13-1/16 \text{ inch to } -12-9/16 \text{ inch}} = (8.15)(0.500) = 4.07 \text{ cm}^3 \text{ total}$$

- (b) Volume, end of T-C well to bottom of inlet tube (3/4 inch from inside bottom)

$$\frac{\text{Volume}}{-12-9/16 \text{ inch to } -12-5/16 \text{ inch}} = (8.35)(1/4) = 2.09 \text{ cm}^3$$

- (c) Volume, bottom of inlet tube to lower spacer bottom (1-1/4 inch from inside bottom)

Volume of inlet tube metal/inch:

$$\text{OD} = 0.375 \text{ inch}$$

$$\text{Wall} = 0.020 \text{ inch}$$

$$\text{ID} = 0.335 \text{ inch}$$

$$\text{Volume} = \frac{\pi}{4} [0.375^2 - 0.335^2] (1)(16.4) = 0.332 \text{ cm}^3/\text{inch}$$

$$\text{Net volume /inch} = 8.35 - 0.33 = 8.02 \text{ cm}^3/\text{inch}$$

$$\frac{\text{Volume}}{-12-5/16 \text{ inch to } -11-13/16 \text{ inch}} = (8.02)(0.5) = 4.01 \text{ cm}^3$$

- (d) Volume, bottom of spacer to top of spacer (1.328 inch from inside bottom)

$$\text{Spacer thickness} = 0.078 \text{ inch}$$

$$\text{Hole size} = 3/32 \text{ inch diameter}$$

$$\text{Hole spacing} = 1/8 \text{ inch center to center}$$

$$\% \text{ free area} = \left[ \left( \frac{\pi}{4} \right) \left( \frac{3}{32} \right)^2 \div \left( \frac{1}{8} \frac{\sqrt{3}}{2} \right) \right] 100 = 51.0\%$$

$$\begin{aligned} \text{Net volume/inch} &= \left( \frac{\pi}{4} \right) (0.335)^2 (1)(16.4) + \left( \frac{\pi}{4} \right) (\overline{0.805}^2 - \overline{0.375}^2) \cdot \\ &\quad \cdot (1)(16.4)(0.510) \\ &= 4.77 \text{ cm}^3/\text{inch} \end{aligned}$$

$$\frac{\text{Volume}}{-11-13/16 \text{ inch to } -11.734 \text{ inch}} = (4.77)(0.078) = 0.37 \text{ cm}^3$$

- (e) Volume, top of lower spacer to bottom of upper spacer (24.172 inch from inside bottom)

$$\frac{\text{Volume}}{-11.734 \text{ inch to } +11.110 \text{ inch}} = (8.02)(22.844) = 183.1 \text{ cm}^3$$

- (f) Volume, bottom of upper spacer to top of upper spacer (24.250 inch from inside bottom)

$$\frac{\text{Volume}}{+11.110 \text{ inch to } 11.188 \text{ inch}} = 0.37 \text{ cm}^3$$

- (g) Volume, top of upper spacer to inside capsule top (25.625 inch from inside bottom)

$$\frac{\text{Volume}}{+11.188 \text{ inch to } +12.563 \text{ inch}} = (8.02)(1.375) = 11.01 \text{ cm}^3$$

- (h) Volume, capsule to header

$$\text{Volume inside } 3/8 \text{ inch tube} = (\pi/4)(0.335)^2(1)(16.4) = 1.44 \text{ cm}^3/\text{in.}$$

Volume in outer annulus:

$$\text{OD} = 0.625 \text{ inch}$$

$$\text{Wall} = 0.049 \text{ inch}$$

$$\text{ID} = 0.527 \text{ inch}$$

$$\text{Volume} = (\pi/4)(\overline{0.527}^2 - \overline{0.375}^2)(1)(16.4) = 1.77 \text{ cm}^3/\text{in.}$$

$$\text{Total volume/inch} = 3.21 \text{ cm}^3/\text{inch}$$

Total vertical length, inside top of capsule to inside bottom of header = 87-1/16 inch from loop drawings. Allow 2 inches for spiral of tubes in concrete shield.

Volume, inside top of capsule to inside bottom of header  
 = (89)(3.21) = 286 cm<sup>3</sup>

(i) Volume, header (approximate volume only):

$$\begin{aligned} \text{Volume} &= \left[ \left( \frac{\pi}{4} \right) \left( \frac{7}{8} \right)^2 \left( \frac{25}{32} + \frac{1}{2} \right) \right] \\ &\quad - \left[ \frac{\pi}{4} (0.620)^2 \left( \frac{3}{16} \right) + \frac{\pi}{4} (\overline{0.620^2} - \overline{0.350^2}) \left( \frac{13}{16} \right) \right. \\ &\quad \quad \left. - \frac{\pi}{4} (\overline{0.339^2}) \left( \frac{0.620 - 0.332}{2} \right) \right] \\ &\quad - \left[ \left( \frac{\pi}{4} \right) (\overline{0.375^2} - \overline{0.335^2}) \left( \sim \frac{1}{2} \right) \right] \\ &\quad - \left[ \left( \frac{\pi}{4} \right) (\overline{0.4375^2} - \overline{0.3395^2}) \left( \sim \frac{1}{4} \right) \right] \text{ in.}^3 \\ &\cong 8.7 \text{ cm}^3 \cong 9 \text{ cm}^3 \end{aligned}$$

The variation of the volume per inch with position relative to the center of the core is given in Figure 3.23 of Chapter 3. The total in-pile section volume is given in Table A3.8.

(2) Measurement of Total In-Pile Volume Including Header

In the measurement of the volume, 102 inches of 7/16 inch OD X 0.049 inch wall tubing was connected to the in-pile section.

Volume/inch =  $(\pi/4)(0.3395)^2(1)(16.4) = 1.48 \text{ cm}^3/\text{inch}$

Tubing volume =  $(102)(1.48) = 151 \text{ cm}^3$

Average total volume measured =  $640 \text{ cm}^3$

Volume of in-pile section =  $640 - 151 = 489 \text{ cm}^3$

Summary: Volume measured =  $489 \text{ cm}^3$

Volume calculated =  $500 \text{ cm}^3$

Discrepancy = 2%



Agreement between the measured and calculated in-pile volume is within the experimental and calculational errors.

Table A3. 8. Total In-Pile Volume

Capsule	4.07
	2.09
	4.01
	0.37
	183.1
	0.27
	<u>11.01</u>
	205.02 $\equiv$ 205 cm <sup>3</sup> $\pm$ 2 cm <sup>3</sup>
Inside top of capsule to inside bottom of header	286
Header	<u>9</u>
Total	500 cm <sup>3</sup> $\pm$ 10 cm <sup>3</sup>

## APPENDIX 4. 1

ENERGY ABSORBED OR GENERATED IN THE ORGANIC SAMPLES  
BECAUSE OF CHEMICAL CHANGES

Under irradiation, chemical changes take place in the three organic materials used in this experiment. Depending on whether the products formed are more or less stable than the undegraded material, energy in the form of sensible heat is released or removed from the organic material. This effect could introduce an error in the measured dose rate, since the heating rate is the measured quantity in the measurement.

Chemical bond energies are generally of the order of 5 ev or less per chemical bond. This value is an upper limit on the energy effects due to chemical reactions. If stable end products are formed having a bond energy close to that of the undegraded material, the energy involved per chemical reaction will be much less. For polystyrene, Bovey (A4. 1) reports that about 600 to 800 ev of energy are absorbed per cross link between molecules and 3000 to 4000 ev per scission of a polymer molecule. For this material, chemical effects involving energies of the order of 5 ev or less are insignificant compared to the total energy absorbed and released as thermal energy.

The case of polyethylene and Santowax OMP is somewhat questionable. Bovey (A4. 1) reports for polyethylene that probably 100 ev are absorbed per cross link produced and 31 to 55 ev for each scission. For pure Santowax OMP, it has been found in the present experiment that approximately 0.3 molecules are changed per 100 ev of energy absorbed. A chemical energy effect of 5 ev could result in an error of approximately 15 per cent in the measured heating rate for polyethylene and 1.5 per cent in the case of Santowax OMP. However, the results obtained with polyethylene have, in general, been in good agreement with the polystyrene results, indicating that the effect is much smaller than indicated above; probably stable products are formed which are chemically quite similar

to the original material so that the energy involved per chemical event is much less than 5 ev. The results obtained from Santowax OMP have been consistently high relative to the polystyrene and polyethylene results; it is believed this discrepancy is due to an inaccuracy in the heat capacity measurement for Santowax OMP rather than chemical effects.

The conclusion that the effect of chemical changes on the thermal energy liberated in an organic material on irradiation is insignificant is supported by Dyne and Thurston (A4. 2) who state: "Even when there is appreciable radiation damage, not more than 0.1 per cent of the energy is ever stored in structural alterations".

#### APPENDIX 4. 2

#### SOURCES OF FAST NEUTRON AND GAMMA RADIATION AND THEIR TIME VARIATION AFTER STARTUP OF A NUCLEAR REACTOR

A total of  $204 \pm 7$  Mev of energy is released per fission. Weinberg and Wigner (A4. 3) give the following values for the different contributions:

Kinetic energy of fission fragments	$167 \pm 6$ Mev
Prompt gamma radiation	$6 \pm 1^{(1)}$
Kinetic energy of fission neutrons	$5 \pm 1$
Fission product decay gamma radiation	$6 \pm 1^{(1)}$
Fission product decay beta radiation	$8 \pm 1.5$
Neutrinos	<u><math>12 \pm 2.5</math></u>
	$204 \pm 7$ Mev

The fission fragments are stopped in the fuel plates and therefore do not contribute to the dose rate. Prompt and delayed gamma radiations reach the organic material. The decay beta radiation cannot reach the organic material since its range is insufficient to traverse the aluminum,  $D_2O$ , and stainless steel between the fuel plates and the organic. However, Fischer (A4. 4) has estimated that 1/2 Mev of the 8 Mev of beta radiation might appear as bremsstrahlung radiation which could be absorbed in the organic material. In addition to these radiations, radiation from thermal

---

(1) To the gamma energies listed should be added about 7 Mev/fission due to (n,  $\gamma$ ) reactions.

neutron activation of materials such as the stainless steel capsule and aluminum thimble will contribute to the dose rate, although the contribution will generally be much smaller than radiations coming from the fission process.

Of these various radiations, the dose rate due to fission and scattered neutrons and to the prompt gamma radiation emitted will be directly proportional to the reactor power level. The dose rate due to fission product decay gamma radiation will be dependent on the previous operating history of the reactor. However, most of the fission products have a short half-life and Goldstein (A4. 5) has estimated that three-fourths of the 6 Mev due to fission product decay is released within 1/2 hour after the fission event. It is thus seen that, assuming the fast neutron dose rate to be one-third of the total, approximately two-thirds of the total dose is proportional to the reactor power. If 75 per cent of the remaining one-third due to fission product decay has been added after 1/2-hour operation, the dose rate has reached approximately 92 per cent of its total value, assuming the reactor was operating at equilibrium with all fission products. This equilibrium condition is never reached in the MITR as the reactor is operated only 4-1/4 days/week so that equilibrium of the fission product build-up and decay is never reached.

The time behavior of the gamma dose rate is indicated in Figure A4. 1, where 50 per cent of the equilibrium dose is assumed due to prompt gammas and 50 per cent due to fission product decay gammas. The calculations are based on the expression given by Weinberg and Wigner (A4. 3) for gamma radiation from decay of fission products over the time interval of 1 sec to  $10^5$  sec after the fission event where  $t$  is the time in seconds after the fission:

$$E(t) = 1.40t^{-1.2} \text{ Mev/sec} \quad (\text{A4. 1})$$

For comparison with the  $6 \pm 1$  Mev given above, integration of this expression from 1 sec to  $10^5$  sec gives a total emitted gamma energy of 6.29 Mev per fission. Now, let  $T$  = time of reactor operation

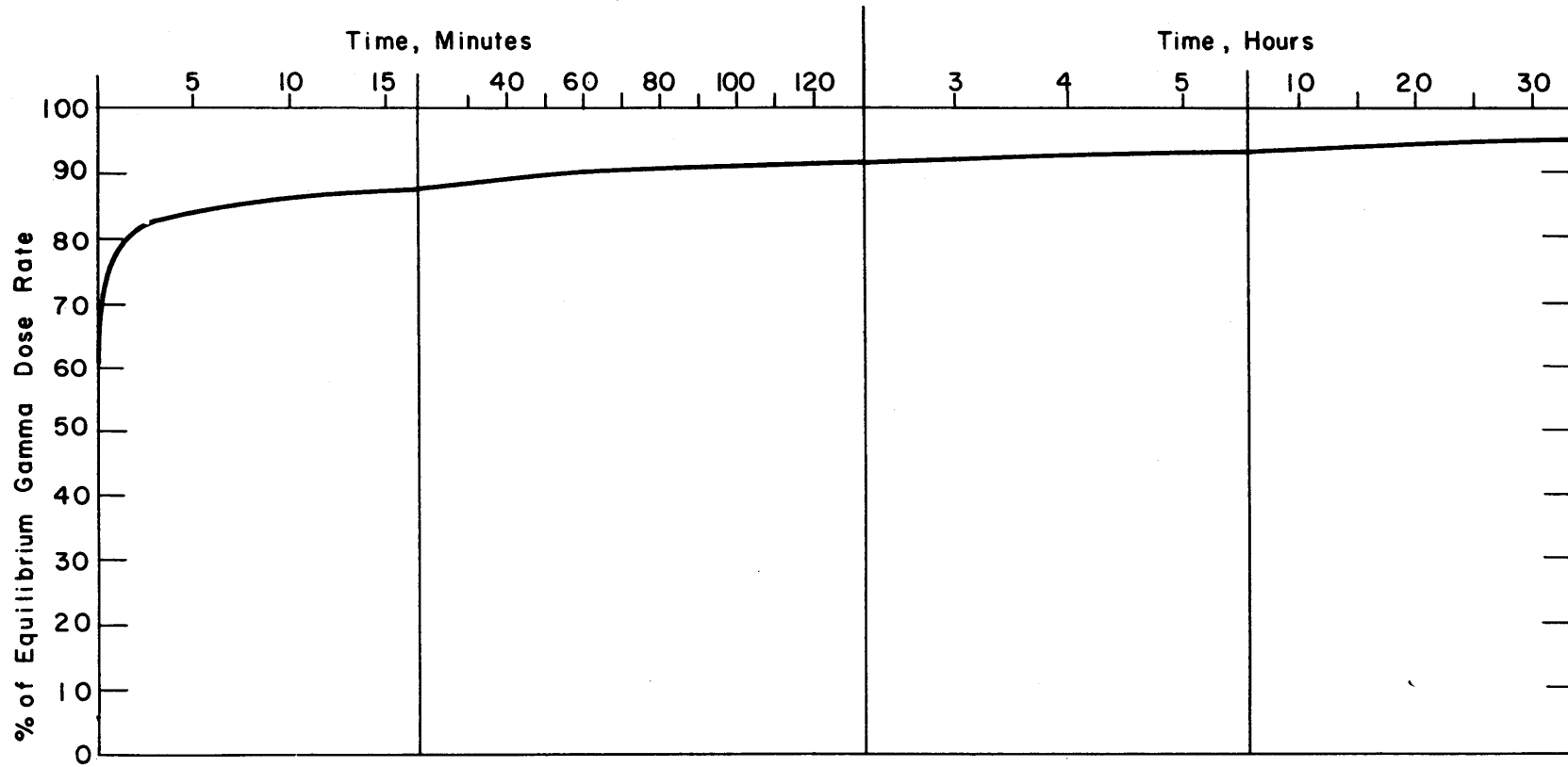


FIGURE A4.1 PERCENTAGE OF EQUILIBRIUM GAMMA DOSE RATE AS A FUNCTION OF TIME AFTER REACTOR STARTUP

after startup and  $F_0$  the fission rate in fissions/sec. The decay time at  $T$  of fission products formed at time  $t$  is then  $T-t$  and the release rate from these fission products formed over a time interval  $dt$  is

$$E(T-t) F_0 dt \quad (\text{A4. 2})$$

Integrating from 0 to  $T$  gives for  $H(T)$ , the energy emission rate at  $T$ ,

$$\begin{aligned} H(T) &= F_0 \int_0^T E(T-t) dt \frac{\text{Mev}}{\text{sec}} \\ &= F_0 \int_0^{T-1} 1.40(T-t)^{-1.2} dt + F_0 \int_{T-1}^T E(T-t) dt \end{aligned} \quad (\text{A4. 3})$$

Now, the last integral represents the contribution due to very short-lived fission products and hence should be a constant for all  $T$ 's. Hence,

$$\begin{aligned} H(T) - C &= F_0 \int_0^{T-1} 1.40(T-t)^{-1.2} dt \\ &= 7.00 F_0 [1 - T^{-0.2}] \frac{\text{Mev}}{\text{sec}} \end{aligned} \quad (\text{A4. 4})$$

The value of the constant  $C$  representing the fission products formed during the second before  $T$  is difficult to estimate accurately and is probably included, in any case, as a contribution to the prompt fission gammas. It should be noted that integration of Equation (A4. 1) from 1 to 2 seconds gives an emission of 0.9 Mev, compared to the total of 6.29 Mev over the period of 1 to  $10^5$  seconds. In obtaining Figure A4. 1,  $C$  was assumed to be included with the prompt fission gammas, since the fission product gammas are given as  $6 \pm 1$  Mev in agreement with the 6.29 Mev obtained by integration; the long-lived contributors were also neglected since they add only a small percentage to the total gamma dose rate.

It is thus seen that, assuming a constant reactor power and constant fission rate in all fuel elements, a small weekly variation

in the gamma dose rate can be expected, particularly in the first day of operation after the weekend shutdown; the fast neutron dose rate should be constant and independent of time under these conditions except as influenced by changes in the thermal flux or reactor power. In general, the variation in the dose rate is small enough to be neglected in determining the dose rate in the organic material and has not been detected in the calorimeter measurements made between 1/2 hour and 10 hours after reactor startup, the variation in the dose rate evidently being less than the experimental standard deviation of the measurements.

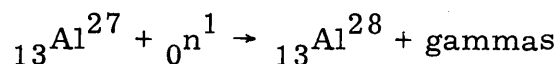
### APPENDIX 4. 3

#### ESTIMATION OF BETA AND GAMMA ENERGY ABSORBED IN THE CALORIMETER SAMPLES DUE TO THERMAL NEUTRON REACTIONS (Based on Calculations by Turrichia (A4. 6))

Thermal neutrons do not contribute directly to the energy generation rate in a material. When a thermal neutron is captured by the material, however, beta and gamma radiation may be produced which can be totally or partially absorbed in the material, resulting in the generation of thermal energy. To obtain the desired energy generation rate due only to fast neutron and gamma radiation from the reactor, the energy released as the result of these thermal neutron interactions in the samples must be subtracted from the total measured energy generated. This appendix presents the method of calculation and the results as developed by Turrichia (A4. 6).

#### A4. 3. 1 ALUMINUM

The capture cross section of  $\text{Al}^{27}$  (which comprises 100 per cent of natural aluminum) is 0. 23 barns for 2200 meter/sec neutrons. The reaction is:



The Q value for this reaction is 7. 724 Mev and the energy of the capture

gamma rays emitted can vary from almost zero up to the Q value. Troubetzkoy and Goldstein (A4. 7) present a tabulation of the gamma rays emitted from thermal neutron capture in which the number of photons emitted in different energy intervals is given; they also indicate that approximately 2 photons are emitted per thermal neutron capture.

In addition to this radiation, the isotope,  $\text{Al}^{28}$ , produced by the reaction also decays with a half-life of 2.3 minutes by an allowed beta transition plus gamma emission. The gamma ray energy is 1.8 Mev and the maximum and average energies of the beta particles are 2.87 Mev and 1.26 Mev, respectively.

The gamma radiation produced directly by the  $n, \gamma$  reaction builds up immediately when the sample is placed in a thermal neutron flux and is constant throughout an experiment. The beta and gamma radiation from decay of  $\text{Al}^{28}$  build up asymptotically with time as  $A_0(1 - e^{-\lambda t})$  where  $A_0$  is the equilibrium activity,  $\lambda$  is the decay constant for  $\text{Al}^{28}$ , and  $t$  is the time after the absorber was placed in the neutron flux. These different sources will now be considered separately.

#### (1) Absorption of Capture Gamma Radiation in Aluminum Absorber

Henderson and Whittier (A4. 8) have reported the fraction of gamma energy escaping from an infinite cylinder and from a sphere, both of which have a uniformly distributed internal source. The results are presented as a function of  $\mu R$  where  $R$  is the radius and  $\mu$  the attenuation coefficient. Calculations for an infinite cylinder with a radius of 1/4 inch (0.635 cm) and for an equivalent sphere having the same volume as the calorimeter samples (diameter = 0.987 cm) give close agreement with respect to the fraction of energy escaping. In estimating the fraction of energy escaping, the total linear energy absorption coefficient,  $\mu_a$ , rather than the total linear attenuation coefficient,  $\mu_0$ , has been used since it is believed this factor gives a better estimate of the fraction of scattered plus unscattered gamma energy



escaping from the sample. The calculations are summarized in Table A4. 1. The number of photons emitted per energy interval as given by Troubetzkoy and Goldstein have been arbitrarily adjusted so that the summation of the products of the average energy for each energy interval and the number of photons emitted in that energy interval add up to approximately the Q value of the reaction. The energy absorbed in each energy interval is taken as the product of the average energy and the energy absorption coefficient based on that energy. It is seen that an estimated 4. 5 per cent of the gamma energy generated is absorbed in the aluminum sample.

The total energy released per unit thermal flux per gram of aluminum is:

$$E = \frac{N}{A_{Al}} \sigma_{2200} \frac{\Sigma n E_{avg}}{100} = \frac{6.025 \times 10^{23}}{26.98} (0.23 \times 10^{-24}) (7.73) (1.6 \times 10^{-13})$$

$$= 6.35 \times 10^{-15} \frac{\text{watt sec cm}^2}{\text{gm}}$$

The energy absorbed per unit flux is then

$$(0.045) (6.35 \times 10^{-15}) = 2.86 \times 10^{-16} \frac{\text{watt sec cm}^2}{\text{gm}}$$

For a thermal flux of  $1.41 \times 10^{13}$  n/cm<sup>2</sup>-sec (approximate center of core at 1.00 MW), the energy absorbed is 0.00403 watts/gm which is about 1.7 per cent of the total dose rate in aluminum.

## (2) Absorption of 1.8 Mev Gamma from Al<sup>28</sup> Decay

Following the same calculational procedure as in part 1 of this appendix, the following values are obtained for the 1.8 Mev gamma at equilibrium:

$$E = 1.48 \times 10^{-15} \frac{\text{watt sec cm}^2}{\text{gm}} = \text{total energy emitted at equilibrium per unit thermal flux.}$$

$$\mu_a = (0.023) (2.7) = 0.062 \text{ cm}^{-1}$$

TABLE A4.1  
 CALCULATION OF FRACTION OF GAMMA ENERGY  
 LIBERATED BY THERMAL NEUTRON CAPTURE WHICH IS  
 ABSORBED BY THE ALUMINUM SAMPLE

ENERGY INTERVAL MEV	n, GAMMAS EMITTED PER 100 CAPTURES	TOTAL ENERGY OF GENERATED GAMMAS (n E <sub>AVG</sub> ) MEV	$\mu_a$ , cm <sup>-1</sup>	$\mu_a R$	P, FRACTION OF ENERGY ESCAPING	GAMMA ENERGY CAPTURED (1-P)(n E <sub>AVG</sub> ) Mev
7-9	20.5	155	0.050	0.0493	0.96	6
5-7	14.6	88	0.051	0.0503	0.96	4
3-5	40	160	0.054	0.0533	0.96	6
2-3	41	107	0.060	0.0592	0.95	5
1-2	95	143	0.067	0.0660	0.95	7
1	240	120	0.079	0.0780	0.94	7
		773				35

% of Energy Liberated which is absorbed =  $\frac{35}{773} = 4.5\%$ .

For a cylinder,  $R = 0.635$  cm  
 $\mu_a R = 0.0394$   
 $P \cong 0.95 =$  fraction escaping

For a sphere,  $R_{\text{eff}} = 0.987$  cm  
 $\mu_a R = 0.0611$   
 $P \cong 0.95$

Hence, the energy absorbed at equilibrium for a unit flux is

$$(1-0.95)(1.48 \times 10^{-15}) = 7.4 \times 10^{-17} \text{ watt-sec-cm}^2/\text{gm}.$$

For a thermal flux of  $1.41 \times 10^{13}$  n/cm<sup>2</sup>-sec, the energy absorbed is 0.00104 watts/gm which is about 0.45 per cent of the total dose rate.

### (3) Absorption of Beta Radiation from Al<sup>28</sup> Decay

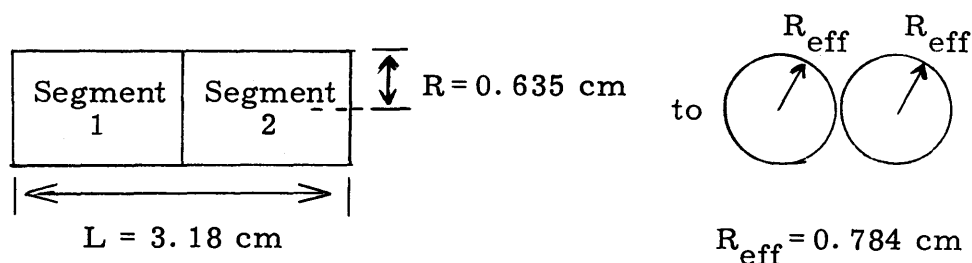
Hine and Brownell (A4.9) have reported calculations for a sphere of the ratio of the average dose rate in the sphere to the dose rate at the center of the sphere. The results are presented as a function of  $\sqrt{R}$  where  $\sqrt{\phantom{x}}$  is an experimentally determined attenuation coefficient and  $R$  is the sphere radius. The data presented are based on an infinite and homogeneous medium containing a small spherical volume of the same composition with a uniform distribution of activity.

In the present case, the internal absorption in a finite cylinder is desired. To use the calculations presented by Hine and Brownell, it has been assumed that the internal absorption in a sphere having the same volume as the cylindrical sample is the same as in the cylindrical sample. For calorimeters III and II, the effective radii are 0.987 cm and 1.046 cm, respectively. These radii are longer than the range of a 2.87 Mev beta particle in aluminum so that the dose rate at the center of the sphere is the same as the energy generation rate.

The absorption coefficient,  $\sqrt{\phantom{x}}$ , for an allowed beta transition has been calculated as  $3.92 \text{ cm}^2/\text{g}$ , using the relation

$\nu = \frac{16.3}{(E_0 - 0.036) 1.37} \text{ cm}^2/\text{gm}$  for aluminum (A4.9). With this  $\nu$  and the radii above, the fraction of energy liberated in the sample which is absorbed is 86 per cent for calorimeter III and 87 per cent for calorimeter II.

As a check on the assumption of a sphere having the same volume as the sample, the calculation was repeated by dividing the volume into two spheres of the same size, the radius of each for calorimeter III being 0.784 cm:



For the two spheres, the calculated fraction absorbed is 83 per cent. This represents an underestimation since part of the energy released by one sphere is absorbed by the other. The fraction of the total energy escaping (17 per cent) from one sphere which was intercepted by the other is estimated for each segment as the ratio for the cylindrical sample of the area shared by the two segments to the total surface area of that segment. This ratio is

$$\frac{\pi(0.635)^2}{\frac{3.18}{2} (2\pi)(0.635) + 2[\pi(0.635)^2]} = 0.143 = 14.3\%.$$

The fraction of the 17% of the total energy escaping from both absorbers which is intercepted and absorbed is then  $[17\%][2(0.143)] = 4.86\%$ . The total fraction escaping then is  $83\% + 5\% = 88\%$ , which is in reasonable agreement with the calculation based on one sphere.

The above calculations are for the case where the spherical source is assumed to be an infinite medium having the same composition as the

source. The calculation thus includes back-scattered radiation from the surroundings. In the actual case, a vacuum separates the aluminum absorber and the aluminum sheath, so that this condition is not exactly met. However, back-scattered beta radiation from the aluminum capsule should be approximately the same as if the sample were immediately surrounded by aluminum.

The value of 88% was used as the fraction of the released beta energy which was absorbed. The energy absorbed per unit flux at equilibrium is given below.

$$\begin{aligned} \text{Energy released} &= \frac{N}{A_{Al}} \sigma_{2200} \bar{E}_{\beta} \\ \text{Energy absorbed} &= 0.88 \left[ \frac{N}{A_{Al}} \sigma_{2200} \bar{E}_{\beta} \right] \\ &= 0.88 \left[ \left( \frac{6.025 \times 10^{23}}{26.98} \right) (0.23 \times 10^{-24}) (1.26) (1.60 \times 10^{-13}) \right] \\ &= 9.12 \times 10^{-16} \text{ watt sec cm}^2/\text{gm}. \end{aligned}$$

For a thermal flux of  $1.41 \times 10^{13}$  n/cm<sup>2</sup>-sec, the dose rate due to the beta particles emitted at equilibrium is 0.0129 watt/gm, or approximately 5.5 per cent of the total dose rate.

#### (4) Summary

Combining all three effects, the total energy absorption rate due to thermal neutron capture in aluminum at a 2200 meter/sec thermal flux of  $1.41 \times 10^{13}$  n/cm<sup>2</sup>-sec is:

$$R_{Al}^{th} = 0.00403 + 0.0139(1 - e^{-0.30t}) \text{ watt/gm} \quad (\text{A4.5})$$

where  $t$  is the time in minutes after starting irradiation. At saturation,  $R_{Al}^{th}$  is about 8 per cent of the total energy absorption rate at the center of the core. This result was changed by the ratio of the thermal flux at any position to  $1.41 \times 10^{13}$  to obtain  $R_{Al}^{th}$  for that position.

Anderson and Waite (A4. 10) have calculated the energy due to thermal neutron capture for an aluminum sample 2. 54 cm long  $\times$  1. 27 cm diameter. They used approximately the same procedure for gamma radiation as used here, but used equations derived by Richard and Rubin (A4. 11) for the absorption of beta radiation. Their results at saturation are compared in Table A4. 2 with the values calculated in this section at a flux of  $1. 41 \times 10^{13}$  n/cm<sup>2</sup>-sec. The gamma results agree almost perfectly, whereas the beta absorption calculated by Turrichia is 18 per cent larger than that calculated by Anderson and Waite. Considering the approximations involved in the calculations, this agreement is satisfactory.

Table A 4. 2

Energy Absorption from Beta and Gamma Radiation in Aluminum Sample from Thermal Neutron Capture,  $\phi_{2200} = 1. 41 \times 10^{13}$  n/cm<sup>2</sup>-sec.

	Energy Absorbed, watt/gm		
	Gamma	Beta	Total
Calculated in this appendix	$0. 51 \times 10^{-2}$	$1. 29 \times 10^{-2}$	$1. 80 \times 10^{-2}$
Calculated by Anderson and Waite (A4. 10)	$0. 50 \times 10^{-2}$	$1. 09 \times 10^{-2}$	$1. 59 \times 10^{-2}$

It is believed the calculations presented here are accurate to about  $\pm 15\%$ . The maximum error which could be introduced in the net fast neutron and gamma dose rate by this uncertainty is  $[8\%][\pm 0. 15] = \pm 1. 2\%$  based on a saturation activity of Al<sup>28</sup> and an 8% contribution by thermal neutron capture to the total dose rate. This error is based on subtracting the saturation value due to thermal neutron capture from the total aluminum dose rate. Actually, the Al<sup>28</sup> activity never reaches saturation since the aluminum temperature curve generally crosses the wall temperature approximately 2 to 3 minutes after the start of an irradiation; hence, the error introduced can conservatively be given as  $\pm 1. 0\%$ .

### A4. 3. 2 PLASTIC AND BERYLLIUM ABSORBERS

Hydrogen has a thermal absorption cross section for 2200 meter/sec neutrons of 0.332 barns. The  $(n, \gamma)$  reaction emits a 2.2 Mev gamma ray. Calculations by Turrìchia (A4. 6), using the same procedure as for aluminum, indicate that the energy absorbed in polyethylene (which has the highest hydrogen density) due to these gammas is less than one per cent of the total dose rate; this correction has been neglected in the calculations. The thermal absorption cross sections of carbon and beryllium are low enough so that neutron capture in these materials can be neglected.

## APPENDIX 4. 4

### ASSUMPTION OF ONLY COMPTON SCATTERING OF GAMMA RADIATION IN CALORIMETER EXPERIMENT

It has been assumed in estimating the relative gamma energy absorption rates in the different materials that the energy absorbed due to photo-electric and pair production interactions are small compared to the energy absorbed by Compton scattering interactions, so that the ratio of gamma dose rates in different materials to that in aluminum,  $R^\gamma / R_{Al}^\gamma$ , can be represented by  $(Z/A) / (Z/A)_{Al}$  (see section 4. 2. 4). This assumption has been based on the fact that for low  $Z$  materials, the Compton interaction is the predominant mode over a large range of gamma energies. For example, in Table A4. 3, the energies at which the photoelectric ( $\tau$ ) and pair production ( $\kappa$ ) linear attenuation coefficients are equal to the Compton attenuation coefficient ( $\sigma$ ) are given; between the energies listed, Compton interactions are the predominant, and except at energies near those listed, the controlling mode. The energy range of Compton predominance is reduced slightly if the energy absorption coefficient, instead of the total attenuation coefficient, is compared. However, in any event, it is seen that Compton interactions are predominant over a large range of gamma energies.

To estimate quantitatively the maximum error involved in assuming

Table A4. 3

The Energies ( $E_{1/2}$ ) at Which the Photoelectric ( $\tau$ ) and Pair Production ( $\kappa$ ) Linear Attenuation Coefficients are Equal to the Compton Coefficient ( $\sigma$ ). Between the energies listed, Compton interactions are the Predominant Mode (A4. 5).

Z	Element	$E_{1/2}$ , Mev $\tau = \sigma$	$E_{1/2}$ , Mev $\sigma = \kappa$
1	Hydrogen	$10^{-4}$	78
4	Beryllium	0.011	35
6	Carbon	0.016	28
13	Aluminum	0.046	15

that only Compton interactions occur, calculations of the relative energy absorbed in hydrogen, carbon, and aluminum have been made using published gamma ray spectra for the fission process. The gamma energy absorbed in any material can be written as:

$$R^{\gamma} = \int_0^{\infty} g(E) I(E) E \left[ \frac{\tau_a}{\rho} + \frac{\sigma_a}{\rho} + \frac{\kappa_a}{\rho} \right] dE \frac{\text{Mev}}{\text{gm-sec}} \quad (\text{A4. 6})$$

where

$g(E)$  = attenuation of gamma rays by aluminum thimble or other material separating samples from radiation source.

$I(E)$  = intensity of the gamma field, photons/cm<sup>2</sup>-sec-Mev.

$\tau_a(E)$  = photoelectric energy absorption coefficient, cm<sup>-1</sup>.

$\sigma_a(E)$  = Compton energy absorption coefficient, cm<sup>-1</sup>.

$\kappa_a(E)$  = pair production energy absorption coefficient, cm<sup>-1</sup>.

$\rho$  = density, gm/cm<sup>3</sup>.

$E$  = photon energy, Mev.

In making calculations using this equation, the gamma ray spectra for prompt fission gamma rays and for short-lived fission product decay



gamma rays presented by Goldstein (A4. 5) have been used. From 1. 0 Mev to 7. 0 Mev, he recommends the following relation for the prompt fission and short-lived fission produce decay gamma radiation:

$$N(E) = 14 e^{-1.10E} \text{ Mev}^{-1} \quad (\text{A4. 7})$$

where

$N(E)$  = number of photons emitted per Mev of energy per fission.

$E$  = gamma energy, Mev.

Below 1. 0 Mev, the spectrum is best represented by the relation:

$$N(E) = 46.9 e^{-2.30E} \text{ Mev}^{-1} \quad (\text{A4. 8})$$

The application of this last equation below approximately 0. 1 Mev is questionable, since the photoelectric absorption coefficient becomes very large below this energy and the gamma spectrum is undoubtedly strongly depressed in this energy region. For example, at 0. 02 Mev, the photoelectric absorption coefficient for aluminum is  $8.1 \text{ cm}^{-1}$  which is equivalent to a mean-free path of only 0. 12 cm in aluminum. Hence, any gamma radiation produced in this energy range should be absorbed very close to its source and the gamma spectrum decreased.

To obtain a conservative upper limit on the error due to photoelectric interactions, Equation (A4. 8) has been assumed to describe the spectrum down to zero energy gamma radiation even though the spectrum will be depressed in this lower energy range. It has also been assumed that the aluminum or stainless steel thimble and the aluminum calorimeter capsule wall provide attenuation of this reactor gamma field. This effect has been included in the calculations by means of an attenuation factor,  $g(E)$ , given in Equation (A4. 6) and defined as (for shields 1 and 2):

$$g(E) \cong \frac{I}{I_0} = e^{-\mu_1 x_1} e^{-\mu_2 x_2} \quad (\text{A4. 9})$$

where  $\mu$  represents the total energy absorption coefficient (which is predominantly the photoelectric effect in this low energy range). Use of this

$g(E)$  provides an effective cutoff of approximately 0.05 Mev on the gamma spectrum to which a sample in the aluminum capsule and stainless steel thimble is exposed.

The results of calculations of the relative energy absorbed due to photoelectric, Compton, and pair production interactions will now be presented for aluminum, hydrogen, and carbon. Energy absorption coefficients tabulated by Evans (A4.12), Kaplan (A4.13), and Davisson and Evans (A4.14) were used with the gamma spectrum given by Equations (A4.7) and (A4.8) to calculate the energy absorbed due to each type of interaction. Graphical integrations of Equation (A4.6) were used in calculations for each type of interaction and for attenuation factors based on (1) attenuation by the aluminum thimble (0.035 inch) and the aluminum capsule (0.10 inch) and (2) attenuation by the stainless steel thimble (0.049 inch) and the aluminum capsule (0.10 inch). In Tables A4.4 and A4.5, the calculations used for the graphical integrations in the case of aluminum samples are presented, Table A4.4 being the calculations for the aluminum thimble and Table A4.5 being the calculations for the stainless steel thimble. The calculated results are plotted in Figures A4.2, A4.3, and A4.4 for energy intervals of 0 to 0.10 Mev, 0.10 to 1.0 Mev, and 1.00 to 7.00 Mev. The areas under these curves are the desired integrals. The integrated values for aluminum are presented in Table A4.6. A summary of similar calculations for hydrogen and carbon (and for polyethylene based on the hydrogen and carbon calculations) is presented in Table A4.7.

It is seen from Table A4.7 that for hydrogen, only 0.2 per cent of the total gamma energy absorbed is due to interactions other than Compton, so that the assumption of only Compton scattering is very good for this material. The assumption is also quite good for carbon since only 1.3 per cent (for the stainless steel thimble) and 1.7 per cent (for the aluminum thimble) are estimated to come from interactions other than Compton scattering. For aluminum, on the other hand, the calculations indicate that 8.9 per cent (for the aluminum thimble) and 4.4 per cent (for the stainless steel thimble) of the gamma

Calculations Made for Graphical Integration to Determine Relative Photoelectron, Compton, and Pair Production Absorption Rates in Aluminum, Attenuation by Aluminum Thimble (0.035 inch wall) and Capsule (0.10 inch wall).

$$R_{Al}^Y(\text{Photo}) \propto \int_0^\infty g(E) I(E) E \frac{\tau_a}{\rho} dE$$

$$R_{Al}^Y(\text{Compton}) \propto \int_0^\infty g(E) I(E) E \frac{\sigma_a}{\rho} dE$$

$$R_{Al}^Y(\text{Pair}) \propto \int_0^\infty g(E) I(E) E \frac{\kappa_a}{\rho} dE$$

$$g(E) = e^{-\mu_{Al} x_1} e^{-\mu_{Al} x_2} = e^{-\mu_{Al} (x_2 + x_1)} = e^{-0.343 \mu_{Al}}$$

where

$$\mu_{Al} = \left[ \frac{\tau_a}{\rho} + \frac{\sigma_a}{\rho} \right] \rho$$

E Mev	g(E)	$N(E) \propto I(E)$	$\frac{\tau_a}{\rho}$	$\frac{\sigma_a}{\rho}$	$\frac{\kappa_a}{\rho}$	$\frac{dR_{Al}^Y(\text{Photo})}{dE}$	$\frac{dR_{Al}^Y(\text{Compton})}{dE}$	$\frac{dR_{Al}^Y(\text{Pair})}{dE}$
		$\frac{1}{\text{cm}^2\text{-Mev-sec}}$	$\text{cm}^2/\text{gm}$	$\text{cm}^2/\text{gm}$	$\text{cm}^2/\text{gm}$	$\frac{1}{\text{cm sec}} \times 10^5$	$\frac{1}{\text{cm sec}} \times 10^5$	$\frac{1}{\text{cm sec}} \times 10^5$
7.0	1.0	0.0063	~0	0.013	0.0061	~0	57	26.9
6.0		0.0193		0.014	0.0052		162	60.2
5.0		0.0574		0.015	0.0043		430	123
4.0		0.172		0.017	0.0032		1170	220
3.0		0.518		0.0195	0.0018		3030	280
2.0		1.55		0.023	$6.21 \times 10^{-4}$		7140	193
1.5		2.68		0.025	$1.59 \times 10^{-4}$		10050	64
1.0		4.69		0.027	$2.79 \times 10^{-5}$		12280	13
0.9		5.90		0.027	~0		14320	~0
0.8		7.45		0.028			16700	
0.7		9.39		0.029			19050	
0.6		11.80	$7.2 \times 10^{-5}$	0.0295		51	20800	
0.5		14.85	$1.16 \times 10^{-4}$	0.030		86	22300	
0.4		18.65	$2.15 \times 10^{-4}$	0.030		161	22400	
0.3		23.5	$5.10 \times 10^{-4}$	0.028		360	19720	
0.2		29.6	$1.9 \times 10^{-3}$	0.026		1125	15400	
0.15		33.2	$4.6 \times 10^{-3}$	0.024		2290	11950	
0.10		37.2	$1.6 \times 10^{-2}$	0.020		5950	7440	
0.09	0.958	38.2	$2.4 \times 10^{-2}$	0.019		7900	6250	
0.08	0.954	39.0	$3.3 \times 10^{-2}$	0.018		9810	5350	
0.07	0.940	39.8	$5.0 \times 10^{-2}$	0.017		13100	4450	
0.06	0.907	40.8	$9.0 \times 10^{-2}$	0.015		20000	3330	
0.05	0.844	41.7	0.17	0.013		29900	2290	
0.04	0.710	42.7	0.36	0.011		43600	1332	
0.03	0.460	43.7	0.83	0.009		50100	547	
0.02	0.0621	44.8	3.0	0.0065		16700	36.2	
0.015	0.00152	44.9	7.0	0.0050		716	~0	
0.01	~0	45.8	23.0	0.0036		~0	~0	

TABLE A4.5

Calculations Made for Graphical Integration to Determine Relative Photoelectric, Compton, and Pair Production Absorption Rates in Aluminum, Attenuation by Stainless Steel Thimble (0.049 inch wall) and Aluminum Capsule (0.10 inch wall)

$$g(E) = e^{-\mu_{ss}(0.1245)} e^{-\mu_{Al}(0.254)}$$

where

$$\mu = \left[ \frac{\tau_a}{p} + \frac{\sigma_a}{p} \right] p$$

E, Mev	$\mu_{Fe}$ $cm^{-1}$	$\mu_{Al}$ $cm^{-1}$	$g(E)$	$\frac{dR_{Al}^Y(\text{Photo})}{dE}$ $\frac{1}{cm \text{ sec}} \times 10^5$	$\frac{dR_{Al}^Y(\text{Compton})}{dE}$ $\frac{1}{cm \text{ sec}} \times 10^5$
>0.20			Assumed 1.00	see Table A4.4	See Table A4.4
0.20	0.379	0.0755	0.935	1051	14,400
0.15	0.630	0.0783	0.906	2080	10,810
0.10	1.73	0.0971	0.786	4670	5,840
0.09	2.18	0.116	0.739	6100	4,820
0.08	3.31	0.138	0.640	6590	3,590
0.07	4.60	0.181	0.539	7500	2,550
0.06	7.68	0.284	0.357	7870	1,310
0.05	13.0	0.494	0.175	6200	475
0.04	25.9	1.00	0.031	1900	58,1
0.03	65.0	2.26	0.00028	30.5	
0.02	198	8.10	Negligible		

TABLE A4.6

CALCULATED ENERGY ABSORPTION RATES IN ALUMINUM DUE TO  
PHOTOELECTRIC, COMPTON, AND PAIR PRODUCTION  
INTERACTIONS

(A) Attenuation by Al Thimble and Al Capsule

Energy Range, Mev	Relative Energy Absorbed, $\frac{\text{Mev}}{\text{gm-sec}}$		
	Photoelectric	Compton	Pair
1.00-7.00	0.00	0.176	0.00906
0.100-1.00	0.00378	0.162	0.00
0.00-0.100	0.0205	0.00266	0.00
Total	0.0243	0.341	0.0091

Total 0.374

% Due to Compton Interactions = 91.1%

% Due to Photoelectric Interactions = 6.5%

% Due to Pair Production Interactions = 2.4%

(B) Attenuation by SS Thimble and Al Capsule

Energy Range, Mev	Relative Energy Absorbed, $\frac{\text{Mev}}{\text{gm-sec}}$		
	Photoelectric	Compton	Pair
1.00-7.00	0.00	0.176	0.00906
0.100-1.00	0.00358	0.160	0.00
0.00-0.100	0.00288	0.00149	0.00
Total	0.00646	0.337	0.0091

Total 0.352

% Due to Compton Interactions = 95.6%

% Due to Photoelectric Interactions = 1.8%

% Due to Pair Production Interactions = 2.6%

TABLE A4.7

Calculated Contributions of Photoelectric, Compton,  
and Pair Production Interactions to the Gamma Dose  
Rate for Different Materials

(A) Attenuation by Al Thimble and Al Capsule

Material	Calc. Total Dose Mev/gm-sec	Calculated % of Total Gamma Dose Rate			$R^Y/R_{Al}^Y$		
		Photoelectric	Compton	Pair	Calc.	$\frac{(Z/A)}{(Z/A)_{Al}}$	% Diff.
Aluminum	0.374	6.5	91.1	2.4	1.00	1.00	—
Hydrogen	0.708	0.0	99.8	0.2	1.891	2.06	9%
Carbon	0.357	0.4	98.3	1.3	0.954	1.038	9%
Polyethylene	0.407	—	—	—	1.088	1.184	9%

(B) Attenuation by SS Thimble and Al Capsule

Material	Calc. Total Dose Mev/gm-sec	Calculated % of Total Gamma Dose Rate			$R^Y/R_{Al}^Y$		
		Photoelectric	Compton	Pair	Calc.	$\frac{(Z/A)}{(Z/A)_{Al}}$	% Diff.
Aluminum	0.352	1.8	95.6	2.6	1.00	1.00	—
Hydrogen	0.708	0.0	99.8	0.2	2.01	2.06	2.5
Carbon	0.356	0.0	98.7	1.3	1.010	0.038	2.8
Polyethylene	0.406	—	—	—	0.152	1.184	2.9

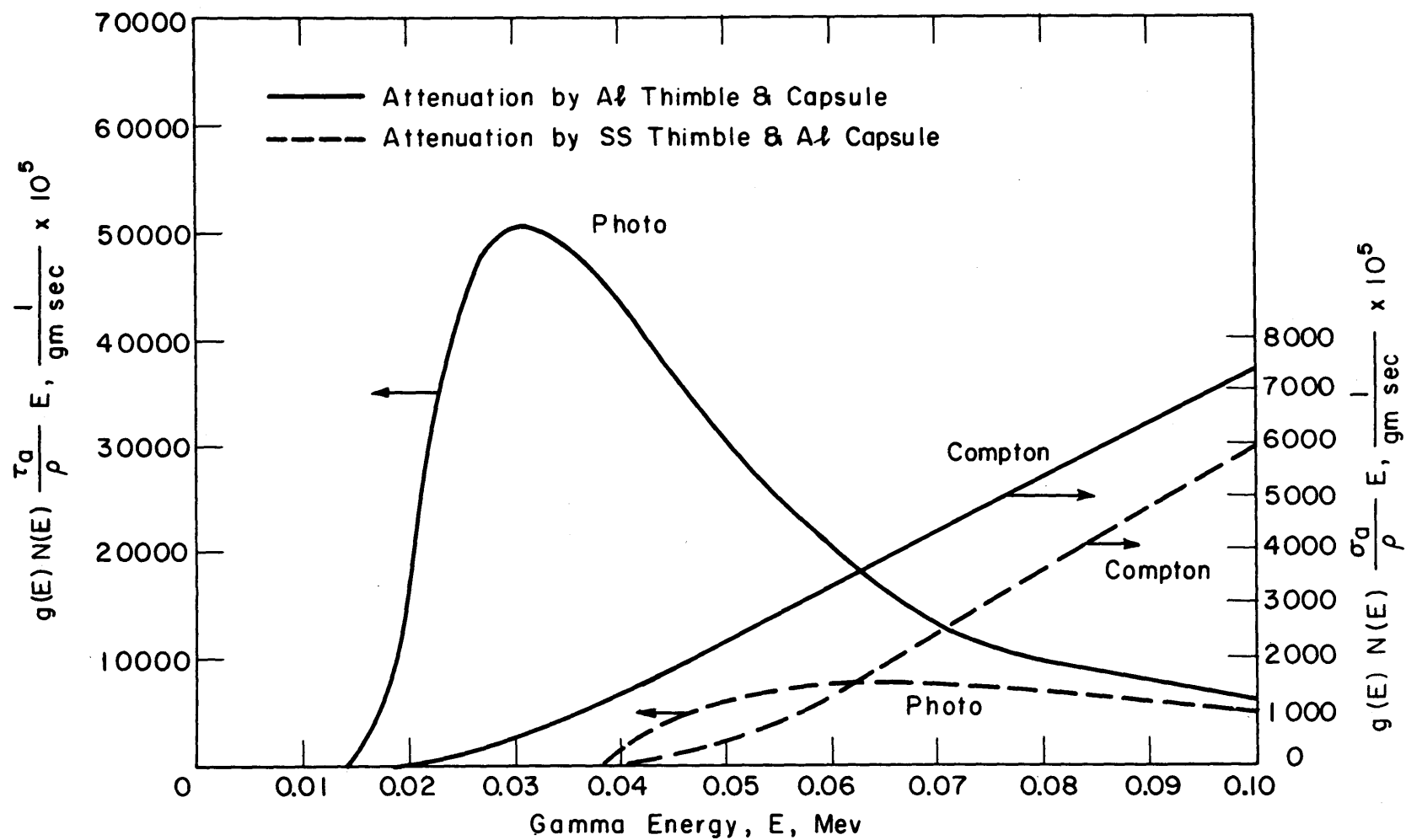


FIGURE A4.2 DIFFERENTIAL RELATIVE ENERGY ABSORPTION RATE DUE TO GAMMA INTERACTIONS, 0.00-0.10 MEV, ALUMINUM SAMPLE

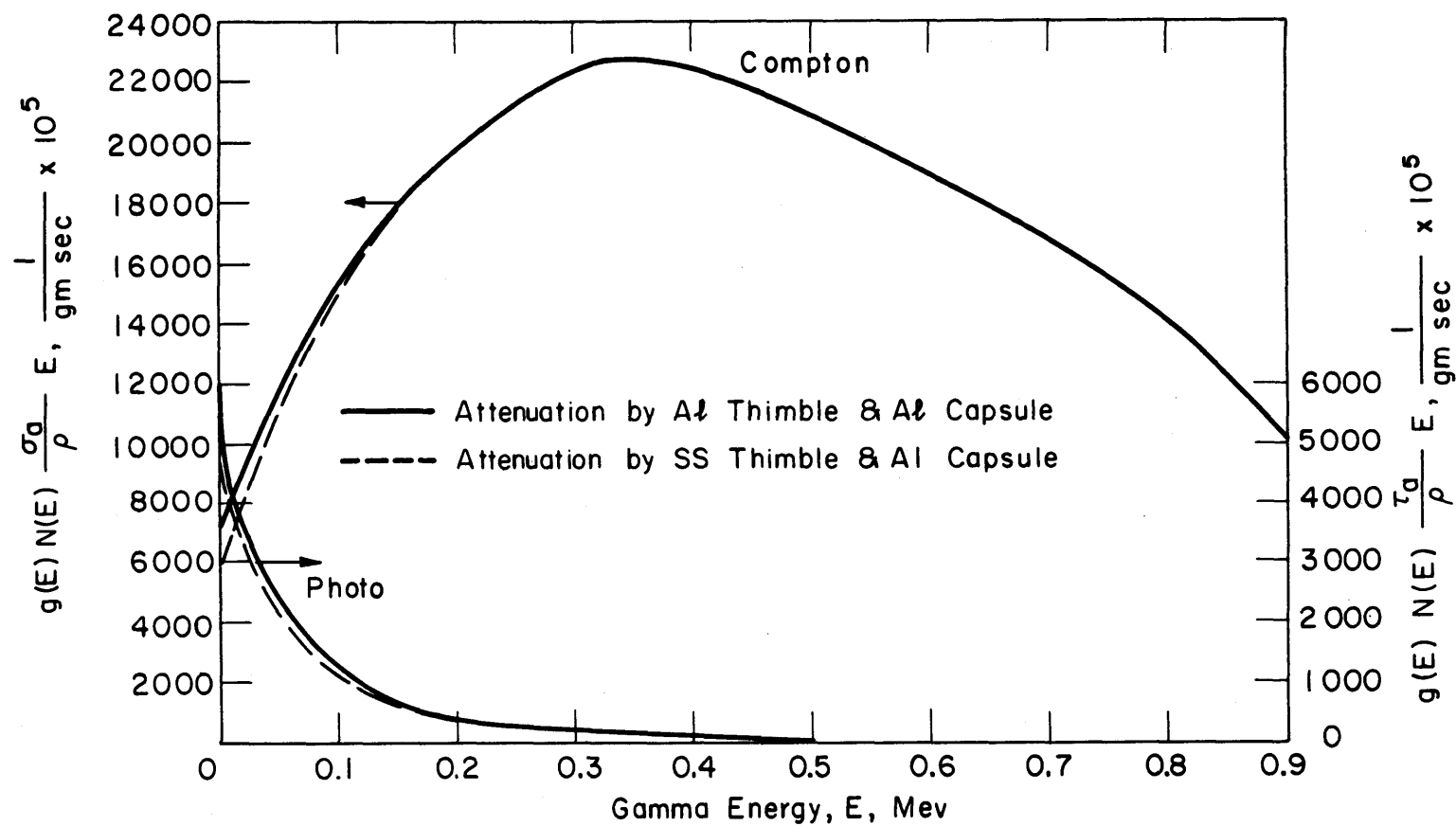


FIGURE A4.3 DIFFERENTIAL RELATIVE ENERGY ABSORPTION RATE DUE TO GAMMA INTERACTIONS, 0.100 - 1.00 Mev, ALUMINUM SAMPLE



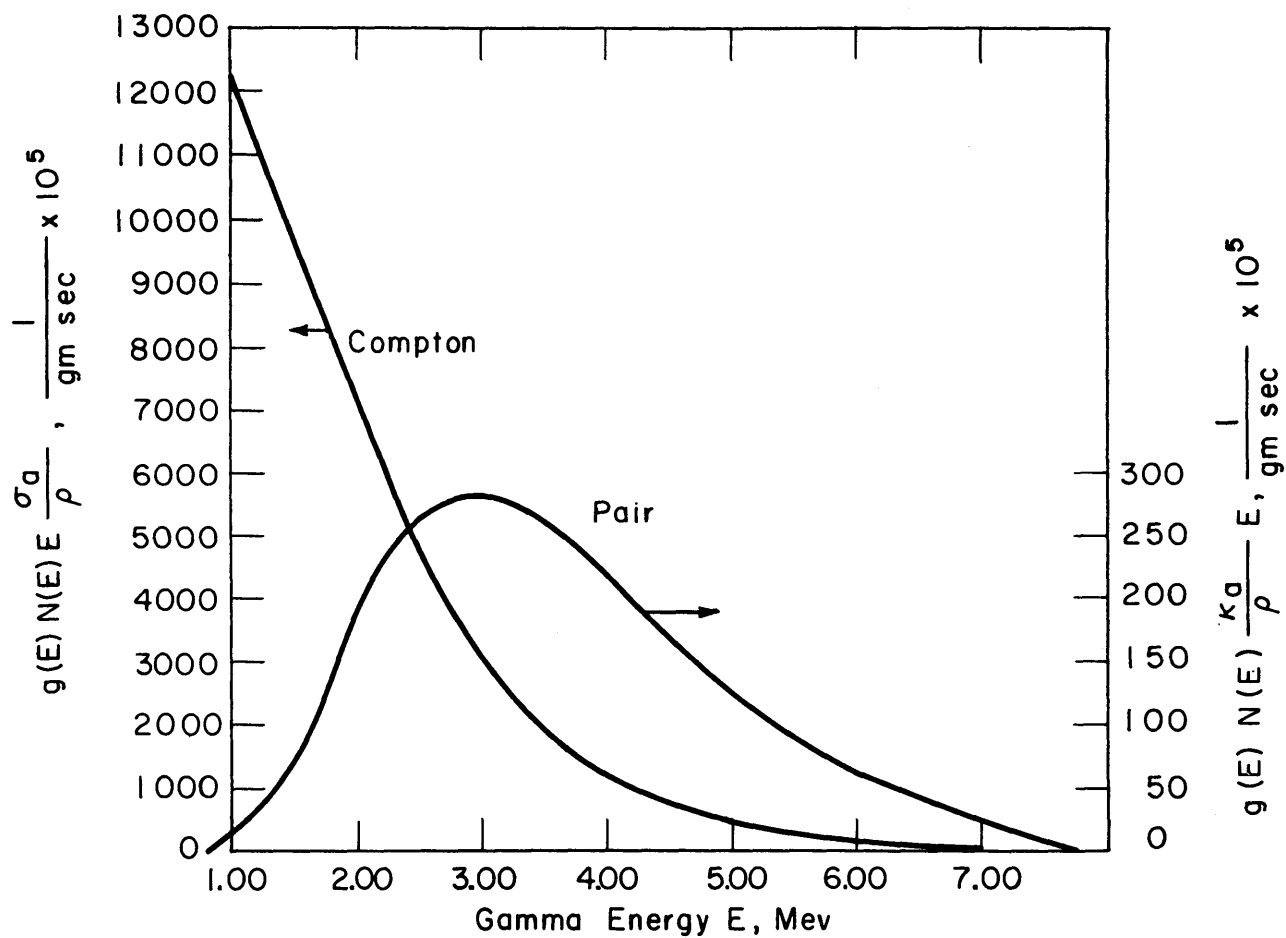


FIGURE A4.4 DIFFERENTIAL RELATIVE ENERGY ABSORPTION RATE DUE TO GAMMA INTERACTIONS, 1.00 - 7.00 MEV, ALUMINUM SAMPLE

energy absorbed comes from interactions other than Compton scattering. The effect of this relatively large contribution by non-Compton interactions in aluminum is evident from the  $R^\gamma/R_{Al}^\gamma$  ratios which are presented in Table A4. 7. Values of the ratio based on the calculations of this appendix are compared with the ratios of  $(Z/A)/(Z/A)_{Al}$  which have been assumed equal to  $R^\gamma/R_{Al}^\gamma$  in interpreting the calorimeter data. It is seen that, for the aluminum and the stainless steel thimbles, the differences between the ratios are  $\sim 9$  per cent and  $\sim 3$  per cent, respectively. The approximation of using  $R^\gamma/R_{Al}^\gamma = (Z/A)/(Z/A)_{Al}$  is thus quite adequate for the measurements in the stainless steel thimble, but somewhat questionable for the measurements in the aluminum thimble. However, the largest calculated contributor to non-Compton interactions in the aluminum thimble is the photoelectric process which, as previously mentioned, is probably over-estimated in the calculation because of the conservative assumption made regarding the gamma spectrum below 0.05 Mev. Considering the uncertainty in the gamma spectrum as well as the inexactness of the graphical integration performed, it is believed that the assumption of  $R^\gamma/R_{Al}^\gamma = (Z/A)/(Z/A)_{Al}$  is as good or better than any other estimate of  $R^\gamma/R_{Al}^\gamma$ . This is particularly true for the measurements in the stainless steel thimble where the maximum error introduced is believed to be no more than 3 per cent; the dose rate in Santowax OMP in the in-pile section is based on the calorimeter measurements in the stainless steel thimble.

#### APPENDIX 4.5

##### TOTAL GRAMS OF URANIUM IN CENTRAL FUEL ELEMENT

In Figure A4. 5, the total grams of uranium in the central fuel element is presented as a function of the date. The values plotted are based on burnup calculations by the MITR operating staff (A4. 15) by a procedure summarized below. The actual variation of the uranium content would be represented by a saw-tooth curve rather than a smooth curve because of the normal MITR operating schedule of 4-1/4 days

operation and 2-3/4 days downtime. For the purpose of this report, the accuracy of a smooth curve as drawn in Figure A4. 5 is sufficient. The steps in calculating the burnup are summarized below (A4. 15):

- (a) The initial grams of uranium in each fuel element before irradiation is specified by the manufacturer.
- (b) Calculate the power in the central fuel element at 1000 kw as:

$$P = \frac{\sum_{i=1}^N \left[ \Sigma_f^c A_c F_c \frac{\bar{\phi}_c}{\phi_o} \right]_i}{\sum_{i=1}^N \left[ \Sigma_f A F \frac{\bar{\phi}}{\phi_o} \right]_i} 1000 \quad (\text{A4. 10})$$

where

c = subscript or superscript referring to central fuel element.

$\Sigma_f$  = average macroscopic fission cross section for thermal neutrons in the homogenized fuel volume.

i = subscript referring to any of N fuel elements in the reactor.

$\bar{\phi}$  = average homogenized core thermal flux in any fuel element.

$\phi_o$  = maximum homogenized core thermal flux.

A = cross sectional area of fuel region in any fuel element.

$$F = \frac{1 + \frac{V_m}{V_F}}{1 + \frac{\bar{\phi}_m}{\bar{\phi}_F} \frac{V_m}{V_F}} \quad \text{for each fuel element.}$$

$\frac{V_m}{V_F}$  = ratio of volume of moderator to volume of fuel.

$\frac{\bar{\phi}_m}{\bar{\phi}_F}$  = disadvantage factor = ratio of average flux in moderator to average flux in fuel.

The flux ratios as well as other properties used in the estimation are based on calculations by Larson (A4. 16).

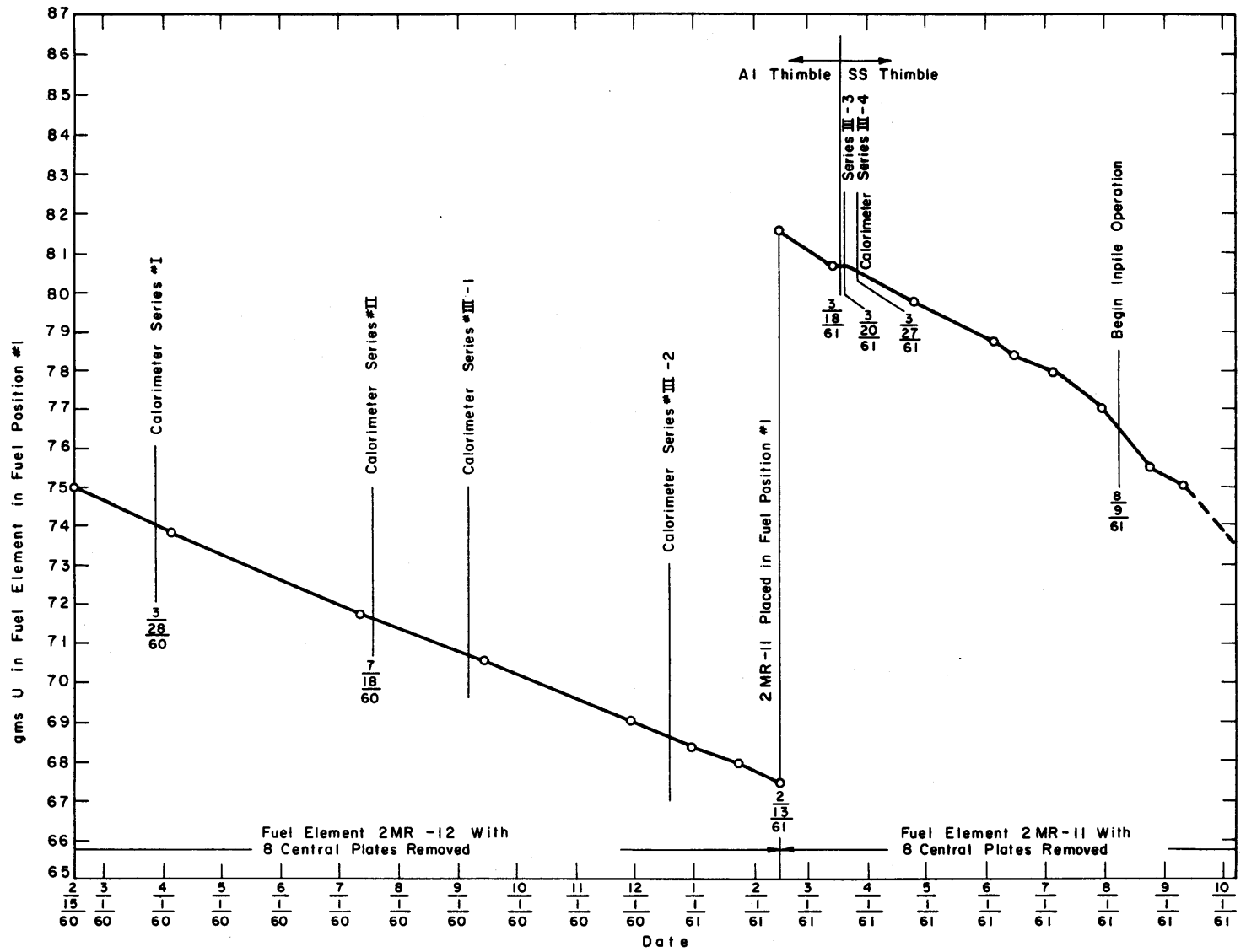


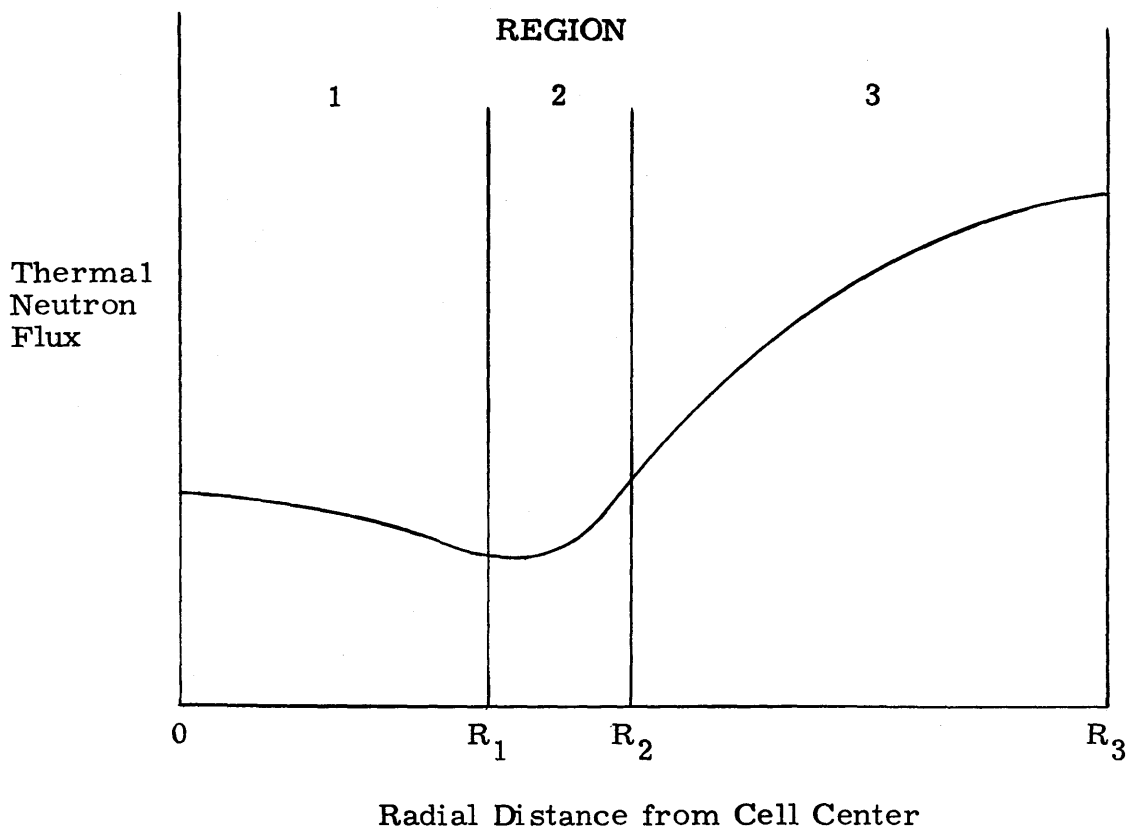
FIGURE A4.5 VARIATION OF THE TOTAL GRAMS OF URANIUM IN CENTRAL FUEL ELEMENT (FUEL POSITION NO.1) WITH DATE

- (c) Once the power in the fuel element is known, the grams or uranium burned up per hour of reactor operation (grams/MWHR) is calculated from the energy yield of the fission process and the ratio of the total cross section to the fission cross section for uranium.
- (d) This burnup rate is assumed constant over a relatively small increment of reactor operation (measured in MWHR) and the total grams of uranium burned up during the increment is calculated.
- (e) This burnup in grams is subtracted from the grams present in the element at the beginning of the increment to give the grams of uranium remaining in the element. Using this value,  $\Sigma_f$  is adjusted for all of the fuel elements and the calculation repeated for the next increment.

## APPENDIX 4. 6

METHOD OF CALCULATING THERMAL FLUX DIFFERENCES  
FOR ALUMINUM AND STAINLESS STEEL THIMBLE

The method is based on a two-group calculation for a unit cell, assuming a constant and flat fast flux over the fuel element. Larson (A4. 16) has shown that this method gives good agreement with measured disadvantage factors. The calculation is based on a cylindrical unit cell, as shown in Figures A4. 6 and A4. 7 which compare the actual geometry with that of the cylindrical unit cell. The effective radii of each section are based on the area of each section in the actual geometry. The flux profile will be similar to that shown in the sketch below:



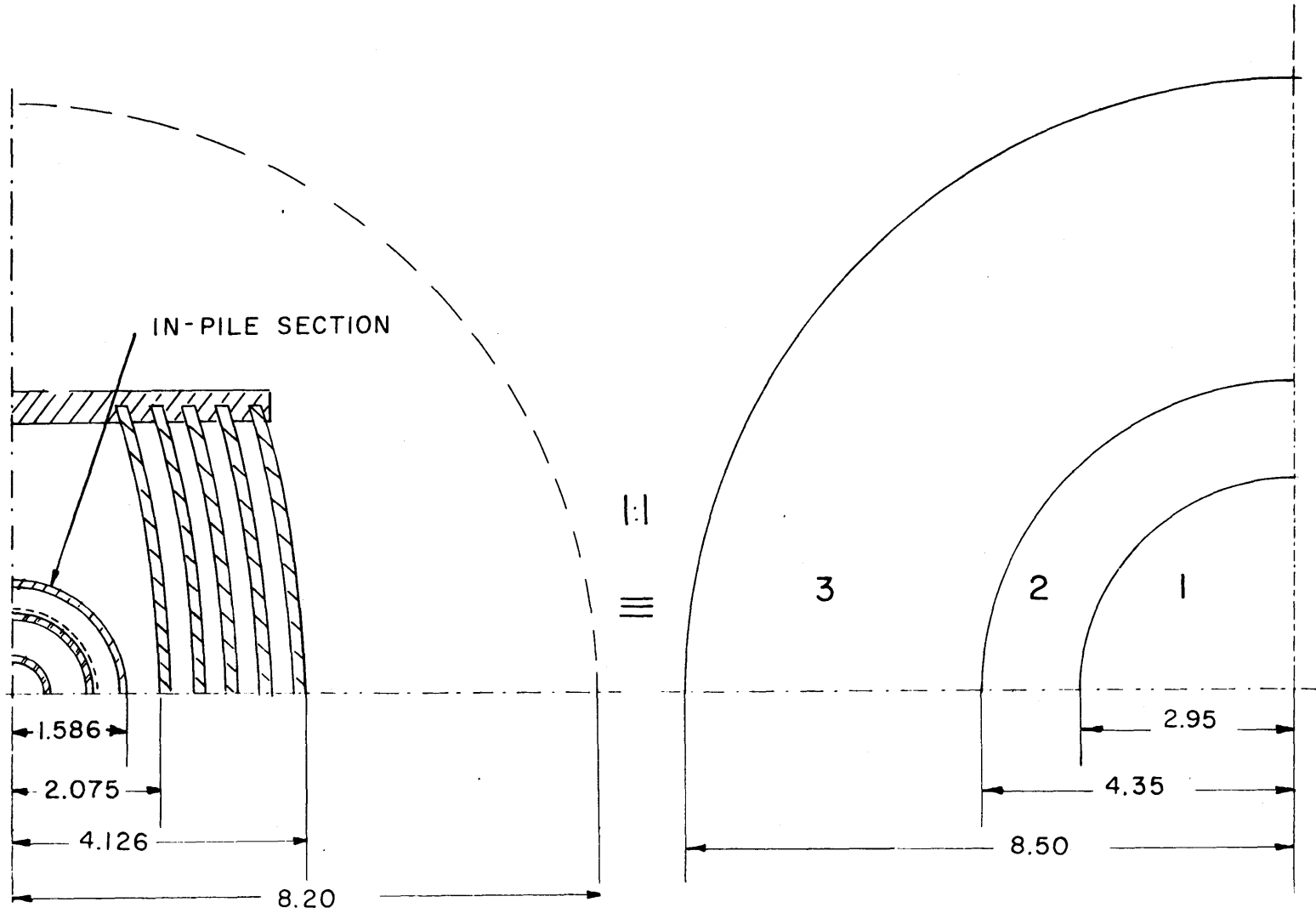


FIG. A 4.6 CROSS SECTION OF THE IN-PILE SECTION IN THE CORE OF THE REACTOR AND EQUIVALENT CYLINDRICAL UNIT CELL , DIMENSIONS IN CENTIMETERS

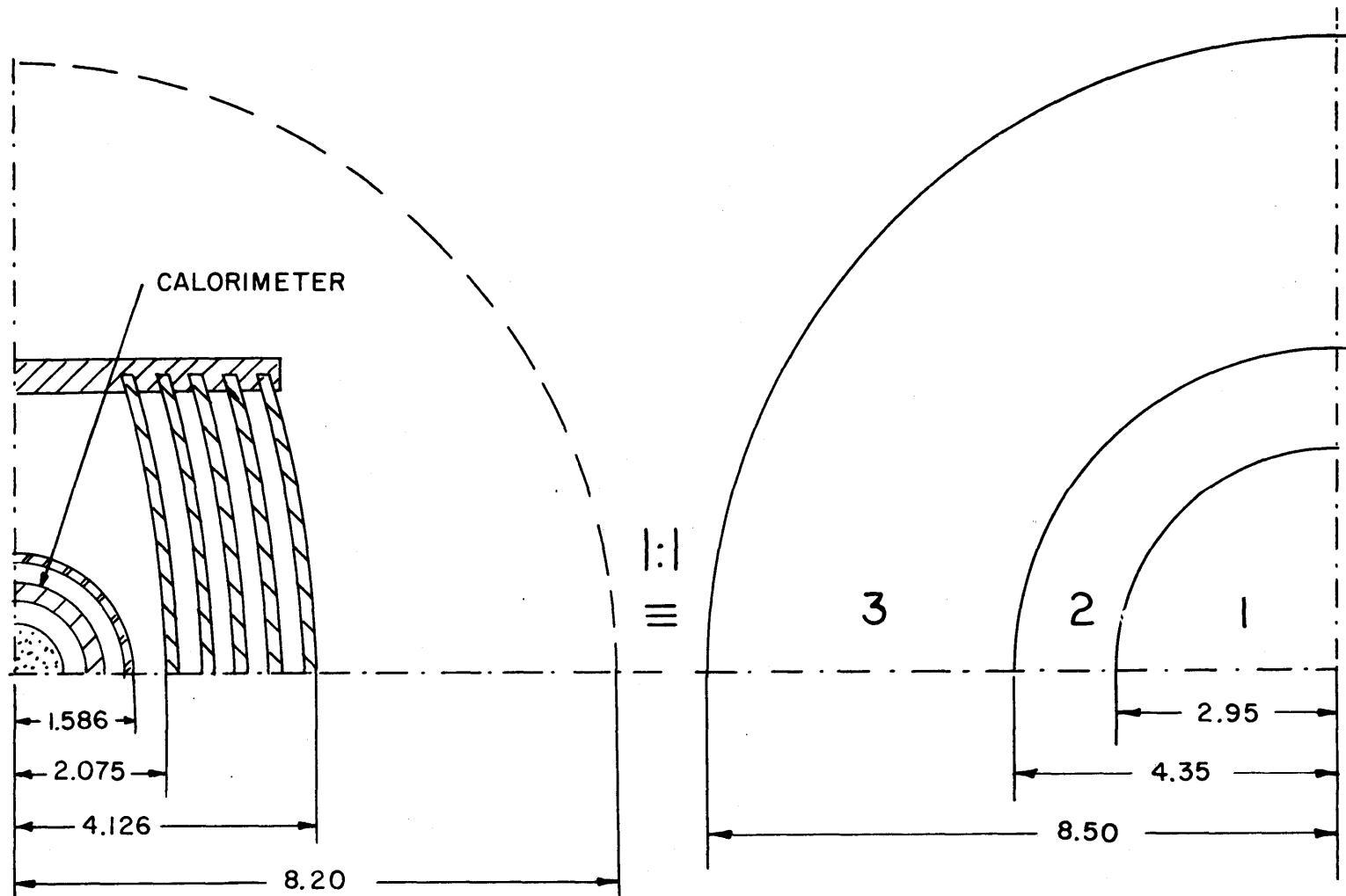


FIG. A4.7 CROSS SECTION OF THE CALORIMETER IN THE CORE OF THE REACTOR AND EQUIVALENT CYLINDRICAL UNIT CELL, DIMENSIONS IN CENTIMETERS



In the three regions shown, all materials are homogenized. Region 1 is a homogeneous mixture of the thimble plus contents and the  $D_2O$  surrounding the thimble. Region 2 is a homogeneous mixture of  $D_2O$ , aluminum, and uranium. Region 3 is pure  $D_2O$ . As previously mentioned, the fast flux is assumed constant across the unit cell and independent of the thimble or its contents.

A thermal neutron balance for each region can be written as below:

$$\begin{aligned} D_1 \nabla^2 \phi_1 - \Sigma_1 \phi_1 + q_1 &= 0 \\ D_2 \nabla^2 \phi_2 - \Sigma_2 \phi_2 + q_2 &= 0 \\ D_3 \nabla^2 \phi_3 - \Sigma_3 \phi_3 + q_3 &= 0 \end{aligned} \quad (A4. 11)$$

$$-(\text{leakage}) - (\text{absorption}) + (\text{production}) = 0$$

where  $\phi$  is the thermal flux,  $n/cm^2$ -sec.

$D$  is the diffusion coefficient, cm.

$\Sigma$  is the macroscopic absorption coefficient for thermal neutrons,  $cm^{-1}$ .

$q$  is the slowing down density for neutrons entering the thermal group,  $n/cm^3$ -sec.

$q$  can be written as  $\bar{\xi} \Sigma_s \int E \phi(E)$  for each region where

$$\bar{\xi} = \frac{\sum_{i=1}^{i=N} \Sigma_{s1} \xi_1}{\Sigma_s} \quad (A4. 12)$$

Now, each  $\nabla^2 \phi$  can be divided into a radial and axial part,

$$\begin{aligned} \nabla^2 \phi &= \nabla_r^2 \phi + \nabla_H^2 \phi \\ &= \nabla_r^2 \phi - B_H^2 \phi \end{aligned} \quad (A4. 13)$$

where  $B_H^2$  is the axial buckling. Considering the homogeneous part of the equation first,

$$\nabla_r^2 \phi - B_H^2 \phi - \frac{\Sigma}{D} \phi = 0$$

$$\nabla_r^2 \phi = \left( \frac{\Sigma}{D} + B_H^2 \right) \phi = \bar{\kappa}^2 \phi$$
(A4. 14)

where

$$\bar{\kappa}^2 = \frac{\Sigma}{D} + B_H^2$$

The general solution of this equation is,

$$\phi = C_1 I_0(\bar{\kappa} r) + C_2 K_0(\bar{\kappa} r)$$
(A4. 15)

A particular solution is given by

$$\nabla_r^2 \phi + \frac{q}{D} = \bar{\kappa}^2 \phi$$

or

$$\phi = \frac{q}{\bar{\kappa}^2 D} = Q$$
(A4. 16)

Hence, this solution for all three regions is,

$$\begin{aligned} \phi_1 &= C_1 I_0(\bar{\kappa}_1 r) + C_2 K_0(\bar{\kappa}_1 r) + Q_1 \\ \phi_2 &= C_3 I_0(\bar{\kappa}_2 r) + C_4 K_0(\bar{\kappa}_2 r) + Q_2 \\ \phi_3 &= C_5 I_0(\bar{\kappa}_3 r) + C_6 K_0(\bar{\kappa}_3 r) + Q_3 \end{aligned}$$
(A4. 17)

Since the fast flux has been assumed constant, the ratio of slowing down density in any region to that in the other is given as:

$$\frac{q_1}{q_2} = \frac{\bar{\xi}_1 \Sigma_{s1}}{\bar{\xi}_2 \Sigma_{s2}}$$
(A4. 18)

Six boundary conditions are required:

$$\begin{aligned} 1) \quad r = R_3 \quad \frac{d\phi_3}{dr} &= 0 \\ 2) \quad \phi_1 \text{ is finite at } r = 0 & \end{aligned}$$
(A4. 19)

$$\begin{aligned}
3) \quad r = R_1 \quad \phi_1 &= \phi_2 \\
4) \quad r = R_1 \quad D_1 \frac{d\phi_1}{dr} &= D_2 \frac{d\phi_2}{dr} \\
5) \quad r = R_2 \quad \phi_2 &= \phi_3 \\
6) \quad r = R_2 \quad D_2 \frac{d\phi_2}{dr} &= D_3 \frac{d\phi_3}{dr}
\end{aligned} \tag{A4. 19}$$

Applying these boundary conditions gives for the final results,

$$\begin{aligned}
\phi_1 &= C_1 I_0(\bar{\mathcal{K}}_1 r) + Q_1 \\
\phi_2 &= C_3 I_0(\bar{\mathcal{K}}_2 r) + C_4 K_0(\bar{\mathcal{K}}_2 r) + Q_2 \\
\phi_3 &= C_5 \left[ I_0(\bar{\mathcal{K}}_3 r) + \frac{I_1(\bar{\mathcal{K}}_3 R_3)}{K_1(\bar{\mathcal{K}}_3 R_3)} K_0(\bar{\mathcal{K}}_3 r) \right] + Q_3
\end{aligned} \tag{A4. 20}$$

where

$$Q = \frac{q}{\bar{\mathcal{K}}^2 D} \quad \bar{\mathcal{K}} = \frac{\Sigma}{D} + B_H^2 \quad \frac{q_1}{q_2} = \frac{\bar{\xi}_1 \Sigma_{s1}}{\bar{\xi}_2 \Sigma_{s2}}$$

and the coefficients  $C_1$ ,  $C_3$ ,  $C_4$ , and  $C_5$  are given by a solution of:

$$\begin{aligned}
C_1 \{ I_0(\bar{\mathcal{K}}_1 R_1) \} - C_3 \{ I_0(\bar{\mathcal{K}}_2 R_1) \} - C_4 \{ K_0(\bar{\mathcal{K}}_2 R_1) \} &= Q_2 - Q_1 \\
C_1 \left\{ \frac{D_1}{D_2} \bar{\mathcal{K}}_1 I_1(\bar{\mathcal{K}}_1 R_1) \right\} - C_3 \{ \bar{\mathcal{K}}_2 I_1(\bar{\mathcal{K}}_2 R_1) \} + C_4 \{ \bar{\mathcal{K}}_2 K_1(\bar{\mathcal{K}}_2 R_1) \} &= 0 \\
C_3 \{ I_0(\bar{\mathcal{K}}_2 R_2) \} + C_4 \{ K_0(\bar{\mathcal{K}}_2 R_2) \} - C_5 \{ I_0(\bar{\mathcal{K}}_3 R_2) + B_{13} K_0(\bar{\mathcal{K}}_3 R_2) \} &= Q_3 - Q_2 \\
C_3 \left\{ \frac{D_2}{D_3} \bar{\mathcal{K}}_2 I_1(\bar{\mathcal{K}}_2 R_2) \right\} - C_4 \left\{ \frac{D_2}{D_1} \bar{\mathcal{K}}_2 K_1(\bar{\mathcal{K}}_2 R_2) \right\} \\
- C_5 \{ \bar{\mathcal{K}}_3 I_1(\bar{\mathcal{K}}_3 R_2) - B_{13} \bar{\mathcal{K}}_3 K_1(\bar{\mathcal{K}}_3 R_2) \} &= 0
\end{aligned} \tag{A4. 21}$$

$$\text{where } B_{13} = \frac{I_1(\bar{\mathcal{K}}_3 R_3)}{K_1(\bar{\mathcal{K}}_3 R_3)}$$

Crout's method was used for the solution of these equations (A4.17). For details of the nuclear properties used and the calculation of the results plotted in Figure 4.14, reference is made to Turricchia (A4.6).

#### APPENDIX 4.7

##### CALCULATION OF FAST NEUTRON DOSE RATE, $I_C/I_H$ , AND $I_{Al}/I_H$ FROM FAST NEUTRON FLUX MEASUREMENTS

Using the fast flux measurements presented, it is possible to calculate the fast neutron dose rate in Santowax OMP for comparison with results from the calorimeter measurements. The accuracy of this calculation is limited by uncertainties in the flux spectrum, particularly in the region between 570 ev and 2.90 Mev where no flux measurements have been made and which accounts for the largest fraction of the absorbed dose due to fast neutron interactions. The calculations should serve as a check of the calorimeter results, however. The calculations also provide values of  $I_C/I_H$  and  $I_{Al}/I_H$  which are required for analysis of the calorimeter data. As indicated by the calculations, these ratios are relatively insensitive to the assumed spectrum. Calculations have been made for hydrogen, carbon, and aluminum, of the fast neutron dose rate in watts/atom or equivalently  $I_H$ ,  $I_C$ , and  $I_{Al}$  as given in Equation (4.3) of Chapter 4; the fast neutron dose rate in any material containing these three elements can then be calculated by multiplying these values by the atoms/gm for that particular element. In calculating  $I_H$ ,  $I_C$ , and  $I_{Al}$ , either a graphical or numerical integration was used for Equation (4.3). In general, for all of the calculations, the total cross section was assumed to be the scattering cross section and data from BNL-325 (A4.18) were used.

In Tables 4.7 and 4.8 of Chapter 4, the results of the calculations based on five different neutron flux vs. energy curves are presented. The first four spectra used are given in Figure 4.25 of Chapter 4 and were used by Sefchovich (A4.19) in calculations for hydrogen and carbon. The fifth spectrum is given in Figure A4.8 and was used in calculations

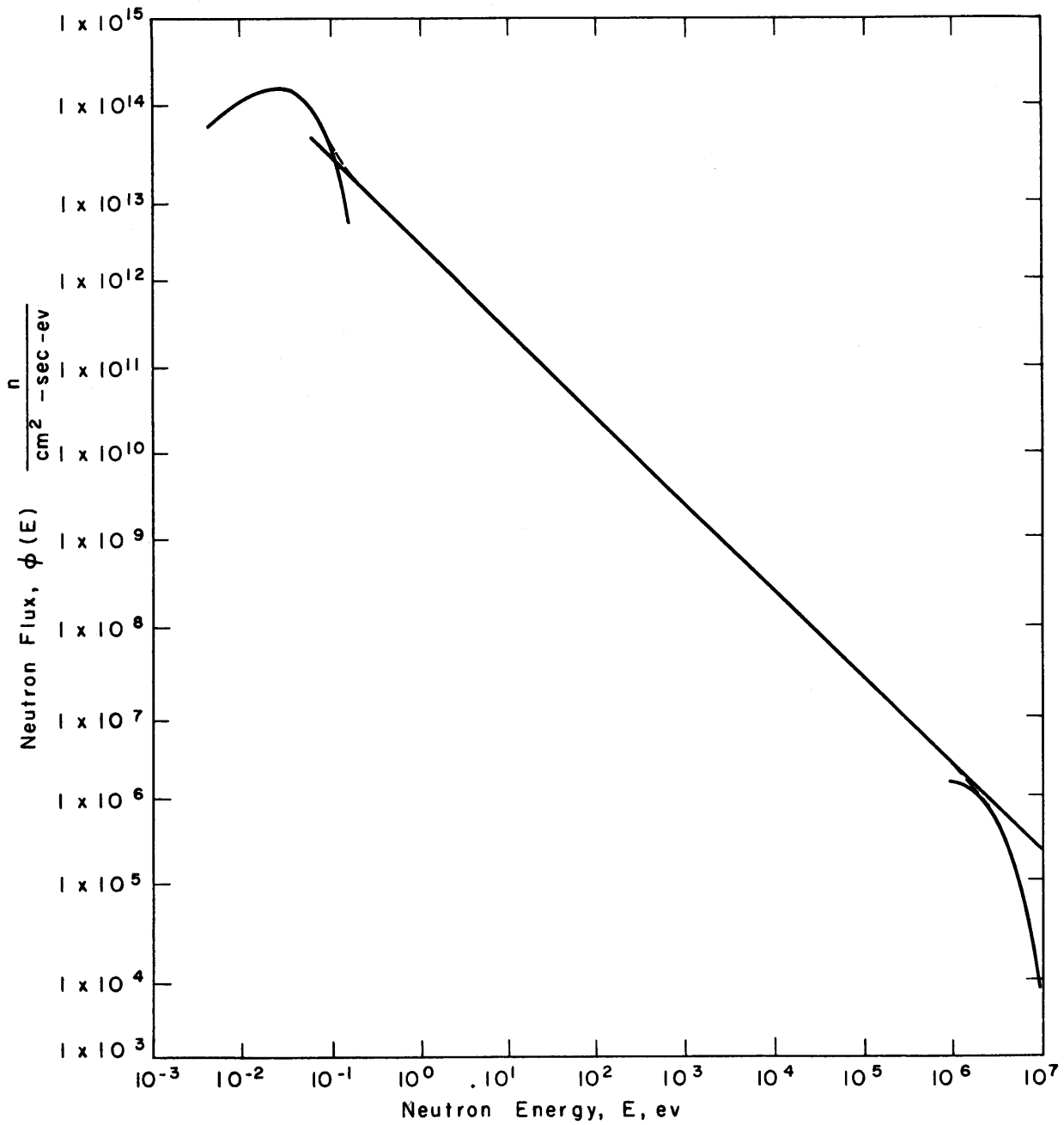


FIGURE A4.8 NEUTRON FLUX SPECTRUM AT AXIAL CENTER OF CORE USED FOR CALCULATION OF FAST NEUTRON DOSE RATE IN SANTOWAX OMP AND  $\frac{I_C}{I_H}$  AND  $\frac{I_{AI}}{I_H}$

for this report for hydrogen, carbon, and aluminum. The fluxes on which this fifth spectrum is based are close to those of the monitor tube. The calculations performed using this fifth spectrum will be briefly summarized in the remainder of this appendix.

In Table A4. 8, the fluxes on which the fifth spectrum is based are compared with the fluxes in the stainless steel thimble and in the monitor tube. The complete neutron spectrum over all neutron energies based on the fluxes for Curve V is drawn in Figure A4. 8. The thermal flux per unit energy interval was calculated by means of the Maxwell-Boltzmann relation from the measured flux for 2200 meter/sec thermal neutrons. In the resonance region, the flux is based on  $\phi(E) = \phi_0/E$ , where  $\phi_0$  was taken as the value for cobalt or  $2.60 \times 10^{12}$  n/cm<sup>2</sup>-sec. In the region above 2.0 Mev, a fission spectrum was drawn, based on an average for the three flux measurements listed. From integrated values for the Watt spectrum,  $\phi(E) = K[0.483 e^{-E} \sinh \sqrt{2E}]$ ,

$$\begin{aligned} K_{2.90} &= 3.11 \times 10^{12} \\ K_{6.3} &= 3.88 \times 10^{12} \\ K_{8.6} &= 6.05 \times 10^{12} \\ K_{\text{avg}} &= 4.35 \times 10^{12} \end{aligned} \tag{A4. 22}$$

and

$$\phi(E) = 2.10 \times 10^{12} e^{-E} \sinh \sqrt{2E}$$

Calculations with this fifth spectrum were made for hydrogen, carbon, and aluminum. The calculation for hydrogen is straightforward since no resonances occur in the hydrogen cross section and no inelastic scattering occurs. For carbon and particularly for aluminum, resonances occur. Also, above approximately 1.0 Mev for aluminum and 5.0 Mev for carbon, a small fraction of the total cross section is due to inelastic scattering. For carbon, the calculation was made by two methods:

- (1) Using a smooth curve drawn through the resonances in the  $\sigma_T(E)$  vs E curve as Sefchovich did.

TABLE A4.8  
 COMPARISON OF FLUXES AT AXIAL CENTER POSITION  
 WITH THOSE USED FOR CURVE V (Figure A4.8)

	$\phi_{2200}$ , n/cm <sup>2</sup> -sec	$\phi_0$ n/cm <sup>2</sup> -sec		$\int_E^{\infty} \phi(E)dE$ , n/cm <sup>2</sup> -sec		
		Co	Cu	E=2.90 Mev	E=6.3 Mev	E= 8.6 Mev
Curve V	$1.51 \times 10^{13}$	$2.60 \times 10^{12}$	$4.96 \times 10^{12}$	$7.13 \times 10^{11}$	$7.85 \times 10^{10}$	$2.14 \times 10^{10}$
Monitor Tube	$1.51 \times 10^{13}$	$2.45 \times 10^{12}$	-	$7.7 \times 10^{11}$	$7.9 \times 10^{10}$	$2.2 \times 10^{10}$
Stainless Steel Thimble	$1.41 \times 10^{13}$	$2.25 \times 10^{12}$	$4.70 \times 10^{12}$	$9.2 \times 10^{11}$	$11.4 \times 10^{10}$	$2.73 \times 10^{10}$

(2) Approximating each resonance as a square peak with height half that of the actual resonance and width equal to the resonance base width. It was also assumed that inelastic scattering does not contribute to the absorbed energy and the estimated inelastic cross section was subtracted from the total.

Using both methods, the same result given in Table 4. 7 of Chapter 4 was obtained. For aluminum, the second calculational procedure (outlined above for carbon) was used.

The calculations for curve V were made separately for energy intervals of 0. 0001 Mev to 0. 001 Mev, 0. 001 Mev to 0. 01 Mev, etc., up to a neutron energy where the absorption rate was negligible due to the small flux at that energy. With this procedure, the fraction of the total neutron dose rate which is absorbed in any energy interval is thus determined. The results are tabulated for Santowax OMP in Table 4. 8 (of Chapter 4).

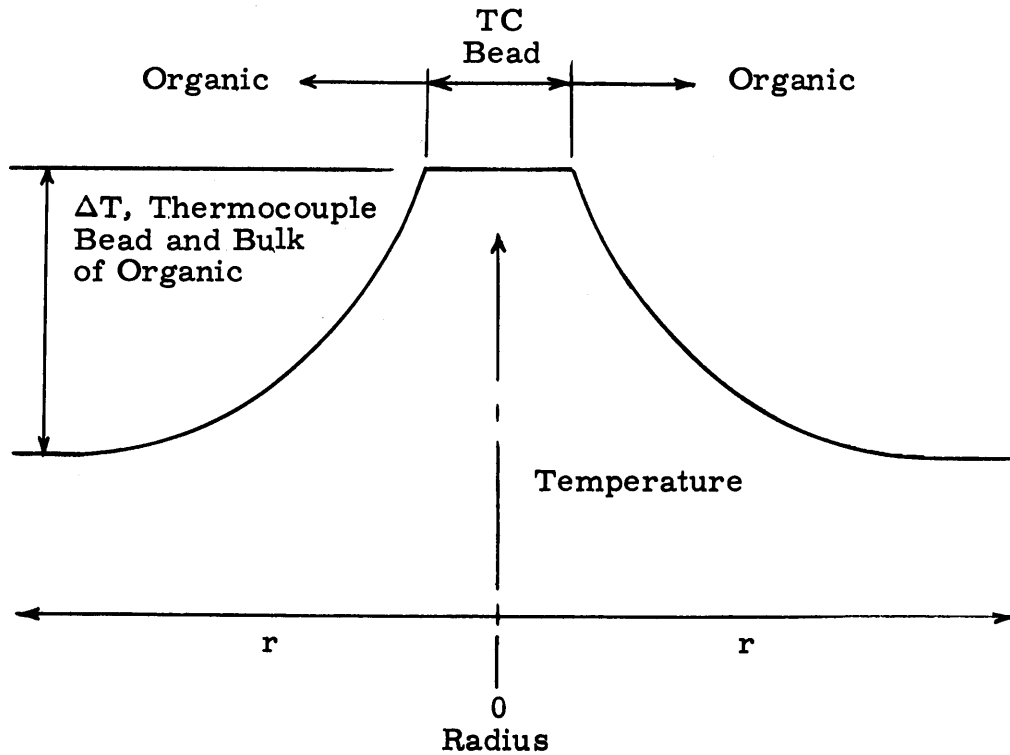
#### APPENDIX 4. 8

##### EQUILIBRIUM TEMPERATURE DIFFERENCE BETWEEN THERMOCOUPLE BEAD AND CALORIMETER SAMPLES

Because of heat generated in the thermocouple bead and conduction of heat by the thermocouple lead wires, a temperature difference can exist between the thermocouple bead and the calorimeter sample when perfect thermal contact is assumed. This effect is of particular importance for the organic samples because of their low thermal conductivity. In this appendix, the equilibrium (steady-state) temperature difference is developed as a function of the temperature gradient in the lead wire at the bead. The assumptions are made that (1) the thermocouple bead is isothermal, (2) the temperature in the organic sample is independent of time and position in the absence of the thermocouple, (3) the thermocouple bead is spherical and has its entire surface area available for transfer of heat to the absorber, and (4) the absorber is infinite with respect to the temperature perturbation introduced by the



thermocouple bead. The temperature profile in the organic and thermocouple is indicated in the following sketch for the case where heat is flowing from the thermocouple bead to the organic:



Using spherical geometry, the general heat transfer equation which applies in the organic without internal heat generation is:

$$T = -\frac{C_1}{r} + C_2 \quad (\text{A4. 23})$$

where

$T$  = temperature, °F, of the organic.

$r$  = radius, ft.

Letting  $q$  equal the energy transfer rate, Btu/hr, from the thermocouple bead to the absorber and  $R$  equal the radius of the bead, ft, the applicable boundary conditions are:

(1) At  $r = R$ ,

$$q = -k_o 4\pi R^2 \frac{dT}{dr}$$

or

$$\left(\frac{dT}{dr}\right)_{r=R} = - \frac{q}{4\pi R^2 k_o} \quad (\text{A4. 24})$$

where

$$k_o = \text{thermal conductivity of organic, } \frac{\text{Btu}}{\text{hr } ^\circ\text{F-ft}}$$

(2) At  $r = R$ ,  $T = T_{TC}$  where  $T_{TC}$  is the thermocouple bead temperature,  $^\circ\text{F}$ .

Applications of these boundary conditions gives the equation,

$$T_{TC} - T = \frac{q}{4\pi k_o} \left[ \frac{1}{R} - \frac{1}{r} \right] \quad (\text{A4. 25})$$

The heat transfer rate,  $q$ , can be written at equilibrium as:

$$q = Q_{TC} \frac{4}{3} \pi R^3 - k_{TC} \frac{\pi}{4} D_{TCW}^2 \left( \frac{\partial T_{TC}}{\partial x} \right)_{x=0} \quad (\text{A4. 26})$$

where  $Q_{TC}$  = volumetric internal heat generation rate in thermocouple,  $\text{Btu/hr-}^\circ\text{F-ft}$

$k_{TC}$  = thermal conductivity of thermocouple lead wire,  $\text{Btu/hr-}^\circ\text{F-ft}$ .

$D_{TCW}$  = effective diameter of lead wire, ft.

$x$  = distance along lead wire measured from thermocouple bead, ft.

$\left( \frac{\partial T_{TC}}{\partial x} \right)_{x=0}$  = temperature gradient in the lead wire at the thermocouple bead,  $^\circ\text{F/inch}$ .

Substitution in Equation A4. 25 and letting  $r = \infty$  to get the maximum

$T_{TC} - T$  gives:

$$T_{TC} - T = \frac{Q_{TC} \left( \frac{4}{3} \pi R^3 \right) - k_{TC} \frac{\pi}{4} (D_{TCW})^2 \left( \frac{\partial T_{TC}}{\partial x} \right)_{x=0}}{4 \pi k_o R} \quad (A4. 27)$$

Calculations are presented below for polystyrene at 100 kw reactor power.

$$k_o = 0.060 \text{ Btu/hr-ft-}^\circ\text{F}$$

$$k_{TC} = 35 \text{ Btu/hr-ft-}^\circ\text{F}$$

$$R = 1/64 \text{ inch} = 0.00130 \text{ ft}$$

$$D_{TCW} = 1.49 \times 10^{-3} \text{ ft (for 28-gage wire)}$$

$$\begin{aligned} Q_{TC} &= 0.020 \text{ watts/gm} \times 3.413 \text{ Btu/hr-watt} \times (8.9)(62.4) \text{ lb/ft}^3 \\ &\quad \times 453.6 \text{ gm/lb} \\ &= 1.72 \times 10^4 \text{ Btu/hr-ft}^3 \end{aligned}$$

Substitutions gives:

$$T_{TC} - T = 0.162 - 0.749 \left( \frac{\partial T_{TC}}{\partial x} \right)_{x=0} \text{ }^\circ\text{F} \quad (A4. 28)$$

where  $\left( \frac{\partial T_{TC}}{\partial x} \right)_{x=0}$  is the gradient in  $^\circ\text{F/in.}$  For polyethylene,  $k_o = 0.19 \text{ Btu/hr-ft-}^\circ\text{F}$ , and

$$T_{TC} - T = 0.051 - 0.236 \left( \frac{\partial T_{TC}}{\partial x} \right)_{x=0} \text{ }^\circ\text{F} \quad (A4. 28)$$

#### APPENDIX 4.9

##### TEMPERATURE-TIME HISTORY OF CENTER AND SURFACE OF CALORIMETER SAMPLE FOR HYPOTHETICAL RUN

Calculations are presented below for a hypothetical case of the time variation of the center and surface temperature of polystyrene. The calculations are based on a constant wall temperature and an

initial sample temperature 6°F below the aluminum capsule temperature at a time of zero. This basis should represent an over-estimation of the error since the wall and sample temperatures are generally never more than 1-2°F apart until the sample temperature has exceeded the capsule temperature (see Figure 4. 6).

The assumption is made that the absorbers are infinite in length. Using cylindrical geometry, the general heat transfer equation is:

$$\frac{\partial^2 T}{\partial r^2} + \frac{1}{r} \frac{\partial T}{\partial r} + \frac{W_i}{k} = \frac{1}{a_t} \frac{\partial T}{\partial \tau} \quad (\text{A4. 29})$$

where

T = temperature, °F.

r = radius, ft.

k = thermal conductivity, Btu/hr-ft-°F.

$\tau$  = time, hr.

$W_i$  = internal heat generation, Btu/hr-ft<sup>3</sup>.

$a_t$  = thermal diffusivity, ft<sup>2</sup>/hr.

The solution to this equation can be written as the sum of a steady state term,  $T_s(r)$ , and an unsteady state term,  $T_t(r, \tau)$ .

$$T = T_s(r) + T_t(r, \tau) \quad (\text{A4. 30})$$

The solution can then be divided into steady and unsteady state parts:

$$\frac{\partial^2 T_s}{\partial r^2} + \frac{1}{r} \frac{\partial T_s}{\partial r} + \frac{W_i}{k} = 0 \quad (\text{A4. 31})$$

$$\frac{\partial^2 T_t}{\partial r^2} + \frac{1}{r} \frac{\partial T_t}{\partial r} = \frac{1}{a_t} \frac{\partial T_t}{\partial \tau} \quad (\text{A4. 32})$$

The general solutions of these equations for a solid cylinder are:

$$T_s = -\frac{W_i r^2}{4k} + C_1 \ln r + C_2 \quad (\text{A4. 33})$$

$$T_t = K e^{-a_t a^2 \tau} J_0(ar) \quad (\text{A4. 34})$$

Letting the relative aluminum wall temperature equal zero, the boundary conditions are:

$$\begin{aligned}
 (1) \quad & \frac{\partial T(r_o, \tau)}{\partial r} = -\frac{h}{k} T(r_o, \tau) \\
 (2) \quad & T(r, 0) = T^* \\
 (3) \quad & \frac{\partial T_s(0)}{\partial r} = 0 \\
 (4) \quad & \frac{\partial T_s(0)}{\partial r} = -\frac{h}{k} T_s(r_o)
 \end{aligned} \tag{A4. 35}$$

Applying boundary conditions (3) and (4) to Equation (A4. 33) gives for the steady state solution:

$$T_s(r) = \frac{W_i r_o^2}{4k} \left[ 1 - \frac{r^2}{r_o^2} + \frac{2k}{r_o h} \right] \tag{A4. 36}$$

Converting boundary conditions (1) and (2) to the transient temperature boundary conditions (by means of Equation (A4. 36) ) gives:

$$\begin{aligned}
 (5) \quad & \frac{\partial T_t(r_o, \tau)}{\partial r} = -\frac{h}{k} T_t(r_o, \tau) \\
 (6) \quad & T_t(r, 0) = T^* - T_s(r)
 \end{aligned} \tag{A4. 37}$$

Substitution of boundary condition (5) gives for the Eigenvalues

$$(\alpha_n r_o) J_1(\alpha_n r_o) = \frac{hr_o}{k} J_0(\alpha_n r_o) \tag{A4. 38}$$

where

$$T_t = \sum_{n=1}^{\infty} K_n e^{-\alpha_n^2 \tau} J_0(\alpha_n r) \tag{A4. 39}$$

Applying boundary condition (6), multiplying by  $r J_0(\alpha_m r) dr$ , and integrating from zero to  $r_o$  gives a relation for  $K_n$ . The complete solution is summarized below:

$$T = T_s + T_t \quad (\text{A4. 40})$$

$$T_s = \frac{W_i r_o^2}{4k} \left[ 1 - \frac{r^2}{r_o^2} + \frac{2k}{r_o h} \right] \quad (\text{A4. 41})$$

$$T_t = \sum_{n=1}^{\infty} K_n e^{-a_n^2 t} J_0(a_n r) \quad (\text{A4. 42})$$

$$K_n = \frac{\int_0^{r_o} r J_0(a_n r) [T^* - T_s(r)] dr}{\int_0^{r_o} r J_0^2(a_n r) dr} \quad (\text{A4. 43})$$

$$(a_n r_o) J_1(a_n r_o) = \frac{hr_o}{k} J_0(a_n r_o) \quad (\text{A4. 44})$$

A numerical calculation for a power of 50 kw will now be presented for polystyrene. Integration of  $K_n$  gives

$$K_n = \frac{2T^* \frac{1}{a_n} J_1(a_n r_o)}{r_o [J_0^2(a_n r_o) + J_1^2(a_n r_o)]} - 2 \frac{W_i h}{r_o k} \frac{1}{k} \left\{ \frac{1}{a_n^2 \left[ \left( \frac{h}{k} \right)^2 + a_n^2 \right] J_0(a_n r_o)} \right\} \quad (\text{A4. 45})$$

The following properties were used.

$$h = 1.15 \text{ Btu/hr-ft-}^\circ\text{F}$$

$$k = 0.060 \text{ Btu/hr-ft-}^\circ\text{F}$$

$$W_i = 1.44 \times 10^3 \text{ Btu/hr-ft}^3 \equiv 0.0141 \text{ watts/gm}$$

$$r_o = 1/4 \text{ inch} = 0.0208 \text{ ft}$$

$$T^* = -6^\circ\text{F}$$

$$C_p = 0.32 \text{ Btu/lb-}^\circ\text{F}$$

With these values of  $h$ ,  $r_o$ , and  $k$ , the Eigenvalues,  $\alpha_n r_o$ , are 0.8516, 3.9344, 7.0723, 10.213 . . .

Values of  $K_n$  at these Eigenvalues are -22.33, +0.846, -0.318, +0.185 . . .

Calculation of the inside and outside temperature for various times using Equations (A4.40) through (A4.45) gives the results tabulated in Table A4.9. The results are plotted in Figure 4.26.

Table A 4. 9. Temperature Variation of Inside and Outside of Polystyrene Absorber.

Time, minutes	Temperature (wall temperature = 0°F), °F	
	Inside	Outside
0	-6	-6
3	-1.9	-1.4
6	1.9	1.7
9	4.9	4.1
12	7.4	6.25
15	9.04	7.58

#### APPENDIX 4. 10

#### CONTRIBUTION TO ENERGY ABSORPTION FROM THE GAMMA AND BETA RADIATION EMITTED BY THE ALUMINUM CAPSULE

As discussed in more detail in Appendix A4.3, capture of thermal neutrons by  $Al^{27}$  produces 7.72 Mev of gamma radiation and  $Al^{28}$  which then decays by emitting a beta particle, ( $E_{max} = 2.87$  Mev), and a 1.8 Mev gamma ray. Since an aluminum capsule surrounds the calorimeter samples, the capsule acts as a beta and gamma source and will contribute to the total dose rate in the samples. The fraction of the measured dose rate due to this effect is estimated in this appendix, using methods developed by Turricchia (A4.6) and by Anderson and Waite (A4.10).

## A4. 10. 1 BASED ON TURRICCHIA'S CALCULATIONS

For purposes of the estimation, the cylindrical sample is transformed into a sphere of equal volume and the aluminum capsule into a spherical shell whose thickness is equal to the real thickness; the inner radius of the shell is selected so the spacing from the central sphere is equal to the spacing existing radially between the cylindrical sample and capsule. The appropriate dimensions in the real and transformed cases are summarized below:

Real Case (Cylindrical geometry)		Transformed Case (Spherical geometry)
2. 44 cm	OD of capsule	$D_o = 3. 13 \text{ cm}$
1. 93	ID of capsule	$D_i = 2. 63$
1. 27	Diameter of sample	$D = 1. 97$
3. 18	Length of sample	

Using spherical geometry, Turricchia shows that the fraction of radiation isotropically emerging from the spherical shell which is intercepted by the central sphere is given by:

$$f \cong \frac{1}{2} [1 - \cos \phi] \quad (\text{A4. 46})$$

where

$$\phi = \sin^{-1} \frac{D}{D_{\text{avg}}}$$

$D$  = diameter of sphere.

$D_{\text{avg}}$  = average diameter of spherical shell.

Substitution of the numerical values gives  $f \cong 0. 142$ . The calculational procedure will now be summarized for the gamma and beta radiation emanating from the capsule wall.



The 7.72 Mev of gamma radiation produced by the  $\text{Al}^{27}(n, \gamma) \text{Al}^{28}$  reaction is, as discussed in Appendix A4. 3, distributed on the average among several photons of different energies. For the purpose of the present approximate estimate, it will be assumed that the radiation is emitted in 3 photons having an average energy of 2.58 Mev. It will also be assumed conservatively that (1) no self-absorption occurs in the capsule wall so that all gamma radiation produced is emitted and (2) the path of gamma radiation in the spherical sample is equal to the diameter of the sphere. With these conditions, the dose rate due to this source per unit mass in a sample,  $E_a^\gamma$ , can then be written as:

$$E_a^\gamma \cong \frac{\left(\frac{N^*}{A}\right)(\rho_{\text{Al}})\left(\frac{\pi}{6}\right)\left(D_o^3 - D_i^3\right)(\sigma)(3E_\gamma)\left(1 - e^{-\mu_a D}\right) f\phi}{\frac{\pi}{6} D^3 \rho_s} \frac{\text{Mev}}{\text{gm-sec}} \quad (\text{A4. 47})$$

where

$N^*$  = Avogadro's number,  $6.025 \times 10^{23}$  atoms/gm atom.

$A$  = atomic weight of aluminum, 27 gms/gm atom.

$\rho_{\text{Al}}$  = density of aluminum, 2.70 gms/cm<sup>3</sup>.

$\rho_s$  = density of sample, gms/cm<sup>3</sup>.

$D_o, D_i$  = outside and inside diameters of capsule wall (spherical geometry), 3.13 and 2.63 cm, respectively.

$E_\gamma$  = energy of gamma rays emitted, assumed to be 2.58 Mev.

$\mu_a$  = energy absorption coefficient for each sample, cm<sup>-1</sup>.

$D$  = diameter of sample (spherical geometry), 1.97 cm.

$\sigma$  = thermal neutron cross section of  $\text{Al}^{27}$ , 0.23 barns.

$\phi$  = thermal neutron flux, n/cm<sup>2</sup>-sec.

Substitution of properties and conversion of units gives:

$$E_a^\gamma \cong 4.00 \times 10^{-15} \frac{1 - e^{-1.97\mu_a}}{\rho_s} \phi \frac{\text{watt}}{\text{gm}} \quad (\text{A4. 48})$$

The calculations for the materials of interest are summarized in part A of Table A4. 10; the results for the equilibrium gamma activity of  $Al^{28}$  (1. 8 Mev) calculated using this same procedure are also presented in this table.

For the beta radiation emitted on decay of  $Al^{28}$ , the calculation is based on the equilibrium activity of  $Al^{28}$  in the capsule wall. Relations given by Richard and Rubin (A4. 11) are used to estimate the fraction of the beta energy emerging from the jacket; these relations indicate that for a source having a thickness equal to the maximum beta range and for beta energies  $\geq 1$  Mev, one-eighth of the beta energy escapes from one side of the source. It is assumed that all beta radiation intercepted by the sample is absorbed and the calculation is based on the average beta energy. With these conditions, the dose rate due to this source per unit mass,  $E_a^\beta$ , can then be expressed as:

$$E_a^\beta = \frac{\left(\frac{N^*}{A}\right) (\rho_{Al}) \left(\frac{\pi}{6}\right) \left[(D_i + R)^3 - D_i^3\right] (\sigma) (\bar{E}_\beta) (P) (2f) \phi}{\frac{\pi}{6} D^3 \rho_s} \frac{\text{Mev}}{\text{gm-sec}} \quad (\text{A4. 49})$$

where

R = maximum range of beta particle in aluminum,  $\sim 0.20$  cm.

$\bar{E}_\beta$  = average beta energy, 1. 25 Mev.

P = fraction of beta energy produced in the capsule wall (from  $D_i$  to  $D_i + R$ ), which escapes from the inside of the wall,  $\sim 0.125$ .

2f = fraction of beta radiation emitted from inside of wall which is absorbed by sample, 0. 284.

Substitution of properties and conversion of units gives:

$$E_a^\beta = \frac{1.24 \times 10^{-16}}{\rho_s} \phi \frac{\text{watt}}{\text{gm}} \quad (\text{A4. 50})$$

The results obtained are presented in part A of Table A4. 10 for aluminum, polyethylene, and polystyrene.

TABLE A4.10

ENERGY ABSORBED BY VARIOUS MATERIALS FROM GAMMA AND BETA  
RADIATION ORIGINATING IN THE ALUMINUM CAPSUL

Thermal Flux =  $1.41 \times 10^{-13}$  n/cm<sup>2</sup>-sec

(A) Based on Turricchia's Method (A4.6)

MATERIAL	ENERGY ABSORPTION RATE, watts/gm				% OF MEASURED DOSE RATE
	CAPTURE GAMMA RADIATION	GAMMA RADIATION-DECAY OF Al <sup>28</sup>	BETA RADIATION DECAY OF Al <sup>28</sup>	TOTAL	
Aluminum	0.0023	0.0006	0.0006	0.0035	1.6
Polyethylene	0.0024	0.0006	0.0019	0.0049	1.0
Polystyrene	0.0024	0.0006	0.0016	0.0046	1.2

(B) Based on Anderson and Waite's Method (A4.10)

MATERIAL	ENERGY ABSORPTION RATE, watts/gm				% OF MEASURED DOSE RATE
	CAPTURE GAMMA RADIATION	GAMMA RADIATION-DECAY OF Al <sup>28</sup>	BETA RADIATION DECAY OF Al <sup>28</sup>	TOTAL	
Aluminum	0.0013	0.0003	0.0011	0.0027	1.2
Polyethylene	0.0013	0.0003	0.0031	0.0047	0.9
Polystyrene	0.0013	0.0003	0.0027	0.0043	1.1

(C) Best Estimate (Based on Anderson and Waite's Gamma Calculations and Turricchia's Beta Calculations)

MATERIAL	ENERGY ABSORPTION RATE			% OF MEASURED DOSE RATE
	GAMMA RADIATION	BETA RADIATION	TOTAL	
Aluminum	0.0016	0.0006	0.0022	1.0
Polyethylene	0.0016	0.0019	0.0035	0.7
Polystyrene	0.0016	0.0016	0.0032	0.9

## A4. 10. 2 BASED ON ANDERSON AND WAITE'S CALCULATIONS

Anderson and Waite (A4. 10) have also estimated the energy absorption rates due to radiation originating in the aluminum capsule for a geometry similar to that of the present calorimeter. Their method of calculation is different from that of Turrichia and is presented as an independent check of the calculations based on Turrichia's method. In their calculations, the actual cylindrical geometry was approximated by transformation to spherical geometry as described above for Turrichia's calculations.

For gamma radiation, the gamma flux at the center of the sphere due to gamma radiation originating in the spherical shell is given by the relation:

$$I = AE_{\gamma} \quad (A4. 51)$$

where

$I$  is the gamma flux,  $\text{ev}/\text{cm}^2\text{-sec}$ .

$A$  is the surface activity,  $\text{dis}/\text{cm}^2\text{-sec}$ .

$E_{\gamma}$  is the gamma photon energy,  $\text{ev}$ .

The energy absorption rate in the sample is then given by  $\left(\frac{\mu_a}{\rho}\right)_s I \frac{\text{Mev}}{\text{gm-sec}}$ .

In the present case, with the same dimensions as used by Turrichia, the following calculations apply, assuming as before that three 2.58 Mev gamma photons are emitted on neutron capture:

$$A = \frac{\pi}{6} (3.13^3 - 2.63^3)(2.7) \left(\frac{6.025 \times 10^{23}}{27}\right) (0.23 \times 10^{-24})$$

$$\left(\frac{1}{\pi(2.88)^2}\right) \phi \frac{\text{interactions}}{\text{cm}^2\text{-sec}}$$

$$= 34.9 \times 10^{-4} \phi \frac{\text{interactions}}{\text{cm}^2\text{-sec}}$$

$$I = (34.9 \times 10^{-4} \phi)(3)(2.58 \times 10^6) \frac{\text{ev}}{\text{cm}^2\text{-sec}} = 2.70 \times 10^4 \phi \frac{\text{ev}}{\text{cm}^2\text{-sec}}$$

$$E_a^\gamma = 2.70 \times 10^4 \phi \left( \frac{\mu_a}{\rho} \right)_s \frac{\text{ev}}{\text{gm-sec}} = 4.32 \times 10^{-15} \phi \left( \frac{\mu_a}{\rho} \right)_s \frac{\text{watts}}{\text{gm}}$$

A similar calculation gives for the 1.8 Mev gamma emitted by Al<sup>28</sup>:

$$E_a^\gamma = 1.00 \times 10^{-15} \phi \left( \frac{\mu_a}{\rho} \right)_s \frac{\text{watts}}{\text{gm}}$$

For beta radiation, Anderson and Waite used Richards and Rubin's (A4. 11) results to estimate the fraction of the beta energy escaping from the capsule wall as did Turricchia. They assumed, however, that the fraction of the emitted beta energy absorbed in the samples is proportional to the surface area of the sample relative to that of the spherical shell, instead of the solid angle subtended by the sample as did Turricchia. Hence, the fraction of the beta energy emitted from the inside capsule wall which is captured by the sample is, with this approximation,  $(1.93/2.83)^2 = 0.464$ ; this is a factor of 1.63 higher than the value of  $2f = 0.284$  used in the calculations based on Turricchia's method. In part B of Table A4. 10, the results obtained based on Anderson and Waite's procedures are given.

### A4. 10. 3 DISCUSSION

It will be seen from Table A4. 10 that the estimated total percentage of the measured dose rate coming from radiation originating in the aluminum capsule is of the order of one per cent for both methods of calculation. Also, it is seen that Turricchia's method gives gamma absorption rates approximately twice those based on Anderson's and Waite's method. It is believed that Anderson and Waite's method probably gives the more reliable estimate for the gamma radiation since Turricchia made the conservative assumption that any gamma radiation striking the sample passed through the entire thickness of the sample. In the case of beta radiation, as mentioned previously, Anderson and Waite's method gives results 1.63 times those obtained using Turricchia's method. In this case, it is believed Turricchia's method gives the more accurate result since his calculation is based on the solid angle which the sample subtends with respect to any point

on the shell. The best estimate of the energy absorption rate is therefore based on Anderson and Waite's method for the gamma radiation and Turricchia's method for beta radiation. The results are given in part C of Table A4. 10 where it is seen the percentage is estimated to be of the order of 0. 7 to 1. 0 per cent of the total measured dose rate. No correction has been applied to the measured dose rates, however, because of (1) the limited accuracy and small magnitude of the estimated energy absorption rates and (2) the fact that, as discussed in Appendix A4. 11, the energy gained by radiation originating in the capsule is balanced to some extent by loss from the sample of energetic electrons produced by gamma interactions.

#### APPENDIX 4. 11

#### NET ABSORBED ENERGY LOSS FROM SAMPLES DUE TO ESCAPE OF COMPTON ELECTRONS FROM SAMPLES AND CAPTURE OF COMPTON ELECTRONS EMANATING FROM ALUMINUM CAPSULE

The absorption of gamma radiation by the Compton process produces electrons having an energy range varying from zero to almost the energy of the gamma photon. The escape of these energetic electrons from the samples could amount to an appreciable percentage of the total absorbed gamma energy in the sample. This loss will be counterbalanced, however, by capture by the samples of Compton electrons as well as beta and gamma radiation (see Appendix 4. 10) emanating from the aluminum capsule.

This effect is quite difficult to estimate accurately because of (1) the variation in energy and, hence, in range of the electrons produced by monoenergetic gamma radiation, (2) the wide range of gamma energies encountered in a nuclear reactor, and (3) the difficulty of accurately calculating the fraction of the electron energy absorbed in a small sample with a uniform source distribution of electrons.

Anderson and Waite (A4. 10) have made calculations for this effect based on the electron energy distribution produced by 2 Mev gamma

radiation. Their calculations are based on a division of the Compton electrons produced into nine different energy groups from zero to the maximum electron energy of 1.8 Mev. For each electron energy interval, a mean electron energy was assumed and the electron range computed. The electron escape formulae derived by Richards and Rubin (A4. 11) were used to estimate for each energy interval the fraction of the total absorbed energy represented by those electrons which are lost from the calorimeter sample. The calculations were made for a calorimeter sample 2.54 cm long by 1.27 cm diameter. Their results are presented in Table A4. 11 for aluminum and polyethylene. Included also in Table A4. 11, is a correction factor for the total energy absorption rate based on the assumptions that the Compton electrons lost from the aluminum sample are exactly balanced by absorption of Compton electrons from the aluminum capsule and that 50 per cent of the total dose rate in polyethylene is due to gamma interactions. Based on these assumptions, the correction to the total dose rate is estimated to be approximately 2-1/2 per cent. This correction has not been applied to the data since, as stated by Anderson and Waite, the corrections "are in general within the experimental error . . . and, as the absolute corrections are uncertain due to the various assumptions made in their estimates, they have been ignored in quoting the corrected values of energy absorption." Based on these calculations, an error of  $\pm 1$  per cent for aluminum and  $\pm 3$  per cent for all other absorbers will be assumed as the contribution to the total error from this source as well as the beta and gamma radiation produced in the aluminum capsule by thermal neutron reactions. If a more accurate evaluation of this effect is desired, it is recommended that calorimetric measurements be performed in samples having different radii.

TABLE A4.11  
 LOSS OF ABSORBED ENERGY DUE TO COMPTON GAMMA INTERACTIONS BY  
 ESCAPE OF COMPTON ELECTRONS FROM ABSORBER  
 (From Anderson and Waite (A4.10))

MATERIAL	PERCENTAGE OF GAMMA ENERGY LOST BY ESCAPE OF COMPTON ELECTRONS	DIFFERENCE BETWEEN PERCENTAGE LOSS AND PERCENTAGE GAINED BASED ON 0% DIFFERENCE FOR ALUMINUM	% CORRECTION TO TOTAL MEASURED ENERGY ABSORPTION BASED ON 0% CORRECTION FOR ALUMINUM AND 50% OF ENERGY ABSORBED DUE TO GAMMA RAYS IN POLYETHYLENE
Al	8.26	0	0
(CH <sub>2</sub> ) <sub>n</sub>	13.1	4.8	+ 2.4



## APPENDIX 4. 12

SAMPLE CALCULATION OF  $R_{Al}^{\gamma}$  AND  $I_H$ 

The calculation procedure for  $R_{Al}^{\gamma}$  and  $I_H$  has been outlined in section 4. 2. 4. In this appendix, a sample calculation is given using the maximum dose rate data quoted in Table 4. 12 for calorimeter series III-2 at 100 kw. The data are:

$$R_{Al}^T = 0. 232 \text{ watts/gm}$$

$$R_{PE}^T = 0. 513 \text{ watts/gm}$$

$$R_{PS}^T = 0. 376 \text{ watts/gm}$$

At the center position of the reactor with the stainless steel thimble in place, the 2200 meter/sec thermal flux is (from Figure 4. 17)  $1. 41 \times 10^{13} \text{ n/cm}^2 \text{ sec}$ . From Appendix 4. 3 at this flux,  $R_{Al}^{th} = 0. 00403 + 0. 0139 (1 - e^{-0. 30t}) \text{ watt/gm}$ ; with  $t = 6 \text{ minutes}$ ,  $R_{Al}^{th} = 0. 016 \text{ watts/gm}$ . Now, from section 4. 2. 4, the equations for the dose rate in aluminum, polyethylene, and polystyrene are:

$$R_{Al}^T - R_{Al}^{th} = R_{Al}^{\gamma} + 0. 221 \times 10^{22} I_H$$

$$R_{PE}^T = 1. 184 R_{Al}^{\gamma} + 9. 32 \times 10^{22} I_H \quad (\text{A4. 52})$$

$$R_{PS}^T = 1. 119 R_{Al}^{\gamma} + 5. 39 \times 10^{22} I_H$$

Substituting the data into these equations results in:

$$0. 216 = R_{Al}^{\gamma} + 0. 221 \times 10^{22} I_H$$

$$0. 513 = 1. 184 R_{Al}^{\gamma} + 9. 32 \times 10^{22} I_H$$

$$0. 376 = 1. 119 R_{Al}^{\gamma} + 5. 39 \times 10^{22} I_H$$

$R_{Al}^{\gamma}$  is then calculated for two values of  $I_H$  for each equation and plotted as in Figure A4. 9. The best value of  $R_{Al}^{\gamma}$  and of  $I_H$  is selected so that  $R_{Al}^{\gamma}$  from the aluminum sample is the average of that from the two plastic samples. The errors are obtained, as described in section 4. 4. 3. 4, from the spread of the values of  $R_{Al}^{\gamma}$  and  $I_H$  around the best values. The selected values, based on Figure A4. 9, are:

$$R_{Al}^{\gamma} = 0. 210 \pm 0. 006 \text{ watts/gm}$$

$$I_H = (2. 74 \pm 0. 13) \times 10^{-24} \text{ watts/atom}$$

The fast neutron and gamma dose rates in Santowax OMP are calculated using the following equation given in section 4. 2. 4:

$$R_{SW}^T = 1. 100 R_{Al}^{\gamma} + 4. 43 \times 10^{22} I_H = R_{SW}^{\gamma} + R_{SW}^n \quad (\text{A4. 53})$$

$$R_{SW}^{\gamma} = 0. 231 \text{ watts/gm}$$

$$R_{SW}^n = 0. 121 \text{ watts/gm}$$

$$R_{SW}^T = 0. 352 \text{ watts/gm}$$

For comparison with the measured values, the calculated total dose rates are given in Table A4. 12.

Table A4. 12. Comparison of Measured and Calculated Total Dose Rates

Material	Measured	Calculated	% Difference
Aluminum	$R_{Al}^T - R_{Al}^{th} = 0. 216$	0. 216	0
Polyethylene	$R_{PE}^T = 0. 513$	0. 505	-1. 6%
Polystyrene	$R_{PS}^T = 0. 376$	0. 383	+1. 8%

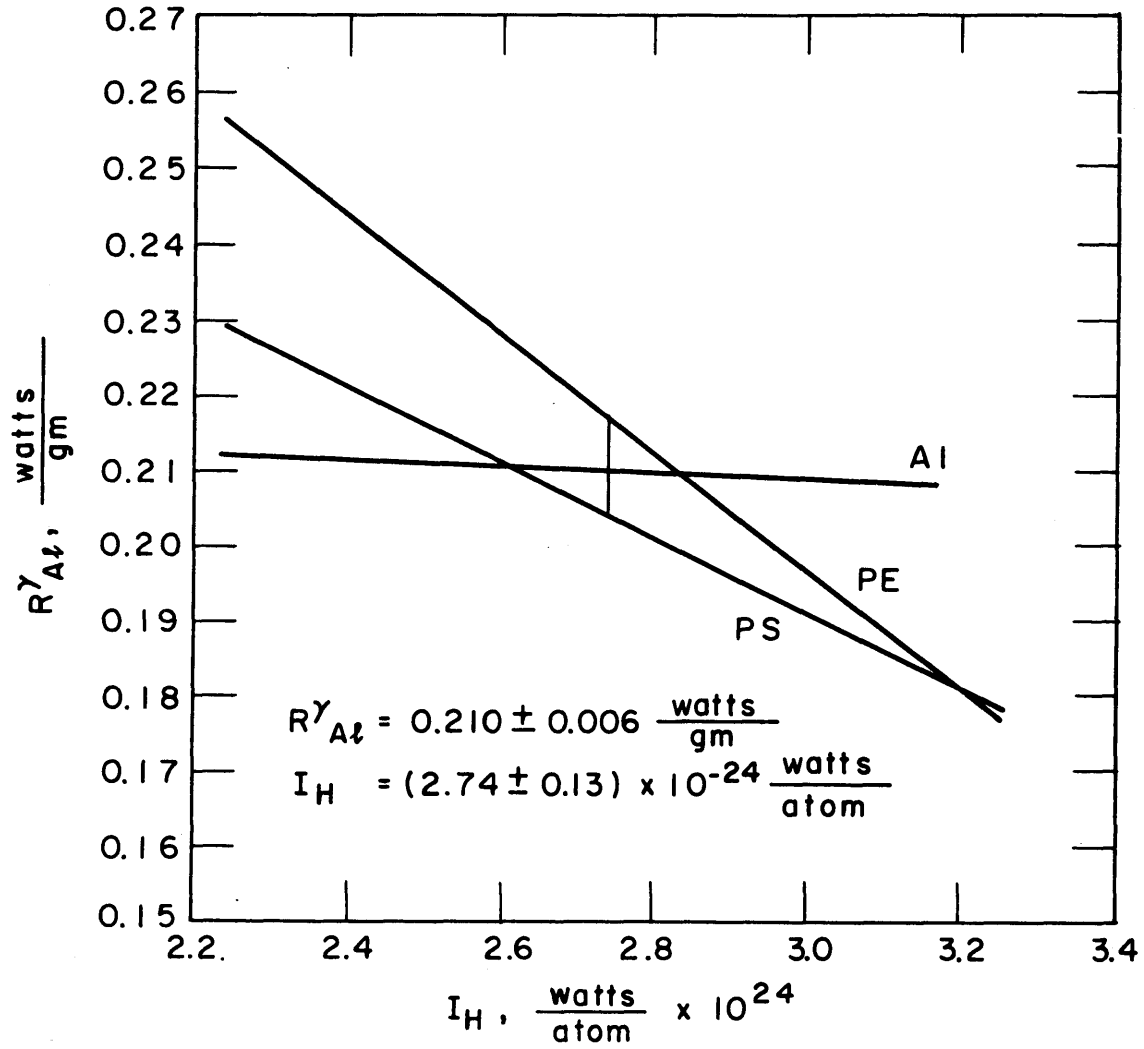


FIGURE A4.9 PLOT OF  $R^{\gamma}_{Al}$  VS  $I_H$  USED IN DETERMINING BEST VALUES OF  $R^{\gamma}_{Al}$  AND OF  $I_H$

## APPENDIX 4.13

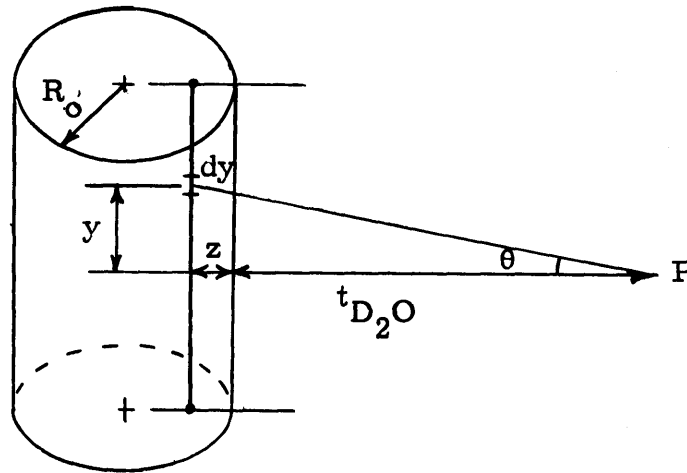
ESTIMATION OF GAMMA AND FAST NEUTRON DOSE RATE  
CONTRIBUTION FROM CENTRAL FUEL ELEMENT RELATIVE  
TO THAT FROM SURROUNDING FUEL ELEMENTS

As discussed in Chapter 4, the fast neutron dose rate measured in the stainless steel thimble and fuel element 2MR-11 is approximately 18 per cent greater than that measured in the aluminum thimble and fuel element 2MR-12, whereas the gamma dose rate is greater by only about 2 to 5 per cent. The main differences between the two cases were an increase in the fuel loading in the central fuel element (68.6 gms to 80.7 gms) and substitution of the stainless steel thimble for the aluminum thimble. In order to see whether this relatively large increase in the fast neutron dose rate compared to the increase in the gamma dose rate is realistic, it is necessary to have an estimate of the fraction of the fast neutron dose rate, and of the gamma dose rate, at the center of the core which is due to fissions in the central fuel element. The procedure used in estimating these two fractions is described in this appendix. The relative contributions of the aluminum and stainless steel thimbles to the gamma dose rate are considered in Appendix 4.1.4.

## A4.13.1 GAMMA DOSE RATE

The positions of the fuel elements in the MITR and the cross section of the fuel element are illustrated in Figures 3.2 and 3.3, respectively. The central fuel element position is surrounded by a ring of six fuel elements, the centers of which are 16.2 cm from the radial center of the core. Outside of this ring of six, another ring of twelve fuel elements is located at a distance of 30.2 cm from radial center of the core. Gamma radiation from the control rods which are located between the two fuel element rings will be neglected, since the rods are generally almost out of the core when the reactor is operating. The fuel elements are 24 inches (61.0 cm) long.

For the purpose of the calculations, it will be assumed that the fuel elements can be transformed into homogeneous cylindrical sources of infinite length consisting of a mixture of  $D_2O$ , uranium, and aluminum. According to Rockwell (A4. 20) and Blizard (A4. 21), the dose rate from a cylindrical source can be represented by an equivalent line source positioned as shown in the following sketch:



where

$z$  = self-attenuation distance presented graphically by Rockwell (A4. 20) and Blizard (A4. 21).

$t_{D_2O}$  = thickness of  $D_2O$  between outside of source and the point, P (center of reactor in this case).

$R_0$  = radius of source, cm.

For a monoenergetic line source, the dose rate due to a differential element of length can be represented by the following equation:

$$dD \cong \frac{(S_v)(\pi R_0^2)(dy) \left(\frac{\mu_a}{\rho}\right) (E_\gamma) e^{-(\mu_{D_2O} t_{D_2O} + \mu_s z) \sec \theta} B_{\mu_{D_2O} t_{D_2O}}}{4\pi(t_{D_2O} + z)^2 \sec^2 \theta} \quad (A4. 54)$$

where

$S_v$  = volumetric source strength, photons/cm<sup>3</sup>-sec

$E_\gamma$  = gamma energy, Mev/photon

$\frac{\mu_a}{\rho}$  = energy absorption coefficient for the material in which the dose rate is desired,  $\text{cm}^2/\text{gm}$ .

$\mu_s$  = linear attenuation coefficient in source,  $\text{cm}^{-1}$ .

$\mu_{\text{D}_2\text{O}}$  = linear attenuation coefficient in  $\text{D}_2\text{O}$ ,  $\text{cm}^{-1}$ .

$dD$  = dose rate due to segment  $dy$ ,  $\text{Mev}/\text{gm}\text{-sec}$ .

$B_{\mu_{\text{D}_2\text{O}}^t \text{D}_2\text{O}}$  = isotropic point source buildup factor.

In this equation, buildup of scattered radiation in the source is neglected and a buildup factor is included only for attenuation through the  $\text{D}_2\text{O}$ .

While not exact, this approximation should not introduce a large error.

Now,

$$\tan \theta = \frac{y}{t_{\text{D}_2\text{O}} + z} \quad \text{or} \quad dy = (t_{\text{D}_2\text{O}} + z) \sec^2 \theta d\theta$$

Substitution and integration gives:

$$D = \frac{S_v R_o^2 E \gamma \frac{\mu_a}{\rho}}{4(t_{\text{D}_2\text{O}} + z)} \int_{\theta_l}^{\theta_u} e^{-(\mu_{\text{D}_2\text{O}}^t \text{D}_2\text{O} + \mu_s z) \sec \theta} B_{\mu_{\text{D}_2\text{O}}^t \text{D}_2\text{O}} d\theta \quad (\text{A4. 55})$$

For an infinite line source,  $\theta_u = +\frac{\pi}{2}$  and  $\theta_l = -\frac{\pi}{2}$  so that:

$$D = \frac{S_v R_o^2 E \gamma \frac{\mu_a}{\rho}}{2(t_{\text{D}_2\text{O}} + z)} \int_0^{\pi/2} e^{-(\mu_{\text{D}_2\text{O}}^t \text{D}_2\text{O} + \mu_s z) \sec \theta} B_{\mu_{\text{D}_2\text{O}}^t \text{D}_2\text{O}} d\theta \quad (\text{A4. 56})$$

In integrating this expression, the buildup factor can be represented according to Rockwell and Blizard as:

$$B_{\mu_{\text{D}_2\text{O}}^t \text{D}_2\text{O}} = A_1 e^{-a_1 \mu_{\text{D}_2\text{O}}^t \text{D}_2\text{O}} + A_2 e^{-a_2 \mu_{\text{D}_2\text{O}}^t \text{D}_2\text{O}} \quad (\text{A4. 57})$$

Substitution of this expression gives:

$$D = \frac{S R_o^2 E_\gamma \frac{\mu_a}{\rho}}{2(t_{D_2O} + z)} \left\{ A_1 \int_0^{\pi/2} e^{-[\mu_s z + (1+a_1) \mu_{D_2O} t_{D_2O}]} \sec \theta \, d\theta \right. \\ \left. + A_2 \int_0^{\pi/2} e^{-[\mu_s z + (1+a_2) \mu_{D_2O} t_{D_2O}]} \sec \theta \, d\theta \right\} \quad (A4. 58)$$

Finally,

$$D = \frac{S R_o^2 E_\gamma \frac{\mu_a}{\rho}}{2(t_{D_2O} + z)} \left[ A_1 F\left(\frac{\pi}{2}, b_{2m}\right) + A_2 F\left(\frac{\pi}{2}, b_{2n}\right) \right] \quad (A4. 59)$$

where

$$b_{2m} = \mu_s z + (1+a_1) \mu_{D_2O} t_{D_2O}$$

$$b_{2n} = \mu_s z + (1+a_2) \mu_{D_2O} t_{D_2O}$$

$$F\left(\frac{\pi}{2}, b_2\right) = \int_0^{\pi/2} e^{-b_2 \sec \theta} \, d\theta$$

Values of  $F(\pi/2, b_2)$  are given graphically by Rockwell (A4. 20) and by Henderson and Whittier (A4. 8) among others.

This equation will now be applied to the present case. For the eighteen fuel elements surrounding the central fuel element, the cross sectional area is 9. 20 in.<sup>2</sup> and the effective radius of a cylindrical source having this area is 1. 71 inches or 4. 35 cm. The calculation will first be made for the ring of six fuel elements immediately surrounding the central element. The gamma energy will be assumed to be 1. 0 Mev since approximately half of the energy absorbed in the organic due to gamma radiation comes from gamma photons with energies greater than 1. 0 Mev and approximately half from gammas with energies less than 1. 0 Mev.

$$R_o = 4.35 \text{ cm}$$

$$t_{D_2O} = 16.2 - 4.35 = 11.8 \text{ cm}$$

Average  $\mu_s$ :

$$\left(\frac{\mu}{\rho}\right)_{Al} = 0.0614 \frac{\text{cm}^2}{\text{gm}} \quad \mu_{Al} = 0.166 \text{ cm}^{-1} \quad \text{Area} = 3.67 \text{ in.}^2$$

$$\left(\frac{\mu}{\rho}\right)_U = 0.0779 \frac{\text{cm}^2}{\text{gm}} \quad \mu_U = 1.452 \text{ cm}^{-1} \quad \text{Area} = 0.00136 \text{ in.}^2$$

$$\left(\frac{\mu}{\rho}\right)_{D_2O} = 0.062 \frac{\text{cm}^2}{\text{gm}} \quad \mu_{D_2O} = 0.0682 \text{ cm}^{-1} \quad \text{Area} = 5.51 \text{ in.}^2$$

$$\mu_s = 0.166 \frac{3.67}{9.20} + 1.452 \frac{0.00136}{9.20} + 0.0682 \frac{5.51}{9.20} = 0.107 \text{ cm}^{-1}$$

Self-attenuation distance:

$$\mu_{D_2O} t_{D_2O} = (0.0682)(11.8) = 0.804$$

$$\mu_s (R_o + t_{D_2O}) = (0.107)(16.2) = 1.739$$

From plots by Blizard (A4. 21),

$$\frac{\mu_s z}{m} = 1.10 \quad m = 0.35 \quad \text{and} \quad z = 3.60$$

Constants for buildup factor: these are assumed to be the same as for  $H_2O$  and are taken from Blizard (A4. 21) for 1.0 Mev photons,

$$A_1 = 11$$

$$A_2 = -10$$

$$a_1 = -0.104$$

$$a_2 = 0.028$$

$$b_{2n} = (0.107)(3.60) + (0.0682)(1.028)(11.8) = 1.211$$

$$b_{2m} = (0.107)(3.60) + (0.0682)(0.896)(11.8) = 1.106$$



From plots by Henderson and Whittier (A4. 8),

$$F(\pi/2, b_{2n}) = 0. 250$$

$$F(\pi/2, b_{2m}) = 0. 290$$

Substitution gives for six fuel elements:

$$D = (6) \frac{S_v (4. 35)^2 \frac{\mu_a}{\rho} E_\gamma}{(2)(11. 8 + 3. 6)} [ (11)(0. 290) - (10)(0. 250) ] = 2. 54 \left( S_v \frac{\mu_a}{\rho} E_\gamma \right)$$

For the ring of 12 fuel elements,

$$R_o = 4. 35 \text{ cm}$$

$$t_{D_2O} = 30. 2 - 4. 35 = 25. 8 \text{ cm}$$

$$z = 4. 09 \text{ cm}$$

$$b_{2n} = 2. 246$$

$$b_{2m} = 2. 015$$

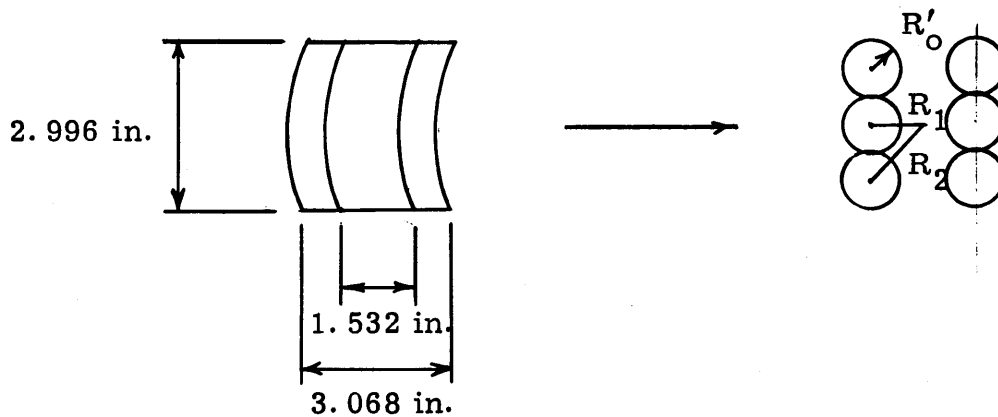
$$F(\pi/2, b_{2n}) = 0. 068$$

$$F(\pi/2, b_{2m}) = 0. 087$$

$$D = 1. 046 \left( \frac{\phi_{12}}{\phi_6} \right) \left( S_v \frac{\mu_a}{\rho} E_\gamma \right)$$

where  $\phi_{12}/\phi_6$  = ratio of thermal neutron flux in ring of 12 fuel elements to that in ring of 6 fuel elements.

For the central fuel element, the geometry can be transformed with good approximation as indicated in the following sketch:



$$\text{Area of each fuel section} = \frac{3.068 - 1.532}{2} (2.996) = 2.30 \text{ in.}^2$$

$$\text{Area of each cylinder} = \frac{2.30}{3} \text{ in.}^2 = \pi(R'_O)^2$$

$$R'_O = 0.496 \text{ in.} = 1.26 \text{ cm}$$

$$R_1 = \left( \frac{3.068 - 1.532}{2} \right) \left( \frac{1}{2} \right) + \frac{1.532}{2} = 1.151 \text{ in.} = 2.92 \text{ cm}$$

$$R_2 = \sqrt{(2.92)^2 + [(2)(1.26)]^2} = 3.86 \text{ cm}$$

The graphs presented by Blizard (A4. 21) for the determination of  $z$  do not cover the small cylinders for the present case. It is thus assumed that  $z = R'_O$  for these small radius cylinders. For the two middle cylinders,

$$t_{D_2O} = 2.92 - 1.26 = 1.66 \text{ cm}$$

$$z = 1.26 \text{ cm}$$

$$b_{2n} = (0.107)(1.26) + (0.0682)(1.028)(1.66) = 0.2510$$

$$b_{2m} = (0.107)(1.26) + (0.0682)(0.896)(1.66) = 0.2360$$

$$F(\pi/2, b_{2n}) = 0.99$$

$$F(\pi/2, b_{2m}) = 1.01$$

For the two middle cylinders, then,

$$D = 2 \frac{S_v (1.26)^2 \left( \frac{\mu_a}{\rho} E_\gamma \right)}{(2)(1.26 + 1.66)} [(11)(1.01) - (10)(0.99)] \frac{\phi_c}{\phi_6} = 0.653 \frac{\phi_c}{\phi_6} \left( S_v \frac{\mu_a}{\rho} E_\gamma \right)$$

For the four outer cylinders,

$$t_{D_2O} = 3.86 - 1.26 = 2.60$$

$$z = 1.26$$

$$b_{2n} = 0.3168$$

$$b_{2m} = 0.2938$$

$$F(\pi/2, b_{2n}) = 0.88$$

$$F(\pi/2, b_{2m}) = 0.91$$

$$D = 0.987 \frac{\phi_c}{\phi_6} \left( S_v \frac{\mu_a}{\rho} E_\gamma \right)$$

Total for central fuel element,  $D = 1.64 \frac{\phi_c}{\phi_6} \left( S_v \frac{\mu_a}{\rho} E_\gamma \right)$ . The percentage of the gamma dose due to the central fuel element is then:

$$\% = \frac{1.64 \frac{\phi_c}{\phi_6}}{1.64 \frac{\phi_c}{\phi_6} + 2.54 + 1.046 \frac{\phi_{12}}{\phi_6}}$$

Calculations for the MIT Reactor have indicated the following flux ratios:

$$\frac{\phi_c}{\phi_6} = 1.059 \quad \frac{\phi_{12}}{\phi_6} = 0.883$$

Substitution of these flux ratios gives 33 per cent as the fraction of the gamma dose rate due to the central fuel element.

## A4. 13. 2. FAST NEUTRON DOSE RATE

Intuitively, it would be expected that the fast neutron dose rate in the organic material would be due to fast neutrons almost exclusively from the central fuel element because of the relatively short slowing down distance of the neutrons. This is particularly true since, as shown in Table 4.8, approximately 50 per cent of the fast neutron dose rate is due to fast neutrons having energies above 1.0 Mev and 90 per cent to fast neutrons having energies above 0.1 Mev.

The estimation of the relative contribution of the different fuel elements in the reactor to the fast neutron dose rate in Santowax OMP will be made with the assumption of Fermi Age theory. While Fermi Age theory is not strictly applicable to a  $D_2O$  medium, the accuracy of the approximation should be sufficient for the present purpose. It will also be assumed that the fuel elements can be represented as infinite line sources with a correction considered for self-absorption in the fuel element.

MacGreblian and Holmes (A4. 22) give the following equation for the slowing down density for an infinite line source in an infinite medium:

$$q(\rho, u) = \frac{q_0 e^{-\rho^2/4\tau(u)}}{4\pi\tau(u)} \quad (\text{A4. 60})$$

where

$u$  = lethargy =  $\ln \frac{E_0}{E}$  where  $E_0$  is the source neutron energy.

$\rho$  = radial distance from the line source, cm.

$q(\rho, u)$  = slowing down density as function of  $\rho$  and  $u$  = number of neutrons per unit volume per unit time whose energies are changed from some value above  $E$  to some value below  $E$ .

$q_0$  = source neutrons per unit time per unit length of source released at  $\rho = 0, \tau = 0$ .

$\tau(u)$  = Fermi age as function of lethargy,  $\text{cm}^2$ .

The neutron flux is related to the slowing down density by:

$$\phi(u) = \frac{q(u)}{\xi \Sigma_s(u)} \quad (\text{A4. 61})$$

and the collision rate is:

$$\int_0^u \Sigma_s(u) \phi(u) du \quad (\text{A4. 62})$$

where

$$\xi = 1 + \frac{\alpha \ln \alpha}{1 - \alpha} \quad \alpha = \left( \frac{A-1}{A+1} \right)^2$$

$\Sigma_s(u)$  = macroscopic scattering cross section,  $\text{cm}^{-1}$ .

The Fermi age for a nonabsorbing medium is given by:

$$\tau(u) = \int_0^u \frac{D(u)}{\xi \Sigma_s(u)} du \quad (\text{A4. 63})$$

By means of these relations, the relative dose rate in Santowax OMP at the core center can be calculated for the different fuel elements in the reactor. The calculations performed for the present case are given in Tables A4. 13 and A4. 14 and Figures A4. 11 and A4. 12; the method of calculation is outlined below. A 2.0 Mev monoenergetic source is assumed.

#### (a) Estimation of Fermi Age for Different Neutron Lethargies

The slowing down of fast neutrons in heavy water is governed mainly by scattering with the deuterium atoms. The scattering cross section for deuterium does not vary greatly between 1.0 ev and 2.0 Mev increasing from 2.6 barns at 2.0 Mev to 3.0 barns at 1 Mev to 3.4 barns at 0.1 Mev. Below this energy, the cross section is approximately constant, down to an energy range of 1.0 ev. It will thus be assumed that the scattering cross section is constant over this energy range. With this assumption,

$$\tau(u) = \frac{\bar{D}}{\xi \bar{\Sigma}_s} u \quad (\text{A4. 64})$$

TABLE A4.13

CALCULATIONS FOR DETERMINATION OF SOURCE STRENGTH  
AS FUNCTION OF NEUTRON LETHARGY

E, Mev	$u \ln \frac{2.0}{E}$	$\tau(u)$ = 19.6u	$\bar{\tau} = L_s$	$R_o = 4.35\text{cm}$		$R_o = 1.26\text{cm}$	
				$R_o/L_s$	F	$R_o/L_s$	F
2.0	0	0	0		1.00		1.00
1.98	0.00996	0.195	0.441	9.87	0.76	2.86	0.33
1.96	0.0198	0.388	0.623	6.98	0.71	2.02	0.17
1.94	0.0305	0.598	0.772	5.64	0.645	1.632	0.10
1.92	0.0402	0.787	0.886	4.91	0.595	1.422	0.065
1.90	0.0507	0.994	0.997	4.36	0.54	1.263	0.040
1.85	0.0760	1.490	1.220	3.57	0.44	1.032	0.0
1.80	0.1052	2.005	1.414	3.08	0.37	--	--
1.70	0.1648	3.225	1.795	2.42	0.25	--	--
1.60	0.223	4.37	2.09	2.08	0.18	--	--
1.40	0.358	7.01	2.65	1.642	0.10	--	--
1.20	0.511	10.00	3.16	1.378	0.055	--	--
1.00	0.694	13.60	3.68	1.18	0.025	--	--

TABLE A4.14

INFORMATION FOR GRAPHICAL INTEGRATION OF EQUATION A4.75,

$$\frac{N_C}{N_H} = \frac{4.72}{3.66} \quad \frac{\xi_C}{\xi_H} = \frac{0.142}{0.500} = 0.284$$

E, Mev	$u = \ln \frac{2.0}{E}$	$\tau(u) = 7.04u$ cm <sup>2</sup>	$\sigma_S^H(u) +$ $0.366 \sigma_S^C(u)$ barns	$e^{-u}$	$q_6$	$[\sigma_S^H(u) + 0.366 \sigma_S^C(u)] q_6 e^{-u}$	$q_c$	$[\sigma_S^H(u) + 0.366 \sigma_S^C(u)] q_c e^{-u}$
2.0	0	0	-	1.0	0	0	0	0
1.75	0.133	0.935	3.84	0.875	~0	~0	0.1244	$418 \times 10^{-3}$
1.50	0.288	2.02	4.16	0.750	~0	~0	0.2746	$856 \times 10^{-3}$
1.40	0.358	2.52	4.29	0.700	~0	~0	0.2937	$880 \times 10^{-3}$
1.25	0.470	3.31	4.60	0.625	~0	~0	0.2967	$852 \times 10^{-3}$
1.00	0.694	4.89	5.24	0.500	~0	~0	0.2706	$710 \times 10^{-3}$
0.80	0.917	6.45	5.85	0.400	~0	~0	0.2388	$559 \times 10^{-3}$
0.60	1.202	8.47	6.77	0.300	$1.441 \times 10^{-3}$	$2.93 \times 10^{-3}$	0.2039	$413 \times 10^{-3}$
0.40	1.61	11.32	8.23	0.200	$7.50 \times 10^{-3}$	$12.32 \times 10^{-3}$	0.1672	$275 \times 10^{-3}$
0.20	2.30	16.20	11.15	0.100	$30.5 \times 10^{-3}$	$34.0 \times 10^{-3}$	0.1273	$142 \times 10^{-3}$
0.10	3.00	21.1	14.2	0.0500	$59.5 \times 10^{-3}$	$42.2 \times 10^{-3}$	0.1022	$72.5 \times 10^{-3}$
0.08	3.22	22.6	15.1	0.0400	$68.8 \times 10^{-3}$	$41.5 \times 10^{-3}$	-	
0.06	3.51	24.7	16.3	0.0300	$80.5 \times 10^{-3}$	$39.4 \times 10^{-3}$	-	
0.04	3.91	27.5	17.9	0.0200	$94.5 \times 10^{-3}$	$33.8 \times 10^{-3}$	0.0812	$29.1 \times 10^{-3}$
0.02	4.61	32.4	19.6	0.0100	$115.8 \times 10^{-3}$	$22.7 \times 10^{-3}$		
0.01	5.30	37.3	20.7	0.0050	$131.0 \times 10^{-3}$	$13.52 \times 10^{-3}$		
0.008	5.53	38.9	21.7	0.0040	$135.0 \times 10^{-3}$	$11.71 \times 10^{-3}$		
0.004	6.21	43.7	21.7	0.002	$144.1 \times 10^{-3}$	$6.26 \times 10^{-3}$		

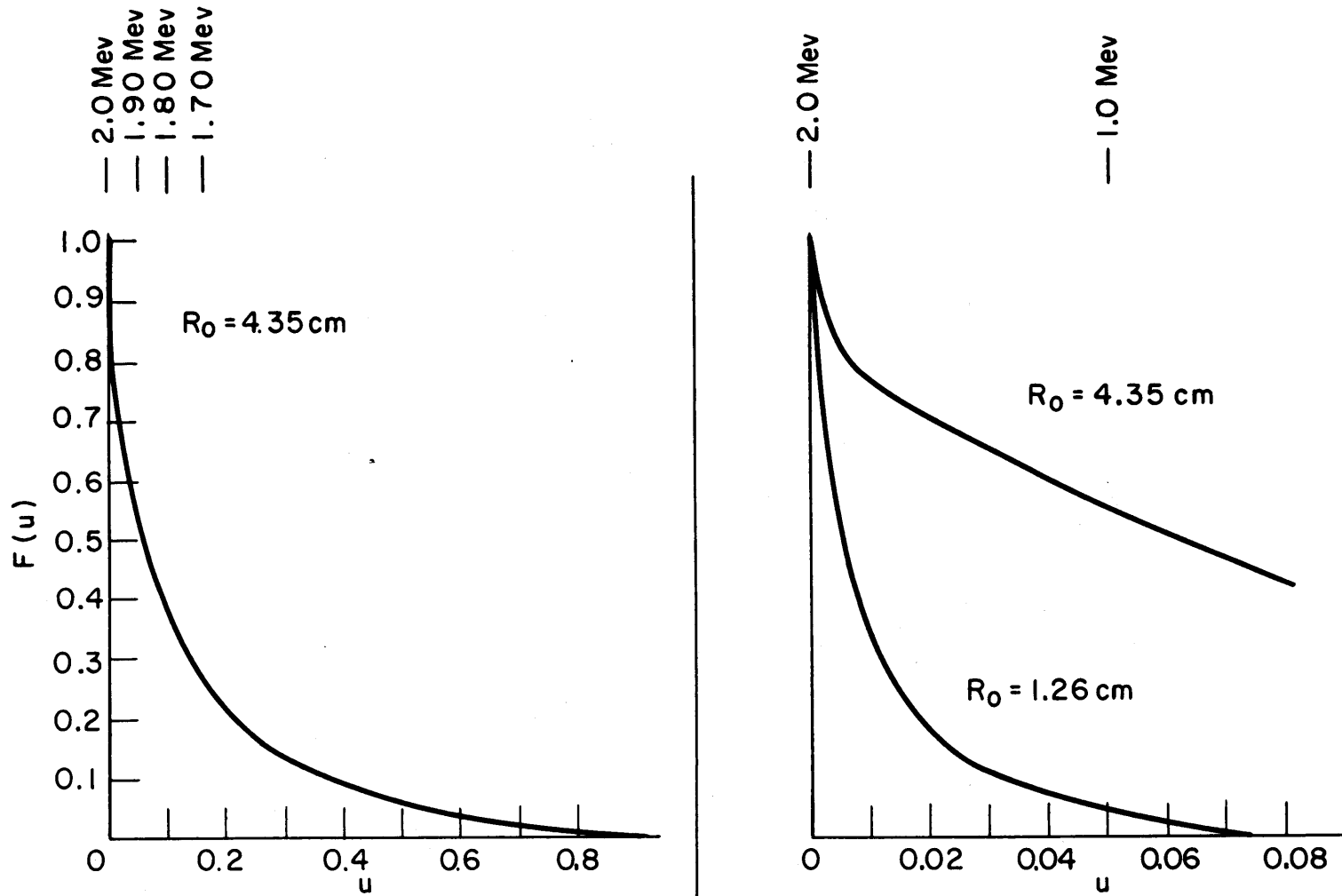


FIGURE A4.10 CURVES FOR DETERMINATION OF SOURCE STRENGTH AS FUNCTION OF NEUTRON LETHARGY



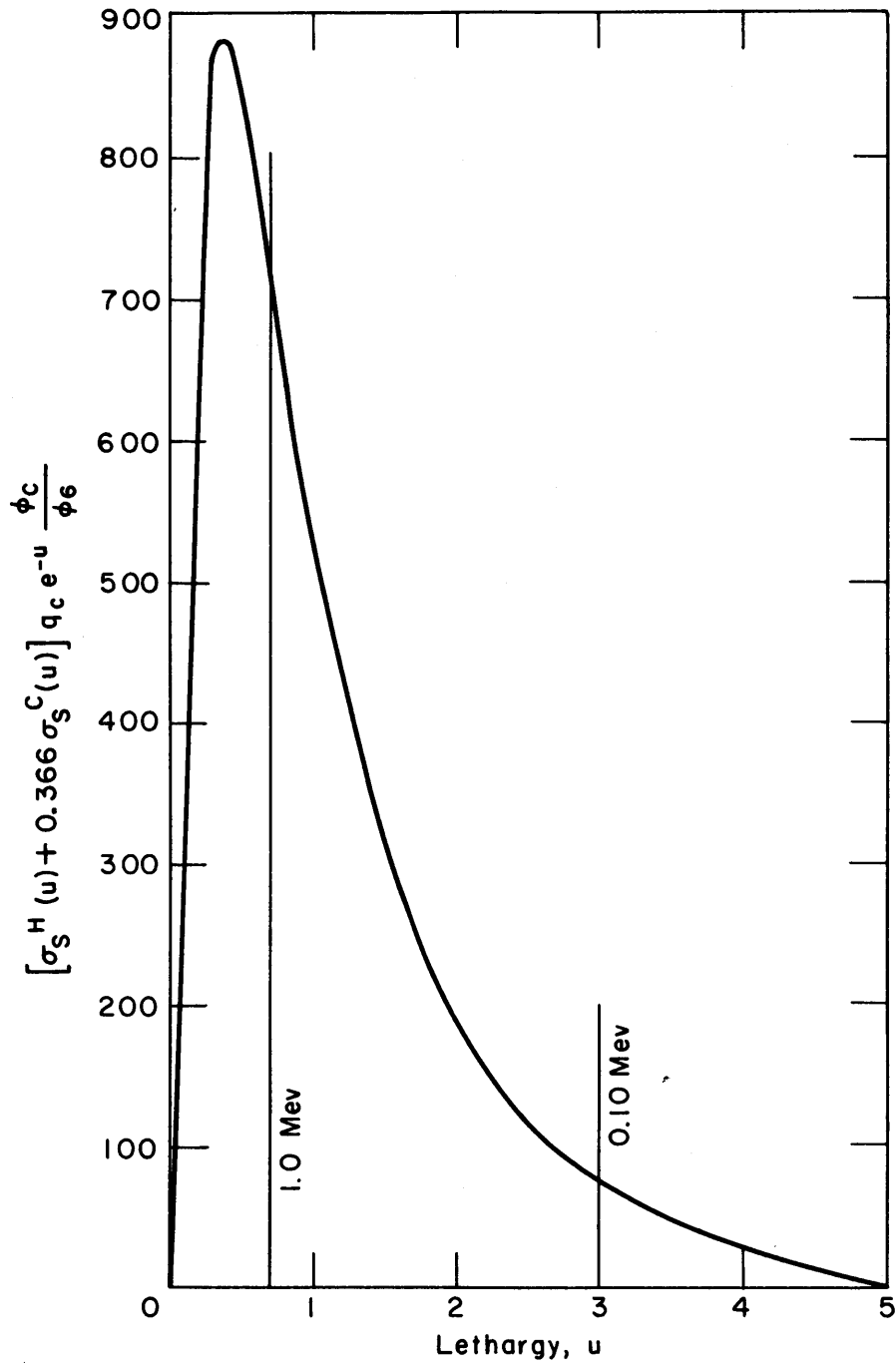


FIGURE A4.11 PLOT FOR GRAPHICAL INTEGRATION TO DETERMINE RELATIVE CONTRIBUTION OF CENTRAL FUEL ELEMENT TO FAST NEUTRON DOSE RATE

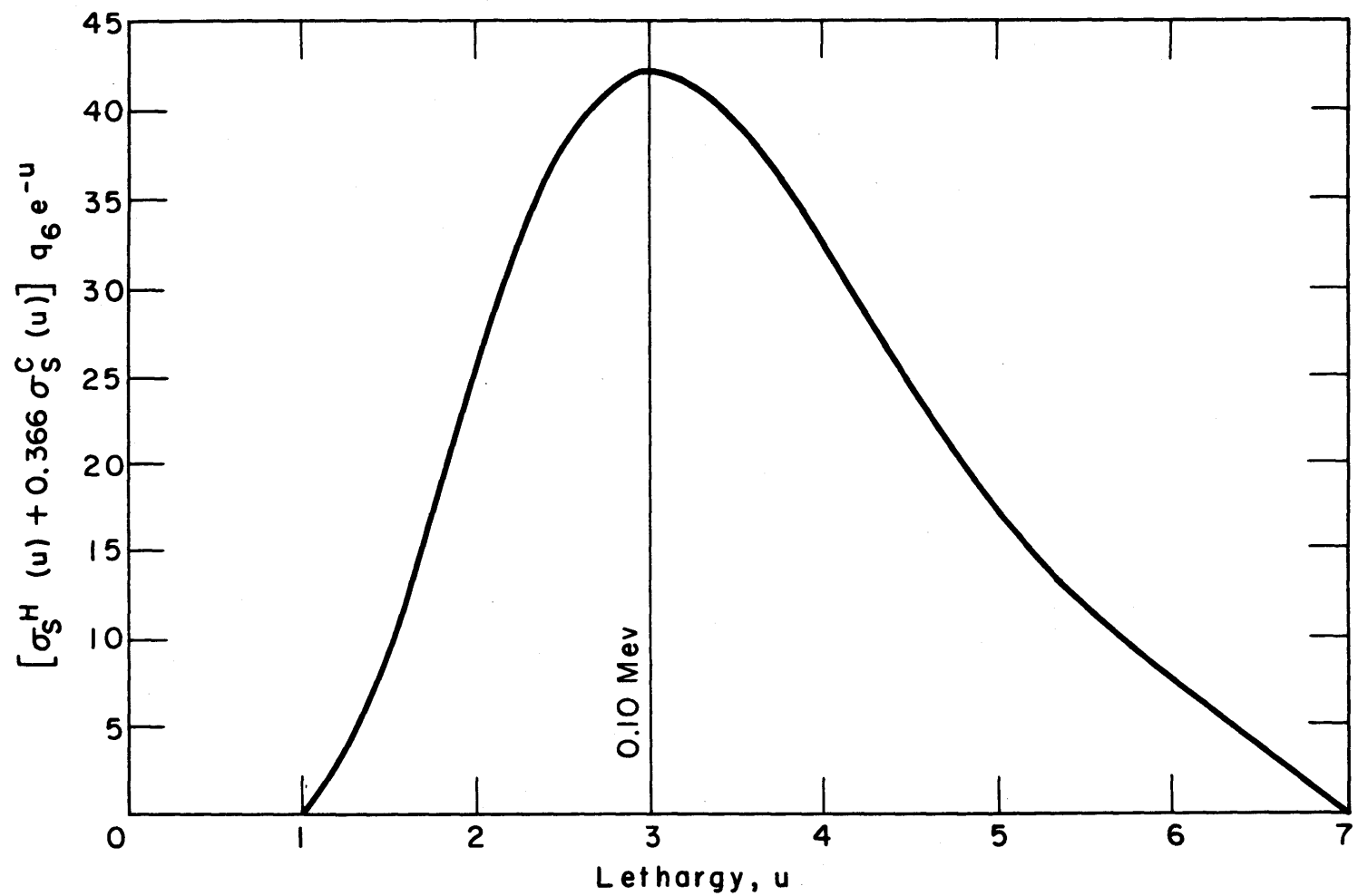


FIGURE A4.12 PLOT FOR GRAPHICAL INTEGRATION TO DETERMINE RELATIVE CONTRIBUTION OF RING OF SIX FUEL ELEMENTS TO FAST NEUTRON DOSE RATE

The ratio of the Fermi age at one lethargy to the Fermi age at another lethargy is given, therefore, by:

$$\frac{\tau(u_1)}{\tau(u_2)} = \frac{u_1}{u_2} \quad (\text{A4. 65})$$

The Fermi age for fission neutrons to the 1.44 ev ( $u = \ln \frac{2.0 \times 10^6}{1.44} = 14.2$ ) resonance of indium is  $100 \text{ cm}^2$  for pure  $\text{D}_2\text{O}$  (A4. 3). Hence,

$$\tau(u)_{\text{D}_2\text{O}} = 100 \frac{u}{14.2} = 7.04 u \text{ cm}^2$$

For the fuel region, the Fermi Age will be larger primarily because of the decreased  $\text{D}_2\text{O}$  content in this region. If the assumption is made that the uranium and aluminum do not contribute appreciably to the slowing down, then, since the fraction of volume occupied by  $\text{D}_2\text{O}$  in fuel section,  $f$ , is  $\frac{5.51}{9.20} = 0.600$ ,

$$\frac{\tau(\text{Pure D}_2\text{O})}{\tau(\text{Fuel region})} \cong f^2 = 0.36$$

$$\tau(u)_{\text{Fuel region}} \cong \frac{\tau(\text{Pure D}_2\text{O})}{0.36} = 19.6 u \text{ cm}^2$$

#### (b) Estimation of Source of Neutrons from Fuel Element

Henderson and Whittier (A4. 8) have calculated the fraction of neutrons slowed down past a given neutron energy within a cylinder of radius,  $a$ . This fraction,  $F$ , is given for a uniform source distribution as a function of  $a/L_s$  where  $L_s$  is the slowing down length for neutrons of that energy ( $\sqrt{\tau}$ ) and  $a$  is the radius of the source. For the fuel element, with all sixteen fuel plates,  $a$  is 4.35 cm. For the central element, the same approximation will be made as in the case of the gamma calculation where the fuel element was transformed into six small cylinders;  $a$  was 1.26 cm for each of these cylinders.

Using values of  $F$  for different Fermi Ages, the neutron energy distribution emerging from the source can be determined.

Let

$Y(u)$  = neutrons escaping from fuel element per unit lethargy per unit length of source, neutrons/cm.

$q'_0$  = source strength, neutrons/cm<sup>3</sup>-sec.

$R_0$  = radius of cylindrical source, cm.

At any lethargy,  $u$ ,  $1 - F(u)$  = fraction of neutrons which have escaped with lethargies less than  $u$ . Then, for a unit length of source,

$$\int_0^u Y(u) du = [1 - F(u)] q'_0 (\pi R_0^2) \quad (\text{A4. 66})$$

Differentiating gives:

$$Y(u) = -(q'_0 \pi R_0^2) \frac{dF(u)}{du} \quad (\text{A4. 67})$$

This relation can be used for calculating the source strength  $Y(u)$  as a function of lethargy,  $u$ . The results of a calculation are given in Table A4. 13 and Figure A4. 10 where  $F(u)$  is plotted vs.  $u$  for radii of 4. 35 cm. and 1. 26 cm. It is seen that in both cases, the curve is very steep at lethargies close to zero, indicating that most of the neutrons escape with energies close to the source energy. Because of this steep slope, it is difficult to get accurate slopes of the curve at energies close to the source energy. Since only an approximate estimate is desired, it will therefore be assumed that absorption within the cylindrical sources is negligible so that they can be considered as monoenergetic line sources of 2. 0 Mev neutrons. This assumption will tend to overestimate the contribution from the outer fuel elements relative to that from the center fuel element because of the larger size of the outer fuel elements.

## (c) Estimation of Contribution by Fuel Elements Surrounding Central Fuel Element

$$q_o = q'_o (\pi R_o^2) \quad R_o = 4.35 \text{ cm}$$

$$q(\rho, u) = \frac{q'_o (\pi R_o^2) e^{-\rho^2/4\tau(u)}}{4\pi\tau(u)} \quad (\text{A4.68})$$

For the ring of six fuel elements,  $\rho = 16.2 \text{ cm}$ .

$$q_6 = 6q'_o (4.73) \frac{e^{-65.7/\tau}}{\tau} = 28.4 q'_o \frac{e^{-65.7/\tau}}{\tau} \quad (\text{A4.69})$$

For the ring of twelve fuel elements,  $\rho = 30.2 \text{ cm}$ .

$$q_{12} = 12q'_o (4.73) \frac{e^{-228/\tau}}{\tau} = 56.7 q'_o \frac{e^{-228/\tau}}{\tau} \quad (\text{A4.70})$$

Because of the large factor in the exponential for the ring of twelve fuel elements, the dose rate from this ring is negligible compared to that from the ring of six fuel elements.

## (d) Estimation of Contribution of Central Fuel Element

The same transformation is used here as was used in estimating the gamma contribution from the central fuel element. For the middle two cylinders,  $\rho = 2.92 \text{ cm}$ .

$$q_c = 2 \frac{\phi_c}{\phi_6} q'_o (0.395) \frac{e^{-2.13/\tau}}{\tau} = 0.790 q'_o \frac{e^{-2.13/\tau}}{\tau} \quad (\text{A4.71})$$

For the outer four cylinders,  $\rho = 3.86 \text{ cm}$ .

$$q_c = 4 \frac{\phi_c}{\phi_6} q'_o (0.395) \frac{e^{-3.72/\tau}}{\tau} = 1.580 q'_o \frac{e^{-3.72/\tau}}{\tau}$$

Hence,

$$q_c^{\text{Total}} = q'_o \left[ 0.790 \frac{e^{-2.13/\tau}}{\tau} + 1.580 \frac{e^{-3.72/\tau}}{\tau} \right] \frac{\phi_c}{\phi_6} \quad (\text{A4.72})$$

## (e) Estimation of Ratio of Dose Rate from Each Source

From the above equations, values of  $q_6$  and  $q_c^{\text{Total}}$  vs. neutron energy or lethargy can be calculated. The energy absorbed by Santowax OMP is then given as follows:

$$\phi(u) = \frac{q(u)}{\xi_{D_2O} \Sigma_s} = Aq(u) \quad (\text{A4. 73})$$

where A is assumed constant.

Also,

$$\phi(u) = E\phi(E) \quad (\text{A4. 74})$$

The energy absorption rate in Santowax OMP is then:

$$D = \int_0^{E_0} \left[ g_H N_H \sigma_s^H(E) + g_C N_C \sigma_s^C(E) \right] \phi(E) E dE \quad (\text{A4. 75})$$

Now, since,  $\phi(u) du = -\phi(E) dE$  and  $E = E_0 e^{-u}$ ,

$$D = \int_0^u \left[ g_H N_H \sigma_s^H(u) + g_C N_C \sigma_s^C(u) \right] \phi(u) E_0 e^{-u} du \quad (\text{A4. 76})$$

Finally,

$$D = AN_H g_H E_0 \int_0^u \left[ \sigma_s^H(u) + \frac{g_C N_C}{g_H N_H} \sigma_s^C(u) \right] q(u) e^{-u} du \quad (\text{A4. 77})$$

Hence,

$$\frac{D_c}{D_6} = \frac{\int_0^u \left[ \sigma_s^H(u) + \frac{g_C N_C}{g_H N_H} \sigma_s^C(u) \right] q_c^{\text{total}} e^{-u} du}{\int_0^u \left[ \sigma_s^H(u) + \frac{g_C N_C}{g_H N_H} \sigma_s^C(u) \right] q_6 e^{-u} du} \quad (\text{A4. 78})$$

In Table A4. 14 and Figures A4. 11 and A4. 12, the information used in a graphical integration to obtain  $D_c/D_6$  is given. The results are presented in Table A4. 15 for a  $\phi_c/\phi_6$  of 1.06; to obtain an idea of the reliability of

TABLE A4.15

RESULTS OF CALCULATION OF FAST NEUTRON DOSE RATE  
FROM CENTER FUEL ELEMENT RELATIVE TO THAT FROM  
RING OF SIX ELEMENTS

ENERGY INTERVAL	FROM RING OF SIX	FROM CENTER	TOTAL	% OF TOTAL	
				CALCULATION FROM FERMI AGE	CALCULATION FROM MEASURED SPECTRUM
Above 1.0 Mev	0.0	450	450	33.0	53.1
0.1 Mev to 1.0 Mev	45.5	740	786	57.7	37.6
Below 0.1 Mev	63.3	64	127	9.3	9.3
Total	108.8	1254	1363	100.0	100.0

$$\% \text{ of Total From Ring of Six} = \frac{108.8}{1363} 100 = 8.0\%$$

$$\% \text{ of Total From Center} = 92.0\%$$

the calculational method, the percentage of the total dose rate due to different neutron energy intervals is compared with that obtained by calculations from the measured spectrum. It is seen that the present method underestimates the contribution of the high energy neutrons as might be expected, since the calculation presented here is based on a monoenergetic source whereas the actual source is a fission spectrum of neutrons. The use of Fermi age theory for deuterium could also introduce some error. In general, however, the agreement is satisfactory for the present purpose and it is seen that the circle of six fuel elements is estimated to contribute 8 per cent of the fast neutron dose rate with the central plate contributing the remaining 92 per cent. If it is assumed that the calculations below an energy of 1.0 Mev are reliable and the fast neutron contribution above 1.0 Mev is arbitrarily increased to give approximately the same percentage for a given energy interval as obtained from calculations based on the measured fast neutron spectrum, the results of Table A4. 16 are obtained.

#### APPENDIX 4. 14

##### CONTRIBUTION OF GAMMA RADIATION FROM THE STAINLESS STEEL AND ALUMINUM THIMBLES AND FROM THE IN-PILE SECTION TO THE DOSE RATE

Gamma radiation is produced in the stainless steel and aluminum thimbles as well as in the in-pile section by thermal neutron capture. In this appendix, the contribution of these sources to the dose rate in Santowax OMP at the center of the thimble will be approximately estimated. The calculation will be made assuming an infinite line source for which the dose rate, assuming only geometric attenuation, can be represented for a monoenergetic source as:

$$R^{\gamma} = \frac{SE}{4r} \frac{\mu_a}{\rho} \quad (\text{A4. 79})$$



TABLE A4.16

CORRECTED RESULTS OF CALCULATION OF FAST NEUTRON DOSE RATE FROM  
CENTRAL FUEL ELEMENT RELATIVE TO THAT FROM RING OF SIX ELEMENTS

ENERGY INTERVAL	FROM RING OF SIX	FROM CENTER	TOTAL	% OF TOTAL
Above 1.0 Mev	0.0	1030	1030	53.0
0.1 Mev to 1.0 Mev	45.5	740	785	40.4
Below 0.1 Mev	63.3	64	127	6.6
TOTAL	108.8	1834	1942	100.0

% of total from ring of six = 5.6%  
% of total from center = 94.4%

Where

$\rho$  = density of material absorbing radiation, gm/cm<sup>3</sup>.

$r$  = distance from line source to point, cm.

$\mu_a$  = energy absorption coefficient of material absorbing radiation, cm<sup>-1</sup>

$S$  = source strength, photons/cm-sec.

$E$  = energy of photons, Mev/photon.

$R^\gamma$  = dose rate in material, Mev/gm-sec.

In the present case, the gamma radiation will be emitted at many energies and it is desirable to write the above equation as the summation over several energy intervals where the values of  $E$ ,  $\mu_a/\rho$ , and  $S_i$  are taken as average values for that interval. Hence,

$$R^\gamma = \frac{1}{4r} \sum_{i=1}^N \frac{\mu_{ai}}{\rho} S_i E_i \quad (\text{A4. 80})$$

The source can also be written as

$$S_i = (m)(G_i) \quad (\text{A4. 81})$$

where

$G_i$  = photons emitted in the  $i^{\text{th}}$  energy interval per gram of material.

$m$  = grams of material/cm of source length.

The calculations for each specific case will now be presented.

#### A4. 14. 1 STAINLESS STEEL THIMBLE

Since stainless steel is a mixture of many elements which, in general, emit gamma radiation with different energies on neutron capture,  $G_i$  must be calculated for each element in stainless steel. For the  $k^{\text{th}}$  element,

$$G_{i, k} = \left[ (\sigma_{ak} \phi) \frac{1}{A} N_{AV} w_k \right] \left[ n_{i, k} \right] \quad (\text{A4. 82})$$

where

$w_k$  = weight fraction of element k in stainless steel.

$n_{i,k}$  = number of photons emitted in  $i^{th}$  energy interval per capture in the element k.

Troubetzkoy and Goldstein (A4. 7) report the number of photons emitted per energy interval for the elements of interest. In general, it has been noticed that the summation of  $n_{i,k} E_i$  does not equal the Q value for the reaction and it is desirable for the present purpose to arbitrarily change  $n_{i,k}$  so that the sum is approximately the Q value of the reaction. Since each element generally consists of several isotopes with different cross sections and Q values and the data by Troubetzkoy and Goldstein are given only for the elements, it is necessary to calculate average Q values. These were calculated by the following relation for each element:

$$Q_{avg} = \frac{\sum (Abund)_i \sigma_{ai} Q_i}{\sum (Abund)_i \sigma_{ai}} \quad (A4. 83)$$

The average Q values calculated for the elements of interest are:

Fe	7.68 Mev
Cr	9.25 Mev
Ni	6.85 Mev
Mo	8.91 Mev
Mn	7.27 Mev

In estimating the absorption, the following values of  $\mu_a/\rho$  were used:

Energy Interval Mev	0-1	1-2	2-3	3-5	5-7	7-9	> 9
$\mu_a/\rho, \text{cm}^2/\text{gm}$	0.037	0.025	0.022	0.020	0.019	0.0185	0.0185

The detailed calculations are given in Table A4. 17 for iron and summarized for all other materials.

TABLE A4.17

CALCULATIONS LEADING TO ESTIMATION OF DOSE RATE  
FROM STAINLESS STEEL THIMBLE

(A) Detailed Calculations for Iron

$$\sigma_a \frac{N_{AV}}{A} w = 1.785 \times 10^{-2} \frac{\text{cm}^2}{\text{gm SS}}$$

Energy Interval, Mev	$n_i$	$n_i E$ Mev	$\frac{\mu_{a1}}{\rho} n_i E_i, \frac{\text{Mev cm}^2}{\text{gm}}$
> 9 $\cong$ 9.3	0.02	0.19	$0.35 \times 10^{-2}$
7-9	0.38	3.04	$5.62 \times 10^{-2}$
5-7	0.25	1.50	$2.85 \times 10^{-2}$
3-5	0.23	0.92	$1.84 \times 10^{-2}$
2-3	0.27	0.68	$1.49 \times 10^{-2}$
1-2	0.60	0.90	$2.25 \times 10^{-2}$
0-1	0.75	0.38	$1.41 \times 10^{-2}$
TOTAL		7.61	$15.81 \times 10^{-2}$

(B) Summary of Calculations for all Materials

MATERIAL	$\sigma_a \frac{N_{AV}}{A} w, \frac{\text{cm}^2}{\text{gm SS}}$	$\sum \frac{\mu_a}{\rho} n_i E,$ $\frac{\text{Mev cm}^2}{\text{gm}}$	$[\sigma_a \frac{N_{AV}}{A} w] [\sum \frac{\mu_{a1}}{\rho} n_i E_i]$ $\frac{\text{cm}^4 \text{ Mev}}{\text{gm}^2}$
Fe	$1.785 \times 10^{-2}$	$15.81 \times 10^{-2}$	$28.2 \times 10^{-4}$
Cr	$0.610 \times 10^{-2}$	$19.06 \times 10^{-2}$	$11.6 \times 10^{-4}$
Ni	$0.615 \times 10^{-2}$	$14.06 \times 10^{-2}$	$8.64 \times 10^{-4}$
Mn	$0.292 \times 10^{-2}$	$15.86 \times 10^{-2}$	$4.63 \times 10^{-4}$
Mo	$0.042 \times 10^{-2}$	$19.50 \times 10^{-2}$	$0.818 \times 10^{-4}$
TOTAL			$53.9 \times 10^{-4}$

For the stainless steel thimble,

$$m_{SS} = \pi[(1.588)^2 - (1.465)^2][1][8.03] = 9.44 \text{ gm/cm}$$

$$r_{avg} = 1.526 \text{ cm}$$

Substituting these quantities as well as the total given in part B of Table A4. 17 gives:

$$\begin{aligned} R^\gamma &= \frac{m_{SS}}{4r} \left[ \sum_{k=1}^M \left( \sigma_{ak} \frac{N_{AV}}{A} w_k \right) \left( \sum_{i=1}^N \frac{\mu_{ai}}{\rho} n_{i,k} E_i \right) \right] \phi & (A4. 84) \\ &= \frac{9.44}{(4)(1.526)} [53.9 \times 10^{-4}] \phi \\ &= 83.4 \times 10^{-4} \phi \frac{\text{Mev}}{\text{gm-sec}} \\ &= 13.4 \times 10^{-16} \phi \frac{\text{watts}}{\text{gm}} \end{aligned}$$

At 1.0 MW,

$$\phi = 1.41 \times 10^{13} \text{ n/cm}^2\text{-sec}$$

$$R^\gamma = (13.4 \times 10^{-16})(1.41 \times 10^{13}) = 0.0189 \text{ watts/gm}$$

The gamma dose rate at the center  $\cong 0.23$  watts/gm. Hence, the percentage contribution to the gamma dose rate from the stainless steel thimble is estimated to be  $\frac{0.0189}{0.23} 100 = 8.2$  per cent.

#### A4. 14. 2 ALUMINUM THIMBLE

The calculations procedure for the aluminum thimble is exactly the same as that for the stainless steel thimble. The equilibrium decay of  $\text{Al}^{28}$  is included in the calculations which are summarized in Table A4. 18.

For the aluminum thimble,

$$m_{Al} = 2.30 \text{ gms/cm}$$

$$r_{avg} = 1.542 \text{ cm}$$

TABLE A4.18

CALCULATIONS LEADING TO ESTIMATION OF  
DOSE RATE FROM ALUMINUM THIMBLE

Energy Interval Mev	$n_i$ Photons Capture	$n_i E_i$ Mev	$\frac{\mu_{a1}}{\rho} n_i E_i$ $\frac{\text{Mev cm}^2}{\text{gm}}$
> 9	0.0	0.0	0.0
7-9	0.205	1.55	$2.87 \times 10^{-2}$
5-7	0.146	0.88	$1.63 \times 10^{-2}$
3-5	0.40	1.60	$3.20 \times 10^{-2}$
2-3	0.41	1.07	$2.36 \times 10^{-2}$
1-2	1.95*	3.21	$8.04 \times 10^{-2}$
0-1	2.40	1.20	$4.44 \times 10^{-2}$
Total			$22.5 \times 10^{-2}$

\*Includes decay of  $\text{Al}^{28}$ 

$$\sigma_a \frac{N_{AV}}{A} = 5.13 \times 10^{-3} \frac{\text{cm}^2}{\text{gm}}$$

$$\left( \sigma_a \frac{N_{AV}}{A} \right) \left( \sum_{i=1}^{i=N} \frac{\mu_{a1}}{\rho} n_i E_i \right) = 1.155 \times 10^{-3} \frac{\text{cm}^4 \text{Mev}}{\text{gm}^2}$$

Substitution gives for a flux of  $1.41 \times 10^{13}$  n/cm<sup>2</sup> sec,

$$R^\gamma = \frac{2.30}{(4)(1.542)} [1.155 \times 10^{-3}] 1.41 \times 10^{13} \text{ Mev/gm-sec}$$

$$= 0.000971 \text{ watts/gm}$$

Hence, the percentage contribution due to the aluminum thimble is estimated to be

$$\frac{(0.000971)(100)}{0.23} = 0.42 \text{ per cent.}$$

#### A4.14.3 IN-PILE SECTION

The in-pile section consists of an aluminum thimble, stainless steel capsule, and various auxiliary items such as trace heaters and thermocouples. In estimating the gamma dose rate, only the aluminum thimble and stainless steel capsule will be considered since these should be the primary contributors.

The aluminum thimble is exactly the same as that considered in section A4.14.2. Hence, neglecting the attenuation resulting from the stainless steel capsule, the dose rate will be exactly the same or 0.00097 watts/gm.

The effect of the stainless steel is quite difficult to accurately estimate because of the geometry involved. The calculation will be made at the center line of the capsule, assuming as before that no attenuation occurs. In addition, the stainless steel outlet tube will be considered as part of the capsule. The following quantities will be used:

$$m_{ss} = 4.97 \text{ gms/cm}$$

$$r_{avg} = 1.075 \text{ cm}$$

Using the calculations of A4.14.1,

$$R_{ss}^\gamma = 0.0189 \frac{1.526}{1.075} \frac{4.97}{9.44} = 0.0141 \text{ watts/gm}$$

Summing the results for the stainless steel capsule and aluminum thimble gives:

$$R_{ss+Al}^{\gamma} = 0.0141 + 0.0010 = 0.0151 \text{ watts/gm}$$

This is about 25 per cent smaller than the contribution calculated for the stainless steel thimble. However, the trace heaters and thermocouple wires will also contribute to the gamma dose rate in the case of the in-pile section and, considering the accuracy of the calculations, it seems reasonable to assume that the gamma contributions (due to thermal neutron capture) from the stainless steel thimble and in-pile section are the same.

#### APPENDIX 4.15

#### CALCULATION OF AVERAGE ENERGY ABSORPTION RATE FOR EACH DAY OF IRRADIATION OF SANTOWAX OMP

The energy absorption rate integrated over the volume of organic exposed to radiation, is given by Equation (4.40) as:

$$R_{SW}^{TI} = (61.3 \pm 2.9) \rho_{avg} \text{ watts/MW}$$

where  $\rho_{avg}$  = average density of the organic in the in-pile section over some relatively short period of time (taken as one day in the present case). The average density for any day is based on the average organic temperature for that day and the %DP corresponding to the average total MWHR of reactor operation on that day. Equation (5.38) was used to calculate the density from these properties.

In Figure A4.13, a plot illustrating the procedure used for calculating the average organic temperature for any day is given. The organic temperatures in the in-pile section as recorded on the loop operation log sheets were plotted vs. time and graphical integration used to determine the average temperature for any day. In Table A4.19, a summary of the calculations for the days shown in this figure is given. The calculated values of  $R_{SW}^{TI}$  are plotted in Figure 4.37.



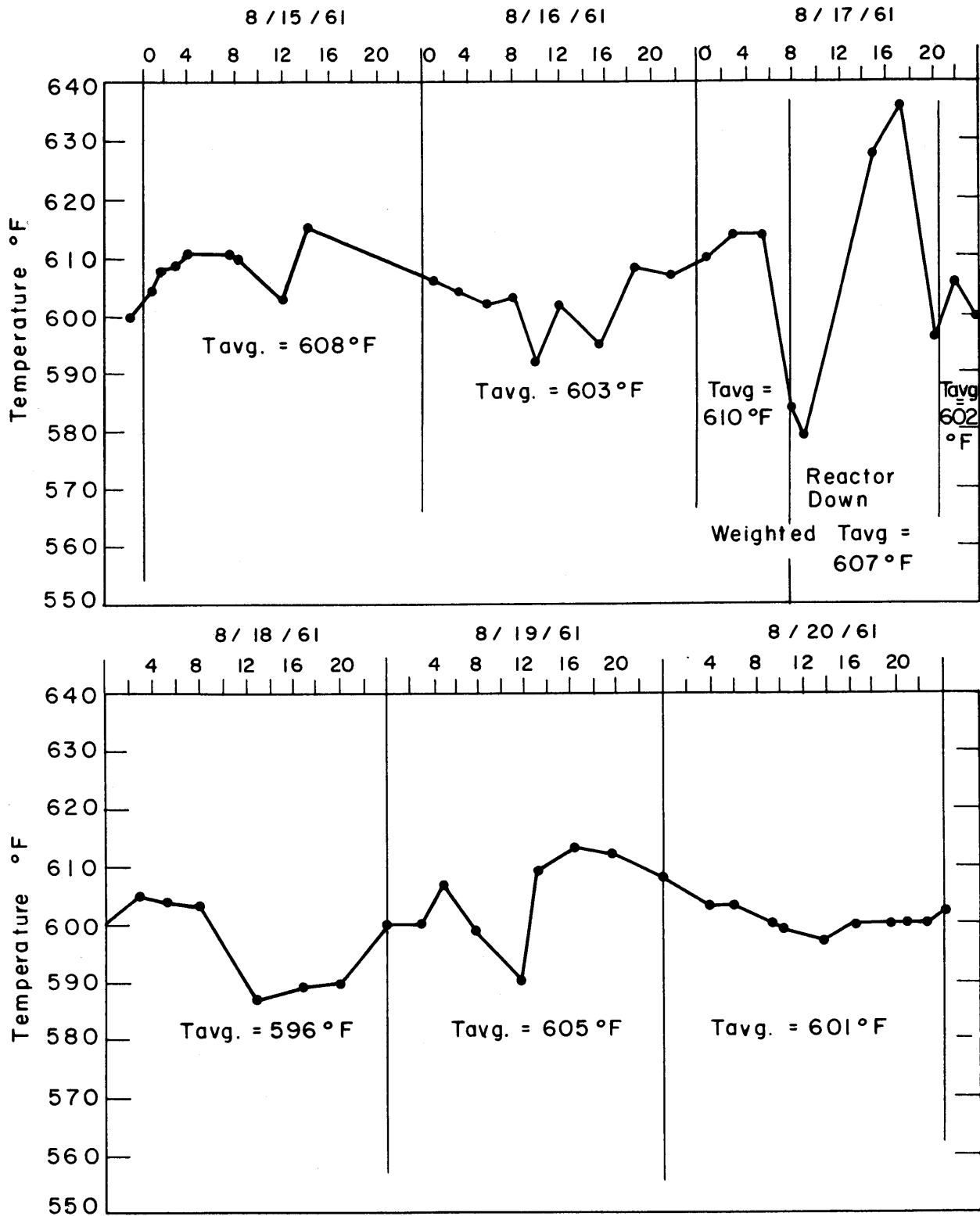


FIGURE A4.13 TEMPERATURE OF SANTOWAX OMP IN IN-PILE SECTION, 8/15/61 - 8/20/61

TABLE A4.19

SAMPLE CALCULATIONS OF  $R_{TI}^{SW}$  FOR  
INDIVIDUAL DAYS OF LOOP OPERATION

Day	MWHR Exposure During Day	Total Average MWHR for Day	Average In-Pile Organic Temp. °F	%DP at Average MWHR for Day	$\rho$ avg, Average Density for Day, $\frac{gm}{cm^3}$	$\frac{watt\ hr}{MWHR}$
Aug. 15, 1961	44.2	273.7	608	10.0	0.868	53.2
16	44.1	317.8	603	11.1	0.872	53.5
17	20.0	349.9	607	12.0	0.871	53.4
18	43.6	381.7	596	13.0	0.877	53.7
19	43.7	425.3	605	14.0	0.874	53.5
20	43.5	469.0	601	15.0	0.877	53.7

## APPENDIX 4. 16

RECOMMENDATIONS FOR IMPROVING ACCURACY  
OF DOSE RATE DETERMINATION

While the dose rate determination made for the first in-pile operation of the loop is quite satisfactory, an effort should be made to improve the accuracy in future measurements and to study experimentally the effect of such items as the central fuel element loading on the dose rate. Recommendations are presented in this appendix for these purposes.

A4. 16. 1 IMPROVEMENTS IN ACCURACY OF CALORIMETER  
MEASUREMENTS

Since the dose rate determination is based primarily on the calorimeter measurements, every effort should be made to improve their reliability and accuracy. In general, this can be accomplished with the present calorimeter design by increasing the reliability of the sample heat capacities and of the measured adiabatic rate of temperature increase. To reduce the errors introduced by unreliable heat capacity values, either or both of the following procedures is advisable:

(1) Construct a calorimeter for measuring the heat capacity of each absorber with an accuracy of 1 per cent or better.

(2) Construct a small electrical heater in each absorber so that the rate of temperature increase can be related directly to the rate of energy generation in the absorber. For the plastic absorbers, caution must be used in constructing these heaters because of the low thermal conductivity of the organics. Otherwise, an error will be introduced due to large temperature gradients over the absorber and a large temperature difference between the heater wire and the absorber. These considerations may prohibit the use of such a calibrating heater for the organic absorbers.

To reduce errors due to temperature measurements, it is necessary to increase the thermal conductivity of the absorbers at the same time retaining a high hydrogen density. One method of accomplishing this would be to use either polystyrene or polyethylene samples containing various

amounts of fine carbon powder homogeneously mixed to increase the thermal conductivity of the plastic and to give various hydrogen densities. A pure graphite absorber could also be used. Letting  $w$  = weight fraction of carbon in an absorber, the total dose rate in this case can be written (for polystyrene):

$$\begin{aligned} R^T &= R_C^\gamma w + R_C^n w + R_{PS}^\gamma (1-w) + R_{PS}^n (1-w) \\ &= w \left[ R_C^T - R_{PS}^T \right] + R_{PS}^T \end{aligned} \quad (\text{A4. 86})$$

Then, measurements with pure graphite and four absorbers with different carbon contents would permit a plot similar to that of Figure A4. 14 to be made and  $R_{PS}^T$  and  $R_C^T$  could be accurately determined.  $I_H$  and  $R_C^\gamma$  could be determined from the following relations obtained following the same procedure as that used in section 4. 2. 2:

$$\begin{aligned} R_{PS}^T &= 1.080 R_C^\gamma + 5.39 \times 10^{22} I_H \\ R_C^T &= R_C^\gamma + 0.823 \times 10^{22} I_H \end{aligned} \quad (\text{A4. 87})$$

The use of samples containing only carbon and hydrogen would also reduce any uncertainties resulting from energy absorbed because of thermal neutron activation or non-Compton interactions, both of which introduce small errors in the case of aluminum samples. If a metallic sample is desired, the use of beryllium rather than aluminum would also greatly reduce these effects.

An additional uncertainty results from differences between the experimental configuration used for the calorimeter measurements and that of the in-pile section filled with organic. While it is believed that use of the stainless steel thimble provides a close approximation to the effect of the in-pile section on the dose rate, it would be desirable to perform measurements in a geometry approaching closer to that of the actual case. Comparison of thermal and fast neutron flux measurements inside (1) the in-pile section when filled

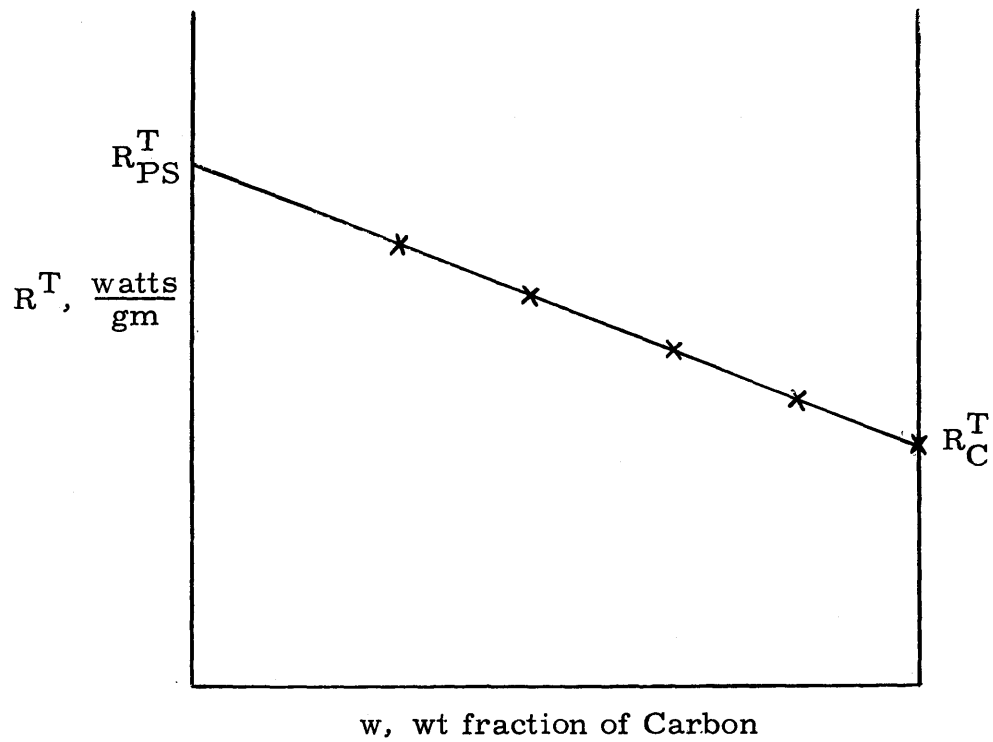


Figure A4. 14. Sketch of Dose Rate Variation with Weight Fraction of Carbon in Plastic for Proposed Calorimeter.

with organic (at the conclusion of an experiment and just before the old in-pile section is removed from the reactor); (2) the monitor tube; and (3) the stainless steel thimble (or other facility used for calorimeter measurements) would be of great use also in this respect. It should be mentioned that in future flux measurements inside the thimbles, arrangements should be made to accurately position the detector wires on the centerline of the thimble. In the measurements reported in this report, no attempt was made to do this so that variations in the flux at different positions inside the thimble could have resulted in the scatter of the measured fluxes noted in some instances.

#### A4. 16. 2 MEASUREMENT OF TIME DEPENDENCE OF DOSE RATE OVER LONG PERIOD OF TIME

As discussed in section 4. 4. 3. 4, there is strong indication that the fast neutron dose rate is strongly dependent on the fuel loading of the central fuel element. In an irradiation covering a long period of time in which a significant fraction of the uranium in the fuel element will be burned up, a decrease in the fast neutron dose rate might be expected. The effect on the gamma dose rate should be much less, since all fuel elements in the reactor contribute to the gamma dose rate. The following recommendations are made to study these variations:

(1) Calorimeter measurements of the fast neutron and gamma dose rates should be made before and after each long term irradiation in the loop. These measurements should indicate any differences which might occur.

(2) Fast flux measurements should be made periodically in the monitor tube throughout the irradiation. The experimental accuracy of the fast flux measurements should also be improved so that smaller changes can be detected.

(3) As described by Turricchia (A4. 6), a miniature ionization chamber is under development for performing gamma dose rate

measurements in the monitor tube. The development of this chamber should be completed so that possible variations in the gamma dose rate during long term irradiations can be reliably detected.

#### A4. 16. 3 INCREASE OF ACCURACY OF EXTRAPOLATION OF CALORIMETER MEASUREMENTS TO FULL REACTOR POWER

As indicated in section 4 . 4 . 3 . 3, extrapolation of the calorimeter results obtained at reactor power levels of 50, 100, and 200 kw to full reactor power (1800 kw at the present time) can introduce a relatively large error in the dose rate. It would be highly desirable to develop a calorimeter with which measurements can be made at full reactor power so that this effect is eliminated. If the development of such a calorimeter appears prohibitively difficult, more extensive measurements at different reactor power levels should be made using the thermal and fast neutron activation detectors, as well as the type of calorimeter described in the present report.

## APPENDIX 5. 1

## METHOD OF GAS CHROMATOGRAPHY ANALYSIS AT M. I. T.

The irradiated Santowax OMP samples at M. I. T. have been analyzed for biphenyl, ortho-terphenyl, meta-terphenyl, and para-terphenyl, using gas chromatography. A Burrell K-7 high-temperature gas chromatograph with temperature programming has been used for the analyses. The operating conditions for the chromatograph are summarized in Table A5. 1. Part of the measurements were made by programming the temperature from 100°C to 240°C; however, measurements at a steady temperature of 240°C were found to give satisfactory separation of the terphenyl isomers and, furthermore, gave slightly better reproducibility. Accordingly, the remainder of the samples were run at a constant column temperature of 240°C. In Figure A5. 1, a typical M.I.T. chromatogram obtained with temperature programming is presented.

In all measurements, triphenylmethane has been used as an internal standard and benzene as a solvent; a known mixture of the terphenyl isomers and triphenylmethane dissolved in benzene has been used to determine an "f" factor defined as:

$$f_i = \frac{x_i}{x_{st}} \frac{A_{st}}{A_i} \quad (\text{A5. 1})$$

where

$x_i, x_{st}$  = weight fraction of component  $i$  and standard, respectively, in the known organic mixture.

$A_i, A_{st}$  = peak area of the  $i^{\text{th}}$  component and the standard, respectively.

Once the "f" factors are known, the weight fraction of component  $i$  in an unknown sample to which a measured mass of triphenylmethane has been added can be determined using this same relation. The standard mixture is generally made up to approximate the concentration of the unknown. In the M. I. T. measurements, "f" factors are generally measured between every 1-3 analyses.



Table A5. 1. Operating Conditions for Burrell K-7 Gas Chromatograph at M. I. T.

Column	5% Apiezon L on 30-50 mesh fire-brick; column length = 2 meters.
Column Temperature	Initial samples -- Temperature programmed, 100°C to 240°C. Remainder of samples -- Control temperature of 240°C.
Detector	Flame ionization.
He Flowrate	35 to 40 cm <sup>3</sup> /min.
Detector Temperature	340°C.
Injection Block Temperature	350°C.
Internal Standard	Triphenylmethane.
Solvent	Benzene
Nominal Concentration	0.01 grams of triphenylmethane and 0.04 grams of sample per cm <sup>3</sup> of solution.
Sample Size Injected	2-4 $\mu$ liters.

FIG. A5.1

Gas Chromatograph for Sample Containing

1.50% Biphenyl  
9.14% o-Terphenyl  
22.18% Triphenylmethane  
39.08% m-Terphenyl  
24.08% p-Terphenyl  
1.50% Triphenylene (Was not eluted from column at temperature used.)

Column temperature - Programmed from 100°C to 260°C at 5°C/min after which temperature was maintained constant at 260°C.

Detector Temperature - 135°C

Sampler Temperature - 355°C

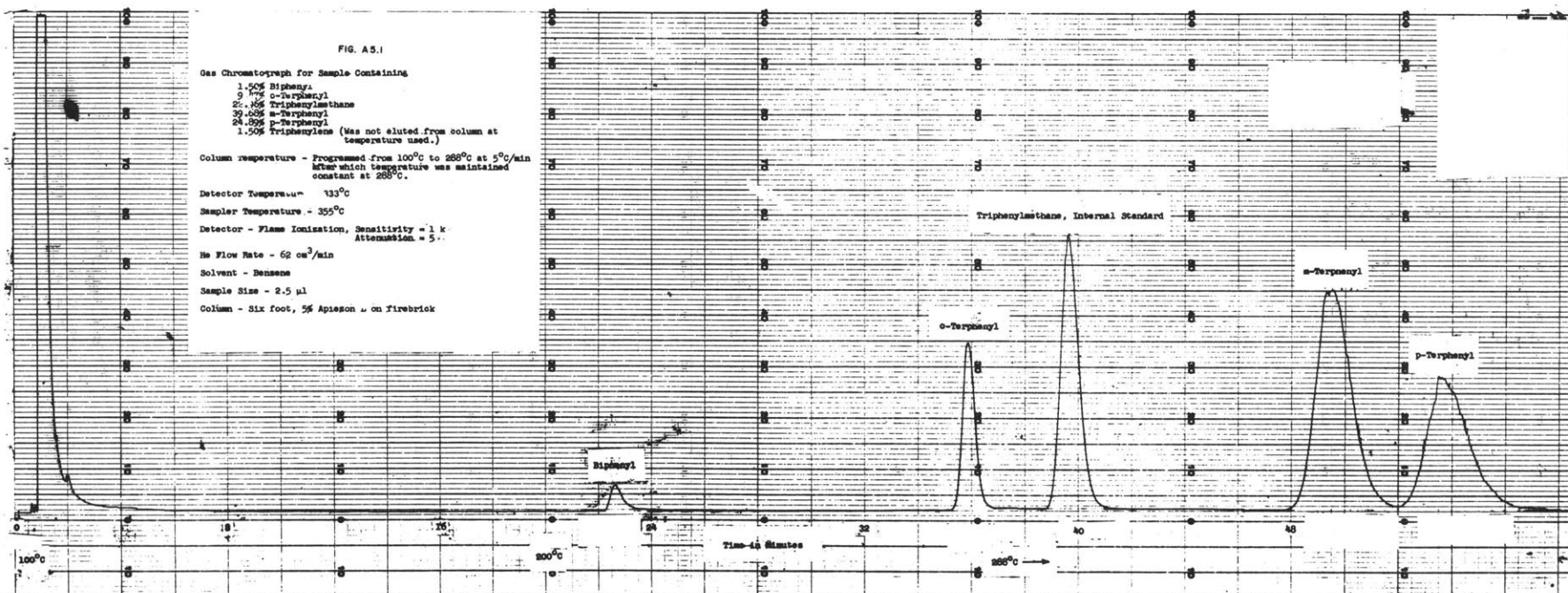
Detector - Flame Ionization, Sensitivity = 1 k  
Attenuation = 5

He Flow Rate - 62 cm<sup>3</sup>/min

Solvent - Benzene

Sample Size - 2.5 µl

Column - Six foot, 5% Apieson  $\mu$  on Firebrick



## APPENDIX 5. 2

## CHEMICAL ANALYSES OF LIQUID SAMPLES

Liquid samples removed from the loop have been analyzed by means of high-temperature gas chromatography for the ortho-, meta-, and para-terphenyl concentrations as well as the biphenyl concentration. As described in section 5. 2. 1, the samples have been analyzed, both at M. I. T. and at Monsanto Chemical Corporation. Two or more analyses have been made for all samples to improve the reliability of the analyses and to provide information on their statistical reliability. The procedure used at M. I. T. for performing the analyses is described in Appendix 5. 1. The detailed results obtained both at M. I. T. and Monsanto are given in Table A5. 2.

In arriving at average concentrations (as well as confidence limits) for each sample for use in correlating the physical property measurements and in determining the liquid degradation rate, the following procedures have been followed:

## (1) Rejection of Extraneous Values

A "Q" test as described by Dean and Dixon (A5. 1) has been applied to the analyses for each sample to screen the data and provide a reasonable and reliable method for rejecting extraneous values. Essentially, this method rejects those observations having a deviation equal to or greater than that which would occur by chance "only 10 per cent of the time at one or the other ends of a set of observations from a normally distributed population" (A5. 1). The procedure is as follows:

## (a) Calculate

$$Q = \frac{x_n - x_{n-1}}{w}$$

where

$x_n$  = doubtful observation.

$x_{n-1}$  = its nearest neighbor after arranging the observations in order of increasing size.

$w$  = range of measurements, i. e., largest value minus smallest value.

## CHEMICAL ANALYSES OF IRRADIATED SANTOWAX OMP-MIT AND MONSANTO DATA

SAMPLE METHOD	SAMPLE NO.	REACTION OPERATION TIME MWHR	POLYPHENYL COMPOSITION, Wt %										
			MIT <sup>(2)</sup>					MONSANTO					
			TOTAL o- $\phi_3$ , m- $\phi_3$ , p- $\phi_3$ , No $\phi_2$	o- $\phi_3$	m- $\phi_3$	p- $\phi_3$	$\phi_2$ <sup>(1)</sup>	TOTAL o- $\phi_3$ , m- $\phi_3$ , p- $\phi_3$ , No $\phi_2$	o- $\phi_3$	m- $\phi_3$	p- $\phi_3$	$\phi_2$	
Drained from Feed Tank	L-8-8-61-16	0		9.9 10.2 10.8 11.5 10.1 10.7	67.4 65.1 63.9 65.4 65.4 65.6	26.7 26.9 23.6 28.0 26.0 24.9	-		9.6 10.4	61.7 60.9	22.2 23.3	0.18 0.4	
		AVG	102.0±1.0	10.5±0.3	65.5±0.5	26.0±0.7	-	94.0±1.6	10.0±0.8	61.3±0.8	22.7±1.1	0.3	
Sample Position No. 1	L-8-12-61-22E	150		10.6 10.4	62.3 60.9	23.7 22.2	-		10.0 9.8	61.8 61.6	23.3 23.5	0.46 0.43	
		AVG	95.0±2.1	10.5±0.2	61.6±1.4	22.9±1.5	-	95.0±0.4	9.9±0.2	61.7±0.2	23.4±0.2	0.45	
	L-8-13-61-24E	175		9.5 10.7	59.5 60.7	19.7 19.2	-		10.7 8.8	61.9 61.2	20.7 20.3	0.34 0.28	
		AVG	89.6±1.8	10.1±1.2	60.1±1.2	19.4±0.5	-	91.8±2.1	9.8±1.9	61.5±0.7	20.5±0.4	0.31	
Sample Position No. 2	L-8-14-61-27G	250		8.5 9.0 9.6 9.0 8.9 9.1 10.2 10.1	55.8 64.5 58.1 58.7 57.3 55.7 55.5 60.5	22.5 19.2 24.6 22.4 22.7 19.5 20.8 21.2	-		9.5 9.4	59.9 60.1	22.7 23.0	0.31 0.35	
		AVG	88.0±1.0	9.0±0.1	57.4±0.7	21.6±0.7	-	92.3±0.4	9.5±0.1	60.0±0.2	22.8±0.3	0.33	
	L-8-18-61-35E	393		9.7 10.2	58.6 57.6	19.6 19.1	-		10.6 10.5	63.7 63.0	22.9 22.4	0.44 0.41	
		AVG	87.4±1.2	9.9±0.5	58.1±1.0	19.4±0.5	-	96.5±0.9	10.5±0.1	63.4±0.7	22.6±0.5	0.42	
	L-8-18-61-37A	400		9.8 10.0 9.8	58.3 58.7 59.1	16.3 17.7 19.6	-		9.9 9.7 9.0 9.3	59.0 56.7 56.6 57.9	21.3 20.9 19.2 20.2	- - 0.07 0.08	
		AVG	86.5±1.4	9.9±0.1	58.7±0.3	17.9±1.4	-	87.5±1.0	9.5±0.3	57.6±0.7	20.4±0.6	0.08	
	L-8-24-61-42H	646		8.8 9.0 9.3 9.4 8.8 9.9 7.6 8.2	52.6 50.6 50.2 56.5 59.0 57.9 51.6 54.0	18.4 19.0 20.0 19.8 18.0 18.9 (15.7) (15.8)	-		8.8 9.0	52.1 53.4	18.9 19.3	0.39 0.39	
	AVG	81.9±1.4	8.9±0.3	54.0±1.3	19.0±0.3	-	80.7±1.4	8.9±0.2	52.7±1.3	19.1±0.4	0.39		
L-8-31-61-47E	816			8.3 8.3	50.8 49.8	16.8 18.4	0.32 0.40		8.0 7.9 7.7	51.1 49.7 48.8	16.6 16.0 15.7	0.36 0.35 0.38	
		AVG	76.2±1.9	8.3±0.2	50.3±1.0	17.6±1.6	0.36	73.7±1.0	7.8±0.1	49.8±0.9	16.1±0.4	0.36	

(1) Dash mark means analysis was not sensitive to biphenyl.

(2) Parenthesis means analysis not included in evaluating average.

## CHEMICAL ANALYSES OF IRRADIATED SANTOWAX OMP-MIT AND MONSANTO DATA

SAMPLE METHOD	SAMPLE NO.	REACTION OPERATION TIME MHR	POLYPHENYL COMPOSITION Wt %									
			MIT <sup>(2)</sup>					MONSANTO				
			TOTAL, o-φ <sub>3</sub> , m-φ <sub>3</sub> p-φ <sub>3</sub> , No φ <sub>2</sub>	o-φ <sub>3</sub>	m-φ <sub>3</sub>	p-φ <sub>3</sub>	φ <sup>(1)</sup> <sub>2</sub>	TOTAL, o-φ <sub>3</sub> , m-φ <sub>3</sub> p-φ <sub>3</sub> , No φ <sub>2</sub>	o-φ <sub>3</sub>	m-φ <sub>3</sub>	p-φ <sub>3</sub>	φ <sub>2</sub>
Sample Position No.2	L-9-7-61-50E	928		8.3 8.8	48.6 49.5	17.5 16.3	0.45 0.18		8.2 8.2 8.2	52.4 52.1 53.0	19.1 18.9 19.2	0.7 0.6 0.4
	AVG		74.5±1.6	8.5±0.5	49.1±0.9	16.9±1.2	0.32	79.7±0.4	8.2±0.0	52.5±0.4	19.0±0.1	0.6
	L-9-14-61-51E	1073		8.2 8.0	45.3 45.5	16.9 15.7	0.19 0.28		7.5 8.4 7.4	47.0 52.5 46.6	18.2 18.9 17.1	0.31 0.32 0.35
	AVG		69.8±1.2	8.1±0.2	45.4±0.2	16.3±1.2	0.24	74.6±2.7	7.8±0.4	48.7±2.6	18.1±0.7	0.33
	L-9-19-61-52EL	1170		8.0 7.9 7.9	46.3 46.5 46.7	13.8 14.1 17.2	- - -		6.9 7.1	43.4 45.8	14.6 14.9	0.25 0.32
	AVG		69.4±1.5	7.9±0.1	46.5±0.2	15.0±1.5	-	66.4±2.4	7.0±0.2	44.6±2.4	14.8±0.3	0.28
	L-9-29-61-59HL	1466		7.8 7.9 8.0	42.2 40.8 40.4	12.9 13.2 12.3	- - -		6.6 6.7	42.4 43.5	14.1 14.5	0.44 0.41
	AVG		64.8±0.9	7.6±0.1	42.8±0.7	14.4±0.5	-	63.9±1.2	6.7±0.1	42.9±0.1	14.3±0.4	0.42
	L-10-5-61-62AL	1616		6.8 6.9 6.9	42.7 42.3 43.5	16.1 16.5 16.0	- - -		5.7 5.8	39.7 39.5	13.5 13.2	0.16 0.15
	AVG		64.5±0.5	6.8±0.2	42.4±0.3	15.3±0.3	0.32	58.7±0.4	5.8±0.1	39.6±0.2	13.3±0.3	0.15
	L-10-5-61-62A	1616		6.7 6.7 6.6	40.3 41.0 40.2	13.7 13.4 13.5	0.28 0.24 0.26		--	--	--	--
	AVG		60.7±0.4	6.7±0.1	40.5±0.4	13.5±0.1	0.26	--	--	--	--	--
	L-10-6-61-63BL	1652		8.0 7.9 8.5	46.5 45.5 46.5	16.9 17.6 17.5	- - -		7.5 7.3	43.1 45.2	15.7 15.3	0.31 0.33
	AVG		72.9±0.5	8.4±0.2	46.6±0.3	17.9±0.3	0.33	67.0±2.1	7.4±0.2	44.1±2.1	15.5±0.4	0.32

(1) Dash mark means analysis was not sensitive to biphenyl.

(2) Parenthesis means analysis not included in evaluating average.

## CHEMICAL ANALYSIS OF IRRADIATED SANTOWAX OMP-MIT AND MONSANTO DATA

SAMPLE METHOD	SAMPLE NO.	REACTION OPERATOR TIME MWHR	POLYPHENYL COMPOSITION, Wt %										
			MIT <sup>(2)</sup>					MONSANTO					
			TOTAL o- $\phi_3$ , m- $\phi_3$ , p- $\phi_3$ , No $\phi_2$	o- $\phi_3$	m- $\phi_3$	p- $\phi_3$	$\phi_2$ <sup>(1)</sup>	TOTAL o- $\phi_3$ , m- $\phi_3$ , p- $\phi_3$ , No $\phi_2$	o- $\phi_3$	m- $\phi_3$	p- $\phi_3$	$\phi_2$	
Sample Position No.2	L-10-6-61-63B	1652	71.0 68.7 68.9	8.6 8.4 8.4	46.5 45.4 45.1	15.7 14.7 15.2	0.2 0.2 0.2	-	-	-	-	-	
		AVG	69.4 $\pm$ 0.7	8.5 $\pm$ 0.1	45.7 $\pm$ 0.6	15.2 $\pm$ 0.4	0.2						
		66F	1786		9.3 8.9 9.0 8.0 7.4 7.6	46.1 44.7 44.2 45.0 43.7 43.4	15.6 12.6 14.7 19.6 16.3 15.9	0.1 0.1 0.1 - - -		6.5 6.5	42.7 42.7	15.7 16.5	0.20 0.21
	AVG		68.7 $\pm$ 1.3	8.4 $\pm$ 0.4	44.5 $\pm$ 0.5	15.8 $\pm$ 1.1	0.1	65.3 $\pm$ 0.8	6.5 $\pm$ 0	42.7 $\pm$ 0	16.1 $\pm$ 0.8	0.20	
	74J	2158			7.8 7.5 7.8	43.2 42.5 43.6	15.1 13.7 14.7	0.25 0.34 0.24		6.1 5.9	37.9 37.9	13.3 13.8	0.3 0.3
					7.6 7.0 7.9	40.7 40.1 41.0	14.7 14.2 14.9	0.3 0.2 0.1					
			AVG		64.0 $\pm$ 0.8	7.6 $\pm$ 0.2	41.8 $\pm$ 0.7	14.6 $\pm$ 0.2	0.2	57.4 $\pm$ 0.5	6.0 $\pm$ 0.2	37.9 $\pm$ 0.0	13.5 $\pm$ 0.5
	82JL	2378			9.0 8.6 7.6	38.6 38.7 38.3	14.3 14.9 12.9	0.36 0.40 0.39					
					6.9 6.8 6.7	36.4 36.0 35.8	13.6 13.5 12.9	0.3 0.3 0.3					
			AVG		58.5 $\pm$ 0.8	7.6 $\pm$ 0.5	37.3 $\pm$ 0.6	13.6 $\pm$ 0.3	0.3				

(1) Dash mark means analysis was not sensitive to biphenyl.

(2) Parenthesis means analysis not included in evaluating average.

(b) If  $Q$  exceeds the values tabulated below, the questionable observation may be rejected with 90 per cent confidence that the observation is extraneous.

<u>Number of Observations</u>	<u>Rejection Quotient <math>Q_{0.90}</math></u>
2	--
3	0.94
4	0.76
5	0.64
6	0.56
7	0.51
8	0.47
9	0.44
10	0.41
$\infty$	0.00

In the present case, only four analyses for all of the samples were rejected by this technique.

(2) Estimation of Average Concentration for Each Sample and of 70 Per Cent Confidence Limit

The average concentration of each component for each sample was estimated from the analyses for that sample which had not been rejected in part 1. The average concentration is defined as  $\bar{C} = \frac{\sum C}{N}$  where  $N$  is the number of observations. The 70 per cent confidence limit for the average concentration for each sample was then calculated by the procedure outlined below, using student's "t". The 70 per cent confidence limit was selected since this is a close approximation to the meaning of one standard deviation (68 per cent) and since student's "t" is tabulated for the 70 per cent confidence limit.

(a) Calculate for each sample:

$$\bar{x} = \text{average of all analyses} = \frac{\sum x}{N} .$$

S = standard deviation of N analyses.

$$= \sqrt{\frac{\sum_{i=1}^N (x - \bar{x})^2}{N - 1}}$$

$S_{\bar{x}}$  = standard error of average.

$$= \frac{S}{\sqrt{N}}$$

(b) Apply student's "t" to determine 70 per cent confidence limit.

70 per cent confidence limit =  $\bar{x} \pm tS_{\bar{x}}$  where t = student's "t" for 70 per cent probability that the true  $\bar{x}$  is within the range  $\bar{x} \pm tS_{\bar{x}}$ . Values of t for various numbers of observations are given below:

<u>Number of Observations</u>	<u>t(70% Probability)</u>
2	1.963
3	1.386
4	1.250
5	1.190
6	1.156
7	1.134
8	1.119
9	1.108
10	1.100



## APPENDIX 5. 3

## CALCULATION OF THE MWHR'S OF REACTOR OPERATION

In determining the MWHR's of reactor exposure, the thermal power as recorded every hour by the reactor operators was divided into regions of approximately constant power where only random fluctuations (generally of one per cent or less) occurred. Over each of the time periods, the MWHR's was taken as the product of the hours of reactor operation and the arithmetic average of the reactor power during this period. On reactor startup or shutdown, the times were measured from the time when the reactor first reached full reactor power on start-up and to the time when the shim rods were dropped on shutdown. The dose rate at nominal zero power is negligible, being only one per cent or less of that at full reactor power. The contribution to the MWHR's of reactor operation while raising the power to 1.80 MW is negligible, since most of the time required to raise the reactor to full power is at low power levels. Once the reactor has reached a power level of 10 kw, only about 5 minutes are required to attain 1.80 MW. The contribution to the exposure time is similarly negligible on shutdown.

The calculations for the first three days of loop operation are given in Table A5. 3 to illustrate the method used. On August 9, 1961, the reactor was slowly raised to full power in steps, since this was the first operation of the reactor with the in-pile section of the loop in place.

The MWHR of reactor operation at which the various samples were taken was calculated in a manner similar to that of Table A5. 3. For example, sample L-8-10-61-18G was taken at 1203 on August 10, 1961. The MWHR's for this sample is therefore (from Table A5. 3)  $35.6 + 1.82 + 1.828 (1203-0100) = 57.6$  MWHR.

TABLE A5.3

## SAMPLE CALCULATION OF MWHR'S OF REACTOR OPERATION

DATE	TIME OF DAY, HRS, MIN.	TIME INTERVAL HRS.	AVERAGE REACTOR POWER LEVEL, MW	REACTOR OPERATION TIME, MWHR	CUMULATIVE TOTAL EXPOSURE MWHR
8/9/61	0309-432	31/60	0.0916	0.047	
		31/60	0.458	0.237	
		21/60	0.917	0.321	
		45/60	1.65	1.24	
		0517-1806	12.82	23.09	
		1806-2400	5.90	10.70	
		TOTAL		35.6	
8/10/61	0000-0100	1.00	1.82	1.82	
	0100-1404	13.07	1.828	23.88	
	1404-1534	--	0	--	
	1534-2400	15.34	1.82	15.34	
	TOTAL			41.05	
8/11/61	0000-0210	2.17	1.820	3.95	
	0210-2400	21.83	1.832	40.02	
	TOTAL			43.97	

## APPENDIX 5.4

## LEAST SQUARES FIT OF CONCENTRATIONS VS. MWHR DATA

## A5.4.1 Introduction

As discussed in section 5.2.1, the concentration data for a given material can be represented with good accuracy by an equation of the following type:<sup>(1)</sup>

$$C = B e^{-bZ} \quad (\text{A5.2})$$

where

C is the concentration, wt %.

B and b are constants.

Z is the MWHR's of reactor operation.

In order to obtain the best estimate of the concentration at any time, as well as to provide a measure of the reliability of the estimate, the averaged chemical analyses for each sample have been used in a least squares calculation of the best values of the constants, B and b. This appendix describes the procedure used in this calculation, as well as a complete calculation for the total terphenyl concentration based on the M. I. T. data. The calculations performed for other concentrations are summarized.

## A5.4.2 Method of Calculation

Since the method of least squares applies to a linear equation, Equation (A5.2) has been transformed to a linear equation by taking logarithms of both sides:

$$\text{Log } C = \text{Log } B - (b \log e) Z \quad (\text{A5.3})$$

---

(1) In section 5.2.1, this equation was written as  $C_i = B_i e^{-b_i Z}$ , where i refers to a particular material. In this appendix, this indexing subscript is not used for simplicity, but it should be remembered that an equation of this type applies for each of the terphenyl isomers, as well as the total terphenyl concentration.

Letting

$$\begin{aligned} Y &= \text{Log } C \\ A &= \text{Log } B \\ m &= -b \log e \\ X &= Z \end{aligned}$$

Equation (A5. 3) can be written as:

$$Y = A + mX \quad (\text{A5. 4})$$

The method of least squares is therefore applied to this linear equation relating Log C to Z.

Application of the method of least squares to the above transformed equation without a different weighting of each data point does not give equal weight to all of the samples, since the squares of the deviation of Log C rather than C is being minimized. In the present case, all of the samples used for the least squares calculation are of the same order of accuracy and it is desired to weight each sample equally. A weighted least squares analysis is thus required for application of Equation (A5. 4).

In a weighted least squares calculation, the weight, w, of each point is generally taken as the reciprocal of the variance of the dependent variable so that (A5. 2, A5. 3):

$$w = \frac{1}{\sigma^2(y)} \quad (\text{A5. 5})$$

where y represents an actual data point of the population which is being represented by Equation (A5. 4). In general, the variance of any quantity, Q, can be written as:

$$\sigma^2(Q) = \sum_m \left( \frac{\partial Q}{\partial q_m} \right)^2 \sigma^2 q_m \quad (\text{A5. 6})$$

Since, in this case,  $y = \text{Log } C'$  where  $C'$  is the measured concentration for a particular sample,

$$\sigma^2(y) = \frac{1}{(C')^2} \sigma^2(C') \quad (\text{A5. 7})$$

Since  $\sigma^2(C')$  has been assumed to be constant, i. e., each sample has equal weight, substitution of Equation (A5. 7) into Equation (A5. 5) gives:

$$w = \frac{(C')^2}{\sigma^2(C')} = (\text{constant})(C')^2 \quad (\text{A5. 8})$$

The weighting factor to be used in the least squared fit of the data to Equation (A5. 4) is therefore proportional to the square of the dependent variable or  $(C')^2$ .

The equations used for the weighted least squares calculation have been obtained by analogy with equations from Gore (A5. 4) for an unweighted least squares calculation. The equations used are summarized in Table A5. 4 where the equations applying to the unweighted case are also given for comparison.

#### A5. 4. 3 Sample Calculation

A sample calculation is presented in this section for the total terphenyl concentration based on the M. I. T. data. As discussed in section 5. 2. 1, only samples 35E through 62A were considered representative of the circulating organic in the loop and were used in the least squares calculation. Hence, the recommended range of validity of the equations is from  $Z = 400$  to  $Z = 1616$  MWHR. In Table A5. 5, the calculation sheet prepared for this case is presented. Using values from this table and equations tabulated in Table A5. 4, the following calculations can be made:

$$m = \frac{8025.914 - \frac{(4318.951)(9.55050)}{5.07572}}{4.46709 \times 10^6 - \frac{(4318.951)^2}{5.07572}} = -1.2705 \times 10^{-4}$$

$$b = \frac{m}{\log e} = -2.93 \times 10^{-4}$$

$$A = \frac{9.55050}{5.07572} - (-1.2705 \times 10^{-4}) \left( \frac{4318.951}{5.07572} \right) = 1.98971$$

TABLE A5.4  
EQUATIONS USED FOR LEAST SQUARES CALCULATION

Form of Equation:  $Y = A + m X$

Form of Data: Values of the dependent variable,  $y$ , have been measured for various values of the independent variable,  $x$ . It is assumed that  $x$  is exactly known or, equivalently,  $\sigma^2(y) \gg \sigma^2(x)$ .

Weighting Factor:  $w$

Number of Observations:  $N$

QUANTITY	EQUATIONS FOR CALCULATION OF QUANTITY	
	UNWEIGHTED	WEIGHTED
$m$	$\frac{\sum xy - \frac{\sum x \sum y}{N}}{\sum x^2 - \frac{(\sum x)^2}{N}}$	$\frac{\sum wxy - \frac{\sum wx \sum wy}{\sum w}}{\sum wx^2 - \frac{(\sum wx)^2}{\sum w}}$
$A$	$A = \bar{y} - b\bar{x}$	$A = \bar{y} - b\bar{x}$
$\bar{y}$	$\bar{y} = \frac{\sum y}{N}$	$\bar{y} = \frac{\sum wy}{\sum w}$
$\bar{x}$	$\bar{x} = \frac{\sum x}{N}$	$\bar{x} = \frac{\sum wx}{\sum w}$
$S_{y(est)}^{(1)}$	$S_y \sqrt{(1-r^2) \frac{N-1}{N-2}}$	$S_y \sqrt{(1-r^2) \frac{N-1}{N-2}}$
$S_y^{(1)}$	$\sqrt{\frac{\sum y^2 - \frac{(\sum y)^2}{N}}{N-1}}$	$\sqrt{\frac{\sum wy^2 - \frac{(\sum wy)^2}{\sum w}}{\frac{\sum w}{N} [N-1]}}$
$S_m^{(1)}$	$\frac{S_{y(est)}}{\sqrt{\sum x^2 - \frac{(\sum x)^2}{N}}}$	$\frac{S_{y(est)}}{\sqrt{\left[ \sum wx^2 - \frac{(\sum wx)^2}{\sum w} \right] \frac{N}{\sum w}}}$
$S_A^{(1)}$	$\sqrt{\frac{S_{y(est)}^2}{N} + S_m^2 \bar{x}^2}$	$\sqrt{\frac{S_{y(est)}^2}{N} + S_m^2 \bar{x}^2}$
Confidence Limit <sup>(2)</sup>	$\begin{array}{c} + t S_m \\ + t S_A \\ - t S_m \\ - t S_A \end{array}$	$\begin{array}{c} + t S_m \\ + t S_A \\ - t S_m \\ - t S_A \end{array}$

(1)  $S \equiv$  standard error

(2)  $t \equiv$  student's  $t$ .

TABLE A5.5

CALCULATION SHEET FOR LEAST SQUARES CALCULATION FOR TOTAL TERPHENYL CONCENTRATION  
BASED ON MIT DATA

Z = x	C'	y = Log C'	xy	$x^2 \times 10^{-6}$	$y^2$	$(C')^2 = w$ $\times 10^{-4}$	w x y	wx	wy	$wy^2$	$wx^2 \times 10^{-6}$
393	87.4	1.94151	762.8523	0.154449	3.769461	0.763876	582.7246	300.2033	1.483073	2.879940	0.117980
400	86.5	1.93702	774.8080	0.1600	3.752046	0.748225	579.7307	299.2900	1.449327	2.807375	0.119716
646	81.9	1.91328	1235.9789	0.417316	3.660640	0.670761	829.0464	433.3116	1.283354	2.455415	0.279919
816	76.2	1.88195	1535.6712	0.665856	3.541736	0.580644	891.6783	473.8055	1.092743	2.056488	0.386625
928	74.5	1.87216	1737.3645	0.861184	3.504983	0.555025	964.2807	515.0632	1.039096	1.945353	0.477979
1073	69.8	1.84386	1978.4618	1.151329	3.399820	0.487204	963.9145	522.7699	0.898336	1.656059	0.560932
1170	69.4	1.84136	2154.3912	1.36890	3.390607	0.481636	1037.6324	563.5141	0.886865	1.633038	0.659312
1466	64.8	1.81158	2655.7763	2.149156	3.281822	0.419904	1115.1711	615.5793	0.760690	1.378050	0.902439
1616	60.7	1.78319	2881.6350	2.611456	3.179767	0.368449	1061.7355	595.4136	0.657015	1.171582	0.962188
TOTAL						5.075724	8025.9142	4318.9505	9.550499	17.983300	4.467090

$$B = \text{anti-log } A = 97.66$$

$$r = \frac{8025.914 - \frac{(4318.951)(9.55050)}{5.07572}}{\sqrt{\left[4.46709 \times 10^6 - \frac{(4318.951)^2}{5.07572}\right] \left[17.98330 - \frac{(9.55050)^2}{5.07572}\right]}} = -0.98983$$

$$S_y = \sqrt{\frac{17.98330 - \frac{(9.55050)^2}{5.07572}}{\frac{5.07572}{9} \cdot 8}} = 0.0537$$

$$S_{y_{\text{est}}} = 0.0537 \sqrt{\left[1 - 0.98983^2\right] \frac{8}{7}} = 0.00816$$

$$S_m = \frac{0.00816}{\sqrt{\left[4.46709 \times 10^6 - \frac{(4318.951)^2}{5.07572}\right] \frac{9}{5.07572}}} = 0.0690 \times 10^{-4}$$

$$S_b = \frac{0.0690 \times 10^{-4}}{\log e} = 0.159 \times 10^{-4}$$

$$S_A = \sqrt{\frac{(0.00816)^2}{9} + (0.0690 \times 10^{-4})^2 \left(\frac{4318.951}{5.07572}\right)^2} = 6.46 \times 10^{-3}$$

Now, since  $A = \text{Log } B$ , and using Equation (A5.6),

$$S_B = \frac{BS_A}{\text{Log } e} = \frac{(97.66)(6.46 \times 10^{-3})}{0.43429} = 1.45$$

With nine observation (seven degrees of freedom), student's t values are:

$$t(70\%) = 1.119$$

$$t(95\%) = 2.365$$



Hence, the confidence limits on the constants are:

70% Probability:

$$S_b = (0.159 \times 10^{-4})(1.119) = 0.178 \times 10^{-4}$$

$$S_A = (1.45)(1.119) = 1.62$$

$$C = (97.7 \pm 1.6) e^{-(2.93 \pm 0.18) \times 10^{-4} Z}$$

95% Probability:

$$C = (97.7 \pm 3.4) e^{-(2.93 \pm 0.38) \times 10^{-4} Z}$$

The equations in which an error corresponding to the 70 per cent confidence limit is given are tabulated in section 5. 2. 1 for the individual and total terphenyl isomers based on M. I. T.'s data and for the total terphenyls based on Monsanto's data. The equations with errors corresponding to the 95 per cent confidence limit are summarized below. The calculation for the total terphenyl concentration, based on Monsanto's data, have been based only on seven samples (samples 37A through 59H), since sample 35E appeared to be definitely in error and Monsanto had analyzed only sample 62AL and not 62A; 62AL was from the lines on the ends of the sampling capsule, so that some material may have been lost from this sample and it is not considered representative. With 95 per cent confidence, the following equations apply:

(95% Confidence Limits)

Total terphenyl (M. I. T. data)

$$C_{\text{omp}\phi_3} = (97.7 \pm 3.4) e^{-(2.93 \pm 0.38) \times 10^{-4} Z} \quad (\text{A5. 9})$$

Total terphenyl (Monsanto data)

$$C_{\text{omp}\phi_3} = (98.0 \pm 11.9) e^{-(2.98 \pm 1.31) \times 10^{-4} Z} \quad (\text{A5. 10})$$

Meta-terphenyl (M. I. T. data)

$$C_{m\phi_3} = (65.4 \pm 1.8) e^{-(3.02 \pm 0.38) \times 10^{-4} Z} \quad (\text{A5. 11})$$

Para-terphenyl (M. I. T. data)

$$C_{p\phi_3} = (21.5 \pm 3.7) e^{-(2.71 \pm 0.86) \times 10^{-4} Z} \quad (\text{A5. 12})$$

Ortho-terphenyl (M. I. T. data)

$$C_{o\phi_3} = (10.9 \pm 0.6) e^{-(2.80 \pm 0.57) \times 10^{-4} Z} \quad (\text{A5. 13})$$

#### APPENDIX 5. 5

##### ESTIMATION OF THERMAL DECOMPOSITION RATE

For the polyphenyls, Bley (A5. 5) reports an upper limit on the pyrolysis rate at 600°F of approximately  $3 \times 10^{-4}$  wt per cent/hr. For an organic mass of 4500 grams at 600°F, the thermal degradation rate is therefore  $(3 \times 10^{-6} \text{ gms degraded/gm-hr})(4500 \text{ gms}) = 0.0135 \text{ gms/hr}$ . At a reactor power of 1.80 MW and 0% DP, the radiolytic degradation rate for the total terphenyls is  $(1.17 \text{ grams/MWHR})(1.80 \text{ MWHR/hr}) = 2.10 \text{ grams/hr}$ . Hence, the thermal degradation rate is a maximum of only  $\frac{(0.0135)}{2.10} 100 = 0.64\%$  of the radiolytic degradation rate and can safely be neglected in this case. If irradiations are carried out at a higher temperature in the future, the thermal degradation rate may become significant and should be evaluated carefully. For example, an increase of the bulk organic temperature to 700°F results in a thermal degradation rate in the loop which is 15 per cent of the radiolytic degradation rate (measured at 600°F), again using the upper limit reported by Bley.

## APPENDIX 5. 6

## MASS OF CIRCULATING ORGANIC IN LOOP

## A5. 6. 1 Summary of Loop Volumes and Temperatures Used in Estimating Circulating Mass in Loop

In Table A5. 6, a summary of the volumes and temperatures used for different sections of the loop in estimating the circulating organic mass in the loop are presented for a nominal organic temperature of 600°F in the loop. Details of the method used in evaluating the effective volume and temperature of the different sections given in this table are described in section A5. 6. 2. Using the values quoted and the organic density in the loop at any time, the circulating mass of the organic can be estimated.

## A5. 6. 2 Circulating Mass of Organic in Loop Just Before Removal of Sample 62A, Based on Loop Volume and Organic Density

Due to fluctuations of the sight glass level of as much as  $\pm 2$  inches during the first two weeks of loop operation, the circulating organic mass in the loop just before removal of liquid sample L-10-5-61-62A was calculated. At this time, the sight glass level fluctuations had been no larger than approximately  $\pm 1/2$  inch for more than three weeks of operation, permitting an accurate determination of the mass in the surge tank.

In some sections of the loop, the entire volume of the section is a part of the main organic flow so that the organic in these sections is well-mixed. In other sections, dead-end spaces exist in which the organic may or may not be well-mixed. In some sections of the loop, the organic temperature is not well-known and must be estimated. In the following discussion, the effect of these uncertainties on the calculated mass is estimated. In all cases, the measured density of the irradiated Santowax OMP was used in determining the mass from the organic volume. As discussed in section 5. 4. 2, the density can be obtained from Equation (5. 38).

TABLE A5.6

SUMMARY OF VOLUMES AND TEMPERATURES FOR DIFFERENT LOOP SECTIONS USED IN ESTIMATING EFFECTIVE CIRCULATING MASS OF ORGANIC (ESTIMATED UNCERTAINTY IN ESTIMATED MASS =  $\pm$  200 GRAMS)

ASSUMED CONDITIONS	LOOP SECTION	VOLUME CM <sup>3</sup>		AVERAGE ORGANIC TEMPERATURE, °F
		TOTAL FOR LOOP SECTION	CIRCULATING	
Positive circulation in Entire Volume with Known and Approximately Constant Temperatures	In-Pile Section to Right Angle Bend in Space Between Upper and Lower Shield Plugs	500	500	600
	Lines Between In-Pile Section and Hydraulic Console	465	465	
	Valve 27 to Surge Tank	106	106	
	Test Heater to Valves 23,24	188	188	
	Test Heater No. 1	183	183	
	Sampling Position No. 2	173	173	
	Flowmeter (One)	118	118	
	Filter (One)	420	420	
	TOTAL	2152	2152 $\approx$ 2150	
Sections with Dead-End Spaces in which Organic may not be well-mixed.	Surge Tank to Filter (V-18 to V-19,20,1,2)	256	133	580
	Filter to Pumps (V-3,4 to V-5,6)	198	120	
	Pump to Flowmeter (V-7,8 to V-9,10)	169	90	
	Flowmeter to Test Heater (V-11,12 to V-13,14)	161	130	
	TOTAL	784	473 $\approx$ 475	
Positive Circulation in Entire Volume but with Different Organic Temperatures	Chempump (One)	1260	600	600
			660	400
	Coolers	608	268	600
			340	500
Variable Volume	Surge Tank (x=level of gage glass)	$V_{ST} = 115 + 61.1 \frac{\rho(350^{\circ}F)}{\rho(600^{\circ}F)} x$	$V_{ST} = 115 + 61.1 \frac{\rho(350^{\circ}F)}{\rho(600^{\circ}F)} x$	600

(1) Organic Mass on 10-5-61 in Sections of Loop Having Positive Circulation of Organic and Known Temperatures

In some sections of the loop, such as the in-pile section, there are no dead spaces or spaces with poor mixing, and the entire organic volume is a part of the main circulating stream of the organic. While there are small differences (of the order of 10 to 20°F) in the organic temperature in these different sections, an estimated average temperature can be used with good accuracy to predict the mass. The volumes determined as described in Appendix 3.6, as well as the estimated mass, are presented in Table A5.7. Based on the reproducibility of the volume measurements as well as a consideration of the method of measuring the volume, it is believed the volume measurements are accurate to within  $\pm 3$  per cent.

(2) Organic Mass on 10-5-61 in Sections with Dead-End Spaces in which Organic May Not Be Well-Mixed

There are some sections of the loop in which dead-end spaces exist, in which the organic volume is probably not well-mixed. These spaces occur in the lines leading to the feed-and-dump tank and in the cross-lines between flow paths one and two provided so various components could be valved off. As discussed in Appendix 3.4, two 1/16-inch tubes have been provided to produce circulation in the two largest dead-end volumes. However, the effectiveness of these tubes is not known and they are not considered in the following discussion in which the calculational procedure used and the results for sections containing dead-end spaces are presented.

The total volume, including any dead spaces not in the circulating organic flow, has been measured for the different sections of the loop. Based on these measured volumes and estimates of the tubing length of each section obtained from the layout drawing (Figure A3.32), it has been determined by a trial and error procedure that the holdup volume of each valve is approximately  $70 \text{ cm}^3$ , of which  $25 \text{ cm}^3$  is on the upstream side and  $45 \text{ cm}^3$  on the downstream side (due to construction of the bellows-sealed valves). In estimating the circulating volume of organic in these sections, it is assumed that the first 0.5 feet of any valved-off line is

TABLE A5.7

Organic Mass on 10-5-61 in Sections with Positive  
Circulation of Organic and Known  
Temperature, % DP = 39.1

(A) Volume

<u>Loop Section</u>	<u>Volume, cm<sup>3</sup></u>
In-Pile	500
Lines Between In-Pile Section and Hydraulic Console	465
Valve 27 to Surge Tank	106
Test Heater to Valves 23,24	188
Test Heater No. 1	183
Sampling Position	173 <sup>(1)</sup>
Flowmeter (One)	118
Filter (one)	420
Total	<u>2153 cm<sup>3</sup> <math>\equiv</math> 2150 <math>\pm</math> 60 cm<sup>3</sup></u>

(B) Mass (% DP = 39.1)

<u>Average Temperature, °F</u>	<u>Density, <math>\frac{\text{gm}}{\text{cm}^3}</math></u>	<u>Mass, gms</u>
590	0.911	1960 $\pm$ 55
600	0.906	1950 $\pm$ 54
610	0.902	1940 $\pm$ 54

(C) Best Value = 1950  $\pm$  65 gms

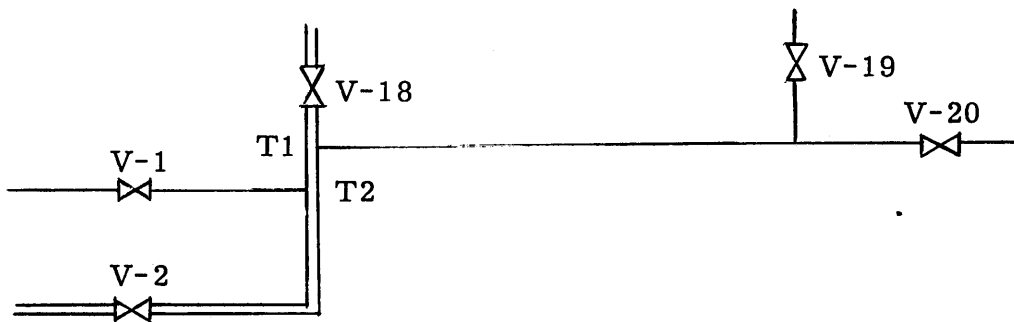
- (1) Length of tubing in sampling position  $\approx$  3 ft.  
Tubing size in sampling position = 0.250 inch OD x 0.049 inch  
wall.  
Tubing size of test heater = 0.250 inch OD x 0.020 inch wall.

$$\text{Volume} = 183 \text{ cm}^3 - (36) \left( \frac{\pi}{4} \right) (0.210^2 - 0.152^2) (16.4) = 183 - 9.7 \text{ cm}^3 = 173 \text{ cm}^3$$

well-mixed, and that the remainder of the line is not mixed at all. An upper error limit is specified which allows for complete mixing in the dead-end space up to but not including the valves at the end of the space (except where stated differently). The lower error limit assumes no mixing at all in the dead-end space. It is believed that the correct answer will fall within these limits. As in part 1, the calculation is made for a range of average temperatures. The calculations for the different sections will now be presented.

(a) Surge Tank to Filter

In the sketch below, this volume is presented, in which the flow path is indicated as a double line. The total measured volume between



valves V-1, V-2, V-18, V-19, and V-20 is 256 cm<sup>3</sup>. The tubing is 7/16 inch O. D. by 0.049 inch wall tubing with a unit volume of 17.75 cm<sup>3</sup>/ft. From the loop layout, the following tubing lengths and volumes have been estimated.

<u>Section of Tubing</u>	<u>Length, ft</u>	<u>Volume, cm<sup>3</sup></u>
V-18 to T2	1.5	27
T2 to V-1	1	18
T2 to V-2	1	18
T1 to V-19, V-20	3	<u>53</u>
Total		118

The valve volumes are as follows:

4 upstreams	100 cm <sup>3</sup>
1 downstream	<u>45</u>
Total	145 cm <sup>3</sup>

The total calculated volume is thus 263 cm<sup>3</sup>, which compares favorably with the measured volume of 256 cm<sup>3</sup>. The circulating volume is therefore estimated to be:

1 downstream side of valve	45 cm <sup>3</sup>
1 upstream side of valve	25
V-18 to T2	27
T2 to V-2	18
0.5 ft, T1 to V-19, V-20	9
0.5 ft, T2 to V-1	<u>9</u>
	133 cm <sup>3</sup> = 135 cm <sup>3</sup>

The upper limit is:

1 downstream side of valve	45 cm <sup>3</sup>
1 upstream side of valve	25
V-18 to T2	27
T2 to V-2	18
3 ft, T1 to V-19, V-20	53
1 ft, T2 to V-1	<u>18</u>
	186 cm <sup>3</sup> = 185 cm <sup>3</sup>

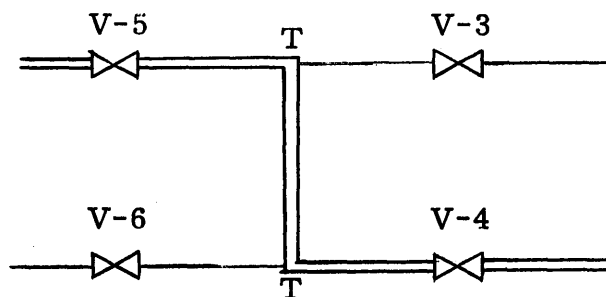
The lower limit is the sum of the first three of these volumes, or 97 cm<sup>3</sup> = 100 cm<sup>3</sup>.

The final volume is, then,

$$135 + 50 - 35 \text{ cm}^3$$



## (b) Filter to Pumps



The measured total volume is  $198 \text{ cm}^3$ . From the loop layout, the following tubing lengths and volumes have been estimated.

<u>Volume Description</u>	<u>Tubing Length, ft</u>	<u>Volume, <math>\text{cm}^3</math></u>
V-3 to V-5	0.5	9
V-4 to V-6	0.5	9
T to T	2	36
2 upstreams	-	50
2 downstreams	-	<u>90</u>
		194

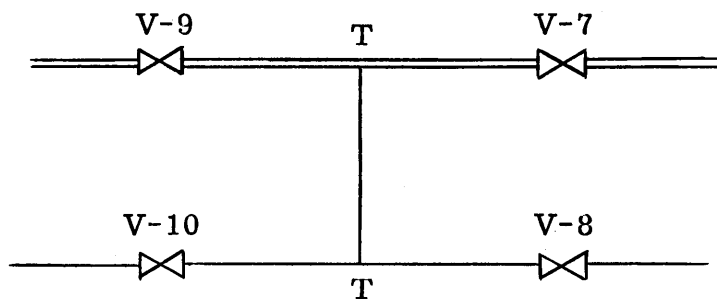
The circulating volume is:

V-3 to V-5	$9 \text{ cm}^3$
V-4 to V-6	9
T to T	36
1 downstream	45
1 upstream	<u>25</u>
	$120 \text{ cm}^3$

Because of the short length of tubing to the valves here, part or all of the organic in the closed valves may be well-mixed and the upper error limit in this case is therefore taken as the total volume. The volume of the flowpath only is about  $10 \text{ cm}^3$  less than the calculated volume so that the estimated volume is:

$$120 + 70 - 10 \text{ cm}^3$$

## (c) Pump to Flowmeter



The total measured volume is  $169 \text{ cm}^3$ . The calculated volume is:

Tubing, V-8 to V-10	0.5 ft	$9 \text{ cm}^3$
Tubing, V-7 to V-9	0.5	9
Tubing, T to T	0.75	14
2 upstreams	-	50
2 downstreams	-	<u>90</u>
		$172 \text{ cm}^3$

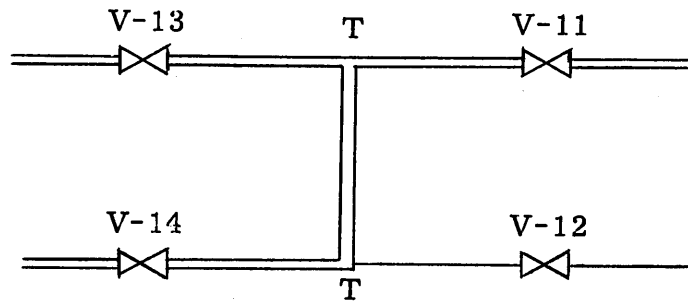
The circulating volume is:

Tubing, V-7 to V-9	$9 \text{ cm}^3$
0.5 ft, T to T	9
1 upstream	25
1 downstream	<u>45</u>
	$88 \text{ cm}^3 \approx 90 \text{ cm}^3$

The upper limit is approximately  $110 \text{ cm}^3$  and the lower limit  $80 \text{ cm}^3$  so that the circulating volume is

$$90 \begin{matrix} +20 \\ -10 \end{matrix} \text{ cm}^3$$

## (d) Flowmeter to Test Heater



The measured volume is  $161 \text{ cm}^3$  and the calculated total volume is the same as in part (c), or  $172 \text{ cm}^3$ . The circulating volume is:

Tubing, V-11 to V-13	0.5 ft	$9 \text{ cm}^3$
Tubing, V-12 to V-14	0.5	9
Tubing, T to T	0.75	14
1 downstream	-	45
2 upstreams	-	<u>50</u>
		$127 \text{ cm}^3 \approx 130 \text{ cm}^3$

The upper limit is taken as the total calculated volume, or  $170 \text{ cm}^3$ , and the lower limit as  $10 \text{ cm}^3$  less than the calculated volume. The final circulating volume is:

$$130 \begin{array}{r} + 40 \\ - 10 \end{array} \text{ cm}^3$$

## (e) Total Volume and Estimated Mass

The total circulating volume of the system is:

$$475 \begin{array}{r} + 180 \\ - 65 \end{array} \text{ cm}^3$$

The total estimated error is taken as the total of the estimated errors for each section rather than the square root of the sum of the errors, since the errors are not random. For comparison, the total measured volume for these sections (circulating and non-circulating) is  $784 \text{ cm}^3$ .

In estimating the mass, an additional uncertainty is added because of the unknown average temperature of the organic. The largest fraction of

the organic is in the main circulating volume of the loop and will be close to 600°F; the organic in the dead-end spaces will be at a somewhat lower temperature. The mass is estimated below for a range of temperatures which is believed to include the actual average temperature.

Average Temperature of Organic, °F	Density, gm/cm <sup>3</sup>	Mass of Organic gm.
560	0.924	440 + 166 - 60
580	0.915	435 + 165 - 60
600	0.906	430 + 163 - 59

The final estimate of the mass for these sections is:

$$435 + 165 \\ - 60 \text{ grams}$$

(3) Organic Mass on 10-5-61 in Sections in Which the Organic Is Well-Mixed but for Which Part of the Organic Is at a Different Temperature than the Main Organic Flow

In the Chempumps and coolers, the organic is well-mixed with the main organic flow. However, part of the organic volume in these components is cooled to a lower temperature than in the main organic volume. Only the total volume of these components is known and the temperatures and fraction of the volume at a given temperature must be estimated.

(a) Chempump

The motor section of the Chempump is cooled by means of Dowtherm A, which acts as a coolant for the stator and cools a bypass organic stream to cool the rotor. The total volume of organic in the pump and connecting tubing is 1260 cm<sup>3</sup>. The fraction of this organic volume which is in the impeller section at approximately 600°F

and the fraction in the low temperature bypass stream is not known. While the average temperature of the organic in the bypass stream is not known exactly, it can be estimated fairly closely. The calculations tabulated in Table A5. 8 are believed to cover the maximum range of these variables. It is seen that even with a large uncertainty in the volumes and temperatures, only a relatively small error is introduced in the mass. The final estimate of the mass is  $1200 \pm 40$  gms.

Table A5. 8. Organic Mass on 10-5-61 in Chempump

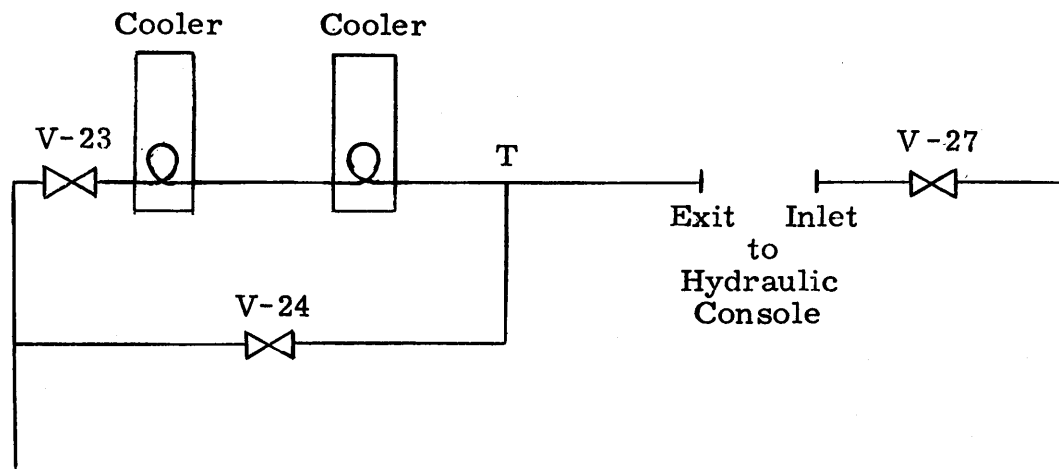
Total volume of pump =  $1260 \text{ cm}^3$

% DP = 39. 1

Organic Volume at 600°F $\text{cm}^3$ ( $\rho=0.906$ )	Organic Volume at Lower Temp. $\text{cm}^3$	Total Mass of Organic at Different Lower Temperatures, gms		
		350°F ( $\rho=1.015$ )	400°F ( $\rho=0.993$ )	450°F ( $\rho=0.973$ )
400	860	1236	1217	1199
600	660	1214	1200	1186
800	460	1192	1182	1173

#### (b) Coolers

To cool the organic material, two coolers are provided in series. A bypass line around the coolers is also provided. Under normal operation, the main loop flow passes through the bypass line at a temperature of approximately 600°F. A small flow of organic is maintained through the coolers; the average temperature of this stream is not exactly known but is estimated to be between 450°F and 550°F. The total volume for this section is  $608 \text{ cm}^3$ , from V-23 and V-24 to V-27, not including the connection from inlet to outlet. The calculated volume is given below.



Cooling coils in coolers	14.2 ft	252 cm <sup>3</sup>
Line between coolers	3.5	62
V-23 to cooler	1.75	31
Loop inlet to valve 27	2.5	44
V-24 to T	2.5	44
T to cooler	1.5	27
T to outlet	0.75	13
2 downstreams		90
1 upstream		<u>25</u>
		588 cm <sup>3</sup>

This calculated value is 20 cm<sup>3</sup> less than the measured volume. The volume circulating at a reduced temperature is:

Cooling coils in cooler	252 cm <sup>3</sup>
Line between coolers	62
T to cooler	<u>27</u>
	341 cm <sup>3</sup> $\approx$ 340 cm <sup>3</sup>

The remaining volume of 268 cm<sup>3</sup> will be assumed to be at 600°F. The calculations are tabulated in Table A5.9.

Table A5. 9. Organic Mass on 10-5-61 in Coolers

% DP = 39. 1

Average Lower Temperature, °F	Density gm/cm <sup>3</sup>	Mass at Lower Temperature, gms	Mass at 600°F (ρ=0. 906 gm/cm <sup>3</sup> )	Total Mass, gms
450	0. 972	330	243	573
500	0. 950	323	243	566
550	0. 928	316	243	559

The best estimate is  $565 \pm 10$  gms for this volume.

## (4) Summation of Masses and Estimation of Mass in Surge Tank on 10-5-61

The summation of the masses calculated up to now are given below. All of the circulating volume is included with the exception of the organic in the surge tank.

Positive circulation and known temperature	1950 ± 65 gms
Volumes with dead-end spaces	435 + 165 - 60
Well-mixed volumes, but different temperature:	
Chempump	1200 ± 40
Coolers	565 ± 10
	4150 + 190 - 110 gms

The error here is taken as the square root of the sum of the squared errors. As discussed in Appendix A5. 6. 4, the relation between the surge tank level,  $y$ , and the gage glass level,  $x$ , at 39. 1 % DP, is given by

$$y = (1. 120 \pm 0. 011) x.$$

The level in the surge tank gage before taking sample 62A and recharging the loop was  $3\text{-}3/4 \pm 1/2$  inch. Hence,  $y = 4. 20 \pm 0. 56$  inches. The volume of the surge tank is given by  $V_{ST} = 115 + 61. 1y$ , so that the organic volume is  $115 + 256 \pm 34 = 371 \pm 34$  cm<sup>3</sup>. With a density of 0. 906 gm/cm<sup>3</sup>, the mass

is  $336 \pm 31$  grams (equivalent to  $340 \pm 30$  grams). Adding this to the previous total, the circulating mass just before sample 62A was taken and the loop recharged is estimated to be  $4490 \begin{smallmatrix} + 190 \\ - 120 \end{smallmatrix}$  grams. The rounded-off value of  $4500 \begin{smallmatrix} + 190 \\ - 120 \end{smallmatrix}$  grams will be used as the mass of the system at this time.

### A5. 6. 3 Circulating Mass in Organic Loop as Function of MWHR Exposure

The circulating mass of the organic loop has decreased throughout the first experiment (up to the time of recharging), due to liquid sampling. In this section, the mass as a function of the MWHR exposure is determined by adding the mass removed in sampling to the calculated mass present just before liquid sample L-10-5-61-62 was taken and the loop recharged. This mass balance is then checked by calculating the initial mass following the same procedure as in section A5. 6. 2.

#### (1) Mass as Function of MWHR Exposure

The circulating mass just before sample 62A was taken and the loop recharged was  $4500 \begin{smallmatrix} + 190 \\ - 120 \end{smallmatrix}$  grams (see Appendix A5. 6. 2). The mass at any MWHR exposure can be determined by adding to this circulating mass the total mass removed by liquid sampling during the period following the MWHR of reactor operation being considered, to the time at which sample 62A was taken. It is assumed that the mass removed by gas sampling is negligible. The mass removed by each sample is calculated from the measured volume of the sample ( $19 \text{ cm}^3$  for the nominal  $10 \text{ cm}^3$  samples and  $78 \text{ cm}^3$  for the  $75 \text{ cm}^3$  samples), and the density of the organic at that time. The results are tabulated in Table A5. 10. Corrections are made for changes in the flow to test heater 2 or sampling position No. 2 during the first days of operation. The initial circulating mass is determined to be 4830 grams.

#### (2) Initial Mass of Circulating Organic in Loop from Loop Volume and Organic Density

The same procedure as used in A5. 6. 2 will be used here to estimate the initial circulating mass of the organic for comparison



TABLE A5.10

## CIRCULATING ORGANIC MASS IN LOOP AS FUNCTION OF MWHR EXPOSURE

LIQUID SAMPLE NO.	MWHR WHEN TAKEN	SAMPLE SIZE, cm <sup>3</sup>	TEMP. OF, AT WHICH SAMPLE TAKEN	% DP, SMOOTHED	DENSITY gm/cm <sup>3</sup>	MASS OF SAMPLES, gms	ORG. MASS BEFORE SAMPLES TAKEN, gms
-	-	-	-	-	-	-	4429 <sup>(1)</sup>
L- 10-5-61-62A	1616	78	600	39.1	0.906	71	4500
L- 9-29-61-59H	1466	19	600	36.3	0.903	17	4517
L- 9-19-61-52E	1170	19	600	30.6	0.896	17	4534
L- 9-14-61-51E	1073	19	600	28.7	0.894	17	4551
L- 9-7-61-50E	928	19	600	25.6	0.890	17	4568
L- 8-30-61-47E	816	19	600	23.1	0.887	17	4585
L- 8-24-61-42H	646	19	600	19.2	0.883	17	4602
L- 8-18-61-37A	400	78	600	13.1	0.875	68	4670
L- 8-18-61-35E	393	19	600	13.1	0.875	17	4687
L- 8-16-61-28G	318	19	600	11.2	0.873	17	4704
L- 8-14-61-27G	250	19	600	9.3	0.871	16	4720 <sup>(2)</sup>
	250						4578 <sup>(2)</sup>
L- 8-13-61-26G	180	19	300	7.0	0.999	19	4597
L- 8-13-61-24E	175	19	300	7.0	0.999	19	4616
L- 8-12-61-22E	150	19	300	6.0	0.998	19	4635
L- 8-11-61-21F	96.5	19	300	4.0	0.996	19	4654 <sup>(3)</sup>
	59.1		600	2.5	0.862		4811 <sup>(3)</sup>
L- 8-10-61-18G	57.6	19	300	2.5	0.994	19	4830
L- 16	0	-	-	0	-	-	4830

(1) Mass after liquid sample L-10-5-61-62A removed and before organic makeup added to loop.

(2) Sample position No. 2 added to circulating volume replacing test heater No. 2. Organic in the lines from the test heater tubing connections to valves 14 and 16 was added to circulating mass of organic. This organic had been trapped in these lines since 59.1 MWHR when test heater No. 2 was valved off. The organic volume added to circulation is:

$$\text{Total Volume of Section Between Valves 14 and 16} = 183 \text{ cm}^3 \quad \equiv \quad 185 \text{ cm}^3$$

$$\text{Volume of Test Heater} = 3 \text{ ft} \left[ \frac{\pi}{4} (0.210)^2 (12) (16.4) \frac{\text{cm}^3}{\text{ft}} \right] = 20 \text{ cm}^3$$

$$\text{Net Volume of Organic Added to Circulation} = 165 \text{ cm}^3$$

$$\text{Mass of Organic Added to Circulation} (\rho = 0.862 \frac{\text{gm}}{\text{cm}^3}) = 142 \text{ gm}$$

(3) Test heater No. 2 was valved off and 183 cm<sup>3</sup> of organic removed from the circulating organic mass. The % DP at this MWHR is approximately 2.5% equivalent to a density of 0.862 gm/cm<sup>3</sup>. The mass removed from circulation is therefore 157 grams.

with the value of 4830 grams calculated in part 1 of this section. No uncertainty limits will be carried through the calculations, as they should be close to those used in estimating the mass on 10-5-61.

- (a) Initial Mass in Volumes with Positive Circulation of Organic and Known Temperatures

Volume

Same as in section A5. 5. 2 except test heater No. 2 is substituted for the sampling position resulting in an estimated increase in the volume of 10 cm<sup>3</sup>. Volume = 2160 cm<sup>3</sup>.

Mass (% DP = 0%)

$$\rho(600^{\circ}\text{F}) = 0.860 \quad \text{Mass} = 1858 \text{ gms.}$$

- (b) Initial Mass in Volumes with Dead-End Spaces in which Organic May Not Be Well-Mixed

Volume

The volumes are the same as those specified in A5. 5. 2, where the total volume containing circulating organic was estimated as 475 cm<sup>3</sup>.

Mass

$$\rho(580^{\circ}\text{F}) = 0.869$$

$$\text{Mass} = 413 \text{ gms}$$

- (c) Initial Mass in Volumes which Are Well-Mixed but for which Part of the Organic Is at a Different Temperature Than the Main Organic Flow

Chempump

$$\text{Volume at } 600^{\circ}\text{F} = 600 \text{ cm}^3 \quad \rho(600^{\circ}\text{F}) = 0.860$$

$$\text{Volume at } 400^{\circ}\text{F} = 660 \text{ cm}^3 \quad \rho(400^{\circ}\text{F}) = 0.947$$

$$\text{Mass} = 516 + 625 = 1141 \text{ gms}$$

Cooler

$$\text{Volume at } 600^{\circ}\text{F} = 268 \text{ cm}^3 \quad \rho(600^{\circ}\text{F}) = 0.860$$

$$\text{Volume at } 500^{\circ}\text{F} = 340 \text{ cm}^3 \quad \rho(500^{\circ}\text{F}) = 0.904$$

$$\text{Mass} = 230 + 308 = 538 \text{ gms}$$

## (d) Summation of Above Mass and Mass in Surge Tank

Summation of masses with exception of the surge tank gives 3950 gms.

It will be assumed that the liquid in the gage glass is at 350°F as before.

$$\rho(350^{\circ}\text{F}) = 0.969.$$

$$y = 1.129x.$$

The surge tank volume is:

$$V_{ST} = 115 + 61.1y = 115 + 69.0x \text{ cm}^3.$$

The mass of organic in the surge tank as a function of x is then given at 600°F by:

$$M_{ST} = 99 + 59.3x \text{ gms.}$$

Hence, the total circulating organic mass is given by:

$$4049 + 59.3x \text{ gms.}$$

where x is the level in the sight glass. To have the same initial volume of 4830 gms as calculated in part 1, the surge tank sight glass level is given by:

$$4830 = 4049 + 59.3x.$$

$$x = \frac{781}{59.3} = 13.2 \text{ inches}$$

This is considerably lower than the initial liquid level which fluctuated from approximately 16 inches to above 19-1/2 inches where the liquid level is out of the top of the sight glass. There were, however, some anomalous drops in the level in the gage glass. Three instances of such a drop are given in Table A5. 11. These anomalous drops and fluctuations in the liquid level in the surge tank gage are the reason the calculated mass on 10-5-61, just before removal of liquid sample L-10-5-61-62, was used as the best estimate of the mass in the loop. There has been no indication of any leakage which would account for these decreases in gage level reading. One possible explanation is that there were pockets of gas in dead spaces which somehow were dissolved or dislodged, causing a drop in the surge tank level.

Table A5. 11. Three Occasions When Anomalous Drops Occurred in Surge Tank Level.

Date	Approximate Drop in Liquid Level in Gage Glass	Disturbances to Loop
8/14/61	From 16-18 inches To ~ 13 inches	Replacement of test heater No. 2 with new sampling position. Volume of tubing filled $\cong 10 \text{ cm}^3$ .
8/17/61	From ~ 13-1/4 inches To 10-1/4 - 11-1/2 inches	Power failure by Cambridge Electric stopped Chempump and circulation for approximately 10 minutes.
8/18/61	From 10-1/4 - 11-1/4 inches To 8-3/4 inches	No recorded disturbances.

#### A5. 6. 4 Calculation of Expected Concentration Change on Dilution on 10-5-61, Just After Sample 62A Was Taken

After 1617 MWHR of reactor operation, it was necessary to add fresh organic makeup to replace the organic removed by sampling. Theoretically, from the amount of organic added and the concentration change of the terphenyl isomers in the loop, an estimate of the circulating mass in the loop can be obtained: In this first dilution, however, inaccuracies in the mass of material added to the loop, as well as in the measured concentration, resulted in a very large uncertainty in the circulating mass estimated by this method. Accordingly, in this report, a comparison is made for each of the terphenyl isomers as well as the total terphenyls, of the estimated change in concentration expected using the circulating mass estimated based on the loop volume measurements.

The final concentration,  $C_2$ , of the terphenyl components on which a mass balance is being performed can be written as:

$$C_2 = \frac{MC_1 + AC_3}{M + A} \quad (\text{A5. 14})$$

where

A = total grams of organic makeup added to the loop.

M = circulating mass in loop before addition of fresh organic, grams.

$C_1$  = concentration of terphenyl isomer in loop before addition of fresh organic, wt %.

$C_2$  = concentration of terphenyl isomer in loop after addition of fresh organic, wt %.

$C_3$  = concentration of terphenyl isomer in the organic added to the loop.

The quantity of organic added, A, can be determined from the decrease in the feed and dump tank level or from the increase in the surge tank level. It is believed the value obtained from the feed and dump tank represents the best value because of frequently anomalous and unpredictable behavior of the level indicated by the surge tank gage. The liquid level in the feed and dump tank decreased on feed of organic to the loop from a level of 6-7/8 inches to 1-7/8 inches; the temperature of the organic in the feed tank was 398°F when added to the loop.

Initial feed tank level	= 6-7/8 ± 1/8 inch
Final feed tank level	= 1-7/8 ± 1/8 inch
Level change	= 5.00 ± 0.18 inch
Volume feed tank	= 223 cm <sup>3</sup> /in.
Volume charged	= 1115 ± 40 cm <sup>3</sup>
$\rho$ (398°F, 0% DP)	= 0.945 gm/cm <sup>3</sup>
Mass charged	= 1050 ± 40 gm

For comparison, a similar calculation for the surge tank level change is presented. The surge tank level must be corrected for the difference in density of the organic in the sight glass and in the tank as a result of a large temperature difference. In the case of the feed tank, this effect can be neglected, as only small temperature differences are encountered. For the surge tank, it will be assumed that

the liquid in the gage is at a temperature of  $350 \pm 25^\circ\text{F}$ . Letting  $y$  be the actual surge tank level and  $x$  the sight glass level, and using densities at a degradation product concentration of 39.1 per cent,

325°F	$\rho = 1.026$	$y = \frac{1.026}{0.906}x = 1.131x$
350°F	$\rho = 1.015$	$y = 1.120x$
375°F	$\rho = 1.004$	$y = 1.109x$
600°F	$\rho = 0.906$	

The best estimate is  $y = (1.120 \pm 0.011)x$  and  $y_2 - y_1 = (1.120 \pm 0.011)(x_2 - x_1)$ .

Initial surge tank gage level ( $x_1$ )	=	$3-1/2 \pm 1/2$ inch
Final surge tank gage level ( $x_2$ )	=	$17.0 \pm 1/2$ inch
Gage glass level change	=	$13-1/2 \pm 0.70$ inch
Surge tank level change	=	$15.11 \pm 0.78$ inch
Volume surge tank	=	$61.1 \text{ cm}^3/\text{inch}$
Volume charged	=	$924 \pm 48 \text{ cm}^3$
$\rho(600^\circ\text{F}, \sim 30.0\% \text{ DP})$	=	$0.895 \text{ gm}/\text{cm}^3$
Mass charged	=	$827 \pm 43 \text{ gm} \equiv 830 \pm 45 \text{ gm}$

This value is considerably smaller than that calculated from the feed and dump tank. As mentioned earlier, the value from the feed and dump tank is believed to be the most reliable and will be used in the calculations.

The concentrations in the loop before dilution were calculated using Equations (5.2-5.5) and are summarized below (at 1617 MWHR):

$$C_1(\text{omp}\phi_3) = 60.9$$

$$C_1(\text{m}\phi_3) = 40.1$$

$$C_1(\text{p}\phi_3) = 13.9$$

The composition of the organic charged to the loop is taken to be the same as the initial charge to the loop. The composition is assumed to be given by Equations (5. 2-5. 5) and is summarized below:

$$C_3(\text{omp}\phi_3) = 97.7$$

$$C_3(\text{m}\phi_3) = 65.4$$

$$C_3(\text{p}\phi_3) = 21.5$$

$$C_3(\text{o}\phi_3) = 10.9$$

The mass,  $M$ , of the system on charging is 4430 grams (from section A5. 5. 2). Substitution of these quantities into Equation (A5. 14) gives for the concentrations after dilution ( $C_2 = 0.809C_1 + 0.1916C_3$ ):

$$C_2(\text{omp}\phi_3) = 68.0$$

$$C_2(\text{m}\phi_3) = 44.9$$

$$C_2(\text{p}\phi_3) = 15.3$$

$$C_2(\text{o}\phi_3) = 7.70$$

These results are plotted in Figures 5. 2 and 5. 3, using the same slopes as were obtained before dilution. All concentrations based on M. I. T. analyses of samples after dilution are seen to be greater than expected, based on the above calculations. The agreement is fairly good for the Monsanto analyses except for ortho-terphenyl.

## APPENDIX 5.7

SAMPLE CALCULATION OF TOTAL TERPHENYL DEGRADATION  
RATES BY METHODS I AND II AND DECOMPOSITION YIELDS  
FROM DEGRADATION RATE

## A5. 7. 1 Method I for Calculation of Degradation Rate

The calculational procedure has been outlined in section 5. 2. 2. 2. The equations used for the weighted least squares analysis are also the same as those tabulated in Table A5. 4 and used for fitting an equation to the concentration vs. Z data. The calculations presented are based only on samples 35E through 62A, as recommended in section 5. 2. 2. 4, and on M. I. T.'s chemical analyses. The calculated results are therefore applicable for  $400 \leq Z \leq 1616$  MWHR.

In Table A5. 12, the calculation sheet used for this case is presented. Following the same calculational format as in Appendix 5. 4, the following results are obtained (see Appendix 5. 4 for tabulation of equations):

$$\begin{aligned}
 m &= +1.1849 \times 10^{-4} \\
 b &= \frac{+1.1849 \times 10^{-4}}{\text{Log } e} = +2.728 \times 10^{-4} \\
 A &= 3.67166 \\
 B &= \text{anti-log } A = 4695.2 \\
 r &= -0.99027 \\
 S_y &= 0.0499 \\
 S_{y(\text{est})} &= 0.00744 \\
 S_m &= 6.27 \times 10^{-6} \\
 S_b &= \frac{S_m}{\text{Log } e} = 0.145 \times 10^{-4} \\
 S_A &= 0.00593 \\
 S_B &= \frac{S_A B}{\text{Log } e} = 64.0
 \end{aligned}$$



TABLE A5.12  
 CALCULATION SHEET FOR TOTAL DEGRADATION RATE OF ORTHO- META, AND PARA- TERPHENYLS

Equations: 
$$M(Z) C_1(Z) + \sum_j S_j C_{j,i} = B_1 e^{-b_1 Z}$$

$$\log [M(Z) C_1(Z) + \sum_j S_j C_{j,i}] = \log B_1 - (b_1 \log e) Z$$

$$Y_i = A_i + m_i Z$$

Sample No.	Z MWHR at Sampling,	M(Z) Before Sampling, grams	C <sub>1</sub> (Z) Sample wt %	M(Z)C <sub>1</sub> (Z) Grams	S <sub>j</sub> (Z) Removal, Grams Added or Removed to Loop	S <sub>j</sub> (Z)C <sub>j,i</sub> (Z) Grams	Σ S <sub>j</sub> (Z)C <sub>j,i</sub> (Z) Grams	I M(Z)C(Z) + Σ S <sub>j</sub> (Z)C <sub>j,i</sub> (Z) Grams	y = log I	y <sup>2</sup>	w = I <sup>2</sup> x 10 <sup>-7</sup>	xy	x <sup>2</sup> x 10 <sup>-6</sup>	wxy	wx	wy	wx <sup>2</sup> x 10 <sup>-6</sup>	wy <sup>2</sup>	
16	0	4830	102.0	4926.60	-		0	4927	-	-	-	-	-	-	-	-	-	-	
18G	57.6	4830	(95.0)	-	19	18.0	0	-	-	-	-	-	-	-	-	-	-	-	
Th2 Valved Off	59.1	4811	(95.0)	-	157	149.0	18.0	-	-	-	-	-	-	-	-	-	-	-	
21F	96.5	4654	(94.0)	-	19	17.9	167.0	-	-	-	-	-	-	-	-	-	-	-	
22E	150	4635	95.0	4403.25	19	18.0	184.9	4588	-	-	-	-	-	-	-	-	-	-	
24E	175	4616	89.6	4135.94	19	17.0	202.9	4339	-	-	-	-	-	-	-	-	-	-	
26G	180	4597	(91.9)	-	19	17.5	219.9	-	-	-	-	-	-	-	-	-	-	-	
New Sampling Position	250	4578	88.0	4028.64	-142 <sup>(2)</sup>	-124.9	237.4	4266	-	-	-	-	-	-	-	-	-	-	
27G	250	4720	88.0	4153.60	16	14.1	112.5	4266	-	-	-	-	-	-	-	-	-	-	
28G	318	4704	(88.2)	-	17	15.0	126.6	-	-	-	-	-	-	-	-	-	-	-	
35E	393	4687	87.4	4096.44	17	14.8	141.6	4238	3.62716	13.1563	1.79606	1425.47	0.154449	2560.230	705.852	6.51460	0.2773997	23.62950	
37A	400	4670	86.5	4039.55	68	58.8	156.4	4196	3.62284	13.1250	1.76064	1449.14	0.160	2551.414	704.256	6.3785170	0.281702	23.10840	
42H	646	4602	81.9	3769.04	17	13.9	215.2	3984	3.60032	12.9623	1.58723	2325.81	0.417316	3691.595	1025.351	5.714536	0.662376	20.57415	
47E	816	4585	76.2	3493.77	17	12.9	228.1	3722	3.57078	12.7505	1.38533	2913.76	0.665856	4036.519	1130.429	4.946709	0.922430	17.663650	
50E	928	4568	74.5	3403.16	17	12.7	240.8	3644	3.56158	12.6849	1.32787	3305.15	0.861184	4388.810	1232.263	4.729315	1.143540	16.843898	
51E	1073	4551	69.8	3176.60	17	11.9	252.7	3430	3.53529	12.4983	1.17649	3793.37	1.15133	4462.862	1262.374	4.159233	1.354528	14.704125	
52E	1170	4534	69.4	3146.60	17	11.8	264.5	3412	3.53301	12.4822	1.16417	4133.62	1.36890	4812.236	1362.079	4.113024	1.593632	14.531403	
59H	1466	4517	64.8	2927.02	17	11.0	275.5	3203	3.50556	12.2890	1.02592	5139.15	2.14916	5272.357	1503.999	3.596424	2.204866	12.607531	
62A	1616	4500	60.7	2731.50	71	-	286.5	3018	3.47972	12.1085	0.910832	5623.23	2.61146	5121.818	1471.905	3.169440	2.378601	11.028809	
												12.13454			36897.841	10398.508	43.32180	10.819074	154.69147

(1) Parenthesis indicates analysis obtained from smoothed curve for estimating S<sub>j</sub> C<sub>j,i</sub>.  
 (2) Composition = 95.0%DP.

$$t(70\%) = 1.119$$

$$t(95\%) = 2.365$$

$$S_b(70\% \text{ confidence}) = 0.162 \times 10^{-4}$$

$$S_b(95\% \text{ confidence}) = 0.344 \times 10^{-4}$$

$$S_B(70\% \text{ confidence}) = 74.5$$

$$S_B(95\% \text{ confidence}) = 152$$

The final equations are:

70% Confidence

$$M(Z) C_i(Z) + \sum_j S_j C_{j,i} = (4695 \pm 75) e^{-(2.73 \pm 0.16) \times 10^{-4} Z} \text{ grams} \quad (\text{A5.15})$$

95% Confidence

$$M(Z) C_i(Z) + \sum_j S_j C_{j,i} = (4695 \pm 152) e^{-(2.73 \pm 0.34) \times 10^{-4} Z} \text{ grams} \quad (\text{A5.16})$$

The derivative of these equations gives  $-\frac{dH(Z)}{dZ}$  or the negative of the grams of ortho-, meta-, and para-terphenyls which are degraded per MWHR of reactor operation. Hence, using the 70% confidence equation,

$$\frac{dH(Z)}{dZ} = (1.281 \pm 0.061) e^{-(2.73 \pm 0.16) \times 10^{-4} Z} \frac{\text{grams}}{\text{MWHR}} \quad (\text{A5.17})$$

The error in  $\frac{dH(Z)}{dZ}$  can be obtained as follows:

Let:

$$\frac{dH(Z)}{dZ} = F e^{+bZ} \quad (\text{A5.18})$$

Since:

$$S^2(Q) = \sum_m \left( \frac{\partial Q}{\partial q_m} \right)^2 S^2(q_m) \quad (\text{A5.19})$$

where  $S^2(Q)$  is the error squared for  $Q$ , it follows that:

$$S^2\left(\frac{dH(Z)}{dZ}\right) = e^{2bZ} S^2(F) + Z^2 F^2 e^{+2bZ} S^2(b) \quad (\text{A5.20})$$

Hence, the final result is:

(A5. 21)

$$\frac{dH(Z)}{dZ} = \left[ 1.281 e^{-2.73 \times 10^{-4} Z} \right] \pm \left[ e^{-5.46 \times 10^{-4} Z} (0.00370 + 4.20 \times 10^{-10} Z^2) \right]^{1/2}$$

The final results are given in Table A5. 13 and compared with values calculated using in addition samples 16, 22E, 24E, and 27G which, as discussed in section 5. 2. 2. 4, are not included in the recommended calculations because of the limited reliability of these samples. It is seen that inclusion of these samples, in any case, does not introduce large differences from the recommended values. The calculation of the decomposition yields or grams degraded per watt-hr of radiation absorbed is the same as in Method II and is described there.

Table A5. 13. Comparison of  $\frac{dH(Z)}{dZ}$  Calculated Using Samples 35E through 62A, 27G through 62A, and 16 through 62A. The Calculations Based on Samples 35E through 62A Are the Recommended Values.

Z, MWHR	Samples 35E-62A (Best Estimate)	$\frac{dH(Z)}{dZ}$ , $\frac{\text{grams}}{\text{MWHR}}$	
		Samples 27G-62A	Samples 16-62A
400	1.15 ± 0.055	1.10	1.19
600	1.09 ± 0.056	1.04	1.13
800	1.03 ± 0.057	0.986	1.07
1000	0.975 ± 0.058	0.935	1.01
1200	0.923 ± 0.059	0.887	0.950
1400	0.874 ± 0.060	0.842	0.899
1600	0.827 ± 0.062	0.800	.850

### A5. 7. 2 Method II for Calculation of Degradation Rate and Decomposition Yield

The calculational procedure has been outlined in section 5. 2. 2. 2. In Table A5. 14, the equations used and sample calculations for the total terphenyls are presented.

## APPENDIX 5. 8

### METHOD OF DETERMINING GAS SOLUBILITY

The procedure for determination of the gas solubility is the same as that developed at Atomics International and described by Ewbank (A5. 6). A schematic of the apparatus is given in Figure A5. 2. Briefly, the procedure involves connection of the stainless steel capsule containing the organic sample directly to the reflux boiler. The entire system is then leak-tested to insure no gas inleakage during the measurement, evacuated, and the buret used for the volume measurement filled with mercury to stopcock S-1. The organic sample in the sampling capsule is then melted, using a glass insulated heating tape, and the sample is transferred to the reflux boiler. A heating mantle is used to heat the organic sample in the reflux boiler. All gases in the boiling sample are then pumped into the buret by means of the Toepler pump. An ice-water cold trap is provided to trap all condensable materials escaping from the reflux boiler. Once all of the dissolved gases have been pumped into the calibrated buret, the volume of gases at standard temperature and pressure is determined from the volume of gas in the buret and the pressure as determined by the height of the mercury in the buret. The volume of gases and weight of sample provides the gas solubility at the loop conditions when the sample was taken. Finally, the glass bulb for collection of the sample is evacuated and the sample transferred into the bulb for mass spectrographic analysis of the composition. For a more detailed description of the procedure, reference is made to Ewbank (A5. 6).

Equations Used and Sample Calculations for Degradation Rate and Decomposition Yields for Total Terphenyls Using Method II - 70% Confidence Limits Used - the Numerical Values are given for Z = 400 MWHR

QUANTIFY	EQUATIONS	SAMPLE CALCULATIONS FOR TOTAL TERPHENYLS
Concentration and Uncertainty	$C = B e^{-bZ}$ $\sigma^2(C) = \sigma_B^2 \{C^2 Z^2\} + \sigma_B^2 \{e^{-bZ}\}^2$	<p>From Appendix 5.4</p> $C = (97.7 \pm 1.6) e^{-(2.93 \pm 0.18) \times 10^{-4} Z} \text{ wt } \%$ $\sigma^2(C) = 3.24 \times 10^{-10} C^2 Z^2 + 2.56 (e^{-2.93 \times 10^{-4} Z})^2$ <p>at Z = 400 MWHR,</p> $C = 87.8 \text{ wt } \%$ $\sigma^2(C) = 2.42 \quad \sigma(C) = 1.6 \text{ wt } \%$
Concentration Gradient and Uncertainty	$\frac{dC}{dZ} = -b B e^{-bZ}$ $\sigma^2\left(\frac{dC}{dZ}\right) = \sigma_B^2 \{C^2 (1-bZ)^2\} + \sigma_B^2 \{(b e^{-bZ})^2\}$	$\frac{dC}{dZ} = -0.0286 e^{-2.93 \times 10^{-4} Z} \frac{\text{wt } \%}{\text{MWHR}}$ $\sigma^2\left(\frac{dC}{dZ}\right) = 3.24 \times 10^{-10} C^2 (1-bZ)^2 + (2.20 \times 10^{-7}) (e^{-2.93 \times 10^{-4} Z})^2$ <p>at Z = 400 MWHR</p> $\frac{dC}{dZ} = -0.0254 \frac{\text{wt } \%}{\text{MWHR}}$ $\sigma^2\left(\frac{dC}{dZ}\right) = 2.12 \times 10^{-6} \quad \sigma\left(\frac{dC}{dZ}\right) = 0.00145 \frac{\text{wt } \%}{\text{MWHR}}$
Degradation Rate and Uncertainty	$\frac{dH(Z)}{dZ} = -\frac{1}{100} M(Z) \frac{dC(Z)}{dZ}$ $\sigma\left(\frac{dH(Z)}{dZ}\right) = \frac{dH(Z)}{dZ} \sqrt{\left(\frac{\sigma(M(Z))}{M(Z)}\right)^2 + \left(\frac{\sigma\left(\frac{dC(Z)}{dZ}\right)}{\frac{dC(Z)}{dZ}}\right)^2}$	$\frac{dH(Z)}{dZ} = M(Z) \left[ 2.86 \times 10^{-4} e^{-2.93 \times 10^{-4} Z} \right] \frac{\text{GRAMS}}{\text{MWHR}}$ <p>Values of M(Z) are given in Figure 5.6.</p> $\sigma\left(\frac{dH(Z)}{dZ}\right) = \frac{dH(Z)}{dZ} \sqrt{\left(\frac{200}{M(Z)}\right)^2 + \left(\frac{\sigma\left(\frac{dC(Z)}{dZ}\right)}{\frac{dC(Z)}{dZ}}\right)^2}$ <p>A value of <math>\pm 200</math> grams has been used for <math>\sigma(M(Z))</math> in all calculations.</p> <p>at Z = 400 MWHR</p> $\frac{dH(Z)}{dZ} = 4602 \left[ 2.86 \times 10^{-4} e^{-2.93 \times 10^{-4} (400)} \right] = 1.17 \frac{\text{GRAMS}}{\text{MWHR}}$ $\sigma\left(\frac{dH(Z)}{dZ}\right) = 1.17 \sqrt{51.4 \times 10^{-4}} = 1.17(0.0717) = 0.0838 \frac{\text{GRAMS}}{\text{MWHR}}$
Decomposition Yields and Uncertainty	$G_m(-1) = \left(\frac{dH(Z)}{dZ}\right) / R_{SW}^{TI}$ $G(-1) = 11.65 G_m(-1)$ $G^*(-1) = \frac{G(-1)}{(C/100)}$ $\sigma(G_m(-1)) = G_m(-1) \sqrt{\left(\frac{\sigma(R_{SW}^{TI})}{R_{SW}^{TI}}\right)^2 + \left(\frac{\sigma\left(\frac{dH(Z)}{dZ}\right)}{\frac{dH(Z)}{dZ}}\right)^2}$ $\sigma(G(-1)) = 11.65 \sigma(G_m(-1))$ $\sigma(G^*(-1)) = G^*(-1) \sqrt{\left(\frac{\sigma(G(-1))}{G(-1)}\right)^2 + \left(\frac{\sigma(C)}{C}\right)^2}$	<p>From Section 4.5,</p> $R_{SW}^{TI} = 59.9 \cdot 7.02 e^{-2.93 \times 10^{-4} Z} \frac{\text{watt-hr}}{\text{MWHR}}$ <p>at Z = 400 MWHR</p> $G_m(-omp \phi_3) = \frac{1.17}{53.7} = 0.0218 \frac{\text{GRAMS}}{\text{watt-hr}}$ $G(-omp \phi_3) = 0.254 \frac{\text{MOLECULES}}{100 \text{ ev}}$ $G^*(-omp \phi_3) = \frac{0.254}{(87.8/100)} = 0.289 \frac{\text{MOLECULES}}{100 \text{ ev}}$ <p>In evaluating the uncertainty, an uncertainty of <math>\pm 5\%</math> in <math>R_{SW}^{TI}</math> has been used at all values of Z.</p> $\sigma(G_m(-omp \phi_3)) = 0.0218 \sqrt{(0.05)^2 + \left(\frac{0.0838}{1.17}\right)^2} = (0.0218)(0.0873) = 0.0019 \frac{\text{GRAMS}}{\text{watt-hr}}$ $\sigma(G(-omp \phi_3)) = 0.022 \frac{\text{MOLECULES}}{100 \text{ ev}}$ $\sigma(G^*(-omp \phi_3)) = 0.289 \sqrt{\left(\frac{0.022}{0.254}\right)^2 + \left(\frac{1.6}{87.8}\right)^2} = (0.289)(0.0885) = 0.027 \frac{\text{MOLECULES}}{100 \text{ ev}}$
Summary of Final Results as Presented in Table 5.5		<p>Z = 400 MWHR</p> $G_m(-omp \phi_3) = 0.0218 \pm 0.0019 \frac{\text{GRAMS}}{\text{watt-hr}}$ $G(-omp \phi_3) = 0.254 \pm 0.022 \frac{\text{MOLECULES}}{100 \text{ ev}}$ $G^*(-omp \phi_3) = 0.289 \pm 0.027 \frac{\text{MOLECULES}}{100 \text{ ev}}$

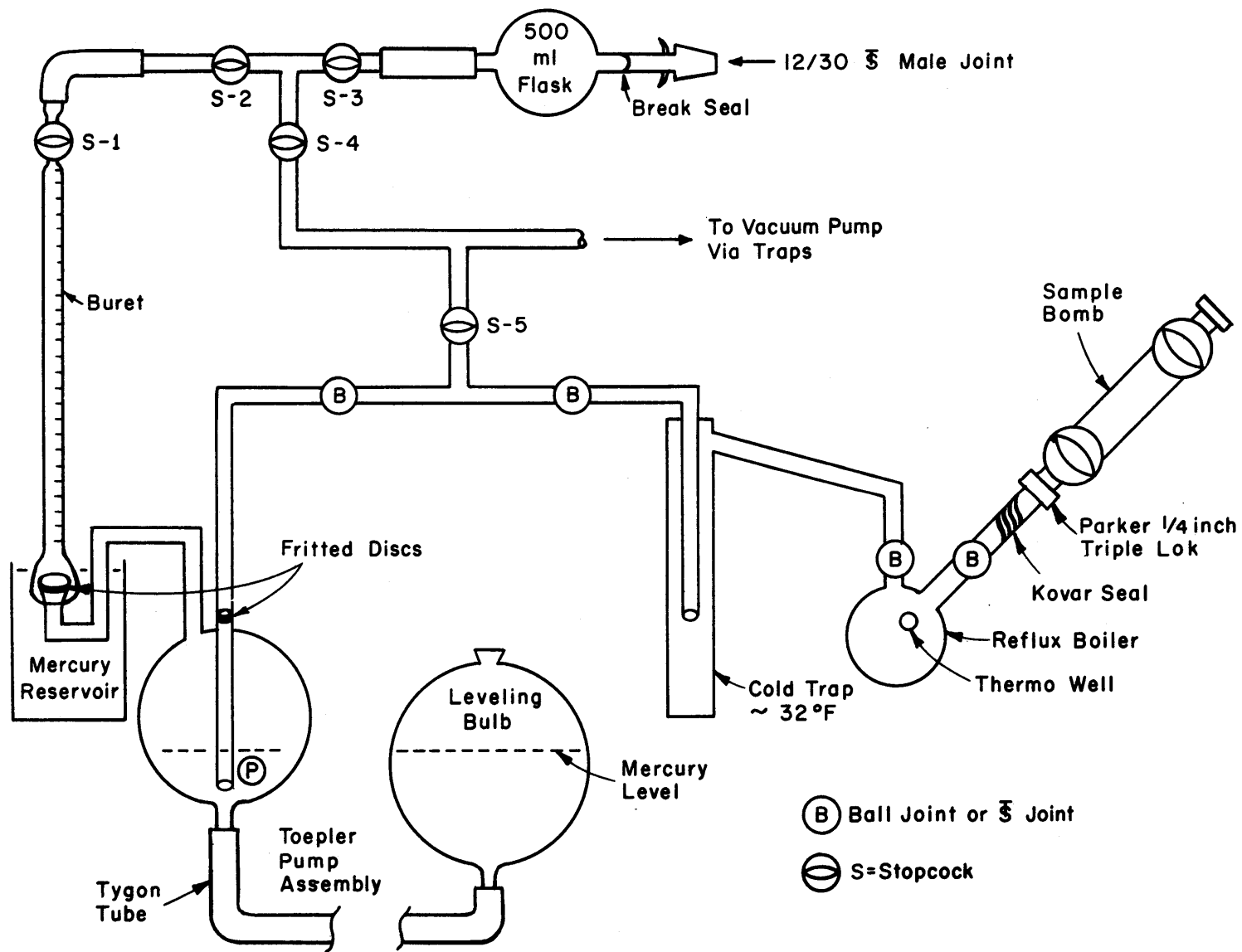


FIG. A 5.2 SCHEMATIC OF APPARATUS FOR GAS SOLUBILITY DETERMINATION FROM REFERENCE (A 5.6)

## APPENDIX 5.9

## GAS BALANCE ON LOOP

A gas balance on the loop has been performed at different times throughout this first run to determine the total gas evolution rate of irradiated Santowax OMP. The basic equation used for the mass balance is given in Equation (5.26) of Chapter 5. In this appendix, the procedures used are described in detail and the detailed calculations presented.

## A5.9.1 Gas Removed by Gas Sampling

During this first run, the accuracy of determination of the gas removed by gas sampling is limited to some extent, since the actual volume at standard temperature and pressure of gas removed has not been measured, but must be estimated from the pressure and temperature at which the gas sample was removed and the measured volume of the gas sampling capsule. While the pressure at which the sample was removed is the loop pressure and is well known, the temperature at which the gas sample was removed has not been measured for all samples and must be estimated. In Figure A5.3, the gas capsule temperature is presented for one case as a function of time after connection to the gas sampling position. Generally, most of the samples have been taken between 2 to 10 minutes after installation of the gas sample capsule but some have been taken after the capsule has been in position a longer time. The capsule temperature for all samples will be taken in the present case as  $130 \pm 20^\circ\text{F}$ ; it is believed an error of  $\pm 20^\circ\text{F}$  should represent the maximum limit for all the samples collected since this uncertainty covers a time period for collection of the sample from 1.5 to 15.5 minutes, based on Figure A5.3.

Another uncertainty is encountered due to a possible temperature difference between the gas in the sample capsule and the sample capsule itself when the valve is closed collecting the sample. The gas entering the sample capsule is at about  $600^\circ\text{F}$  and will be cooled by the capsule walls. Generally, 1 to 2 minutes have elapsed between opening and

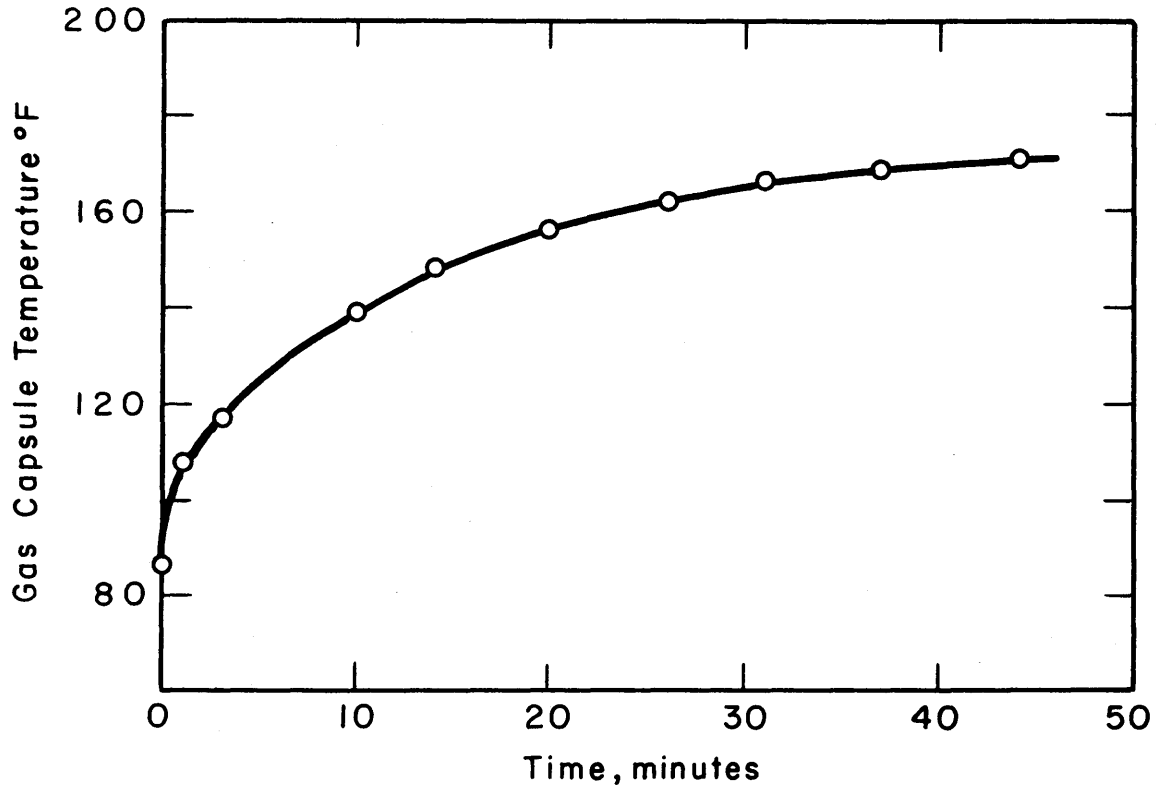


FIG. A5.3 TEMPERATURE OF GAS SAMPLE CAPSULE  
AFTER CONNECTION TO SAMPLING  
POSITION



closing of the sample valve. In order to obtain an order of magnitude estimate for this effect, a simple calculation will be performed. The calculation will be performed using air as the gas, since this should represent a conservative estimate for the decomposition gases which contain approximately 40 mol % H<sub>2</sub>, 20-40% N<sub>2</sub>, and various hydrocarbon gases (see Table 5.10). For air, McAdams (A5.7) reports the heat transfer coefficient for vertical surfaces as:

$$h_c = 0.29 \left( \frac{T_g - T_s}{L} \right)^{0.25} \quad (\text{A5.22})$$

where

$h_c$  is the natural convection heat transfer coefficient, Btu/hr-ft<sup>2</sup>-°F.

$T_g - T_s$  is the temperature difference between the gas and surface temperature.

$L$  is the height of the vertical surface, ft.

Now, for a fixed mass of gas,

$$\frac{dT_g}{d\tau} = \frac{q}{mC_V} = - \frac{h_c A (T_g - T_s)}{mC_V} = - \frac{A}{mC_V} \frac{0.29}{L^{0.25}} (T_g - T_s)^{1.25} \quad (\text{A5.23})$$

where

$\tau$  is time, hours.

$q$  is the heat transfer rate, Btu/hr.

$m$  is the mass of gas in the capsule, lbm.

$C_V$  is the heat capacity at constant volume, Btu/lbm-°F.

Integration of the above equation gives:

$$\int_{T_{g_i}}^{T_{g_f}} \frac{dT_g}{(T_g - T_s)^{1.25}} = - \frac{A}{mC_V} \frac{0.29}{L^{0.25}} \int_0^{\tau} d\tau$$

or

$$T_{g_f} = T_s + \frac{1}{\left[ \frac{A(0.29)(0.25)}{mC_V L^{0.25}} \tau + \frac{1}{(T_{g_i} - T_s)^{0.25}} \right]^4} \quad (\text{A5. 24})$$

The following quantities are used:

$$L \cong 0.5 \text{ ft.}$$

$$A \cong (\pi)(1/2)(0.5) = 0.131 \text{ ft}^2.$$

$$m \cong 82 \frac{492}{1060} \frac{115}{14.7} \text{ cm}^3 \text{ (STP)} \times \frac{\text{gm-mole}}{22,400 \text{ cm}^3 \text{ (STP)}}$$

$$\times \frac{28 \text{ gms}}{\text{gm-mole}} \times \frac{\text{lb}}{453.6 \text{ gms}} \cong 8.2 \times 10^{-4} \text{ lb.}$$

$$C_p \cong 0.3 \text{ Btu/lb-}^\circ\text{F.}$$

$$C_V = C_p - R \cong 0.3 - \frac{1.986}{28} = 0.3 - 0.071 = 0.23 \text{ Btu/lb-}^\circ\text{F.}$$

$$T_{g_i} = 600^\circ\text{F.}$$

$$T_s = 130^\circ\text{F.}$$

Substitution gives

$$T_{g_f} \cong 130 + \frac{1}{[\tau + 0.214]^4} \text{ }^\circ\text{F} \quad (\text{A5. 25})$$

where  $\tau$  is in minutes. Hence, within one minute, the gas temperature has dropped to within approximately  $0.5^\circ\text{F}$  of the surface temperature. Hence, even considering the very approximate nature of the above calculation, it is believed safe to assume the gas temperature is at the capsule wall temperature. The gas temperature will therefore be taken as  $130 \pm 20^\circ\text{F}$ . With this temperature, the volume of gas removed per gas sample at STP ( $32^\circ\text{F}$ ,  $14.7 \text{ psia}$ ) is:

$$V_{STP} = 82 \pm 3 \frac{492}{590 \pm 20} \frac{P \pm 5}{14.7} = 4.65 P \pm 7\% \quad (A5. 26)$$

where  $P$  is the loop pressure after the sample valve is opened, psia.

#### A5. 9. 2 Gas Removed by Liquid Sampling

An appreciable volume of gas is dissolved in the organic material. Hence, removal of liquid samples removes gas from the loop. In Appendix 5. 10, the gas solubility of the loop has been considered and a value of  $7.1 \pm 0.7 \times 10^{-3} \text{ cm}^3(\text{STP})/\text{psia-gm}$  recommended. With this value, the volume of gas at standard conditions removed in a liquid sample is:

$$V_{STP} = (7.1 \pm 0.7) \times 10^{-3} (S_j \pm 2)(P \pm 5) = (7.1 \times 10^{-3}) S_j P \pm 15\% \quad (A5. 27)$$

where  $S_j$  is the grams of organic removed in the sample.

$P$  is the loop pressure at which the sample was taken, psia.

#### A5. 9. 3 Volume of Undissolved Gas

From Appendix 5. 10, the volume of gas in the surge tank at standard temperature and pressure can be written as:

$$V_{STP} = \left\{ \left[ 1540 - 61.1 \frac{\rho(350)}{\rho(600)} y \right] \pm 100 \right\} \frac{492(P \pm 5)}{(1060)(14.7)} \\ = \left\{ \left[ 48.6 - 1.93 \frac{\rho(350)}{\rho(600)} y \right] \pm 3.16 \right\} (P \pm 5) \quad (A5. 28)$$

The density is given by the following relations obtained from Equations (5. 2) and (5. 38):

$$\rho(350^\circ\text{F}) = 1.087 - 0.1151 e^{-2.93 \times 10^{-4} Z} \\ \rho(600^\circ\text{F}) = 0.978 - 0.1151 e^{-2.93 \times 10^{-4} Z} \quad (A5. 29)$$

## A5. 9. 4 Volume of Dissolved Gas Circulating in Loop

$$\begin{aligned}
 V_{\text{STP}} &= [(7.1 \pm 0.7) \times 10^{-3}] [M \pm 200] [P \pm 5] \\
 &= 7.1 \times 10^{-3} MP \pm 12\%
 \end{aligned}
 \tag{A5. 30}$$

where M is the circulating organic mass, grams.

## A5. 9. 5 Total Gas in Loop Plus Gas Removed by Sampling

The gas evolution rate can be determined from the total amount of gas in the loop at any time plus the cumulative amount of gas removed by gas and liquid sampling (see Equation (5. 26)). The calculations performed in estimating this last quantity are presented in Table A5. 15. For comparison, a summary of the results of calculations performed using a gas solubility of  $2.6 \times 10^{-2} \text{ cm}^3(\text{STP})/\text{psia}$  are presented in Table 5. 11 of the main body.

## APPENDIX 5. 10

## ESTIMATION OF GAS SOLUBILITY

Due to difficulties encountered in measuring the solubility of the gases dissolved in the organic coolant, only two measurements of the gas solubility were made up to recharging of the loop on October 5, 1961, just after sample 62A was taken. Since recharging of the loop, several more measurements have been made. The results of measurements of the gas solubility, both before and after recharging of the loop on October 5, 1962, are presented in Table A5. 16. It will be noticed that the value obtained with sample L-52E is considerably lower than those from the other measurements. It is believed this is due to the delay of 2-1/2 weeks between taking this sample and performing the measurement, so that gases could have slowly leaked from the sample. Within the accuracy of the measurements performed to date, there does not appear to be any trend indicating

TABLE A5.15  
GAS BALANCE ON LOOP

SAMPLE NO.	MWHR OF REACTOR OPERATION	LOOP PRES. AFTER SAMPLE REMOVAL, psia	cm <sup>3</sup> (STP) REMOVED IN GAS SAMPLES	GRAMS OF ORGANIC REMOVED	cm <sup>3</sup> (STP) REMOVED IN LIQUID SAMPLES	(I)	y, LIQUID LEVEL AFTER REMOVAL OF SAMPLE, INCH	(II)	MASS OF ORGANIC IN LOOP AFTER SAMPLE, gms.	(III)	cm <sup>3</sup> (STP) I + II + III
						TOTAL GAS REMOVAL INCLUDING SAMPLE cm <sup>3</sup> (STP)		UNDISSOLVED GAS AFTER SAMPLE, cm <sup>3</sup> (STP)		DISSOLVED GAS AFTER SAMPLE cm <sup>3</sup> (STP)	
-	0	130	-	-	-	0	20.0	662	4830	4450	5112
L-18G	57.6	145	-	19	19.5	19.5	19.5	900	4811	4940	5860
-	59.1	145	-	157	162	182	-	-	-	-	-
G-20C	-	137	638	-	-	820	-	-	-	-	-
L-21F	96.5	147	-	19	19.8	839	19.1	1042	4635	4830	6711
L-22E	149.6	159	-	19	21.4	861	19.1	1128	4616	5200	7189
L-24E	174.7	162	-	19	21.8	883	-	-	-	-	-
L-26G	179.5	162	-	19	21.8	904	-	-	-	-	-
-	250.5	159	-	-142	-160	744	-	-	-	-	-
L-27G	250.5	159	-	16	21.4	766	-	-	-	-	-
L-28G	317.6	160	-	17	21.6	787	12.5	3420	4687	5320	9527
G-29C	-	152	704	-	-	1491	-	-	-	-	-
G-30C	-	146	676	-	-	2167	-	-	-	-	-
G-31C	-	144	666	-	-	2833	-	-	-	-	-
G-32C	-	138	639	-	-	3472	-	-	-	-	-
G-33C	-	133	616	-	-	4088	-	-	-	-	-
G-34C	-	127	591	-	-	4679	-	-	-	-	-
L-35E	393	127	-	17	15.3	4695	-	-	-	-	-
L-37A	400.5	126	-	68	60.9	4755	9.1	3630	4670	4170	12555
G-38C	-	136	630	-	-	5385	-	-	-	-	-
G-39C	563.0	129	597	-	-	5982	-	-	-	-	-
G-40C	-	123	569	-	-	6551	-	-	-	-	-
G-41C	-	118	546	-	-	7097	-	-	-	-	-
L-42H	646.3	126	-	17	15.2	7113	7.5	4060	4585	4110	15283
G-43C	-	120	555	-	-	7668	-	-	-	-	-
G-44C	-	131	606	-	-	8274	-	-	-	-	-
G-45C	741.3	125	578	-	-	8852	-	-	-	-	-
G-46C	-	123	569	-	-	9421	-	-	-	-	-
L-47E	816.4	131	-	17	15.8	9437	8.3	4010	4568	4240	17687
G-48C	-	130	602	-	-	10039	-	-	-	-	-
G-49C	-	124	576	-	-	10615	-	-	-	-	-
L-50E	927.9	122	-	17	14.7	10629	5.9	4360	4551	3910	18899
L-51E	1073.3	126	-	17	15.2	10644	6.0	4480	4534	4060	19184
G-53C	-	130	601	-	-	11245	-	-	-	-	-
L-52E	1170	130	-	17	15.7	11261	4.9	4940	4517	4170	20371
G-54C	1204	128	582	-	-	11843	-	-	-	-	-
G-55C	-	134	620	-	-	12463	-	-	-	-	-
G-56C	1380	129	596	-	-	13059	-	-	-	-	-
G-57C	-	129	596	-	-	13655	-	-	-	-	-
G-58C	-	125	578	-	-	14233	-	-	-	-	-
L-59H	1466	125	-	17	15.1	14248	3.7	5070	4500	3990	23308
G-60C	-	126	583	-	-	14831	-	-	-	-	-
G-61C	1575	125	578	-	-	15409	-	-	-	-	-
(1)	1575	(1)	2090 <sup>(1)</sup>	-	-	17499	-	-	-	-	-
L-62A	1616	96	-	71	48.4	17546	3.3	3980	4429	3020	24548

(1) Gas lost from loop here.

Undissolved Gases

$P_i = 110$  psig  
 $P_f = 81$  psig  
 $\rho(350^\circ\text{F}) = 1.015$   
 $\rho(600^\circ\text{F}) = 0.906$   
 $y = 4$  inches  

$$\Delta V_{\text{STP}} = (48.6 - 1.93 \frac{1.015}{0.906} 4)(110-81)$$

$$= 1160 \text{ cm}^3 \text{ (STP)}$$

Dissolved Gases

Mass of organic = 4500 grams  

$$\text{Solubility} = 7.1 \times 10^{-3} \frac{\text{cm}^3 \text{ (STP)}}{\text{gm-psia}}$$

$$\text{Gas volume} = (4500)(7.1 \times 10^{-3})(110-81) = 926 \text{ cm}^3 \text{ (STP)}$$

TABLE A5.16

MEASURED VALUES OF GAS SOLUBILITY IN ORGANIC COOLANT

\*-Denotes Measurements taken on Samples from loop before recharging with organic.

SAMPLE NO.	MWHR	LOOP PRESSURE psig	SURGE TANK TEMP., °F	GAS SOLUBILITY	
				S $\frac{\text{cm}^3(\text{STP})}{\text{gm}}$	$\frac{\text{cm}^3(\text{STP})}{\text{gm} - \text{psia}} = \frac{1}{k'_{\text{avg}}}$
*L-52E	1170	115	603	0.34	$2.62 \times 10^{-3}$
*L-59H	1466	110	598	0.85	$6.80 \times 10^{-3}$
L-82J	2378	108	598	0.88	$7.15 \times 10^{-3}$
L-100H	3219	110	600	0.74	$5.91 \times 10^{-3}$
L-118J	3885	105	606	1.01	$8.41 \times 10^{-3}$

Average not including L-52E =  $(7.1 \pm 0.7) \times 10^{-3} \frac{\text{cm}^3(\text{STP})}{\text{gm-psia}}$

where the limits represent the 70 % confidence level.

a change in the gas solubility with changes in the degradation product composition. Hence, the average of determinations on samples L-59H through L-118J will be used as the best estimate of the gas solubility at the present time.

To account for variations in the solubility with pressure, Henry's law will be used for the small pressure variations occurring during operation of the loop. For each gaseous component in the loop,

$$p_i = k_i N_i = k'_i S_i \quad (\text{A5. 32})$$

where

$p_i$  is the partial pressure of component  $i$ .

$k_i$  and  $k'_i$  are Henry's law coefficients for component  $i$ .

$N_i$  is the mole fraction of component  $i$  in the liquid.

$S_i$  is the solubility of component  $i$ , cc (STP)/gram of material.

Neglecting the vapor pressure of the coolant which is only about 3 psia at 600°F, the total loop pressure,  $p$ , can then be written as:

$$p = \sum p_i = \sum k'_i S_i \quad (\text{A5. 33})$$

For a given composition of gases, this can be written as

$$p = k'_{\text{avg}} S \quad (\text{A5. 34})$$

where

$$S = \sum S_i$$

$$k'_{\text{avg}} = \sum k'_i \frac{S_i}{S} \quad (\text{A5. 35})$$

In the present case, the composition of the gases as well as organic coolant has not remained constant and  $k'_{\text{avg}}$  would be expected to be a function of the MWHR of reactor operation. As can be seen from Table A5. 16, the changes in  $k'_{\text{avg}}$  are evidently smaller than the experimental errors so that Equation (A5. 34) can be assumed to apply with a constant  $k'_{\text{avg}}$  during the time covered in this report; the values of  $k$  and  $S$  obtained are obviously related to the operating temperature of about 600°F.

The solubility in the loop is then given by:

$$S = p \frac{1}{k'_{avg}} \frac{\text{cc(STP)}}{\text{gm}} = (7.1 \pm 0.7) \times 10^{-3} p \quad (\text{A5. 36})$$

where  $p$  is the total loop pressure in psia.

An estimate of the gas solubility can also be obtained from the pressure change of the loop when six consecutive gas samples were removed from the loop. The relation between the quantity of gas removed, gas solubility, and pressure change in the loop can be written as:

$$\sum_{j=1}^n V_{sj} \frac{(492)(P_{sj})}{(T_{sj})(14.7)} = V_g \frac{492[P_i - P_f]}{(T_g)(14.7)} + \left( \frac{1}{k'_{avg}} \right) M [P_i - P_f] \quad (\text{A5. 37})$$

where

$V_{sj}$  = volume of sample removed,  $\text{cm}^3$ .

$P_{sj}$  = pressure in sample removed from loop, psia.

$T_{sj}$  = temperature of sample removed from loop,  $^{\circ}\text{R}$ .

$V_g$  = volume of gas space in surge tank,  $\text{cm}^3$ .

$P_i$  and  $P_f$  are the initial and final pressures, respectively, in the surge tank, psia.

$T_g$  is the gas temperature in the surge tank,  $^{\circ}\text{R}$ , which is assumed to be equal to the organic temperature.

$M$  is the mass of organic in the loop, grams.

The desired unknown is  $1/k'_{avg}$ ,  $\text{cm}^3$  (STP)/gram-psia.

The value of  $V_g$  can be estimated only with limited accuracy. The volume of the surge tank above a level equivalent to the top of the gage glass is estimated from the construction drawings to be approximately  $200 \text{ cm}^3$ . The tubing above the surge tank is estimated to be approximately  $150 \text{ cm}^3$ . At the beginning of the irradiation, the gage



glass level in the surge tank was approximately 20 inches (slightly above top of gage glass) but, as discussed in Appendix 5. 6, fluctuated considerably. Using relations given in Appendix 5. 6, the volume of organic in the surge tank is then:

$$V_{ST} = 115 + (69.0)(20) = 1495 \text{ cm}^3$$

The total surge tank volume is  $115 + (61.1)(19.5) + 350 = 1655 \text{ cm}^3$ . The difference gives an initial gas space of  $160 \text{ cm}^3$ . The gas volume at different sight glass levels,  $y$ , can be estimated from this initial volume by the relation below:

$$V_g = 160 + \left[ (69.0)(20) - (61.1) \frac{\rho(350)}{\rho(600)} y \right] = 1540 - 61.1 \frac{\rho(350)}{\rho(600)} y \quad (\text{A5. 38})$$

An error of  $\pm 100 \text{ cm}^3$  will be assumed for  $V_g$ .

No attempt has been made to control the temperature,  $T_{sj}$ , at which the sample is removed from the loop. However, from Appendix 5. 9,  $T_{sj}$  is estimated to be  $590 \pm 20^\circ\text{R}$  for all samples. The gas volume removed by sampling,  $V_{sj}$ , has been measured and is  $82 \pm 3 \text{ cm}^3$ ; the sample pressure is equal to the loop pressure after the sample has been taken. A calculation will now be given for the consecutive removal of samples G-8-16-61-29C through G-8-16-61-34C (six samples):

$M$  = mass of organic in loop =  $4680 \pm 200$  grams.

$y$  = surge tank gage glass level = 13. 3 inches.

Coolant composition  $\cong 11\%$  DP.

$\rho(350^\circ\text{F}) = 0.984$ .

$\rho(600^\circ\text{F}) = 0.875$ .

$V_g = 1540 - 61.1 \frac{0.984}{0.875} (13.3) = 627 \cong 630 \pm 100 \text{ cm}^3$ .

$P_i$  = initial pressure =  $157 \pm 5$  psia.

$P_f$  = final pressure =  $129 \pm 5$  psia.

$$\begin{aligned}
 \Sigma V_{sj} \frac{492 P_{sj}}{T_{sj} 14.7} &= \frac{(82 \pm 3)(492)}{(590 \pm 20)(14.7)} \Sigma P_{sj} \\
 &= (4.65 \pm 5\%) [(152 \pm 5) + (146 \pm 5) + (144 \pm 5) \\
 &\quad + (138 \pm 5) + (133 \pm 5) + 127 \pm (5)] \\
 &= 3900 \pm 200 \text{ cm}^3
 \end{aligned}$$

Substitution gives:

$$\begin{aligned}
 \frac{1}{k'_{avg}} &= \frac{(3900 \pm 200) - (630 \pm 100) \frac{(492)(28 \pm 7)}{(1060)(14.7)}}{(4680 \pm 200)(28 \pm 7)} \\
 &= (2.6 \pm 0.6) \times 10^{-2} \frac{\text{cc(STP)}}{\text{gm-psi}}
 \end{aligned}$$

This is higher by a factor of approximately three than the value obtained from samples removed from the loop. The reason for the difference is unknown at present.

#### APPENDIX 5.11

##### CALCULATION OF RADIOLYTIC GAS YIELDS

As discussed in section 5.3.3, an equation of the following type fits the gas yield data:

$$V = V_1 + P(1 - e^{-bZ})$$

or

$$Y = A + mX$$

(A5.39)

An unweighted least squares has been applied to this equation, using equations given in Table A5.4. Following the same procedure as outlined in Appendix 5.4 (except using the unweighted equations), the following results were obtained, using the data given in Table 5.11 and assuming  $b = (2.93 \pm 0.18) \times 10^{-4} \text{ MWHR}^{-1}$ .

$$m = P = 5.21 \times 10^4 \text{ cm}^3 \text{ (STP)}$$

$$A = V_1 = 5564 \text{ cm}^3 \text{ (STP)}$$

$$r = 0.9932$$

$$S_y = 6590$$

$$S_{y(\text{est})} = 804$$

$$S_m = 4620$$

$$S_A = 845$$

$$\text{Student's } t = 1.093$$

Hence,

$$\sigma(m) = 5050$$

$$\sigma(A) = 924$$

$$V = (5560 \pm 920) + (5.21 \pm 0.51) \times 10^4 \left[ 1 - e^{-(2.93 \pm 0.18) \times 10^{-4} Z} \right] \text{ cm}^3 \text{ (STP)} \quad (\text{A5. 40})$$

Differentiation of this equation gives:

$$\frac{dV}{dZ} = 15.25 e^{-2.93 \times 10^{-4} Z} \frac{\text{cm}^3 \text{ (STP)}}{\text{MWHR}} \quad (\text{A5. 41})$$

The uncertainty in this quantity is given by:

$$\sigma^2 \left( \frac{dV}{dZ} \right) = [0.878(1 - 2.93 \times 10^{-4} Z)^2 + 2.23] \left( e^{-2.93 \times 10^{-4} Z} \right)^2 \quad (\text{A5. 42})$$

Values of  $G(\text{gas})$  and  $G^*(\text{gas})$  were calculated from the above quantities following procedures outlined in Appendix 5.4 and using Equation (4.41) for  $R_{\text{SW}}^{\text{TI}}$  and Equation (5.2) for  $C_{\text{omp}\phi_3}$ . The results obtained are tabulated in Table 5.12 of the main body.

## APPENDIX 5.12

MEASUREMENT TECHNIQUE FOR THE VISCOSITY AND  
DENSITY OF SANTOWAX OMP UP TO 800°F

## A5. 12. 1 Measurement of Viscosity

## A5. 12. 1A Introduction

The viscosity of Santowax OMP is determined by measuring efflux times in a semi-micro capillary viscometer of the Ostwald type. The viscometer is pressurized with nitrogen gas to prevent boiling of the organic. A molten nitrate salt bath is used as a constant temperature bath. In this appendix, the necessary equations for viscosity measurements over a range of temperatures are presented; the equipment used is described in some detail, and the results of the measurement of the viscosity of samples of unirradiated Santowax OMP are presented, including calibration of the viscometers. The data are used to test two relations for correlating viscosity with temperature changes.

A5. 12. 1B Basic Equations and Errors of Viscosity Measurements  
(A5. 8, A5. 9, A5. 10, A5. 11)

In this section are presented the basic equations of capillary flow viscometry and a discussion of the various errors which can occur. Extension of a low temperature calibration to higher temperatures is discussed.

Errors of Viscosity Measurements - The basic equation for viscosity measurements using laminar flow through a capillary tube is:

$$\nu = \frac{\mu}{\rho} = \left\{ \frac{\pi g h r^4 t}{8 l V} - \frac{m V}{8 \pi l t} \right\} B \quad (\text{A5. 43})$$

where

$\nu$  = kinematic viscosity, stokes

$\mu$  = dynamic viscosity, poises

$\rho$  = density, gms/cm<sup>3</sup>

$g$  = gravitational constant, cm per sec<sup>2</sup>

$h$  = fluid head, cm

$r$  = radius of capillary, cm

$t$  = efflux time, sec

$l$  = capillary length, cm

$m$  = kinetic energy coefficient

$V$  = efflux volume, cm<sup>3</sup>

$B$  = conversion factor, cm<sup>2</sup>/sec to stokes

In this equation, the first term on the right represents fully developed laminar flow in the capillary tube and the second term a kinetic energy correction due to contraction and expansion losses at the entrance and exit of the capillary. The various errors possible in measuring the viscosity will now be discussed.

**Kinetic Energy Correction** - In using Equation (A5. 43), the second term on the right has been neglected. To obtain an estimate of the error due to this effect, the ratio of the second term on the right to the first term will be estimated:

$$\text{Ratio} = \left( \frac{mV}{8\pi l t} \right) \bigg/ \frac{\pi g h r^4 t}{8l V} = \frac{mV}{\pi^2 g h} \frac{1}{t^2} \frac{V}{r^4} \quad (\text{A5. 44})$$

The ratio of  $V/r^4$  can be obtained from the calibration of the viscometer with water. From data presented in a later section of this appendix, a flow time of 531.5 seconds was measured for water at 25°C at which temperature the kinematic viscosity is 0.00896 cm<sup>2</sup>/sec. Also, the calibration measurements give a value of  $h_{V_{25}^{\text{std}}} d^2 = 7.02 \text{ cm}^3$  for a

liquid volume of 1.63 cm<sup>3</sup> where  $d$  is the diameter of the fluid reservoir at the bottom of the viscometer and  $h_{V_{25}^{\text{std}}}$  is the effective head of the liquid;  $d$  is approximately 0.8 cm so that  $h \cong 11.0$  cm and  $l$  is approximately 10 cm. Substituting these quantities into Equation (A5. 43) and neglecting the second term on the right gives:

$$0.00896 = \frac{\pi g h t}{8l} \frac{r^4}{V} = \frac{(\pi)(980)(11)(531.5)}{(8)(10.0)} \frac{r^4}{V}$$

or

$$\frac{r^4}{V} = 3.98 \times 10^{-8} \text{ cm}$$

Values of  $m$  from zero to slightly above one have been reported; a value of 1.00 will be used in the present case. The efflux volume of the viscometer is not known exactly but is believed to be less than  $0.5 \text{ cm}^3$ . For a conservative estimation,  $0.5 \text{ cm}^3$  will be used for  $V$ . Substituting these quantities into Equation (A5.44) gives the following result:

$$\text{Ratio} = \frac{(1)(0.5)}{(\pi)^2(980)(11.0)(3.98 \times 10^{-8}) t^2} = \frac{118}{t^2}$$

For a 0.5 per cent error or less,

$$\frac{118}{t^2} \leq 0.005 \quad \text{or} \quad t \geq 154 \text{ sec}$$

The smallest flow time observed in the viscosity measurements has been approximately 160 sec. for unirradiated organic at a temperature close to  $800^\circ\text{F}$ . Thus, the error introduced by neglecting the second term on the right of Equation (A5.43) is always less than 0.5 per cent. Generally, the error is much smaller than this since the flow times at the lower temperatures are considerably higher than 160 sec.

**Covette Correction** - As the fluid emerges from the capillary, it has a tendency to retain the shape of the capillary for a finite distance, resulting in an apparent increase in the length of the capillary. This effect is difficult to estimate but is believed to be negligible in the present case because of the small radius (approximately 0.15 mm) and relatively long length of the capillary. Also, the effect will be at least partially compensated since all viscosity measurements are made relative to water which is used for calibration of the viscometers.

**Drainage Errors** - Since the measurements are based on calibration of the viscometers with water, errors may arise from

the fact that not all liquids drain from a surface with equal ease. Barr (A5. 8) reports that this error is generally small and can be safely neglected.

Surface Tension - Surface tension can lead to a change in the effective head in improperly designed viscometers and result in an error in measurements made relative to a calibrating fluid. The change in effective head can be written as:

$$\Delta h = \frac{2}{g} \left[ \frac{1}{r_1} - \frac{1}{r_2} \right] \left[ \frac{\sigma_1}{\rho_1} - \frac{\sigma_2}{\rho_2} \right] \quad (\text{A5. 45})$$

where

$\Delta h$  = change in effective head, cm

$r_1$  = radius of efflux bulb, cm

$r_2$  = radius of lower reservoir, cm

$\sigma_1$  = surface tension of calibrating liquid, gm/sec<sup>2</sup>

$\sigma_2$  = surface tension of test liquid, gm/sec<sup>2</sup>

$\rho_1$  = density of calibrating liquid, gm/cm<sup>3</sup>

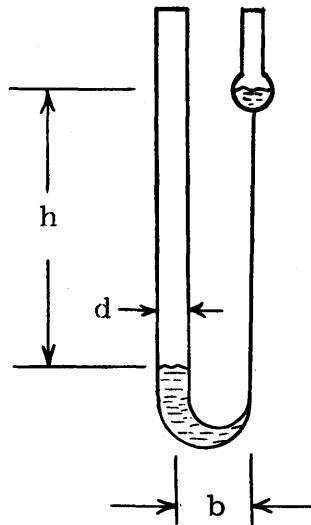
$\rho_2$  = density of test liquid, gm/cm<sup>3</sup>

This error is thus zero if either  $r_1 = r_2$  or  $\sigma_1/\rho_1 = \sigma_2/\rho_2$ . Generally, viscometers should be designed so that  $r_1 = r_2$  and the effect can be neglected, regardless of the surface tension of the materials. For the viscometers used in this experiment, the exact radius of the efflux bulb which is spherical in shape is not known. However, it appears that the radius,  $r_1$ , is somewhat less than the radius,  $r_2$ . For a rough and conservative estimation of this effect, it will be assumed that  $r_1 = \frac{1}{2} r_2$  where  $r_2 = 0.4$  cm. The surface tension of water at 25°C is 72 gm/sec<sup>2</sup> and the density is 0.9971 gm/cm<sup>3</sup>. For the organic, it will be assumed that the surface tension is the same as that of benzene or toluene at 20°C or 28.5 gm/sec<sup>2</sup> (A5. 12). An organic density of 0.85 gm/cm<sup>3</sup> will be assumed. Hence,

$$\Delta h = \frac{2}{980} \left[ \frac{1}{0.2} - \frac{1}{0.4} \right] \left[ \frac{72}{0.997} - \frac{28.5}{0.85} \right] = 0.2 \text{ cm}$$

This is approximately 2 per cent of the total fluid head of 11.0 cm.

Non-Vertical Alignment - Consider the sketch below.



If the viscometer makes an angle,  $\alpha$ , with the vertical, the relative error of the hydrostatic pressure amounts to

$$\frac{h-h'}{h} = (1 - \cos \alpha) + \frac{b}{h} \sin \alpha \quad (\text{A5.46})$$

where  $h'$  = the effective value of the fluid head. With proper procedure, this error is negligible. When inserting a viscometer in the salt bath, vertical alignment was made by means of plumb bobs suspended in front of the two windows of the bath. These windows are  $90^\circ$  apart in the horizontal plane. It is believed that the maximum alignment error,  $\alpha$ , would be  $1^\circ$ . For this angle and using  $h = 11.0$  cm and  $b = 2$  cm,

$$\frac{h-h'}{h} = (1 - 0.99985) + \left( \frac{2}{11.0} \right) (0.01745) = 0.00333$$

Hence, the maximum error introduced due to non-vertical alignment is believed to be 0.3 per cent.



Non-Newtonian Behavior - Equation (A5. 43) is based on the assumption of Newtonian behavior of the fluid; that is, that the shear stress,  $\tau$ , is a linear function of the rate of shear,  $D$ . This assumption can be expressed as:

$$\tau = \mu D \frac{\text{gmf}}{\text{cm}^2}$$

$$D = \frac{\partial v}{\partial r} \text{ sec}^{-1}$$
(A5. 47)

where  $v$  is velocity, cm/sec. The viscosity coefficient,  $\mu$ , is a constant. For a Newtonian fluid, the same value of viscosity is determined regardless of size of the capillary or the flow rate of the fluid (as long as laminar flow occurs and the end effects do not become appreciable). For a non-Newtonian fluid,  $\tau$ , is not a linear function of  $D$  and additional factors must be considered to describe the flow in addition to or in place of  $\mu$ .

In the present case, indications are that Santowax OMP behaves as a Newtonian fluid. Burns, et al, (A5. 13), report measurements on p-terphenyl, Santowax R, and irradiated organics using an open-ended viscometer near the melting point to avoid vaporization. The shear rate in these measurements was varied by using different nitrogen pressures to change the effective head of the fluid. The measured viscosity was found to be independent of the rate of shear over the range of  $5.42 \times 10^2 \text{ sec}^{-1}$  to  $6.80 \times 10^3 \text{ sec}^{-1}$ . If desired, the Newtonian behavior of the irradiated material in the present case can be checked at higher temperatures since the pressurizing system has been set up so a differential pressure can be put across the viscometer to increase the effective head.

Non-Parabolic Flow in Both Ends of the Capillary - This effect should be negligible for the small radius capillary and large capillary length used in the present experiment.

Measurement of Efflux Time and Variation of Temperature in Temperature Bath - The timer used for measuring efflux times is accurate and readable to 0.1 seconds. The variation of temperature in both the calibrating water bath (25.0°C) and salt bath is sufficiently

small so that flow times reproducible within 0.5 per cent are routinely observed.

**Volume Expansion of Liquid and of Glass** - A correction must be applied for the expansion of the liquid as the temperature is increased during a measurement. Analysis of the effect of expansion of the glass with temperature indicates that this effect is negligible up to 800°F. The effect of these factors on the viscometer coefficient are considered in some detail in the following section.

#### A5. 12. 1C Viscometer Coefficient for Viscosity Measurement of Santowax OMP at Temperatures from 400 to 800 °F

The viscometers used for measurement of the viscosity of Santowax OMP have been calibrated with water at 25°C. Since the viscosity measurements on the organic materials are made at temperatures varying from 400 to 800°F, with a constant mass of sample, a correction must be applied to the viscometer coefficient for volumetric expansion of the liquid and may be necessary for volumetric expansion of the glass. This section evaluates these corrections.

Neglecting the kinetic energy correction, Equation (A5. 43) can be written as

$$\frac{\mu}{\rho} = Ct \quad (\text{A5. 48})$$

where

$$C = \text{viscometer coefficient} = \frac{\pi h g r^4}{8 l V} \quad (\text{A5. 49})$$

The following definitions for the various coefficient will be used.

$C_{V_{25}^{\text{std}}}$  = coefficient determined with water as a standard at 25°C when the viscometer contains  $V_{25}^{\text{std}} \text{ cm}^3$  of water.

$C_{V_T}$  = coefficient for an organic volume  $V_T \text{ cm}^3$  at a temperature, T°F.  $V_T$  is calculated from the organic mass and the density of the organic at T°F.

Application of Equation (A5. 49) gives:

$$\frac{C_{V_T}}{C_{V_{25}^{std}}} = \frac{h_T}{h_{V_{25}^{std}}} \frac{\ell_{25}}{\ell_T} \frac{V_{25}^{std}}{V_T} \left( \frac{r_T}{r_{25}} \right)^4 \quad (\text{A5. 50})$$

Letting  $e$  = the linear coefficient of expansion of glass,  $^{\circ}\text{C}^{-1}$ ,

$$\begin{aligned} r_T &= r_{25} [1 + e(T-25)] \\ \ell_T &= \ell_{25} [1 + e(T-25)] \\ V_T &\cong V_{25} [1 + 3e(T-25)] \end{aligned} \quad (\text{A5. 51})$$

The effective head,  $h$ , will be changed by volume changes due to the volumetric expansion of both the liquid and the glass. Furthermore, an additional increase in the effective head results from the increase in length of the viscometer due to expansion of the glass. These changes can be written as follows:

$$\frac{h_T}{h_{V_{25}^{std}}} = \frac{h_{25}^{std} + \Delta h_T}{h_{V_{25}^{std}}} = 1 + \frac{\Delta h_T}{h_{V_{25}^{std}}} \quad (\text{A5. 52})$$

where  $\Delta h_T$  is the change in the effective head in going from a temperature of  $25^{\circ}\text{C}$  and standard volume at  $25^{\circ}\text{C}$  to a temperature,  $T$ , and volume,  $V_T$ , determined from the mass and density of the sample. Now, letting  $d$  = the effective diameter of the reservoir, the following approximation can be derived:

$$\frac{h_T}{h_{V_{25}^{std}}} = 1 - \frac{V_T [1 - 3e(T-25)] - V_{25}^{std}}{\frac{\pi}{4} h_{V_{25}^{std}} d_{25}^2 [1 + 2e(T-25)]} + e(T-25) \quad (\text{A5. 53})$$

Substitution of Equations (A5. 51), (A5. 52), and (A5. 53) into (A5. 50) and simplification results in:

$$C_{V_T} \cong C_{V_{25}^{std}} \left\{ 1 + e(T-25) - \frac{[1 - 3e(T-25)] V_T - V_{25}^{std}}{0.787 h_{V_{25}^{std}} d_{25}^2 [1 + 2e(T-25)]} \right\} \quad (A5. 54)$$

If the thermal expansion of glass can be neglected, this relation simplifies to:

$$C_{V_T} = C_{V_{25}^{std}} \left\{ 1 - \frac{V_T - V_{25}^{std}}{0.787 h_{V_{25}^{std}} d_{25}^2} \right\} \quad (A5. 55)$$

In the range of temperature considered here, the glass expansion can be neglected. For example, using a value of  $e$  of  $0.036 \times 10^{-4} \text{ } ^\circ\text{C}^{-1}$ ,  $V_T = 2.00 \text{ cm}^3$ ,  $V_{25}^{std} = 1.00 \text{ cm}^3$ ,  $h_{V_{25}^{std}} d_{25}^2 = 7.00 \text{ cm}^3$  and  $T = 800^\circ\text{F} = 427^\circ\text{C}$ .

$$C_{V_T} = 0.8189 C_{V_{25}^{std}} \quad \text{without correction}$$

% difference = 0.4%

$$C_{V_T} = 0.8225 C_{V_{25}^{std}} \quad \text{with correction}$$

An additional error can result from a change in the liquid head due to vaporization of the organic material. This effect will be apparent only at the higher temperatures where the vapor pressure of Santowax OMP is appreciable. The magnitude of the change can be obtained by estimating the change in  $V_T$  due to vaporization of the organic. At  $800^\circ\text{F}$  ( $427^\circ\text{C}$ ),

$$\rho = 0.780 \text{ gms/cm}^3$$

$$V_T = 2.00 \text{ cm}^3$$

Vapor pressure  $\cong 2100 \text{ mm Hg}$

Height of vapor space  $\cong 25 \text{ cm}$

Diameter of reservoir  $\cong 0.8 \text{ cm}$

$$M. W. = 230$$

$$V_{25}^{\text{std}} = 1.00 \text{ cm}^3$$

Applying the ideal gas law,

$$n = \frac{PV}{RT} = \frac{(2.10)[(\pi/4)(0.8)^2(25)]}{(62.36)(700)} = 6.04 \times 10^{-4} \text{ gm-moles}$$

$$\text{Grams of organic vaporized} = (6.04 \times 10^{-4})(230) = 0.1388$$

$$\text{Total gms of organic in viscometer} = 1.56$$

Calculating  $C_{V_T}$  at 800°F using 1.56 gms and 1.42 gms, respectively, gives:

$$\begin{aligned} C_{V_T, 1.56} &= 0.8189 \\ C_{V_T, 1.42} &= 0.8512 \end{aligned} \quad \% \text{ difference} = 3.8\%$$

Hence, at the higher temperatures, the viscosity measured, assuming no loss of liquid due to vaporization, can be low by as much as 4 per cent. At temperatures below 600°F, this error should be considerably less than one per cent as the vapor pressure of Santowax OMP drops to approximately 275 mm Hg at this temperature. It should be noted that condensation of organic on the walls of the viscometer, the droplets of which generally hang to the side, can result in an error. It is generally more desirable to start at the lowest temperature and go up, rather than start at the highest temperature and go down, when doing a viscosity measurement.

#### A5.12.1D Equipment and Experimental Procedures

The capillary viscometers used in these experiments were size No. 25 Cannon-Manning semi-micro viscometers of the Ostwald type, rated for a range of 0.3 to 1.6 centistokes.<sup>(1)</sup> The viscometers, as

---

<sup>(1)</sup> Cannon Instrument Company, Box 812, State College, Pennsylvania.

received, were lengthened by the addition of glass tubing of the same size as that of the viscometer to each leg of the viscometer to facilitate immersion in the salt bath. In Figure A5. 4, a photograph of the viscometer used is presented. The tubing used for lengthening the viscometer was selected so as to fit 1/4-inch and 1/2-inch Swagelok fittings, respectively; Teflon ferrules were used with these fittings for connecting the viscometer to the pressurizing system.

A molten salt bath was used as a constant temperature medium for the measurements. The bath used is eutectic mixture, melting at 120°C and usable up to 450°C. The mixture is

53%  $\text{KNO}_3$

7%  $\text{NaNO}_3$

40%  $\text{NaNO}_2$

A "Simply-Trol" proportional temperature<sup>(1)</sup> controller with a range of 0 to 1000°F and calibrated for an Iron-Constantan Thermocouple sensing element was used for controlling the bath temperature to  $\pm 1$  to 2°F. Figure A5. 5 is a schematic sketch of the salt bath and Figure A5. 6, a photograph of the actual salt bath.<sup>(2)</sup>

Since the maximum temperatures to be used are above the boiling temperature of the organic materials at room temperature, it is necessary to pressurize the viscometer. In the present case, provision was also made for varying the shear rate of the viscosity measurement by putting a differential nitrogen pressure across the viscometer in addition to the normal liquid head. Figure A5. 7 is a sketch of the pressurizing system, where it can be seen that provision is also made for evacuating the viscometer and pycnometer (for density measurements) preparatory to pressurizing to remove oxygen which might lead to chemical changes in the organic material

---

(1) Assembly Products, Inc., Chesterland, Ohio.

(2) Safety precautions must be taken when molten nitrate salt baths are used as the nitrates are spontaneously explosive if handled improperly.

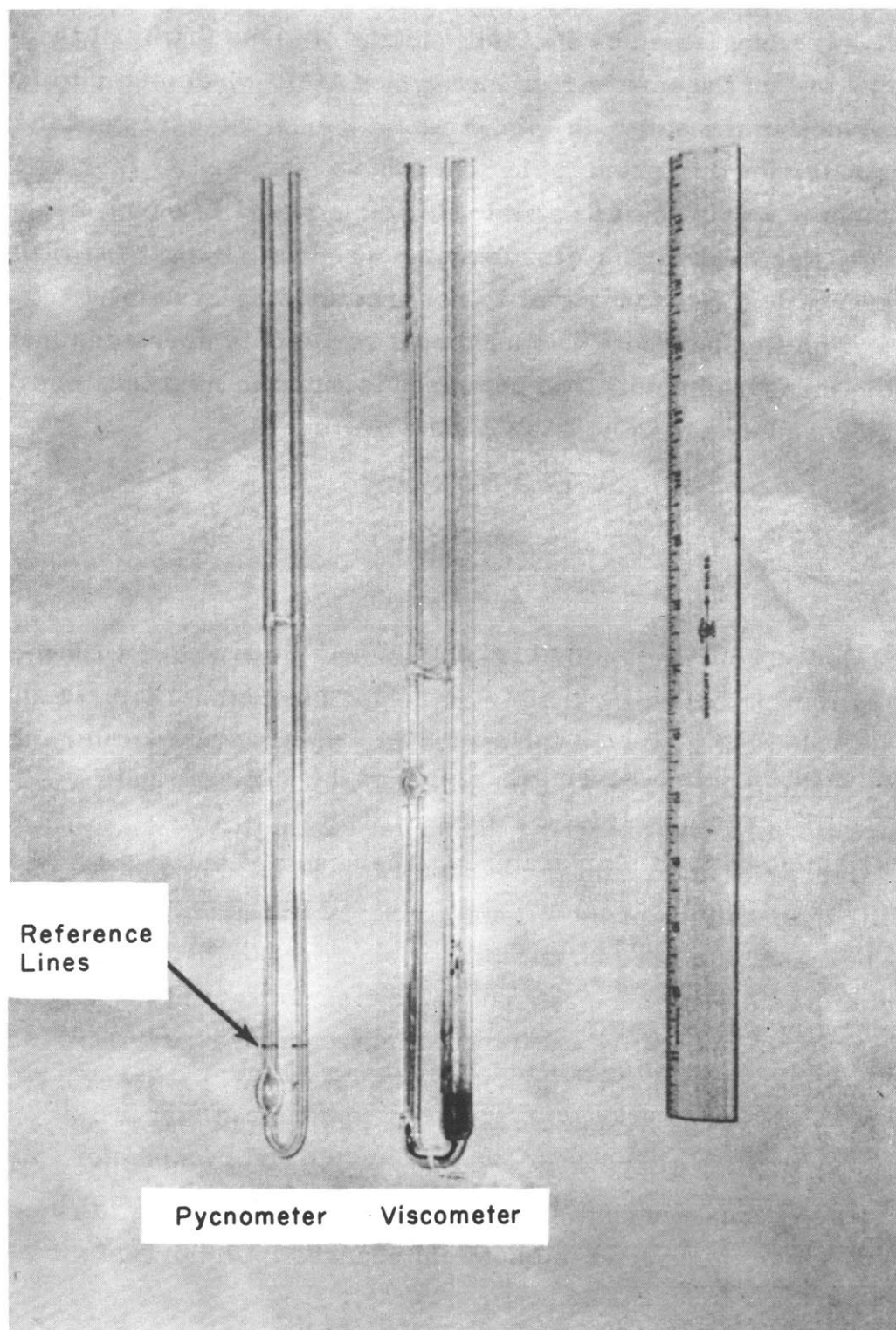


FIG. A5.4 PHOTOGRAPH OF VISCOMETER AND PYCNOMETER USED FOR VISCOSITY AND DENSITY MEASUREMENTS OF SANTOWAX OMP

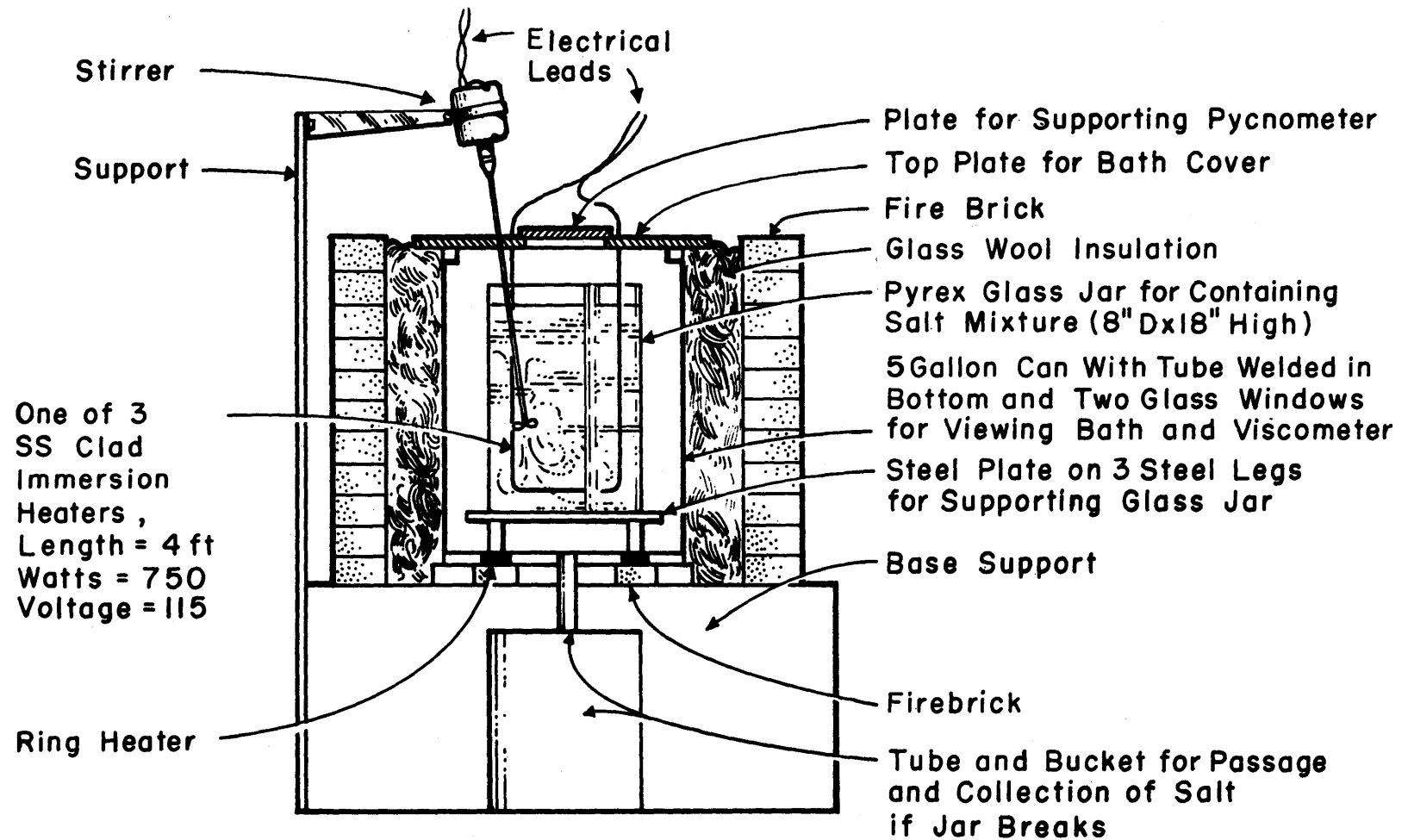


FIG. A5.5 SCHEMATIC OF SALT BATH



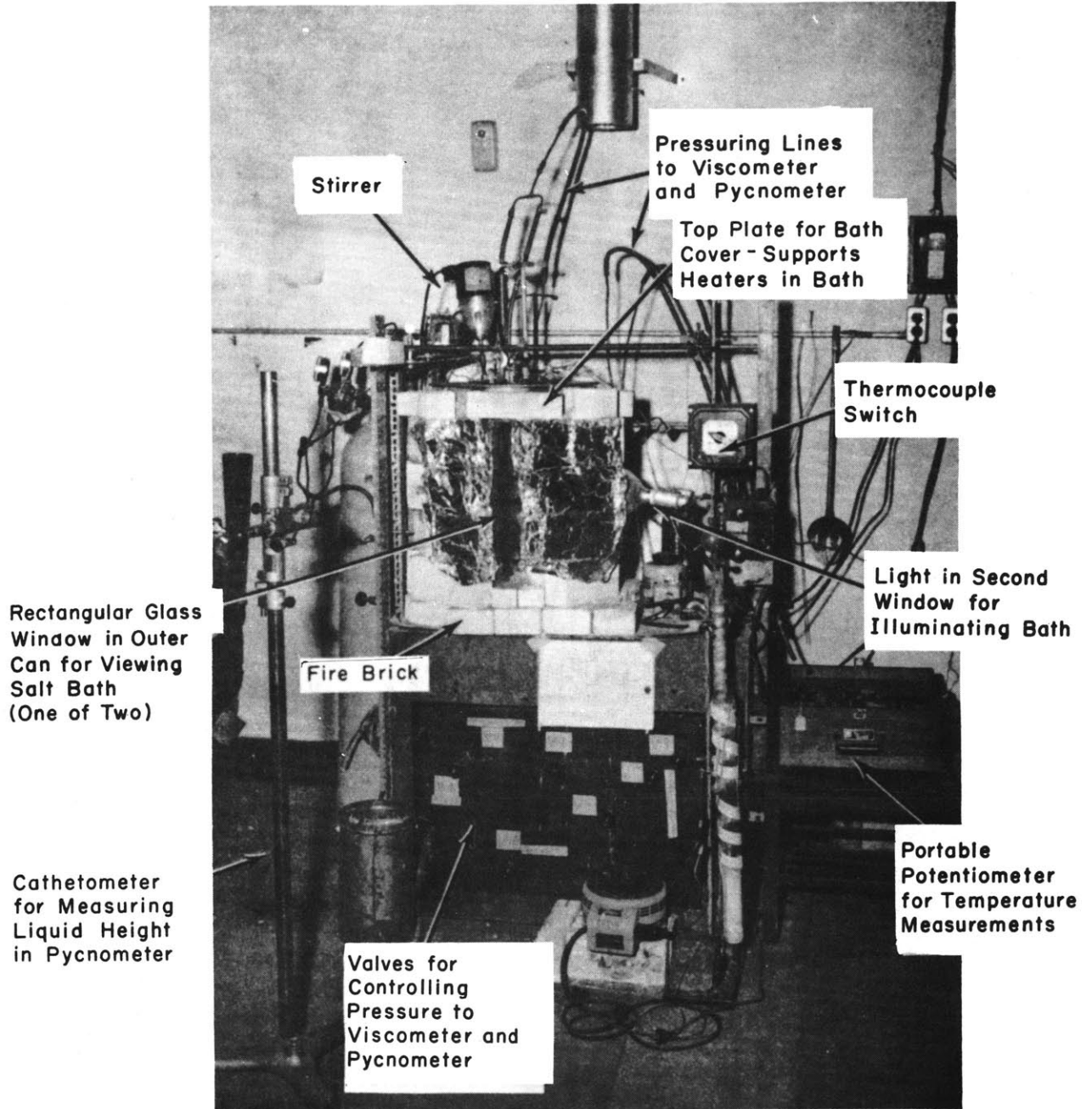


FIG. A5.6 PHOTOGRAPH OF MOLTEN SALT BATH FOR DENSITY AND VISCOSITY MEASUREMENTS

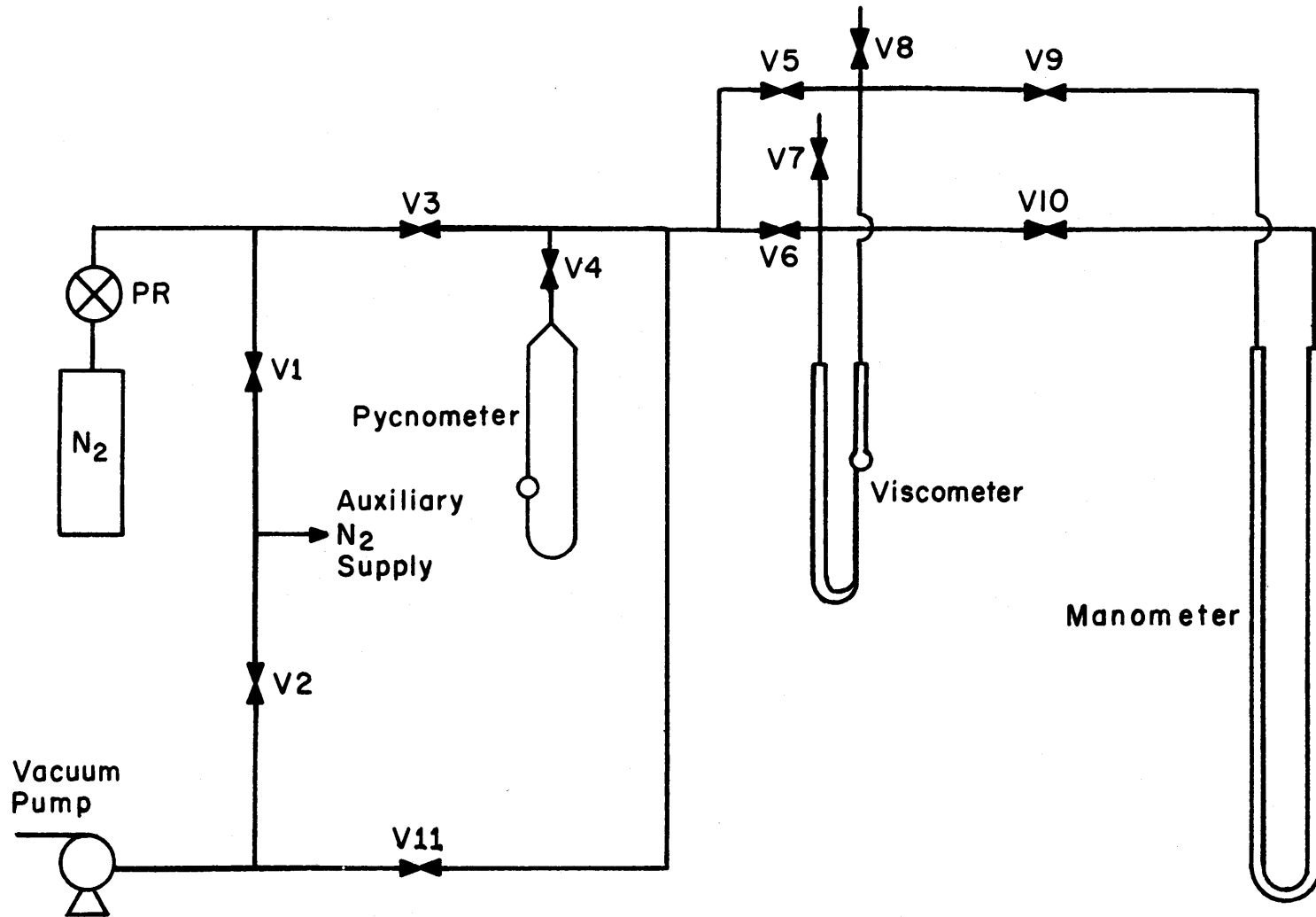


FIG. A5.7 SCHEMATIC OF PRESSURE AND EVACUATING SYSTEM FOR DENSITY AND VISCOSITY MEASUREMENT

during the measurement.

It should be noted that for viscometers with the small capillary used here, it is absolutely necessary to filter all liquids added to the viscometer through a sintered glass filter to prevent plugging of the capillary (a coarse-grade filter is satisfactory).

#### A5.12.1E Sample Experimental Results

In this section, the results for two preliminary viscosity measurements performed in checking out the measurement techniques are presented to illustrate the procedure used in measuring the viscosities. The measurements were performed on random batches of Santowax OMP and is not the same material used to charge the loop for this first experiment. Viscometer A140 used in obtaining the results presented for the first measurement and viscometer A138 used for the second measurement were calibrated at 25°C with water. The flowtime was measured with several different volumes of water and the data used to obtain  $h_{V_{25}^{std}} d_{25}^2$  for these viscometers. From Equation (A5.55), it is seen that a plot of  $C_{V_{25}^{std}}$  vs.  $(V_{25} - V_{V_{25}^{std}})$  should be a straight line with an intercept of  $C_{V_{25}^{std}}$  and slope of

$$-\frac{C_{V_{25}^{std}}}{0.787 h_{V_{25}^{std}} d_{25}^2}$$

Sample results for three water volumes for viscometer A140 are presented in Table A5.17 and the complete results for both viscometers are given in Figure A5.8. The calibration was repeated before and after the viscosity measurements with viscometer A140. As can be seen from Figure A5.8, a linear relationship is indeed obtained with only a slight difference between the calibrations for A140 made before and after the measurement. The constants obtained were:

$$V_{25}^{std} = \text{assumed value of } 1.6385 \text{ cm}^3 \text{ for A140 and A138.}$$

$$C_{V_{25}^{std}} = 1.526 \times 10^{-3} \text{ cp cm}^3 / \text{gm-sec for A140.}$$

Table A5. 17. Sample Calibration Runs for Viscometer A140.

Temperature = 25. 0°C

$$\mu_{25}^{\text{H}_2\text{O}} = 0. 8937 \text{ cp (A5. 12)}$$

$$\rho_{25}^{\text{H}_2\text{O}} = 0. 99707 \text{ (A5. 12)}$$

$$V_{25}^{\text{std}} = \text{assumed value of } 1. 6385 \text{ cm}^3$$

Wt. H <sub>2</sub> O grams	Volume H <sub>2</sub> O cm <sup>3</sup>	Flowtime, seconds	$\frac{1}{t} \frac{\mu}{\rho} = C V_{25}$ $\frac{\text{cp cm}^3}{\text{gm-sec}}$	$V_{25} - V_{25}^{\text{std}}$ cm <sup>3</sup>
1. 0572	1. 0603	531. 5 531. 9 531. 4 531. 1 531. 5 Avg. = 531. 5	$1. 686 \times 10^{-3}$	-0. 5782
1. 3341	1. 3380	554. 1 553. 8 554. 4 553. 7 Avg. = 554. 0	$1. 618 \times 10^{-3}$	-0. 3005
1. 6337	1. 6385	586. 5 587. 8 587. 7 586. 9 Avg. = 587. 2	$1. 526 \times 10^{-3}$	0. 0000

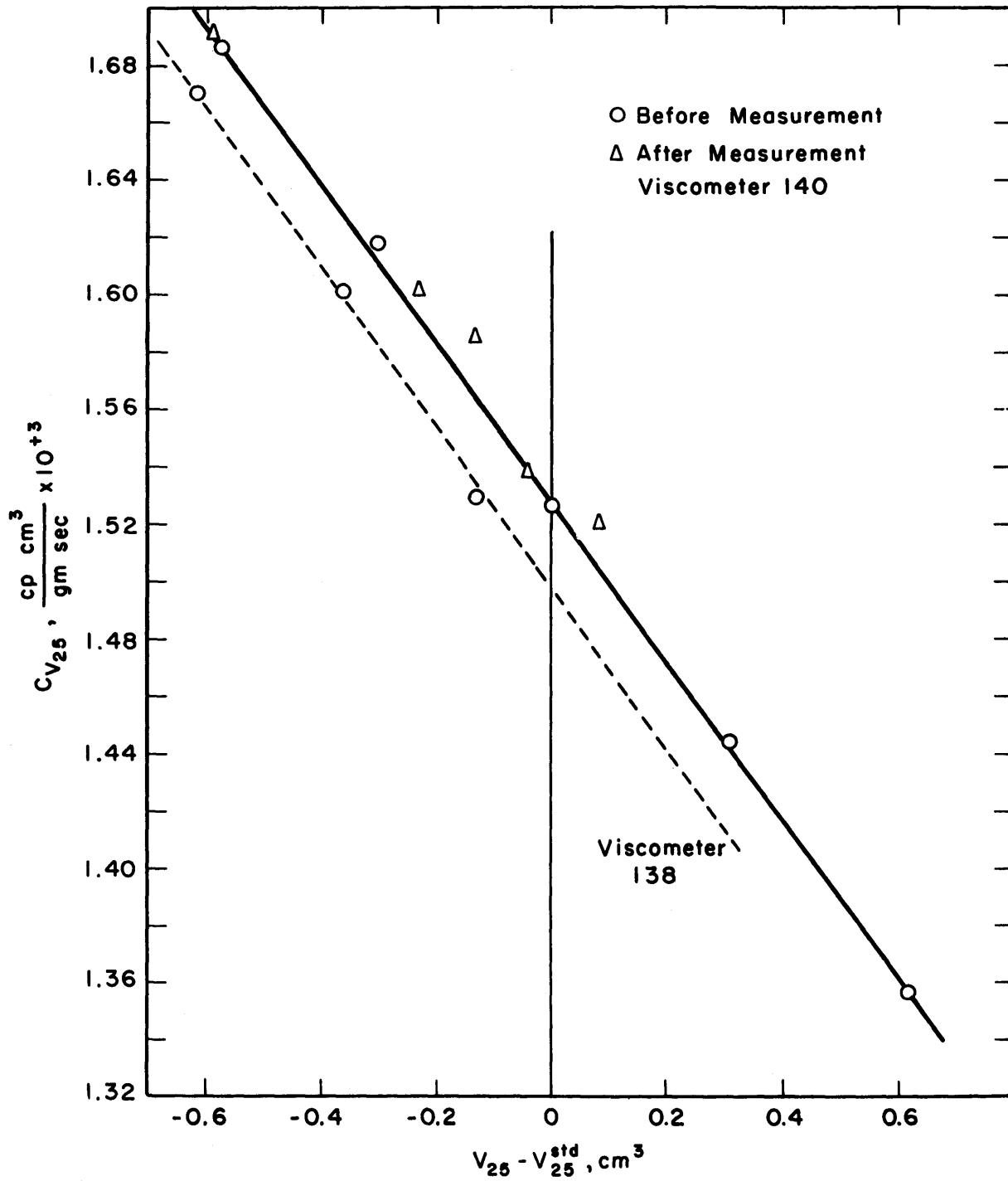


FIG. A5.8 VARIATION OF VISCOMETER CONSTANT WITH VOLUME OF LIQUID IN VISCOMETER

$$C_{V_{25}^{\text{std}}} = 1.497 \times 10^{-3} \text{ cp cm}^3/\text{gm-sec for A138}$$

$$h_{V_{25}^{\text{std}}} d_{25}^2 = 7.02 \text{ cm}^3 \text{ for A140 and A138}$$

Sample results obtained for the viscosity of Santowax OMP are presented in Table A5. 18 for viscometer A140. The density values used were calculated from Equation (A5. 62) based on the density measurements reported in section A5. 12. 2. The variation of viscosity with temperature has been the subject of various studies, a summary of which is given in reference (A5. 11). Generally, it has been found that the experimental data can be described by equations of the following type:

$$\mu = \mu_0 e^{\beta/T} \quad (\text{A5. 56})$$

$$\mu = \mu_0 v^{-1/3} e^{\beta/vT} \quad (\text{A5. 57})$$

where

$v$  = specific volume of the fluid.

The data from both viscometers are plotted on the basis of these two equations in Figures A5. 9 and A5. 10, where it can be seen that Equation (A5. 57) appears to agree with the experimental data slightly better than Equation (A5. 56). The agreement with Equation (A5. 56) is satisfactory, however, and has been used in presenting the data for irradiated Santowax OMP, since it is a simpler relation. There is a slight difference between the two viscosity measurements, but this is probably due to concentration differences in the two Santowax OMP samples. For comparison, data of Bates, *et al*, (A5. 14), for Santowax R are presented on Figure A5. 9.

Table A5. 18. Sample Results of Viscosity Measurement on Santowax OMP

Wt. of sample = 1. 1284 grams

Nitrogen pressure = 30 psig

 $v$  = specific volume of organic,  $\text{cm}^3/\text{gm}$ 

Corrected Temperature, °F			Density, $\text{gm}/\text{cm}^3$	Flow time, sec.	$C_{VT}$ $\frac{\text{cp cm}^3}{\text{gm sec}}$	$\frac{\mu}{\rho}$ $\frac{\text{cp cm}^3}{\text{gm}}$	$\mu$ cp	$\mu v^{1/3}$ $\frac{\text{cp cm}}{\text{gm}^{1/3}}$
Top	Middle	Bottom						
434	434	432	0. 939	457. 3 456. 9 457. 7 Avg. = 457. 3	$1. 647 \times 10^{-3}$	0. 753	0. 706	0. 721
577	578	577	0. 874	278. 2 278. 3 278. 6 Avg. = 278. 4	$1. 594 \times 10^{-3}$	0. 444	0. 388	0. 406
778	779	779	0. 781	169. 4 168. 7 168. 7 Avg. = 168. 9	$1. 551 \times 10^{-3}$	0. 262	0. 204	0. 222

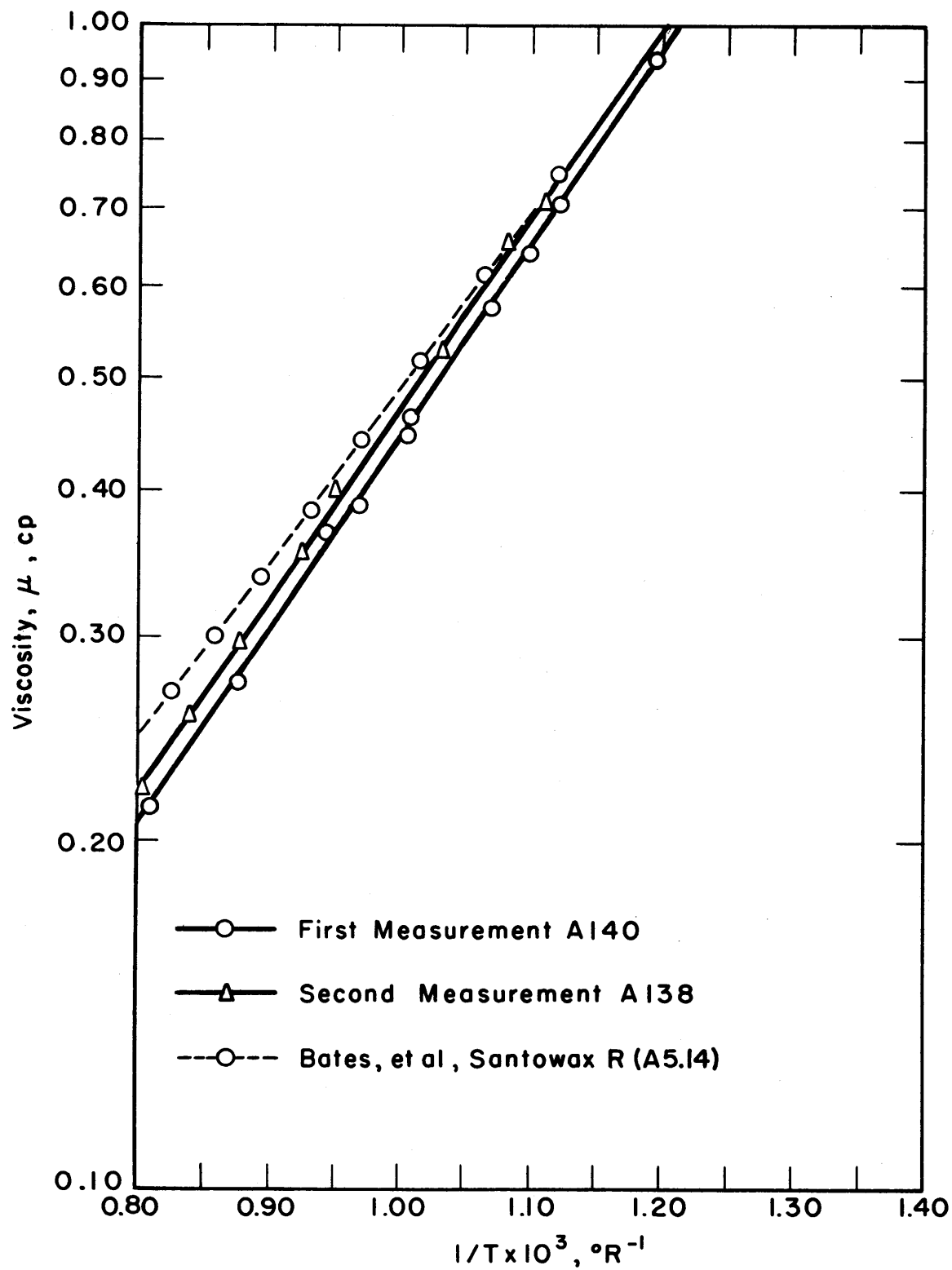


FIG. A5.9 VARIATION OF VISCOSITY WITH  $1/T$  ON SEMI-LOG PLOT



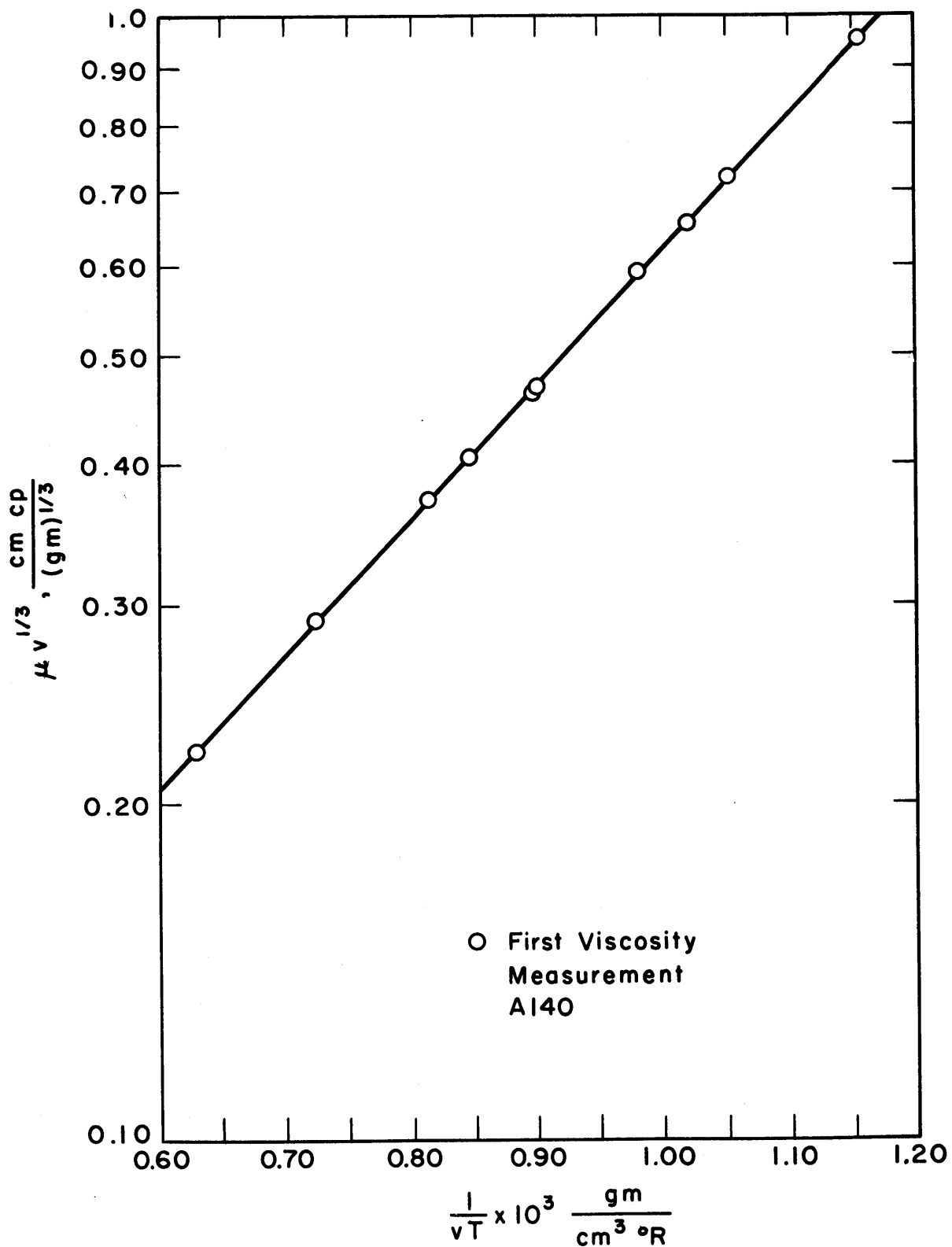


FIG. A 5.10 VARIATION OF  $\mu v^{1/3}$  WITH  $\frac{1}{vT}$  ON SEMI-LOG PLOT

## A5.12.2 Measurement of Density of Santowax OMP Up to 800°F

## A5.12.2A Method of Measurement

The density of Santowax OMP up to 800°F is measured by using a pycnometer in which the volume of a known mass of the organic is determined by measuring the liquid height in two capillary tubes connected to a small reservoir of fluid. In Figure A5.4, a photograph of the pycnometer is presented. The specifications for the pycnometers have been selected so as to accurately cover a density range of approximately 0.75 - 1.00 gm/cm<sup>3</sup> with an organic loading of  $1.0 \pm 0.1$  cm<sup>3</sup>; the specifications are:

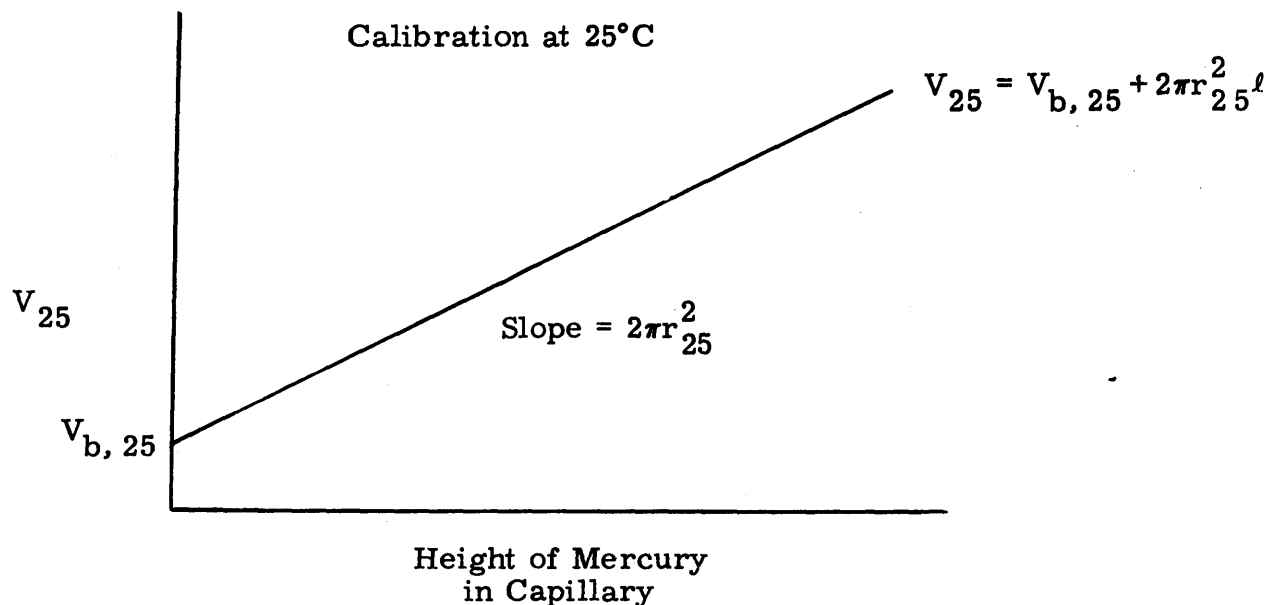
Volume of bulb at bottom to be filled with organic material slightly above melting point (~300°F)	$1.0 \pm 0.1$ cm <sup>3</sup>
Capillary size	$1.25 \pm 0.05$ mm
Length, red reference marks to top of tubing (the top 2 inches of the tubing is not normally used in the measurement).	36 cm

The pycnometers were made by a commercial glass blower.

During a measurement, the pycnometer is suspended in the same constant temperature bath as used for the viscosity measurements and is pressurized with nitrogen as described in the previous section on viscosity. The height in the capillary tube at any level is measured using a cathetometer readable to 0.05 mm. The volume of the pycnometer is calibrated by inserting incremental quantities of mercury by means of a hypodermic syringe fitted with a 25 cm length stainless steel needle, weighing to determine the mass of mercury added, and measuring the height of the mercury after each addition. The pycnometer is suspended in a 25.0°C water bath during the calibration. The results obtained during checkout of the measurement technique will now be presented to illustrate the procedure used in measuring densities.

## A5. 12. 2B Calibration of Pycnometers

As described in A4. 12. 2A, the pycnometer is calibrated using mercury at 25°C. At 25°C, then, the calibration curve is illustrated in the sketch below:



where

$V_{25}$  = total volume at 25°C for a specific level in the pycnometer legs relative to the reference line.

$V_{b, 25}$  = total volume below reference mark at 25°C.

$r_{25}$  = radius of each capillary.

$l$  = distance from reference mark to liquid level.

Since density measurements are to be made up to 800°F, the effect of temperature changes on this calibration will now be considered. Letting  $e$  = the linear coefficient of expansion of glass, °C<sup>-1</sup>, the bulb volume below the reference mark at any temperature,  $V_{b, T}$ , can be written as

$$V_{b, T} \cong V_{b, 25}(1 + 3e(T-25)) \quad (\text{A5. 58})$$

For the section above the reference line, the height,  $l$ , is a measured quantity and fixed. The radius will change, however, with temperature:

$$r_T = r_{25} [1 + e(T-25)] \quad (\text{A5. 59})$$

Now, letting  $V_T$  = the total volume of the pycnometer at a level,  $l$ , above the reference line,

$$V_T = V_{b, 25} [1 + 3e(T-25)] + 2l\pi r_{25}^2 [1 + 2e(T-25)] \quad (\text{A5. 60})$$

Rewriting gives:

$$V_T = V_{25} + e(T-25)[3V_{b, 25} + 4l\pi r_{25}^2] \quad (\text{A5. 61})$$

$$V_{25} = V_{b, 25} + 2l\pi r_{25}^2$$

The magnitude of the temperature effect can be seen by substituting the following typical values:

$$V_{b, 25} = 1.00 \text{ cm}^3$$

$$l = 20 \text{ cm}$$

$$2\pi r_{25}^2 = 0.0250 \text{ cm}^2$$

$$T = 800^\circ\text{F} = 427^\circ\text{C}$$

$$e = 0.036 \times 10^{-4} / ^\circ\text{C}$$

Substitution gives

$$\begin{aligned} V_T &= 1.50 + (0.036 \times 10^{-4})(402)[(3)(1.00) + (2)(20)(0.0250)] \\ &= 1.50 \text{ cm}^3 + 0.00579 \text{ cm}^3 \end{aligned}$$

Hence, at the maximum temperature to be encountered, the temperature correction is only 0.6 per cent and can be neglected so that the calibration prepared at  $25^\circ\text{C}$  can be used for all temperatures. The error due to vaporization of the organic will be small due to the small volume of the capillary tubes.

Calibration measurements have been made on two types of pycnometers, one having a relatively large diameter bore and one having the

specifications listed in the preceding section which is now used for density measurements in order to get a larger increase in liquid height with temperature. The results for the former pycnometer (large bore) are presented in Table A5. 19 and the results for both pycnometers are plotted in Figure A5. 11.

#### A5. 12. 2C Density Measurement

The results of one density measurement on Santowax OMP are presented in Table A5. 20 and Figure A5. 12. The data are represented by the equation:

$$\rho = 1.138 - 4.58 \times 10^{-4}T \quad (\text{A5. 62})$$

where T is in °F and  $\rho$  in gm/cm<sup>3</sup>.

Table A5. 19. Calibration of Large Capillary Pycnometer for Density Determinations  
Reported in Section A5. 12. 2C.

Distance, top meniscus to top red line		Position, cm						Total gms of Hg added	Total volume at 25. 0°C $\rho_{25} = 13. 5336$
		Bulb Side			Other Side				
Bulb	Other	Top of red line	Top of meniscus	End of meniscus	Top of red line	Top of meniscus	End of meniscus		
-0. 165	-0. 055	91. 240	91. 075	91. 050	91. 230	91. 175	91. 140	20. 0497	1. 4815
+0. 340	+0. 490	91. 205	91. 545	91. 520	91. 170	91. 660	91. 610	20. 5318	1. 5171
+1. 720	+1. 905	91. 525	93. 245	93. 225	91. 485	93. 390	93. 355	21. 8023	1. 6110
+3. 735	+3. 920	91. 525	95. 260	95. 235	91. 490	95. 410	95. 385	23. 6398	1. 7474
+6. 990	+7. 030	92. 300	99. 290	99. 265	92. 280	99. 310	99. 280	26. 5565	1. 9623

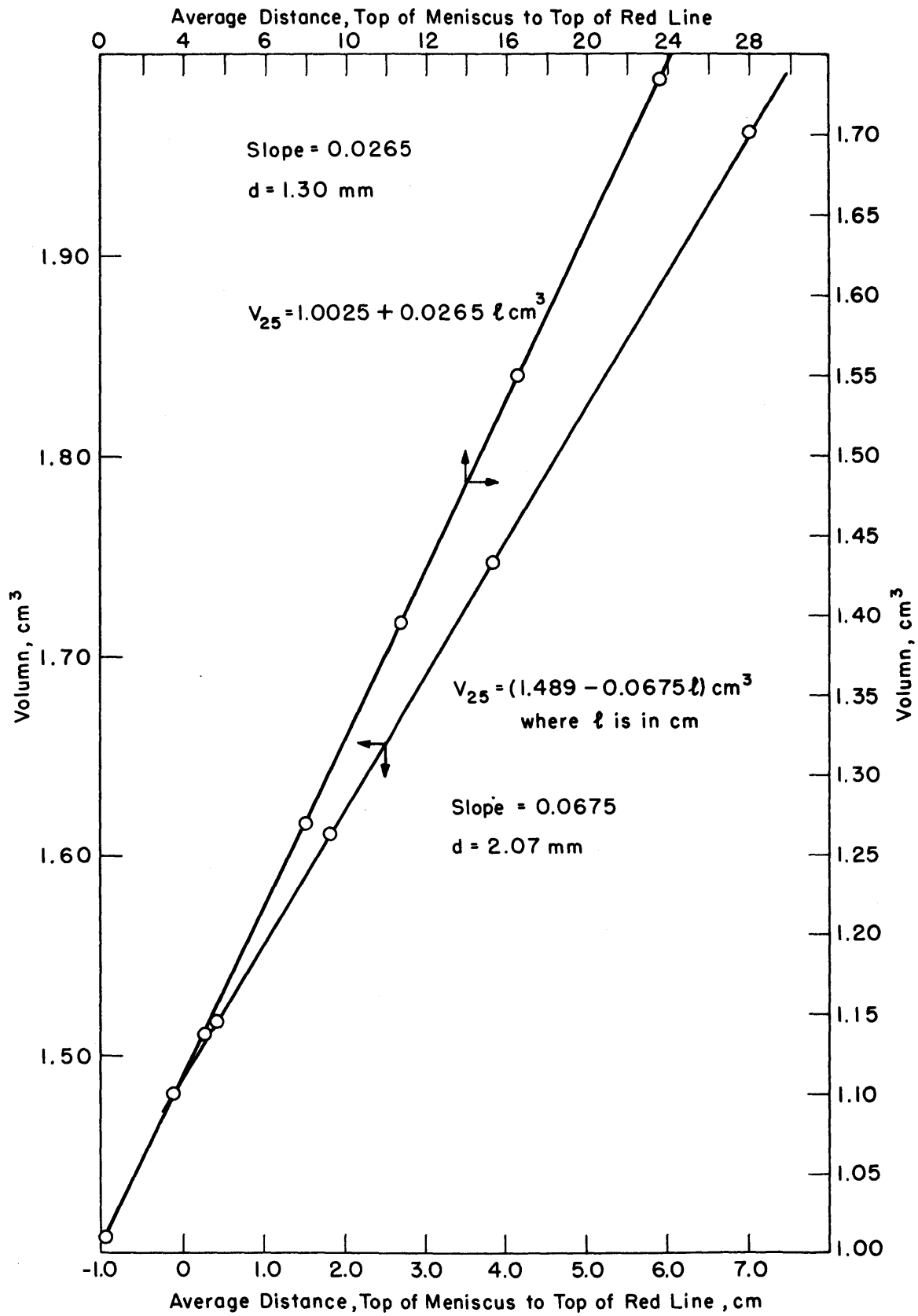


FIG. A5.II CALIBRATION OF PYCNOMETERS

Table A5. 20. Density Measurement of Santowax OMP, Large Capillary Pycnometer,  
Sample Mass = 1. 425 grams.

Corrected Temp., °F			Height of Liquid, cm				Differential Height, cm		Vol. of Organic cm <sup>3</sup>	Density gms/cm <sup>3</sup>
			Bulb Leg		Other Leg					
Upper	Middle	Lower	Red Line	Liquid	Red Line	Liquid	Bulb	Other		
373	373	372	75. 945	75. 765	75. 925	75. 805	-0. 180	-0. 120	1. 479	0. 9635
442	442	440	75. 945	76. 355	75. 925	76. 405	+0. 410	+0. 480	1. 519	0. 9381
522	522	521	75. 945	77. 230	75. 925	77. 270	+1. 285	+1. 345	1. 578	0. 9030
587	587	586	75. 945	78. 215	75. 925	78. 100	+2. 270	+2. 175	1. 639	0. 8694
684	685	686	75. 945	79. 490	75. 925	79. 455	+3. 545	+3. 530	1. 728	0. 8247
752	753	754	75. 945	80. 480	75. 925	80. 480	+4. 535	+4. 555	1. 795	0. 7939



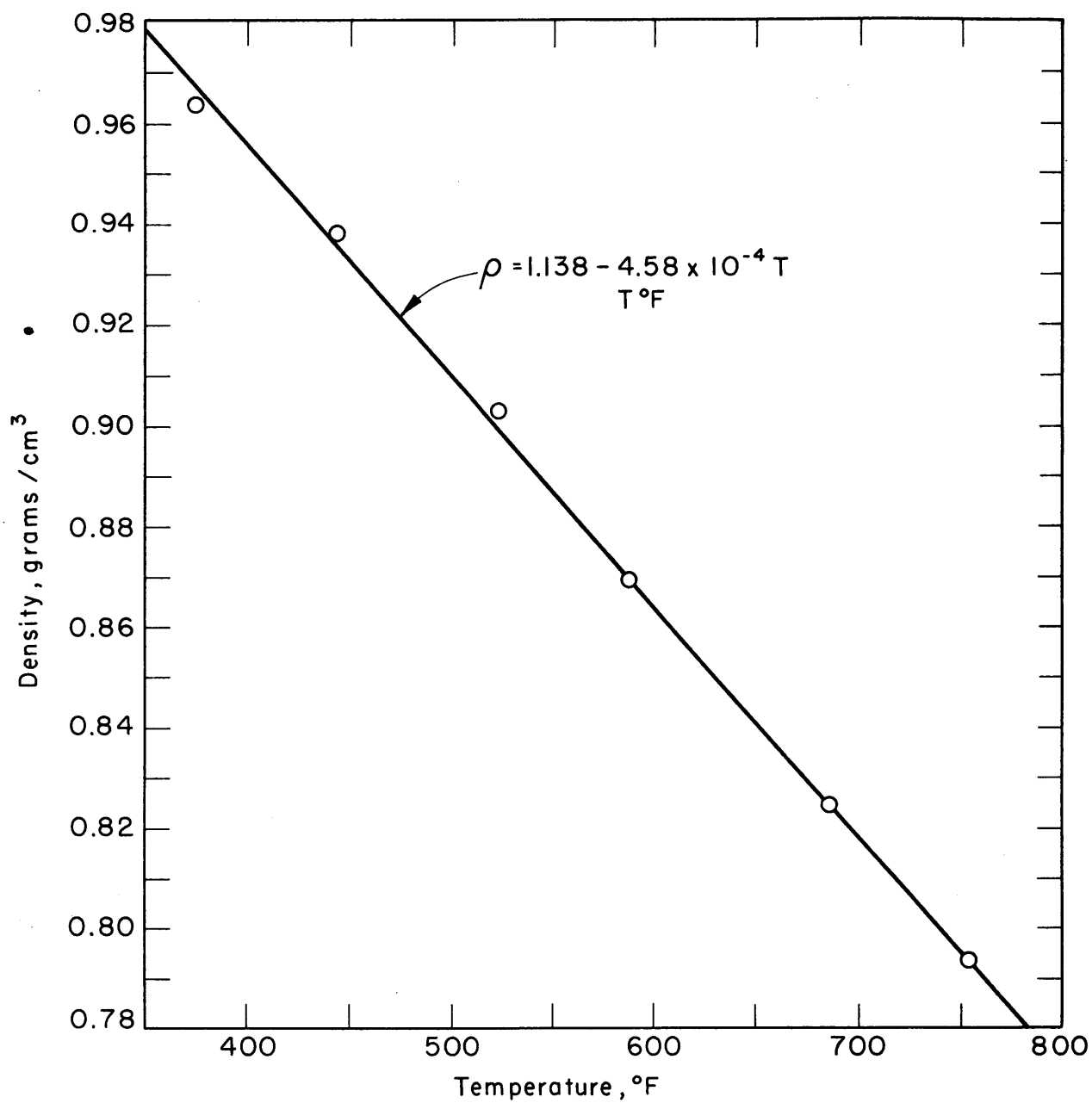


FIG. A5.12 DENSITY OF UNIRRADIATED SANTOWAX OMP

APPENDIX 6.1

DIMENSIONS OF TEST HEATER TH-5\*

Points E through R, see Fig. 3.12 - Points E<sub>1</sub> through E<sub>4</sub> refer to wall thickness measurements around the circumference of the tube.

Position	Outer Diameter				Position	Wall Thickness			
	E <sub>1</sub>	E <sub>2</sub>	E <sub>3</sub>	E <sub>4</sub>		E <sub>1</sub>	E <sub>2</sub>	E <sub>3</sub>	E <sub>4</sub>
E	.2473	.2473	.2473	.2473	E	.0195	.0196	.0202	.0200
F	.2472	.2473	.2472	.2473	F	.0196	.0198	.0201	.0201
G	.2473	.2473	.2473	.2473	G	.0198	.0197	.0202	.0202
H	.2473	.2472	.2473	.2472	H	.0197	.0197	.0201	.0201
J	.2472	.2473	.2472	.2473	J	.0195	.0197	.0201	.0202
K	.2472	.2472	.2472	.2472	K	.0197	.0197	.0202	.0202
L	.2472	.2472	.2472	.2472	L	.0195	.0198	.0202	.0203
M	.2473	.2473	.2473	.2473	M	.0197	.0199	.0202	.0203
N	.2472	.2473	.2472	.2473	N	.0196	.0198	.0202	.0202
P	.2472	.2472	.2472	.2472	P	.0198	.0198	.0202	.0201
Q	.2471	.2471	.2471	.2471	Q	.0198	.0199	.0202	.0202
R	.2472	.2472	.2472	.2472	R	.0196	.0198	.0202	.0201

\* Measurements made by Atomics International, a division of North American Aviation, Inc.

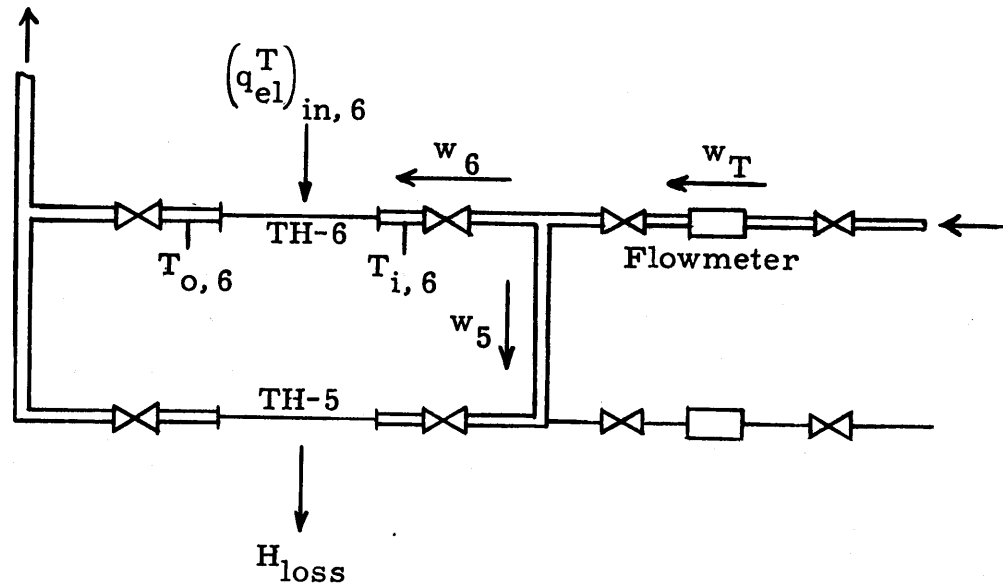
## APPENDIX 6. 2

PROCEDURE AND SAMPLE RESULTS FOR  
CALIBRATION OF TEST HEATER THERMOCOUPLES  
AND DETERMINATION OF HEAT LOSSES

To insure accurate temperature measurements for the determination of the heat transfer coefficient, the test heater wall and outlet bulk organic thermocouples were calibrated in place relative to the inlet bulk organic thermocouples which were used as standards. The procedure followed and sample results are presented in this appendix.

The basic method was to pass organic through the test heater without any power input at various velocities with a constant inlet organic temperature; at each velocity, the inlet and outlet bulk organic thermocouple readings, as well as all test heater wall thermocouple readings, were measured. The thermocouple readings in millivolts were then plotted vs.  $1/V$  (or equivalently to  $1/w'$  where  $w'$  is the organic flowrate, gpm) and extrapolated to  $1/V = \text{zero}$ . Since this is equivalent to an infinite velocity, there should be no difference between the temperature of the entering and leaving organic and the inside wall temperature of the test heater should be at the organic temperature (since  $h \rightarrow \infty$  as  $V \rightarrow \infty$ ). Neglecting the normally small temperature drop across the test heater wall due to heat losses, the extrapolated thermocouple readings of all thermocouples should thus be equivalent to the same temperature. Hence, using the inlet thermocouple as a standard, corrections for all of the remaining thermocouples can be determined.

In actually performing the calibration, it was necessary to use one of the duplicate test heaters as a heat source to maintain a constant organic temperature while the other test heater was being calibrated. The following sketch illustrates the experimental arrangement used for the calibration of test heater TH-5; test heater TH-6 was used as a heat source to maintain a constant organic inlet temperature. In this procedure, only the total flowrate,  $w_T$  lb/hr, was measured using the flowmeter. The flowrate through TH-5 was determined from the measured temperature rise across test heater TH-6. At the beginning of a set of measurements  $(q_{el}^T)_{in, 6}$  was set



at the proper level to give the desired organic temperature. With full flow through test heater TH-6, ( $w_5 = 0$ ) -- represented by values marked with \*,  $w_6^* \equiv w_T^*$  and:

$$\left( q_{el}^T \right)_{in,6}^* = w_6^* C_{p,6}^* (T_{o,6}^* - T_{i,6}^*) \quad (A6.1)$$

Now, when part of the flow is bypassed through test heater TH-5, the heat balance can be written as:

$$\left( q_{el}^T \right)_{in,6} = w_6 C_{p,6} (T_{o,6} - T_{i,6}) \quad (A6.2)$$

The flowrate,  $w_6$ , through test heater TH-6, with flow through test heater TH-5, is thus given by:

$$w_6 = w_6^* \frac{\left( q_{el}^T \right)_{in,6}}{\left( q_{el}^T \right)_{in,6}^*} \frac{C_{p,6}^*}{C_{p,6}} \frac{T_{o,6}^* - T_{i,6}^*}{(T_{o,6} - T_{i,6})} \quad (A6.3)$$

#### A 6. 4

The flow rate through test heater TH-5 is given by:

$$w_5 = w_T - w_6 \quad (\text{A6. 4})$$

In Figure A6. 1, a typical plot used in determining the correction factors is presented. It will be noticed that a linear plot is obtained, permitting an accurate extrapolation to  $1/w' = 0$ . In Figure A6. 2, a plot of the thermocouple correction factors for three wall thermocouples are presented vs. the millivolt reading of the chromel-alumel thermocouple.

The total heat loss from the test heater was also obtained from the calibration procedure based on the following equation:

$$H_{\text{loss}} = w_5 C_{p, 5} (T_{o, 5} - T_{i, 5}) \quad (\text{A6. 5})$$

The results obtained for the total heat loss from test heater TH-5, including losses from the electrodes and through the thermal insulation, are given in Figure A6. 3 as a function of the outside wall temperature.

#### APPENDIX 6. 3

##### ESTIMATION OF TEMPERATURE DIFFERENCE BETWEEN INSIDE AND OUTSIDE OF TEST HEATER WALL

In performing heat transfer measurements, the outside wall temperature has been measured by means of thermocouples. Since the inside wall temperature is the desired temperature, the temperature difference across the wall must be estimated. An equation for this estimation is derived in this appendix. It will be assumed that the energy generated in the test heater wall by the electric current is constant and uniformly distributed. In cylindrical coordinates, the general steady state equation with internal energy generation is:

$$T_w = - \frac{Qr^2}{4k} + C_1 \ln r + C_2 \quad (\text{A6. 6})$$

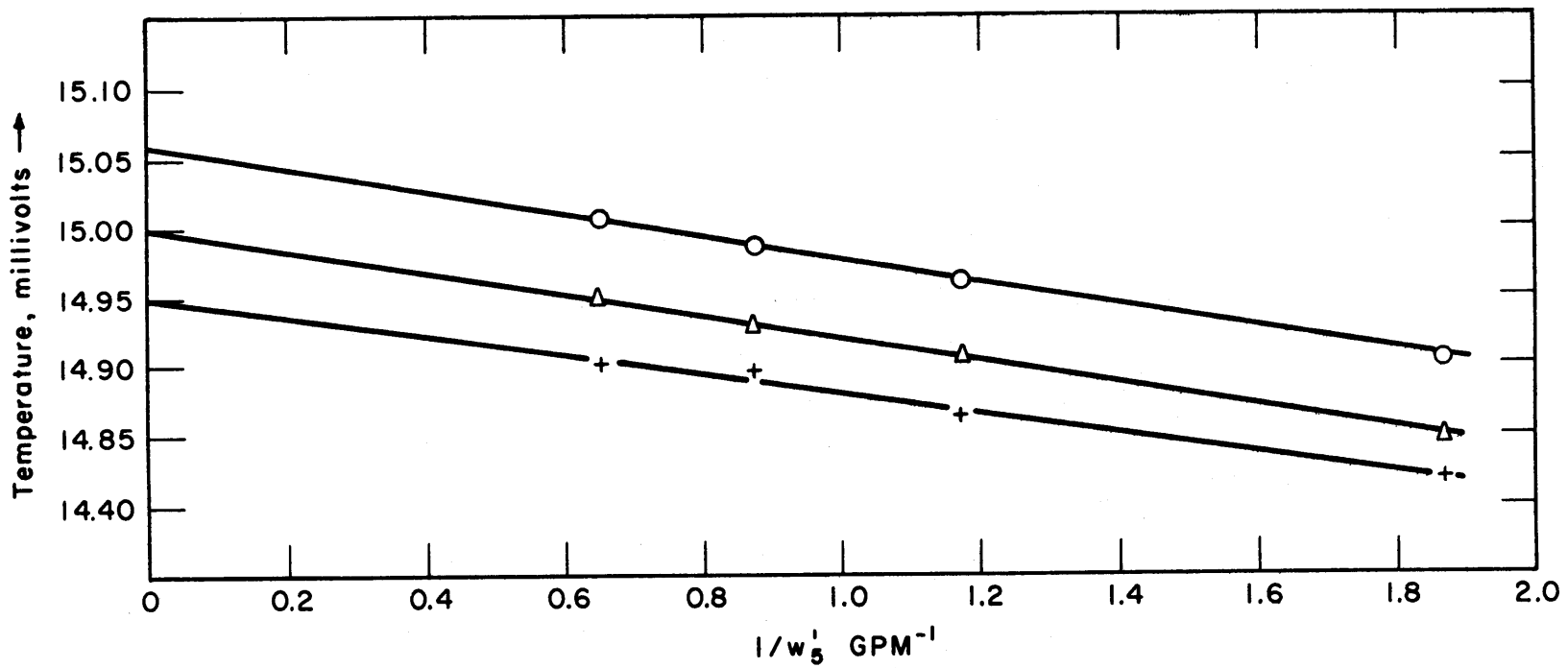


FIG. A6.1 SAMPLE OF METHOD USED TO DETERMINE THERMOCOUPLE CALIBRATION

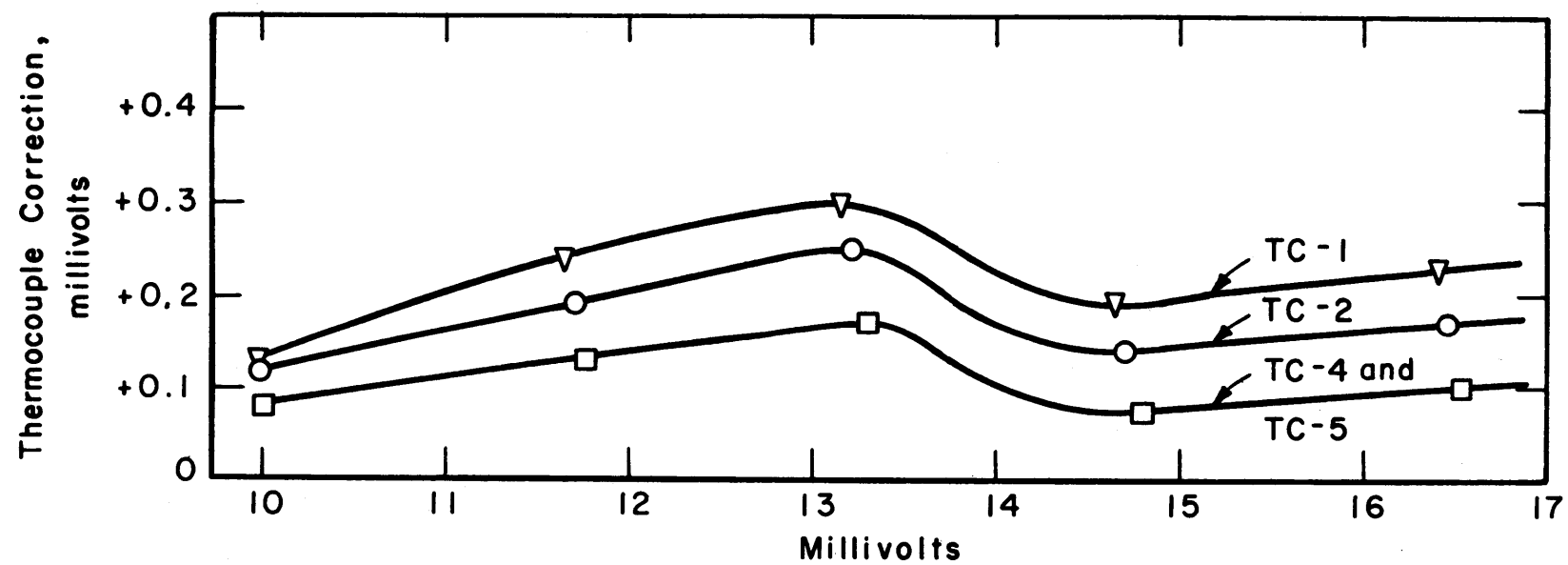


FIG. A6.2 SAMPLE OF THERMOCOUPLE CALIBRATION

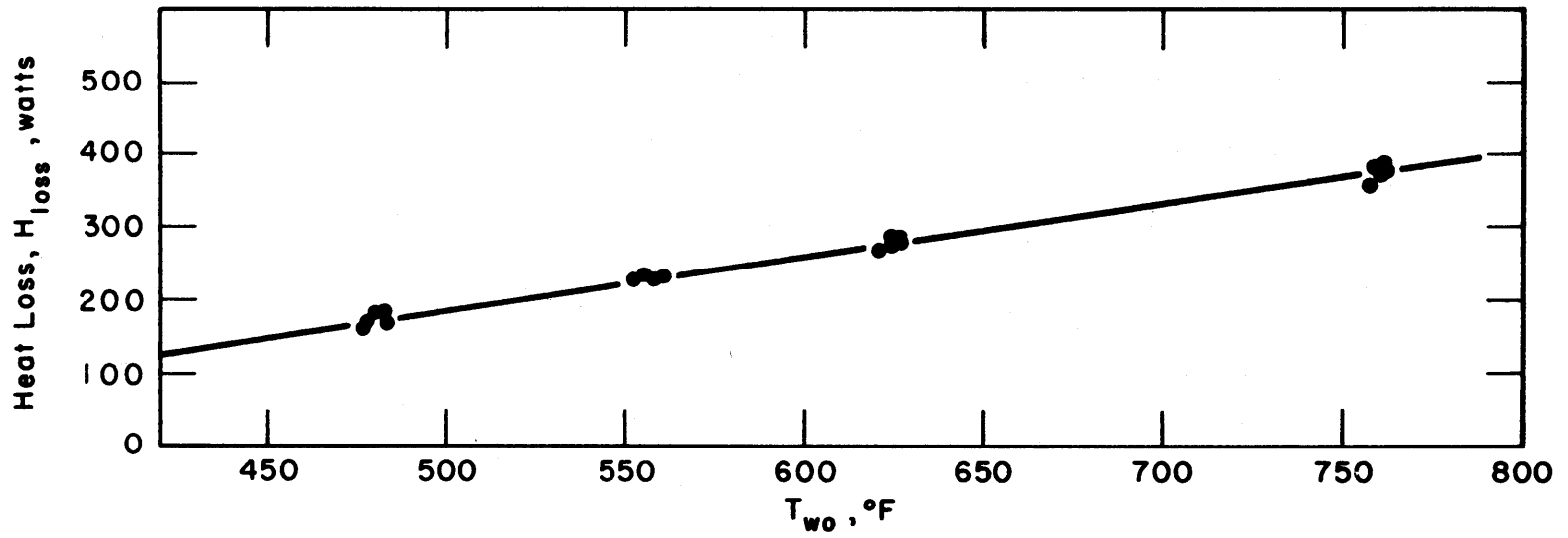


FIG. A6.3 TOTAL HEAT LOSSES FROM BOTH HEATER SECTIONS vs. OUTSIDE AVERAGE WALL TEMPERATURE



where

$Q$  is the volumetric energy generation rate, Btu/hr-ft<sup>3</sup>.

$r$  is the radius, ft.

$k$  is the thermal conductivity, Btu/hr-ft-°F.

$C_1$  and  $C_2$  are constants.

$T_w$  is the temperature, °F.

The boundary conditions are:

(1) At  $r = r_o =$  outside radius of tube,

$$\left( \frac{dT_w}{dr} \right)_{r=r_o} = - \left( \frac{H_{loss}}{L} \right) \left( \frac{1}{(k)(2\pi r_o)} \right)$$

where  $H_{loss}/L =$  heat loss rate from test heater, Btu/hr-ft.

(2) At  $r = r_o$ ,  $T_w = T_{wo} =$  outside wall temperature.

Applying boundary condition 1 gives:

$$C_1 = \frac{2Qr_o^2}{4k} - \frac{(H_{loss}/L)}{2\pi k} \quad (A6. 7)$$

or

$$T_w = -\frac{Qr^2}{4k} + \frac{2Qr_o^2}{4k} \ln r - \frac{H_{loss}/L}{2\pi k} \ln r + C_2 \quad (A6. 8)$$

Applying boundary condition 2 gives:

$$C_2 = T_{wo} + \frac{Qr_o^2}{4k} - \frac{2Qr_o^2}{4k} \ln r_o + \frac{H_{loss}/L}{2\pi k} \ln r_o \quad (A6. 9)$$

or

$$T_w = T_{wo} + \frac{Qr_o^2}{4k} \left[ 1 + 2 \ln \frac{r}{r_o} - \frac{r^2}{r_o^2} \right] + \frac{H_{loss}/L}{2\pi k} \left[ \ln \frac{r_o}{r} \right] \quad (A6. 10)$$

Substitution of  $r = r_i$  in this equation gives  $T_{wi}$ , the desired inside wall temperature. The following parameters were used in estimating the temperature correction:

$$r_o = \frac{0.247}{2} \text{ inches} = 0.0103 \text{ ft.}$$

$$r_i = \frac{0.207}{2} \text{ inches} = 0.00862 \text{ ft.}$$

$$k_w = 12.05 \text{ Btu/hr-ft-}^\circ\text{F.}$$

$$Q = \frac{q}{L} \text{ watts/ft} \times 3.413 \text{ Btu/hr-watt} \times \frac{1}{\pi[0.0103^2 - 0.00862^2]}$$

$$= 3.41 \times 10^4 \frac{q}{L} \text{ Btu/hr-ft}^3.$$

where  $q/L$  is the power input to one 12-inch section of the test heater. Substitution of these quantities into Equation A6. 10 with  $r = r_i$  gives

$$T_{wo} - T_{wi} = 4.20 \times 10^{-3} \frac{q}{L} - 8.09 \times 10^{-3} \left( \frac{H_{\text{loss}}}{L} \right) \quad (\text{A6. 11})$$

where

$$T_{wo} - T_{wi} = \text{temperature difference between outside wall and inside wall, } ^\circ\text{F.}$$

$$q/L = \text{watts generated in one 12-inch section.}$$

$$H_{\text{loss}}/L \text{ is the heat loss from one 12-inch section of the test heater, watts.}$$

The above equations neglect axial conduction in the heater tube wall which may be important near the electrodes.

## APPENDIX 6. 4

## ELECTRICAL RESISTANCE OF TEST HEATER TH-5

As indicated by Equation (6. 6), the power input to the test heater is determined from the measured voltage drop across the heater and from the electrical resistance of the test heater. The electrical resistance of test heater TH-5 was measured as a function of temperature for this purpose. The test heater was wound with a double-glass insulated heating tape and then with a layer of glass wool insulation. The thermocouples on the test heater were used to give the local temperature of the test heater tube for each resistance measurement and an average temperature calculated. A precision Wheatstone bridge was used for the resistance measurements. Copper leads were connected to each electrode of the test heater for the measurement; the resistance of the copper leads was also measured and subtracted from the total measured resistance, to give the resistance of the test heater only. The influence of temperature on the resistance of the copper leads was checked and found to be negligible since only a small length of the lead was in the high temperature region.

Based on the results obtained, the total series resistance of both sections of test heater TH-5 can be represented by the following equation:

$$R_T = 0.0471 + 2.16 \times 10^{-5} T \text{ ohms} \quad (\text{A6. 12})$$

where T is °F. The resistance for each section of the test heater can be taken as  $R_T/2$ .

## APPENDIX 6. 5

ADDITIONAL RESULTS OBTAINED IN CORRELATION  
OF HEAT TRANSFER DATA

As discussed in Chapter 6, when least squares evaluations of all constants in the heat transfer correlations [Equations (6. 17) and (6. 19)] have been made, using the heat transfer data obtained up to November 10, 1961, the constants have generally been significantly different than those

normally reported for correlation of heat transfer data. The correlation obtained using Equation (6. 19) is:

$$q/A \cong 200,000 \text{ Btu/hr-ft}^2 \text{ data}$$

$$(\text{Nu})_b = 0.00952 (\text{Re})_b^{0.867} (\text{Pr})_b^{0.779} \left(\frac{\mu_b}{\mu_w}\right)^{-1.24} \quad (\text{A6. 13})$$

RMS deviation of Nu =  $\pm 7.7\%$

$$q/A \cong 100,000 \text{ Btu/hr-ft}^2 \text{ data}$$

$$(\text{Nu})_b = 0.00779 (\text{Re})_b^{0.859} (\text{Pr})_b^{0.781} \left(\frac{\mu_b}{\mu_w}\right)^{-1.15} \quad (\text{A6. 14})$$

RMS deviation of Nu =  $\pm 8.7\%$

These correlations are compared in Figure A6. 4 with the experimental data where it is seen that two distinctly separate correlations with a difference of 23 per cent are obtained for the  $q/A = 200,000 \text{ Btu/hr-ft}^2$  and  $q/A = 100,000 \text{ Btu/hr-ft}^2$  data. It will also be noticed from Equations (A6. 14) and (A6. 13) that a negative coefficient of about 1. 2 is obtained on the  $\mu_b/\mu_w$  in contrast to the usual value of +0. 14. Based on physical reasoning, a positive coefficient would be expected in contrast to the results obtained.

A least squares evaluation of the constants in Equation (6. 17) without the viscosity term has also been made with the following results:

$$q/A = 200,000 \text{ Btu/hr-ft}^2 \text{ data}$$

$$(\text{Nu})_b = 0.00211 (\text{Re})_b^{1.000} (\text{Pr})_b^{0.550} \quad (\text{A6. 15})$$

RMS deviation of Nu =  $\pm 3.3\%$

$$q/A = 100,000 \text{ Btu/hr-ft}^2 \text{ data}$$

$$(\text{Nu})_b = 0.00208 (\text{Re})_b^{0.999} (\text{Pr})_b^{0.556} \quad (\text{A6. 16})$$

RMS deviation of Nu =  $\pm 2.4\%$

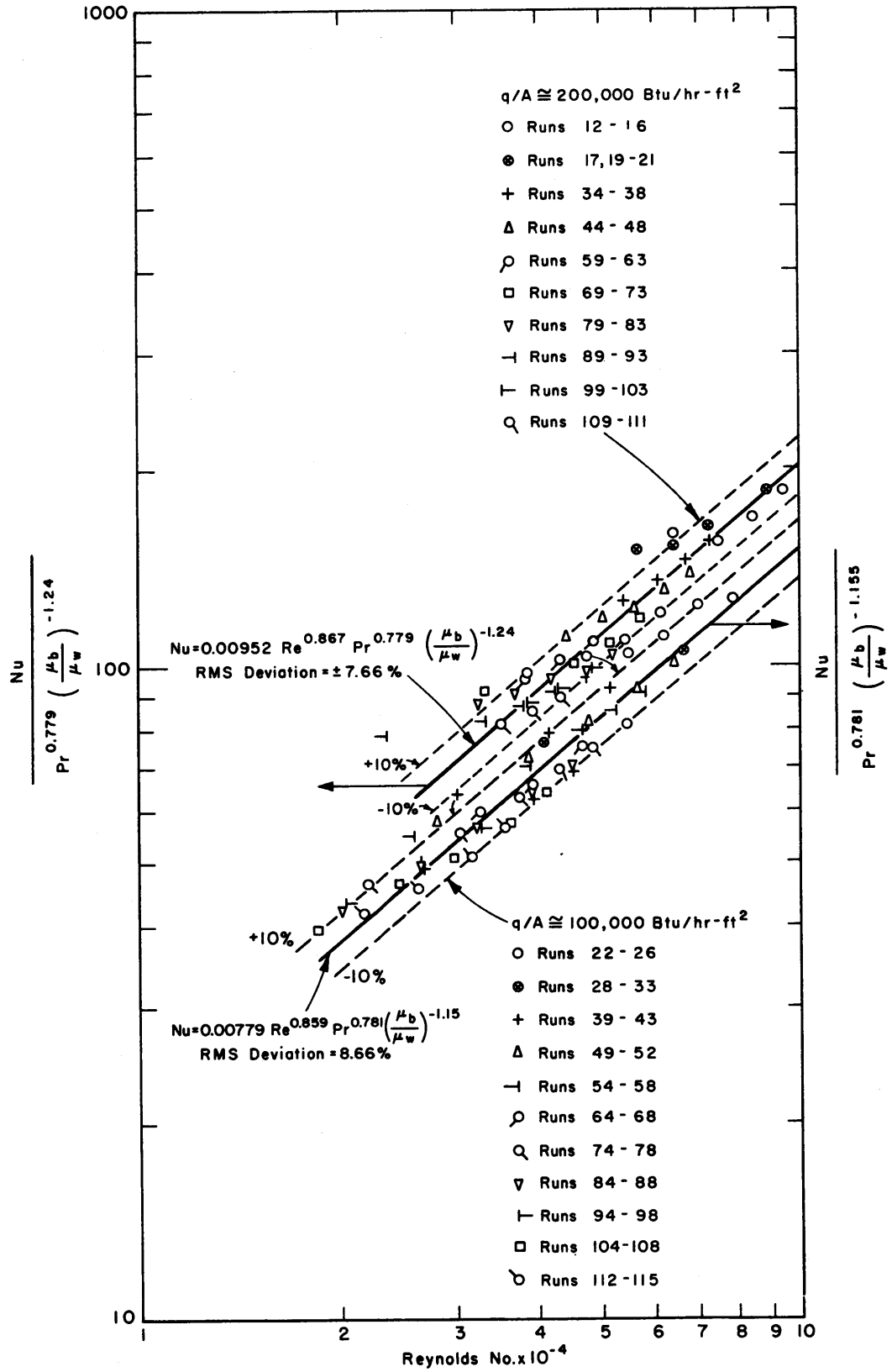


FIG. A6.4 LEAST SQUARES CORRELATION OF HEAT TRANSFER DATA WITH SEIDER - TATE TYPE OF EQUATION - NOMINAL  $q/A \cong 200,000 \text{ Btu/hr-ft}^2$  AND  $100,000 \text{ Btu/hr-ft}^2$

These correlations are compared in Figures A6.5 and A6.6 with the experimental data. Considering the rather small range in values of  $Re$  and  $Pr$  studied to date, presentation of these correlations should not be taken as a suggestion that the dependence of the Nusselt number on  $Re$  and  $Pr$  is indeed different from the conventional correlations of Equations (6.20) and (6.21). As additional heat transfer data are obtained in the course of this study, the computer program will be used to re-evaluate the various methods of correlation.

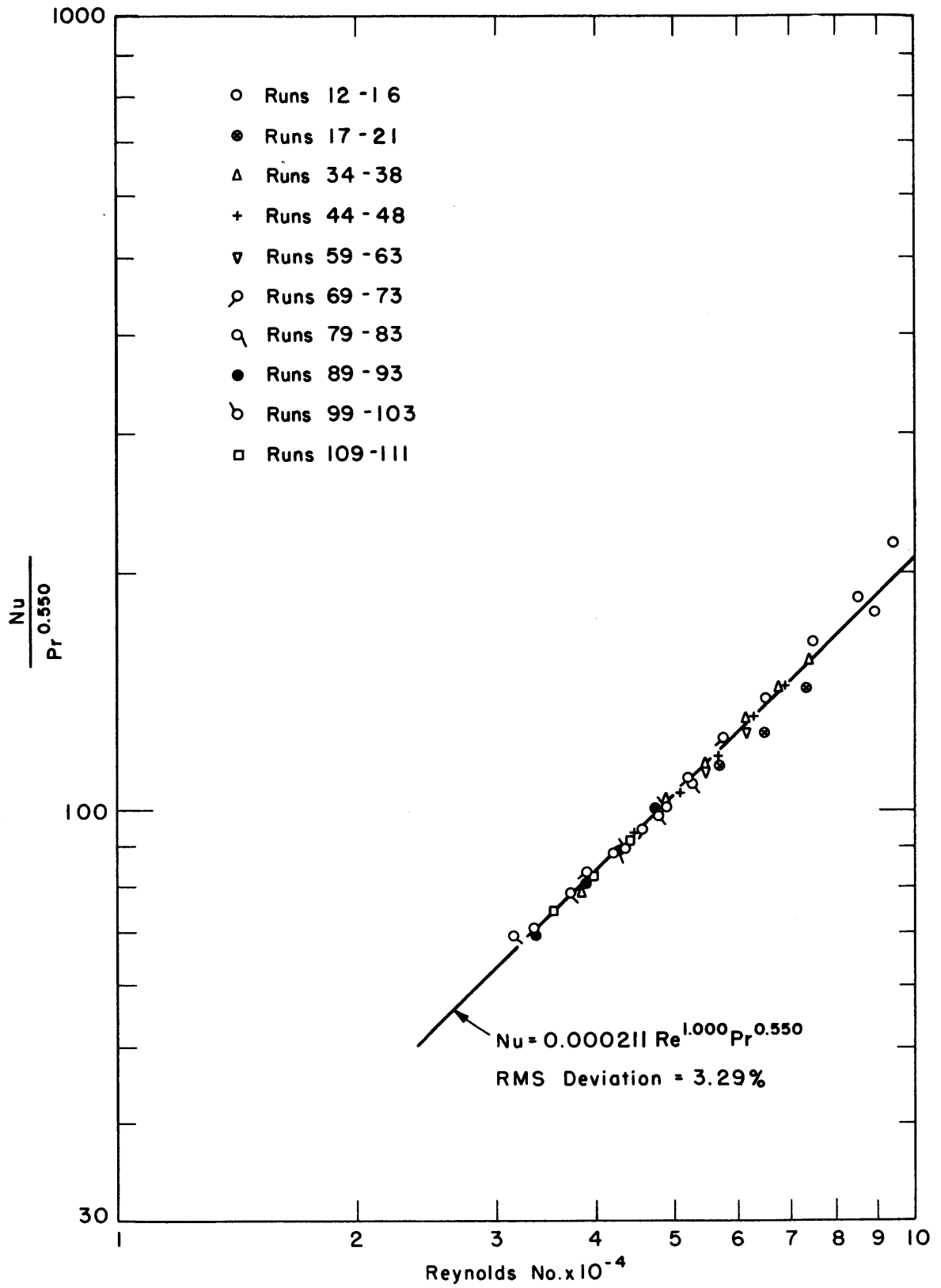


FIG. A6.5 LEAST SQUARES CORRELATION OF HEAT TRANSFER DATA WITH DITTUS-BOELTER TYPE OF EQUATION -NO CONSTANTS SPECIFIED - NOMINAL  $q/A \cong 200,000$  Btu/hr-ft<sup>2</sup>

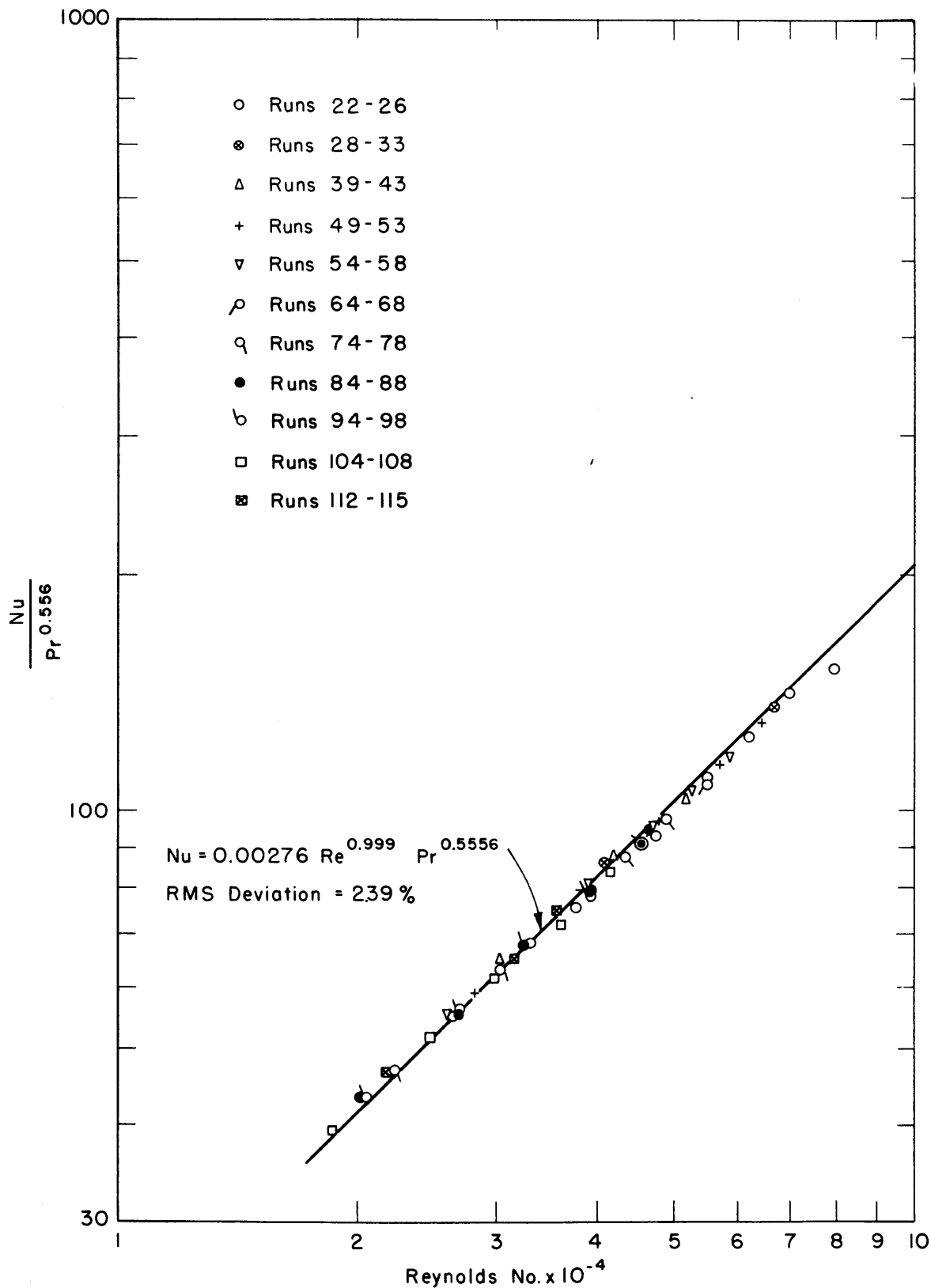


FIG. A6.6 LEAST SQUARES CORRELATION OF HEAT TRANSFER DATA WITH DITTUS - BOELTER TYPE OF EQUATION - NO CONSTANTS SPECIFIED - NOMINAL  $q/A \cong 100,000$  Btu/hr - ft<sup>2</sup>



APPENDIX 7 REFERENCESCHAPTERS 2-67.1 CHAPTER 2

- (2.1) "Annual Technical Progress Report, AEC Unclassified Programs, Fiscal Year 1960", NAA-SR-5350, Atomics International, Canoga Park, Calif., August 1, 1960.
- (2.2) Kline, H. E., N. J. Gioseffi, and W. N. Bley, "Dynamic Corrosion in Polyphenyls Under Irradiation", NAA-SR-2046, Atomics International, Canoga Park, Calif., May 15, 1958.
- (2.3) Gioseffi, N. J., and H. E. Kline, "Behavior of Structural Materials Exposed to an Organic Moderated Reactor Environment", NAA-SR-2570, Atomics International, Canoga Park, Calif., October 1, 1959.
- (2.4) Berg, S., N. W. Ewbank, R. J. Mack, J. Scarborough, and J. F. Zack, Jr., "Irradiations of Santowax OMP at the Curtiss-Wright Research Reactor", NAA-SR-5892, Atomics International, Canoga Park, Calif., January 3, 1961.
- (2.5) "Organic Cooled Reactor Study, Summary of Study", TID-8501 (Pt. 1), Bechtel Corporation and Atomics International, June, 1959.
- (2.6) "AEC Puts Together a Long Range Power Reactor Program-Nucleonics Digests it For You", Nucleonics, 18, No. 4, pp. 71-82, April, 1960.
- (2.7) "Organic Cooled Reactor Study--Reactor Concept Evaluation" TID-8501 (Pt. 3), prepared by Bechtel Corp. and Atomics International, issued July, 1959.

APPENDIX 7 REFERENCES (CONT.)7.1 CHAPTER 2 (CONT.)

- (2.8) Bolt, R.O., and J.G. Carroll, "Organic Reactor Moderator-Coolants, Some Aspects of Their Thermal and Radiation Stabilities", Proc. Int. Conf. on the Peaceful Uses of Atomic Energy, 7, p. 547 1956 .
- (2.9) Colichman, E.L., and R.H.J., Gercke, "Radiation Stability of Polyphenyls", Nucleonics, 14, pp. 50-54, 1956 .
- (2.10) Colichman, E.L., and R.F. Fish, "Resistance of Terphenyls to Heat and Radiation", Nucleonics, 15, pp. 72-74, 1957 .
- (2.11) Smith, H.P., "Compilation of Organic Moderator and Coolant Technology", TID-7007 (Parts I and II), Office of Technical Services, Washington, D.C., 1957 .
- (2.12) Civilian Power Reactor Program Part III, "Status Report on Organic-Cooled Power Reactors as of 1959", TID-8518(7), U.S. Atomic Energy Commission, 1960.
- (2.13) Burns, W.G., W. Wild, and T.F. Williams, "The Effect of Fast Electrons and Fast Neutrons on Polyphenyls at High Temperatures", 2nd United Nations International Conference on the Peaceful Uses of Atomic Energy, Paper A/Conf. 15/P/51, May 26, 1958.
- (2.14) West, W.W., "The Radiolysis of Prospective Organic Reactor Coolants", California Research-AEC Report No. 13, August 13, 1959.
- (2.15) Carroll, J.G., "Circulating Loops for Testing Organic Coolants", AECU-4291, U.S. Atomic Energy Commission, June 30, 1959.

APPENDIX 7 REFERENCES (CONT.)7.1 CHAPTER 2 (CONT.)

- (2.16) Bley, W.N., "An In-Pile Loop Study of the Performance of Polyphenyl Reactor Coolants", NAA-SR-2470, Atomics International, Canoga Park, Calif., September 15, 1958.
- (2.17) "Report on Organic Liquid-Cooled Reactor Development" PR-CM-26, Section 7, Atomic Energy of Canada Limited, Chalk River, Ontario, April 1-June 30, 1961.
- (2.18) Leary, J.E., and D.A. Huber, "Advanced OMR Coolant Screening and Boiling Test Loops", NAA-SR-5070, Atomics International, Canoga Park, Calif., July 30, 1960.
- (2.19) Trilling, C.A., "Experience with Surface Film Formation in Organic Circulation Systems", NAA-SR-Memo-5297, Atomics International, Canoga Park, Calif.
- (2.20) "Evaluation of the Organic Fouling Problem in the OMRE", TID-6882, U.S. Atomic Energy Commission, March 24, 1961.
- (2.21) "Status Report--Coolant and Fuel Element Technology for Organic Reactors", U.S. Atomic Energy Commission, July 1, 1961.
- (2.22) "Proceedings of the Organic Cooled Reactor Forum", October 6-7, 1960, NAA-SR-5688, Atomics International, Canoga Park, Calif.

7.2 CHAPTER 4

- (4.1) Bates, T.H., W. G. Burns, B. Morris, R.W. Wilkinson, and T. F. Williams, "The Radiation and Thermal Stability of Some Potential Organic Moderator-Coolants. Part II. Pile Irradiation of Para-Terphenyl and Santowax R." Report No. AERE C/R 2185 1959 .

APPENDIX 7 REFERENCES (CONT.)7.2 CHAPTER 4 (CONT.)

- (4.2) Berg, S., N. M. Ewbank, R. J. Mack, J. Scarborough, and J. F. Zack, Jr., "Irradiations of Santowax OMP at the Curtiss-Wright Research Reactor, The Effect of Fast Neutrons on Organic Coolants," NAA-SR-5892, January 3, 1961.
- (4.3) Fischer, P., "Calorimetric Dose Rate Measurement in the MIT Reactor," Master's Thesis, M.I.T., Cambridge 39, Mass., September, 1960.
- (4.4) Turricchia, A., "Dose Rate Measurement by Means of Adiabatic Calorimeters and a Miniature Ionization Chamber," Master's Thesis, M.I.T., Cambridge 39, Mass., February, 1962.
- (4.5) Houston, R.W., "Fast Neutron Dosimetry in Pile Irradiations", Nuclear Science and Engineering, 4, 227-238 (1958).
- (4.6) Hughes, D.J., and J. A. Harvey, "Neutron Cross Sections," BNL-325, Brookhaven National Laboratory.
- (4.7) Anderson, A.A., and R. J. Waite, "The Calorimetric Measurement of Energy Absorbed from Reactor Radiation in B.E.P.O.," Report No. AERE C/R 2253, Harwell, England, March, 1960.
- (4.8) Sefchovich-Itzcovich, E., "Neutron Dose Rates in the MIT Reactor," S.M. Thesis, Massachusetts Institute of Technology, January, 1962.
- (4.9) Uthe, P.M., "Attainment of Neutron Flux-Spectra from Foil Activations," S.M. Thesis, Air Force Institute of Technology, Air University, March 1957.

APPENDIX 7 REFERENCES (CONT.)7.2 CHAPTER 4 (CONT.)

- (4.10) Anderson, C.A. Jr., "Measurement of Neutron Energy Spectra With the M.I.T.R. Fast Chopper", Ph. D. Thesis, Department of Nuclear Engineering, M.I.T., Cambridge, Mass., August, 1961.
- (4.11) Profio, A. E., "Operating Manual for the MIT Reactor," Department of Nuclear Engineering, Massachusetts Institute of Technology, Cambridge, Mass., March, 1959.
- (4.12) Larson, C., "Reactivity Studies of a Heavy Water Moderated, Highly Enriched Uranium Reactor," ScD Thesis, MIT, Cambridge, Mass., 1959.
- (4.13) Hodgman, C.D., Editor, Handbook of Chemistry and Physics, 34th Ed., Chemical Rubber Publishing Co., Cleveland, Ohio, 1952.
- (4.14) McAdams, W.H., Heat Transmission, 3rd Ed., McGraw-Hill Book Co., Inc., New York, 1954.
- (4.15) Darwin, G.E., and J. H. Buddery, Beryllium, Butterworths Scientific Publications, London, 1960.
- (4.16) Reti, A., and H. Stern, "Specific Heat Measurements," Report No. 207, MAS-1, Dynatech Corp., Cambridge, Mass., August 17, 1960.

7.3 CHAPTER 5

- (5.1) Annual Technical Progress Report, AEC Unclassified Programs, Fiscal Year, 1959, NAA-SR-3850, Atomics International, Canoga Park, Calif., August 1, 1959.
- (5.2) Annual Technical Progress Report AEC Unclassified Programs, Fiscal Year, 1961, NAA-SR-6370, Atomics International, Canoga Park, Calif., August 15, 1961.

APPENDIX 7 REFERENCES (CONT.)7.3 CHAPTER 5 (CONT.)

- (5.3) Dean, R. B., and W. J. Dixon, "Simplified Statistics for Small Numbers of Observations", *Analytical Chemistry*, 23, No. 4, 636-638, 1951 .
- (5.4) Gercke, R.H.J. and C.A. Trilling, "A Survey of the Decomposition Rates of Organic Reactor Coolants", NAA-SR-3835, *Atomics International*, Canoga Park, Calif., June 10, 1959.
- (5.5) Burns, W. G., W. Wild, and T. F. Williams, "The Effect of Fast Electrons and Fast Neutrons on Polyphenyls at High Temperatures", A/Conf. 15/P/51, Second U.N. International Conference on the Peaceful Uses of Atomic Energy, May 26, 1958.
- (5.6) Berg, S., N. W. Ewbank, R. J. Mack, J. Scarborough, and J. F. Zack, Jr., "Irradiations of Santowax OMP at the Curtiss-Wright Research Reactor", NAA-SR-5892, *Atomics International*, Canoga Park, Calif., January 3, 1961.
- (5.7) Bates, T. H., et al, "The Radiation and Thermal Stability of Some Potential Organic Moderator-Coolants, Part I, Electron Irradiation of Para Terphenyl and Santowax R", AERE-C/R-2121, Harwell, 1957.
- (5.8) Annual Technical Progress Report, AEC Unclassified Programs, Fiscal Year 1961, NAA-SR-6370, *Atomics International*, Canoga Park, Calif., August 15, 1961.
- (5.9) Status Report, Coolant and Fuel Element Technology for Organic Reactors, Idaho Operations Office, AEC, July 1, 1961.
- (5.10) Bley, W.N., "An In-Pile Loop Study of the Performance of Polyphenyl Reactor Coolants", NAA-SR-2470, *Atomics International*, Canoga Park, Calif., September 15, 1958.

APPENDIX 7 REFERENCES (CONT.)7.3 CHAPTER 5 (CONT.)

- (5.11) Burns, W.G., "The Irradiation of Polyphenyls with Different Types of Radiation", Estratto Dagli Atti Ufficiali: Del Congresso Scientifico, Sezione Nucleare, Roma, 16-20 Giugno, 1959.
- (5.12) Bates, T.H., W.G. Burns, B. Morris, A.W. Wilkinson and T.F. Williams, "The Radiation and Thermal Stability of Some Potential Organic Moderator-Coolants, Part II, Pile Irradiation of Para Terphenyl and Santowax R", AERE C/R 2185, Harwell, July, 1959.
- (5.13) Anderson, A.R., and Waite, R.J., "The Calorimetric Measurement of Energy Absorbed from Reactor Radiation in B.E.P.O.", AERE C/R 2253, Harwell, March, 1960.
- (5.14) McEwen, Malcolm, Development Department, Monsanto Chemical Company, St. Louis, Missouri, Personal Correspondence, February 17, 1961.
- (5.15) Burr, J.G., and Scarborough, J.M., "The Radiolysis of Deuterated Biphenyls: Mechanism of Hydrogen Formation", NAA-SR-4961, Atomics International, Canoga Park, Calif., July 30, 1960.
- (5.16) Gercke, R.H.J., and Asanovick, G., "Thermophysical Properties of Irradiated Polyphenyl Coolants, Part I, Density and Viscosity," NAA-SR-4484, Atomics International, Canoga Park, Calif., December 1, 1960.
- (5.17) Rossini, F.D., B.J. Mair, and A.J. Streiff, Hydrocarbons from Petroleum, Reinhold Publishing Corporation, New York, 1953.
- (5.18) Wineman, R.J., Monsanto Research Corp., Everett, Massachusetts, Letter to E. A. Mason, Massachusetts Institute of Technology, Cambridge, Mass., March 30, 1961.

APPENDIX 7 REFERENCES (CONT.)7.3 CHAPTER 5 (CONT.)

- (5.19) Bonnar, R.V., M. Dimbat, and F.H. Stross, Number-Average Molecular Weights, Fundamentals and Determination, Interscience Publishers, Inc., New York, 1958.
- (5.20) "Evaluation of the Organic Fouling Problem in the OMRE", TID-6882, Office of Technical Information, United States Atomic Energy Commission, June 3, 1960.

7.4 CHAPTER 6

- (6.1) McAdams, W.H., Heat Transmission, McGraw-Hill Book Company, Inc., New York, 1954.
- (6.2) Eckert, E.R.G., and Drake, R.M. Jr., Heat and Mass Transfer, McGraw-Hill Book Co., Inc., New York, 1959.
- (6.3) Sawyer, C., Personal Communication, Department of Nuclear Engineering, Massachusetts Institute of Technology Cambridge 39, Mass., May, 1962.
- (6.4) Swierzawski, T.J., "Effect of In-Pile Irradiation on Heat Transfer Characteristics of Santowax OMP," Master's Thesis, Nuclear Engineering Department M.I.T., Cambridge 39, Mass., February, 1962.
- (6.5) Ziebland, H., and Burton, J.T.A., "The Thermal Conductivity of Santowax R Between 155 and 400°C," AERE/X/PR 2653, Harwell, June, 1959.
- (6.6) Bowring, R.W., D.A. Garton, and H.F. Norris, "Measurement of the Specific Heats of Santowax R, Para-, Meta-, and Ortho-Terphenyl, Diphenyl, and Dowtherm A," AEEW-R 38, Atomic Energy Establishment, Winfrith, Dorchester, December, 1960.



APPENDIX 8 REFERENCES, APPENDICESCHAPTERS 3-68.1 CHAPTER 3

- (A3.1) Morgan, R.P., "Design of the In-Pile Section of an Organic Moderator-Coolant Loop," S.M. Thesis, Massachusetts Institute of Technology, Cambridge, Mass., January, 1961.

8.2 CHAPTER 4

- (A4.1) Bovey, F.A., The Effects of Ionizing Radiation on Natural and Synthetic High Polymers, Interscience Publishers, Inc., New York., 1958.
- (A4.2) Dyne, P.J., and W. Thurston, A Calorimetric Determination of Energy Deposition in the J-Rod Annulus of the NRX Reactor, AEGL No. 432, Chalk River, Ontario, April, 1957.
- (A4.3) Weinberg, A.M., and E. P. Wigner, The Physical Theory of Neutron Chain Reactors, The University of Chicago Press, Chicago, Illinois, 1958.
- (A4.4) Fischer, P., Calorimetric Dose Rate Measurement in the MIT Reactor, Master's Thesis, M.I.T., Cambridge 39, Mass., September, 1960.
- (A4.5) Goldstein, H., Fundamental Aspects of Reactor Shielding, Addison-Wesley Publishing Co., Inc., Reading, Mass., 1959.

APPENDIX 8 REFERENCES, APPENDICES (CONT.)8.2 CHAPTER 4 (CONT.)

- (A4.6) Turricchia, A., "Dose Rate Measurement by Means of Adiabatic Calorimeters and a Miniature Ionization Chamber," Master's Thesis, M.I.T., Cambridge 39, Mass., February, 1962.
- (A4.7) Troubetzkoy, E., and H. Goldstein, "Gamma Rays from Thermal-Neutron Capture," Nucleonics, 18, pp. 171-173, No. 11, November, 1960.
- (A4.8) Henderson, W.J., and A. C. Whittier, "Handbook of Shielding and Heat Production Calculations for the N.R.U. Reactor", CRR-578 or AECL-403, 1957.
- (A4.9) Hine, G.J., and G.L. Brownell, Radiation Dosimetry, Academic Press, Inc., New York, 1956.
- (A4.10) Anderson, A.A., and R.J. Waite, "The Calorimetric Measurement of Energy Absorbed from Reactor Radiation in B.E.P.O.," Report No. AERE C/R 2253, Harwell, England, March, 1960.
- (A4.11) Richard, P.I., and B.A. Rubin, "Irradiation of Small Volumes by Contained Radioisotopes", Nucleonics 6, 42, 1950.
- (A4.12) Evans, R.D., The Atomic Nucleus, McGraw-Hill Book Company, Inc., New York, 1955.
- (A4.13) Kaplan, I, Nuclear Physics, Addison-Wesley Publishing Company, Inc., Cambridge, Mass., 1955.
- (A4.14) Davisson, C.M. and Evans, R.D., "Gamma Ray Absorption Coefficients," Reviews of Modern Physics, 24, 79-107, April, 1952.
- (A4.15) Lanning, D., Personal Communication, Department of Nuclear Engineering, M.I.T. Cambridge, Mass., November, 1961.

APPENDIX 8 REFERENCES, APPENDICES (CONT.)8.2 CHAPTER 4 (CONT.)

- (A4.16) Larson, C., "Reactivity Studies of a Heavy Water Moderated Highly Enriched Uranium Reactor," ScD Thesis, MIT, 1959.
- (A4.17) Hildebrand, F.P., **Methods of Applied Mathematics**, Prentice-Hall, Inc., Englewood Cliffs, N.J., 1952.
- (A4.18) Hughes, D.J., and J.A. Harvey, **Neutron Cross Sections**, BNL-325, Brookhaven National Laboratory, July 1, 1955.
- (A4.19) Sefchovich, E., "Neutron Dose Rate in the MIT Reactor," S.M. Thesis, MIT, Nuclear Engineering Department, Cambridge, Mass., January, 1962.
- (A4.20) Rockwell, T., Editor, **Reactor Shielding Design Manual**, McGraw-Hill Book Company, Inc., New York, 1956.
- (A4.21) Blizard, E.P., **Nuclear Radiation Shielding**, Notes Prepared for McGraw-Hill Nuclear Reactor Handbook, Oak Ridge National Laboratory, September 17, 1956.
- (A4.22) Meghreblian, R.V., and D.K. Holmes, **Reactor Analysis**, McGraw-Hill Book Company, Inc., New York, 1960.

8.3 CHAPTER 5

- (A5.1) Dean, R.B., and W.J. Dixon, "Simplified Statistics for Small Numbers of Observations", **Analytical Chemistry**, 23, No. 4, 636-638, 1951.
- (A5.2) Daniel, C., "Statistics for Engineers", KZ-6680, Union Carbide Nuclear Company, Oak Ridge, Tenn., 1947.

APPENDIX 8 REFERENCES, APPENDICES (CONT.)8.3 CHAPTER 5 (CONT.)

- (A5.3) Mickley, H.S., T.K. Sherwood, and C.E. Reed, "Applied Mathematics in Chemical Engineering", 2nd Ed., McGraw-Hill Book Company, Inc., 1957.
- (A5.4) Gore, W.L., Statistical Methods for Chemical Experimentation, Interscience Publishers, Inc., New York, 1952.
- (A5.5) Bley, W.N., "An In-Pile Loop Study of the Performance of Polyphenyl Reactor Coolants", NAA-SR-2470, Atomics International, Canoga Park, Calif., September 15, 1958.
- (A5.6) Ewbank, N.M., "Procedure for the Determination of Gas Solubility in OMRE Coolant", IOL to R.H.J. Gercke Atomics International, Canoga Park, Calif., September 18, 1958.
- (A5.7) McAdams, W.H., Heat Transmission, 3rd Ed., McGraw-Hill Book Co., Inc., New York, 1954.
- (A5.8) Barr, G., Monograph of Viscosity, Oxford University Press, London, 1931.
- (A5.9) "First Report on Viscosity and Plasticity" Prepared by the Committee for the Study of Viscosity of the Academy of Sciences at Amsterdam Uitgave Van de N.V. Noord-Hollandsche Uitgevers-Maatschappij, Amsterdam, 1935.
- (A5.10) Cannon, M.R., and M.R. Fenske, "Viscosity Measurement", Ind. and Eng. Chem., Anal Ed., 10, p. 297, (1938).
- (A5.11) "Second Report on Viscosity and Plasticity," Prepared by the Committee for the Study of Viscosity of the Academy of Sciences at Amsterdam, N.V. Noord-Hollandsche Uitgevers-Maatschappij, Amsterdam, 1938.
- (A5.12) Hodgman, C.D., Editor, Handbook of Chemistry and Physics, 34 Ed., Chemical Rubber Publishing Co., Cleveland, Ohio, 1952.
- (A5.13) Burns, W.G., B. Morris, and R.W. Wilkinson, "An Apparatus for the Viscosity of Organic Liquids at High Temperatures", Journal of Scientific Instruments, 35, No. 8, p. 291, 1958 (August).

APPENDIX 8 REFERENCES, APPENDICES (CONT.)8.3 CHAPTER 5 (CONT.)

- (A5.14) Bates, T.H., W.G. Burns, B. Morris, R.W. Wilkinson, and T.F. Williams, "The Radiation and Thermal Stability of Some Potential Organic Moderator-Coolants, Part I. Electron Irradiation of Para-Terphenyl and Santowax R", A.E.R.E. c/R 2121, p. 18, Harwell, 1957.

## APPENDIX 9

## NOMENCLATURE

$A$  = area,  $\text{ft}^2$ .

$A, A_1, A_2$  = constants.

$A$  = area,  $\text{ft}^2$ .

$A$  = surface activity,  $\text{dis}/\text{sec}\text{-cm}^2$ .

$A$  = total grams of organic makeup added to the loop on dilution.

$A, A_i$  = atomic or molecular weight of material  $i$  where  $i$  refers to aluminum (Al), polyethylene (PE), polystyrene (PS), beryllium (Be), and Santowax OMP (SW).

$A_B, A_{Cd}$  = activity of irradiated flux detectors,  $\text{dis}/\text{sec}$ , when irradiated bare and cadmium covered.

$A_i$  = inside area,  $\text{ft}^2$ .

$A_i, A_{st}$  = peak area of the  $i^{\text{th}}$  component and the standard, respectively, in gas chromatography measurement.

$a$  = constant.

$a$  = radius,  $\text{cm}$ .

$a_t$  = thermal diffusivity,  $\text{ft}^2/\text{hr}$ .

$B$  = conversion factor,  $\text{cm}^2/\text{sec}$  to stokes.

$B_H^2$  = the axial buckling.

$B_i$  = constant.

$B_j$  = atoms of element  $j$  per molecule.

$B_{\mu t}$  = buildup factor as function of  $\mu t$ .

$b$  = subscript corresponding to evaluation of coolant properties at the bulk temperature of the coolant.

$b, b_i$  = constants.

$b_{2n}, b_{2m}$  = parameters for evaluation of gamma ray shielding.

$C, C_i, C_i(Z)$  = concentration of component,  $i$ , in coolant, wt % or wt fraction, where  $i$  refers to meta-terphenyl ( $m\phi_3$ ), para-terphenyl ( $p\phi_3$ ), ortho-terphenyl ( $o\phi_3$ ), and the total terphenyls ( $omp\phi_3$ ).

$C'$  = measured concentration for a particular sample, wt per cent.

$C(DP)$  = wt per cent of degradation products in coolant.

$C_{j,i}$  = weight fraction of the isomer,  $i$ , in the  $j^{\text{th}}$  sample.

$C_1, C_2, C_3$  = wt % of terphenyl isomer before and after addition of organic makeup and concentration of the organic makeup, respectively.

$C_V$  = heat capacity of gas at constant volume, Btu/lb-°F.

$C, C_p, c_p$  = heat capacity of material, watt-sec/gm-°C.

$C$  = viscometer coefficient.

$C_{V_{25}^{\text{std}}}$  = calibration constant for the viscometer containing  $V_{25}^{\text{std}}$  cm<sup>3</sup> of fluid.

$C_{V_T}$  = calibration constant for viscometer measurement for an organic volume,  $V_T$ , cm<sup>3</sup>.

$D$  = diameter, ft.

$D$  = diffusion coefficient for thermal neutrons, cm.

$D$  = rate of shear, sec<sup>-1</sup>.

$D$  = total absorbed dose, watt hrs.

$D$  = dose rate, Mev/gm-sec.

$D_{TCW}$  = effective thermocouple bead diameter, ft.

$d$  = diameter of the fluid reservoir at the bottom of the viscometer, cm.

$d$  = the scale thickness, ft.

$E$  = potential drop across test heater section, volts.

$E$  = neutron energy, ev or Mev.

$E_0$  = assumed neutron source strength, Mev.

$E$  = total energy released by thermal neutron activation per gram of aluminum per unit thermal flux.

$E(t)$  = Mev/sec of gamma radiation from decay of fission products at a time,  $t$ , after the fission event.

$E_{avg}$  = average gamma energy for a given gamma energy interval, Mev.

$E_\gamma$  = energy of gamma rays emitted, Mev.

$E_a^\beta, E_a^\gamma$  = energy absorption in the calorimeter samples due to beta and gamma radiation emanating from the aluminum capsule, Mev/gm-sec.

$\overline{E}_\beta$  = average beta energy, Mev.

$E_{1/2}$  = energy, Mev, at which the photoelectric ( $\tau$ ) and pair production ( $\kappa$ ) linear attenuation coefficients are equal to the Compton coefficient ( $\sigma$ ).

$E_C$  = cadmium cutoff energy, ev.

$E_1$  = energy at which the resonance flux joins the thermal flux, ev.

$E_{eff}$  = effective threshold energy, Mev, for fast neutron threshold detectors.

$E_{th}$  = actual threshold energy for threshold fast neutron reaction, ev or Mev.

$e$  = linear coefficient of expansion of glass,  $^{\circ}\text{C}^{-1}$ .

$F$  = conversion factor,  $\frac{\text{ev}}{\text{sec-atom}}$  to  $\frac{\text{watts}}{\text{atom}}$  or  $\frac{\text{ev}}{\text{sec-gm}}$  to  $\frac{\text{watts}}{\text{gm}}$ .



$$F = \frac{1 + \frac{V_m}{V_F}}{1 + \frac{\bar{\phi}_m}{\bar{\phi}_F} \frac{V_m}{V_F}} \quad \text{for calculation of fission rate in fuel element.}$$

$F$  = fraction of gamma dose rate for calorimeter series III-3 from all fuel elements.

$F$  = fraction of neutrons slowed down past a given neutron energy within a cylinder of radius,  $a$ .

$$F\left(\frac{\pi}{2}, b_2\right) = \int_0^{\pi/2} e^{-b_2 \sec \theta} d\theta.$$

$F_{c2}, F_{c3}$  = fission rate for center fuel element for calorimeter series III-2 and III-3, respectively.

$F_{o2}, F_{o3}$  = total fission rate for outer fuel elements for calorimeter series III-2 and III-3, respectively.

$F_o$  = fission rate in reactor, fissions/sec.

$f$  = fraction of radiation emerging from spherical shell which is intercepted by central sphere.

$f_i$  = "f" factor for gas chromatograph measurements.

$G(\text{gas})$  = molecules of total gas evolved per 100 ev absorbed in the coolant.

$$G^*(\text{gas}) = \frac{G(\text{gas})}{C} \frac{\text{molecules}}{100 \text{ ev}}.$$

$G^{*n}(\text{gas}), G^{*\gamma}(\text{gas})$  = gas evolution yield for fast neutrons and gamma radiation, respectively, for the coolant.

$G_m(-i), G(-i)$  = radiolytic decomposition yield of component  $i$  in the coolant expressed in units of grams/watt-hr and molecules/100 ev, respectively, where  $i$  refers to meta-terphenyl ( $m\phi_3$ ), para-terphenyl ( $p\phi_3$ ), ortho-terphenyl ( $o\phi_3$ ), and the total terphenyls ( $omp\phi_3$ ).

$$G_m^*(-i) = \frac{G_m(-i)}{C_i(Z)} \text{ molecules/100 ev.}$$

$$G^*(-i) = \frac{G(-i)}{C_i(Z)} \text{ molecules/100 ev.}$$

$G^{*n}(-i)$ ,  $G^{*\gamma}(-i)$  = decomposition yield for fast neutron and gamma radiation, respectively, for material i.

$g_j$  = average fraction of the neutron energy lost on collision with an atom of element j where j refers to aluminum (Al), hydrogen (H), and carbon (C).

$G_i$  = photons emitted in the  $i^{\text{th}}$  energy interval per gram of material.

$g$ ,  $g_c$  = gravitational constant,  $\text{cm}^2/\text{sec}$  and conversion factor.

$g(E)$  = attenuation factor.

$H(Z)$ ,  $H_i(Z)$  = grams of component i degraded at Z MWHR's, where i refers to meta-terphenyl ( $m\phi_3$ ), para-terphenyl ( $p\phi_3$ ), ortho-terphenyl ( $o\phi_3$ ), and the total terphenyls ( $omp\phi_3$ ).

$H(T)$  = gamma energy emission rate at time, T, due to decay of fission products.

$H_{\text{loss}}/L$  = heat loss rate from test heater, Btu/hr-ft.

h = fluid head, cm.

h = the fluid convective heat transfer coefficient,  $\text{Btu/hr-ft}^2\text{-}^\circ\text{F}$ .

$h_{25}^{\text{std}}$  = effective fluid head, cm, when the viscometer contains  $V_{25}^{\text{std}}$   $\text{cm}^3$  of water.

I,  $I(E)$  = intensity of gamma field,  $\text{photons/cm}^2\text{-sec-Mev}$ .

$I_j$  = energy transfer integral for element, j,  $\frac{\text{watts}}{\text{atom}}$ , where j refers to aluminum (Al), hydrogen (H), and carbon (C).

$I_0(a)$ ,  $I_1(a)$  = Bessel functions.

$J_0(a)$  = Bessel function.

$K, K_n = \text{constant.}$

$K_c = \text{contraction coefficient.}$

$k_1, k_2 = \text{reaction rate constants for evolution of gas on irradiation of terphenyls, cm}^3 \text{ (STP)/MWHR-wt \%}, \text{ where 1 refers to the undegraded terphenyls and 2 to the degradation products.}$

$k_i, k'_i = \text{Henry's law coefficients for component } i.$

$k'_{\text{avg}} = \text{average Henry's law coefficient for mixture of gases.}$

$k = \text{thermal conductivity, Btu/hr-ft-}^\circ\text{F.}$

$k_o, k_{\text{TC}}, \text{ and } k_s = \text{thermal conductivity of organic, thermocouple lead-wire, and scale on heat transfer surface, Btu/hr-ft-}^\circ\text{F.}$

$L_s = \text{slowing down distance, cm.}$

$L = \text{length, ft.}$

$l = \text{axial position in the reactor core, inches.}$

$+l_u = \text{distance in inches of the top of the holdup capsule from the reactor core center.}$

$-l_l = \text{distance in inches of the bottom of the capsule from the reactor core center, inches.}$

$l = \text{distance from reference mark to liquid level, cm.}$

$M_i = \text{molecular weight of component, } i, \text{ of the coolant, grams/gram mole.}$

$M_N = \text{number average molecular weight, grams/gram mole.}$

$M(\text{DP}) = \text{molecular weight of degradation products.}$

$M, M(Z) = \text{mass of organic in loop as a function of } Z, \text{ the MWHR's of reactor operation.}$

$m = \text{constant.}$

$m = \text{mass of gas in sample capsule, lb.}$

$m = \text{grams of material/cm of source.}$

$m = \text{kinetic energy coefficient.}$

$N, N^*, N_{AV}$  = Avogadro's number, molecules/gram molecule.

$N$  = fraction of gamma dose rate for calorimeter series III-3 from outer fuel element.

$N$  = number of observations.

$N_j, N_j^i, N_{i,j}$  = atoms of element  $j$  per gram of material  $i$  where  $j$  refers to hydrogen (H), carbon (C), and aluminum (Al) and  $i$  refers to aluminum (Al), polyethylene (PE), and polystyrene (PS), beryllium (Be), and Santowax OMP (SW).

$N(E)$  = number of photons of energy,  $E$ , emitted on fission and by fission product decay per fission.

$N_i$  = mole fraction of component  $i$ .

$Nu$  = Nusselt number =  $\frac{hD}{k}$ .

$N_{59}, N_{60}$  = atoms of  $Co^{59}$  and  $Co^{60}$  in flux detectors.

$n, n_{i,k}$  = number of photons emitted in  $i^{th}$  gamma energy interval per thermal neutron capture in the element,  $k$ .

$n, n_g$  = gm-moles of material or gas.

$P$  = constant.

$P$  = fraction of beta energy produced in the capsule wall (from  $D_i$  to  $D_i + R$ ) which escapes.

$P$  = pressure, psig or psia.

$P$  = probability of gamma radiation produced in calorimeter sample by thermal neutron activation escaping.

$P$  = power in the central fuel element of the MITR at 1000 kw.

$P$  = reactor power as function of time, MW.

$P_{avg}$  = time-averaged reactor power for one day, MW.

$P_i, P_f$  = initial and final pressures, psia.

$Pr$  = Prandtl number,  $\frac{C_p \mu}{k}$ .

$P_{sj}$  = pressure in  $j^{\text{th}}$  gas sample removed from loop, psia.

$p$  = total pressure, psia.

$p_a$  = partial pressure of acetone, psia.

$p_g$  = partial pressure of gas, psia.

$Q$  = energy released in a nuclear reaction, Mev.

$Q, Q_{0.90}$  = ratio for rejection of extraneous values and 90% confidence rejection quotient, respectively.

$Q$  = volumetric thermal energy generation rate, watts/cm<sup>3</sup>.

$q$  = heat transfer rate, Btu/hr.

$q$  = slowing down density for neutrons entering the thermal group, n/cm<sup>3</sup>-sec.

$q_i, q(\rho, u)$  = slowing down density as a function of  $\rho$  and  $u$ , neutrons/cm<sup>3</sup>-sec, where  $i$  refers to ring of six fuel elements (6) or central fuel element (c).

$q_{el}, q'_{el}$  = electrical input into test heater section  $i$ , watts.

$q_0$  = neutron source strength of line source at  $\rho = 0, \tau = 0$ , neutrons/cm of length-sec.

$q_0^1$  = neutron source strength, neutrons/cm<sup>3</sup>-sec.

$(q_{el}^T)_{in}$  = total heat transferred to organic coolant, watts.

$R, R_o, r, r_{25}$  = radius, cm or ft.

$R$  = ideal gas law constant.

$R$  = maximum range of beta particle in aluminum, cm.

$R_{Cd} = \frac{A_B}{A_{Cd}}$  = cadmium ratio.

$R_T, R(T)$  = electrical resistance of test heater section as function of temperature, ohms.

$Re$  = Reynolds number,  $\frac{DV\rho}{\mu}$ .

$R_f = \frac{1}{h}$  = coolant boundary layer resistance to heat flow.

$R_s$  = fouling or scale resistance to heat flow.

$R_i^n$  = fast neutron dose rate in material,  $i$ , watts/gm, where  $i$  refers to aluminum (Al), polyethylene (PE), polystyrene (PS), Santowax OMP (SW), and beryllium (Be).

$R_2^n, R_3^n$  = fast neutron dose rate measured in calorimeter series III-2 and III-3, respectively.

$R_i^T, R_i^T$  = total dose rate in material  $i$ , watts/gm, where  $i$  refers to aluminum (Al), polyethylene (PE), and polystyrene (PS).

$R/P_o$  = dose rate as function of position,  $l$ , watt/gm-MW.

$R_{SW}^T/P_o$  = total dose rate in organic material as a function of position in the core normalized to a reactor power of 1.0 MW, watts/gm-MW.

$R_i^{th}$  = dose rate due to thermal neutron activation in material  $i$ , watts/gm, where  $i$  refers to aluminum (Al).

$\left(R_{SW}^{TI}\right)_{avg}, \left(R_{SW}^{nI}\right)_{avg}, \left(R_{SW}^{\gamma I}\right)_{avg}$  = average (over one day) total, fast neutron, and gamma energy absorption rates in the organic coolant, watt-hr/MWHR.

$R_i^\gamma, R_i^\gamma$  = gamma dose rate in material  $i$ , watts/gram where  $i$  refers to aluminum (Al), polyethylene (PE), and polystyrene (PS).

$r$  = proportionality constant relating the fission rate in the central fuel element to the fast neutron dose rate in the in-pile section.

$S$  = standard deviation.

$S, S_i$  = source strength, photons/cm-sec, where  $i$  refers to the  $i^{th}$  energy interval.

$S_i$  = gas solubility,  $\text{cm}^3$  (STP)/gm, of component i.

$S_j$  = grams of organic coolant removed from the loop in the  $j^{\text{th}}$  sample  
or by any other means.

$S_{\bar{x}}$  = standard error of average.

$S_v$  = volumetric source strength, photons/ $\text{cm}^3$ -sec.

T = time.

T = total exposure time or time of reactor operation, hours.

T = time of irradiation, sec.

T = absolute temperature, °R, or temperature, °F.

$T_g$  = gas temperature, °F or °R.

$T^*$  = initial temperature of calorimeter samples, °F.

$T_{\text{OR}}$  = bulk organic temperature along the test heater, °F.

$(T_{\text{OR}})_o$ ,  $T_o$  = outlet organic temperature from test heater, °F.

$(T_{\text{OR}})_i$ ,  $T_i$  = inlet organic temperature to test heater, °F.

$T_{s_j}$  = temperature of  $j^{\text{th}}$  gas sample removed from loop, °R.

$T_s$  = gas sample capsule temperature, °F.

$T_s$  = steady state temperature, °F.

$T_t$  = unsteady state temperature, °F.

T(t) = temperature, °C, as a function of time, t.

$T_{\text{TC}}$  = thermocouple junction temperature, °F.

$T_w$  = wall temperature, °F.

$T_{wi}$ ,  $T_{wo}$  = inside wall temperature of test heater, °F, and outside wall  
temperature of test heater, °F, respectively.

t = student's t.

$t$  = thickness, cm.

$t$  = time.

$t_{1/2}$  = half life of radioactive decay.

$U$  = heat transfer coefficient, Btu/hr-ft<sup>2</sup>-°F, from inside of test heater to flowing organic.

$u$  = neutron lethargy.

$V$  = velocity, ft/sec.

$V$  = undissolved and dissolved gas in loop plus cumulative removal by liquid and gas sampling, cm<sup>3</sup> (STP).

$V_1$  = value of  $V$ , cm<sup>3</sup> (STP), at  $Z = 0$  MWHR's.

$V$  = efflux volume, cm<sup>3</sup>.

$V_A$  = volume of acetone added in loop volume measurements.

$V_S$  = actual volume of loop section for which volume is being measured.

$V_T$  = total volume filled with acetone vapor plus gas after filling the loop section with acetone during volume measurement.

$V_{25}$  = volume at 25°C for a specific level in the pycnometer legs, cm<sup>3</sup>, relative to the reference line.

$V_{b, 25}$  = total volume below reference mark at 25°C, cm<sup>3</sup>.

$V_m/V_F$  = ratio of volume of moderator to volume of fuel.

$V_{sj}$  = volume of  $j^{\text{th}}$  gas sample removed, cm<sup>3</sup>.

$V_{STP}$  = volume of gas at standard temperature and pressure, cm<sup>3</sup> (STP).

$V_{ST}$  = volume of organic in surge tank, cm<sup>3</sup>.

$V_T$  = total volume of the pycnometer at a level,  $l$ , above the reference line.

$v$  = specific volume, cm<sup>3</sup>/gm.

$v$  = velocity, cm/sec.



A 9. 12

$W_i$  = internal heat generation, Btu/hr-ft<sup>3</sup>.

$w'$  = organic flow rate, gpm.

$w$  = flow rate, lb/hr.

$w_k$  = weight fraction of element  $k$  in stainless steel.

$w$  = weight for each data point for least squares calculation.

$X$  = independent variable in least squares calculations.

$X$  = fraction of the fission neutron energy absorbed in the coolant.

$x$  = fraction of total dose due to fast neutron interactions.

$x, x_1, x_2$  = organic volume per unit length of the capsule or tubing above the capsule, cm<sup>3</sup>/in, where subscript 1 refers to the capsule and 2 refers to the tubing above the capsule.

$x$  = absorbed dose, watt hr/gram.

$x$  = surge tank liquid level, inches.

$x$  = proportionality constant relating the fission rate in the outer fuel elements to the gamma dose rate in the in-pile section.

$\bar{x}$  = arithmetical average.

$x_i, x_{st}$  = wt fraction of component  $i$  and standard, respectively, for gas chromatography measurements.

$Y$  = fraction of the fission gamma energy absorbed in the coolant.

$Y$  = dependent variable in least squares calculations.

$Y(u)$  = neutrons escaping from fuel element per unit lethargy per unit length of source, neutrons/cm.

$y$  = distance, cm.

$y$  = proportionality constant relating the fission rate in the central fuel element to the gamma dose rate in the in-pile section.

$y$  = surge tank gage glass level, inches.

$Z$  = MWHR's of reactor operation.

$Z, Z_i$  = average atomic number of material  $i$  where  $i$  refers to aluminum (Al), polyethylene (PE), and polystyrene (PS).

$Z_{\text{avg}}$  = average atomic number of a molecule, electrons per molecule.

$z$  = self attenuation distance for shielding calculations, cm.

$\alpha$  = angle.

$$\alpha = \frac{\int_{0.5}^{\infty} \sigma_{\text{res}} \frac{dE}{E}}{\int_{0.5}^{\infty} \sigma_{1/v} \frac{dE}{E}}$$

$\alpha_1, \alpha_2$  = constants.

$\alpha_n$  = constant for Eigenfunctions in transient heat transfer calculations.

$\beta^-, \beta^+$  = beta ray (negatron or positron).

$\beta$  = constant,  $^{\circ}\text{R}^{-1}$ .

$\gamma$  = gamma radiation.

$\delta(i)$  = average error or uncertainty in  $i$ .

$$\bar{\kappa}^2 = \frac{\Sigma}{D} + B_H^2$$

$\theta$  = angle.

$\kappa_a(E)$  = pair production energy absorption coefficient,  $\text{cm}^{-1}$ .

$\lambda$  = decay constant,  $\text{sec}^{-1}$ .

$\mu$  = total linear attenuation absorption coefficient,  $\text{cm}^{-1}$ .

$\mu_a, \mu_i, \mu_a(E)$  = total linear energy absorption coefficient for gamma radiation,  $\text{cm}^{-1}$ .

$\mu_s$  = linear attenuation coefficient in source,  $\text{cm}^{-1}$ .

$\mu$  = viscosity, cp.

$\mu_o$  = constant, cp.

$\nu, \nu'$  = kinematic viscosity, cp-cm<sup>3</sup>/gm.

$\lambda$  = absorption coefficient for attenuation of beta radiation.

$\xi$  = average increase in neutron lethargy per collision.

$\pi$  = total pressure, psia.

$\rho$  = organic density in in-pile section as function of time, gms/cm<sup>3</sup>.

$\rho$  = density, gms/cm<sup>3</sup>.

$\rho$  = radial distance, cm.

$\rho_{avg}$  = time averaged density of the organic in the radiation field, gms/cm<sup>3</sup>, for a period of one day.

$\Sigma$  = summation sign.

$\Sigma$  = macroscopic absorption coefficient for thermal neutrons, cm<sup>-1</sup>.

$\Sigma_f$  = average macroscopic fission cross section for thermal neutrons in the homogenized core, cm<sup>-1</sup>.

$\Sigma_s$  = macroscopic scattering cross section, cm<sup>-1</sup>.

$\sigma$  = surface tension of liquid, gm/sec<sup>2</sup>.

$\sigma$  = thermal neutron cross section, barns.

$\sigma(E)$  = neutron absorption cross section above thermal energies, cm<sup>2</sup>.

$\sigma^2(y)$  = variance of y.

$\sigma_a(E)$  = Compton linear absorption coefficient, cm<sup>-1</sup>.

$e \sigma_a(E)$  = Compton average absorption cross section per electron, cm<sup>2</sup>/electron.

$\left( \frac{\sigma_a(E)}{\rho} \right)_{Eff}$  = effective value of  $\frac{\sigma_a(E)}{\rho}$  for a mixture of elements, cm<sup>2</sup>/gm.

$\bar{\sigma}_{eff}$  = effective cross section for threshold reactions, barns.

$\sigma_{2200}$  = 2200 meter/sec neutron absorption cross section,  $\text{cm}^2$ .

$\sigma_S^j(E)$ ,  $\sigma_S^j(E)$  = scattering cross section of element j,  $\text{cm}^2$ , where j refers to hydrogen (H), carbon (C), and aluminum (Al).

$\sigma_T(E)$  = total neutron cross section,  $\text{cm}^2$ .

$\sigma_{1/v}$  =  $1/v$  component of absorption cross section,  $\text{cm}^2$ .

$\sigma_{\text{res}}$  = resonance component of absorption cross section,  $\text{cm}^2$ .

$\tau$  = shear stress, psi.

$\tau$  = time.

$\tau_a(E)$  = photoelectric energy absorption coefficient,  $\text{cm}^{-1}$ .

$\tau_m$  = specific absorbed dose, watt-hr of radiation energy absorbed per gram of total coolant.

$\tau(u)$  = Fermi age as function of lethargy,  $\text{cm}^2$ .

$\phi$  = angle.

$\phi(E)$  = neutron flux per unit energy,  $\text{n/cm}^2\text{-sec-ev}$ .

$\bar{\phi}$  = average homogenized core thermal flux in any fuel element,  $\text{n/cm}^2\text{-sec}$ .

$\phi_0$  = maximum homogenized core thermal flux,  $\text{n/cm}^2\text{-sec}$ .

$\phi_0$  = epithermal flux constant  $\text{n/cm}^2\text{-sec} = \phi(E) E$ .

$\phi_i$  = thermal neutron flux in region i,  $\text{n/cm}^2\text{-sec}$ .

$\phi_c$ ,  $\phi_6$ , and  $\phi_{12}$  = thermal neutron fluxes in central fuel element, ring of six, and ring of twelve, respectively.

$\frac{\bar{\phi}_m}{\bar{\phi}_F}$  = disadvantage factor = ratio of average flux in moderator to average flux in fuel.

$\phi(u)$  =  $E\phi(E)$  = neutron flux per unit lethargy,  $\text{n/cm}^2\text{-sec}$ .

$\phi_{2200}$  = 2200 meter/sec neutron flux,  $\text{n/cm}^2\text{-sec}$ .

% DP = per cent of degradation products in the coolant.

$\infty$  = infinity.